AD_____

Award Number: W81XWH-07-1-0247

TITLE: Transrectal Near-Infrared Optical Tomography for Prostate Imaging

PRINCIPAL INVESTIGATOR: Daqing Piao, Ph.D.

CONTRACTING ORGANIZATION: Oklahoma State University
Stillwater, OK 74078

REPORT DATE: March 2011

TYPE OF REPORT: Final

PREPARED FOR: U.S. Army Medical Research and Materiel Command
Fort Detrick, Maryland 21702-5012

REPORT DOCUMENTATION PAGE

Form Approved
OMB No. 0704-0188

1. REPORT DATE *(DD-MM-YYYY)*	**2. REPORT TYPE**	**3. DATES COVERED** *(From - To)*
01-03-2011	Final	1 MAR 2007 - 28 FEB 2011

4. TITLE AND SUBTITLE

Transrectal Near-Infrared Optical Tomography for Prostate Imaging

5a. CONTRACT NUMBER

5b. GRANT NUMBER

W81XWH-07-1-0247

5c. PROGRAM ELEMENT NUMBER

6. AUTHOR(S)

Daqing Piao, Ph.D.

E-Mail: daqing.piao@okstate.edu

5d. PROJECT NUMBER

5e. TASK NUMBER

5f. WORK UNIT NUMBER

7. PERFORMING ORGANIZATION NAME(S) AND ADDRESS(ES)

Oklahoma State University
Stillwater, OK 74078

8. PERFORMING ORGANIZATION REPORT NUMBER

9. SPONSORING / MONITORING AGENCY NAME(S) AND ADDRESS(ES)

U.S. Army Medical Research and Materiel Command
Fort Detrick, Maryland 21702-5012

10. SPONSOR/MONITOR'S ACRONYM(S)

11. SPONSOR/MONITOR'S REPORT NUMBER(S)

12. DISTRIBUTION / AVAILABILITY STATEMENT

Approved for Public Release; Distribution Unlimited

13. SUPPLEMENTARY NOTES

14. ABSTRACT

Purpose: to explore the technology of trans-rectal near-infrared (NIR) optical tomography that may benefit accurate, selective prostate biopsy. Updated scope: to develop a TRUS-coupled optical tomography technology for imaging prostate cancer in canine model.
Major findings: (1) the onset of a prostate tumor was detected earlier by the researched technique than by using TRUS alone; (2) the changes of blood concentration of a rapidly growing prostate tumor were quantified; (3) the regression of a TVT mass in a canine prostate was detected as having a gradually decreasing oxygen level and a gradually increasing region of reduced oxygenation in the inner area of the tumor foci, coupled with intermittently increased total hemoglobin in the periphery of the mass; (4) a cystic lesion also presented with slightly increased total hemoglobin with oxygen-reduction in the periphery of the lesion, and the slightly increased total hemoglobin was found by histopathology to be related to intralesional hemorrhage.
Significance and impact: These discoveries are expected to have impact on more accurate imaging guidance for targeted prostate biopsy, and monitoring treatment of locally advanced disease.

15. SUBJECT TERMS

Prostate cancer, optical tomography, canine model, hemoglobin, oxygen saturation, ultrasound

16. SECURITY CLASSIFICATION OF:			**17. LIMITATION OF ABSTRACT**	**18. NUMBER OF PAGES**	**19a. NAME OF RESPONSIBLE PERSON**
a. REPORT	**b. ABSTRACT**	**c. THIS PAGE**			USAMRMC
U	U	U	UU	269	**19b. TELEPHONE NUMBER** *(include area code)*

Table of Contents

INTRODUCTION

The objective of this research is to develop the technology of trans-rectal near-infrared (NIR) optical tomography for prostate imaging that may be applicable to accurate, selective prostate biopsy. Prostate cancer is the most common non-dermatologic cancer in American men. Prostate cancer suspicion is typically based on an elevated serum prostate-specific antigen (PSA) level or a suspicious nodule found during a digital rectal exam (DRE). When the PSA level is elevated or the DRE is abnormal, there is a 25 % chance that cancer is present. The existence of prostate cancer can only be confirmed by a needle biopsy that is guided by trans-rectal ultrasound (TRUS). Since there are no pathognomonic findings for prostate cancer on ultrasound imaging, biopsies are taken following a systematic pattern throughout the prostate with preference given to the peripheral zone wherein most cancer are found. The accuracy of biopsy is questionable and many men undergo multiple biopsies due to the lack of a more specific/sensitive imaging modality. Pathologic studies have demonstrated positive correlation between increased micro-vessel density and the onset of the disease. Near-infrared (NIR) optical tomography is known of sensitive to blood-based contrast, therefore trans-rectally implemented NIR optical tomography may provide a new way of assessing the prostate cancer. *The objective of this research has been to demonstrate the technology of trans-rectally implemented NIR optical tomography, and to perform initial evaluation of the technology on imaging prostate cancer developed in canine model*. *One of the outcomes of trans-rectal NIR tomography of the prostate would be a more accurate imaging guidance for targeted prostate biopsy, and in this study it is also found that trans-rectal NIR tomography has the potential of monitoring treatment of locally advanced disease*.

BODY

Specific aims:

Aim 1: To demonstrate that endoscopic NIR tomography at a probe size of 25mm in diameter can be achieved by use of spread-spectral-encoding from a broad-band light source.

Aim 2: To demonstrate that trans-rectal NIR tomography can image the prostate at the proximity of the rectum with significant tumor-tissue contrast.

Aim 3: To demonstrate that multi-spectral trans-rectal NIR tomography can be implemented with the single trans-rectal imaging probe.

Aim 4: To demonstrate that trans-rectal multi-spectral NIR tomography can quantify the hemoglobin concentration and oxygenation saturation in phantom, and further in prostate tumor model developed in canine species.

Completed works specific to the proposed aims:

Studies specific to the aim 1----development of the trans-rectal applicator: At the beginning of this project, we investigated and developed an axial-imaging trans-rectal NIR tomography probe with a diameter of 20mm that is in size equivalent to a standard TRUS prostate probe. The diameter of the developed probe was 20mm, which was smaller than the originally proposed diameter of 25mm, therefore it was more challenging to fabricate for the same number of optical source and detector channels (8 source

channels and 8 detector channels), but it was more patient-friendly. The design of the probe and the fabricated probe are given in Fig. 1. Image reconstruction algorithm and the novel configuration of using spread-spectral-encoding from a broad-band light source to achieve optical tomography data acquisition were also developed. Using phantoms and animal tissues, axial-imaging trans-rectal optical tomography was successfully demonstrated with the contrast of a normal prostate agreeing with expectation. However, we found that it was challenging to image the optical contrast of a prostatic lesion using this stand-alone axial-imaging trans-rectal optical tomography probe, due to the lack of detailed anatomic information by optical tomography alone to localize the prostate and the lesion, as indicated in Fig. 2, as well as the limited imaging depth due to the axial configuration of the optical channels.

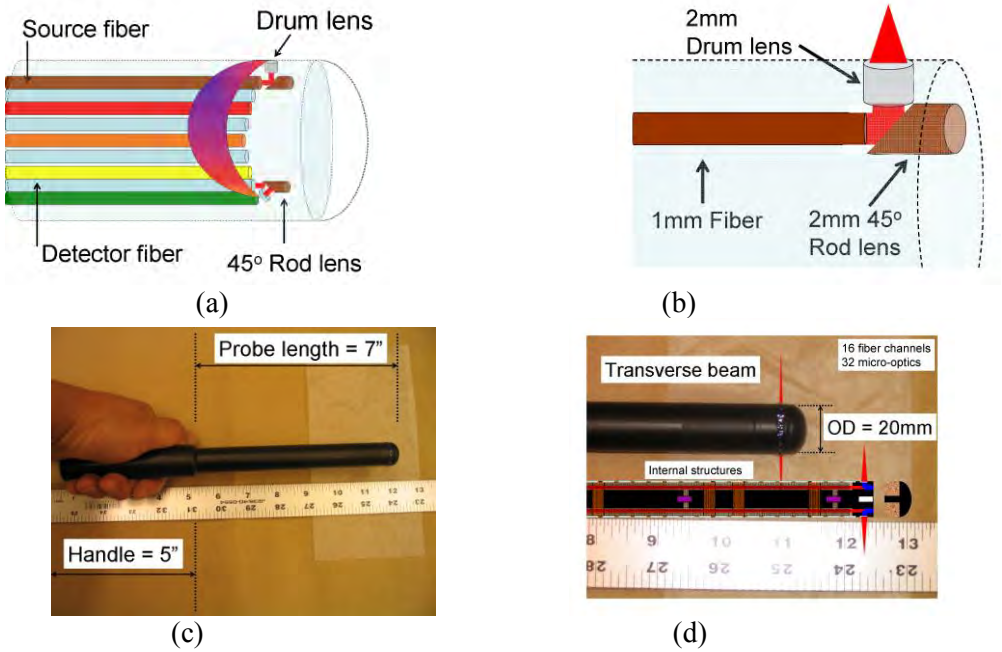

Figure 1. The 20mm axial-imaging applicator for trans-rectal NIR tomography. (a) Illustration of the fiber arrangement inside the applicator. (b) Each source/detector channel consists of a 1mm bare fiber, a 45° rod lens of 2mm in diameter, and a drum lens of 2mm in diameter. The configuration allows side-firing for axial-imaging. (c) Photograph of the probe, where the length of the probe is given. (d) Photograph of the distal part of the probe, where the micro-optics components (drum lenses) with anti-reflection coating are shown and the internal structure of the probe is also sketched.

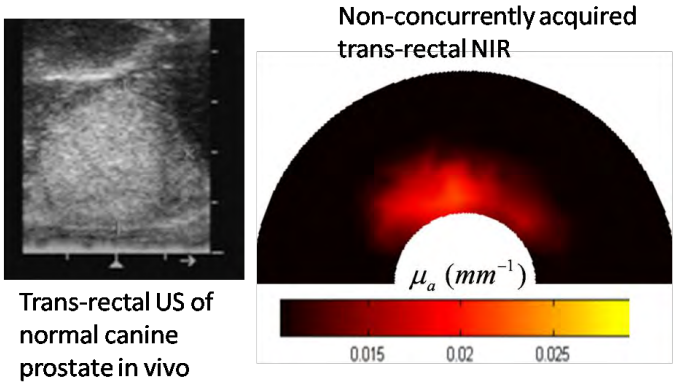

Figure 2. Axial trans-rectal NIR optical tomography of normal canine prostate *in vivo*. The dog prostate was visualized on TRUS first as shown in the left panel, then the TRUS probe was replaced with NIR probe to acquire the NIR tomography image as shown in the right panel. Lack of concurrent US imaging makes correlation of NIR imaging difficult.

We then proposed a novel applicator that acquired sagittal NIR tomography image concurrently with sagittal TRUS as illustrated in Fig. 3(a) [Xu et al, 2008]. The completed probe, as shown in Fig. 3(b), was developed based on an ALOKA bi-plane veterinary US transducer [Jiang et al, 2008]. This TRUS-guided NIR tomography probe allowed the following studies on several dogs for the feasibility of detecting prostate cancer using trans-rectal optical tomography.

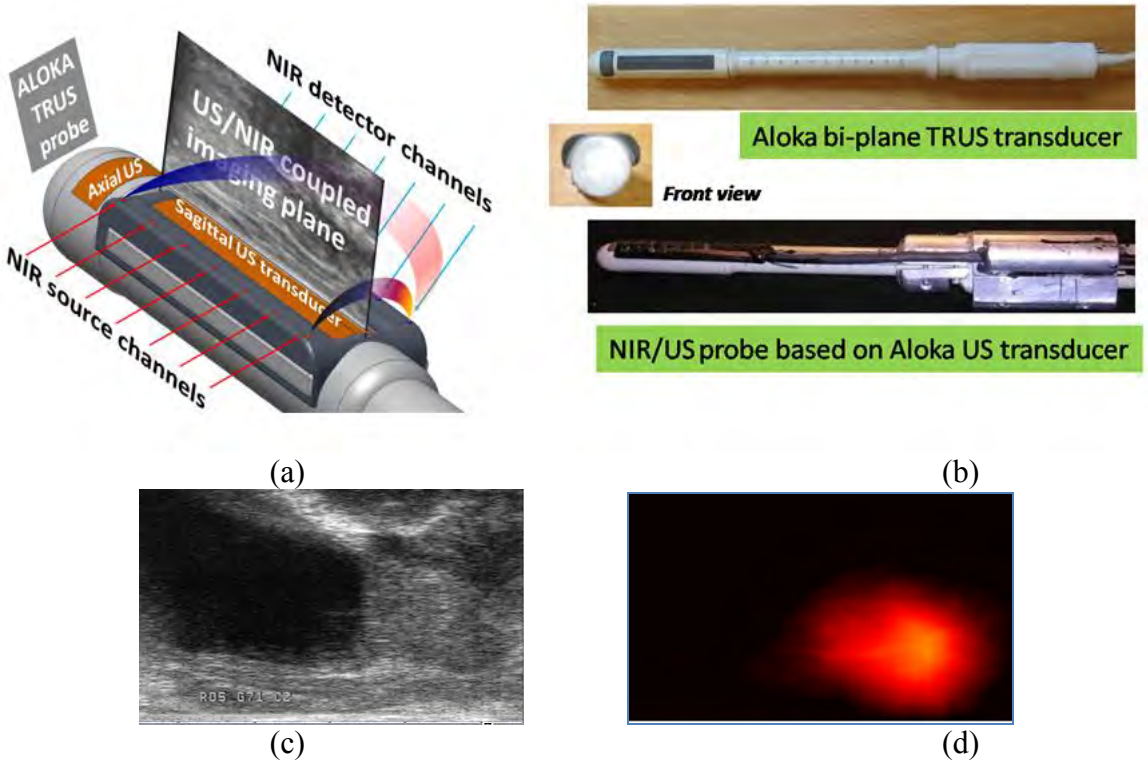

Figure 3. (a): illustration of trans-rectal NIR/US applicator. Trans-retal US is placed in the middle of the trans-rectal NIR applicator (optodes distributed longitudinally) to perform combined NIR/US imaging. (b): photograph of the Aloka trans-rectal US transducer and the completed NIR/US probe used for canine imaging. A sagittal US image (C) of a canine prostate and the concurrently acquired spatially-correlated NIR optical tomography image (D, NIR absorption image).

Studies specific to the aim 2—optical tomography of tumor-tissue contrast in canine prostate in vivo: We have developed a canine model of prostate cancer using canine transmissible venereal tumor (TVT). The TVT cells were propagated in immunocompromised (SCID) mice and transferred to prostate gland of the dog to result in a neoplastic mass effect useful for imaging studies. The study on the first dog that had TVT developed in its prostate demonstrated that optical absorption contrast provided earlier indication of the on-set of the tumor-development than did with grey-scale ultrasonography alone [Jiang et al, 2009; Piao et al, 2010]. For this subject, the TVT cells were seeded along the needle track during needle retraction. The gross and histological findings (8-week post-injection) confirmed intra- and peri-prostatic neoplastic infiltrates with masses also located along the urethra and peri-rectal tissue; the latter related to dissemination along the needle track during TVT inoculation. The necropsy results as shown in the top-panel of Fig. 4 confirmed the retrospective observations by NIR tomography as shown in the bottom-panel of Fig. 4. The trans-rectal US and the NIR images shown in the bottom panel of Fig. 4 were obtained at the middle of the right lobe, the middle-line of the prostate, and the middle of the left lobe, before the TVT injection, 2 weeks after the TVT injection when the US and rectal examination showed no evidence of

tumor growth, and 5 weeks after the TVT injection when the tumor growth was evident on both US and rectal examination. At the 2-week NIR absorption images, hyper-absorptive regions were found dorsal to the prostate in the right lobe, and dorsal to the pelvic bone in the right lobe with potential extension to the middle line. The locations of these hyper-absorptive regions correlated very well with those of the hypo-echoic and hyper-absorptive regions found in week-5. *The growth of the tumor was indicated earlier by the absorption images of trans-rectal NIR than by the trans-rectal US*. *It was also found that the growth of the tumor was shown not as evident on reduced scattering images as in the absorption images*. It is evident that combining the information of trans-rectal US and trans-rectal NIR renders earlier and much more accurate findings of the tumor growth.

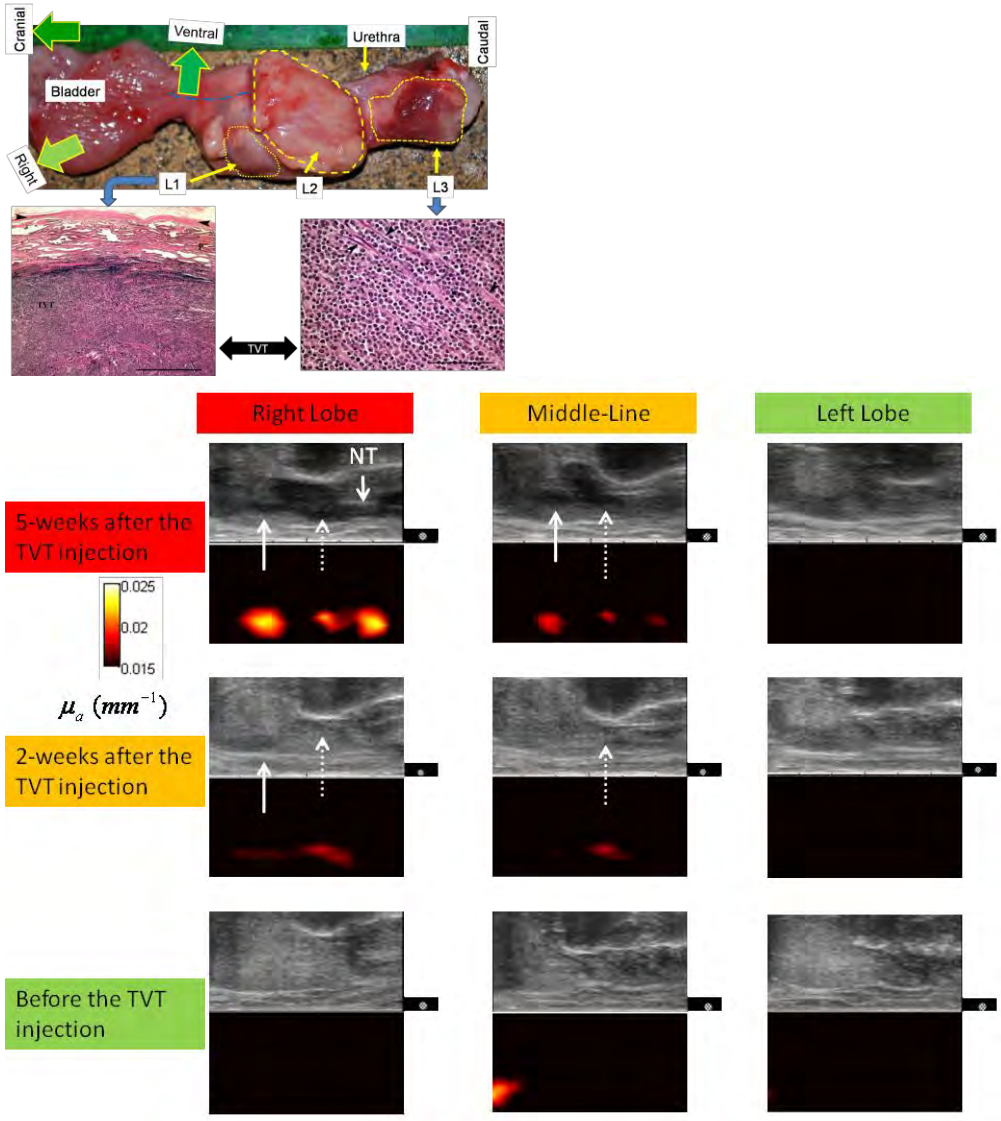

Figure 4 Top panel: necropsy and histology of the pelvic canal with TVT. Bottom panel: comparison between the image-monitoring of TVT development in canine pelvic canal by trans-rectal NIR and US, over a period of 5 weeks. The images were taken at the middle of the right lobe, the middle-line of the prostate, and the middle of the left lobe, before the TVT injection, 2 weeks after the TVT injection when the US and rectal examination showed no evidence of tumor growth ***but the NIR indicated the tumor growth***, and 5 weeks after the TVT injection when the tumor growth was evident on both US and rectal examination.

Studies specific to the aim 3---multi-spectral trans-rectal optical tomography: By coupling light of multiple wavelengths to the source-channels of the trans-rectal probe, multi-spectral trans-rectal optical tomography was achieved. We first integrated the outputs of a 785nm laser diode (LD) and a 830nm LD, by combining them using a bifurcated fiber and sequentially delivering the light to the NIR source channels via a linear-translational fiber switch. The NIR detector channels were coupled to a spectrograph for CCD acquisition of the dual-band imaging data. The use of dual-band data allowed reliable recovering of total hemoglobin information [Jiang et al, 2011a], but the recovery of oxygen saturation information was noisy. We then integrated the outputs of a 705nm LD, a 785nm LD and a 808nm LD, by combining them using a trifurcated fiber and sequentially delivering the light to the NIR source channels via a linear-translational fiber switch. The NIR detector channels were coupled to a spectrograph for CCD acquisition of the triple-band imaging data. The use of triple-band data allowed reliable recovering of total hemoglobin information and oxygen saturation [Jiang et al, 2011b].

Studies specific to the aim 4---trans-rectal optical tomography of tumor-associated hemoglobin concentration and hemoglobin oxygen saturation. Two dogs were used for demonstrating this aim. For the first one, the TVT was injected at two locations in the right aspect of the prostate, one in the cranial aspect, one close to the middle aspect. The base-line US indicated that the prostate measured 6cm from cranial to caudal. The base-line US also revealed a cluster of prostatic cysts resembling a ―face" in the right aspect of the gland. This ―face" landmark, the location of which on US image is arrowed in Fig. 5(a),

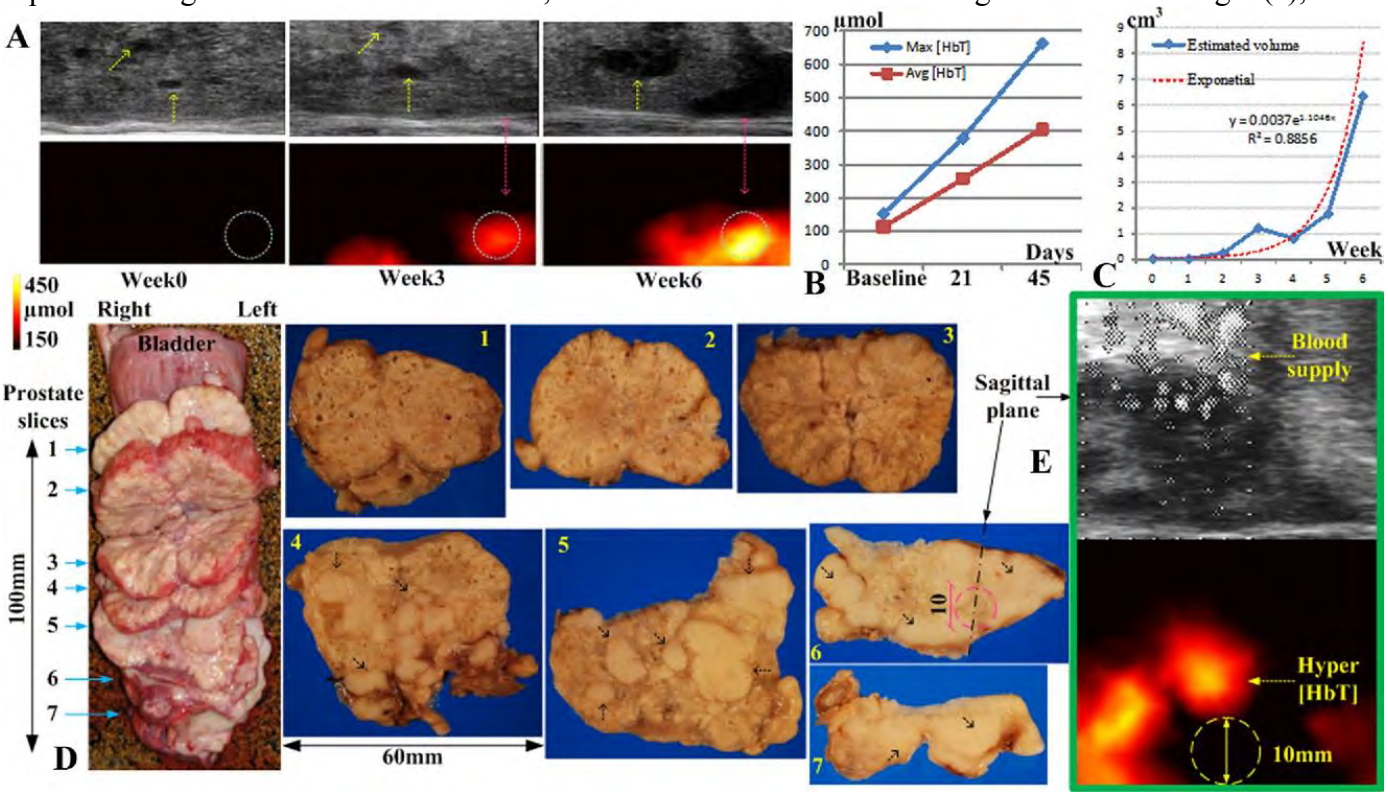

Figure 5. (A) Sagittal images of the right lobe in the middle-caudal aspect at baseline, day 21 (week 3), and day 45 (week 6). (B) Changes in HbT in the 10-mm-diameter region of interest over the 6-week duration. (C) Estimated tumor volume changes from week 1 to week 6. (D) Gross examination of the canine prostate on necropsy. After fixation in 10% buffered formalin, 7 slices of the prostate gland were sectioned from cranial to caudal, at an interval of approximately 15 mm. (E) Doppler US and optical images of the sagittal plane were taken approximately across the line marked on slice 6.

facilitated multiple images taken in the same relative areas in that location over time throughout the course of the imaging study. Figure 5(B) illustrates the changes of [HbT] from baseline to 45-days post-injection in a marked 10mm-diameter region located in the right lobe that correlated to the US hypo-echoic mass observed caudal to the prostate. The average [HbT] in this region changed from 120 μM to 375 μM, a nearly 300% change over the 45-days of development. The volume of [HbT]≥ 150μM within the caudal-aspect of the right lobe corresponding to the week 6 hypoechoic mass was estimated from volumetric NIR reconstruction. The post-injection volumetric change followed an exponential growth pattern as shown in Fig. 5c. The excised prostate (Fig 5(d)) was approximately 10×5×5cm3 in size. The prostate was serially sectioned in the conventional transverse orientation in ~1.5cm slices. The gross examination confirmed multiple coalescing foci of TVT in the caudal-aspect of the gland, and significant infiltration of the tumor from right to the left lobes. After fixation in 10% buffered formalin, the prostatic sections were again closely examined. On slice 6 corresponding to the left-caudal-aspect of the gland, a small pocket (indicated by a 10mm circle) of normal prostatic tissue surrounded by multi-foci TVT was noted. Indication of similar morphology can also be seen as demarcated by the line in the figure (e) on the sagittal NIR image of day-38 as a region of base-line [HbT] enclosed by heterogeneous hyper-[HbT] masses. The simultaneous sagittal Doppler US of day-38 revealed substantially enhanced blood supply ventral to the heterogeneously hypo-echoic mass. This complete study demonstrated that TRUS-coupled spectral optical tomography enhanced the detection of the progression and lateral involvement of the prostatic tumor compared to using TRUS alone [Jiang et al, 2011a].

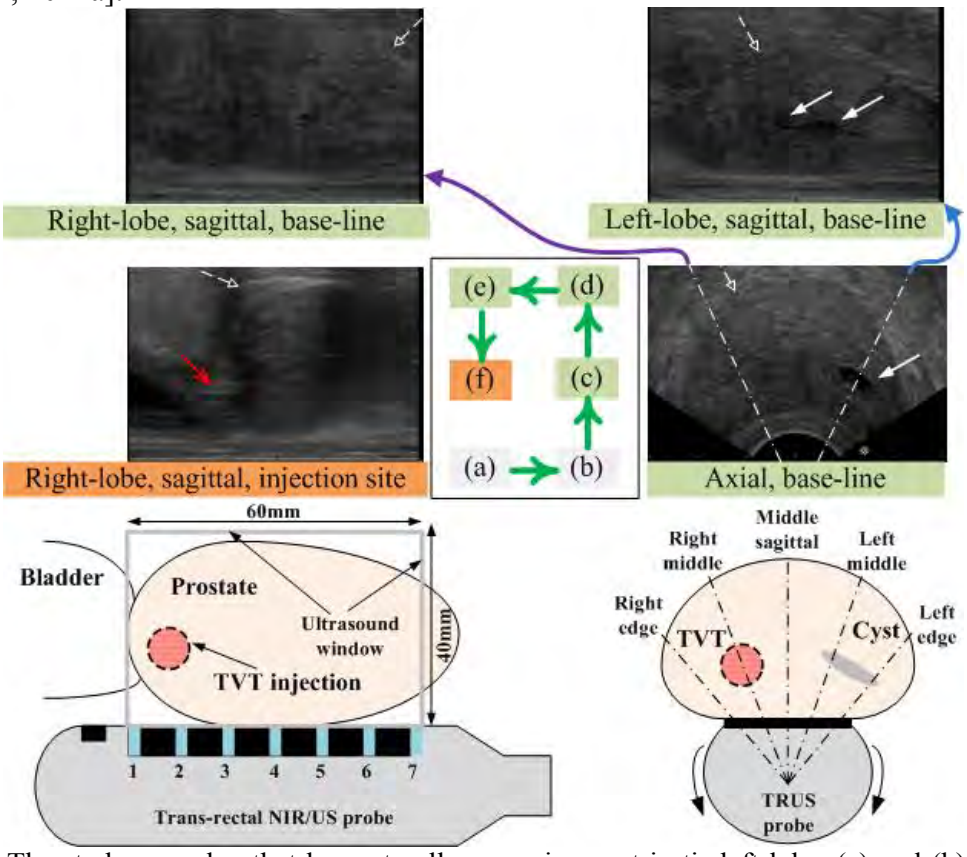

Figure 6. The study on a dog that has naturally occurring cyst in tis left lobe. (a) and (b), imaging geometry; (c) and (d), a large ―scorpion-like" cystic lesion extending irregularly within the left lobe; (e), right lobe was unremarkable on the base-line US; (f), the TVT injection site was noticeable on US as indicated by the red arrow.

The second dog involved in this aim provided an unusual opportunity for comparing the difference between the oxygen-reduction in a necrotic neoplastic lesion and the oxygen-deprivation in a cystic lesion in the same prostate. The TVT in this dog prostate underwent spontaneous regression, which rendered to the best of our knowledge the first trans-rectal optical imaging of tumor hypoxia in canine prostate. Interestingly this dog prostate was found, at base-line, to have a large cystic lesion in a site contra-lateral to the planned TVT implantation. This study, therefore demonstrated the potential of differentiating the malignancy of a localized lesion, and monitoring of its response to treatment over time [Jiang et al, 2011b].

The base-line examination including US indicated a prostate that was presumably benign prostatic hypertrophy and measured 7.0 cm cranial-to-caudal. The base-line US also found a large cystic lesion in the left lobe (see Fig. 6(b) and (c)). The cyst extended irregularly within the left mid-lateral aspect of the prostate, and appeared like a ―scorpion" on some sagittally acquired US images (see Fig. 6(d)). The right mid-lateral aspect of the prostate, though, was unremarkable on the base-line US (see Fig. 6(e)), and after the TVT inoculation, the injection site was noticeable on US as indicated by the red arrow in Fig. 6(f). For all baseline and post-injection examinations, trans-rectal US-integrated optical tomography was performed on five quasi-sagittal planes (Fig. 6(b)), including the middle-sagittal, half-way to the right lateral edge, the right lateral edge, half-way to the left lateral edge, and the left lateral edge of the prostate gland. On each of the five quasi-sagittal planes the imaging was performed at three longitudinal positions for cross-validation.

Shown in Fig. 7 are the images acquired at base-line, day-49, day-56 and day-63 after the injection, of four characteristics, including Doppler US, grey-scale US, [HbT] and StO2, at left-mid-sagittal plane across the cyst (marked by the dashed line in the axial US image in the upper panel) and right-mid-sagittal plane across the planed TVT injection site as well as a later developed tumor mass (marked by the dashed line in the axial US image in the lower panel). The dimension of all images is 60mm (cranial—caudal) × 40mm (dorsal—ventral). As the Doppler-overlapped US images were recorded immediately after acquiring the grey-scale US images, slight differences may be seen between the anatomies shown on Doppler-US and grey-scale US images. The dashed line at the dorsal edge of the US images indicate the actual location of the NIR sensors, which were approximately 3mm ventral to the surface of the US transducer as an outcome of the fabrication. The NIR recovered images are color-scaled at [50 150]μM for [HbT] and [50 90]% for StO2, respectively.

At baseline, the right prostatic lobe had predominantly homogenous StO2 and [HbT]≤50μM. A hypoechoic region at the right-cranial edge of the prostate (marked by the down-pointing hollow arrow) was indicated in NIR images as having a ―bean-shape" of 10-20mm in axes, with clear contrasts of hyper-[HbT] and lower StO2 in the central region of it. Comparatively, the left prostatic lobe had a large anoxic-like region extending longitudinally and corresponding to the anatomy of the extended cystic lesion (marked by the oblique arrow). The large anoxic-like region was shown in NIR images with slightly elevated but relatively homogenous [HbT]. A hypoechoic region at the left-cranial edge of the prostate was visualized in NIR images as having increased [HbT] and somewhat lower StO2 with respect to the indicted prostatic background, but the NIR imaging features of that region were not evident for a ―bean-shape" structure. By day-49, the TVT developed hypoxic core, which became stronger and larger during the next 2 weeks that was consistent with US observation of TVT regression in that period. Strong but intermittent elevation of HbT in the periphery of the TVT correlated inconsistently with visualized blood flow. Over the entire course of monitoring, the cystic lesion consistently had a strong hypoxic interior that was greater in size than the sonographically visualized lesion, and mild heterogeneous elevation of HbT in the periphery of the lesion that did not correlate with visualized blood flow. Histological examinations confirmed necrotic cores within the TVT and found chronic & acute hemorrhages associated with the cystic lesion.

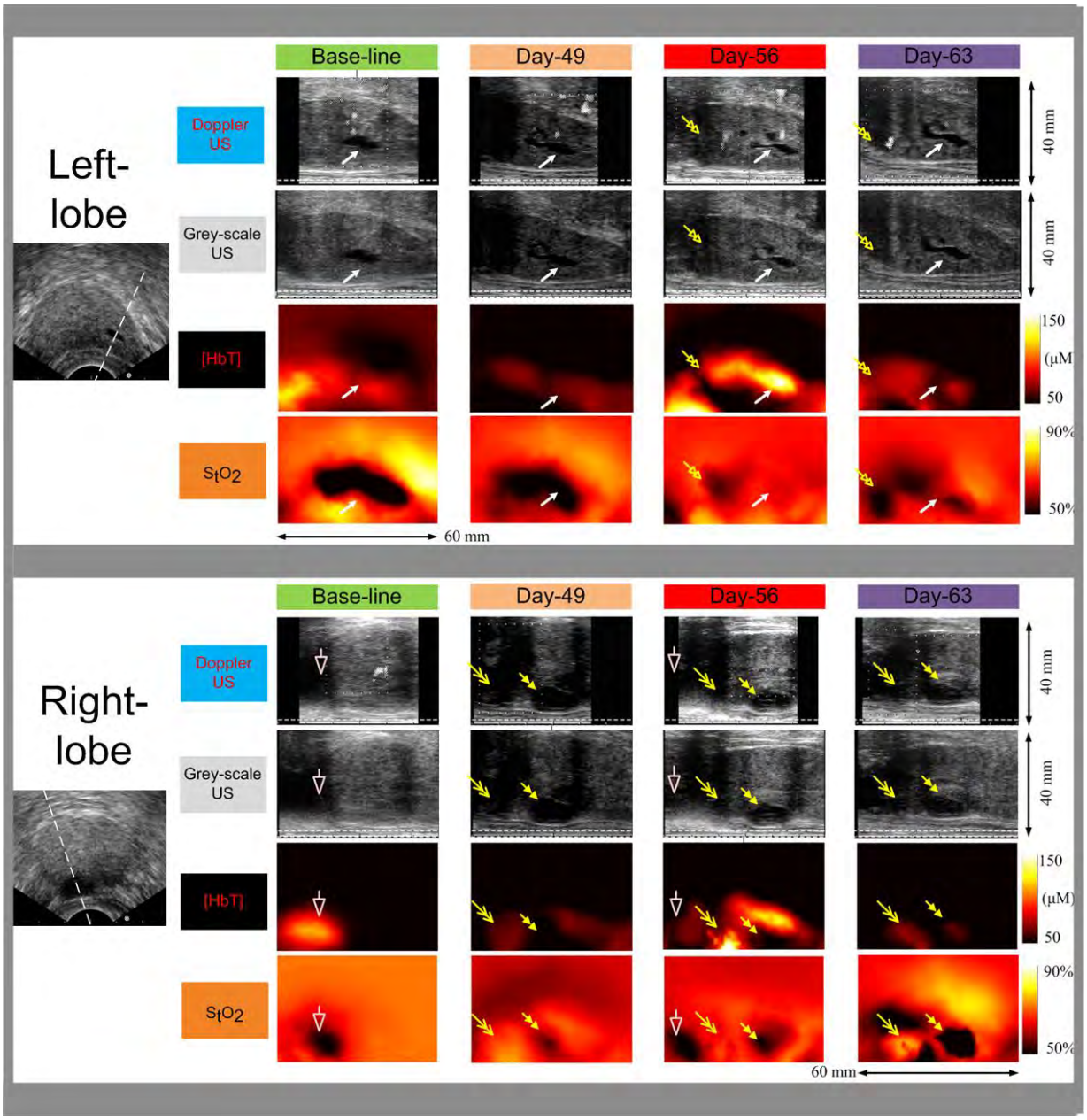

Figure 7. Image dimension----60×40mm2 (cranial-caudal×dorsal-ventral). Images were acquired at base-line, day-49, day-56 and day-63 after the injection, of four characteristics, including Doppler US, grey-scale US, [HbT] and StO2, at left-mid-sagittal plane across the cyst (marked by the dashed line in the axial US image in the upper panel) and right-mid-sagittal plane across the planed TVT injection site as well as a later developed tumor mass (marked by the dashed line in the axial US image in the lower panel). The dashed line at the dorsal edge of the US images indicate the actual location of the NIR sensors, which were approximately 3mm ventral to the surface of the US transducer as an outcome of the fabrication. The NIR recovered images are color-scaled at [50 150]μM for [HbT] and [50 90]% for StO2, respectively. Down-pointing hollow-arrow: pelvic lymph node; oblique double-arrow: a neoplastic nodule; oblique double-solid-arrow: necrotic TVT; oblique double-hollow-arrow: a TVT nodule; oblique arrow: cystic lesion. All lesions indicated by the arrows were confirmed by pathological examinations.

Other studies associated with this research---review of up-to-date optical properties of canine and human prostates: Using light to image prostate is underlined by that benign and cancerous prostate tissues present different optical properties which can be resolved by means of optical interrogation. Revealing the contrast of prostate cancer over normal tissue will be challenging if significant base-line heterogeneities exist in the optical properties of benign tissues. There have been a number of studies on prostate optical properties in which certain consensuses have been made. Although these studies are conducted at different wavelengths, different samples, and different methods, spectrally these studies shall offer information invaluable to understanding the potentials of detecting prostate cancer as well as difficulties facing the optical imaging of prostate. We conducted a review of the optical properties of canine and human prostates known to us up to the date of the submission of the manuscripts [Piao et al, 2009; Piao et al, 2010]. The implications of our review on optical interrogation of the prostate are:

(1). The reduced scattering coefficient of prostate is approximately an order higher than the absorption coefficient of prostate. As this has been confirmed by time-resolved measurements, the prostate can be treated as a scattering-dominant tissue, thereby diffuse optical methods can be applied to modeling the photon propagation as in PDT and image reconstruction in trans-rectal imaging of the prostate as demonstrated by our studies.

(2). There are noticeable inter-subject and intra-organ heterogeneities in optical properties of prostate. The intra-organ heterogeneity poses a substantial challenge to differentiating malignant tissue from normal tissue, since the optical contrast of the malignant tissue over the normal tissue must be greater than the background heterogeneity for the malignant lesion to be resolved. The intra-organ heterogeneity may also partially contribute to the previous finding that the effective attenuation coefficients of benign and malignant human prostate tissues were similar. It is noted that none of the previous measurements of prostate optical heterogeneities have been examined on intact prostate *in vivo*. Our approach of trans-rectal near-infrared diffuse optical tomography, which aims at imaging the intact prostate in its real-time *in vivo* condition, has indeed demonstrated intrinsic optical property contrasts are available for differentiating the malignant prostatic tissue from benign tissue.

Other studies associated with this research---unified theory of steady-state photon diffusion in a homogenous medium bounded externally or internally by an infinitely long circular cylindrical applicator. The solutions to the steady-state photon diffusion associated with concave and convex geometries were derived in a unified theoretical framework, for the first time to our knowledge.

The geometry of a diffusive medium bounded externally by a cylindrical applicator resembles that of imaging externally accessible biological tissue such as the breast using a ring-type array. The geometry of a diffusive medium bounded internally by a cylindrical applicator resembles that of imaging internally accessible biological tissue such as the prostate using a trans-rectal probe. Solutions to steady-state photon diffusion in these two geometries are derived in cylindrical coordinates by applying the extrapolated boundary condition and are expressed in modified Bessel functions of the first and second kinds.

In Part-I of this work [Zhang et al, 2010], approximate solutions for large cylinder radius are also derived in the format close to that for semi-infinite geometry by including a shape-radius-associated term. Numerical evaluations are provided for the cases of having the source and the detector positioned only along the azimuthal or longitudinal directions. The results demonstrate that compared with a semi-infinite boundary, the concave boundary has smaller photon fluence decay in the azimuth direction but greater

photon fluence decay along the longitudinal direction compared with a semi-infinite geometry having the same source–detector distance. On the other hand, the convex boundary has greater photon fluence decay in the azimuth direction but smaller photon fluence decay along the longitudinal direction. As the radius of the concave or convex circular applicator becomes infinitely large, the results for these specific geometries reach the well-known condition for a semi-infinite medium, as expected.

The second part of this work [Zhang et al, 2011] quantitatively examines these predictions from Part I through several approaches, including (a) the finite-element method, (b) the Monte Carlo simulation, and (c) experimental measurement. Despite that the quantitative examinations have to be conducted for finite cylinder applicators with large length-to-radius ratio to approximate the infinite-length condition modeled in Part I, the results obtained by these quantitative methods for two concave and three convex applicator dimensions validated the qualitative trend predicted by Part I and verified the quantitative accuracy of the analytic treatment of Part I in the diffusion regime of the measurement. We have also predicted the existence of a potentially spiral direction on the surface of both the concave cylindrical applicator and the convex cylindrical applicator, along which the decay rate of photon fluence could be equivalent to that in a planar surface or a semi-infinite geometry. The existence of such planar-equivalent spiral direction inside or outside a cylindrical applicator is both theoretically and practically important. If the existence of such a planar-equivalent spiral direction inside or outside a cylindrical applicator is verified, for certain translumenal sensing or imaging applications, the semi-infinite geometry may be implemented for greatly simplified modeling and rapid recovery of tissue optical properties.

Other studies associated with this research---comparing direct-current based image reconstruction versus direct-current included or excluded image reconstruction in optical tomography. We also studied the level of variations of recovered optical properties in optical tomography associated with the measurement uncertainty under three reconstruction configurations of direct-current (DC)-only, the DC-excluded frequency-domain (FD), and the DC-included FD, by analytic and synthetic means. It is demonstrated that, at the same level of measurement uncertainty typical to optical tomography and under pixelwise reconstruction without spatial a priori information, the standard deviations of absorption coefficient over absorption coefficient reconstructed by DC only are at least 1.4 times lower than those obtained by FD methods. The standard deviations of diffusion coefficient (or reduced scattering coefficient) over diffusion coefficient (or reduced scattering coefficient) reconstructed by DC only are slightly lower than those by FD methods. Frequency-domain reconstruction including DC generally outperforms reconstruction excluding DC, but the difference between the two becomes less significant when the total amount of measurements becomes larger. For FD reconstruction with no spatial a priori information and a smaller number of measurements, including DC is recommended. When a priori structural information is available, the three reconstruction configurations investigated in this study perform equally well [Xu et al, 2010].

KEY RESEARCH ACCOMPLISHMENTS

1. The technology of US-coupled trans-rectal NIR tomography at single or multi-spectral detection is demonstrated.

2. A repro reproducible dog model of prostate cancer is developed by using canine transmissible venereal tumor cells.

3. The initial *in vivo* work has demonstrated the following results: (1) The onset of a prostate tumor was detected earlier by the researched technique than by using TRUS alone. (2) The changes of blood concentration of a rapidly growing prostate tumor were quantified. (3) The regression of a TVT mass in a canine prostate was detected as having a gradually decreasing oxygen level and a gradually increasing region of reduced oxygenation in the inner area of the tumor foci, coupled with intermittently increased total hemoglobin in the periphery of the mass. (4) A cystic lesion also presented with slightly increased total hemoglobin with oxygen-reduction in the periphery of the lesion. The slightly increased total hemoglobin was found by histopathology to be related to intra-lesional hemorrhage.

4. The optical properties of canine and human prostates reported in literature, which were all acquired by invasive or in vitro measurements, are comprehensively reviewed. There are noticeable intra-organ optical heterogeneities, which poses a substantial challenge to differentiating malignant tissue from normal tissue in real-time imaging condition. Our approach of trans-rectal near-infrared diffuse optical tomography, however, demonstrated that the prostate cancer can be differentiated from benign prostatic tissue by the intrinsic optical property contrasts.

5. A novel analytic treatment for photon diffusion in a homogenous medium bounded externally or internally by an infinitely long circular cylindrical applicator is presented and experimentally validated. The geometry of a diffusive medium bounded externally by a cylindrical applicator resembles that of imaging externally-accessible biological tissue such as breast using a ring-type array. The geometry of a diffusive medium bounded internally by a cylindrical applicator resembles that of imaging internally-accessible biological tissue such as prostate using trans-rectal probe.

6. We studied the level of image artifacts in optical tomography associated with measurement uncertainty under three reconstruction configurations, namely, by using only direct-current (DC), DC-excluded frequency-domain, and DC-included frequency-domain data. Frequency-domain reconstruction including DC generally outperforms that excluding DC, but as the amount of measurements increases, the difference between the two diminishes. Under the condition of a priori structural information, the performances of three reconstruction configurations are seemingly equivalent.

REPORTABLE OUTCOMES

This award has resulted in following publications or manuscripts:

Journal Papers Published

[01] Xu G, Piao D, Musgrove CH, Bunting CF, Dehghani H, "Trans-rectal ultrasound-coupled near-infrared optical tomography of the prostate Part I: Simulation," ***Optics Express***, Vol. 16, Iss. 22, pp. 17484–17504 (2008).

[02] Jiang Z, Piao D,* Xu G, Ritchey JW, Holyoak GR, Bartels KE, Bunting CF, Slobodov G, Krasinski JS, "Trans-rectal ultrasound-coupled near-infrared optical tomography of the prostate Part II: Experimental demonstration," ***Optics Express***, Vol. 16, Iss. 22, pp. 17505–17520 (2008).

[03] Piao D,* Jiang Z, Bartels KE, Holyoak GR, Ritchey JW, Xu G, Bunting CF, Slobodov G, "*In vivo* trans-rectal ultrasound-coupled near-infrared optical tomography of intact normal canine prostate," ***Journal of Innovative Optical Health Sciences***, Vol. 2, No. 3, pp. 215-225 (2009).

[04] Jiang Z, Holyoak GR, Bartels KE, Ritchey JW, Xu G, Bunting CF, Slobodov G, Piao D*, "*In vivo* trans-rectal ultrasound coupled near-infrared optical tomography of a transmissible venereal tumor model in the canine pelvic canal," ***Journal of Biomedical Optics Letters***, Vol. 14, No. 3, pp. 030506 (2009).

[05] Zhang A, Piao D,* Bunting CF, Pogue BW, "Photon diffusion in a homogeneous medium bounded externally or internally by an infinitely long circular cylindrical applicator ---- Part I: steady-state theory," ***Journal of Optical Society of America, A***, Vol. 27, No. 3, pp. 648-662 (2010).

[06] Piao D,* Bartels KE, Jiang Z, Holyoak GR, Ritchey JW, Xu G, Bunting CF, Slobodov G, "Alternative trans-rectal prostate imaging: A diffuse optical tomography method," ***IEEE Journal of Selected Topics in Quantum Electronics***, Vol. 16, No. 4, pp. 715-729 (2010). "Biophotonics 2" Special Issue, invited paper.

[07] Xu G, Piao D,* Bunting CF, Dehghani H, "Direct-current based image reconstruction versus direct-current included or excluded frequency-domain reconstruction in diffuse optical tomography," ***Applied Optics***, Vol. 49, No. 16, pp. 3059-3070 (2010).

[08] Jiang Z, Piao D,* Holyoak GR, Ritchey JW, Bartels KE, Slobodov G, Bunting CF, Krasinski JS, "Trans-rectal ultrasound-coupled spectral optical tomography of total hemoglobin concentration enhances assessment of the laterality and progression of a transmissible venereal tumor in canine prostate," ***Urology,*** Vol. 77m No. 1, pp. 237-42 (2011).

[09] Zhang A, Xu G, Daluwatte C, Yao G, Bunting CF, Pogue BW, Piao D*, "Photon diffusion in a homogeneous medium bounded externally or internally by an infinitely long circular cylindrical applicator ---- Part II: Quantitative examinations of steady-state theory," ***Journal of Optical Society of America, A***, Vol. 28, No. 2, pp. 66-75 (2011).

Journal Paper Under Preparation

[10] Jiang Z, Piao D,* Bartels KE, Holyoak GR, Ritchey JW, Ownby CL, Rock K, Slobodov G, Culkin D, "Intra-lesional oxygen saturation and peri-lesional hemoglobin concentration differ between a regressing transmissible venereal tumor and a naturally occurring canine prostatic cyst as measured by TRUS integrated spectral optical tomography," under preparation for submission to ***Urology.***

Proceeding Papers---Full Length (up to 15 pages)

[01] Piao D, Jiang Z, Xu, G, Musgrove CH, Bunting CF, "Approach on trans-rectal optical tomography probing for the imaging of prostate with trans-rectal ultrasound correlation", ***Proceedings of SPIE***, Vol. 6850, Paper #68500E (2008) (invited paper).

[02] Jiang Z, Ritchey JW, Holyoak GR, Bartels KE, Xu G, Bunting CF, Slobodov G, Krasinski JS, Piao D, "In vivo trans-rectal ultrasound coupled trans-rectal near-infrared optical tomography of canine prostate bearing transmissible venereal tumor," ***Proceedings of SPIE***, Vol. 7174, Paper #71741U (2009).

[03] Zhang A, Piao D, Yao G, Bunting CF, Krasinski JS, Pogue BW, "Forward modeling of axial trans-lumenal diffuse optical imaging with a cylindrical applicator using continuous-wave photon-illumination," ***Proceedings of SPIE***, Vol. 7174, Paper #717404 (2009).

[04] Xu G, Bunting CF, Dehghani H, Piao D, "A hierarchical spatial prior approach for prostate image reconstruction in trans-rectal optical tomography," ***Proceedings of SPIE***, Vol. 7171, Paper #71710S (2009).

[05] Jiang Z, Piao D, Krasinski JS, "Development of a continuous-wave dual-band trans-rectal optical tomography system for concurrent sagittal imaging with trans-rectal ultrasound," ***Proceedings of SPIE***, Vol. 7171, Paper #71710G (2009).

[06] Piao D, Jiang Z, Bartels KE, Holyoak GR, Ritchey JW, Ownby CL, Rock K, Bunting CF, Slobodov G, *"Optical biopsy of the prostate: can we TRUST (trans-rectal ultrasound-coupled spectral tomography)?"* ***Proceedings of SPIE.*** Paper 7895-18 (2011) (invited paper).

[07] Xu G, Piao D, "Feasibility of rapid near-infrared diffuse optical tomography by swept-spectral-encoded sequential light delivery," ***Proceedings of SPIE.*** Paper 7896-31 (2011).

[08] Jiang Z, Holyoak GR, Ritchey JW, Bartels KE, Rock K, Ownby CL, Slobodov G, Bunting CF, Piao D, "Different optical spectral characteristics in a necrotic transmissible venereal tumor and a cystic lesion in the same canine prostate observed by triple-band transrectal optical tomography under transrectal ultrasound guidance," ***Proceedings of SPIE.*** Paper 7892-24 (2011).

[09] Xu G, Piao D, Dehghani H, "—"Spectral a priori" to "spatial a posteriori" in continuous-wave image reconstruction in near-infrared optical tomography, " ***Proceedings of SPIE.*** Paper 7892-12 (2011).

Proceeding Papers---Short (3-pages)

[01] Xu G, Musgrove CH, Bunting CF, Deghani H, Piao D, "Sagittal-imaging transrectal optical tomography reconstruction with structural guidance: initial simulative study", ***OSA Biomedical Topical Meetings***, St. Petersburg, FL, March 16-19, 2008.

[02] Jiang Z, Xu G, Elgawadi A, Piao D, "Development of a trans-rectal optical tomography probe for concurrent sagittal imaging with trans-rectal ultrasound", ***OSA Biomedical Topical Meetings***, St. Petersburg, FL. March 16-19, 2008.

[03] Jiang Z, Bartels KE, Holoak GR, Ritchey JW, Krasinski JS, Bunting CF, Slobodov G, Piao D, "Trans-rectal ultrasound-coupled spectral optical tomography at 785nm and 830nm detects elevation of total hemoglobin concentration in canine prostate associated with the development of transmissible venereal tumors," ***OSA Biomedical Topical Meetings***, Miami, Apr. 11-14, 2010, BTuD39.

[04] Xu G, Piao D, Bunting CF, Dehghani H, "The pain and gain of DC-based diffuse optical tomography reconstruction---New insights into an old-look problem," ***OSA Biomedical Topical Meetings***, Miami, Apr. 11-14, 2010, BSuD54.

[05] Zhang A, Piao D, Yao G, Pogue BW, "Photon diffusion associated with a cylindrical applicator boundary for axial trans-lumenal optical tomography: experimental examination of the steady-state theory," ***OSA Biomedical Topical Meetings***, Miami, Apr. 11-14, 2010, BSuD25.

[06] Xu G, Piao D, Frederickson CJ, Dehghani H, ""Reverse-uptake" of zinc-specific fluorophore in the prostate by trans-rectal fluorescence diffuse optical tomography," ***OSA Biomedical Topical Meetings***, Miami, Apr. 11-14, 2010, BSuD19.

[07] Jiang Y, Mukherjee S, Stine JE, Bunting CF, Piao D, "FPGA-assisted strategy toward efficient reconstruction (FAStER) in diffuse optical tomography," ***OSA Biomedical Topical Meetings***, Miami, Apr. 11-14, 2010, BSuD18.

Abstracts Presented In Conferences

[01] Piao D, Jiang Z, Xu G, Musgrove CH, Bunting CF, Elgawadi A, "Trans-rectal implementation of near-infrared diffuse optical tomography for non-invasive prostate imaging," ***Saratov Fall Meetings (SFM) 07***, Saratov, Russia, Sep. 25–28, 2007, internet session.

[02] Piao D, Holyoak GR, Bartels KE, Ritchey JW, Jiang Z, Xu G, Bunting CF, "In vivo trans-rectal optical tomography of normal canine prostate---demonstration of optical contrast of intact prostate over its peripheral tissue," Saratov Fall Meetings 2008, Saratov, Russia, Sep. 23-26, 2008 (Internet session invited lecture).

[03] Piao D, Jiang Z, Bartels KE, Holoak GR, Ritchey JW, Xu G, Bunting CF, Slobodov G, "In vivo optical absorption, reduced scattering, and effective attenuation tomography of intact normal and cancerous canine pelvic canal including the prostate," ***Saratov Fall Meetings (SFM) 09***, Saratov, Russia, Sep. 21–24, 2009. (Internet invited lecture).

[04] Piao D, Yao G, Pogue BW, Krasinski JS, "When cross-talk offers signal: feasibility of recovering absorbing target in endoscopic diffuse imaging geometry using spread-spectral-encoding of wide-band light based on the feature of spectral cross-talk among source channels," International Symposium on Biomedical Optics, San Jose, CA, Jan. 24-29, 2009. Paper #7174-65 (poster presentation)

[05] Xu G, Piao D, "Swept-spectral-encoded sequential light delivery for endoscopic near-infrared diffuse optical tomography: principle demonstration," ***Saratov Fall Meetings (SFM' 10)***, Saratov, Russia, Oct. 05-08, 2010. [Internet session lecture].

[06] Zhang A, Piao D, Bunting CF, "Recent advancements of photon diffusion modeling for intra-menal and extra-lumenal sensing," ***Saratov Fall Meetings (SFM' 10)***, Saratov, Russia, Oct. 05-08, 2010. [Internet session invited lecture].

[07] Jiang Z, Bartels KE, Holyoak GR, Ritchey JW, Bunting CF, Slobodov G, Piao D, "The regression of a transmissible venereal tumor in a canine prostate was detected by triple-wavelength trans-rectal optical tomography under trans-rectal ultrasound guidance ," ***SPIE International Symposium on Biomedical Optics, Jan. 22-27, 2011, San Francisco, CA.*** Paper 7883B-38 of Conference 7883B, Date: Saturday, 22 January 2011.

[08] Jiang Y, Piao D, "Analysis of the correlation between the ROIs of transrectal near infrared and transrectal ultrasound images of the prostate cancer using an observer model-based approach," ***SPIE Medical Imaging, Feb. 12-17, Lake Buena Vista, FL***. Paper 7966-59 of Conference 7966, Date: Tuesday, 16 February 2010.

[09] Xu G, Piao D, *"Challenges of and new configurations toward fluorescence diffuse optical tomography of zinc-specific biomarker for prostate cancer detection",* ***2nd Innovative Minds in Prostate Cancer Today (IMPaCT) Conference for research funded by the Department of Defense (DOD) Prostate Cancer Research Program (PCRP), Mar. 09-11, 2011, Orlando, FL.*** Paper PC094694-1920.

[10] Piao D, Jiang Z, Bartels KE, Holyoak GR, Ritchey JW, Xu G, Bunting CF, Slobodov G, *"Transrectal optical tomography with ultrasound guidance: A novel hybrid imaging technology toward prostate cancer detection and characterization",* ***2nd Innovative Minds in Prostate Cancer Today (IMPaCT) Conference for research funded by the Department of Defense (DOD) Prostate Cancer Research Program (PCRP), Mar. 09-11, 2011, Orlando, FL.*** Paper PC060814-1802.

Grants Being Awarded That Can Be Attributed To This Research:

1. PC094694 XU G (PI) 04/30/2010---04/29/2013

DOD Prostate Cancer Research Program----Pre-Doc Training Award $99,124

–*Challenges of Zinc-Specific Transrectal Fluorescence Tomography to Detect Prostate Cancer*"

This study investigates the algorithm and instrumentation challenges associated with detecting zinc-specific near-infrared fluorescence in prostate. Zinc is a well-established marker of prostate cancer, as the zinc-production is virtually turned off in prostate cancer. This research, if successful, may improve the sensitivity and specificity of detecting prostate cancer, by using zinc-tagged near-infrared fluorophore.

Role: Mentor to the pre-doctoral fellowship trainee

2. EN-09-RS-284 Jiang Y (PI) 08/01/12009---07/31/2010

Oklahoma State Regents for Higher Education **$20,000**

"Quantitative Image Analysis for in vivo Trans-Rectal Ultrasound-Coupled Optical Tomography of the Prostate"

This research investigates the potential correlation of the target information between trans-rectal optical tomography and trans-rectal ultrasound. The objective of the subcontract project is to provide images obtained from phantoms and *in vivo* subjects for the image analysis study.

Role: Co-investigator

3. R44 CA096153-03 Oraevsky A (PI),
Bartels K (PI in OSU) 11/16/2009---11/15/2010 (estimated)

NIH/NCI through Fairway Medical Technologies, Inc. **$17,219 (to OSU)**

"Optoacoustic System for Image-guided Biopsy of Prostate Cancer"

This research evaluates the laser optoacoustic and ultrasonic imaging system (LOUIS) in detection of prostate cancer in canine model that is developed at Oklahoma State University.

Role: Co-investigator

Funding Applied For Based On Work Supported By This Award:

Title of Proposal	Funding Agency	Amount Requested	Duration of Performance
In-plane detection of 5-aminolaevulinic acid-induced protoporphyrin IX fluorescence on sagittal transrectal ultrasound	Department of Defense - United States Army Medical Research Acquisition	$99,016.00	9/30/2011-9/29/2014
Transrectal Radiofrequency-Educed Acoustic Tomography (TREAT)	Department of Defense - United States Army Medical Research Acquisition	$619,503.00	9/30/2011-9/29/2014
Trans-rectal Ultrasound-guided Light Imaging of Prostate Cancer	National Institutes of Health (NIH)	$640,860.00	5/1/2011-4/30/2013
Trans-rectal Optical Tomography of Prostate with Concurrent Trans-rectal Ultrasound Guidance - Frequency Domain Measurement	Department of Defense - U.S. Army Medical Research and Materiel Command	$99,811.00	1/1/2009-12/31/2011
Trans-rectal Optical Tomography of Prostate with Concurrent Trans-rectal Ultrasound a Priori — 3-Dimensional Analysis	Department of Defense - U.S. Army Medical Research and Materiel Command	$99,811.00	1/1/2009-12/31/2011
CAREER: Translumenal Spectral Tomography of the Prostate and Spiral-planar-equivalence for Conditionalized Teaching of Photon Diffusion	National Science Foundation (NSF)	$495,084.00	2/1/2011-1/31/2016

Personnel Supported By This Award:

01.	Bartels, Kenneth E	Faculty
02.	Bunting, Charles F	Faculty
03.	Holyoak, G. Reed	Faculty
04.	JIANG, Yuanyuan	MS Student.
05.	JIANG, Zhen	PhD (*Degree in Apr. 2010*)
06.	Musgrove, Cameron F.	MS (*Degree in Dec. 2007*)
07.	Piao, Daqing	Faculty
08.	Ritchey, Jerry W	Faculty
09.	Slobodov, Gennady	Faculty
10.	Xie, Hao	MS (*Degree in Apr. 2008*)
11.	XU, Guan	PhD Candidate
12.	ZHANG, Anqi	PhD Candidate

CONCLUSIONS

The award is to explore the technology of trans-rectal near-infrared (NIR) optical tomography that may benefit accurate, selective prostate biopsy. The award has made some important discoveries that have implications to prostate cancer, including: (1) the onset of a prostate tumor was detected earlier by the researched technique than by using TRUS alone; (2) the changes of blood concentration of a rapidly growing prostate tumor were quantified; (3) the regression of a TVT mass in a canine prostate was detected as having a gradually decreasing oxygen level and a gradually increasing region of reduced oxygenation in the inner area of the tumor foci, coupled with intermittently increased total hemoglobin in the periphery of the mass; (4) a cystic lesion also presented with slightly increased total hemoglobin with oxygen-reduction in the periphery of the lesion, and the slightly increased total hemoglobin was found by histopathology to be related to intralesional hemorrhage. *These discoveries are expected to have impact on more accurate imaging guidance for targeted prostate biopsy, and monitoring treatment of locally advanced disease*.

REFERENCES

Jiang Z, Piao D,* Xu G, Ritchey JW, Holyoak GR, Bartels KE, Bunting CF, Slobodov G, Krasinski JS, ~~–~~Trans-rectal ultrasound-coupled near-infrared optical tomography of the prostate Part II: Experimental demonstration," ***Optics Express***, Vol. 16, Iss. 22, pp. 17505–17520 (2008).

Jiang Z, Holyoak GR, Bartels KE, Ritchey JW, Xu G, Bunting CF, Slobodov G, Piao D*, ~~–~~*In vivo* trans-rectal ultrasound coupled near-infrared optical tomography of a transmissible venereal tumor model in the canine pelvic canal," ***Journal of Biomedical Optics Letters***, Vol. 14, No. 3, pp. 030506 (2009).

Jiang Z, Piao D,* Holyoak GR, Ritchey JW, Bartels KE, Slobodov G, Bunting CF, Krasinski JS, ~~–~~Trans-rectal ultrasound-coupled spectral optical tomography of total hemoglobin concentration enhances assessment of the laterality and progression of a transmissible venereal tumor in canine prostate," ***Urology,*** Vol. 77m No. 1, pp. 237-42 (2011a).

Jiang Z, Piao D,* Bartels KE, Holyoak GR, Ritchey JW, Ownby CL, Rock K, Slobodov G, Culkin D, ~~–~~Intra-lesional oxygen saturation and peri-lesional hemoglobin concentration differ between a

regressing transmissible venereal tumor and a naturally occurring canine prostatic cyst as measured by TRUS integrated spectral optical tomography," under preparation for submission to ***Urology*** (2011b).

Piao D,* Jiang Z, Bartels KE, Holyoak GR, Ritchey JW, Xu G, Bunting CF, Slobodov G, "*In vivo* trans-rectal ultrasound-coupled near-infrared optical tomography of intact normal canine prostate," ***Journal of Innovative Optical Health Sciences***, Vol. 2, No. 3, pp. 215-225 (2009).

Piao D,* Bartels KE, Jiang Z, Holyoak GR, Ritchey JW, Xu G, Bunting CF, Slobodov G, "Alternative trans-rectal prostate imaging: A diffuse optical tomography method," ***IEEE Journal of Selected Topics in Quantum Electronics***, Vol. 16, No. 4, pp. 715-729 (2010). "Biophotonics 2" Special Issue, invited paper.

Xu G, Piao D, Musgrove CH, Bunting CF, Dehghani H, "Trans-rectal ultrasound-coupled near-infrared optical tomography of the prostate Part I: Simulation," ***Optics Express***, Vol. 16, Iss. 22, pp. 17484–17504 (2008).

Xu G, Piao D,* Bunting CF, Dehghani H, "Direct-current based image reconstruction versus direct-current included or excluded frequency-domain reconstruction in diffuse optical tomography," ***Applied Optics***, Vol. 49, No. 16, pp. 3059-3070 (2010).

Zhang A, Piao D,* Bunting CF, Pogue BW, "Photon diffusion in a homogeneous medium bounded externally or internally by an infinitely long circular cylindrical applicator ---- Part I: steady-state theory," ***Journal of Optical Society of America, A***, Vol. 27, No. 3, pp. 648-662 (2010).

Zhang A, Xu G, Daluwatte C, Yao G, Bunting CF, Pogue BW, Piao D*, "Photon diffusion in a homogeneous medium bounded externally or internally by an infinitely long circular cylindrical applicator ---- Part II: Quantitative examinations of steady-state theory," ***Journal of Optical Society of America, A***, Vol. 28, No. 2, pp. 66-75 (2011).

APPENDICES

1. Reprints of published journal papers and one book chapter----------total 150 pages
2. Reprints of published conference proceeding papers and selected abstracts-------total 99 pages

Trans-rectal ultrasound-coupled near-infrared optical tomography of the prostate Part I: Simulation

Guan Xu,[1] Daqing Piao,[1*] Cameron H. Musgrove,[2] Charles F. Bunting, [1]
Hamid Dehghani [3]

[1] *School of Electrical and Computer Engineering, Oklahoma State University, Stillwater, OK, 74078-5032, USA*
[2] *Sandia National Laboratories, Albuquerque, NM, 87155-1330, USA*
[3] *School of Physics, University of Exeter, Exeter, UK, EX4 4QL*
**Corresponding Author: daqing.piao@okstate.edu*

Abstract: We investigate the feasibility of trans-rectal optical tomography of the prostate using an endo-rectal near-infrared (NIR) applicator that is to be integrated with a trans-rectal ultrasound (TRUS) probe. Integration with TRUS ensures accurate endo-rectal positioning of the NIR applicator and the utility of using TRUS spatial *prior* information to guide NIR image reconstruction. The prostate NIR image reconstruction is challenging even with the use of spatial *prior* owing to the anatomic complexity of the imaging domain. A hierarchical reconstruction algorithm is developed that implements cascaded initial-guesses for nested domains. This hierarchical image reconstruction method is then applied to evaluating a number of NIR applicator designs for integration with a sagittal TRUS transducer. A NIR applicator configuration feasible for instrumentation development is proposed that contains one linear array of optodes on each lateral side of the sagittal TRUS transducer. The performance of this NIR applicator is characterized for the recovery of single tumor mimicking lesion as well as dual targets in the prostate. The results suggest a strong feasibility of trans-rectal prostate imaging by use of the endo-rectal NIR/US probe.

OCIS codes: (170.3880) Medical and biological imaging; (170.6960) Tomography; (170.7230) Urology.

References and links

1. A. Jemal, R. Siegel, E. Ward, T. Murray, J. Xu, and M. J. Thun, "Cancer statistics, 2007," CA Cancer J. Clin. **57**, 43-66 (2007).
2. T. J. Polascik, J. E. Oesterling, and A. W. Partin, "Prostate specific antigen: a decade of discovery--what we have learned and where we are going," J. Urol. **162**, 293-306 (1999).
3. G. D. Grossfeld and P. R. Carroll, "Prostate cancer early detection: a clinical perspective," Epidemiol Rev. **23**, 173-80 (2001).
4. T. A. Stamey, M. Caldwell, J. E. McNeal, R. Nolley, M. Hemenez, and J. Downs, "The prostate specific antigen era in the United States is over for prostate cancer: what happened in the last 20 years?," J. Urol. **172**, 1297-1301 (2004).
5. C. R. Pound, A. W. Partin, M. A. Eisenberger, D. W. Chan, J. D. Pearson, and P. C. Walsh, "Natural history of progression after PSA elevation following radical prostatectomy," JAMA. **281**, 1591-1597 (1999).
6. A. C. Loch, A. Bannowsky, L. Baeurle, B. Grabski, B. König, G. Flier, O. Schmitz-Krause, U. Paul, and T. Loch, "Technical and anatomical essentials for transrectal ultrasound of the prostate," World J. Urol. **25**, 361-366 (2007).
7. A. Bill-Axelson, L. Holmberg, M. Ruutu, et al. "Radical prostatectomy versus watchful waiting in early prostate cancer," N. Engl. J. Med. **352**, 1977-1984 (2005).
8. B. Spajic, H. Eupic, D. Tomas, G. Stimac, B. Kruslin, and O. Kraus, "The incidence of hyperechoic prostate cancer in transrectal ultrasound-guided biopsy specimens," Urology **70**, 734-737 (2007).

#99968 - $15.00 USD Received 8 Aug 2008; revised 13 Oct 2008; accepted 14 Oct 2008; published 15 Oct 2008

9. K. Shinohara, T. M. Wheeler, and P. T. Scardino, "The appearance of prostate cancer on transrectal ultrasonography: correlation of imaging and pathological examinations," J. Urol. **142**, 76-82 (1989).
10. C. R. Porter, "Does the number of prostate biopsies performed affect the nature of the cancer identified?" Nat. Clin. Pract. Urol. **4**, 132-133 (2007).
11. V. Scattoni, A. Zlotta, R. Montironi, C. Schulman, P. Rigatti, and F. Montorsi, "Extended and saturation prostatic biopsy in the diagnosis and characterisation of prostate cancer: a critical analysis of the literature," Eur. Urol. **52**,1309-1322 (2007).
12. B. Tromberg, J. Coquoz, O. Fishkin, J. B. Pham, T. Anderson, E. R. Butler, J. Cahn, M. Gross, J. D. Venugopalan, and D. Pham, "Non-invasive measurements of breast tissue optical properties using frequency-domain photon migration," Phil. Trans. R. Soc. Lond. B **352**, 661-668 (1997).
13. B. W. Pogue, S. P. Poplack, T.O. McBride, W. A. Wells, K. S. Osterman, U. L. Osterberg, and K. D. Paulsen," Quantitative hemoglobin tomography with diffuse near-infrared spectroscopy: pilot results in the breast," Radiology **218**, 261-266 (2001).
14. V. Ntziachristos and B. Chance, "Probing physiology and molecular function using optical imaging: applications to breast cancer," Breast Cancer Res. **3**, 41-46 (2001).
15. R. Choe, A. Corlu, K. Lee, T. Durduran, S. D. Konecky, M. Grosicka-Koptyra, S. R. Arridge, B. J. Czerniecki, D. L. Fraker, A. DeMichele, B. Chance, M. A. Rosen, and A. G. Yodh, "Diffuse optical tomography of breast cancer during neoadjuvant chemotherapy: a case study with comparison to MRI," Med. Phys. **32**, 1128-1139 (2005).
16. M. A. Franceschini, K. T. Moesta, S. Fantini, G. Gaida, E. Gratton, H. Jess, W. W. Mantulin, M. Seeber, P. M. Schlag, and M. Kaschke, "Frequency-domain techniques enhance optical mammography: initial clinical results," Proc. Nat. Acad. Sci. USA **94**, 6468-6473 (1997).
17. Q. Zhu, E. B. Cronin, A. A. Currier, H. S. Vine, M. Huang, N. Chen, and C. Xu, "Benign versus malignant breast masses: optical differentiation with US-guided optical imaging reconstruction," Radiology **237**, 57-66 (2005).
18. S. A. Bigler, R. E. Deering, and M. K. Brawer, "Comparison of microscopic vascularity in benign and malignant prostate tissue," Hum. Pathol. **24**, 220-226 (1993).
19. J. H. Ali , W. B. Wang , M. Zevallos, and R. R. Alfano , "Near infrared spectroscopy and imaging to probe differences in water content in normal and cancer human prostate tissues," Technol. Cancer Res. Treat. **3**, 491-497 (2004).
20. M. R. Arnfield , J. D. Chapman, J. Tulip , M. C. Fenning, and M. S. McPhee , "Optical properties of experimental prostate tumors in vivo," Photochem. Photobiol. **57**, 306-311 (1993).
21. T. C. Zhu, A. Dimofte, J. C. Finlay, et al. "Optical properties of human prostate at 732 nm measured in mediated photodynamic therapy," Photochem. Photobiol. **81**, 96-105 (2005).
22. T. Svensson, S. Andersson-Engels, M. Einarsdóttír, and K. Svanberg, "In vivo optical characterization of human prostate tissue using near-infrared time-resolved spectroscopy," J. Biomed. Opt. **12**, 014022 (2007).
23. M. Goel, H. Radhakrishnan, H. Liu, et al. "Application of near infrared multi-spectral CCD imager system to determine the hemodynamic changes in prostate tumor," in *OSA Biomedical Topical Meetings* (Optical Society of America, 2006), paper SH10.
24. H. Liu, Y. Song, K. L. Worden, X. Jiang, A. Constantinescu, and R. P. Mason, "Noninvasive investigation of blood oxygenation dynamics of tumors by near-infrared spectroscopy," Appl. Opt. **39**, 5231-43 (2000).
25. X. Zhou and T. C. Zhu, "Image reconstruction of continuous wave diffuse optical tomography (DOT) of human prostate," in *Proceedings of the COMSOL Users Conference* (2006).
26. S. L. Jacques and M. Motamedi, "Tomographic needles and catheters for optical imaging of prostatic cancer," Proc. SPIE **2395**, 111-118 (1995).
27. C. Li, R. Liengsawangwong, H. Choi, and R. Cheung , "Using *a priori* structural information from magnetic resonance imaging to investigate the feasibility of prostate diffuse optical tomography and spectroscopy: a simulation study," Med. Phys. **34**, 266-274 (2007).
28. C. Musgrove, C. F. Bunting, H. Dehghani, B. W. Pogue, and D. Piao, "Computational aspects of endoscopic near-infrared optical tomography: initial investigations," Proc. SPIE **6343**, 643409 (2007)
29. D. Piao, H. Xie, W. Zhang, G. Zhang, C. H. Musgrove, C. F. Bunting, H. Dehghani, B. W. Pogue, and S. N. Vemulapalli, "Near-infrared optical tomography: endoscopic imaging approach," Proc. SPIE **6431**, 643103 (2007).
30. H. Dehghani, C. M. Carpenter, P. K. Yalavarthy, B. W. Pogue, and J. P. Culver, "Structural *a priori* information in near-infrared optical tomography," Proc. SPIE **6431**, 64310B1 (2007).
31. Q. Zhu, T. Durduran, V. Ntziachristos, M. Holboke, and A. G. Yodh, "Imager that combines near-infrared diffusive light and ultrasound," Opt. Lett. **24**, 1050-1052 (1999).
32. M. J. Holboke, B. J. Tromberg, X. Li, N. Shah, J. Fishkin, D. Kidney, J. Butler, B. Chance, and A. G. Yodh, "Three-dimensional diffuse optical mammography with ultrasound localization in a human subject," J. Biomed. Opt. **5**:237-47 (2000).
33. B. W. Pogue, S. Geimer, T. O. McBride, S. Jiang, U. L. Osterberg, and K. D. Paulsen, "Three-dimensional simulation of near-infrared diffusion in tissue: boundary condition and geometry analysis for finite-element image reconstruction," Appl. Opt. **40**, 588-600 (2001).

#99968 - $15.00 USD Received 8 Aug 2008; revised 13 Oct 2008; accepted 14 Oct 2008; published 15 Oct 2008

34. M. Schweiger, S. R. Arridge, and D. T. Delpy, "Application of the finite-element method for the forward and inverse models in optical tomography," J. Math. Imag. Vision **3**, 263-283 (1993).
35. J. J. More, "Levenberg--Marquardt algorithm: implementation and theory," in *Numerical Analysis*, (Springer Berlin / Heidelberg, 1978), pp. 105-116.
36. X. Yu, G. Chen, and S. Cheng, "Dynamic learning rate optimization of the backpropagation algorithm," IEEE Trans. Neural Netw. **6**, 669-677 (1995).
37. D. Shen, Y. Zhan, and C. Davatzikos, "Segmentation of prostate boundaries from ultrasound images using statistical shape model," IEEE Tran. Med. Imaging **22**, 539-55 (2003).
38. M. Schweiger, S. R. Arridge, O. Dorn, A. Zacharopoulos, and V. Kolehmainen, "Reconstructing absorption and diffusion shape profiles in optical tomography using a level set technique," Opt. Lett. **31**, 471-473 (2006).
39. V. Kolehmainen, S. R. Arridge, W. R. B. Lionheart, M. Vauhkonen, and J. P. Kaipio, "Recovery of region boundaries of piecewise constant coefficients of an elliptic PDE from boundary data," Inverse Probl. **15**, 1375-1391 (1999).
40. V. Kolehmainen, M. Vauhkonen, J. P. Kaipio, and S. R. Arridge, "Recovery of piecewise constant coefficients in optical diffusion tomography," Opt. Express **7**, 468-480 (2000).
41. V. Kolehmainen, S. R. Arridge, M. Vauhkonen, and J. P. Kaipio, "Simultaneous reconstruction of internal tissue region boundaries and coefficients in optical diffusion tomography," Phys. Med. Biol. **45**, 3267-3284 (2000).
42. S. Srinivasan, B. W. Pogue, H. Dehghani, S. Jiang, X. Song, and K. D. Paulsen, "Improved quantification of small objects in near-infrared diffuse optical tomography," J. Biomed. Opt. **9**, 1161-1171 (2004).
43. P. K. Yalavarthy, H. Dehghani, B. W. Pogue, and K. D. Paulsen, "Critical computational aspects of near infrared circular tomographic imaging: Analysis of measurement number, mesh resolution and reconstruction basis," Opt. Express **14**, 6113-6127 (2006).
44. H. Shan, N. Pantong, J. Su, H. Liu, and M. V. Klibanov, "Globally convergent reconstruction algorithm for diffusion tomography of prostate," in *Biomedical Optics/Digital Holography and Three-Dimensional Imaging/Laser Applications to Chemical, Security and Environmental Analysis* on CD-ROM (The Optical Society of America, Washington, DC, 2008), paper BSuE33.
45. A. M. Wise, T. A. Stamey, J. E. McNeal, and J. L. Clayton, "Morphologic and clinical significance of multifocal prostate cancers in radical prostatectomy specimens," Urology **60,** 264-9 92002).
46. G. J. Miller and J. M. Cygan, "Morphology of prostate cancer: the effects of multifocality on histological grade, tumor volume and capsule penetration," J. Urol. **152**(5 Pt 2), 1709-13 (1994).

1. Introduction

Prostate cancer is the second most commonly diagnosed cancer and the second leading cause of cancer deaths in American men [1]. Prostate cancer screening is performed by measurement of serum prostate-specific antigen (PSA) [2], digital rectal examination (DRE), and in many cases a combination of both tests [3]. The introduction of PSA test contributed to substantially increased detection rate of organ-confined prostate cancer or considerable stage migration [4]. However, PSA is not a specific indicator of prostate malignancy and post-treatment tumor recurrence, except after radical prostatectomy [5]. A clearly increased serum PSA value (>20 ng/ml) may indicate the presence of a prostate carcinoma at a very high probability [6]. In the gray zone between 4 and 10 ng/ml the tissue marker PSA is frequently influenced by benign alterations, so that it is not possible, on the basis of the PSA value alone, to differentiate between benign and malignant cases [6, 7]. DRE can often distinguish between prostate cancer and non-cancerous conditions; it may also detect prostate cancers having normal PSA levels. However, palpation during a DRE is subjective, insensitive, and more than half of all prostate cancers detected are not palpable [3]. When the suspicion of prostate cancer is raised by abnormal PSA and/or DRE, the diagnosis is made by biopsy. The technique of trans-rectal ultrasound (TRUS) based trans-rectal prostate biopsy, carried out with a semi-automatic coil spring device and an 18-gauge needle, is to date considered as the gold standard [6].

Prostate neoplastic lesions may be identified on TRUS as being hypoechoic [8]. However at most 60% neoplastic lesions appear hypoechoic on TRUS while most of the remaining neoplastic lesions appear isoechoic [9]. The hypoechoic, cancer-suspicious areas may be histologically either benign or malignant [9]. The lack of TRUS specificity thereby prompts the practice of "systematic biopsy" of the prostate. The current trend is to use 10- to 12-core

#99968 - $15.00 USD Received 8 Aug 2008; revised 13 Oct 2008; accepted 14 Oct 2008; published 15 Oct 2008

biopsy with a preference in the peripheral zone, where most neoplastic lesions are found, as the initial biopsy strategy. It should be noted that the majority of biopsies are found to be negative, and in men with persistent suspicion of prostate cancer after several negative biopsies, more extensive protocols (>12 cores) up to saturation biopsy (24 cores) represent a necessary diagnostic procedure [10]. However, despite years of research, the exact number of biopsies to be taken is still largely unknown [11].

The need of having many biopsy-cores for systematic, yet random, tissue sampling of the prostate may be alleviated if the acoustic contrast that TRUS relies on is augmented with functional or "surrogate" markers of the prostate tumor such that the biopsy is directed to the malignant lesions. A functional imaging modality augmenting TRUS is certainly more desirable if it is non-ionizing and minimally-invasive as is TRUS. Optical tomography based on near-infrared (NIR) light could emerge as such a modality.

Near-infrared measurements of attenuation through tissue have demonstrated significant contrast gradients between blood and parenchymal tissue that is otherwise difficult to obtain [12-17]. The alteration of vascularity or the hemoglobin content in the tumor provides high intrinsic optical contrast between the tumor and benign tissues which has been well-demonstrated in breast cancer imaging [12-17]. When multi-spectral detection is engaged, NIR imaging is also capable of directly quantifying the chromorphore concentrations important for characterization of the malignancy [12-17]. In prostate, studies have shown vascular density gradient in malignant versus benign tissue specimens [18], and different water concentrations in cancerous and benign tissues *in vitro* [19]. Invasive NIR measurements of prostate have been conducted for experimental prostate tumors [20] and human prostate [21, 22]. Surface measurements of implanted prostate tumor have also been reported [23, 24]. All these studies demonstrate the potential of using NIR to detect and characterize prostate cancer. NIR diffuse optical measurement, performed interstitially, is also becoming an important tool for monitoring photodynamic therapy in prostate [21, 22, 25]. Prostate NIR imaging via trans-urethral probing had been analyzed and tested [26]. Recently, trans-rectal prostate NIR imaging has been investigated in simulation in the context of assisting MRI for treatment decision [27].

To our knowledge, experimental work on trans-rectal NIR tomography has not been performed except for our recent attempts [28, 29] which may be largely due to the challenge of fabricating a suitable trans-rectal applicator. Optical tomography typically needs 10s of channels of NIR optodes in order to achieve reasonable spatial resolution as a large tissue volume is being interrogated. The NIR illumination can be delivered by small diameter fibers, but the detection of weak scattered light is in favor of fibers of larger diameters and/or suitably larger numerical apertures. Unlike in breast NIR tomography where there is minimum spatial restriction for the optode configuration, trans-rectal applicator for NIR tomography has to deploy many optodes in a very compact space. This restriction could become more pronounced when trans-rectal NIR applicator is also to be combined with TRUS transducer. Since the depth of tissue interrogation by diffuse NIR light is roughly one-half of the source-detector separation for typical scattering-dominant biological tissue, reaching targets centimeters deep in prostate implies a NIR array of several centimeters in size. Such an NIR array is feasible for trans-rectal application if the optodes are arranged longitudinally, which should provide a sagittal-view in trans-rectal NIR imaging. The images obtained by trans-rectal NIR tomography alone would, however, be difficult to correlate with the anatomy. Unlike in breast imaging where the NIR applicator could be accurately positioned, accurate positioning of a trans-rectal NIR applicator with respect to the prostate is difficult which is due to the "blind" location of the prostate, slow NIR image reconstruction, and lack of anatomic details in NIR tomography images. It is thereby imperative to use a real-time morphological imaging modality concurrently with trans-rectal NIR tomography to provide a positioning guidance for NIR applicator in order to correlate the NIR tomography findings with the prostate anatomy. The structural information of the prostate can further be utilized as

#99968 - $15.00 USD Received 8 Aug 2008; revised 13 Oct 2008; accepted 14 Oct 2008; published 15 Oct 2008

the spatial *prior* [30] to improve the accuracy of NIR image reconstruction. Among the prostate imaging techniques, TRUS is perhaps the best modality for trans-rectal NIR tomography to combine owing to the operational similarity between these two modalities.

The diagnostic benefit of augmenting NIR contrast to US has been demonstrated in breast cancer detection [31, 32]. The methodology of combining NIR & US can certainly be extended from breast imaging to prostate imaging; nevertheless, the technique cannot be extended from imaging the breast to imaging the prostate without an NIR/US applicator suitable for trans-rectal manipulation. In this work, we demonstrate TRUS coupled trans-rectal optical tomography of the prostate. This work is reported in two consecutive papers. The Part-I paper, based on simulation, investigates designs of NIR tomography applicator suitable for integrating with a commercial TRUS transducer. A hierarchical NIR image reconstruction algorithm is developed for utilizing the TRUS structural *a priori* information which is then used to evaluate several NIR applicator configurations for integrating with a TRUS transducer. The Part-II paper implements the probe design suggested in Part-I, presents the instrumentation details of the TRUS coupled trans-rectal NIR tomography probe & system, and demonstrates TRUS-coupled trans-rectal NIR tomography of a canine prostate.

2. The geometry of trans-rectal NIR imaging and the utility of TRUS information

2.1 Configuration of sagittal trans-rectal NIR array for coupling with sagittal TRUS

The TRUS is typically performed in bi-plane (sagittal and transverse) for prostate imaging. The sagittal and transverse views are switched during prostate imaging, but for biopsy procedure, the firing of the spring-loaded needle is monitored in the sagittal plane wherein the needle trajectory may be accurately marked. We have acquired a bi-plane TRUS probe (Aloka UST-672-5/7.5) as is shown in Fig. 1(a), which has a proximal sagittal transducer window of 60mm×10mm and a distal transverse transducer window of 120°×10mm. The cylindrical TRUS probe has a maximum diameter of 20mm. Integrating NIR applicator to a TRUS probe implies that the dimension, particularly the radial one, of the NIR array is quite restricted. As discussed earlier, longer source-detector separation is needed to interrogate deeper targets; therefore the most feasible configuration of an NIR array may be through distributing a linear array of optode on each lateral side of the sagittal TRUS transducer, as illustrated in Fig. 1(b). Taking into account the mechanical structure necessary to support the optodes, the combined

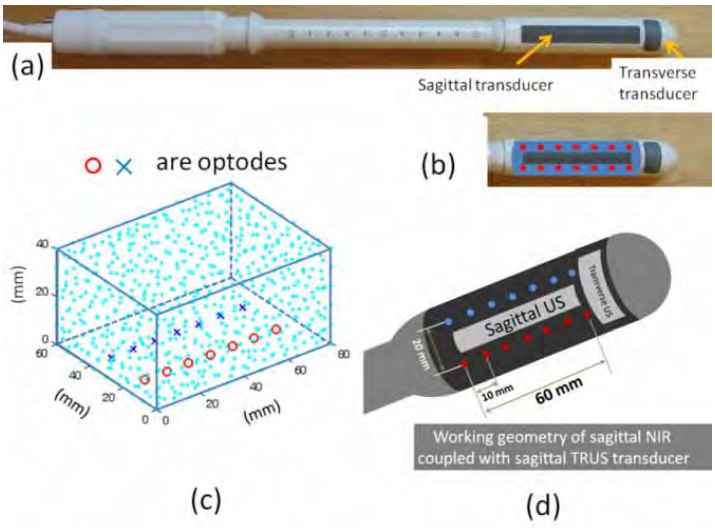

Fig. 1. (a) Photograph of a bi-plane TRUS transducer. (b) Configuration of an NIR array feasible for coupling with sagittal TRUS. (c) The NIR imaging geometry for the one depicted in (b). (d) Illustration of a trans-rectal probe that integrates NIR and US synergistically.

#99968 - $15.00 USD Received 8 Aug 2008; revised 13 Oct 2008; accepted 14 Oct 2008; published 15 Oct 2008

probe will likely have a radial size of at least a few millimeters larger than that of the original TRUS probe. NIR tomography has to use multimode fibers to detect weak diffuse light, and these multimode fibers must be delivered longitudinally before being side-fired. Bending the fiber is not a viable solution here for side-firing unless the fibers are passed inside the TRUS probe. The side-firing alternatively may however be realized by implementing micro-optical components, but the compact space inside or surrounding the probe may not accommodate a large number of such channels. A NIR array, which could couple with TRUS, may be configured by fabricating 7 fiber channels on each lateral side of the TRUS to span 60mm longitudinally as the TRUS does, and placing the optical channels 10mm apart. The NIR array must leave the 10mm-wide sagittal TRUS transducer unblocked; therefore a 20mm spacing of the NIR optodes from one lateral side to the other is perhaps needed. These considerations lead to the NIR array geometry shown in Fig. 1(c) where 14 optodes are spaced 10mm longitudinally and 20mm laterally. Fig. 1(d) illustrates an NIR/US probe if the sagittal NIR array can be fabricated synergistically with the TRUS probe.

2.2 Forward and inverse methods for sagittal trans-rectal optical tomography

The prostate and peripheral tissues are scattering-dominant in NIR [19-22]. We use the diffusion approximation to the radiative transport equation in frequency-domain [33]:

$$\nabla \cdot D(\vec{r})\nabla U(\vec{r},\omega) - (\mu_a + \frac{i\omega}{c})U(\vec{r},\omega) = -S(\vec{r},\omega) \tag{1}$$

where $U(\vec{r},\omega)$ is the photon fluence rate at position $\vec{r}$, $S(\vec{r},\omega)$ is the source, ω is the source modulation frequency, c is the speed of light in the medium, μ_a is the absorption coefficient, and $D = [3(\mu_a + \mu_s')]^{-1}$ is the diffusion coefficient with μ_s' being the reduced or transport scattering coefficient. Finite-element method [34] is used to solve Equ. (1) under the Robin-type boundary condition [33]:

$$U(\vec{r}_0,\omega) + 2DA\hat{n}_0 \bullet \nabla U(\vec{r}_0,\omega) = 0 \tag{2}$$

where $\vec{r}_0$ is the boundary, $\hat{n}_0$ is the outward normal vector of the boundary and A is the refractive index mismatch coefficient. The refractive indices used for air and tissue are 1 and 1.33 respectively, leading to A=2.82 as in [33].

The imaging volume is divided to 4 regions-of-interest (ROIs): the rectum wall, the peri-prostate tissue, the prostate, and the prostate tumor. The Jacobian (sensitivity) values are calculated for each ROI rather than each node which has the form of:

$$J = \begin{bmatrix} \frac{\partial \ln I_{11}}{\partial \mu_{a\_rect}} & \frac{\partial \ln I_{11}}{\partial \mu_{a\_peri}} & \frac{\partial \ln I_{11}}{\partial \mu_{a\_pros}} & \frac{\partial \ln I_{11}}{\partial \mu_{a\_lesi}} & \frac{\partial \ln I_{11}}{\partial \mu_{s\_rect}'} & \frac{\partial \ln I_{11}}{\partial \mu_{s\_peri}'} & \frac{\partial \ln I_{11}}{\partial \mu_{s\_pros}'} & \frac{\partial \ln I_{11}}{\partial \mu_{s\_lesi}'} \\ \frac{\partial \ln I_{12}}{\partial \mu_{a\_rect}} & \ddots & \ddots & \vdots & \vdots & \ddots & \ddots & \vdots \\ \vdots & \ddots & \ddots & \vdots & \vdots & \ddots & \ddots & \vdots \\ \frac{\partial \ln I_{77}}{\partial \mu_{a\_rect}} & \cdots & \cdots & \frac{\partial \ln I_{77}}{\partial \mu_{a\_lesi}} & \frac{\partial \ln I_{77}}{\partial \mu_{s\_rect}'} & \ddots & \ddots & \frac{\partial \ln I_{77}}{\partial \mu_{s\_lesi}'} \\ \frac{\partial \phi_{11}}{\partial \mu_{a\_rect}} & \frac{\partial \phi_{11}}{\partial \mu_{a\_peri}} & \frac{\partial \phi_{11}}{\partial \mu_{a\_pros}} & \frac{\partial \phi_{11}}{\partial \mu_{a\_lesi}} & \frac{\partial \phi_{11}}{\partial \mu_{s\_rect}'} & \cdots & \cdots & \frac{\partial \phi_{11}}{\partial \mu_{s\_lesi}'} \\ \frac{\partial \phi_{12}}{\partial \mu_{a\_rect}} & \ddots & \ddots & \vdots & \vdots & \ddots & \ddots & \vdots \\ \vdots & \ddots & \ddots & \vdots & \vdots & \ddots & \ddots & \vdots \\ \frac{\partial \phi_{77}}{\partial \mu_{a\_rect}} & \cdots & \cdots & \frac{\partial \phi_{77}}{\partial \mu_{a\_lesi}} & \frac{\partial \phi_{77}}{\partial \mu_{s\_rect}'} & \cdots & \cdots & \frac{\partial \phi_{77}}{\partial \mu_{s\_lesi}'} \end{bmatrix} \tag{3}$$

#99968 - $15.00 USD Received 8 Aug 2008; revised 13 Oct 2008; accepted 14 Oct 2008; published 15 Oct 2008

where $I_{ij}\ (i,j=1,2,...,7)$ and $\phi_{ij}\ (i,j=1,2,...,7)$ are the intensity and phase terms of $U(\vec{r},\omega)$, respectively. In Equ. 3, "rect", "peri", "pros", and "lesi" denote "rectum wall", "peri-prostate tissue", "prostate", and "prostate lesion", respectively.

The Levenberg-Marquart (LM) algorithm [35] governs the iterative recovery of the optical properties by updating the ROI-specific values of μ_a and μ_s' according to

$$x_{k+1} = x_k + \alpha \cdot [J^T(x_k)J(x_k) + \lambda I]^{-1} J^T(x_k)\Delta v(x_k) \tag{4}$$

where *x* is the array of parameters to be optimized, Δv is the forward projection error and λ is a penalty or regularization term. A small damping factor α in the range of (0, 1) is introduced in Equ. 4 to stabilize the convergence. It is shown that an empirically chosen α could make the LM algorithm more reliable and computationally more efficient [36].

2.3 TRUS prior assisted finite-element mesh for trans-rectal NIR tomography reconstruction

The TRUS prostate images which are available in open sources [37] are used for the simulation study. The TRUS image was first imported into a pre-processing software 3ds-MAX [Autodesk Inc] (shown in Fig. 2(a)). The 3ds-MAX provides very flexible geometry-deforming functions, with which a basic 3-D geometry of the prostate can be outlined manually. The finalized 3-D mesh of the prostate is then converted to COMSOL Multiphysics [COMSOL AB] compatible format (shown in Fig. 2(b)) using MeshToSolid [Syncode Inc]. The prostate tumor is then mimicked using a spherical shape to allow for flexibility of adjusting its size. The absorption and reduced scattering coefficients of the rectum, peri-prostate tissue, prostate and the tumor are assigned with values as suggested by literature [27]. Figure 3 illustrates one example of the completed FEM-mesh for trans-rectal optical tomography derived from a TRUS image, where x, y and z denoting the longitudinal, lateral and the depth coordinates, respectively. A typical mesh used for this work contains approximately 4000 nodes and 20000 linear tetrahedral elements.

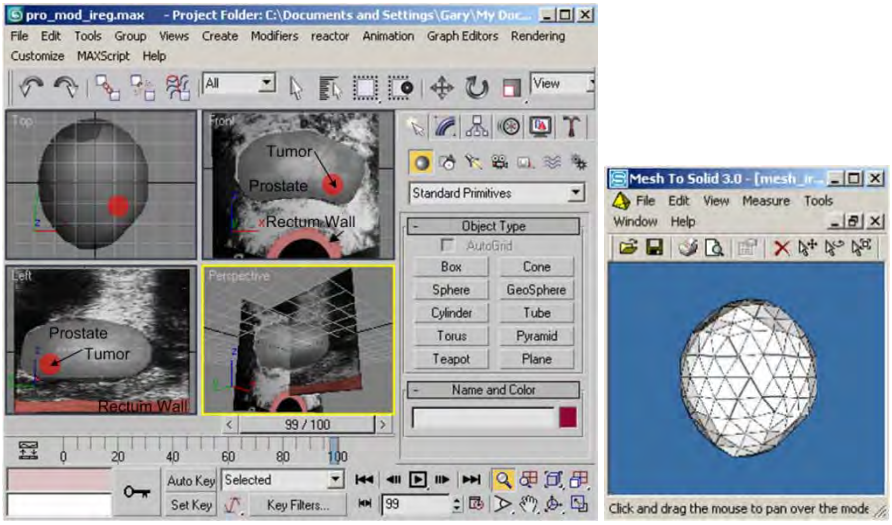

(a) (b)

Fig. 2. (a) 3ds-MAX Interface, (b) Mesh-to-Solid Interface

The mesh in Fig. 3 corresponds to a volume of 80×80×80 mm^3 and the 'walnut' shaped prostate has a dimension of 50×50×30 mm^3. The rectum wall is 4mm thick with a curvature radius of 80 mm. The choice of the curvature radius is due to the fact that the NIR array added to a TRUS probe may have a flat surface that would transform the rectum lumen to an

#99968 - $15.00 USD Received 8 Aug 2008; revised 13 Oct 2008; accepted 14 Oct 2008; published 15 Oct 2008

elliptical shape. A larger radius also gives more flexibility in handling the posterior prostate region within the mesh.

Although only the rectum wall is a physical boundary, treating the other 5 surfaces as physical boundaries (Robin type, Equ. 2) should have negligible effect upon the results as the lateral-medial and ventral-dorsal dimensions well exceed the potential path of photon propagation for the NIR array given in Fig. 1(c). The modulation frequency ω of the source in Equ. 1 is set at 100MHz, and 1% Gaussian noise is added to all forward calculations to form the measurement data.

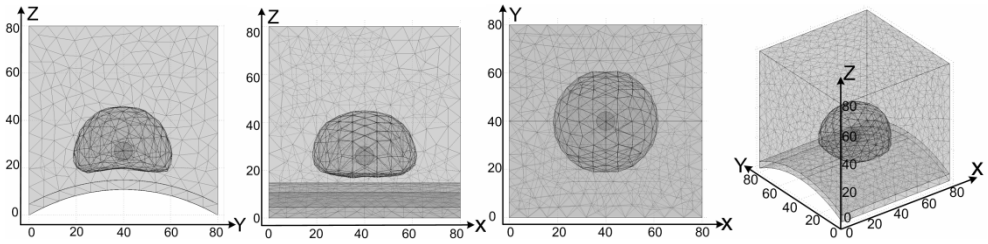

(a) Transverse View (b) Sagittal View (c) Coronal View (d) Perspective View

Fig. 3. FEM mesh generated based on approaches in Fig. 2. [Unit: mm].

3. A hierarchical spatial *prior* approach for trans-rectal NIR tomography reconstruction

3.1 Sensitivity of the sagittal trans-rectal NIR array

The NIR array proposed in Fig. 1(c) has 7 source channels occupying one linear array and 7 detection channels occupying the other array. The sensitivity with respect to a perturbation of a specific optical property is determined by the corresponding Jacobian values in Equ. 3. Figure 4 plots the sensitivity specific to absorption, or $\partial \ln I_{ij} / \partial \mu_a$, for a medium with optical properties of $\mu_a = 0.01mm^{-1}$ and $\mu_s^{'} = 1.0mm^{-1}$, calculated by projecting the Jacobian values along a line in the imaging volume. Figure 4(a) is the longitudinal sensitivity in the mid-sagittal plane for a line from (0, 40, 30) to (80, 40, 30), Fig. 4(b) is the lateral sensitivity in the mid-transverse plan for a line from (40, 0, 30) to (40, 80, 30), and Fig. 4(c) is the depth sensitivity in the mid-sagittal plane for a line from (40, 40, 15.1) (here 15.1 is the z coordinate, but the actual depth from the rectum surface is 0mm owing to the curvature of the rectum) to (40, 40, 80), respectively. The dimension or the locations of the source & detector array is marked on the abscissa of all three plots. The TRUS sagittal plane is located at y=40mm, which is the mid-sagittal plane within the NIR imaging volume.

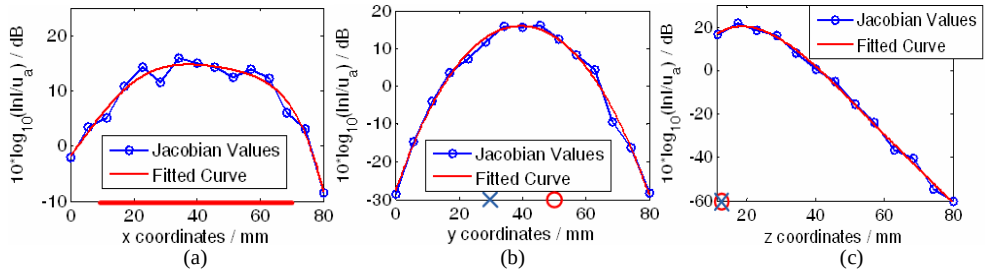

Fig. 4. Sensitivity profile. (a) Mid-sagittal plane, longitudinal sensitivity; (b) mid-transverse plane, lateral sensitivity; (c) mid-saggital plane, depth sensitivity. The marks on abscissa or the origin show the positions of optodes.

Figure 4 indicates that the longitudinal sensitivity has ~6dB variation in the middle 75% range of the array, and the lateral sensitivity peaks at the mid-saggital plane. In the middle-

#99968 - $15.00 USD Received 8 Aug 2008; revised 13 Oct 2008; accepted 14 Oct 2008; published 15 Oct 2008

sagittal plane the sensitivity degrades ~1dB/mm as z-coordinate increases from 20mm, which is apparently due to the side-way placement of the NIR array. The depth-degrading sensitivity will cause deeper targets to be reconstructed at a shallower position [28] if no spatial *prior* is incorporated.

3.2 Trans-rectal NIR image reconstruction without a priori information

The performance of recovering tumor-mimicking target by trans-rectal NIR tomography without any structural *prior* is examined. Figure 5 lists the results for the tumor target being placed at left, middle, and right within the prostate. The top row in Fig. 5 lists the target images of μ_a and $\mu_s^{'}$ generated by the TRUS-defined geometry as shown in Fig. 3. The optical properties of the 10mm diameter tumor target are $\mu_a = 0.02mm^{-1}$ and $\mu_s^{'} = 1.6mm^{-1}$, with the parameters of other regions as listed in Table 1. These target images are used to generate the noise-added simulated measurement data. The image reconstruction is then conducted using a mesh of homogenous element density throughout the entire volume and updated element by element. The results are given in the bottom row of Fig. 5. As seen, the tumor target may be localized, but the recovered resolution or spatial information is poor. The accuracy of optical property recovery is also low. Further, it is found that a tumor target with negative contrast in absorption cannot be accurately recovered using similar settings. It is however expected that the detection and characterization of the tumor target will be improved when the spatial information of prostate and the tumor is available.

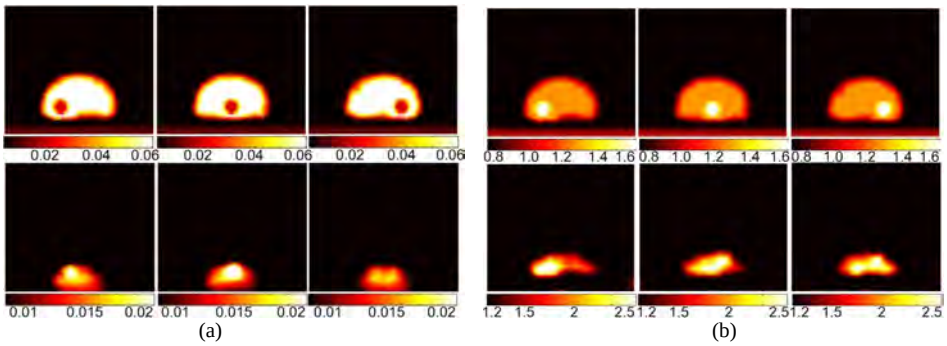

Fig. 5. NIR-only element-based reconstruction of a tumor target in various longitudinal locations. Row 1: target image for calculating the forward data; Row 2: Images reconstructed without any spatial prior. (a): μ_a images; (b): $\mu_s^{'}$ images. [Unit: mm^{-1}]

3.3 A hierarchical spatial prior method for TRUS guided trans-rectal NIR reconstruction

The tissue volume interrogated by trans-rectal NIR imaging constitutes a nested-domain including a thin layer of rectum wall, a large volume of peri-prostate tissue, a relatively absorbing prostate, and the lesion within the prostate. These nested imaging domains may be further complicated by the pelvic bone that could interfere with the light propagation. Schweiger, et al. [38], Kolehmainen et al. [39-41], and Srinivasan et al. [42] have previously investigated the issue of recovering the shapes and optical properties of regions with optical contrast inside a non-nested or nested domains, where the shapes of the ROIs were derived from optical information when no spatial *prior* is available from other complementary imaging modalities. These methods have shown sufficient robustness in recovering the shapes and optical properties of the ROIs, yet the problem of stability and/or slow convergence was noticed in such approaches dealing with nested-domains. In trans-rectal NIR tomography reconstruction the spatial information from TRUS may be implemented by assigning homogenous optical properties within each ROIs of the imaging domain. However the convergence and the accuracy of reconstruction will still depend upon the initial guess in

#99968 - $15.00 USD Received 8 Aug 2008; revised 13 Oct 2008; accepted 14 Oct 2008; published 15 Oct 2008

addition to the accuracy of the *prior* information. The dependence on initial guess in a gradient based solver is due to the local minimum feature [36], as indicated in Fig. 6, which could be exaggerated in prostate imaging due to the possible multiple combinations of optical properties in the nested-structures. The image reconstruction in trans-rectal optical tomography is further complicated by the discrepancy regarding the optical contrast that the prostate tumor could have, namely positive or negative [19-22, 27].

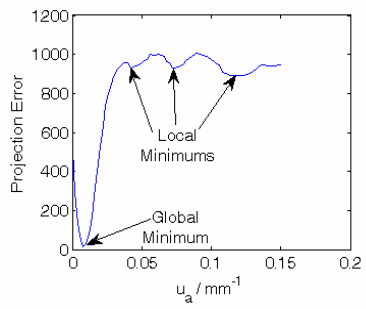

Fig. 6. Local-minimum issue in reconstruction. The forward calculation is based on Fig. 3(a) with assumption of homogeneous imaging volume. The projection error is calculated by using reduced scattering coefficient of the true value (0.008mm^{-1}), and using an absorption coefficient value from 0 to 0.15mm^{-1} at a step of 0.002mm^{-1}, with respect to the forward data. Other than the global minimum, three local minimums can be observed where the iteration can stop incorrectly. This is the effect of varying only one parameter. More local minimums may occur when reconstructing more parameters.

When the TRUS is available, a conventional method of utilizing the spatial information would be the having the optical property of each ROI set as homogenous and updated simultaneously at each iteration. However, we have found that this conventional approach may not lead to reliable convergence for prostate imaging, which is attributed to the local-minimum problem. One example is given in Table 1 for the NIR array shown in Fig. 1(c). The prostate model is generated according to a previous work [27] (details of which are given later in Fig. 8), and a target of 10mm diameter is located at (40, 50, 15) which is 15 mm from the rectal surface. When the four ROIs including the rectum, the peri-prostate tissue, the prostate, and the prostate tumor are updated simultaneously from the same initial guess of μ_a =0.01mm^{-1} and μ_s' =1.0mm^{-1}, the iteration stops after 1 update due to the negative μ_a value obtained for the rectum wall. The iteration fails to continue apparently due to the local minimum issue.

Table 1. Results of simultaneously updating the 4 ROIs from the same initial guess

	μ_a (mm^{-1})				μ_s' (mm^{-1})			
Regions	Surrounding Tissue	Rectum Wall	Prostate	Tumor	Surrounding Tissue	Rectum Wall	Prostate	Tumor
Set value	0.002	0.01	0.06	0.02	0.8	1	1.27	1.6
Simultaneous Update	0.1216	**-0.008**	0.026	0.0215	1.1482	2.3602	0.6173	0.7073

The local minimum problem may be mitigated by a cascaded initial-guess approach or a hierarchical spatial *prior* method. The principle of this method is to first reconstruct the global optical properties of the entire volume, then to reconstruct the optical properties of prostate and rectum wall, and last to reconstruct the tumor lesion area. The 2nd and 3rd steps use the value obtained in the previous step as the initial guess of that specific ROI. Therefore at each step, the perturbation by a relatively smaller region is less influential and convergence of the iteration is better achieved. The detailed steps are shown in Fig. 7 and described in below:

#99968 - $15.00 USD Received 8 Aug 2008; revised 13 Oct 2008; accepted 14 Oct 2008; published 15 Oct 2008

(a) The first iterations assign an entirely homogenous imaging volume. In this round the initial projection error will be large and the convergence is most likely dominated by the global minimum. A single set of μ_a and μ_s' are determined using LM algorithm (Equ. 4) and will be used as the initial guess for the second step.

(b) The second iterations consider three regions, the rectum wall, peri-prostate tissue, and prostate, within the imaging volume. The calculation of the optical properties of these three ROIs start at the same initial guess as provided in step (a) but converges at different values.

(c) The values obtained from step (b) are used as the initial guess for the three ROIs but with a tumor added to the prostate. The tumor and the prostate take the same initial values as determined by the previous step. Each of the four ROIs (rectum wall, peri-prostate tissue, prostate, and tumor) converge to different end value.

The change of the overall projection error for the three steps is plotted in Fig. 7(d), and as evident, rapid and reliable convergence is observed. The hierarchy of the implementation of initial values for iteration is illustrated alternatively in Fig. 7(e).

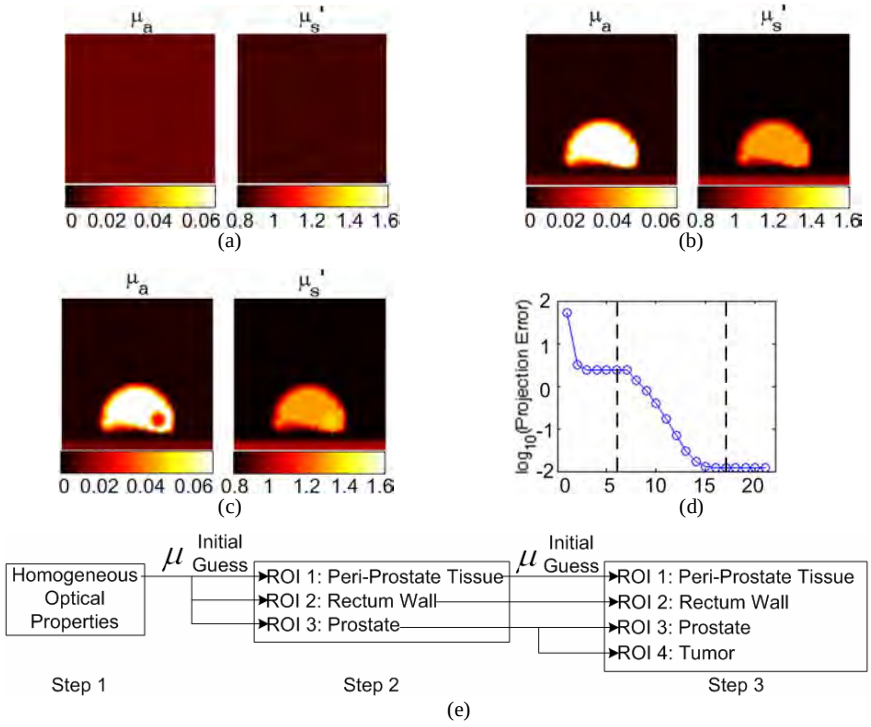

Fig. 7. The 3-step hierarchical reconstruction method (a) Step 1—one ROI for the entire volume; (b) step 2—three ROIs representing rectum wall, peri-prostate tissue, prostate; (c) step 3—four ROIs representing rectum wall, peri-prostate tissue, prostate, tumor; (d) change of the overall projection error, where the dash lines separate the converging of the three steps in (a)—(c); (e) block chart of the hierarchical initial guess assignment. [Unit in (a)---(c): mm^{-1}]

3.4 Validation of the hierarchical spatial prior method

Recently Li et al. reported simulation results for trans-rectal optical tomography in the context of using MRI anatomic information [27], which is referred to as "NIR/MRI" in the following text. The proposed hierarchical spatial *prior* method is evaluated using the same probe geometry, prostate geometry and the optical properties (also in Table 1) presented in the NIR/MRI work. The size and depth of the tumor for simulation were not specified in the NIR/MRI work, but a tumor with diameter of 10 mm and a depth of 15mm from the planar probe surface is considerably close to the one presented in the NIR/MRI paper. The NIR/MRI

#99968 - $15.00 USD Received 8 Aug 2008; revised 13 Oct 2008; accepted 14 Oct 2008; published 15 Oct 2008

work also indicated the challenge of reconstruction that may be due to the local minimum. The authors set an arbitrary searching range for the optical properties (μ_a:0-0.1 mm^{-1}, μ_s':0-2 mm^{-1}), and in 4 sets of the results, 3 of the tumor absorption value reached the limits and were stopped from further iteration, whereas the 4th value converged at a value more than 2 folds of the set value.

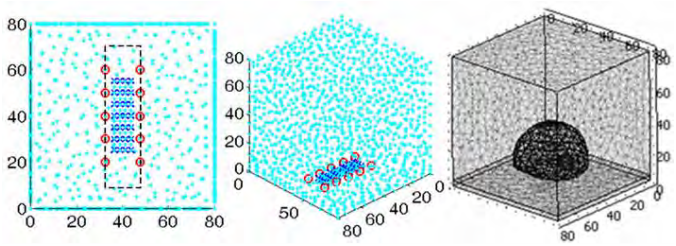

(a) (b) (c)

Fig. 8. The FEM mesh generated by following the geometry in NIR/MRI paper: (a) the geometry of the optodes, where the dash rectangle delineates the dimension of the NIR array that will be evaluated later for integration with US; (b) the 3-d view of the optodes and the imaging volume; (c) FEM containing the prostate and the tumor. [Unit: mm]

In the NIR/MRI work, a stand-alone trans-rectal NIR probe is simulated. The stand-alone NIR probe could have contained more optode channels incorporated than a TRUS-coupled NIR probe. In the NIR/MRI work, the best result is deducted for 10 sources and 28 detectors, which is used to evaluate the hierarchical method. The NIR probe geometry and the imaging domain of the NIR/MRI work are re-plotted in Fig. 8 for clarification and the hierarchical method is also preformed in transverse-view as did the NIR/MRI work. A 1% noise is also used in both methods assuring the consistency of measurement data.

Table 2. Reconstruction of a prostate tumor of negative contrast with respect to the prostate

	μ_a (mm^{-1})				μ_s' (mm^{-1})			
Regions	Surrounding Tissue	Rectum Wall	Prostate	Tumor	Surrounding Tissue	Rectum Wall	Prostate	Tumor
Set value	0.002	0.01	0.06	0.02	0.8	1	1.27	1.6
NIR/MRI	0.0025	0.01	0.0575	0.0448	0.8324	1	1.339	1.075
3-step	0.002	0.0099	0.06	0.0208	0.8012	1.0028	1.2824	1.3495

Table 3. Reconstruction of a prostate tumor of positive contrast with respect to the prostate

	μ_a (mm^{-1})				μ_s' (mm^{-1})			
Regions	Surrounding Tissue	Rectum Wall	Prostate	Tumor	Surrounding Tissue	Rectum Wall	Prostate	Tumor
Set value	0.002	0.01	0.006	0.02	0.8	1	1.27	1.6
3-step	0.0020	0.0100	0.0061	0.0163	0.7998	0.9997	1.2863	1.2434

Table 2 lists the results of the hierarchical method in comparison with those given in NIR/MRI paper. The hierarchical method (listed as "3-step" in the table), as expected, slightly outperforms the NIR/MRI method in terms of the accuracy of recovering optical properties. The results of recovering a target of positive absorption contrast are listed in Table 3 using the NIR/MRI probe geometry and our proposed 3-step method. The case of reconstructing a target with positive absorption contrast is not presented in the NIR/MRI paper, therefore only

#99968 - $15.00 USD Received 8 Aug 2008; revised 13 Oct 2008; accepted 14 Oct 2008; published 15 Oct 2008

the 3-step method is presented in Table 3 for comparison with the set values. In Table 3 the absorption coefficient of prostate is set much lower than that in Table 2 but the tumor optical properties are kept the same as those in Table 2. It is found that if the absorption of prostate in Table 3 is kept the same as in Table 2, the positive absorption target can hardly be reconstructed. The choice of lower prostate absorption is for testing our hierarchical method and the values may be much lower than the values reported of prostate [19-22]. It is noted that the reported values of prostate absorption coefficient vary in literatures where the measurements were taken either from *in vitro* tissue or from *in vivo* tissue using invasive methods. The absorption coefficient of intact or native prostate is in fact unknown, and is likely to be lower than the values reported in literatures.

The reconstructed images for targets of both negative and positive contrasts are listed in Fig. 9. These results demonstrate the capability of our hierarchical spatial *prior* method in reconstructing prostate lesion with either negative or positive absorption contrast.

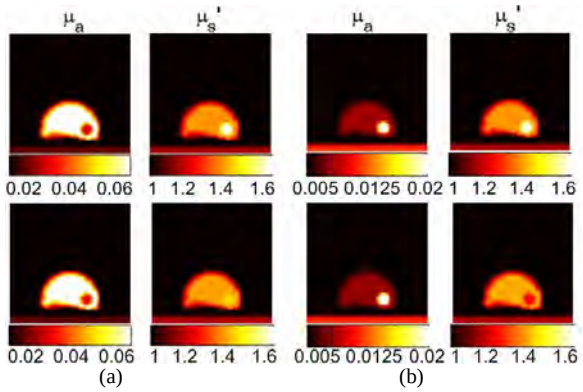

Fig. 9. Reconstructed images for a target with absorption contrast: (a) negative contrast (b) positive contrast. Top row: target setting; Bottom row: reconstructed image. [Unit: mm^{-1}]

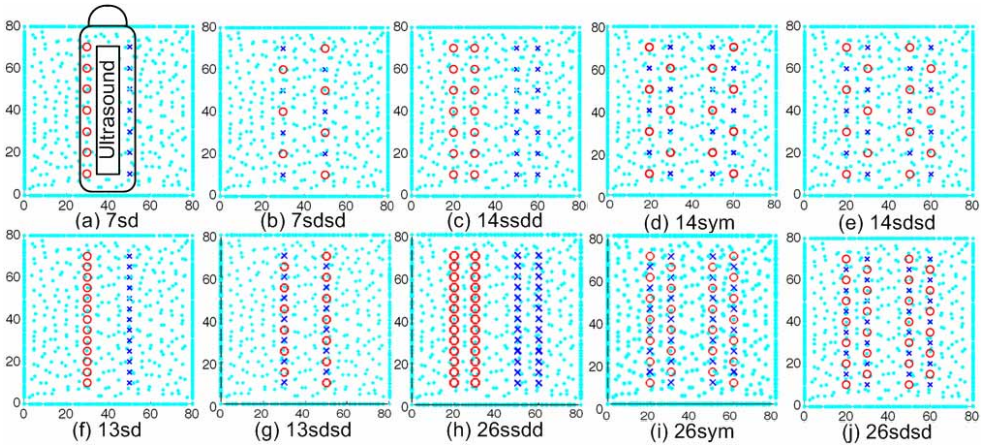

Fig. 10. NIR array designs. The dimension of the sagittal TRUS is shown in (a). The number of the Fig. caption denotes the number of opdotes on each lateral side of the TRUS as is depicted in (a). "sd" denotes one line of source and one line of detector; "ssdd" denotes two lines of source and two lines of detector; "sdsd" denotes mixed source/detector in one line; "sym" denotes symmetric distribution of the optodes with respect to the sagittal TRUS. [Unit: mm]

#99968 - $15.00 USD Received 8 Aug 2008; revised 13 Oct 2008; accepted 14 Oct 2008; published 15 Oct 2008

4. Assessment of NIR applicator designs for coupling NIR with TRUS

It is stated previously that an NIR array of dual-line geometry is feasible for concurrent trans-rectal NIR/US imaging considering the space limitation when coupling NIR with TRUS transducer for endo-rectal application. Based on the fabrication constraints, we have also suggested that each line array consist of 7 channels. The 7 channels could be exclusively source or detector as shown in Fig. 10(a), or interspersed source/detector as in Fig. 10(b). There are certainly a number of NIR geometries that can be coupled to TRUS sagittal transducer if not-limited by difficulties in fabrication or endo-rectal use. Compared with the geometry in Fig. 10(a), more channels could be added to each line-array as shown in Fig. 10(f), more lines can be added as shown in Fig. 10(c), or more lines and more channels added as in Fig. 10(h). More options are also listed in Fig. 10.

The array in Fig. 10(a) is the most desirable in terms of the fabrication easiness and endo-rectal applicability. The designs in Fig. 10(a), (b), (f) and (g) correspond to an NIR probe with a minimum lateral dimension of 20mm. The designs in Fig.10(c)-(e) and (h-j) correspond to NIR probe with a minimum 40mm lateral dimension which is not suitable for endo-rectal use. The geometries in Fig. 10(a)—(e) represent a 10mm spacing between the closest optodes, and the geometries in Fig. 10(f)—(j) require a 5mm spacing between the closest optodes. The smaller spacing in Fig. 10(f)—(j) will be challenging for fabrication considering the number of fiber channels and the side-firing configuration if the probe is to be integrated to TRUS probe unless the internal structural of the TRUS probe can be altered.

4.1 Sensitivity comparison

The sensitivities of all the 10 configurations of Fig. 10 are compared in Fig. 11. The mesh in Fig. 3 with homogeneous optical properties ($\mu_a = 0.01mm^{-1}$ and $\mu_s^{'} = 1.0mm^{-1}$) is used for the sensitivity calculation. The sensitivity in Fig. 10 is evaluated at the lines identical to those in Fig. 4. Only the absorption sensitivity is evaluated.

The observations made from Fig. 11 are: (1) increasing the spatial dimension of source-detector array generally improves the sensitivity; (2) increasing the number of source-detector pairs generally improves the sensitivity, as demonstrated previously [43]; (3) interspersed source-detector layout may have slightly wider lateral sensitivity but is comparable to non-dispersed source-detector layout for other imaging views; (4) the geometry of 26ssdd (the upper thicker line) has the best sensitivity feature among the 10 geometries, therefore it can be used as a standard to evaluate the simple geometry of 7sd (the lower thicker line).

4.2 Comparison between the 7sd design and the 26ssdd design

The 7sd design represents an array which is less challenging in fabrication and more practical for endo-rectal use. The 26ssdd geometry is impractical for endo-rectal application, difficult to fabricate, but has the best performance among the designs listed. It is shown in Fig. 11 that the sensitivity of 7sd design is approximately 10dB lower than that of 26ssdd in the specified longitudinal, lateral, and depth directions. Quantitative comparison of the performance is conducted between these two geometries for representative target variations. The optical properties listed in Table 2 (set values) are used for these comparisons.

#99968 - $15.00 USD Received 8 Aug 2008; revised 13 Oct 2008; accepted 14 Oct 2008; published 15 Oct 2008

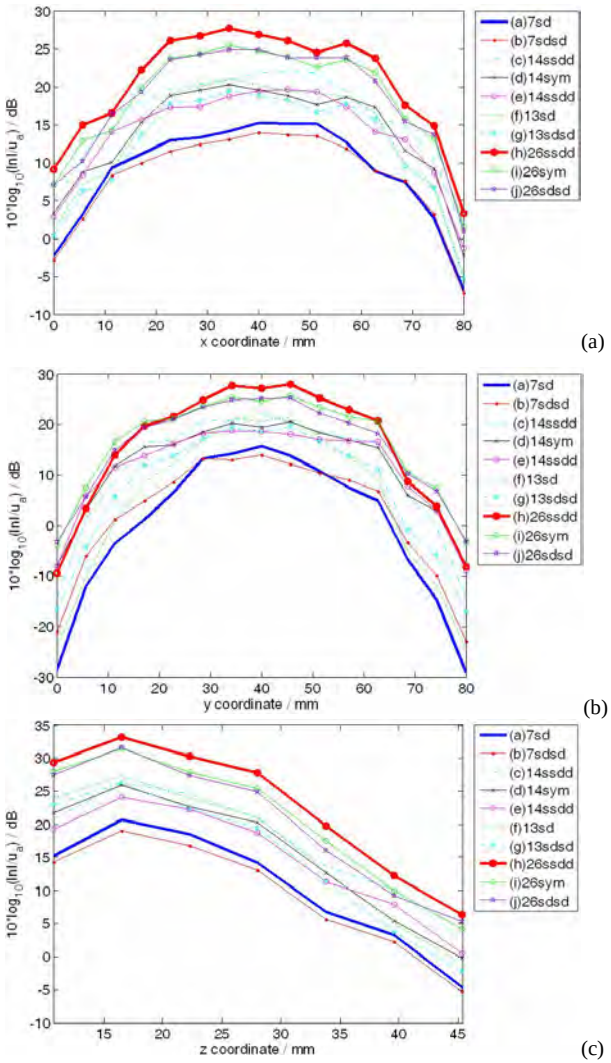

Fig. 11 Sensitivity comparison: (a) longitudinal direction, (b) lateral direction, (c) depth direction. The upper thicker line corresponds to the configuration (h) in Fig. 10, and the lower thicker line corresponds to the desired configuration (a) in Fig. 10.

4.2.1 Reconstruction accuracy versus target longitudinal location

A target of 10mm in diameter is placed at the middle-sagittal plane of y=40mm, z=26mm, and varied in longitudinal coordinates from x=25 to 55mm with a step of 5mm (Fig. 12(a)). The optical properties reconstructed by the two geometries are plotted versus the true values in Fig. 12(b) and (c). The optical properties recovered by 26ssdd and 7sd designs are close to each other at most of the longitudinal locations, but the 7sd design shows a larger variation in the recovered absorption contrast at x=30mm and x=50mm compared to other positions. This may be related to fewer source-detector pairs that contribute to the target detection when close to the boundary or the existence of any irregular elements in the mesh.

#99968 - $15.00 USD Received 8 Aug 2008; revised 13 Oct 2008; accepted 14 Oct 2008; published 15 Oct 2008

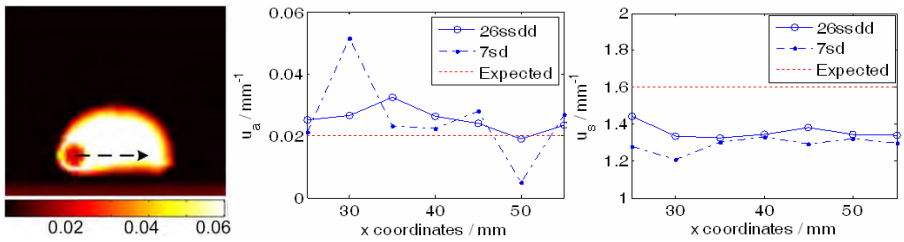

(a) (b) (c)

Fig. 12. Comparison of two geometries for a target varying in longitudinal location in the middle-sagittal plane: (a) illustration of the target location change [Unit: mm^{-1}]; (b) comparison of absorption coefficient reconstruction; (c) comparison of reduced scattering coefficient reconstruction

4.2.2 Reconstruction accuracy versus target depth

A target of 10mm in diameter is placed at the middle-sagittal plane at x=40mm, y=40mm, and the depth is varied from z=25 to 40mm at a step of 2.5mm (the last data point is simulated at z=39mm as at 40mm the target is out of the prostate) (Fig. 13(a)). The reconstructed optical properties are plotted in Fig. 13(b) and (c). The 26ssdd configuration outperforms the 7sd one again, however beyond z=30mm, both designs are incapable of recovering the absorption coefficient of the target from the prostate background. This depth limitation is related to the maximum span of the NIR array, the absorption coefficient of the prostate, and the size of the target. For a larger target with a diameter of 14mm, it is verified that the target may be resolved up to 36mm depth from the NIR array in comparison to 30mm for a target of 10mm diameter. A potentially smaller absorption coefficient of intact prostate may also increase the depth limit of target detection due to an increase in sensitivity.

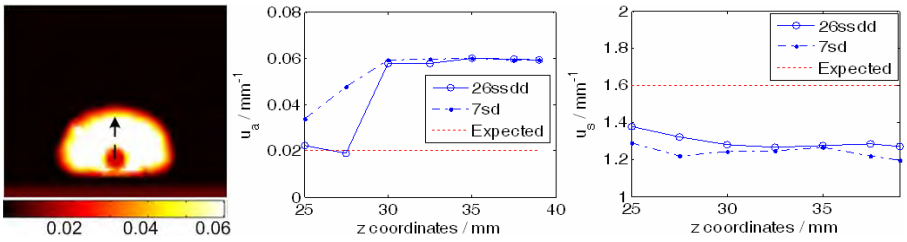

(a) (b) (c)

Fig. 13. Comparison of two geometries for a target varying in depth in the middle-sagittal plane: (a) illustration of the target location change [Unit: mm^{-1}]; (b) comparison of absorption coefficient reconstruction; (c) comparison of reduced scattering coefficient reconstruction

4.2.3 Reconstruction accuracy versus target size

A target is placed at middle-sagittal plane of x=40mm, y=40mm and z=26mm, and the diameter is varied from 4mm to 14mm with a step of 1mm. The target diameter change is illustrated in Fig. 14(a). The reconstructed optical properties are shown in Fig. 14(b) and (c). It is clear that the larger the target, the better the accuracy of reconstruction. The 26ssdd can recover the absorption contrast of the target when the diameter is greater than 6mm and the 7sd can recover the target for target diameter greater than 8mm.

These comparisons suggest that the 7sd design is inferior to the 26ssdd design, especially for the reconstruction of absorption properties. However, the accuracy of reconstructing scattering properties by the 7sd design is close to that of 26ssdd. Considering the challenges in trans-rectal NIR probing for coupling with TRUS, it is fair to develop and test the instrumentation with the 7sd design.

#99968 - $15.00 USD Received 8 Aug 2008; revised 13 Oct 2008; accepted 14 Oct 2008; published 15 Oct 2008

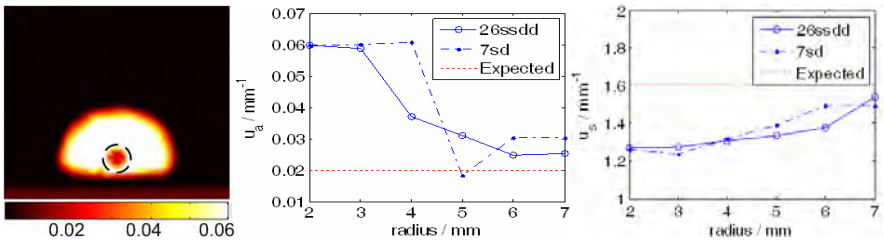

(a) (b) (c)

Fig. 14. Comparison of two geometries for a target varying in size in the middle-sagittal plane: (a) illustration of the target size change [Unit: mm^{-1}]; (b) comparison of absorption coefficient reconstruction; (c) comparison of reduced scattering coefficient reconstruction

4.3 Capability of recovering two targets by the 7sd design in sagittal plane

Capability of differentiating two targets is of particular relevance to prostate cancer imaging owing to the existence of secondary or multifocal tumors [44-46]. The multiple lesions may fall into the same TRUS field-of-view (FOV), or one falls outside the TRUS FOV. For the former case, the US *prior* could be used to guide NIR reconstruction of both targets. For the latter case, as NIR actually performs 3-D imaging it may interrogate the out-of-plane target and help redirecting the US to that target. In this section, however, we investigate only the former case of having two targets in the same sagittal plane. This requires implementing the multi-target location information in the last step of the hierarchical spatial *prior* routine. The following simulations are conducted with the 7sd probe design only.

4.3.1 Reconstruction of two targets located at the same depth in sagittal plane

Figure 15 shows two 10mm-diameter regions being added to the prostate, at coordinates (25, 40, 26) and (55, 40, 26), respectively. In Fig. 15(a) only one region has optical contrast, and in Fig. 15(b) both regions have optical contrasts. In both cases the optical contrast can be reconstructed with good accuracy, as is shown in Table 4. The μ_a of the target with true optical contrast is reconstructed within ±20% of the set value and μ_s' can be reconstructed within ±23% of the set values. The target with no optical contrast is reconstructed with some artifacts, nevertheless, the target with optical contrast can be easily differentiated from the one without.

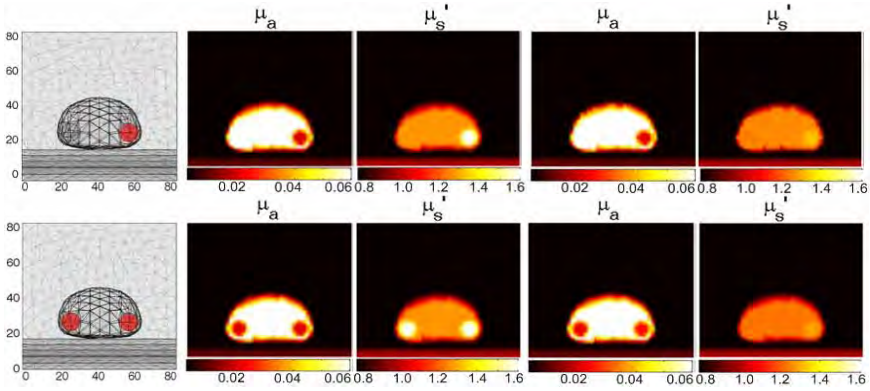

(a)

(b)

Fig. 15. Two suspicious regions at the same depth [Units: mm and mm^{-1}]

#99968 - $15.00 USD Received 8 Aug 2008; revised 13 Oct 2008; accepted 14 Oct 2008; published 15 Oct 2008

Table 4. Comparison of reconstructed optical properties (mm^{-1}) in Fig. 15

μ_a(mm^{-1})						
Fig.	Regions	Peri-prostate	Rectum	Prostate	Target 1	Target 2
(a)	Set value	0.002	0.01	0.06	0.06	0.02
	Reconstructed	0.002	0.0101	0.0601	0.0778	0.0208
(b)	Set value	0.002	0.01	0.06	0.02	0.02
	Reconstructed	0.002	0.01	0.0597	0.0207	0.024
μ_s' (mm^{-1})						
Fig.	Regions	Peri-prostate	Rectum	Prostate	Target 1	Target 2
(a)	Set value	0.8	1.0	1.27	1.27	1.6
	Reconstructed	0.7995	0.9935	1.261	1.2187	1.3216
(b)	Set value	0.8	1.0	1.27	1.6	1.6
	Reconstructed	0.8007	0.9953	1.2343	1.2302	1.2837

4.3.2 Reconstruction of two targets located at different depth in sagittal plane

Two targets of 10mm diameter are added in the prostate at coordinates of (25, 40, 28) and (55, 40, 24), respectively. Figure 16 shows the reconstructed images for the case of both targets having negative contrast and the reconstructed values are listed in Table 5.

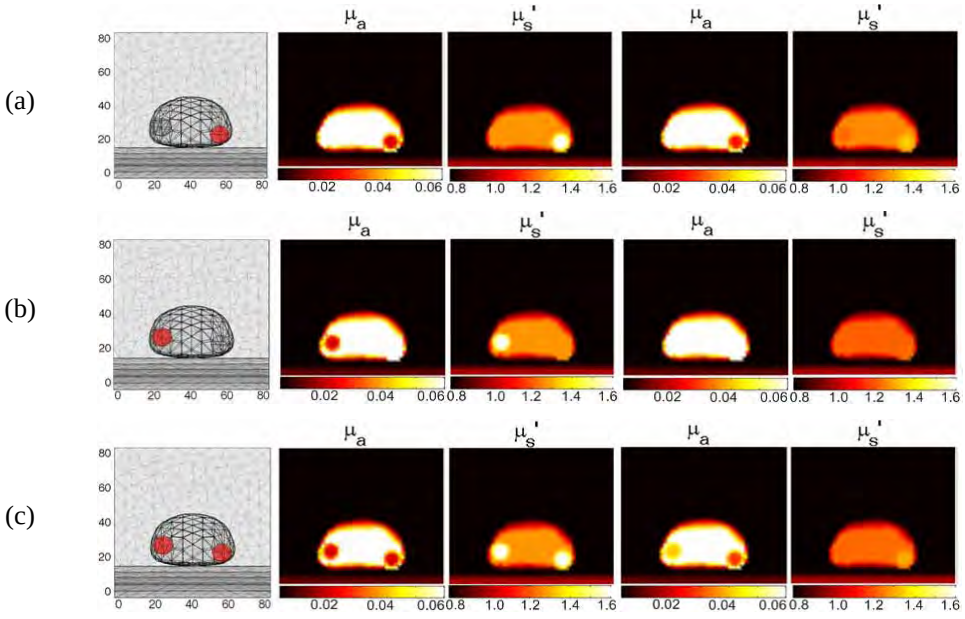

Fig. 16. Two targets at different depths: negative contrast cases [Unit: mm and mm^{-1}]

#99968 - $15.00 USD Received 8 Aug 2008; revised 13 Oct 2008; accepted 14 Oct 2008; published 15 Oct 2008

Table 5. Comparison of reconstructed optical properties (mm^{-1}) in Fig. 16

μ_a (mm^{-1})						
Fig.	Regions	Peri-prostate	Rectum	Prostate	Region 1	Region 2
(a)	Set value	0.002	0.01	0.06	0.06	0.02
	Reconstructed	0.002	0.01	0.0594	0.0674	0.0252
(b)	Set value	0.002	0.01	0.06	0.02	0.06
	Reconstructed	0.002	0.0101	0.0597	0.0592	0.0607
(c)	Set value	0.002	0.01	0.06	0.02	0.02
	Reconstructed	0.002	0.01	0.0596	0.0402	0.0276
μ_s' (mm^{-1})						
Fig.	Regions	Peri-prostate	Rectum	Prostate	Region 1	Region 2
(a)	Set value	0.8	1.0	1.27	1.27	1.6
	Reconstructed	0.8009	0.9977	1.2538	1.2167	1.3286
(b)	Set value	0.8	1.0	1.27	1.6	1.27
	Reconstructed	0.8015	0.9931	1.2102	1.2179	1.2083
(c)	Set value	0.8	1.0	1.27	1.6	1.6
	Reconstructed	0.8015	0.9956	1.2177	1.2024	1.2962

When the target is at a depth of 24mm, the μ_a and μ_s' can be reconstructed within ±20% and ±25% of the set values, respectively. However, a target at 28mm depth cannot be reconstructed. This is due to the prostate's high absorption coefficient of $0.06mm^{-1}$. When the prostate absoption coefficient is reduced to $0.006mm^{-1}$ which will provide positive optical contrast in the two target regions, both tartgets can be recovered as shown in Fig. 17 and Table 6. The μ_a of the target can be reconstructed within ±5% of the set value, while the μ_s' is still reconstructed within ±23% of the expected values.

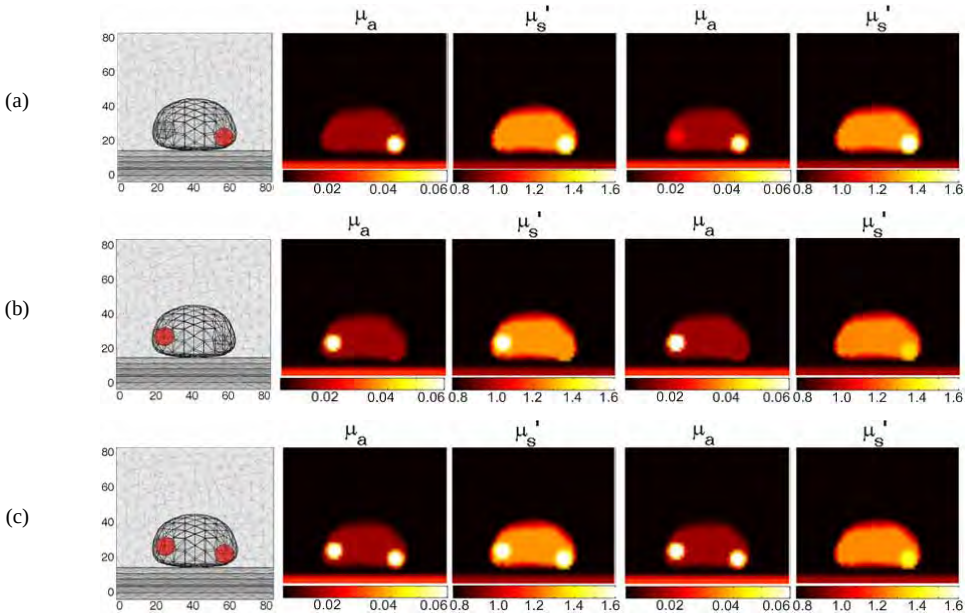

Fig. 17. Two targets at different depths: positive contrast cases [Unit: mm and mm^{-1}]

#99968 - $15.00 USD Received 8 Aug 2008; revised 13 Oct 2008; accepted 14 Oct 2008; published 15 Oct 2008

Table 6. Comparison of reconstructed optical properties (mm^{-1}) in Fig. 17

μ_a(mm^{-1})						
Fig.	Regions	Peri-prostate	Rectum	Prostate	Region 1	Region 2
(a)	Set value	0.002	0.01	0.006	0.006	0.02
	Reconstructed	0.002	0.0101	0.006	0.0083	0.0191
(b)	Set value	0.002	0.01	0.006	0.02	0.006
	Reconstructed	0.002	0.0101	0.006	0.0116	0.0058
(c)	Set value	0.002	0.01	0.006	0.02	0.02
	Reconstructed	0.002	0.0099	0.006	0.0208	0.0199
μ_s' (mm^{-1})						
Fig.	Regions	Peri-prostate	Rectum	Prostate	Region 1	Region 2
(a)	Set value	0.8	1.0	1.27	1.27	1.6
	Reconstructed	0.7993	0.9934	1.2637	1.2689	1.6722
(b)	Set value	0.8	1.0	1.27	1.6	1.27
	Reconstructed	0.8008	0.993	1.259	1.2402	1.3586
(c)	Set value	0.8	1.0	1.27	1.6	1.6
	Reconstructed	0.8049	0.9979	1.2576	1.2538	1.424

5. Discussions

The scope of this work is to investigate the feasibility of trans-rectal NIR tomography of the prostate in the context of concurrent imaging with sagittal TRUS using combined endo-rectal NIR/US probe. Recently there have been considerable interests on trans-rectal NIR tomography to augment existing imaging modalities which cannot be validated without the development of an endo-rectal NIR applicator. With an endo-rectal applicator, trans-rectal NIR tomography of the prostate can be performed stand-alone. However, without a position correlation with a real-time anatomic imaging modality such as TRUS, the images obtained by trans-rectal NIR would be difficult to interpret. Combining the NIR applicator with TRUS is a viable solution for accurate positioning of the NIR probe which would further enable using TRUS anatomy to guide the image reconstruction of trans-rectal NIR tomography. A variety of designs of NIR array for coupling with TRUS are possible, however, the NIR probe dimension and the number of NIR channels on the probe are quite limited.

The utilization of a hierarchical spatial *prior* is under the condition that the anatomic information of the prostate tumor can be extracted explicitly from TRUS. The prostate boundary can be well-delineated in TRUS, and so does a strongly hypo-echoic region indicating a suspicious lesion. This is when the NIR imaging may help determine if the suspicious lesion is malignant or benign based on optical contrasts [31]. However, since as many as 40% of the tumors may be seen as iso-echoic on TRUS, the utility or accuracy of this hierarchical imaging approach is hindered when TRUS images do not specify a suspicious region, or when it is difficult to define the spatial extent of a suspicion region in TRUS. Under these circumstances, the third step of the proposed hierarchical image reconstruction routine may be performed by element-based reconstruction within the prostate instead of region-based reconstruction for the prostate. Such approach is proven effective based on our initial investigations, but the accuracy and robustness may be affected by the depth-dependent sensitivity of the endo-rectal NIR probe and the relatively small number of source/detector channels that may be engineered on the NIR probe. More dedicated investigations could be conducted when the trans-rectal NIR/US approach is experimentally demonstrated. Prostate trans-rectal optical imaging is a relatively new area, thus it is imperative to focus the initial approach of trans-rectal NIR/US on characterizing lesions identifiable on TRUS.

#99968 - $15.00 USD Received 8 Aug 2008; revised 13 Oct 2008; accepted 14 Oct 2008; published 15 Oct 2008

Characterizing lesions marginally suspicious to TRUS or iso-echoic on TRUS may become less-challenging when the knowledge on trans-rectal NIR tomography of lesions most suspicious on TRUS is available.

The simulations studies presented here are largely based on setting the absorption properties of prostate at a high level of $0.06mm^{-1}$. This is significantly larger than that of breast tissue, and it is this parameter that dominates the detection depth of trans-rectal NIR tomography for the NIR array being discussed. Recent studies indicate that improved measurement condition, such as suppressing the bleeding interference, may lead to a lower absorption value of the prostate [22]. If the prostate is measured at its intact or native states by modalities such as trans-rectal optical tomography, an even lower absorption coefficient of the prostate may be obtained. A lower absorption coefficient will allow the same NIR array to detect deeper targets. In fact, a TRUS-coupled trans-rectal NIR tomography may not only help characterize lesions suspicious to TRUS, but also help quantify the optical properties of intact prostate that are unavailable so far.

6. Conclusions

The feasibility of imaging the prostate using a TRUS-coupled NIR applicator is investigated by simulation. A hierarchical iteration algorithm is first developed in order to incorporate the TRUS spatial *prior* more reliably into the trans-rectal NIR image reconstruction. This hierarchical reconstruction method uses a cascaded initial-guess approach to mitigate the local minimum problem common to NIR tomography reconstruction. It is shown that trans-rectal optical tomography based on this method is reliable. This hierarchical reconstruction method is then utilized to evaluate a number of designs of NIR applicator that may be integrated with a sagittal TRUS transducer. A configuration of the endo-rectal NIR applicator is proposed, that contains single line of optode on each lateral side of the sagittal TRUS transducer, with 20mm lateral separation between the two line arrays and 10 mm longitudinal spacing among the total 7 channels on each line-array. The performance of this simple NIR array design is evaluated for the imaging of single tumor target in prostate by comparing with a much more complicated design that is impractical for endo-rectal application. The simple NIR array design is also evaluated for imaging of two targets in the prostate. Results suggest that trans-rectal imaging of the prostate is feasible by coupling this simple NIR array with TRUS.

The following Part-II paper presents the instrumentation of a TRUS-coupled endo-rectal NIR array and demonstrates trans-rectal optical tomography of the prostate by the combined endo-rectal NIR/US applicator. The endo-rectal NIR array has incorporated the design suggested by Fig. 10(a). Concurrent trans-rectal imaging is acquired in the same sagittal plane by both US and NIR optical tomography. The real-time TRUS is used for accurate positioning of the endo-rectal NIR applicator and for guiding NIR image reconstruction with the spatial *a priori* information. Tests on phantoms and tissues using the combined trans-rectal NIR/US imager demonstrate that optical contrast may be recovered by endo-rectal NIR imaging only but with improved accuracy when the TRUS spatial *prior* is incorporated. Trans-rectal imaging of a healthy canine prostate *in situ* administered with tissue contrast validates the endo-rectal utility of the NIR/US probe as well as the hierarchical method for TRUS guided trans-rectal NIR image reconstruction.

Acknowledgments

This work has been supported by the Prostate Cancer Research Program of the U.S. Army Medical Research Acquisition Activity (USAMRAA), 820 Chandler Street, Fort Detrick MD, 21702-5014, through grant #W81XWH-07-1-0247. The content of the information does not necessarily reflect the position or the policy of the USARAA, and no official endorsement should be inferred. Comments and questions may be directed to Daqing Piao at daqing.piao@okstate.edu.

#99968 - $15.00 USD Received 8 Aug 2008; revised 13 Oct 2008; accepted 14 Oct 2008; published 15 Oct 2008

Trans-rectal ultrasound-coupled near-infrared optical tomography of the prostate Part II: Experimental demonstration

Zhen Jiang,[1] Daqing Piao,[1*] Guan Xu,[1] Jerry W. Ritchey,[2] G. Reed Holyoak,[3] Kenneth E. Bartels,[3] Charles F. Bunting,[1] Gennady Slobodov,[4] Jerzy S. Krasinki [1]

[1] *School of Electrical and Computer Engineering, Oklahoma State University, Stillwater, OK 74078 USA*
[2] *Department of Veterinary Pathobiology, Oklahoma State University, Stillwater, OK 74078 USA*
[3] *Department of Veterinary Clinical Sciences, Oklahoma State University, Stillwater, OK 74078 USA*
[4] *Department of Urology, University of Oklahoma Health Science Center, Oklahoma City, OK 73104 USA*
[*] *Corresponding author: daqing.piao@okstate.edu*

Abstract: We demonstrate trans-rectal optical tomography of the prostate using an endo-rectal near-infrared (NIR) applicator integrated with a trans-rectal ultrasound (TRUS) probe. The endo-rectal NIR applicator incorporated a design presented in our previously reported work. A continuous-wave NIR optical tomography system is combined with a commercial US scanner to form the dual-modality imager. Sagittal trans-rectal imaging is performed concurrently by endo-rectal NIR and TRUS. The TRUS ensures accurate positioning of the NIR applicator as well as guides NIR image reconstruction using the spatial prior of the target. The use of a condom, which is standard for TRUS, is found to have minimal effect on trans-rectal NIR imaging. Tests on avian tissues validates that NIR imaging can recover the absorption contrast of a target, and its accuracy is improved when the TRUS spatial prior is incorporated. Trans-rectal NIR/US imaging of a healthy canine prostate in situ is reported.

OCIS codes: (170.3880) Medical and biological imaging; (170.6960) Tomography; (170.7230) Urology; (170.1610) Clinical applications.

References and links

1. G. Xu, D. Piao, C. H. Musgrove, C. F. Bunting, and H. Dehghani, "Trans-rectal ultrasound coupled trans-rectal optical tomography of the prostate Part I: Simulations," Accepted for publication in Opt. Express.
2. G. D. Grossfeld and P. R. Carroll, "Prostate cancer early detection: a clinical perspective," Epidemiol. Rev. **23**, 173-80 (2001).
3. A. C. Loch, A. Bannowsky, L. Baeurle, B. Grabski, B. König, G. Flier, O. Schmitz-Krause, U. Paul, and T. Loch, "Technical and anatomical essentials for transrectal ultrasound of the prostate," World J. Urol. **25**, 361-366 (2007).
4. C. R. Porter, "Does the number of prostate biopsies performed affect the nature of the cancer identified?" Nat. Clin. Pract. Urol. **4**, 132-133 (2007).
5. V. Scattoni, A. Zlotta, R. Montironi, C. Schulman, P. Rigatti, and F. Montorsi, "Extended and saturation prostatic biopsy in the diagnosis and characterisation of prostate cancer: a critical analysis of the literature," Eur. Urol. **52**,1309-1322 (2007).
6. B. Spajic, H. Eupic, D. Tomas, G. Stimac, B. Kruslin, and O. Kraus, "The incidence of hyperechoic prostate cancer in transrectal ultrasound-guided biopsy specimens," Urology **70**, 734-737 (2007).
7. K. Shinohara, T. M. Wheeler, and P. T. Scardino, "The appearance of prostate cancer on transrectal ultrasonography: correlation of imaging and pathological examinations," J. Urol. **142**, 76-82 (1989).
8. B. Tromberg, J. Coquoz, O. Fishkin, J. B. Pham, T. Anderson, E. R. Butler, J. Cahn, M. Gross, J. D. Venugopalan, and D. Pham, "Non-invasive measurements of breast tissue optical properties using frequency-domain photon migration," Phil. Trans. R. Soc. Lond. B **352**, 661-668 (1997).
9. B. W. Pogue, S. P. Poplack, T. O. McBride, W. A. Wells, K. S. Osterman, U. L. Osterberg, and K. D. Paulsen," Quantitative hemoglobin tomography with diffuse near-infrared spectroscopy: pilot results in the breast," Radiology **218**, 261-266 (2001).

#99971 - $15.00 USD Received 8 Aug 2008; revised 13 Oct 2008; accepted 14 Oct 2008; published 15 Oct 2008

10. V. Ntziachristos and B. Chance, "Probing physiology and molecular function using optical imaging: applications to breast cancer," Breast Cancer Res. **3**, 41-46 (2001).
11. R. Choe, A. Corlu, K. Lee, T. Durduran, S. D. Konecky, M. Grosicka-Koptyra, S. R. Arridge, B. J. Czerniecki, D. L. Fraker, A. DeMichele, B. Chance, M. A. Rosen, and A. G. Yodh, "Diffuse optical tomography of breast cancer during neoadjuvant chemotherapy: a case study with comparison to MRI," Med. Phys. **32**, 1128-1139 (2005).
12. M. A. Franceschini, K. T. Moesta, S. Fantini, G. Gaida, E. Gratton, H. Jess, W. W. Mantulin, M. Seeber, P. M. Schlag, and M. Kaschke, "Frequency-domain techniques enhance optical mammography: initial clinical results," Proc. Nat. Acad. Sci. USA **94**, 6468-6473 (1997).
13. Q. Zhu, E. B. Cronin, A. A. Currier, H. S. Vine, M. Huang, N. Chen, and C. Xu, "Benign versus malignant breast masses: optical differentiation with US-guided optical imaging reconstruction," Radiology **237**, 57-66 (2005).
14. B. J. Tromberg, B. W. Pogue, K. D. Paulsen, A. G. Yodh, D. A. Boas, and A. E. Cerussi, "Assessing the future of diffuse optical imaging technologies for breast cancer management," Med Phys. **35**, 2443-51 (2008).
15. J. H. Ali , W. B. Wang , M. Zevallos, and R. R. Alfano , "Near infrared spectroscopy and imaging to probe differences in water content in normal and cancer human prostate tissues," Technol. Cancer Res. Treat. **3**, 491-497 (2004).
16. M. R. Arnfield , J. D. Chapman, J. Tulip, M. C. Fenning, and M. S. McPhee, "Optical properties of experimental prostate tumors in vivo," Photochem. Photobiol. **57**, 306-311 (1993).
17. T. C. Zhu, A. Dimofte, J. C. Finlay, D. Stripp, T. Busch, J. Miles, R. Whittington, S. B. Malkowicz, Z. Tochner, E. Glatstein, and S. M. Hahn, "Optical properties of human prostate at 732 nm measured in mediated photodynamic therapy," Photochem. Photobiol. **81**, 96-105 (2005).
18. T. Svensson, S. Andersson-Engels, M. Einarsdóttír, and K. Svanberg, "In vivo optical characterization of human prostate tissue using near-infrared time-resolved spectroscopy," J. Biomed. Opt. **12**, 014022 (2007).
19. M. Goel, H. Radhakrishnan, H. Liu, et al. "Application of near infrared multi-spectral CCD imager system to determine the hemodynamic changes in prostate tumor," in *OSA Biomedical Topical Meetings* (Optical Society of America, 2006), paper SH10.
20. X. Zhou and T. C. Zhu, "Image reconstruction of continuous wave diffuse optical tomography (DOT) of human prostate," in *Proc. the COMSOL Users Conference* (2006) .
21. S. L. Jacques and M. Motamedi, "Tomographic needles and catheters for optical imaging of prostatic cancer," Proc. SPIE **2395**, 111-118 (1995).
22. C. Li, R. Liengsawangwong, H. Choi, and R. Cheung , "Using *a priori* structural information from magnetic resonance imaging to investigate the feasibility of prostate diffuse optical tomography and spectroscopy: a simulation study," Med. Phys. **34**, 266-274 (2007).
23. H. Dehghani, C. M. Carpenter, P. K. Yalavarthy, B. W. Pogue, and J. P. Culver, "Structural *a priori* information in near-infrared optical tomography," Proc. SPIE **6431**, 64310B1-7 (2007).
24. M. J. Holboke, B. J. Tromberg, X. Li, N. Shah, J. Fishkin, D. Kidney, J. Butler, B. Chance, and A. G. Yodh, "Three-dimensional diffuse optical mammography with ultrasound localization in a human subject," J. Biomed Opt. **5,** 237-247 (2000).
25. A. Li, E. L. Miller, M. E. Kilmer, T. J. Brukilacchio, T. Chaves, J. Stott, Q. Zhang, T. Wu, M. Chorlton, R. H. Moore, D. B. Kopans, and D. A. Boas, "Tomographic optical breast imaging guided by three-dimensional mammography," Appl. Opt. **42**, 5181-90 (2003).
26. M. Guven, B. Yazici, X. Intes, and B. Chance, "Diffuse optical tomography with a priori anatomical information," Phys. Med. Biol. **50**, 2837-58 (2005).
27. D. Piao, H. Xie. W. Zhang, J. S. Kransinski, G. Zhang, H. Dehghani, and B. W. Pogue, "Endoscopic, rapid near-infrared optical tomography," Opt. Lett. **31**, 2876-2878 (2006).
28. N. Iftimia and H. Jiang, "Quantitative optical image reconstruction of turbid media by use of direct-current measurements," Appl. Opt. **39**, 5256-5261 (2000).
29. V. Ntziachristos, "Concurrent diffuse optical tomography, spectroscopy and magnetic resonance imaging of breast cancer," PhD Dissertation, University of Pennsylvania, Philadelphia, PA, 15-16 (2000).
30. R. C. Haskell, L. O. Svaasand, T. T. Tsay, T. C. Feng, M. S. McAdams, B. J. Tromberg, "Boundary conditions for the diffusion equation in radiative transfer," J. Opt. Soc. Am. A. **11**, 2727-41 (1994).
31. R. Aronson, "Boundary conditions for diffusion of light," J. Opt. Soc. Am. A. 12, 2532-9 (1995).
32. D. Piao and B. W. Pogue, "Rapid near-infrared tomography for hemodynamic imaging using a low coherence wideband light source", J. Biomed. Opt. **12**, 014016 (2007).
33. H. Xu, "MRI-coupled broadband near-infrared tomography for small animal brain studies," Ph.D. Dissertation, Dartmouth College, Hanover, NH, 36–36 (2005).
34. S. Arridge, M. Cope, and D. Delpy, "The theoretical basis for the determination of optical pathlengths in tissue: temporal and frequency analysis," Phys. Med. Biol. Vol. 37, No **7**, 1531-1560 (1992).
35. W. F. Cheong, S. A. Prahl, and A. J. Welch, "A review of the optical properties of biological tissues," IEEE J. Quantum Electron. **26**, 2166-2185 (1990).
36. H. Xie, "Dual-spectral endoscopic near-infrared optical tomography for assessment of hemoglobin concentration and oxygen saturation," Master Thesis, Oklahoma State University (2008).

#99971 - $15.00 USD Received 8 Aug 2008; revised 13 Oct 2008; accepted 14 Oct 2008; published 15 Oct 2008

37. A. H. Hielscher, R. E. Alcouffe, and R. L. Barbour, "Comparison of finite-difference transport and diffusion calculations for photon migration in homogeneous and heterogeneous tissues," Phys. Med. Biol. **43**, 1285-302 (1998).
38. Z. Yuan, Q. Zhang, E. Sobel, and H. Jiang, "Three-dimensional diffuse optical tomography of osteoarthritis: initial results in the finger joints," J. Biomed. Opt. **12**, 034001 (2007).
39. A. Custo, W. M. Wells 3rd, A. H. Barnett, E. M. Hillman, and D. A. Boas, "Effective scattering coefficient of the cerebral spinal fluid in adult head models for diffuse optical imaging," Appl. Opt. **45**, 4747-55 (2006).
40. C. Xu, Q. Zhu, "Estimation of chest-wall-induced diffused wave distortion with the assistance of ultrasound," Appl. Opt. **44**, 4255-64 (2005).

1. Introduction

This is a continuation of previously reported work [1] whose objective is to demonstrate the feasibility of trans-rectal ultrasound (TRUS) coupled trans-rectal near-infrared (NIR) tomography of the prostate.

Prostate cancer screening is performed by measurement of serum prostate-specific antigen (PSA), digital rectal examination (DRE), and a combination of these tests [2]. When the suspicion of prostate cancer is raised by abnormal PSA and/or DRE, the diagnosis is made by biopsy performed under US guidance (most often by TRUS). Biopsy is also used to confirm neoplastic lesions and to determine their clinical significance for treatment planning [3]. The current standard of prostate biopsy is to routinely use 10 to 12 cores of tissue obtained throughout the prostate for the initial assessment [4]. It should be noted that the majority of biopsies are found to be negative, and in men with persistent suspicion of prostate cancer after several negative biopsies, more extensive protocols (>12 cores) up to saturation biopsy (24 cores) represent a necessary diagnostic procedure [5]. TRUS-guided prostate biopsy is performed following a "systematic sampling" strategy because less than 60% of neoplastic lesions appear hypoechoic on TRUS while most of the remaining neoplastic lesions appear isoechoic [6]. Also, TRUS does not reliably differentiate neoplastic from benign tumors [7].

We have suggested [1] that the accuracy of prostate biopsy may be improved if the TRUS imaging could be augmented with a functional or "surrogate" marker of a prostate tumor. Based on decades of research on cancer imaging [8-14] and prostate measurements [15-22], near-infrared (NIR) tomography, being non-ionizing and minimally-invasive similar to TRUS, has the potential of providing such functional or "surrogate" markers of prostate tumors. NIR optical tomography, if carried out trans-rectally, may improve the specificity of TRUS imaging such that prostate biopsies could be directed to the most suspicious lesions.

In the first paper of this two part series [1] we discussed the challenges of trans-rectal optical tomography, particularly the fabrication of an endo-rectal NIR applicator for integrating with TRUS. Specifically, since a TRUS-coupled endo-rectal NIR applicator requires deploying many optodes in a very limited space. We suggested [1] that arranging optodes longitudinally is feasible and the configuration would allow interrogating deep prostate tissue in a sagittal imaging geometry. Coupling endo-rectal NIR to TRUS obtains functional information otherwise unavailable from TRUS alone. Coupling endo-rectal NIR to TRUS also renders accurate and real-time anatomic information from TRUS with which to correlate NIR. The structural information obtained from TRUS may further provide the needed spatial *prior* [14, 23-26] to improve the accuracy of NIR image reconstruction. In that initial paper we further suggested [1] an array configuration of the endo-rectal NIR applicator for direct integration with a TRUS transducer.

The work presented here details the development of an endo-rectal NIR probe built on our previous work [1] and demonstrates TRUS-coupled trans-rectal NIR tomography of the prostate. It validates that trans-rectal NIR tomography helps characterize a target identified by TRUS, and the accuracy of quantitative imaging of a target by trans-rectal NIR tomography is improved when the TRUS spatial *prior* is incorporated. TRUS-coupled trans-rectal optical

#99971 - $15.00 USD Received 8 Aug 2008; revised 13 Oct 2008; accepted 14 Oct 2008; published 15 Oct 2008

tomography of a canine prostate *in situ* is performed, indicating the utility of this approach for *in vivo* imaging.

2. Instrumentation

2.1 Development of a TRUS-coupled NIR applicator for trans-rectal optical tomography

The integrated sagittal-imaging trans-rectal NIR/US applicator consists of a custom-built NIR probe and a commercial bi-plane TRUS transducer, as shown in Fig. 1. The bi-plane TRUS probe is equipped with a proximal 7.5MHz sagittal-imaging transducer and a distal 5MHz transverse-imaging transducer. The sagittal TRUS transducer occupies a 60mm×10mm window. The diameters of the sagittal and transverse imaging sections of the TRUS probe are 18mm and 20mm, respectively. Adapting to the un-even TRUS cross-section, the NIR applicator is fabricated to a cap-shape and attached to the TRUS probe (Fig. 1(a) ~(e)). The NIR array substrate was machined from a black polycarbonate material to minimize the surface reflection. This substrate was then connected to an aluminum bracket and securely fastened to the TRUS handle using a bottom clamp. The rectangular TRUS handle (Fig. 1(f) ~(g)) ensured aligning the NIR applicator to the TRUS transducer. A slot of 60mm×10mm was opened up in the NIR applicator to expose the sagittal TRUS transducer.

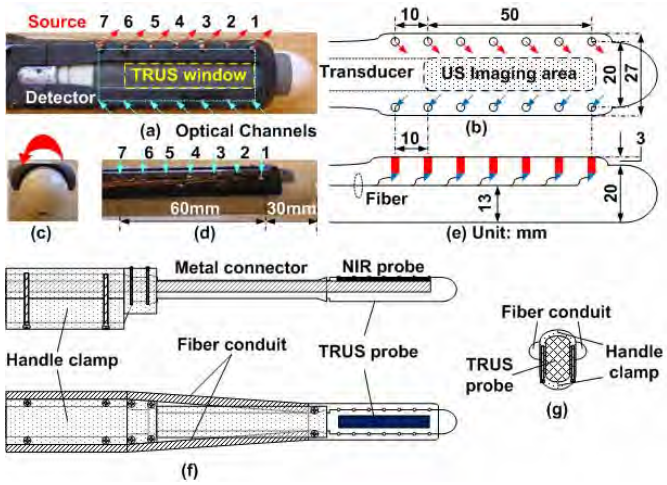

Fig. 1. The combined trans-rectal NIR/US probe: (a) top-view; (b) top-view dimension; (c) front-view; (d) side-view; (e) side-view dimension; (f) side and top views of the NIR/US alignment method; (g) rear-view of the NIR/US alignment method.

The geometry of the NIR array follows the design we previously described [1]. The NIR probe consists of two linear-arrays, one for the source and the other for the detector, separated by 20mm and placed on each side of the sagittal TRUS transducer. Each linear-array consists of 7 channels spaced 10mm apart and covering 60mm in length. The 60mm long NIR array is aligned precisely with the 60mm window of the sagittal TRUS transducer. The sagittal TRUS transducer actually has a longitudinal field-of-view (FOV) of 50mm. Therefore the NIR channels 1 to 6 on each linear-array match with the length of the sagittal TRUS transducer, and the NIR channel 7 of each linear-array is displaced longitudinally 10mm from the sagittal TRUS transducer.

A metal-coated 600μm-core diameter fiber (Oxford Electronics) is chosen for its thin cladding and mechanical strength. The 7 fibers of each linear-array are packaged into one groove of ~4mm×4mm in cross-section formed in the black substrate. Bending the fiber inside the small groove for side-firing at the probe surface is impractical. Instead micro-optics components are used for deflecting the light side-ways. As shown in Fig. 2, each source channel includes 2 gradient-index (GRIN) lenses and 1 prism attached to the fiber while each

#99971 - $15.00 USD Received 8 Aug 2008; revised 13 Oct 2008; accepted 14 Oct 2008; published 15 Oct 2008

detector channel has 1 GRIN lens and 1 prism attached to the fiber. The GRIN lens (Newport Corporation) has a pitch of 0.25, a diameter of 1mm, a length of 2.61mm, and a numerical aperture of 0.46. The prism is a coated 1mm right angle micro-prism (Tower Optics). Each fiber is polished and epoxied to a prism and a GRIN lens is attached to the other side of the micro-prism for illumination and detection at the probe surface. Each source channel has one GRIN lens attached to the proximal end of the fiber for coupling the emission of a superluminescent diode (SLD) using a spread-spectral-encoding configuration [27]. It is shown by ZEMAX (ZEMAX Development Co.) simulation that for collimated incident beam using a GRIN lens and a prism gives 38% more coupling than without the GRIN lens for a micro-prism of 80% reflection at NIR band that is typical for enhanced aluminum coating. A coupling efficiency improvement of 10%~15% is observed experimentally from the completed fiber channels. The overall coupling efficiencies of the 14 home-assembled fiber channels are shown in Table 1. The coupling efficiency is at about 50%, which could be improved if the assembly can be made more precise.

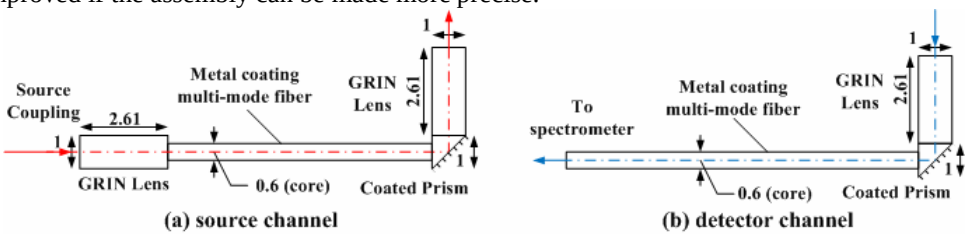

Fig. 2. Micro-optical configurations: (a) source channel; (b) detector channel. Unit: mm

Table 1. Measured coupling efficiency of the source/detector fiber channels

Source channels	s1	s2	s3	s4	s5	s6	s7
Coupling efficiency	46%	48%	49%	49%	51%	43%	49%
Detector channels	d1	d2	d3	d4	d5	d6	d7
Coupling efficiency	54%	48%	49%	51%	53%	52%	50%

2.2 Development of a continuous-wave NIR imager for coupling with US

The combined trans-rectal NIR/US imager is schematically illustrated in Fig. 3(a) and the photograph is given in Fig. 3(b). The US scanner is an ALOKA SSD-900V portable machine. The US images are transferred to the main computer of the combined imager by a PCI image acquisition card (National Instruments PCI-1405). The NIR imager uses a custom-designed superluminescent diode (SLD) (Superlumdiodes Inc.) that is pigtailed to a multi-mode fiber

#99971 - $15.00 USD Received 8 Aug 2008; revised 13 Oct 2008; accepted 14 Oct 2008; published 15 Oct 2008

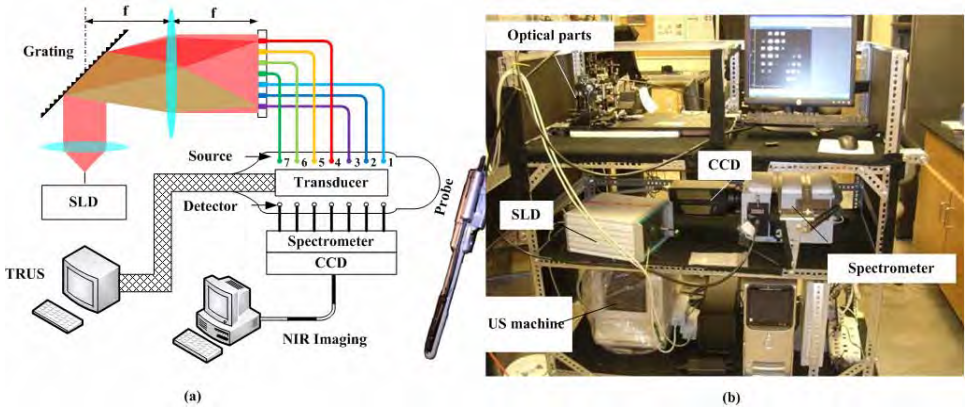

Fig. 3. The combined trans-rectal NIR/US system: (a) System diagram; (b) Photo of the system on a custom designed three-layer cart.

and delivers 100mW of 840nm NIR light with 14.2nm FWHM bandwidth. The SLD output beam is dispersed by a 1200 groves/mm grating and collimated unto linearly aligned 7 fibers connecting to the source channels on NIR applicator. NIR light with slightly different wavelengths are coupled to the 7 fibers to form a spread-spectral-encoding of the source channels [27]. The remitted lights collected by the 7 detection channels are coupled to a spectrometer (Acton Research). The signal corresponding to the individual source channels are discriminated horizontally by the spectrometer. The signals corresponding to the individual detector channels are differentiated vertically based on the position of the detection channels on the spectrometer entrance slit. A 16-bit intensified CCD camera (Princeton Instruments) acquires a complete set of NIR imaging data. The exposure time for one frame of data is in the range of 100s milliseconds, depending on the medium being imaged. The NIR system resides on a custom-built cart that also houses the US scanner.

The CCD has a maximum dynamic range of 48dB, which may not be sufficient to accommodate the full dynamic range of the signals when a medium is highly absorptive, as the minimum and maximum source-detector distances of the trans-rectal NIR array are 20mm and 63mm, respectively. Fortunately, the layout of the dual-line NIR array leads to lesser signal dynamic range for the light illuminated from the sources at the middle portion of the array than the ones at the edges of the array. Reducing the total dynamic range of the signal is possible by proper use of the Gaussian spectrum of the SLD source. The actual light coupling configuration is given in Fig. 4(a), where the stronger spectral components are coupled to the peripheral NIR channels (such as 1 and 7), and the weaker spectral components are coupled to the middle NIR channels (such as 3-5). Comparing with the configuration of coupling the uniform light to all 7 source channels, the strategy in Fig. 4(a) offers a 15dB reduction of the overall signal dynamic range for a medium of 0.0023mm^{-1} absorption coefficient and 1.0mm^{-1} reduced scattering coefficient (equivalent to a 1% Intralipid solution).

#99971 - $15.00 USD Received 8 Aug 2008; revised 13 Oct 2008; accepted 14 Oct 2008; published 15 Oct 2008

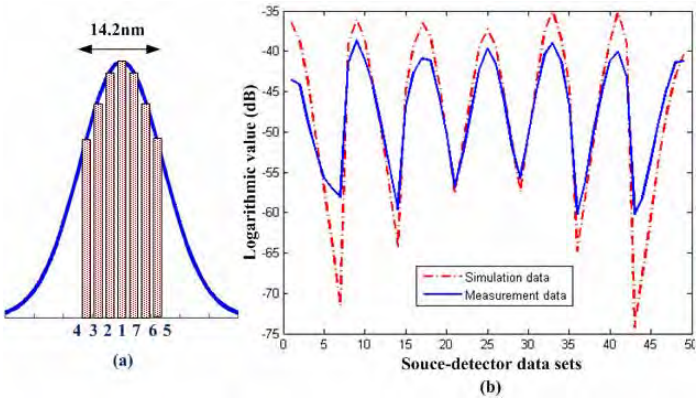

Fig. 4. Source coupling sequence with the Gaussian-spectrum (a), and the received signal dynamic range compared with the case when source channels have even intensities (b).

3. NIR image reconstruction based on continuous-wave data

The steady-state diffusion equation for a photon density U at position $\vec{r}$ can be stated as [28]

$$\nabla \cdot D(\vec{r})\nabla U(\vec{r}) - \mu_a(\vec{r}) \cdot U(\vec{r}) = -S(\vec{r}) \tag{1}$$

where μ_a is the absorption coefficient, $D = \left[3(\mu_a + \mu_s')\right]^{-1}$ is the diffusion coefficient with μ_s' being the reduced scattering coefficient, and S is a source term. For a collimated source and a detector at a semi-infinite boundary, the diffuse reflectance may be described by [29]

$$U(\rho) = \frac{S}{4\pi D\rho^2}\left[-4\left(\mu_a / D\right)^{1/2}\left(z_b^2 + z_b/\mu_s'\right)\right] \cdot \exp\left[-\left(\mu_a / D\right)^{1/2}\rho\right] \tag{2}$$

where ρ is the source-detector distance, and z_b is a length term determined by the refractive index mismatch on the boundary [30, 31].

The raw data acquired by CCD is show in Fig. 5(a). If the SLD spectral components were coupled orderly to the source channels from 1 to 7, the higher intensity signals would have been located along a diagonal line in the CCD acquired image [27, 32]. The modified source coupling configuration described in Fig. 4 leads to the pattern of diagonal-shifted high-intensity signals as shown in Fig. 5(a).

The signal non-uniformity among all source-detector pairs is calibrated using the 1% bulk Intralipid solution based on the linear relationship between $\ln\left[\rho^2 U(\rho)\right]$ and ρ derived from Eq. (2), as shown in Fig. 5(b). One calibrated data set corresponding to the complete 7×7 source-detector pairs is displayed in (c) in comparison to the non-calibrated one.

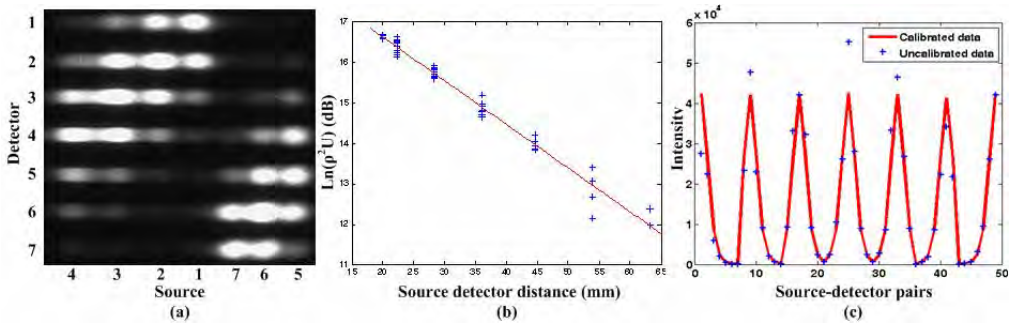

Fig. 5. Data Calibration: (a) raw CCD data; (b) linear fitting of the measurement data based on the semi-infinite model; (c) calibrated data for the signal corresponding to the 49 source-detector pairs.

#99971 - $15.00 USD Received 8 Aug 2008; revised 13 Oct 2008; accepted 14 Oct 2008; published 15 Oct 2008

Recent studies have demonstrated that absorption and reduced scattering coefficients can be reconstructed quantitatively from steady-state measurements, by updating the D and μ_a distributions to minimize a weighted sum of the squared difference between computed and measured data [28]. The method is equivalent to performing the same minimization by mapping the DC signal to frequency-domain [33], which we utilize in the reconstruction.

The frequency-domain diffusion equation [34]

$$\nabla \cdot D(\vec{r})\nabla U(\vec{r},\omega) - \left(\mu_a(\vec{r}) + \frac{i\omega}{c}\right)\cdot U(\vec{r},\omega) = -S(\vec{r},\omega) \tag{3}$$

where ω is the source modulation frequency, is used to map the Equ. (2) using finite-element discretization by setting ω to a small value of 0.1Hz. The optical properties are updated by using

$$x_{k+1} = x_k + \alpha \cdot [J^T(x_k)J(x_k) + \lambda I]^{-1} J^T(x_k)\Delta v(x_k) \tag{4}$$

where x is the parameters to be optimized, J is the Jacobian derived from Equ. (3), Δv is the forward projection error, λ is a penalty or regularization term. A small damping factor α in the range of (0, 1) is introduced to stabilize the convergence [1].

Both absorption and reduced scattering coefficients can be reconstructed from the DC measurement, but it is noted that it appears to be generally more difficult for the scattering image to be reconstructed than the absorption image [28]. In this work we focus on recovering targets having absorption contrast to demonstrate the feasibility of TRUS-coupled endo-rectal NIR optical tomography.

The geometry used for image reconstruction is illustrated in Fig. 6. The NIR image reconstruction uses a 3-dimensional mesh representing 80×40×60mm^3. The TRUS sagittal imaging is performed at the mid-plane of the NIR mesh. The TRUS image is used to develop a mesh with target spatial information. The NIR image is reconstructed in 3-dimension, and displayed at the mid-sagittal plane to correlate with TRUS image. The image reconstruction typically takes ~10 minutes on a 3.0GHz Pentium(R) 4 PC for 10 iterations.

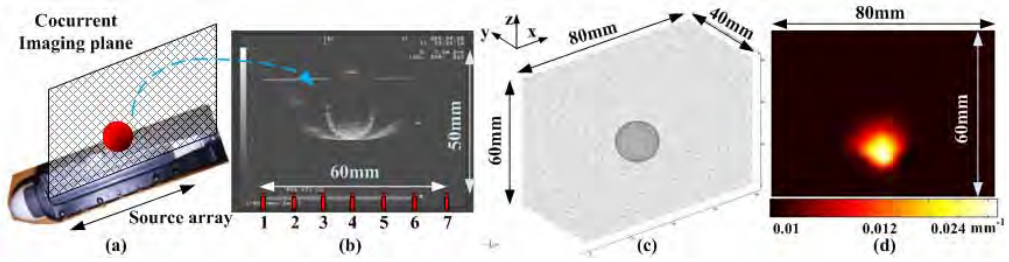

Fig. 6. NIR Imaging geometry: (a) NIR arrays are parallel and symmetric to the TRUS sagittal plane; (b) the positions of NIR channels with respect to the TRUS image; (c) mesh for NIR image reconstruction generated by use of TRUS image; (d) absorption image reconstructed from a simulation data for an absorbing target.

4. Performance evaluation for the TRUS-coupled trans-rectal NIR tomography

4.1 Imaging single target

The performance of phantom imaging by the endo-rectal NIR applicator was evaluated without the use of TRUS *prior*. A 1% bulk Intralipid solution was the background medium. A cylinder-shape solid phantom 15mm in diameter and 25mm long (Fig. 7(a)) was the target. The solid phantom was fabricated from a bulk material that was provided and calibrated by the NIR imaging laboratory of Dartmouth College. The solid phantom has an absorption

#99971 - $15.00 USD Received 8 Aug 2008; revised 13 Oct 2008; accepted 14 Oct 2008; published 15 Oct 2008

coefficient of 0.0056mm^{-1} and a reduced scattering coefficient of 1.03mm^{-1}, in comparison to 0.0023mm^{-1} and 1.0mm^{-1} of the background. The testing setup is depicted in Fig. 7(b).

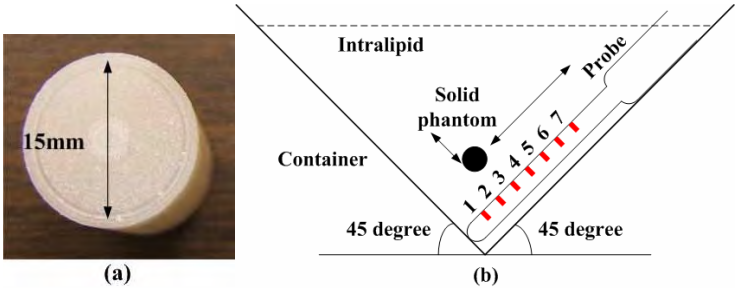

Fig. 7. Solid tissue phantom (a) and experimental setup (b)

Figure 8 lists the images reconstructed without the TRUS *prior* by using a mesh of homogenous density throughout the entire NIR imaging volume. When this mesh is used for reconstruction based on only the NIR information, the optical properties are certainly updated element-by-element in order to recover the heterogeneity being imaged. The solid phantom is placed at the mid-sagittal plane. The NIR images are displayed with a FOV of 80×30mm^2. The left most optode is located at 10mm right to the left edge of the image, and the right-most optode is 10mm left to the right edge of the image. The (a), (b), and (c) correspond to the target depth of 17.5mm at longitudinal locations of 20, 40 and 60mm (counted from left edge), respectively. The (d), (e) and (f) correspond to the phantom depth of 12.5mm at longitudinal locations of 20, 40 and 60mm, respectively. The target is identified clearly against satisfactorily recovered background; however, the absorption contrast of the target is significantly underestimated.

The same data sets were reconstructed using the target spatial information obtained from TRUS. The TRUS image, similar to the one in Fig. 6(b), has artifacts around and shows only the lower half of the cylinder owing to the shadow effect. This image/artifact pattern is specific to the solid cylinder target that reflects much of the US signal on its surface. This type of artifact may not be representative for tissue imaging *in situ.* The artifact is thereby ignored when incorporating the spatial information of the target, by generating a mesh having a homogenous background region and a circular target region as shown in Fig. 6(c). As there are only two regions to reconstruct, the hierarchical iteration routine introduced in [1] involves only 2-steps. The results are given in Table 2 and Figure 9. The absorption coefficient of the background medium is reconstructed at 0.002mm^{-1} for all images. The absorption coefficient of the target is recovered to within 14% of the true value.

#99971 - $15.00 USD Received 8 Aug 2008; revised 13 Oct 2008; accepted 14 Oct 2008; published 15 Oct 2008

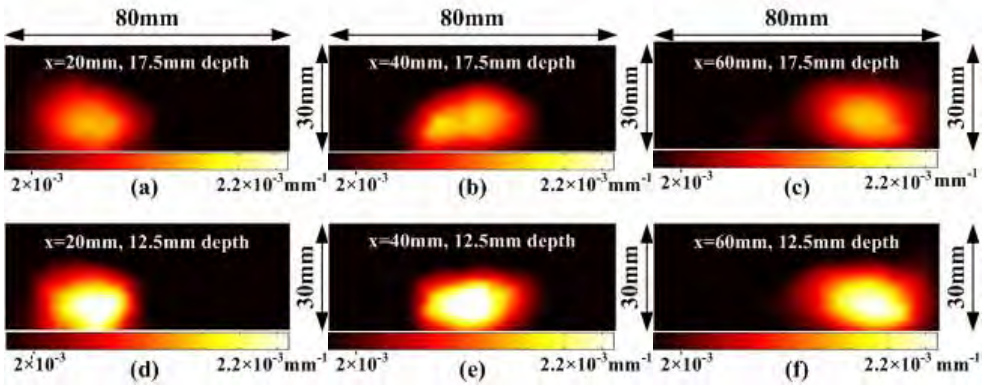

Fig. 8. NIR imaging of a solid tissue phantom having an absorption coefficient of 0.0056mm^{-1}. The reconstructed background absorption coefficients are 0.0019mm^{-1} in (a), (b), (d), (e), and 0.0020 mm^{-1} in (c), (f).

Table 2. NIR image reconstruction guided by TRUS- *prior*

Center depth	**12.5mm**		
Longitudinal location (x)	20mm	40mm	60mm
True Value (mm^{-1})	0.0056	0.0056	0.0056
Reconstructed value (mm^{-1})	0.0067	0.0064	0.0063
Center depth	**17.5mm**		
Longitudinal location (x)	20mm	20mm	20mm
True Value (mm^{-1})	0.0056	0.0056	0.0056
Reconstructed value (mm^{-1})	0.0064	0.0063	0.0061

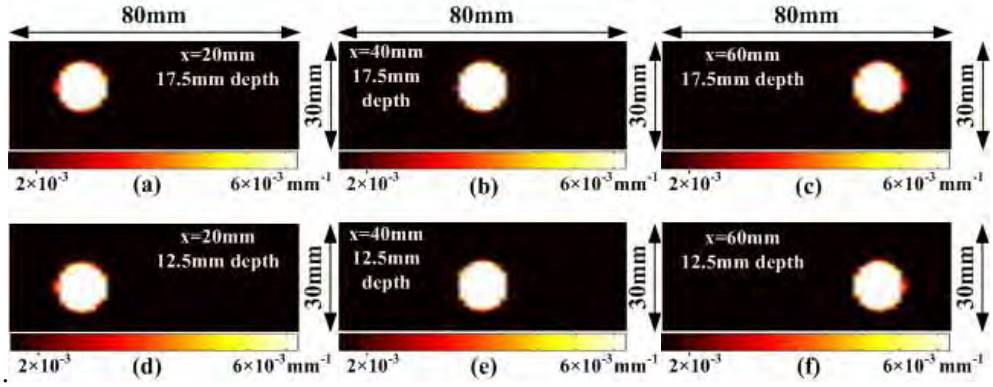

Fig. 9. TRUS guided NIR image reconstruction for solid phantom in homogenous medium

4.2 Imaging two targets

The capability of recovering more than one target by the endo-rectal NIR probe is also examined. Two cylinder-shaped solid tissue phantoms, including the one shown in Fig. 7(a), are used as the target. Both targets are 15mm in diameter and 25mm in length. The newly added solid phantom has an absorption coefficient of 0.0064mm^{-1} and a reduced scattering coefficient of 0.997 mm^{-1} in comparison to the other one of 0.0056mm^{-1} and 1.03mm^{-1}. Figure 10(a) and (b) are the images for placing the two targets at depths of 17.5mm and 22.5mm, respectively, in the mid-sagittal plane, with 20mm longitudinal spacing. When the reconstruction is performed without the target spatial information, the two targets can barely be differentiated at the depth of 17.5mm, and not discriminated at the depth of 22.5mm. The

#99971 - $15.00 USD Received 8 Aug 2008; revised 13 Oct 2008; accepted 14 Oct 2008; published 15 Oct 2008

absorption contrasts of the targets are also significantly underestimated in both cases. Figure 10(c) indicates the results of using the spatial information from the TRUS image. The two targets can be recovered as having different absorption contrasts, at both depths. The reconstructed absorption coefficients listed in Table 3 are also close to the true values.

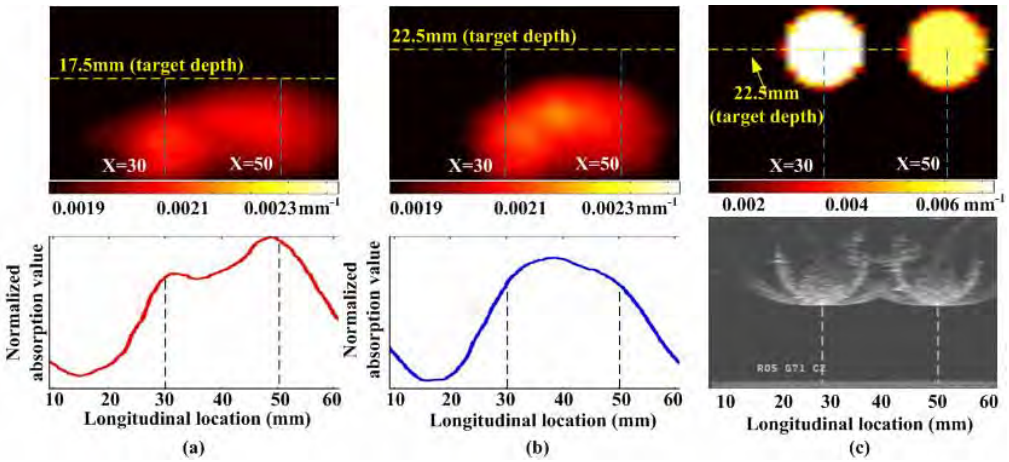

Fig. 10. Imaging of multiple targets: (a) NIR-only reconstruction when the target depth is 17.5mm, the targets can be barely separated; (b) NIR-only reconstruction when the target depth is 22.5mm, the targets cannot be separated; (c) region based reconstruction when the target depth is 22.5mm.

Table 3. Reconstructed absorption coefficients of the two targets in Fig. 12

	Target 1	Target 2
True value (mm^{-1})	0.0064	0.0056
Reconstructed value (mm^{-1})	0.0067	0.0058

4.3 Effects of condom on NIR tomography

The TRUS probe is always covered with a regular latex condom when imaging the prostate. A TRUS-coupled NIR applicator has to be applied with a condom if used in the clinic. In the previous applications of NIR tomography imaging there was no need of applying a latex barrier between an NIR applicator and the tissue being interrogated, therefore the effect of a latex condom on NIR tomography was not reported.

The test being carried out used the setup and solid phantom shown in Fig. 7, by applying US gel to the NIR/US probe, covering the NIR/US with a condom, then pressing the condom to eliminate any gas between the condom and the probe. US gel is not applied on top of the condom when imaging the Intralipid, but is applied for all the tissue imaging tests presented in Section 5. The absorption coefficient of the target reconstructed using TRUS information is listed in Table 4. The overall distribution of the reconstructed absorption coefficient of the target is plotted in Fig. 11(a), and the distribution specific to target position is plotted in Fig. 11(b). These results, which are consistent with those presented in Section 4.1, demonstrate that the condom has minimum effect on NIR imaging. Nevertheless, an attention of the light power is observed, as it takes 10% longer exposure time for CCD to integrate the same amount of signal when the condom is applied.

#99971 - $15.00 USD Received 8 Aug 2008; revised 13 Oct 2008; accepted 14 Oct 2008; published 15 Oct 2008

Table 4. Absorption coefficient reconstructed with the use of condom on the NIR probe (mm^{-1})

Depth (mm)	22.5	25	27.5	30	32.5	35	37.5
True value	0.0056	0.0056	0.0056	0.0056	0.0056	0.0056	0.0056
X=20mm	0.0065	0.0058	0.0070	0.0066	0.0048	0.0043	0.014
X=40mm	0.0053	0.0051	0.0047	0.0049	0.0043	0.0052	0.0063
X=60mm	0.0059	0.0045	0.0066	0.0052	0.0054	0.0095	0.0065

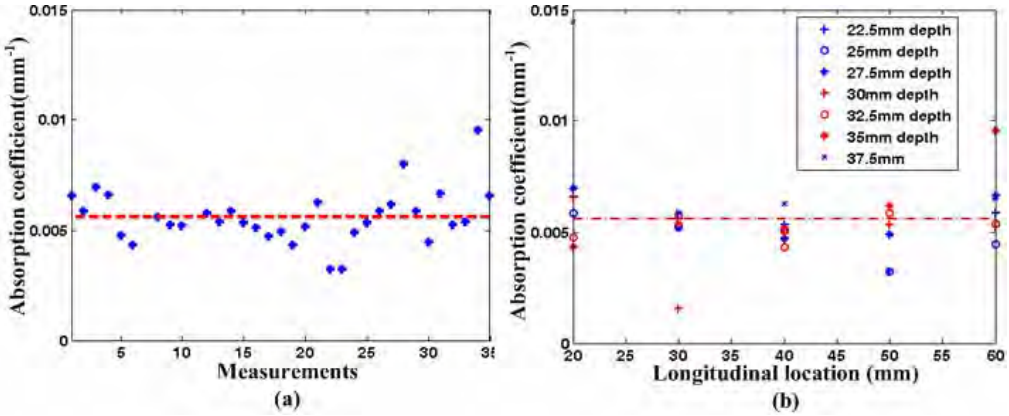

Fig. 11. Test of condom effect on the NIR imaging: (a) reconstructed absorption coefficients for all cases listed in Table 4, and The red dashed line shows the true value; (b) data points in (a) specific to target depths and longitudinal locations.

5. Results of tissue imaging by TRUS-coupled trans-rectal NIR tomography

5.1 Imaging solid absorbing object embedded in avian tissue

The condom-covered NIR/US probe was enclosed within thick layers of chicken breast tissue ($\mu_a = 0.006mm^{-1}$, $\mu_s' = 0.757mm^{-1}$ [35], and a black object (10mm diameter ×10mm length) was embedded as the target. The photographs in Fig. 12(a) and (b) show the setup of tissue sample and the absorbing target being embedded. The tissue without the absorbing target is also imaged as a baseline test. The baseline images by US and NIR are shown in Fig. 12(c), where the NIR image is reconstructed using a homogenous mesh as there was no indication of a target on US. Figure 12(d) to (f) correspond to target being embedded at different longitudinal locations at slightly different depths. The embedded object is clearly visible in the US images as anechoic shadows. The NIR imaging without prior information can clearly recover the object, but with inconsistent and potentially much under-estimated absorption coefficients. When the target location and size information are used to guide the NIR image reconstruction, the target is recovered with consistent absorption coefficients indicating a strongly absorbing object.

5.2 Internal imaging of avian tissues

As shown in Fig. 13(a) the empty abdomen of a whole chicken was filled with chicken breast tissue and a piece of chicken liver was embedded within the breast tissue. The embedded liver shows up as the hypo-echoic region circled in Fig. 13(b). The NIR image reconstructed without any target information is given in Fig. 13(c), in which the absorptive mass does correlate longitudinally with the liver tissue. Fig. 13(d) shows NIR image reconstructed by treating the liver mass as a sphere. Fig. 13(e) shows the NIR image reconstructed by excluding the non-tissue region from the background of Fig. 13(b). Fig. 13(f) shows the NIR

#99971 - $15.00 USD Received 8 Aug 2008; revised 13 Oct 2008; accepted 14 Oct 2008; published 15 Oct 2008

image reconstructed by taking into account the irregular shape of the liver mass. Among the 3 spatial *prior* implementations, the one in Fig. 13(f) is the most accurate wherein the absorption coefficient of the chicken liver mass is also the closest to the realistic value [35].

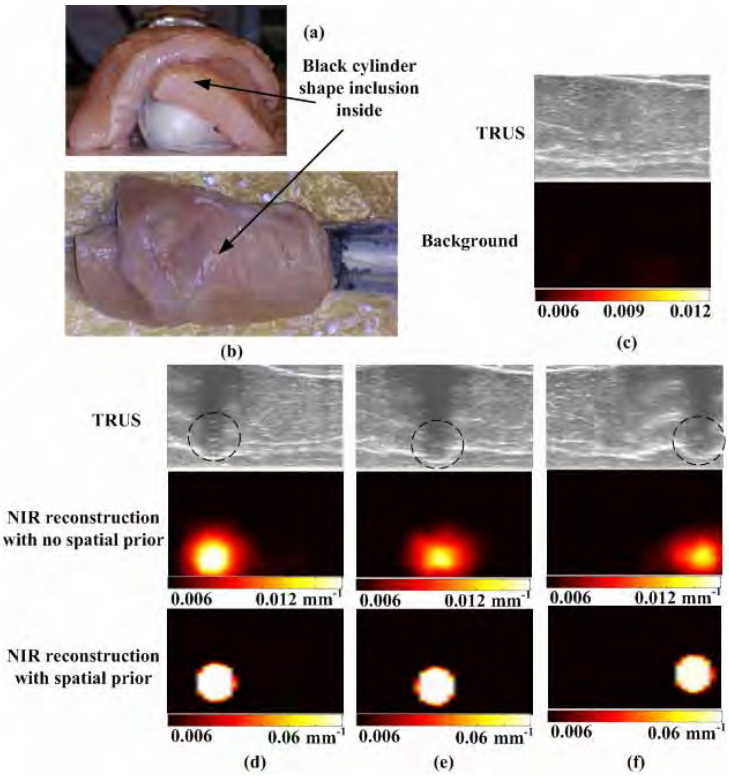

Fig. 12. Avian tissue imaging: (a) front view; (b) top view; (c) no inclusion; (d) inclusion is at 20mm; (e) 35mm; (f) 58mm, longitudinally, respectively.

5.3 TRUS-coupled trans-rectal optical tomography of canine prostate in situ

TRUS-coupled trans-rectal NIR imaging of the prostate is conducted on a canine cadaver. The prostate was exposed and approximately 0.33ml of homogenized foal liver was injected ventral-dorsally, paramedian in the left lobe of the prostate. The prostate was then enclosed in thick layers of peri-prostate tissues. On the TRUS image of Fig. 14(a) the injected liver tissue is visible by the mass proximal to the center of the prostate and the vertical hyper-echoic strip at the ventral side of the prostate. The large hypo-echoic region at the upper half was due to air. The mesh generated in Fig. 14(b) has excluded the air based on the US image. The rectum wall was not outlined in the mesh because of its close proximity and near apposition to the US transducer due to the small size of this canine cadaver. The rectum layer may be included when imaging a larger subject. The finalized mesh given in Fig. 14(b) shows nested-domains where there is a relatively small prostate and a much smaller target in the prostate. The NIR image in Fig. 14(c) is reconstructed by applying the 3-step hierarchical reconstruction method introduced in the previous paper [1]. A highly absorptive mass is clearly recovered out of the injected liver tissue. The absorption coefficient of the foal liver tissue in Fig. 14(c) is lower than that of the avian liver tissue in Fig. 13(f); nevertheless both values are at the order of $0.1mm^{-1}$, indicating high absorption by both tissues. The reconstructed absorption coefficients of the prostate and the peripheral tissue are given in Table 5. It is very interesting to observe that the numbers agree with the values suggested by the literature [16-18, 35].

#99971 - $15.00 USD Received 8 Aug 2008; revised 13 Oct 2008; accepted 14 Oct 2008; published 15 Oct 2008

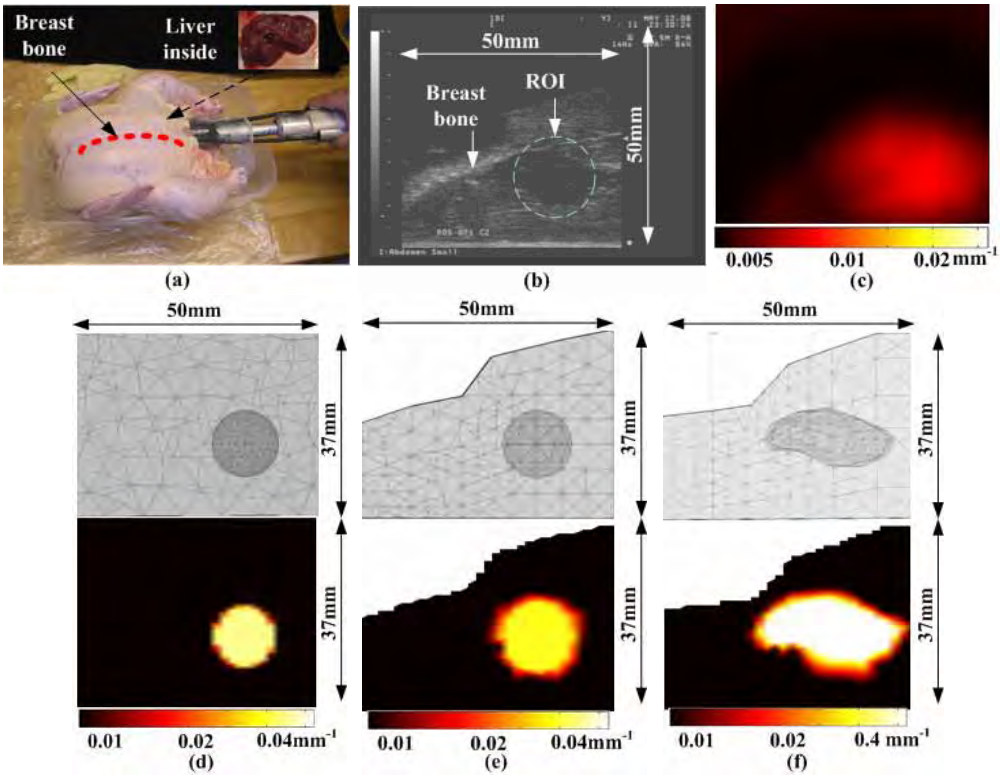

Fig. 13. Internal imaging of avian tissue embedded with a piece of liver. (a) Whole chicken sample; (b) US image of the embedded liver tissue; (c) NIR image reconstructed without US *prior*; (d) NIR image reconstructed assuming a circular target; (e) NIR image reconstructed by adding the boundary profile of the background tissue; (f) NIR image reconstructed by adding the actual contour of the target.

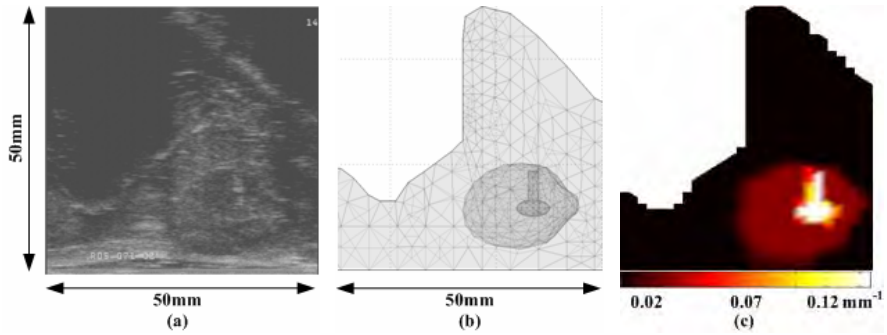

Fig.14. Trans-rectal NIR / US imaging of in vitro canine prostate with exogenous tissue contrast.

Table 5 Reconstructed absorption value of in vitro canine prostate imaging

Region	Background	Prostate	Injected liver
Reconstructed value (mm^{-1})	0.0062	0.0309	0.1301

6. Discussion

In the NIR imager an 840nm superliminescent diode with ~14nm bandwidth is used to simultaneously excite all source channels. The bandwidth would certainly introduce

#99971 - $15.00 USD Received 8 Aug 2008; revised 13 Oct 2008; accepted 14 Oct 2008; published 15 Oct 2008

wavelength-dependent attenuation among source channels for the same tissue chromophore. The reconstructed absorption coefficient is therefore a value averaged over the band coupled into the source channels. Luckily the absorption of the tissue chromorphores like hemoglobin is less wavelength-dependent in the close vicinity of 840nm. If the source coupling method is performed at an additional wavelength, such as 780nm, to quantify the oxygen saturation [36], it may be necessary to compensate the wavelength-dependent absorptions among source channels in image reconstruction.

It is shown that the absorption coefficient can be quantitatively reconstructed by steady-state trans-rectal NIR measurements. The accuracy of reconstruction for a highly heterogeneous domain can be improved dramatically by use of the TRUS spatial *prior*. Implementing frequency-domain detection to the NIR system will also allow more accurate reconstruction of the absorption coefficient owing to the reliable differentiation of it from the scattering by true phase information.

Generating the target mesh from the TRUS image has been based on the assumption that the entire imaging volume and the target are symmetric and centered at the TRUS imaging plane. This is perhaps necessary if only one TRUS image is utilized to form a 3-dimensional mesh for NIR image reconstruction, but is mostly inaccurate. This is particularly problematic in imaging of the prostate if the NIR/US probe is to be directed away from the midline of the prostate. The effect of asymmetric-domain may be corrected if multiple US images are available to generate a mesh representing the true 3-dimensional contents of the imaging volume more faithfully.

The trans-rectal examination of the prostate on the sagittal view is likely being interfered with by the nearby bladder and pelvic bone. If the bladder is empty, the photon propagation may be less interrupted. If the bladder is full, it may become a relatively transparent domain for photon propagation. In this case the bladder likely becomes a diffusion-void domain [37, 38]. A transport-equation based model of photon propagation can be implemented [37, 39] to mitigate the interference of void-domains. The interference from the pelvic bone is similar in principle to that of the chest wall in breast imaging when using a planner NIR array [40]. In this work we applied the Robin-type boundary condition under diffusion equation to the void-tissue interfaces under the diffusion model. This is a rather straightforward approach that is proven helpful for improving the reconstruction accuracy, but more studies are needed to quantitatively evaluate improvement by this approach in comparison to the more rigorous transport-based model.

The probe sensitivity curves in this paper and those in the previous paper [1] were all derived under the assumption of an absorptive NIR probe surface. This boundary condition produces a peak of depth-sensitivity close to, but not at, the probe surface. This feature may be desirable for prostate imaging, since the measurement will be less sensitive to the existence of a rectum layer. On the other hand, the peak also indicates that the measurement is less sensitive to a lesion deeper in the prostate than one closer to the surface of the prostate. Prostate tumors are known to occur more often in the peripheral zone which stretches abaxial from the middle-line of the prostate. For deeper target, we have showed that with TRUS *prior*, the accuracy of target recovery can be improved successfully. However, more dedicated simulation and experimental studies are necessary to evaluate the likelihood of retrieving deeper target *in vivo*.

In all the tests presented in this work, the target of interest is visible or at least sensitive to US, therefore US spatial information of the target is readily rendered to guide the NIR image reconstruction. If the target is ambiguous to US, it may still be recognizable by NIR-only reconstruction. One example is given in Fig. 15 wherein a piece of chicken breast tissue was dyed with diluted Indian ink and then placed in the middle of the natural chicken breast tissue. The approximate boundary of the dyed tissue is marked with the dash-circle in the US image. This embedded tissue is hardly distinguishable in the TRUS image; therefore the NIR image reconstruction was performed without any a *priori* information. The target is identified by

#99971 - $15.00 USD Received 8 Aug 2008; revised 13 Oct 2008; accepted 14 Oct 2008; published 15 Oct 2008

NIR even though the depth and size were not accurate. This result may show positive indication on the clinical application of trans-rectal NIR/US measurement providing the fact that up to 40% of prostate tumors are not sensitive to US [3, 6, 7]. Besides using NIR information to characterize US-sensitive lesions, if the NIR imaging is able to discover a lesion that is otherwise non-suspicious on US, the overall sensitivity and specificity of TRUS-based prostate imaging may be improved.

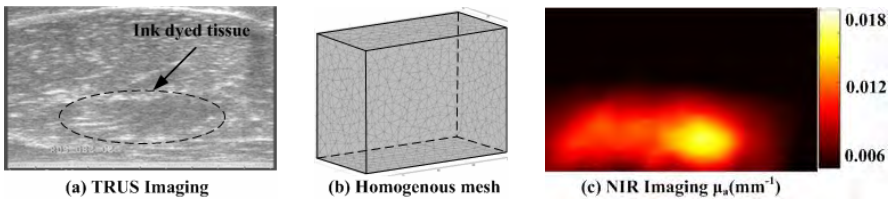

Fig. 15. Imaging of a tissue mass that is ambiguous to TRUS but sensitive to NIR.

7. Conclusions

We implemented the NIR array design suggested in our previous work for direct integration of the NIR array with a TRUS transducer. The combined NIR/US probe & system enabled concurrent acquisition of trans-rectal NIR tomography and TRUS images in the same sagittal plane. Although the NIR imager is constructed in CW mode, accurate quantitative reconstruction of the absorption coefficient is feasible with the TRUS spatial *a priori* information. The use of a condom is found to have minimum affect on NIR tomography measurement, indicating that endo-rectal NIR may be applied concurrently with TRUS in a clinic setting with no alteration of the standard procedures. An absorptive target may also be recovered by trans-rectal NIR only, but the incorporation of TRUS *a priori* information allows trans-rectal NIR tomography to recover an absorption target more accurately, as demonstrated by imaging of the alien tissue in the canine prostate. The previous Part-I and this Part-II papers together have validated prostate imaging as feasible by TRUS-coupled trans-rectal NIR tomography. Work is on-going toward *in vivo* measurement of optical properties in intact prostate as well as development of prostate cancer models in the canine to validate that augmenting TRUS morphology information with trans-rectally acquired NIR contrast may improve the overall accuracy of TRUS prostate imaging.

Acknowledgments

This work has been supported by the Prostate Cancer Research Program of the U.S. Army Medical Research Acquisition Activity (USAMRAA), 820 Chandler Street, Fort Detrick MD, 21702-5014, through grant #W81XWH-07-1-0247. The content of the information does not necessarily reflect the position or the policy of the USARAA, and no official endorsement should be inferred. The authors would like to thank Drs. Brian W. Pogue and Quing Zhu for enlightening discussions and suggestions. Comments and questions may be directed to Daqing Piao whose e-mail address is daqing.piao@okstate.edu.

#99971 - $15.00 USD Received 8 Aug 2008; revised 13 Oct 2008; accepted 14 Oct 2008; published 15 Oct 2008

In vivo trans-rectal ultrasound–coupled optical tomography of a transmissible venereal tumor model in the canine pelvic canal

Zhen Jiang,[a] G. Reed Holyoak,[b] Kenneth E. Bartels,[b] Jerry W. Ritchey,[c] Guan Xu,[a] Charles F. Bunting,[a] Gennady Slobodov,[d] and Daqing Piao[a,*]

[a]Oklahoma State University, School of Electrical and Computer Engineering, Stillwater, Oklahoma 74078
[b]Oklahoma State University, Department of Veterinary Clinical Sciences, Stillwater, Oklahoma 74078
[c]Oklahoma State University, Department of Veterinary Pathobiology, Stillwater, Oklahoma 74078
[d]University of Oklahoma Health Sciences Center, Department of Urology, Oklahoma City, Oklahoma 73104

Abstract. *In vivo* trans-rectal near-infrared (NIR) optical tomography was performed concurrently with, albeit reconstructed without spatial *a prior* of, trans-rectal ultrasound (US) on transmissible venereal tumor (TVT) developed as a model in the canine pelvic canal. Studies were taken longitudinally at prior to, 14 days after, and 35 days after the TVT injection. As the tumor grew, the nodules became increasingly hyperabsorptive and moderately hyperscattering on NIR. The regions of strong NIR contrast, especially on absorption images, correlated well with those of US hypoechoic masses indicative of tumors. Combining the information of trans-rectal NIR and US detected the tumor more accurately than did the US alone at 14 days postinjection. [DOI: 10.1117/1.3149852]

Keywords: prostate cancer; trans-rectal optical tomography; transmissible venereal tumor; trans-rectal ultrasound.

Paper 09010LR received Jan. 14, 2009; revised manuscript received Mar. 9, 2009; accepted for publication Apr. 17, 2009; published online Jun. 8, 2009.

1 Introduction

Near-infrared (NIR) optical tomography is becoming increasingly important for functional imaging of biological tissues[1] because the endogenous or exogenous NIR contrast could benchmark tissue physiology and functionality. NIR optical tomography has contributed to diagnosis and prognosis of cancer,[2] understanding of cerebral response,[3] characterization of rheumatologic dysfunction,[4] and small animal imaging.[5] In all these applications, the tissues have been interrogated noninvasively via external NIR applicators.

NIR optical tomography based on trans-rectal "noninvasive" probing has been investigated recently by the authors, attempting to augment trans-rectal ultrasound (TRUS)[6] of prostate with the unique optical specificity. This approach was motivated by the hypothesis that optical properties of prostate cancer *in vivo* may be different from those of normal intact prostate tissues and was challenged by the difficulty of assessing the prostate in its *in vivo* real-time environment. This work demonstrates *in vivo* trans-rectal NIR optical tomography, conducted concurrently with TRUS, on a dog bearing transmissible venereal tumors (TVTs)[7] in its pelvic canal. This study not only validates the utility of *in vivo* trans-rectal NIR tomography of the prostate but also reveals, for the first time, the NIR contrasts that TVT has over the normal tissues within the canine pelvic canal.

2 Methods and Materials

The studies were conducted under a protocol approved by the Institutional Animal Care and Use Committee of Oklahoma State University. The protocol was also approved and underwent an on-site inspection by the U.S. Army Medical Research and Material Command. For this study, the prostate of a 12-kg sexually intact adult purpose-bred Beagle dog estimated to be approximately four years of age was used. The TVT cell line was obtained cryopreserved from MD Anderson Cancer Center (Houston, Texas). Following two cycles of inoculation into the subcutis of non-obese-diabetic/severe-combined-immunodeficiency (NOD/SCID) mice, neoplastic cells were recovered and homogenized for injection into the canine prostate gland. Approximately 3 cc of TVT cells were aseptically injected transperineally into the right lobe of the prostate using a 6-in. 16-gauge hypodermic needle under TRUS visualization. During retraction of the injection needle, it was assumed that TVT cells could leak from the prostate injection site and be "seeded" along the needle insertion tract. During the first 14 days postinjection, there was no evidence of tumor growth on TRUS and rectal examination. The TRUS examination at 35 days postinjection showed hypoechoic masses in the prostatic parenchyma, periprostatically around the right lobe of the prostate, and perirectaly along the track of needle injection. The dog underwent weekly monitoring for two more weeks and was then humanly euthanized for necropsy and histological examinations at 56 days postinjection.

The trans-rectal NIR/US system was described elsewhere.[6] The NIR probe has been integrated with a 60-mm-long sagittal TRUS transducer. The 60-mm length of the NIR source/detector arrays limits the imaging depth to ~30 mm. The steady-state NIR measurements reconstruct the absorption and reduced scattering images without *a priori* structural information.[6]

3 Results

Figure 1 presents the trans-rectal NIR and US images acquired at the middle of the right lobe, the middle line of the prostate, and the middle of the left lobe, which were obtained before the TVT injection, 14 days postinjection, and 35 days postinjection. The absorption [Fig. 1(a)] and reduced scattering [Fig. 1(b)] images correlate to the same set of US images. The image dimensions are 60×30 mm^2 (cranial-caudal $\times$ dorsal-ventral). On the day-35 US images of the right lobe

*Address all correspondence to: Daqing Piao, Tel: 405-744-5250; E-mail: daqing.piao@okstate.edu

1083-3668/2009/14(3)/030506/3/$25.00

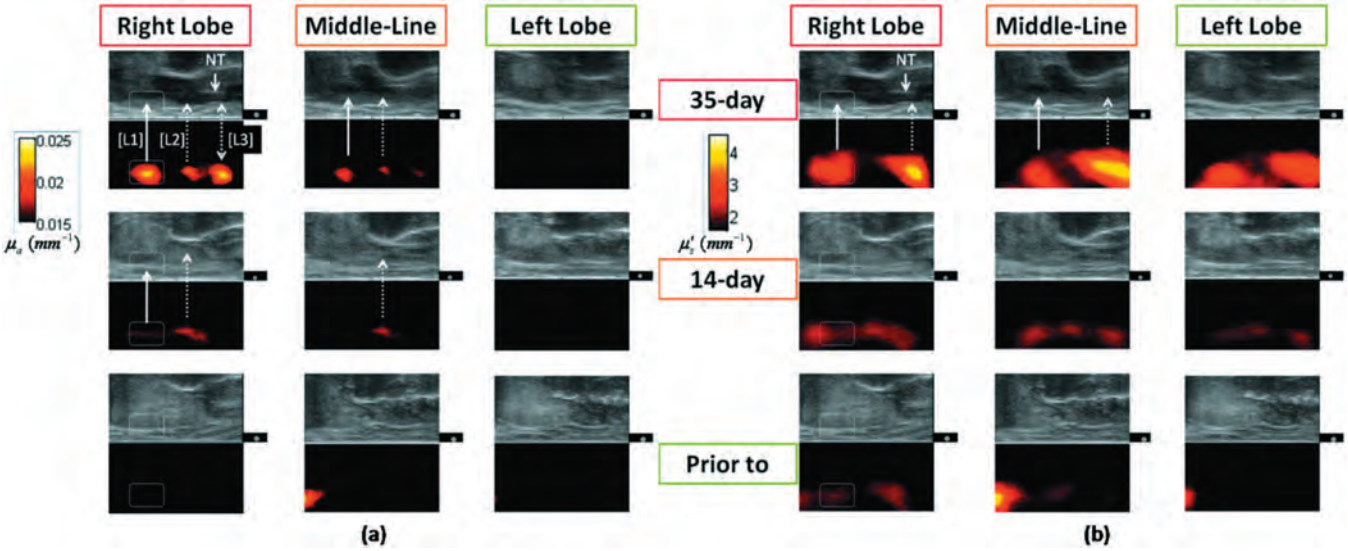

Fig. 1 *In vivo* trans-rectal NIR/US of TVT development in canine pelvic canal. The images were taken before the TVT injection, 14 days after the TVT injection when the US and rectal examination showed no evidence of tumor growth, and 35 days after the TVT injection when the tumor growth was evident on both US and rectal examination. (a) US and NIR absorption images. (b) US and NIR reduced scattering images. The dimensions of the images are 60×30 mm^2 (cranial-caudal $\times$ dorsal-ventral). The rectangular mark enclosing L1 is used in Fig. 2(a), where the peak NIR contrasts within the region are plotted. NT: needle track.

and middle line, the hypoechoic region "L1" indicated an intraprostatic mass; the large hypoechoic region "L2" indicated a mass ventral and caudal to the prostate that could have a connection with L1; the needle track (NT) on the right lobe denoted the needle trajectory for introducing the TVT cells with longitudinal hypoechoic regions, including L3, seen along the NT. On the day-35 NIR image of the right lobe, the hyperabsorptive regions corresponded longitudinally to L1, L2, and L3. The day-35 NIR image of the middle line displayed less and smaller hyperabsorptive masses, indicative of L1, L2, and L3. Trans-rectal NIR/US images performed at the left lobe were shown with no abnormal features on US and no hyperabsorptive regions on NIR. At the day-14 NIR absorption images, hyperabsorptive regions were found intraprostatically in the right lobe only (L1) and dorsal to the pelvic bone in the right lobe (L2), with potential extension to the middle line. The longitudinal locations of these hyperabsorptive regions correlated well with those of the hypoechoic and hyperabsorptive regions found in day-35. Because the NIR array surface is 3 mm ventral to the TRUS surface, the nodules were shown to be slightly dorsal on the NIR versus on the US images. The change of the hyperabsorptive regions from day-14 to day-35 implied tumor growing in the right lobe and extending toward the middle line. The growth of the tumor was indicated earlier by the NIR absorption images than by the TRUS, and combining the information of NIR and TRUS led to earlier and more accurate findings of tumor growth than did TRUS alone.

The hyperabsorptive masses in Fig. 1(a) were shown in Fig. 1(b) with different patterns of the contrast. In Fig. 1(b), the L3 had much higher contrast than did the other masses corresponding to L1 and L2. The growth of tumors L1 and L2 at day-14 in Fig. 1(b) are not as evident as in Fig. 1(a).

The progressions of the peak NIR contrasts within the rectangular region corresponding to L1 as outlined in Fig. 1, with

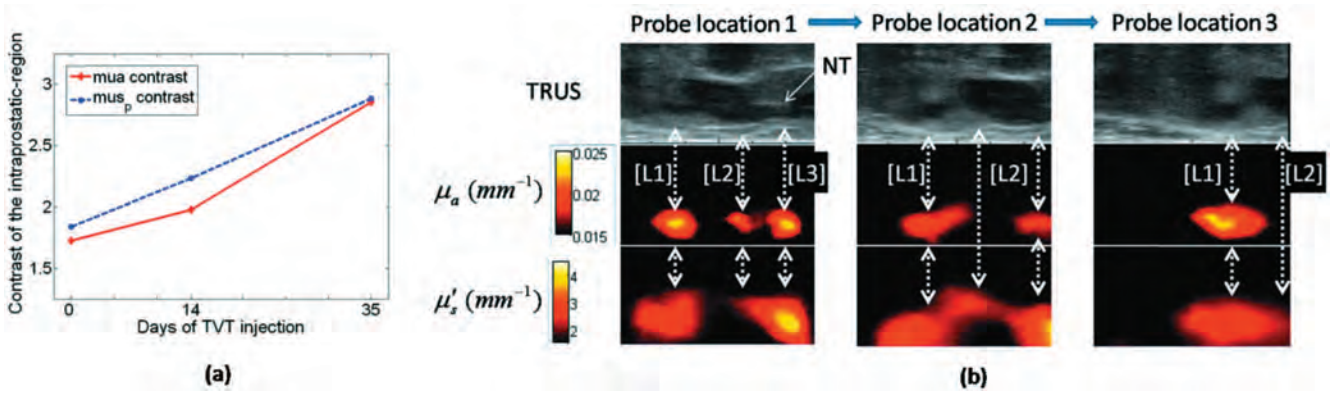

Fig. 2 (a) The progression of peak NIR contrasts within the rectangular region specified in Fig. 1. (b) Sagittal trans-rectal NIR/US imaging in three longitudinal locations. The locations of the left-column images correspond to those of the right lobe taken at day-35 in Fig. 1.

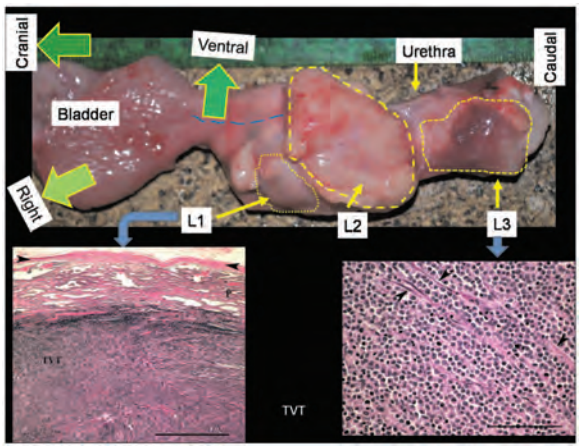

Fig. 3 (Top) Image of prostate gland taken after removal of the urinary bladder and intrapelvic urethra immediately following euthanasia. The prostate gland is markedly expanded and misshapen secondary to intraprostatic (L1) and periprostatic (L2) neoplastic masses. Neoplastic masses were also distributed along the distal intrapelvic urethra (L3) and in the perirectal subcutaneous tissues (not shown). Histologically, expansile masses of TVT (cells bottom left panel) displace and compress prostatic tissue (P). Prostatic capsule (arrowheads), bar =1.8 mm. The TVT infiltrate (bottom right panel) consists of sheets of neoplastic round cells dissecting through preexisting fibrovascular stroma (arrowheads), bar=230 μm.

respect to the background values for normal perirectal parenchyma, are given in Fig. 2(a). The clear trend of contrast increase is believed as the demonstration of imaging the tumor growth because NIR tomography is a nonlinear process in which the enlargement of the target may be reconstructed as having elevated contrast in addition to volume changes when reconstructed without the spatial *prior* information of the target.

Figure 2(b) displays the NIR/US images obtained by placing the probe at three locations along the middle plane of the right lobe. At location 1, L1, L2, and L3 (refer to Fig. 1) were all within the US field of view, whereas at location 2 the L3 was moved out of the US view. At location 3, only L1 was shown on US. The overall NIR hypercontrast masses correlated well with the US hypoechoic regions.

The gross and histological findings (56 days postinjection) in Fig. 3 confirmed intra- and periprostatic neoplastic infiltrates with masses also located along the urethra and perirectal tissue; the latter related to dissemination along the needle track during TVT inoculation. All masses consist of diffuse sheets of a monomorphic population of neoplastic round cells dissecting through preexisting fibrovascular stroma. The neoplastic cells have large hyperchromatic nuclei, single conspicuous nucleoli, and moderate amounts of featureless cytoplasm. The cytological features are consistent with canine TVT.

4 Discussions and Conclusion

The intraprostatic TVT tumors were initiated in a non-immunosuppressed canine model in which the TVT nodules developed at multiple sites intraprostatically and periprostatically. Although not all TVT tumors were confined to the prostate, successful imaging of multiple TVT nodules implies the utility of detecting multiple intraprostatic tumors.

The feature of TVT as strongly hyperabsorptive on NIR tomography is likely due to the hyperchromatic nuclei unique to TVT. The relatively higher scattering of the TVT may be due to the hyperdensity and larger nuclei of the neoplastic cells. As the neoplastic cells are arranged into microlobules by the preexisting fibrovascular stroma, the TVT may also present certain polarization sensitivity. Overall, the NIR features of TVT may be comparable to those revealed by tissue angiogenesis. As studies of microvessel-density within the human prostate demonstrated a clear correlation of increased microvessel density with the presence of cancer,[8] it can be expected that human prostate cancer may have notable contrast on trans-rectal NIR tomography.

In conclusion, this work reports *in vivo* imaging of TVT tumors in the canine pelvic canal by trans-rectal NIR tomography coupled with TRUS. The TVT tumor nodules were presented as hyperabsorptive and hyperscattering with respect to the normal prostatic and other pelvic tissues. Correlation of the TVT locations is found between trans-rectal NIR and TRUS images. These demonstrations encourage testing of trans-rectal NIR tomography with additional animal studies and eventually to the human prostate.

Acknowledgments

The authors acknowledge support from U.S. Army Medical Research and Material Command through Grant No. W81XWH-07-1-0247.

References

1. E. M. Hillman, "Optical brain imaging *in vivo*: techniques and applications from animal to man," *J. Biomed. Opt.* **12**, 051402 (2007).
2. B. J. Tromberg, B. W. Pogue, K. D. Paulsen, A. G. Yodh, D. A. Boas, and A. E. Cerussi, "Assessing the future of diffuse optical imaging technologies for breast cancer management," *Med. Phys.* **35**(6), 2443–2451 (2008).
3. B. W. Zeff, B. R. White, H. Dehghani, B. L. Schlaggar, and J. P. Culver, "Retinotopic mapping of adult human visual cortex with high-density diffuse optical tomography," *Proc. Natl. Acad. Sci. U.S.A.* **104**, 12169–12174 (2007).
4. A. K. Scheel, M. Backhaus, A. D. Klose, B. Moa-Anderson, U. J. Netz, K. G. Hermann, J. Beuthan, G. A. Müller, G. R. Burmester, and A. H. Hielscher, "First clinical evaluation of sagittal laser optical tomography for detection of synovitis in arthritic finger joints," *Ann. Rheum. Dis.* **64**, 239–245 (2005).
5. M. B. Unlu, Y. Lin, O. Birgul, O. Nalcioglu, and G. Gulsen, "Simultaneous *in vivo* dynamic magnetic resonance-diffuse optical tomography for small animal imaging," *J. Biomed. Opt.* **13**, 060501 (2008).
6. Z. Jiang, D. Piao, G. Xu, J. W. Ritchey, G. R. Holyoak, K. E. Bartels, C. F. Bunting, G. Slobodov, and J. S. Krasinski, "Trans-rectal ultrasound-coupled near-infrared optical tomography of the prostate, Part II: experimental demonstration," *Opt. Express* **16**, 17505–17520 (2008).
7. B. Rivera, K. Ahrar, M. M. Kangasniemi, J. D. Hazle, and R. E. Price, "Canine transmissible venereal tumor: a large-animal transplantable tumor model," *Comparative Med.* **55**(4), 335–343 (2005).
8. S. A. Bigler, R. E. Deering, and M. K. Brawer, "Comparison of microscopic vascularity in benign and malignant prostate tissue," *Hum. Pathol.* **24**, 220–226 (1993).

Journal of Innovative Optical Health Sciences
Vol. 2, No. 3 (2009) 215–225

World Scientific
www.worldscientific.com

IN VIVO TRANS-RECTAL ULTRASOUND-COUPLED NEAR-INFRARED OPTICAL TOMOGRAPHY OF INTACT NORMAL CANINE PROSTATE

DAQING PIAO*,†, ZHEN JIANG†, KENNETH E. BARTELS‡, G. REED HOLYOAK‡, JERRY W. RITCHEY§, GUAN XU†, CHARLES F. BUNTING† and GENNADY SLOBODOV¶

†*School of Electrical and Computer Engineering Oklahoma State University, Stillwater, OK 74078 USA*
**daqing.piao@okstate.edu*

‡*Department of Veterinary Clinical Sciences Oklahoma State University, Stillwater, OK 74078 USA*

§*Department of Veterinary Pathobiology Oklahoma State University, Stillwater, OK 74078 USA*

¶*Department of Urology, University of Oklahoma Health Sciences Center, Oklahoma City, OK 73104 USA*

This is the first tomography-presentation of the optical properties of a normal canine prostate, *in vivo,* in its native intact environment in the pelvic canal. The imaging was performed by trans-rectal near-infrared (NIR) optical tomography in steady-state measurement at 840 nm on three sagittal planes across the right lobe, middle-line, and left lobe, respectively, of the prostate gland. The NIR imaging planes were position-correlated with concurrently applied trans-rectal ultrasound, albeit there was no spatial *prior* employed in the NIR tomography reconstruction. The reconstructed peak absorption coefficients of the prostate on the three planes were 0.014, 0.012, and 0.014 mm^{-1}. The peak reduced scattering coefficients were 5.28, 5.56, and 6.53 mm^{-1}. The peak effective attenuation coefficients were 0.45, 0.43, and 0.50 mm^{-1}. The absorption and effective attenuation coefficients were within the ranges predictable at 840 nm by literature values which clustered sparsely from 355 nm to 1064 nm, none of which were performed on a canine prostate with similar conditions. The effective attenuation coefficients of the gland were shown to be generally higher in the internal aspects than in the peripheral aspects, which is consistent with the previous findings that the urethral regions were statistically more attenuating than the capsular regions.

Keywords: Prostate; canine; optical property; optical tomography; trans-rectal ultrasound.

1. Introduction

The knowledge of tissue optical properties relevant to light diffusion or attenuation is important to both the dosimetry of photodynamic therapy (PDT)[1–4] and the analysis based on near-infrared (NIR) diffuse optical imaging.[5–10] The prostate of the dog is usually considered as a model closest to that of the human being, therefore a number of studies have been conducted[11–20] on canine subjects to estimate the optical properties of prostate, *in vitro* or *in vivo*, over a wide range of spectrum (to be reviewed in more detail in Sec. 2 of this

study). A general consensus that has been made from these studies is that significant intra-organ and inter-subject variations of the prostate optical properties do occur. The optical properties being investigated include the absorption coefficient, the reduced or transport scattering coefficient, and the effective attenuation coefficient that is a combination of the above two properties. The reported intra-organ and inter-subject prostate optical heterogeneity imposes the need of individualized and localized measurement for PDT applications,[18] as well as challenges to trans-rectal NIR tomography that aims to resolve the optical contrast, either endogenous[21,22] or exogenous,[23] of prostate cancerous lesions over normal or benign prostate tissues.

It is also important in PDT to know the optical properties of peri-prostatic tissues, such as rectal or peri-rectal regions since the existence of any optical property gradient of the prostate over its peripheral tissue will influence the local peri-prostatic light distribution. For trans-rectal NIR tomography of the prostate, the NIR light is attenuated first by a condom (required for endo-rectal application), then by the rectal wall and the peri-rectal tissue before finally reaching the prostate. The degree of NIR light propagation into the prostate is dependent upon the optical property gradients between the prostatic capsule and peri-prostatic tissue. The *in vivo* or *in vitro* optical contrast of the prostate with respect to peri-rectal or peri-prostatic tissue is therefore fundamental to PDT and prostate NIR tomography, yet to our knowledge it has rarely been evaluated on a single subject. Overall there is very limited information regarding the NIR attenuating features of peri-rectal tissue.[11] Therefore, it is difficult to draw a comparison of the optical properties reported in different studies between the prostate and the peri-rectal tissue. Except the current reported *in vivo* investigation, all of the studies on normal prostate (canine and human) have been taken interstitially on exposed prostate or through trans-perineal imaging. The interstitial measurements, although very reliable and consistent, are likely to alter to some extent the optical properties natural to the tissue being measured.

In this work we present tomographic measurements of optical properties of a normal canine prostate, *in vivo,* in its native intact environment in the pelvic canal. The imaging was performed by trans-rectal NIR optical tomography in steady-state measurement at 840 nm, on three sagittal planes across the right lobe, middle-line, and left lobe, respectively, of the prostate gland. The NIR imaging planes were position-correlated with concurrently applied trans-rectal ultrasound, albeit there was no spatial *prior* employed in the NIR tomography reconstruction. The prostate gland appears as a positive-contrast region in NIR images, particularly in the absorption and effective-attenuation images. The position and profile of the positive-contrast prostate-indicating region correlate well with those of the prostate in the concurrent trans-rectal ultrasound image. The peak absorption coefficients of the prostate-region on the three planes were found to be 0.014, 0.012, and 0.014 mm^{-1}. The peak reduced scattering coefficients were 5.28, 5.56, and 6.53 mm^{-1}. The peak effective attenuation coefficients were 0.45, 0.43, and 0.50 mm^{-1}. The absorption and effective attenuation coefficients were within the ranges that are predictable at 840 nm based on literature values which clustered sparsely from 355 nm to 1064 nm, none of which were performed on a prostate in similar conditions. It is also noted that effective attenuation coefficients of the gland are higher in the internal aspect than in the peripheral aspect, which is consistent with the previous findings of statistically more attenuating urethral regions than the capsular regions.

2. Review of the Optical Property Measurements on Canine Prostate

Tables 1 and 2 summarize what the authors have found to be existing methods, represented graphically by diagram (Table 1), and published values (Table 2) on optical properties of the canine prostate within the spectral range from 355 nm to 1064 nm. In Table 2, the attenuation coefficient is denoted by μ_a, the reduced scattering coefficient by μ_s', and the effective attenuation coefficient by μ_{eff} that is defined as

$$\mu_{\mathrm{eff}} = \sqrt{3\mu_a(\mu_a + \mu_s')}. \tag{1}$$

Oraevsky *et al.* presented *in vitro* μ_a, μ_s', and μ_{eff} of prostate at 355, 532, and 1064 nm, respectively, using opto-acoustic time-resolved fluence rate measurements on slab samples of normal canine prostate tissues.[12] Another post-mortem study by Chen *et al.* estimated prostate μ_a, μ_s', and μ_{eff} at 630 nm, by interstitial measurements on excised

Table 1. Legend indicating the measurement methods used in Table 2.

								
Opto-acoustic on slab tissue	Integrating sphere on slab tissue	Interstitial on exposed prostate	Interstitial on excised prostate	Reflective on exposed prostate	Interstitial close to the capsule	Interstitial close to the urethra	Interstitial close to the base	Interstitial close to the apex

normal prostate.[13] *In vitro* μ_a and μ_s' of slab samples of normal canine prostate tissues were evaluated at 633 nm, by employing steady-state fluence rate measurements using the standard double-integrating sphere technique.[15] Other studies relied on steady-state fluence rate measurements on tissues *in situ*, albeit involving surgical procedures to expose the prostatic tissue to the fiber, to determine μ_{eff} of the normal canine prostate. At wavelengths of 630, 665, 730, 732 nm, interstitial measurements on normal canine prostate *in vivo* were conducted before and after PDT.[14,17,18,20] Perhaps the only *in vivo* study using reflection measurement upon exposed prostate, thereby maintaining the intactness of the gland itself, was performed at 732 nm on exposed normal canine prostate.[19] Trans-perineal interstitial measurement,[16–18] which in principle is more accurate than interstitial measurement on exposed prostate, demonstrated with statistical significance that the μ_{eff} of prostatic urethral regions is higher than that of the prostatic capsular regions.[16,17]

In Table 2, there are some individual values of μ_a and μ_s', but nevertheless most original values listed are regarding μ_{eff} only, which are readily available from steady-state fluence rate measurements. Because the data are clustered in a wide spectrum, summarizing all these studies to a single category for spectrally-resolved comparative evaluation can only be made by utilizing μ_{eff} since it represents the coupled effect of μ_a and μ_s'. When the standard deviations of μ_a and μ_s', denoted by $\sigma\mu_a$ and $\sigma\mu_s'$, respectively, are available, the standard deviation of μ_{eff} in Table 2 is calculated based on Eq. (1) by

$$\sigma\mu_{eff} = \sqrt{\left(\frac{\partial\mu_{eff}}{\partial\mu_a}\sigma\mu_a\right)^2 + \left(\frac{\partial\mu_{eff}}{\partial\mu_s'}\sigma\mu_s'\right)^2}. \qquad (2)$$

3. Methods and Materials

3.1. *Trans-rectal US-coupled NIR tomography*

The details of the trans-rectal US-coupled NIR tomography system can be found elsewhere.[21,22] Figure 1 illustrates the configuration of the trans-rectal NIR/US probe and the prostate imaging geometry. Since NIR imaging depth is typically 1/2 of the array dimension, the NIR optodes are distributed longitudinally in parallel to the sagittal US to allow interrogating deep prostatic tissues. The NIR arrays are also put symmetrically on the lateral sides of the sagittal US transducer, enabling accurate correlation of the middle-sagittal NIR imaging plane with the sagittal US imaging.

The completed trans-rectal NIR/US probe and imager are shown in Fig. 2. The US probe was a bi-plane sector and linear array trans-rectal probe fitted to an ALOKA SSD-900V unit. The NIR applicator was integrated over the 7.5 MHz sagittal-imaging transducer. The NIR probe consisted of one source and one detector array separated 20 mm laterally and placed symmetrically to the sagittal US transducer. The NIR source and detector array, each having seven channels, were 60 mm in longitudinal dimension, which was identical to the longitudinal length of the sagittal US transducer. Each NIR optode channel had a micro prism-lens pair for coupling the light to and from the probe surface. The NIR light from a super-luminescent diode of 100 mW at 840 nm was focused sequentially onto seven source fibers of the NIR applicator by a home-made translating fiber multiplexer. The NIR remissions collected by the seven detection fibers were acquired by a 16-bit intensified CCD camera through a spectrometer (not necessary for acquiring the data but used for system integrity). Acquisition of NIR signals from seven source channels took less than five seconds after the prostate was localized by the sagittal US using an Aloka SSD-900V portable US scanner, which provides 50 mm longitudinal field of view when performing sagittal imaging with the 60 mm long 7.5 MHz US transducer. The absorption and reduced scattering coefficients of the prostate were reconstructed from steady-state measurements[22] using a model-based non-linear optimization method.[22,25,26] The effective attenuation coefficient is then calculated based on Eq. (1).

Table 2. Optical properties of normal canine prostate tissue as reported in various published studies. N is the number of samples. This table follows the template for human prostate in Ref. 24.

Study [Ref.]	Year	Sample	N	Method	λ (nm)	μ_a (mm^{-1})	μ_s' (mm^{-1})	μ_{eff} (mm^{-1})
Oraevsky *et al.* [12]	1997	*In vitro*	2		355	0.852	5.22	3.94
Oraevsky *et al.* [12]	1997	*In vitro*	2		532	0.233	2.45	1.37
Chen *et al.* [13]	1997	*In vivo*	17		630	0.04 ± 0.02	2.6 ± 2.1	0.5 ± 0.1
Chen *et al.* [13]	1997	*Ex vivo*	10		630	0.030 ± 0.007	2.6 ± 0.8	0.48 ± 0.09
Lee *et al.* [14]	1997	*In vivo*	7		630			0.47 ± 0.05
Nau *et al.* [15]	1999	*In vitro* (fresh)	10		633	0.073 ± 0.007	0.225 ± 0.005	0.256 ± 0.015*
Nau *et al.* [15]	1999	*In vitro* (frozen)	13		633	0.076 ± 0.003	1.00 ± 0.11	0.495 ± 0.027*
Lilge *et al.* [16]^	2004	*In vivo*	7	 Capsule	660	0.0030 ± 0.0021	0.92 ± 0.65	0.184 ± 0.040^
Lilge *et al.* [16]^	2004	*In vivo*	7	 Urethra	660	0.0014 ± 0.0013	3.23 ± 2.76	***0.206 ± 0.035***^
Jankun *et al.* [17]	2004	*In vivo*	13	 Capsule	665			0.171 ± 0.071
Jankun *et al.* [17]	2004	*In vivo*	13	 Urethra	665			*0.192 ± 0.027*
Jankun *et al.* [17]	2004	*In vivo*	13	 Capsular base	665			0.259 ± 0.193
Jankun *et al.* [17]	2004	*In vivo*	13	 Urethral base	665			*0.275 ± 0.131*
Jankun *et al.* [17]~	2004	*In vivo*	13	 Capsular apex	665			0.176 ± 0.031^^
Jankun *et al.* [17]	2004	*In vivo*	13	 Urethral apex	665			*0.190 ± 0.065*
Jankun *et al.* [18]	2005	*In vivo*	5	 Base	665			0.247 ± 0.06
Jankun *et al.* [18]	2005	*In vivo*	5	 Apex	665			0.203 ± 0.026
Solonenko *et al.* [19]	2002	*In vivo*	4		730		1.27 ± 0.06	
Zhu *et al.* [20]	2003	*In vivo*	12		732	0.003–0.058	0.1–2.0	0.03–0.49
Nau *et al.* [15]	1999	*In vitro* (fresh)	7		1064	0.027 ± 0.003	1.76 ± 0.13	0.381 ± 0.026*
Nau *et al.* [15]	1999	*In vitro* (frozen)	10		1064	0.071 ± 0.006	0.79 ± 0.05	0.428 ± 0.023*
Oraevsky *et al.* [12]	1997	*In vitro*	2		1064	0.009	0.63	0.13

Note: *Calculation of the effective attenuation coefficient based on Eqs. (1) and (2).
^The values in the abstract of Ref. 16 are contrary to those in the text of Ref. 16. The results in the text were used here.
^^The results given in Ref. 17 were "0.176 ± 0.314 mm^{-1}," which had the standard deviation larger than the mean value. The authors made a "reasonable" estimation of "0.176 ± 0.0314 mm^{-1}" for this set of literature data.

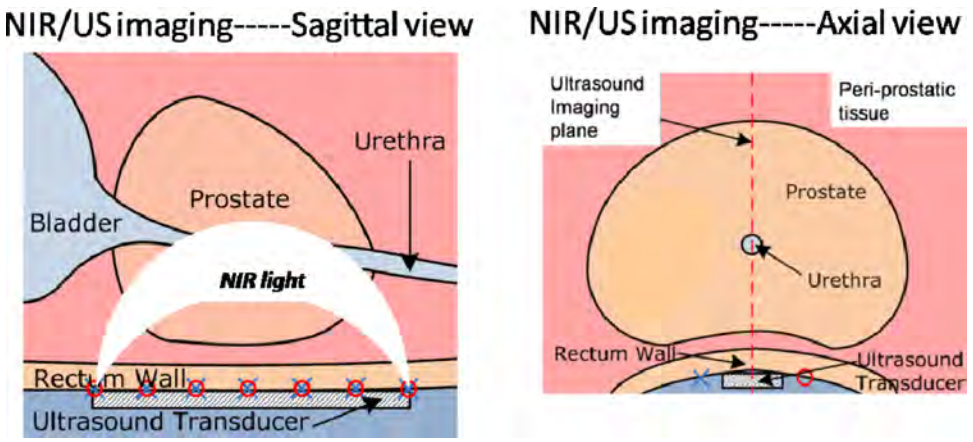

Fig. 1. Illustration of trans-rectal NIR/US of the prostate. Trans-rectal US is placed in the middle of the trans-rectal NIR applicator (optodes distributed longitudinally) to perform combined and correlated NIR/US imaging of the prostate at the sagittal plane.

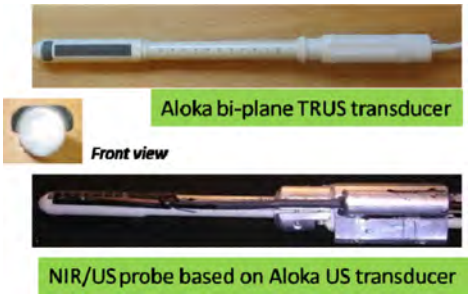

(a)

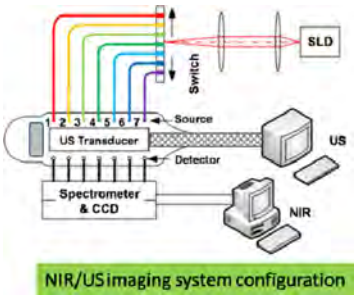

(b)

Fig. 2. (a) Photograph of the trans-rectal Aloka US transducer and the completed NIR/US probe. (b) Schematic diagram of the trans-rectal NIR/US imaging system that consists of a custom-built NIR imager and a commercial ALOKA SSD-900V portable US scanner.

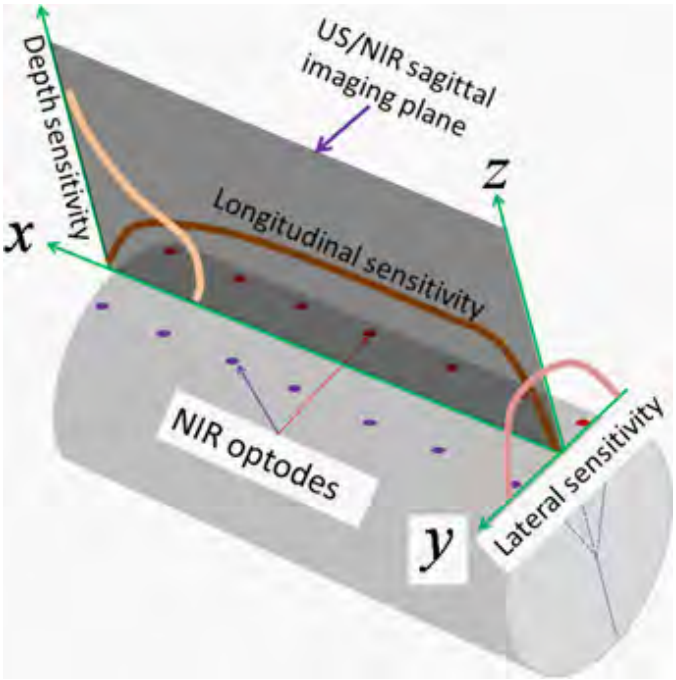

Fig. 3. Sensitivity profiles of the NIR imaging probe along the lateral, longitudinal and depth directions.

3.2. *Sensitivity features of the trans-rectal NIR imaging*

Since the purpose of this study was to examine the inherent NIR contrast that the prostate may demonstrate over the peri-prostatic tissue, the NIR image was reconstructed without any spatial *prior* information. The accuracy or the robustness of the NIR reconstruction is thereby dependent upon the sensitivity of NIR array to the heterogeneity of the optical properties within the volume being interrogated. Figure 3 illustrate the sensitivity profiles, with respect to the absorption, of the NIR applicator based on the previous study.[21] The longitudinal sensitivity is relatively uniform over the entire NIR array dimension, but it tapers off at the distal and proximal edges of the NIR array. The lateral sensitivity peaks at the middle-sagittal plane that coincides with the sagittal TRUS plane, while the

depth sensitivity generally degrades along with the increase of the depth. The sensitivity to the scattering or total attenuation would have similar patterns. Based on these sensitivity features, one could expect that a target may be reconstructed with better contrast if it is located within the regions of higher NIR sensitivity. It is also anticipated that for multiple targets located longitudinally on the same sagittal plane, the contrast-comparison would be reliable.

3.3. *Animal model*

This study was approved by the Institutional Animal Care and Use Committee of Oklahoma State University. The protocol was also approved and underwent an on-site inspection by the US Army Medical Research and Material Command. A 20-kg sexually intact, adult mixed-breed dog, approximately four years of age, was anesthetized using an intravenous injection of propofol (8 mg/kg) followed by intubation and halothane/oxygen inhalation for anesthetic maintenance. The animal was placed in left lateral recumbency for bowel preparation and physical examination (rectal palpation) of the prostate. TRUS visualization was performed using the combined trans-rectal NIR/US probe with condom-and-gel coverage. Both the physical examination and ultrasound revealed a normal prostate for this dog. The prostate was examined weekly using similar procedures, with consistent evaluation results being classified as "normal," until the dog was euthanized nine weeks after the initial exam with an overdose of pentobarbital sodium. A complete necropsy was performed and the prostate and peri-prostatic structures were submitted for histologic examination.

4. Results

Figure 4 displays one set of sagittal trans-rectal NIR tomography images and the correlated TRUS performed at the right lobe, middle-line, and the left lobe of the normal canine prostate gland. The dimensions of the NIR and correlated TRUS images are 50 mm (cranial-to-caudal) × 30 mm (dorsal-to-ventral). Each of the images represents one of three highly consistent measurements taken at each location.

The NIR absorption coefficient images are displayed at a color-scale of [0.007 0.014] mm^{-1}. The NIR transport scattering coefficient images are displayed at a color-scale of [3.000 6.000] mm^{-1}. The NIR effective attenuation coefficient images are displayed at a color-scale of [0.250 0.500] mm^{-1}. The color-scales in all images represent a background threshold at $1/2$ of the maximum value of the color-scale. At this scale, the locations of the NIR regions indicating the prostate had excellent position correlation with prostatic images obtained using TRUS. The urinary bladder is shown as an anechoic structure on TRUS, which is similar to images using NIR. Most of the peri-rectal tissues are also not identified using NIR except at the periphery of the urinary bladder. The prostate is consistently demonstrated in NIR images as having positive-contrast with respect to the peri-prostatic tissues, with an average of more than two-folds of contrast in absorption, reduced scattering, and effective attenuation. In addition, the prostate is more optically heterogeneous in the middle-line and more optically attenuating toward the internal aspects of the prostate than in the peripheral aspects of the gland.

At this scale setting, it is noted that areas of prostatic regions on NIR images resemble the actual cross-sections being interrogated on the gland. The cranial-caudal length dimensions of the prostate at the right lobe and left lobe NIR images are smaller than that at the middle-line NIR images. The dorsal-ventral thickness dimensions of the prostate in the right and left lobe NIR images are shown greater than that at the middle-line NIR images. Overall, the prostate is longitudinally elongated in the middle line than in the right and left lobes. This profile of the canine prostate interpreted from NIR regions implies a walnut-shape with lobular anatomy.

Figure 4 illustrates peak absorption coefficients of this prostate specimen on the three planes to be 0.014, 0.012, and 0.014 mm^{-1}; the peak reduced scattering coefficients to be 5.28, 5.56, and 6.53 mm^{-1}; and the peak effective attenuation coefficients to be 0.45, 0.43, and 0.50 mm^{-1}. The validity of these numbers has been examined in the context of values summarized in Table 2 and by the spectra plots in Fig. 5. The majority of the previous measurements in Table 2 were performed in the spectral range of 630 nm to 732 nm, with some extension to the ultraviolet end of 355 nm and the infrared end of 1064 nm. The data points of this study, performed at 840 nm, represent the values of absorption, reduced scattering, and effective attenuation averaged over the peak values of right lobe, middle line, and left lobe. It is noted that the absorption coefficients of this study are

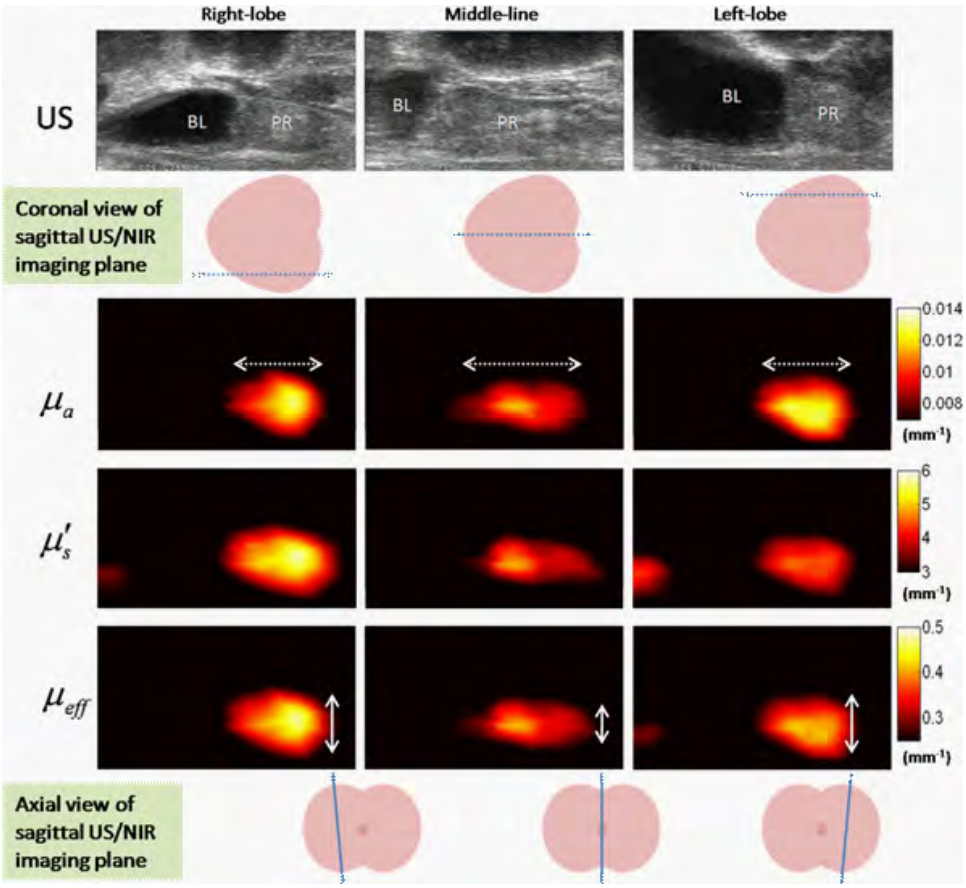

Fig. 4. Trans-rectal NIR/US of normal canine prostate *in vivo*: The US and NIR images were taken at the right lobe (left column), middle-line (middle column), and the left lobe (right column). The 1st row, US; the 2nd row, coronal view of the locations of sagittal NIR/US planes; the 3rd row, absorption coefficient; the 4th row, transport scattering coefficient; the 5th row, effective attenuation coefficient; the 6th row, axial view of the locations of sagittal NIR/US planes. The dimensions of all images are 50 mm × 30 mm (cranial-caudal × dorsal-ventral). BL-urinary bladder, PR-prostate.

narrowly distributed in a range predicted by the reported values closest to 840 nm. The reduced scattering values of this study are much higher (2–3 folds) than what may be estimated from the previously reported values, yet the effective attenuation coefficients of this study are narrowly distributed within the range predictable by reported values.

5. Gross and Histological Examination of the Prostate Gland

The prostate gland exhibited diffuse, symmetrical (and mild) enlargement (4.5 cm ×4.5 cm×2.5 cm). On cross-section, the tissue was grossly normal with the exception of a discrete, 0.5 cm in diameter focus of grey/tan tissue [arrowhead, Fig. 6(b)] located in the region of the right prostatic lobe. Histologically, this focus corresponded to moderate interstitial fibrosis with infiltration by primarily lymphocytic inflammatory cells [arrow, Fig. 6(d)]. The remainder of the prostatic tissue exhibited diffuse slight enlargement of the prostatic epithelium with occasional papillary projections and cystic dilation of prostatic glands consistent with early benign prostatic hyperplasia/hypertrophy. Otherwise, the tissue was histologically unremarkable [Fig. 6(c)]. The histological results confirmed that the NIR optical contrasts presented in this work are of a normal canine prostate.

6. Discussions

This study revealed the *in vivo* optical properties of an intact normal canine prostate in its normal anatomic position in the pelvic canal. The absorption, reduced scattering and effective attenuation coefficients of the canine prostate at approximately 840 nm have not been reported previously. However,

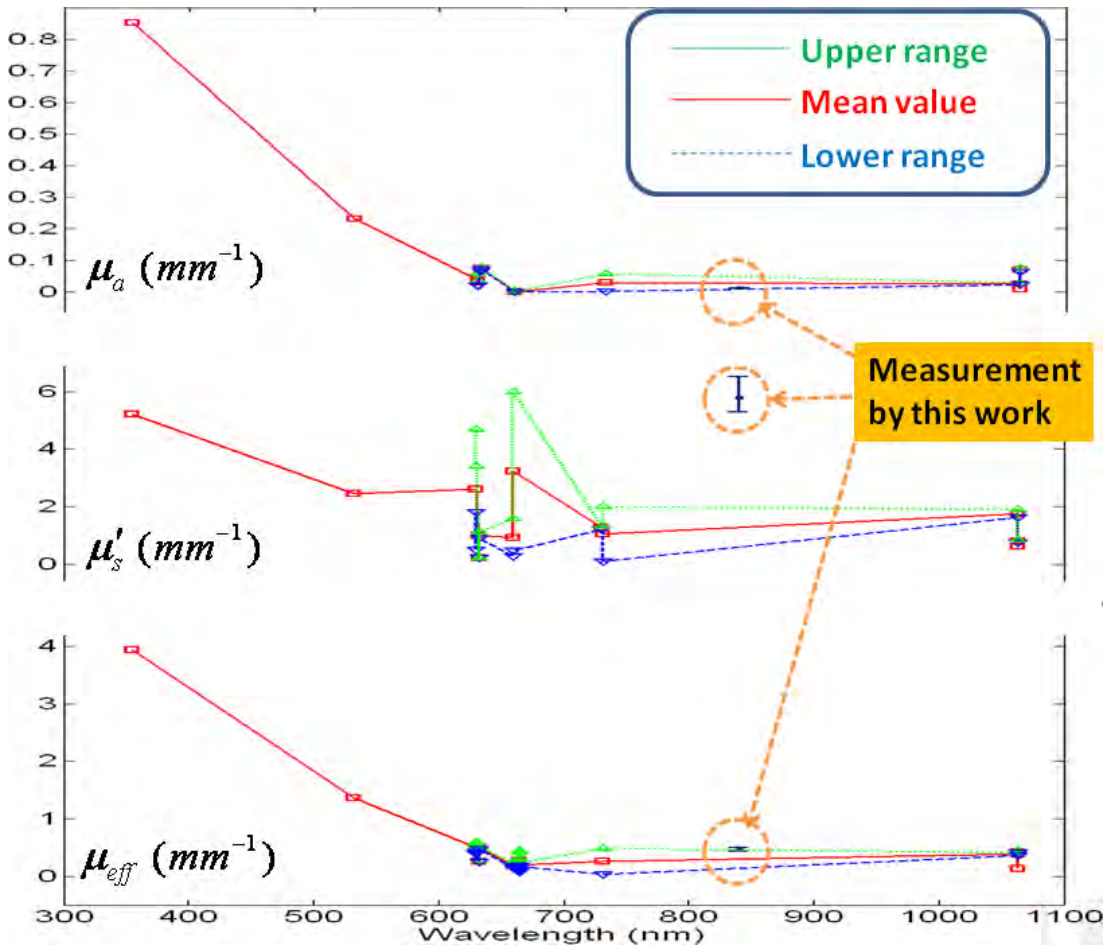

Fig. 5. Spectra of the optical properties of canine prostate based on the values given in Table 2. The measurements by this work at 840 nm were the average of the peak values of the right lobe, middle line, and left lobe.

an examination of the spectra in Fig. 5 allowed estimation of these values to be around that value. Given that the prostate is a gland with relatively rich vasculature, it is not difficult to correlate the absorption spectrum of the prostate to that of the total hemoglobin content, which has a low NIR absorption at and above the near-infrared band, as well as a relatively leveled absorption at wavelengths greater than the isosbestic point of 805 nm. The reduced scattering spectrum is rather "noisy" in the NIR band, yet globally it seems to follow the empirical power-law model of $\mu_s' = A\lambda^{-b}$, where A and b are model parameters for scattering amplitude and scattering power, respectively,[27] when there is a broad range of scattering particle sizes. The effective attenuation spectrum is close to that of the absorption, a result that may be anticipated from Eq. (1). Among the three optical properties being measured or calculated, both the absorption and effective attenuation coefficients are well within what can be predicted from the current literature. The predicted average reduced scattering values at 840 nm from the literature may be much smaller than the measured values in this study but there is a fairly large error of distribution within the cited values of the spectra. It is thereby impractical to predict the reduced scattering coefficient at 840 nm within a narrow range based on the literature spectra. On the other hand, this study utilized non-*prior* guided pure optical-based reconstruction for trans-rectal optical tomography. Our previous study indicated that when an accurate spatial *prior* to trans-rectal NIR tomography reconstruction is not employed, the absorption coefficients may be under-estimated, and the reduced scattering coefficients may be over-estimated.[21] The image reconstruction of trans-rectal NIR tomography in this study requires a 3D mesh being used due to the geometry of the NIR applicator. Extracting an accurate 3D prostate profile based on sagittal TRUS images, however, remains a challenging task. If the optical properties were reconstructed with an accu-

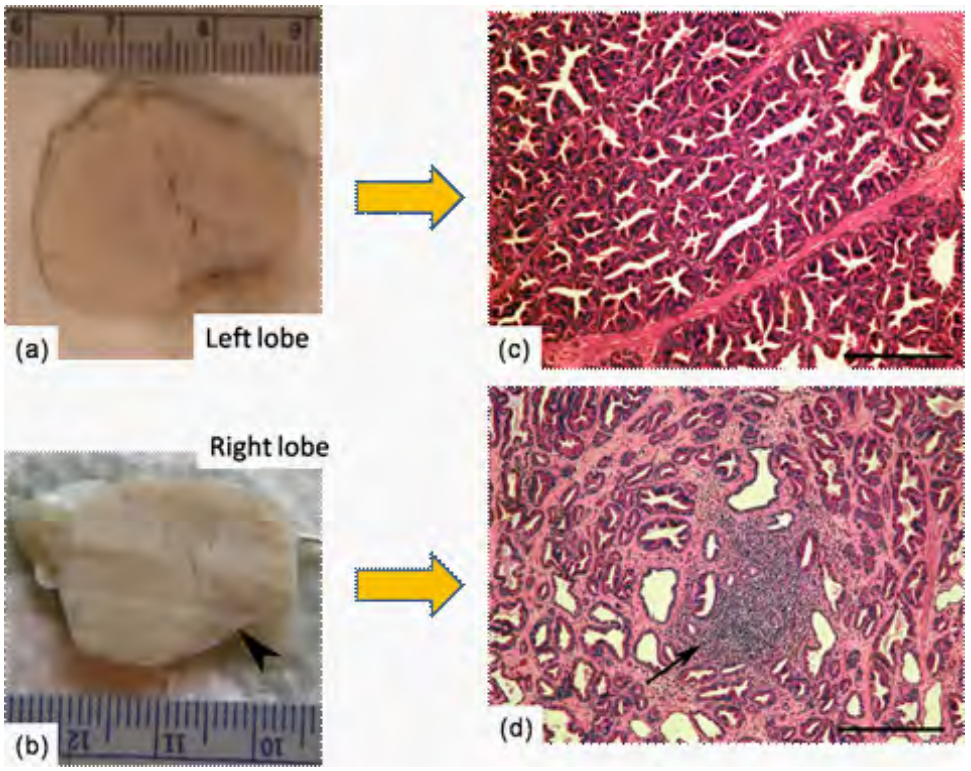

Fig. 6. Canine prostate gland. The prostate gland was slightly enlarged (4.5 cm × 4.5 cm × 2.5 cm) and on cross-section was predominantly unremarkable (a). The right lobe of the prostate contained a 0.5-cm in diameter focus of grey/tan tissue [arrowhead in (b)]. Histologically, most of the prostate gland exhibited inconspicuous lesions of early prostatic hyperplasia/hypertrophy consisting of increased prostatic epithelial cell size (c), scattered papillary projections and cystic dilation of prostatic acini. The gross lesion in the right prostatic lobe consisted of a focus of interstitial fibrosis and lymphocytic prostatitis [arrow in (d)]. Hematoxylin and Eosin stain, Bar = 360 μm.

rate spatial *prior*, the reduced scattering coefficients could have better correlation with the literature predictions.

This study also revealed the optical property contrasts that a normal canine prostate has over other structures within the canine pelvic canal. The prostate is shown as having positive-contrast over its peripheral tissue in absorption, reduced scattering, and effective attenuation of the NIR light. There are a number of factors that could make the prostate hyper-attenuating on trans-rectal NIR tomography. First, the unique thin-layers of prostatic capsule may be refractive-index mismatched with respect to the peri-prostatic tissue, thereby causing specular reflection on the prostatic capsule that contributes to the elevated light attenuation of the prostate. Second, the prostate is known to have relatively rich vasculature that may impose stronger NIR absorption within the prostate. Third, the intra-prostatic parenchyma is known to be optically heterogeneous,[12–20] a condition favorable to high scattering attenuation. The origin of the intra-prostatic optical heterogeneity is not well understood, but is likely due to multiple factors. These factors may include (1) the radially-distributed blood vessels giving non-uniform blood vessel count throughout the prostate, (2) the unique intra-prostatic anatomy that is complicated by the existence of urethra and ejaculation ducts, and (3) the different cellular structures in the different zonal areas of the prostate. Among these factors, the first and second may also cause the higher effective attenuation in the urethral region than in the capsular region that is clearly demonstrated in Refs. 15 and 16.

7. Conclusions

In conclusion, the optical properties of a normal canine prostate, *in vivo*, in its native intact environment in pelvic canal have been acquired for the first time by trans-rectal NIR optical tomography at 840 nm, under TRUS position-correlation but with

no spatial *prior* employed in the reconstruction. The absorption and effective attenuation coefficients are within the ranges predictable at 840 nm by literature values which clustered sparsely from 355 nm to 1064 nm. The effective attenuation coefficients are found higher in the internal aspects of the prostate than in the peripheral aspects, which agrees with the previous findings that the urethral regions were statistically more attenuating than the capsular regions.

Acknowledgment

This work has been supported by the Prostate Cancer Research Program of the US Army Medical Research Acquisition Activity (USAMRAA), 820 Chandler Street, Fort Detrick, MD, 21702-5014, through a Grant #W81XWH-07-1-0247.

References

1. Q. Chen, Z. Huang, D. Luck, J. Beckers, P. H. Brun, B. C. Wilson, A. Scherz, Y. Salomon, F. W. Hetzel, "Preclinical studies in normal canine prostate of a novel palladium-bacteriopheophorbide (WST09) photosensitizer for photodynamic therapy of prostate cancers," *Photochem. Photobiol.* **76**, 438–445 (2002).
2. K. K. Wang, L. Lutzke, L. Borkenhagen, W. Westra, M. W. Song, G. Prasad, N. S. Buttar, "Photodynamic therapy for Barrett's esophagus: Does light still have a role?" *Endoscopy* **40**, 1021–1025 (2008).
3. J. B. Wang, L. X. Liu, "Use of photodynamic therapy in malignant lesions of stomach, bile duct, pancreas, colon and rectum," *Hepatogastroenterology* **54**, 718–724 (2007).
4. M. A. D'Hallewin, D. Kochetkov, Y. Viry-Babel, A. Leroux, E. Werkmeister, D. Dumas, S. Gräfe, V. Zorin, F. Guillemin, L. Bezdetnaya, "Photodynamic therapy with intratumoral administration of lipid-based mTHPC in a model of breast cancer recurrence," *Lasers Surg. Med.* **40**, 543–549 (2008).
5. B. J. Tromberg, J. Coquoz, O. Fishkin, J. B. Pham, T. Anderson, E. R. Butler, J. Cahn, M. Gross, J. D. Venugopalan, D. Pham, "Non-invasive measurements of breast tissue optical properties using frequency-domain photon migration," *Phil. Trans. R. Soc. Lond. B* **352**, 661–668 (1997).
6. B. W. Pogue, S. P. Poplack, T. O. McBride, W. A. Wells, K. S. Osterman, U. L. Osterberg, K. D. Paulsen, "Quantitative hemoglobin tomography with diffuse near-infrared spectroscopy: Pilot results in the breast," *Radiology* **218**, 261–266 (2001).
7. V. Ntziachristos, B. Chance, "Probing physiology and molecular function using optical imaging: Applications to breast cancer," *Breast Cancer Res.* **3**, 41–46 (2001).
8. R. Choe, A. Corlu, K. Lee, T. Durduran, S. D. Konecky, M. Grosicka-Koptyra, S. R. Arridge, B. J. Czerniecki, D. L. Fraker, A. DeMichele, B. Chance, M. A. Rosen, A. G. Yodh, "Diffuse optical tomography of breast cancer during neoadjuvant chemotherapy: A case study with comparison to MRI," *Med. Phys.* **32**, 1128–1139 (2005).
9. M. A. Franceschini, K. T. Moesta, S. Fantini, G. Gaida, E. Gratton, H. Jess, W. W. Mantulin, M. Seeber, P. M. Schlag, M. Kaschke, "Frequency-domain techniques enhance optical mammography: Initial clinical results," *Proc. Nat. Acad. Sci. USA* **94**, 6468–6473 (1997).
10. Q. Zhu, E. B. Cronin, A. A. Currier, H. S. Vine, M. Huang, N. Chen, C. Xu, "Benign versus malignant breast masses: Optical differentiation with US-guided optical imaging reconstruction," *Radiology* **237**, 57–66 (2005).
11. H. M. Ross, J. A. Smelstoys, G. J. Davis, A. S. Kapatkin, F. Del Piero, E. Reineke, H. Wang, T. C. Zhu, T. M. Busch, A. G. Yodh, S. M. Hahn, "Photodynamic therapy with motexafin lutetium for rectal cancer: A preclinical model in the dog," *J. Surg. Res.* **135**, 323–330 (2006).
12. A. A. Oraevsky, S. L. Jacques, F. K. Tittel, "Measurement of tissue optical properties by time-resolved detection of laser-induced transient stress," *Appl. Opt.* **36**, 402–415 (1997).
13. Q. Chen, B. C. Wilson, S. D. Shetty, M. S. Patterson, J. C. Cerny, F. W. Hetzel, "Changes in *in vivo* optical properties and light distributions in normal canine prostate during photodynamic therapy," *Radiat. Res.* **147**, 86–91 (1997).
14. L. K. Lee, C. Whitehurst, Q. Chen, M. L. Pantelides, F. W. Hetzel, J. V. Moore, "Interstitial photodynamic therapy in the canine prostate," *Br. J. Urol.* **80**, 898–902 (1997).
15. W. H. Nau, R. J. Roselli, D. F. Milam, "Measurement of thermal effects on the optical properties of prostate tissue at wavelengths of 1,064 and 633 nm," *Lasers Surg. Med.* **24**, 38–47 (1999).
16. L. Lilge, N. Pomerleau-Dalcourt, A. Douplik, S. H. Selman, R. W. Keck, M. Szkudlarek, M. Pestka, J. Jankun, "Transperineal *in vivo* fluence-rate dosimetry in the canine prostate during SnET2-mediated PDT," *Phys. Med. Biol.* **49**, 3209–3225 (2004).
17. J. Jankun, L. Lilge, A. Douplik, R. W. Keck, M. Pestka, M. Szkudlarek, P. J. Stevens, R. J. Lee, S. H. Selman, "Optical characteristics of the canine prostate at 665 nm sensitized with tin etiopurpurin dichloride: Need for real-time monitoring of photodynamic therapy," *J. Urol.* **172**, 739–743 (2004).

18. J. Jankun, R. W. Keck, E. Skrzypczak-Jankun, L. Lilge, S. H. Selman, "Diverse optical characteristic of the prostate and light delivery system: Implications for computer modelling of prostatic photodynamic therapy," *B. J. U. Int.* **95**, 1237–1244 (2005).
19. M. Solonenko, R. Cheung, T. M. Busch, A. Kachur, G. M. Griffin, T. Vulcan, T. C. Zhu, H. W. Wang, S. M. Hahn, A. G. Yodh, "*In vivo* reflectance measurement of optical properties, blood oxygenation and motexafin lutetium uptake in canine large bowels, kidneys and prostates," *Phys. Med. Biol.* **47**, 857–873 (2002).
20. T. C. Zhu, S. M. Hahn, A. S. Kapatkin, A. Dimofte, C. E. Rodriguez, T. G. Vulcan, E. Glatstein, R. A. Hsi, "*In vivo* optical properties of normal canine prostate at 732 nm using motexafin lutetium-mediated photodynamic therapy," *Photochem. Photobiol.* **77**, 81–88 (2003).
21. G. Xu, D. Piao, C. H. Musgrove, C. F. Bunting, H. Dehghani, "Trans-rectal ultrasound-coupled near-infrared optical tomography of the prostate Part I: Simulation," *Opt. Exp.* **16**, 17484–17504 (2008).
22. Z. Jiang, D. Piao, G. Xu, J. W. Ritchey, G. R. Holyoak, K. E. Bartels, C. F. Bunting, G. Slobodov, J. S. Krasinski, "Trans-rectal ultrasound-coupled near-infrared optical tomography of the prostate Part II: Experimental demonstration," *Opt. Exp.* **16**, 17505–17520 (2008).
23. J. Boutet, L. Guyon, M. Debourdeau, J. M. Dinten, D. Vray, P. Rizo, "Advances in bi-modal optical and ultrasound detection of prostate cancer diagnosis," *Proc. SPIE* **7171**, 71710E (2009).
24. T. Svensson, S. Andersson-Engels, M. Einarsdóttír, K. Svanberg, "*In vivo* optical characterization of human prostate tissue using near-infrared time-resolved spectroscopy," *J. Biomed. Opt.* **12**, 014022 (2007).
25. N. Iftimia, H. Jiang, "Quantitative optical image reconstruction of turbid media by use of direct-current measurements," *Appl. Opt.* **39**, 5256–5261 (2000).
26. H. Xu, *MRI-Coupled Broadband Near-Infrared Tomography for Small Animal Brain Studies*, Ph.D. Dissertation, Dartmouth College, Hanover, NH, p. 36 (2005).
27. F. Bevilacqua, A. J. Berger, A. E. Cerussi, D. Jakubowski, B. J. Tromberg, "Broadband absorption spectroscopy in turbid media by combined frequency-domain and steady-state methods," *Appl. Opt.* **39**, 6498–6510 (2000).

Direct-current-based image reconstruction versus direct-current included or excluded frequency-domain reconstruction in diffuse optical tomography

Guan Xu,[1] Daqing Piao,[1,*] Charles F. Bunting,[1] and Hamid Dehghani[2]

[1]School of Electrical and Computer Engineering, Oklahoma State University, Stillwater, Oklahoma, USA 74078

[2]University of Birmingham, Birmingham B15 2TT, UK

*Corresponding author: daqing.piao@okstate.edu

Received 25 September 2009; revised 16 March 2010; accepted 29 March 2010; posted 8 April 2010 (Doc. ID 117721); published 25 May 2010

We study the level of image artifacts in optical tomography associated with measurement uncertainty under three reconstruction configurations, namely, by using only direct-current (DC), DC-excluded frequency-domain, and DC-included frequency-domain data. Analytic and synthetic studies demonstrate that, at the same level of measurement uncertainty typical to optical tomography, the ratio of the standard deviation of μ_a over μ_a reconstructed by DC only is at least 1.4 times lower than that by frequency-domain methods. The ratio of standard deviations of D (or μ_s') over D (or μ_s') reconstructed by DC only are slightly lower than those by frequency-domain methods. Frequency-domain reconstruction including DC generally outperforms that excluding DC, but as the amount of measurements increases, the difference between the two diminishes. Under the condition of *a priori* structural information, the performances of three reconstruction configurations are seemingly equivalent.

OCIS codes: 170.3880, 170.3010, 170.6960, 170.5270.

1. Introduction

Diffuse optical tomography (DOT) based on measurement of near-infrared (NIR) light diffused through thick biological tissue aims to quantify the heterogeneities of NIR-absorbing chromophors and scattering particles [1]. There are generally three categories of DOT measurements: (1) continuous wave (CW), wherein only steady-state or direct-current (DC) detection is carried out, (2) time domain, wherein the attenuation and pulse-width broadening of the excitation light are the measurands [2–5], and (3) frequency domain, which is mathematically the Fourier-transform equivalent of the time-domain method [6–17] but is considerably less complicated in instrumentation. Frequency-domain detection ideally renders three types of information: the DC attenuation, the modulation intensity change (AC), and the modulation phase shift (PHS). Some frequency-domain DOT works, however, have utilized AC and PHS [6–12,14,15], rather than the complete measurands of DC, AC, and PHS. Excluding the DC in frequency-domain DOT reconstruction implied that the DC information was considered unlikely to improve the outcome of reconstruction when the AC and PHS are available. Such consideration could have been prompted if the DC information had been redundant in frequency-domain reconstruction, but indeed it has not been either justified or negated.

On the other hand, many works in DOT have relied on only the DC measurements [18–26]. Although lacking phase information will certainly reduce the accuracy or confidence of quantitative reconstruction, almost all these studies have demonstrated that the absorption and reduced scattering characteristics can

0003-6935/10/163059-12$15.00/0

be separately and absolutely reconstructed by use of DC information only. But all these works lack a direct comparison of the outcome of DC-based reconstruction with that of frequency-domain reconstruction, which is needed to provide a basis to assess the compromise for reconstruction based solely upon DC information. Out of these DC-based DOT reconstructions, there also exists a common but not widely stated feature in the images—the recovered background is usually more homogeneous than the general level of background artifacts seen in images reconstructed in the frequency domain. Fewer image artifacts in the background may be beneficial for identifying the target of interest over a relatively heterogeneous background, but what contributes to fewer image artifacts in the background has not been well understood.

This work studies the level of artifacts associated with measurement uncertainties in three modes of image reconstruction, namely DC, AC + PHS, and DC + AC + PHS. The studies are conducted both analytically and by synthetic measurements, to address why the DC-based reconstruction results in fewer background artifacts and to demonstrate that including DC information in frequency domain generally improves the reconstruction outcome. Clearly, the analysis of this study shall be based upon the propagation of measurement noises to the image. Contributing to the image artifacts are a number of noise sources, among which is an error due to coupling loss, as studied by Schweiger *et al.* [27]. That study treated coupling errors as coupling coefficients appended to the solution space, and demonstrated reconstruction of frequency-domain data contaminated with synthetic coupling errors. Similar studies are necessary to understanding reconstruction with contaminated DC data.

The level of artifacts is a critical indicator of the capability of reliably recovering the optical heterogeneity. Ntziachristos *et al.* [28] demonstrated that the reconstruction of localized lesions deteriorated as a function of background heterogeneity. They also found that increasing the dataset size, specifically the number of detectors used, improves the reconstruction of the lesion structure, but does not remove the artifacts. Those results, performed on frequency-domain synthetic and experimental data, indicate that certain artifacts are inherent to image formation and, thereby, cannot be removed completely. The cause of such artifacts must also be inherent to DC-based reconstruction, wherein the outcome relative to frequency-domain reconstruction is unknown.

The analytic approach of this study is based primarily upon a method introduced by Fantini *et al.* [29] to model the accuracies or, equivalently, the errors associated with a two-distance measurement technique for quantifying the optical properties of a bulk homogeneous medium. Reconstructing optical properties in a homogeneous medium is essentially a process of fitting the slopes of measurements with respect to different source–detector distances, for which Fantini *et al.* introduced their models of the "relative error" of absorption and reduced scattering coefficients using the intensity exponential factor, the AC exponential factor, and the phase factor between the measurements made at two different source–detector distances. The tomography of optical heterogeneity relies on multiple measurements among spatially resolved sources and detectors, and image reconstruction is a process of optimizing the local optical properties to minimize the difference of model prediction for these source–detector pairs with respect to the measured values. The accuracy of reconstruction is thereby dependent upon the capability of distinguishing the signal variations for a single source–detector pair due to all types of measurement fluctuations, as well as local changes of tissue optical properties, such variations among different source–detector pairs, and mapping such variations to the image space. Hence, the "relative error" initially discussed in [29] equally applies to tomography of optical heterogeneity, because the "relative error" of measurement determines the upper limit of reconstruction accuracy; in other words, it sets the "parameter-recovery-uncertainty level" (PRUL) in the tomography images.

This study analyzes the PRULs of the absorption coefficient, the reduced scattering coefficient, and the diffusion coefficient, for the measurement conditions of DC, AC + PHS, and DC + AC + PHS and examines their representations as image artifacts in synthetic models. Much of the analytic approach of this study is based upon the method established in [29]; however, there are substantial differences in the measurement configurations investigated, and also, in this novel study, the analytic results partially suggested by [29] are quantitatively evaluated to compare the PRULs among these configurations. It is also noted that [29] considered the measurement configurations of DC + AC, AC + PHS, and DC+ PHS. When frequency-domain (FD) information is available, it is straightforward to apply AC + PHS, as employed by many works [6–12,14,15], to image reconstruction. The utilization of DC + AC and DC + PHS are mathematically valid; however, those configurations have seldom been used for image reconstruction. This study investigates the level of artifacts in the DC, AC + PHS, and DC + AC + PHS configurations, as they are the most likely implemented approaches toward image reconstruction. Therefore, among the results previously stated in [29], only those related to AC + PHS have been included in this study when appropriate. The AC + PHS result for the absorption coefficient in [29] is cited directly, but the AC + PHS result in [29] for reduced scattering is revised to a more generalized form that is consistent with the result for the absorption coefficient. Table 1 in Subsection 2.A is introduced to make clear these distinctions. This study also investigates reconstruction of the diffusion coefficient, because, not only are the absorption and reduced scattering coefficients coupled, but also generally the diffusion

Table 1. Comparison of the Analytic Derivations in This Work with That in [29]

	Measurements				
	DC	DC + AC	AC + PHS	DC + PHS	DC + AC + PHS
$\frac{\Delta\mu_a}{\mu_a}\left(\frac{\sigma_{\mu_a}}{\mu_a}\right)$	This study	[29]	[29]	[29]	This study
$\frac{\Delta\mu_s'}{\mu_s'}\left(\frac{\sigma_{\mu_s'}}{\mu_s'}\right)$	This study	[29]	[29] [a]	[29]	This study
$\frac{\Delta D}{D}\left(\frac{\sigma_D}{D}\right)$	This study		This study		This study

[a]The derivation was revised to a more generalized form.

coefficient is involved in the reconstruction process *prior* to formulating the reduced scattering coefficient. The diffusion coefficient image may provide new insights to the study even though its artifacts are expected to be close to those seen in reduced scattering image.

The rest of the paper is organized in the following sections. Section 2 analyses the PRUL for three categories: (1) D.C. only, (2) AC + PHS, and (3) DC+ AC + PHS. Tissue and measurement parameters typical to optical tomography applications are implemented to evaluate quantitatively the PRULs expected in the images. Section 3 uses synthetic data to examine the uncertainty of the parameters recovered for homogeneous medium, single inclusion with different types of optical contrast, and multiple inclusions with specific optical contrasts. These synthetic models are also evaluated selectively for the condition of having spatial *a priori* information in the image reconstruction. Section 4 discusses the implications of the results.

2. Theory

The reconstruction accuracy of optical tomography is determined by many factors, including the accuracy of the forward model, the determinacy of inverse formulation, and the characteristics of instrument noise [30]. An analytic approach has been introduced in [29] to demonstrate that the uncertainty (or error) in the measurement maps to the uncertainty of recovering the assembled optical properties of bulk tissue. The same uncertainty (or error) of the measurement, when involved in tomographic reconstruction to recover spatially resolved tissue optical properties, will translate to spatially varying artifacts that reduce the contrast-to-noise ratio (CNR) of the target of interest. This effect may seem obvious; however, the extent of it is not well understood. This work closes this gap of knowledge in three conditions of DOT measurements, namely DC, AC+ PHS, and complete frequency-domain information by DC + AC + PHS.

A. Parameter-Recovery-Uncertainty Level

The variation of the recovered optical properties is modeled as PRUL, which for AC + PHS has been derived in [29] in terms of the attenuation of the AC amplitude and phase shift versus a change of source–detector distances. We implement the approach in [29], but extend it to DC-only and DC + AC + PHS configurations, and apply it to diffusion coefficients in addition to absorption and reduced scattering coefficients.

The frequency-domain measurement of photon density consists of a steady state and time-varying components as $U_{\mathrm{FD}}(\vec{r},\omega) = U_{\mathrm{DC}}(\vec{r}) + U_{\mathrm{AC}}(\vec{r},\omega)$, where $\vec{r}$ is the position vector and ω is the angular modulation frequency of the light source. The $U_{\mathrm{FD}}(\vec{r},\omega)$ satisfies the photon diffusion equation of

$$\left(-\frac{\mu_a(\vec{r})}{D(\vec{r})} + \frac{i\omega}{vD(\vec{r})}\right)U_{\mathrm{FD}}(\vec{r},\omega) + \nabla^2 U_{\mathrm{FD}}(\vec{r},\omega) = -\frac{S(\vec{r},\omega)}{D(\vec{r})}, \tag{1}$$

where v is the speed of light in the medium, μ_a is the absorption coefficient, $D = [3(\mu_a + \mu_s')]^{-1}$ is the diffusion coefficient, μ_s' is the reduced scattering coefficient, and the source term $S(\vec{r},\omega)$ has a DC component $S_{\mathrm{DC}}(\vec{r})$ and a time-varying component $S_{\mathrm{AC}}(\vec{r},\omega)$. For a homogeneous infinite medium with a detector at $\vec{r}$ and a source at $\vec{r}'$, thereby a source–detector distance of $d = |\vec{r}' - \vec{r}|$, we have

$$\begin{aligned} U_{\mathrm{FD}}(r,\omega) &= U_{\mathrm{DC}}(r) + |U_{\mathrm{AC}}(r,\omega)|\exp(i\Phi_{\mathrm{AC}}) \\ &= \frac{S_{\mathrm{DC}}(r')}{4\pi Dd}\exp(-k_{\mathrm{DC}}d) \\ &\quad + \frac{S_{\mathrm{AC}}(r',\omega)}{4\pi Dd}\exp(-k_{\mathrm{AC}}d)\cdot\exp(ik_{\mathrm{PHS}}d), \end{aligned} \tag{2}$$

where

$$k_{\mathrm{DC}} = \sqrt{\frac{\mu_a}{D}}, \qquad k_{\mathrm{AC}} = \sqrt{\frac{\mu_a}{2D}\left(\sqrt{1+\frac{\omega^2}{v^2\mu_a^2}}+1\right)}, \qquad k_{\mathrm{PHS}} = \sqrt{\frac{\mu_a}{2D}\left(\sqrt{1+\frac{\omega^2}{v^2\mu_a^2}}-1\right)}. \tag{3}$$

It is noted that $k_{\mathrm{AC}} > k_{\mathrm{DC}}$ and k_{AC} is correlated with, but not linearly dependent upon, k_{DC}. The attenuation of the DC component of the photon density is thus not equal to or linearly dependent upon that of the AC component, which is an indication that the DC information would not be a duplication of any of AC or PHS.

Denoting $d_2 > d_1$ and $\rho = |d_1 - d_2|$ as the difference of source–detector distance between two mea-

surements corresponding to the same source, one has [29] (reproduced here for convenience)

$$\delta = \ln\left(\frac{d_2}{d_1}\frac{U_{\mathrm{DC}}(d_2)}{U_{\mathrm{DC}}(d_1)}\right) = -\rho\cdot k_{\mathrm{DC}} = -\rho\cdot\sqrt{\frac{\mu_a}{D}},$$

$$\alpha = \ln\left(\frac{d_2}{d_1}\frac{U_{\mathrm{AC}}(d_2)}{U_{\mathrm{AC}}(d_1)}\right) = -\rho\cdot k_{\mathrm{AC}}$$

$$= -\rho\cdot\sqrt{\frac{\mu_a}{2D}\left(\sqrt{1+\frac{\omega^2}{v^2\mu_a^2}}+1\right)},$$

$$\phi = \Phi(d_2) - \Phi(d_1) = \rho\cdot k_{\mathrm{PHS}}$$

$$= \rho\cdot\sqrt{\frac{\mu_a}{2D}\left(\sqrt{1+\frac{\omega^2}{v^2\mu_a^2}}-1\right)}. \quad (4)$$

Table 1 lists the PRUL of five different measurement configurations, among which three were investigated in [29]. As stated previously, the configuration of DC + AC and DC + PHS were seldom used for image reconstruction, therefore, only the AC + PHS results of [29] are cited for this comparative study.

In CW measurement, we have

$$\mu_a|_{\mathrm{DC}} = D\cdot\left(\frac{\delta}{\rho}\right)^2. \quad (5)$$

References [31,32] suggest that, for steady-state surface measurements, μ_a and D collectively determine the diffuse reflectance, denoted as R_∞, by the relationship $[\mu_a\cdot D] = K(R_\infty)$. It is noted that the diffuse reflectance is not $U_{\mathrm{DC}}(\vec{r})$, which implies treating $K(R_\infty)$ as not significantly dependent upon $U_{\mathrm{DC}}(\vec{r})$, thereby Eq. (5) may be converted to

$$\mu_a|_{\mathrm{DC}} = \frac{\sqrt{K(R_\infty)}}{\rho}\cdot\delta, \quad (6)$$

and estimating the PRUL of μ_a for DC by

$$\left.\frac{\sigma_{\mu_a}}{\mu_a}\right|_{\mathrm{DC}} = \frac{1}{\mu_a}\left[\frac{\partial\mu_a}{\partial\delta}\sigma_\delta\right] = \frac{\sigma_\delta}{\delta} \quad \text{or} \quad \left(\frac{\sigma_\delta^2}{\delta^2}\right)^{1/2}. \quad (7)$$

We have, for AC + PHS [29],

$$\mu_a|_{\mathrm{AC+PHS}} = \frac{\omega}{2v}\left(\frac{\phi}{\alpha}-\frac{\alpha}{\phi}\right), \quad (8)$$

and a PRUL of [29]

$$\left.\frac{\sigma_{\mu_a}}{\mu_a}\right|_{\mathrm{AC+PHS}} = \frac{1}{\mu_a}\left[\left(\frac{\partial\mu_a}{\partial\alpha}\right)^2\sigma_\alpha^2+\left(\frac{\partial\mu_a}{\partial\phi}\right)^2\sigma_\phi^2\right]^{1/2}$$

$$= \frac{\alpha^2+\phi^2}{\alpha^2-\phi^2}\left(\frac{\sigma_\alpha^2}{\alpha^2}+\frac{\sigma_\phi^2}{\phi^2}\right)^{1/2}. \quad (9)$$

For DC + AC + PHS measurement, we have

$$\mu_a|_{\mathrm{DC+AC+PHS}} = -\frac{\omega}{v}\cdot\frac{\delta^2}{2\alpha\phi} \quad (10)$$

and, accordingly, a PRUL of

$$\left.\frac{\sigma_{\mu_a}}{\mu_a}\right|_{\mathrm{DC+AC+PHS}}$$

$$= \frac{1}{\mu_a}\left[\left(\frac{\partial\mu_a}{\partial\delta}\right)^2\sigma_\delta^2+\left(\frac{\partial\mu_a}{\partial\alpha}\right)^2\sigma_\alpha^2+\left(\frac{\partial\mu_a}{\partial\phi}\right)^2\sigma_\phi^2\right]^{1/2}$$

$$= \left(4\frac{\sigma_\delta^2}{\delta^2}+\frac{\sigma_\alpha^2}{\alpha^2}+\frac{\sigma_\phi^2}{\phi^2}\right)^{1/2}. \quad (11)$$

The PRULs in Eqs. (7), (9), and (11) all have the shape of

$$\frac{\sigma_\mu}{\mu} = \eta\cdot(\xi)^{1/2}, \quad (12)$$

which contains a multiplication factor η and a square-root term $\sqrt{\xi}$. The relative levels of these PRULs become comparable as $\frac{\sigma_\phi^2}{\phi^2}$, $\frac{\sigma_\alpha^2}{\alpha^2}$, and $\frac{\sigma_\delta^2}{\delta^2}$ are practically the same [29]. It is indicated in Table 2 that the PRUL of μ_a will be the lowest in DC-based reconstruction, but whether the PRUL of μ_a is lower in AC + PHS or in DC + AC + PHS depends upon the difference in α and ϕ.

Because the image reconstruction recovers D to formulate μ_s', it is imperative to analyze the PRUL of D. For the case of DC, similar to the derivation for μ_a, we have

$$D|_{\mathrm{DC}} = K(R_\infty)\cdot\left(\frac{\rho}{\delta}\right), \quad (13)$$

Table 2. Comparison on PRUL of $\mu_a(\sigma_{\mu_a}/\mu_a)$

		η		$\sqrt{\xi}$		
Eq.	Condition	Expression	Value	Expression	Normalized value	Normalized $\eta\cdot\sqrt{\xi}$
(7)	DC		1	$\left(\frac{\sigma_\delta^2}{\delta^2}\right)^{1/2}$	1	1
(9)	AC + PHS	$\left(\frac{\alpha^2+\phi^2}{\alpha^2-\phi^2}\right)$	>1	$\left(\frac{\sigma_\alpha^2}{\alpha^2}+\frac{\sigma_\phi^2}{\phi^2}\right)^{1/2}$	1.41	>1.41
(11)	DC + AC + PHS		1	$\left(4\frac{\sigma_\delta^2}{\delta^2}+\frac{\sigma_\alpha^2}{\alpha^2}+\frac{\sigma_\phi^2}{\phi^2}\right)^{1/2}$	2.45	2.45

Table 3. Comparison on PRUL of D

Eq.	Condition	Expression	Normalized Value
(14)	DC	$\left(\frac{\sigma_\delta^2}{\delta^2}\right)^{1/2}$	1
(16)	AC + PHS & DC +AC + PHS	$\left(\frac{\sigma_\alpha^2}{\alpha^2}+\frac{\sigma_\phi^2}{\phi^2}\right)^{1/2}$	~1.41

$$\left.\frac{\sigma_D}{D}\right|_{\mathrm{DC}}=\frac{1}{D}\left[\frac{\partial D}{\partial \delta}\sigma_\delta\right]=\frac{\sigma_\delta}{\delta}\ \text{or}\left(\frac{\sigma_\delta^2}{\delta^2}\right)^{1/2}. \tag{14}$$

For AC + PHS and DC + AC + PHS, the expressions are the same:

$$D|_{\mathrm{AC+PHS}}=D|_{\mathrm{DC+AC+PHS}}=-\frac{\omega\rho^2}{2v}\cdot\frac{1}{\alpha\phi}. \tag{15}$$

Therefore,

$$\begin{aligned}\frac{\sigma_D}{D}|_{\mathrm{AC+PHS}}&=\frac{\sigma_D}{D}|_{\mathrm{DC+AC+PHS}}\\&=\frac{1}{D}\left[\left(\frac{\partial D}{\partial \alpha}\right)^2\sigma_\alpha^2+\left(\frac{\partial D}{\partial \phi}\right)^2\sigma_\phi^2\right]^{1/2}\\&=\left(\frac{\sigma_\alpha^2}{\alpha^2}+\frac{\sigma_\phi^2}{\phi^2}\right)^{1/2}.\end{aligned} \tag{16}$$

The PRULs of D in Eqs. (14) and (16) are compared in Table 3. Apparently, when AC and phase are employed, the DC component is redundant for the recovery of D.

The PRUL of μ_s' is derived by

$$\begin{aligned}\frac{\sigma_{\mu_s'}}{\mu_s'}&=\frac{1}{\mu_s'}\left[\left(\frac{\partial \mu_s'}{\partial D}\right)^2\sigma_D^2+\left(\frac{\partial \mu_s'}{\partial \mu_a}\right)^2\sigma_{\mu_a}^2\right]^{1/2}\\&=\left[\frac{1}{3D}-\mu_a\right]^{-1}\cdot\left[\left(\frac{1}{3D}\right)^2\left(\frac{\sigma_D}{D}\right)^2+(\mu_a)^2\left(\frac{\sigma_{\mu_a}}{\mu_a}\right)^2\right]^{1/2},\end{aligned} \tag{17}$$

so the PRUL of μ_s' for DC is

$$\left.\frac{\sigma_{\mu_s'}}{\mu_s'}\right|_{\mathrm{DC}}=\left[\frac{1}{3D}-\mu_a\right]^{-1}\left[\left(\frac{1}{3D}\right)^2\cdot\left(\frac{\sigma_\delta^2}{\delta^2}\right)+\mu_a^2\cdot\left(\frac{\sigma_\delta^2}{\delta^2}\right)\right]^{1/2}. \tag{18}$$

For AC + PHS, it is [29,33]

$$\begin{aligned}\left.\frac{\sigma_{\mu_s'}}{\mu_s'}\right|_{\mathrm{AC+Phs}}&=\left[\frac{1}{3D}-\mu_a\right]^{-1}\cdot\left[\left(\frac{1}{3D}\right)^2\left(\frac{\sigma_\alpha^2}{\alpha^2}+\frac{\sigma_\phi^2}{\phi^2}\right)\right.\\&\left.+\mu_a^2\cdot\left(\frac{\alpha^2+\phi^2}{\alpha^2-\phi^2}\right)^2\cdot\left(\frac{\sigma_\alpha^2}{\alpha^2}+\frac{\sigma_\phi^2}{\phi^2}\right)\right]^{1/2},\end{aligned} \tag{19}$$

and for DC + AC + PHS, it is

$$\begin{aligned}\frac{\sigma_{\mu_s'}}{\mu_s'}|_{\mathrm{DC+AC+Phs}}&=\left[\frac{1}{3D}-\mu_a\right]^{-1}\\&\cdot\left[\left(\frac{1}{3D}\right)^2\left(\frac{\sigma_\alpha^2}{\alpha^2}+\frac{\sigma_\phi^2}{\phi^2}\right)+\mu_a^2\right.\\&\left.\cdot\left(4\frac{\sigma_\delta^2}{\delta^2}+\frac{\sigma_\alpha^2}{\alpha^2}+\frac{\sigma_\phi^2}{\phi^2}\right)\right]^{1/2}.\end{aligned} \tag{20}$$

Based on the estimation leading to Table 2, the PRULs in Eqs. (19) and (20) can be normalized with respect to Eq. (18). The results are given in Table 4. Again, the PRUL of μ_s' will be the lowest for DC. Whether the PRUL of μ_s' is lower in AC + PHS or in DC + AC + PHS depends also upon the difference in α and ϕ as for the PRUL of μ_a, but, because of the dominance of $1/3D$ over μ_a, the difference between AC + PHS and DC + AC + PHS will be less than that observed for PRUL of μ_a in Table 2.

B. Summary of the PRUL Analyses

The DC-only reconstruction seems to give the least level of relative uncertainty of the parameter in the reconstruction. The AC + PHS configuration seems to be equivalent to DC + AC + PHS in the level of PRULs of reduced scattering and diffusion coefficient, but it is unclear for the absorption coefficient. These analyses have been conducted for an infinite homogeneous medium, but the results will be readily translatable to a medium with boundaries and with inclusions.

3. Synthetic Studies

Simulations are carried out to study the practical issues of PRUL, such as background noise, the accuracy of optical property recovery, and the interparameter cross coupling, of the three measurements setups.

A. Synthetic Model

The forward model is carried out by the finite-element method (FEM) solution of Eq. (1) using the Robin-type boundary condition [34]:

Table 4. Comparison on PRUL of μ_s'

Eq.	Condition	Expression	Normalized as
(18)	DC	$\left[\left(\frac{1}{3D}\right)^2\left(\frac{\sigma_\delta^2}{\delta^2}\right)+\mu_a^2\cdot\left(\frac{\sigma_\delta^2}{\delta^2}\right)\right]^{1/2}$	1
(19)	AC + PHS	$\left[\left(\frac{1}{3D}\right)^2\left(\frac{\sigma_\alpha^2}{\alpha^2}+\frac{\sigma_\phi^2}{\phi^2}\right)+\mu_a^2\cdot\left(\frac{\alpha^2+\phi^2}{\alpha^2-\phi^2}\right)^2\cdot\left(\frac{\sigma_\alpha^2}{\alpha^2}+\frac{\sigma_\phi^2}{\phi^2}\right)\right]^{1/2}$	>1.41
(20)	DC + AC + PHS	$\left[\left(\frac{1}{3D}\right)^2\left(\frac{\sigma_\alpha^2}{\alpha^2}+\frac{\sigma_\phi^2}{\phi^2}\right)+\mu_a^2\cdot\left(4\frac{\sigma_\delta^2}{\delta^2}+\frac{\sigma_\alpha^2}{\alpha^2}+\frac{\sigma_\phi^2}{\phi^2}\right)\right]^{1/2}$	>1.41

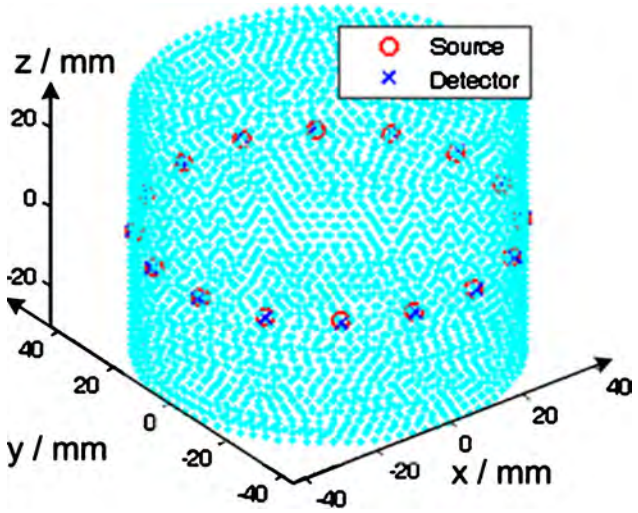

Fig. 1. (Color online) Imaging geometry for a homogeneous medium.

$$U(\vec{r}_0,\omega) - 2DA\hat{n}_0 \cdot \nabla U(\vec{r}_0,\omega) = 0, \tag{21}$$

where A is related to refractive index mismatch and $\hat{n}_0$ is an outgoing normal vector. The Jacobian is structured to the form of

$$J = \begin{bmatrix} \mathrm{DC} \\ \mathrm{AC} \\ \mathrm{PHS} \end{bmatrix} = \begin{bmatrix} \frac{\partial \ln U_{\mathrm{DC}}}{\partial \mu_a} & \frac{\partial \ln U_{\mathrm{DC}}}{\partial D} \\ \frac{\partial \ln |U_{\mathrm{AC}}|}{\partial \mu_a} & \frac{\partial \ln |U_{\mathrm{AC}}|}{\partial D} \\ \frac{\partial \Phi_{\mathrm{AC}}}{\partial \mu_a} & \frac{\partial \Phi_{\mathrm{AC}}}{\partial D} \end{bmatrix}, \tag{22}$$

where the indices of each block of the Jacobian could be node based for pixelwise reconstruction or region based for *prior*-guided regionwise reconstruction. Utilizing only the first row leads to CW, utilizing the second and third rows renders AC + PHS, and utilizing all three rows gives DC + AC + PHS. The inverse solver implements the Levernberg–Marquardt algorithm as

$$x_{k+1} = x_k + \alpha \cdot [J^T(x_k)J(x_k) + \lambda I]^{-1} J^T(x_k)\Delta v(x_k), \tag{23}$$

where x is the array of unknown parameters, $\Delta\nu$ is the forward projection error and λ is a penalty or regularization term. The value of λ is initially set as 100, and is reduced to its fourth root with each continued iteration. The damping factor, α, in the range of (0, 1), is introduced when only regionwise reconstruction is performed to facilitate stable convergence [35] and is set at 0.5 in this study when included. For pixelwise reconstructions using NIRFAST [36,37], α is set to 1.

B. Simulation Results

Synthetic data are generated for a homogeneous medium, a medium with a single inclusion, and a medium with multiple inclusions with mixed types of optical heterogeneities.

1. *PRULs in a Homogeneous Medium*

A cylinder-applicator geometry [38] of 60 mm in height and 86 mm in diameter with 16 optodes is adopted, like the one shown in Fig. 1. The optodes are turned on sequentially for the measurements being taken by all other optodes, generating a total of 240 measurements for each dataset.

The volume is discretized into a FEM mesh of 12,695 nodes for forward computation, while a smaller FEM mesh of 600 nodes is used in the reconstruction. Because this synthetic study specifically investigates the level of artifacts reconstructed to the same level of recovered parameters in an otherwise homogeneous medium, the same optical properties of $\mu_a = 0.01\ \mathrm{mm}^{-1}$ and $\mu_s' = 0.01\ \mathrm{mm}^{-1}$ are used for both forward computation and as the initial values of the inverse routine, with 1% noise added to the forward simulation data to maintain the same measurement error. In addition, all controlling parameters of the inverse model are maintained the same for DC, AC + PHS, and DC + AC + PHS configurations.

Table 5 demonstrates that the variations recovered to the parameters of a homogeneous medium are lowest in DC, as expected from the analytic analysis. The DC + AC + PHS slightly outperforms AC + PHS in μ_a recovery, but AC + PHS slightly outperforms DC + AC + PHS in μ_s'/D recovery.

The normalized numbers (1.45–1.64) for μ_s'/D recovery are considerably close to those in the analytical derivation—with the same average optical properties, the background standard deviation of the images reconstructed by FD system measurements is at least 1.41 times larger than those reconstructed by the CW system. However, in μ_a reconstruction, the variations in FD configurations are about twice those predicted in Table 2. It is noted that the analytic results in this study are based upon perturbation analysis. It is well known that DOT is a nonlinear process, wherein the absorption perturbation is more

Table 5. Mean Value and Standard Deviation Reconstructed for Homogeneous Medium[a]

		$\sigma_{\mu_a}(\mathrm{mm}^{-1})$			$\sigma_{\mu_s'}(\mathrm{mm}^{-1})$			$\sigma_D(\mathrm{mm})$	
	$\bar{\mu}_a$	Abs.	Norm.	$\bar{\mu}_s'$	Abs.	Norm.	$\bar{D}$	Abs.	Norm.
DC	0.01	0.69×10^{-6}	1	1.00	0.80×10^{-4}	1	0.33	2.64×10^{-3}	1
AC + PHS	0.01	3.13×10^{-6}	4.50	1.00	1.18×10^{-4}	1.47	0.33	3.83×10^{-3}	1.45
DC + AC + PHS	0.01	2.98×10^{-6}	4.29	1.00	1.31×10^{-4}	1.64	0.33	4.24×10^{-3}	1.60

[a]"Abs." denotes the absolute value of the standard deviation. "Norm." denotes the standard deviation normalized with respect to the standard deviation of DC. The same notations apply to Tables 6 and 8.

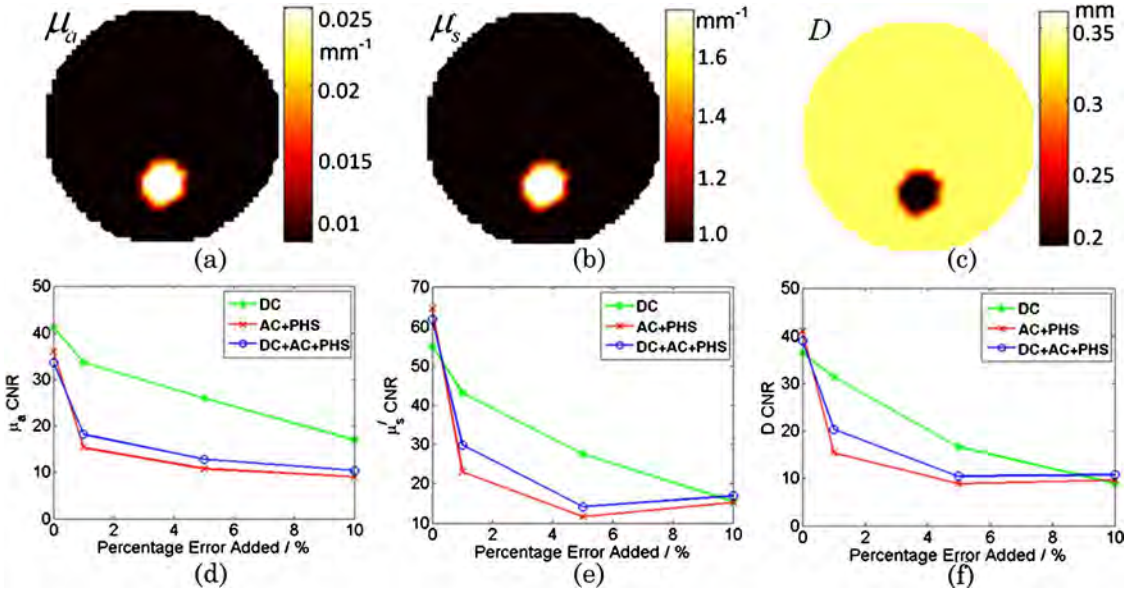

Fig. 2. (Color online) Contrast-to-noise-ratio (CNR) with respect to the measurement noise levels. (a), (b), (c) $\mu_a/\mu_s'/D$ distribution in the $z = 0$ plane of forward model; (d) μ_a CNR comparison; (e) μ_s' CNR comparison; (f) D CNR comparison.

pronounced than scattering perturbation. In this specific model of homogeneous medium, the signal perturbation is evenly distributed to the entire volume of the homogeneous medium instead of mostly confined to smaller lesions with higher optical property contrast, as in the later examinations. Therefore, the perturbations from AC and PHS could have been coupled to and nonlinearly amplified as the variation of absorptions.

2. *Contrast-to-Noise Ratio Analysis for Single Target*

The results in Subsection 3.B.1 indicate that, for 1% noise in the measurement of homogeneous medium, DC-only reconstruction clearly maintains a lower artifact level compared to DC + AC + PHS and AC + PHS. This study examines the contrast of a target inclusion in an otherwise homogeneous medium at different measurement noise levels when reconstructed by DC, AC + PHS, and DC + AC + PHS configurations. The synthetic model is similar to that in Subsection 3.B.1, but with a spherical heterogeneity added at ($x = 0$ mm. $y = -20$ mm, $z = 0$ mm), with $\mu_a = 0.025$ mm^{-1} and $\mu_s' = 1.75$ mm^{-1}. The reconstruction basis of 2760 nodes is larger than the one used for Subsection 3.B.1. Varying noise levels, of 0% to 10%, are integrated into the forward data to examine the CNR of the target (CNR = [max (target-region-value) − mean(background-value)]/ background-standard-deviation) with respect to the background artifacts. The background deviation is calculated by excluding the areas within a distance of 1.5 times the target radius away from its center [39]. The calculated CNRs are given in Fig. 2 for the three types of target contrast. It is observed in Fig. 2 that the CNR levels of μ_a and D look similar when compared to that of μ_s', which supports the

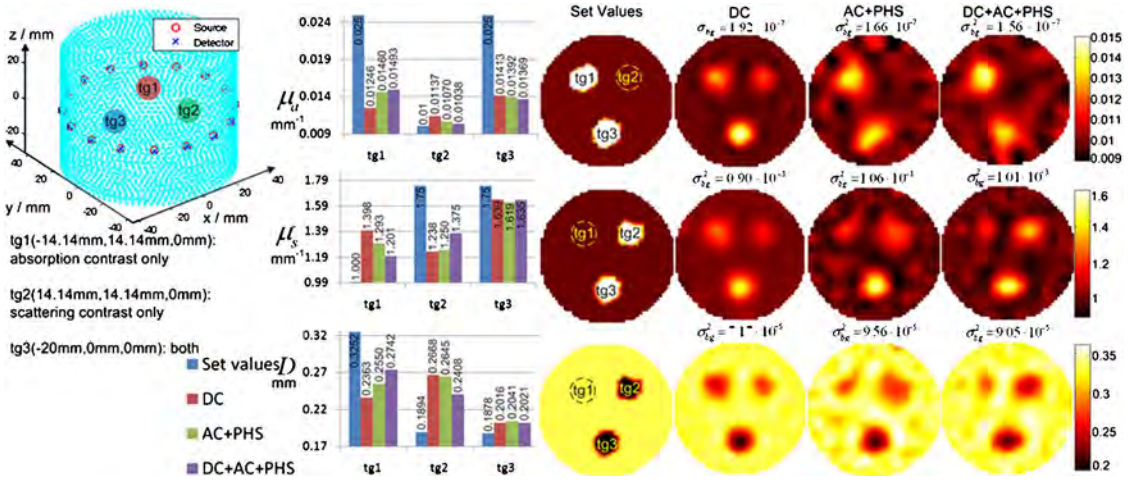

Fig. 3. (Color online) Simulation studies for reconstructing multiple targets in a three-dimensional cylindrical geometry with the optodes and targets located on one plane.

Table 6. Standard Deviation of Background Optical Properties in Fig. 3

	$\sigma_{\mu_a}(\text{mm}^{-1})$		$\sigma_{\mu_s'}(\text{mm}^{-1})$		$\sigma_D(\text{mm})$	
	Abs.	Norm.	Abs.	Norm.	Abs.	Norm.
DC	1.92×10^{-4}	1	2.46×10^{-2}	1	7.25×10^{-3}	1
AC + PHS	3.63×10^{-4}	1.89	2.88×10^{-2}	1.17	9.01×10^{-3}	1.24
DC + AC + PHS	3.45×10^{-4}	1.79	2.49×10^{-2}	1.01	7.75×10^{-3}	1.07

assumptions made for deriving PRULs of μ_a and D in Eqs. (7) and (14). In Fig. 2, the CNR levels of μ_a are found to be lower than that of μ_s', which may be due to underestimation of μ_a and overestimation of μ_s' in such a pixelwise image reconstruction [24]. Despite this, several features can be observed in Fig. 2. (1) At a zero noise level, the three methods are comparable in the CNR. (2) When the noise becomes higher, the D.C. clearly outperforms the other two in CNR, while DC + AC + PHS slightly outperforms AC+ PHS. (3) At a 10% noise level, the CNRs of all methods are similar for μ_s' and D recovery, but DC still outperforms the other two in μ_a reconstruction.

3. *Multiple Target Case*

The geometry for having multiple inclusions is shown in Fig. 3, where three spherical targets with radii of 7.5 mm are located in the longitudinal middle plane ($z = 0$) of the cylindrical imaging volume and are all 20 mm away from the center of the circular cross section, ensuring the same spatial sensitivity at their positions. Target 1, at the upper left ($x = -14.14$ mm, $y = 14.14$ mm, $z = 0$ mm), has only absorption contrast ($\mu_a = 0.025$ mm^{-1}, $\mu_s' = 1$ mm^{-1}), target 2, at upper right ($x = 14.14$ mm, $y = 14.14$ mm, $z = 0$ mm), has only scattering contrast ($\mu_a = 0.01$ mm^{-1}, $\mu_s' = 1.75$ mm^{-1}), and target 3, at lower side ($x = 0$ mm, $y = -20$ mm, $z = 0$ mm), has contrasts of both absorption and reduced scattering ($\mu_a = 0.025$ mm^{-1}, $\mu_s' = 1.75$ mm^{-1}). The dashed line in the figure marks the position of the target when it presents no contrast in that category. Table 6 lists the deviation of the background optical property in the reconstructed images. Standard deviation values in Table 6 are normalized along each column versus those of DC-only reconstruction.

For background homogeneity, comparison in Table 6 indicates that DC only demonstrates the lowest artifact level in the image background, while the background artifact levels of DC + AC + PHS and AC + PHS are approximately 1 to 2 times higher. Although the numerical simulative result does not exactly match the values in Tables 2–4, it qualitatively agrees with the analytical derivations. The analytical derivations given in Tables 2–4 indicate that DC + AC + PHS and AC + PHS produce similar background homogeneities, but the simulation results all indicated a slightly lower background artifact level in DC + AC + PHS reconstruction. For target accuracy, the reconstructed images in Fig. 3 and the data comparison in Table 7 are seen with DC + AC + PHS as superior to AC + PHS, which, along with the comparison on the background homogeneity, indicates that including DC generally improves the FD reconstruction. In terms of interparameter cross coupling, DC has more coupling than FD, which is well known. The cross coupling

Table 7. Comparison of the Accuracy of Recovered Optical Properties in Fig. 3

	$\mu_{a1}(\text{mm}^{-1})$		$\mu_{s1}'(\text{mm}^{-1})$		$D_1(\text{mm})$	
	Value	Error	Value	Error	Value	Error
Set	0.025		1		0.325	
DC	0.0125	−50.16%	1.398	39.84%	0.236	−27.35%
AC + PHS	0.0146	−41.62%	1.293	29.27%	0.255	−21.59%
DC + AC + PHS	0.0149	−40.30%	1.201	20.06%	0.274	−15.67%
	$\mu_{a2}(\text{mm}^{-1})$		$\mu_{s2}'(\text{mm}^{-1})$		$D_2(\text{mm})$	
	Value	Error	Value	Error	Value	Error
Set	0.01		1.75		1.75	
DC	0.0114	13.68%	1.238	−29.25%	1.639	−6.34%
AC + PHS	0.0107	6.95%	1.250	−28.56%	1.619	−7.47%
DC + AC + PHS	0.0104	3.81%	1.375	−21.45%	1.635	−6.55%
	$\mu_{a3}(\text{mm}^{-1})$		$\mu_{s3}'(\text{mm}^{-1})$		$D_3(\text{mm})$	
	Value	Error	Value	Error	Value	Error
Set	0.025		1.75		0.188	
DC	0.0141	−43.48%	1.639	−6.34%	0.2012	7.37%
AC + PHS	0.0139	−44.31%	1.619	−7.47%	0.204	8.70%
DC + AC + PHS	0.0137	−45.24%	1.635	−6.55%	0.202	7.64%

Table 8. Standard Deviation of Background Optical Properties in Fig. 4

	$\sigma_{\mu_a}(\text{mm}^{-1})$		$\sigma_{\mu_s'}(\text{mm}^{-1})$		$\sigma_D(\text{mm})$	
	Abs.	Norm.	Abs.	Norm.	Abs.	Norm.
DC	2.26×10^{-4}	1	3.00×10^{-2}	1	8.47×10^{-3}	1
AC + PHS	4.07×10^{-4}	1.80	3.26×10^{-2}	1.09	9.78×10^{-3}	1.15
DC + AC + PHS	3.95×10^{-4}	1.75	3.18×10^{-2}	1.06	9.51×10^{-3}	1.12

in DC + AC + PHS is slightly less severe than that in AC + PHS.

A similar study is conducted for the same targets in a three-ring setup [38] in Fig. 4, which has three identical rings of optodes at the azimuthal planes of $z = -10$ mm, $z = 0$ mm, and $z = 10$ mm. Each set of data contains a total of 2256 measurements by turning on one source and detecting at all other optodes. The key values are compared in Tables 8 and 9. Most features of the three aspects discussed for the single-ring case can be reconfirmed, except that the target contours recovered by FD reconstructions are more accurately defined, but, nonetheless, the difference between DC + AC + PHS and AC + PHS is insignificant.

Prior-guided region-based reconstructions are also performed on both of the imaging geometries of Figs. 3 and 4 to examine if including accurate *a priori* structural information of the target affects the outcome of the three reconstruction configurations. As is shown in Figs. 5 and 6, with forward models the same as those in Figs. 3 and 4, the inverse model has integrated spatial *a priori* information by assuming a homogeneous target of the accurate size in a homogeneous background. Results of both cases indicate that, with the structural *a priori* information, the performances of the three configurations are essentially equivalent.

4. Discussions

Using only the DC information to simultaneously recover the absorption and diffusion (or the reduced scattering) distributions has been controversial. The nonuniqueness that may be inherent to DC-only measurements was described in a seminal study [40]. However, despite the negative predictions in [40] that there could be an infinite number of diffusion and absorption pairs leading to the same surface measurements, Harrach [41] proved that, at most, one of them consists of a piecewise constant diffusion and piecewise analytic absorption, and if the true medium has these properties, as in virtually any practical condition, a reconstruction algorithm favoring these properties will pick the right combination of profiles. Harrach's study theoretically justified the experiences in many works that the absorption and scattering distributions have been separately and uniquely recovered by surface measurement of DC only [18–26].

The primary aim of this work is to understand the expectation for DC-based reconstruction in a more systematic approach, thereby establishing a certain level of confidence for the recovered information when only DC information can be relied upon. This work, conveyed by a side-by-side comparison of the reconstructions based on DC, AC + PHS, and DC + AC + PHS, does provide direct evidence that DC-based reconstruction is much less accurate in recovering the absolute optical properties of the target of interest when no additional spatial information is available to confine the reconstruction, as having been universally recognized by the DOT community. However, apart from these well-expected shortcomings, it seems that DC-based reconstruction may not be completely unfavorable. This study generalized the analytical approach initially proposed in [29]

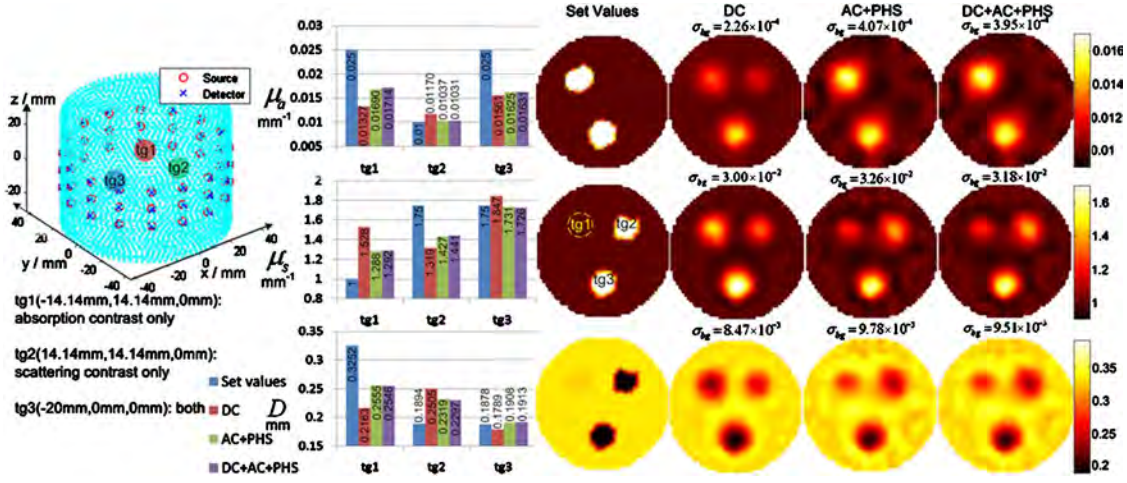

Fig. 4. (Color online) Simulation studies for reconstructing multiple targets in a three-dimensional cylindrical geometry with the optodes located on three different planes and targets located on the middle plane.

Table 9. Comparison of the Accuracy of Recovered Optical Properties in Fig. 4

	$\mu_{a1}(\text{mm}^{-1})$		$\mu'_{s1}(\text{mm}^{-1})$		$D_1(\text{mm})$	
	Value	Error	Value	Error	Value	Error
Set	0.025		1		0.325	
DC	0.0133	−46.93%	1.528	52.81%	0.216	−33.49%
AC + PHS	0.0169	−32.39%	1.288	28.77%	0.256	−21.43%
DC + AC + PHS	0.0171	−31.42%	1.292	29.21%	0.255	−21.70%
	$\mu_{a2}(\text{mm}^{-1})$		$\mu'_{s2}(\text{mm}^{-1})$		$D_2(\text{mm})$	
	Value	Error	Value	Error	Value	Error
Set	0.01		1.75		0.189	
DC	0.0117	16.95%	1.319	−24.63%	0.251	32.26%
AC + PHS	0.0104	3.73%	1.427	−18.45%	0.232	22.46%
DC + AC + PHS	0.0103	3.09%	1.441	−17.66%	0.230	21.31%
	$\mu_{a3}(\text{mm}^{-1})$		$\mu'_{s3}(\text{mm}^{-1})$		$D_3(\text{mm})$	
	Value	Error	Value	Error	Value	Error
Set	0.025		1.75		0.188	
DC	0.0156	−37.57%	1.847	5.57%	0.178	−4.73%
AC + PHS	0.0163	−35.02%	1.731	−1.10%	0.191	1.61%
DC + AC + PHS	0.0163	−34.77%	1.726	−1.38%	0.191	1.88%

to quantify the level of image artifacts that is expressed by the standard deviation of a parameter over the parameter itself. Parameters representative of tissue measurements are used to evaluate the analytic results and conduct the synthetic studies, in both of which the DC reconstruction produced a lower level of relative variation in the optical parameters recovered, and some advantages in the CNR. It may be argued that DC flattens images, leading to a lower standard deviation in the background and, because the background standard deviation is the denominator of CNR, the CNR of DC could become better. But, if there were flattening of the image, then the numerator of the CNR would also be flattened, and perhaps flattened more strongly owing to the nonlinearity of DOT and, thereby, underestimated at a higher level, which collectively might reduce the CNR rather than increase the CNR. The slight but notable CNR advantage of DC-based over FD-based reconstruction demonstrated in this study strongly suggests some inherent advantages of DC, but it could be just because DC has lower information content, similar to what one could expect by reducing the amount of data available or increasing the regularization in FD-based reconstructions.

It is worthwhile to note that this study (as well as most other synthetic studies) assumes a step change of the optical properties of the target of interest with respect to the background. This is not a faithful representation of actual tissue-imaging applications, wherein the target of interest frequently has a tapered or smooth change of contrast over the background. The stronger cross talk between absorption and scattering seen for DC-only reconstruction in this study, as well as many other studies, could have been the outcome of the nonuniqueness, revealed by [40], which is pronounced when the target of interest has a step contrast over the background. In fact, the DC-based reconstruction of *in vivo* measurements has encountered notably different absorption and scattering patterns of a target of interest [42], which may indicate a weaker cross talk for smoother contrast of the target of interest. It is also noted that this study, as well as most other synthetic studies, assumes a globally homogenous yet locally heterogeneous background. An actual tissue environment could be locally homogenous but globally strongly heterogeneous, such as is found in the prostate [26]. In such conditions, a balance or trade-off may exist between the ability of suppressing the background heterogeneity and the likelihood of identifying a

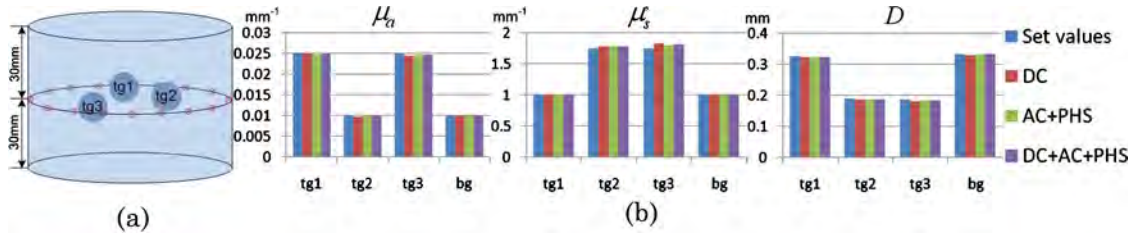

Fig. 5. (Color online) Region-based reconstruction for multiple targets in a three-dimensional cylindrical geometry with the optodes and targets located on one plane. (a) Imaging geometry and the regions of interest; (b) comparison of the results for DC, AC + PHS, and DC + AC + PHS.

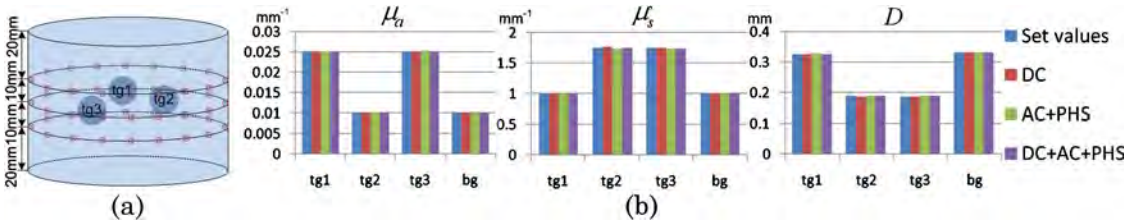

Fig. 6. (Color online) Region-based reconstruction for multiple targets in a three-dimensional cylindrical geometry with the optodes located on three different planes and targets located on the middle plane. (a) Imaging geometry and the regions of interest; (b) comparison of the results for DC, AC + PHS, and DC + AC + PHS.

target of interest in which the contrast is strong locally but weak globally.

This study has also indicated that including DC information in FD reconstruction can sometimes lead to better images than those obtained by ignoring it. The expressions of δ and α in Eq. (4) demonstrate that the DC attenuation is not linearly dependent upon the AC attenuation, and the difference between the two attenuation values increases as the modulation frequency increases. The necessity of including DC in order to optimize the FD reconstruction is made evident by the results in Subsections 3.B.2 and 3.B.3, wherein the DC + AC + PHS results have always been slightly better than the AC + PHS results on the background artifacts, the target properties, and the cross coupling between μ_a and μ_s'/D. However, the slightly better performance of DC + AC + PHS over AC + PHS diminishes as the total number of measurements goes up, as is shown in the three-ring case in Subsection 3.B.3. When fewer measurements are available in application situations, including the DC information in the limited FD measurements likely will improve the overall reconstruction outcome.

This study is carried out for the measurements at a single wavelength. Investigating the PRUL issues in the context of multiband FD measurements will be a natural and more practical extension of this work because most optical tomography measurements are conducted with some kind of spectral information. Besides, similar approaches may be extended to other applications wherein the measurement data contains multiple aspects of information, from which the data usage may be optimized for the specific system configuration.

5. Conclusions

The level of variations of recovered optical properties in optical tomography associated with the measurement uncertainty under three reconstruction configurations of DC-only, the DC-excluded FD, and the DC-included FD is studied by analytic and synthetic means. It is demonstrated that, at the same level of measurement uncertainty typical to optical tomography and under pixelwise reconstruction without spatial *a priori* information, the standard deviations of μ_a over μ_a reconstructed by DC only are at least 1.4 times lower than those obtained by FD methods. The standard deviations of D (or μ_s') over D (or μ_s') reconstructed by DC only are slightly lower than those by FD methods. Frequency-domain reconstruction including DC generally outperforms reconstruction excluding DC, but the difference between the two becomes less significant when the total amount of measurements becomes larger. For FD reconstruction with no spatial *a priori* information and a smaller number of measurements, including DC is recommended. When *a priori* structural information is available, the three reconstruction configurations investigated in this study perform equally well.

This work has been supported in part by the Prostate Cancer Research Program of the U.S. Army Medical Research Acquisition Activity (USAMRAA) through grant W81XWH-07-1-0247, and the Health Research Program of Oklahoma Center for the Advancement of Science and Technology (OCAST) through grant HR06-171. We are grateful to the anonymous reviewers for their constructive comments that enriched the discussions of this work.

References and Notes

1. S. R. Arridge, "Optical tomography in medical imaging," Inverse Probl. **15**, R41–R93 (1999).
2. F. Gao, H. Zhao, Y. Tanikawa, and Y. Yamada, "Optical tomographic mapping of cerebral haemodynamics by means of time-domain detection: methodology and phantom validation," Phys. Med. Biol. **49**, 1055–1078 (2004).
3. H. Rinneberg, D. Grosenick, K. T. Moesta, J. Mucke, B. Gebauer, C. Stroszczynski, H. Wabnitz, M. Moeller, B. Wassermann, and P. M. Schlag, "Scanning time-domain optical mammography: detection and characterization of breast tumors in vivo," Technol. Cancer Res. Treat. **4**, 483–496 (2005).
4. T. Tanifuji and M. Hijikata, "Finite difference time domain (FDTD) analysis of optical pulse responses in biological tissues for spectroscopic diffused optical tomography," IEEE Trans. Med. Imaging **21**, 181–184 (2002).
5. W. Mo and N. Chen, "Fast time-domain diffuse optical tomography using pseudorandom bit sequences," Opt. Express **16**, 13643–13650 (2008).
6. B. W. Pogue, M. S. Patterson, H. Jiang, and K. D. Paulsen, "Initial assessment of a simple system for frequency domain diffuse optical tomography," Phys. Med. Biol. **40**, 1709–1729 (1995).
7. B. W. Pogue, T. O. McBride, J. Prewitt, U. L. Osterberg, and K. D. Paulsen, "Spatially variant regularization improves diffuse optical tomography," Appl. Opt. **38**, 2950–2961 (1999).
8. J. Wang, S. Jiang, K. D. Paulsen, and B. W. Pogue, "Broadband frequency-domain near-infrared spectral tomography using a mode-locked Ti:sapphire laser," Appl. Opt. **48**, D198–D207 (2009).
9. D. M. Hueber, M. A. Franceschini, H. Y. Ma, Q. Zhang, J. R. Ballesteros, S. Fantini, D. Wallace, V. Ntziachristos,

and B. Chance, "Non-invasive and quantitative near-infrared hemoglobin spectrometry in the piglet brain during hypoxic stress, using a frequency-domain multidistance instrument," Phys. Med. Biol. **46**, 41–62 (2001).
10. M. A. Franceschini, K. T. Moesta, S. Fantini, G. Gaida, E. Gratton, H. Jess, W. W. Mantulin, M. Seeber, P. M. Schlag, and M. Kaschke, "Frequency-domain techniques enhance optical mammography: initial clinical results," Proc. Natl. Acad. Sci. USA **94**, 6468–6473 (1997).
11. N. G. Chen, M. Huang, H. Xia, D. Piao, E. Cronin, and Q. Zhu, "Portable near-infrared diffusive light imager for breast cancer detection," J. Biomed. Opt. **9**, 504–510 (2004).
12. M. J. Holboke, B. J. Tromberg, X. Li, N. Shah, J. Fishkin, D. Kidney, J. Butler, B. Chance, and A. G. Yodh, "Three-dimensional diffuse optical mammography with ultrasound localization in a human subject," J. Biomed. Opt. **5**, 237–247 (2000).
13. B. J. Tromberg, B. W. Pogue, K. D. Paulsen, A. G. Yodh, D. A. Boas, and A. E. Cerussi, "Assessing the future of diffuse optical imaging technologies for breast cancer management," Med. Phys. **35**, 2443–2451 (2008).
14. E. S. Papazoglou, M. S. Weingarten, L. Zubkov, L. Zhu, S. Tyagi, and K. Pourezaei, "Near infrared diffuse optical tomography: improving the quality of care in chronic wounds of patients with diabetes," Biomed. Instrum. Technol. **41**, 83–87 (2007).
15. G. Gulsen, O. Birgul, M. B. Unlu, R. Shafiiha, and O. Nalcioglu, "Combined diffuse optical tomography (DOT) and MRI system for cancer imaging in small animals," Technol. Cancer Res. Treat. **5**, 351–363 (2006).
16. J. P. Culver, R. Choe, M. J. Holboke, L. Zubkov, T. Durduran, A. Slemp, V. Ntziachristos, B. Chance, and A. G. Yodh, "Three-dimensional diffuse optical tomography in the parallel plane transmission geometry: evaluation of a hybrid frequency domain/continuous wave clinical system for breast imaging," Med. Phys. **30**, 235–247 (2003).
17. H. K. Kim, U. J. Netz, J. Beuthan, and A. H. Hielscher, "Optimal source-modulation frequencies for transport-theory-based optical tomography of small-tissue volumes," Opt. Express **16**, 18082–18101 (2008).
18. N. Iftimia and H. Jiang, "Quantitative optical image reconstruction of turbid media by use of direct-current measurements," Appl. Opt. **39**, 5256–5261 (2000).
19. A. M. Siegel, J. J. A. Marota, and D. A. Boas, "Design and evaluation of a continuous-wave diffuse optical tomography system," Opt. Express **4**, 287–298 (1999).
20. Y. Xu, X. Gu, T. Khan, and H. Jiang, "Absorption and scattering images of heterogeneous scattering media can be simultaneously reconstructed by use of dc data," Appl. Opt. **41**, 5427–5437 (2002).
21. Z. Yuan and H. Jiang, "Image reconstruction scheme that combines modified Newton method and efficient initial guess estimation for optical tomography of finger joints," Appl. Opt. **46**, 2757–2768 (2007).
22. H. Jiang, K. D. Paulsen, U. L. Osterbergy, and M. S. Patterson, "Improved continuous light diffusion imaging in single- and multi-target tissue-like phantoms," Phys. Med. Biol. **43**, 675–693 (1998).
23. Y. Pei, H. L. Graber, and R. L. Barbour, "Normalized-constraint algorithm for minimizing inter-parameter cross-talk in DC optical tomography," Opt. Express **9**, 97–109 (2001).
24. Z. Jiang, D. Piao, G. Xu, J. W. Ritchey, G. R. Holyoak, K. E. Bartels, C. F. Bunting, G. Slobodov, and J. S. Krasinski, "Trans-rectal ultrasound-coupled near-infrared optical tomography of the prostate Part II: Experimental demonstration," Opt. Express **16**, 17505–17520 (2008).
25. A. H. Hielscher, A. D. Klose, A. K. Scheel, B. Moa-Anderson, M. Backhaus, U. Netz, and J. Beuthan, " Sagittal laser optical tomography for imaging of rheumatoid finger joints," Phys. Med. Biol. **49**, 1147–1163 (2004).
26. K. K. Wang and T. C. Zhu, "Reconstruction of in-vivo optical properties for human prostate using interstitial diffuse optical tomography," Opt. Express **17**, 11665–11672 (2009).
27. M. Schweiger, I. Nissilä, D. A. Boas, and S. R. Arridge, "Image reconstruction in optical tomography in the presence of coupling errors," Appl. Opt. **46**, 2743–2756 (2007).
28. V. Ntziachristos, A. H. Hielscher, A. G. Yodh, and B. Chance, "Diffuse optical tomography of highly heterogeneous media," IEEE Trans. Med. Imaging **20**, 470–478 (2001).
29. S. Fantini, M. A. Franceschini, J. B. Fishkin, B. Barbieriand, and E. Gratton, "Quantitative determination of the absorption spectra of chromophores in strongly scattering media: a light-emitting-diode based technique," Appl. Opt. **33**, 5204–5213 (1994).
30. D. Boas, T. Gaudette, and S. R. Arridge, "Simultaneous imaging and optode calibration with diffuse optical tomography," Opt. Express **8**, 263–270 (2001).
31. S. L. Jacques, "Reflectance spectroscopy with optical fiber devices and transcutaneous bilirubinometers," in *Biomedical Optical Instrumentation and Laser-Assisted Biotechnology*, A. M. Verga Scheggi, S. Martellucci, A. N. Chester, and R. Pratesi, eds. (Kluwer Academic, 1996), pp. 83–94.
32. F. Fabbri, M. A. Franceschini, and S. Fantini, "Characterization of spatial and temporal variations in the optical properties of tissuelike media with diffuse reflectance imaging," Appl. Opt. **42**, 3063–3072 (2003).
33. The original derivation in [29] for $\sigma_{\mu_s'}/\mu_s'$ has ρ in the equation, which is inconsistent with that obtained for σ_{μ_a}/μ_a. Equation (19) corrected this inconsistency.
34. B. W. Pogue, S. Geimer, T. O. McBride, S. Jiang, U. L. Osterberg, and K. D. Paulsen, "Three-dimensional simulation of near-infrared diffusion in tissue: boundary condition and geometry analysis for finite-element image reconstruction," Appl. Opt. **40**, 588–600 (2001).
35. G. Xu, D. Piao, C. H. Musgrove, C. F. Bunting, and H. Dehghani, "Trans-rectal ultrasound-coupled near-infrared optical tomography of the prostate, part I: simulation," Opt. Express **16**, 17484–17504 (2008).
36. H. Dehghani, B. W. Pogue, S. Jiang, B. Brooksby, and K. D. Paulsen, "Three-dimensional optical tomography: resolution in small-object imaging," Appl. Opt. **42**, 3117–3128 (2003).
37. H. Dehghani, M. E. Eames, P. K. Yalavarthy, S. C. Davis, S. Srinivasan, C. M. Carpenter, B. W. Pogue, and K. D. Paulsen, "Near infrared optical tomography using NIRFAST: algorithms for numerical model and image reconstruction algorithms," Commun. Numer. Meth. Eng. **25**, 711–732 (2009).
38. P. K. Yalavarthy, H. Dehghani, B. W. Pogue, and K. D. Paulsen, "Critical computational aspects of near infrared circular tomographic imaging: Analysis of measurement number, mesh resolution and reconstruction basis," Opt. Express **14**, 6113–6127 (2006).
39. M. Huang and Q. Zhu, "A dual-mesh optical tomography reconstruction method with depth correction using *a priori* ultrasound information," Appl. Opt. **43**, 1654–1662 (2004).
40. S. R. Arridge and W. R. B. Lionheart, "Nonuniqueness in diffusion-based optical tomography," Opt. Lett. **23**, 882–884 (1998).
41. B. Harrach, "On uniqueness in diffuse optical tomography," Inverse Probl. **25**, 055010 (2009).
42. Z. Jiang, G. R. Holyoak, K. E. Bartels, J. W. Ritchey, G. Xu, C. F. Bunting, G. Slobodov, and D. Piao, "In vivo trans-rectal ultrasound coupled near-infrared optical tomography of a transmissible venereal tumor model in the canine pelvic canal," J. Biomed. Opt. **14**, 030506 (2009).

Alternative Transrectal Prostate Imaging: A Diffuse Optical Tomography Method

Daqing Piao, *Member, IEEE*, Kenneth E. Bartels, Zhen Jiang, Gilbert Reed Holyoak, Jerry W. Ritchey, Guan Xu, Charles F. Bunting, *Member, IEEE*, and Gennady Slobodov

(Invited Paper)

***Abstract*—This paper presents a transrectal dual-modality near-infrared (NIR) diffuse optical tomography technique coupled with ultrasonography that provides an integrated method for detecting prostate cancer (PCa). The study that provides an alternative transrectal prostate imaging system stems from the perceived inadequacy of conventional transrectal ultrasound (TRUS) in PCa imaging. The transrectally applied diffuse optical tomography aims to characterize the spatially resolved optical properties of the *intact* prostate that are known to have intraorgan and intersubject heterogeneities. A canine model of PCa using canine transmissible venereal tumor was used to demonstrate the utility of this technology in detecting PCa. Tumors in the pelvic canal, including tumors in the prostate, were found to be detectable at 2-week postinjection based upon the NIR absorption contrast, which was detected a few weeks earlier than using NIR-reduced scattering and effective attenuation contrasts, as well as TRUS. Transrectal optical tomography detection of cancerous tissues *in vivo* in *intact* canine prostate based upon NIR contrasts may prove useful for diagnostic imaging of PCa and potentially aid in pretreatment planning for phototherapy applications.**

***Index Terms*—Biomedical acoustics, biomedical optical imaging, diffuse optical tomography, prostate cancer (PCa).**

I. Introduction

THE PROSTATE gland may not be considered as a life-sustaining organ, but prostate cancer (PCa) claims the lives of about 28 000 American men every year [1]. Lifetime risks for a diagnosis of PCa and as the cause of death for American men are 16% and 3%, respectively [2], [3]. Although the death rate of PCa has declined steadily in the past decade [1], [4], PCa remains a compelling medical health problem in American men [5].

Manuscript received July 31, 2009; revised September 10, 2009 and September 28, 2009; accepted September 30, 2009. Date of publication November 13, 2009; date of current version August 6, 2010. This work was supported by the U.S. Department of Defense Army Medical Research Program under Grant W81XWH-07-1-0247.

D. Piao, Z. Jiang, G. Xu, and C. F. Bunting are with the School of Electrical and Computer Engineering, Oklahoma State University, Stillwater, OK 74078 USA (e-mail: daqing.piao@okstate.edu; zhen.jiang@okstate.edu; gary.xu@okstate.edu; reverb@okstate.edu).

K. E. Bartels and G. R. Holyoak are with the Department of Veterinary Clinical Sciences, Oklahoma State University, Stillwater, OK 74078 USA (e-mail: kenneth.bartels@okstate.edu; reed.holyoak@okstate.edu).

J. W. Ritchey is with the Department of Veterinary Pathobiology, Oklahoma State University, Stillwater, OK 74078 USA (e-mail: jerry.ritchey@okstate.edu).

G. Slobodov is with the Department of Urology, University of Oklahoma Health Sciences Center, Oklahoma City, OK 73104 USA (e-mail: Gennady-Slobodov@ouhsc.edu).

Color versions of one or more of the figures in this paper are available online at http://ieeexplore.ieee.org.

Digital Object Identifier 10.1109/JSTQE.2009.2034026

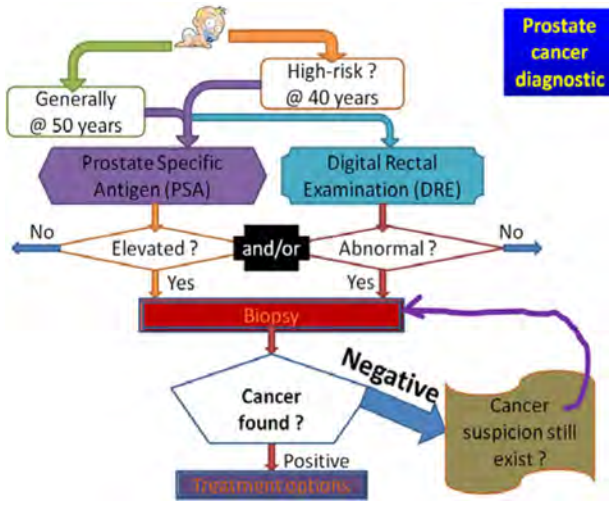

Fig. 1. Procedures involved in a PCa diagnostic.

There is broad consensus that current methods of diagnosing, staging, and treating PCa are inadequate [5], [6]. The diagnosis of PCa currently involves determination of prostate-specific antigen (PSA) and digital rectal examination (DRE), recommended to begin at 50 years of age for men with general risk or at 40 years of age for men with high risk, such as those individuals having a family history of PCa [7]. An abnormal PSA or DRE that provides a presumptive diagnosis of PCa is typically followed by biopsy procedures (illustrated in Fig. 1), which are performed on approximately 1 million American men each year. Prostate biopsy involves ultrasound (US)-guided transrectal needle insertion that provides at least six cores of tissue samples. Sampling 12–16 cores is the most commonly used template, but when indicated, saturation biopsies of up to 24–50 cores may be performed [8]–[10]. These multiple needle cores or "chips," each ~1 mm wide and ~2 cm long, are sampled systematically from the entire gland, with some preference given to the peripheral zone of the prostate wherein most cancers are found [11]. Sampling of more than one core during the biopsy procedure is necessary because up to 85% of PCas are multifocal [12]; however, current systematic biopsy techniques have an overall cancer-positive rate of only 20%–25% [11], [13]. This low "positive" biopsy rate illustrates shortcomings to reliably detect and localize PCa using current outpatient imaging modalities.

Of the ~200 000 patients diagnosed with PCa each year, men with high-grade disease have a significantly greater survival rate with radical treatment (total excision), but men with low-grade

PCa have a smaller absolute survival rate with radical treatment that is further compromised by the potentially adverse effects of current radical therapies [14]. Optimal treatment is thus directed toward eradicating clinically relevant cancer, while at the same time leaving nonpathologic structures surrounding the prostate intact [14]. The optimal "targeted treatment" may include therapeutic choices, such as photodynamic therapy (PDT) [15] or photothermal therapy [16], for localized or recurrent PCa. The efficacy of phototherapy is dependent upon many factors, including the accuracy of profiling the cancer in the prostate, which is largely based upon transrectal ultrasound (TRUS) during treatment monitoring.

The need for more accurate imaging modalities, for both "targeted biopsy" and "targeted treatment," have evoked investigation and development of a number of novel imaging technologies besides the standard modalities, such as US, MRI, computed tomography (CT), etc. Some of these novel approaches, which will be briefly reviewed in this paper, have emerged as alternative prostate imaging methods that provide new insights valuable in differentiating PCa from benign tissues. Among these emerging alternative prostate imaging technologies, the approach using near-infrared (NIR) light has seemed to provide unique information regarding optical properties of the *intact* prostate that may be useful for detecting malignant tissue and pretreatment dosimetry planning. Interpretation of the "noninvasively" acquired optical tomography images of the prostate relies on previous knowledge of prostate optical properties; therefore, a summary of what is known regarding the optical properties of both the canine and human prostate is also necessary.

This paper comprises following sections. In Section II, a brief review is provided regarding emerging alternative transrectally applicable prostate imaging modalities. In Section III,the known optical properties of canine and human prostates are summarized. The remaining sections discuss the transrectal diffuse optical tomography approach that is integrated with standard TRUS, and demonstrate the capability of detecting PCa *in vivo* in the canine model using transmissible venereal tumor (TVT).

II. Emerging Alternative Transrectal Imaging Technologies for Prostate Imaging

The deep intrapelvic position of the prostate dictates employing "transrectal" application in most prostate imaging modalities. Unlike MRI or CT scanners that are capable of imaging the whole body, but with the option of imaging a specific organ or tissue volume (such as in MRI using surface coils) for improved resolution, US is optimal for imaging a specific organ like the prostate gland, since the tissue–ultrasonic interaction requires dedicated transducer designs. The TRUS has become a "gold standard" for outpatient evaluation of the prostate because of its ability to reveal in real time the prostate morphology as well as the blood flow or tissue harmonic responses within the gland. For any alternative prostate imaging modalities developed for outpatient use, it is most likely that the modality would have to integrate with or rely on TRUS, unless the modality itself has real-time capability of visualizing the identifiable prostate morphology. A number of new approaches for prostate imaging, most of which have been demonstrated "transrectally" and some of which are in the stage of advancing to "transrectal" mode, are briefly reviewed later to provide a "side-by-side" comparison of these modalities and their potential for PCa detection.

A. Alternative Transrectal Prostate Imaging Approaches Based on Tissue Mechanical Properties

The conventional TRUS images are formed based on the echogenicity originating from the acoustic index mismatches within the tissue. By taking advantages of tissue mechanical properties other than the acoustic indexes and other forms of tissue–ultrasonic interactions, a number of modalities are under development for prostate imaging.

The prostate mechanical imaging unit developed by Artann Laboratories, Trenton, NJ, employed a transrectal probe fitted with pressure sensor arrays and a 3-D orientation sensor. The pressure sensor array in the head of the probe evaluates spatial distribution of tissue hardness by measuring changes in pressure pattern in response to palpation of the prostate. The technique permitted real-time, cross-sectional imaging of the prostate and produced 3-D reconstructed elasticity images of the gland [17], [18].

The elastography or strain imaging is based on the fact that the backscattered US signal changes its local characteristic pattern only to a comparably small extent if the insonified tissue is slightly compressed and decompressed during the examination [19]. The time or space differences between local regions of interest under different compression ratios change with differences in compressibility of the insonified tissue. As the compressibility of local tissue regions is dependent upon the surrounding tissue and the applied compression force, estimation of tissue elasticity helps to discriminate hard-tissue from soft-tissue regions [19]. Prostate imaging has also been investigated by use of acoustic radiation force that produces a map of the mechanical response of an object to a dynamic force applied at each point. The method remotely exerts a localized acoustic stress field, at a desired frequency, within or on the surface of an object, and records the resultant acoustic response or acoustic emission. Depending on the elastic properties of the object, the radiation force may cause the object to vibrate at a predetermined frequency. Such acoustic response is a measure of the tissue viscoelasticity that has shown differences between malignant and benign prostate tissues [20], [21].

All these modalities have relied upon mechanical signatures that PCa may have. The advantages of these modalities, for those employing ultrasonic energy, are the minimal modification necessary to the US transducer, signal detection, and image formation when comparing with other approaches.

B. Alternative Transrectal Prostate Imaging Approaches Based on Tissue Electrical Properties

The electrical property of tissue is primarily a result of its underlying morphology [22]. The relative intracellular and extracellular fluid volumes and ionic concentrations, and the cellular membrane extent in the tissue, respectively, constitute a frequency-dependent reactive component of bioimpedance,

which also has a relatively frequency-independent resistive component [23]. The complex electrical properties represented by bioimpedance include conductivity and relative permittivity. Imaging of these electrical properties [24] have been proposed by using transrectal electrical impedance tomography [22], [23] coupled with TRUS that may act as a screening device secondary to PSA monitoring or serve as an imaging technique with enhanced lesion specificity for biopsy guidance. Such development has been based on pilot studies suggesting that the electrical properties of PCa may be noticeably different from those of benign tissues within the gland; specifically, the conductivity of malignant tissue in the prostate is found less than that of benign tissues [22], [23].

C. Alternative Transrectal Prostate Imaging Approaches Based on Tissue Optical Properties

Recently, there are several investigations into using NIR light to detect PCa. All these methods are based on optical contrasts of chromophores, either intrinsic or exogenous, which have different concentration in malignant and benign tissues. If the intrinsic optical contrast comes from the difference of hemoglobin content (e.g., total hemoglobin and proportion of oxygenated hemoglobin), it is considered to be associated with angiogenesis and hypoxic changes that are characteristic for a proliferating tumor. One example of utilizing the intrinsic optical contrast is a hybrid laser optoacoustic and ultrasonic imaging method [25], [26]. Transient acoustic signals are generated by pressure that precedes thermal expansion of tissue following the absorption of a short laser pulse. The optoacoustic imaging reconstructs ultrasonic images of intrinsic light absorber that shows regions of tissue with enhanced absorption contrast. Some other approaches have implemented optical contrasts that are exogenously administered, such as utilizing gold-nanorod contrast agent [27], Cytate [28], and other fluorescent imaging approaches [29]. All these modalities are suited for transrectal development.

The aforementioned approaches involve using NIR light. It is noted that the efficacy of light-based imaging modalities not only depends upon the existence of an intrinsic or exogenous optical contrast associated with the cancer, but also the optical properties of the normal tissue, which determines if the photon illumination can reach a specific tissue volume, and if the optical contrast of the malignant tissue over normal tissue is resolvable out of any background heterogeneity. In this regards, it is necessary to examine the current knowledge of the prostate optical properties.

III. Optical Properties of Canine and Human Prostates

Using light to image prostate cancer will not be achievable unless a benign and cancerous prostate tissues present different optical properties that can be resolved by means of optical interrogation. Revealing the contrast of PCa over normal tissue will be challenging if significant baseline heterogeneities exist in the optical properties of benign tissues. There have been a number of studies on prostate optical properties in which certain consensuses have been made. Although these studies are conducted at different wavelengths, in different samples, and using different methods, spectrally these studies shall offer information invaluable to understanding the potentials of detecting PCa as well as difficulties facing the optical imaging of prostate. In this section, we give a side-by-side review of the known optical properties of canine and human prostates.

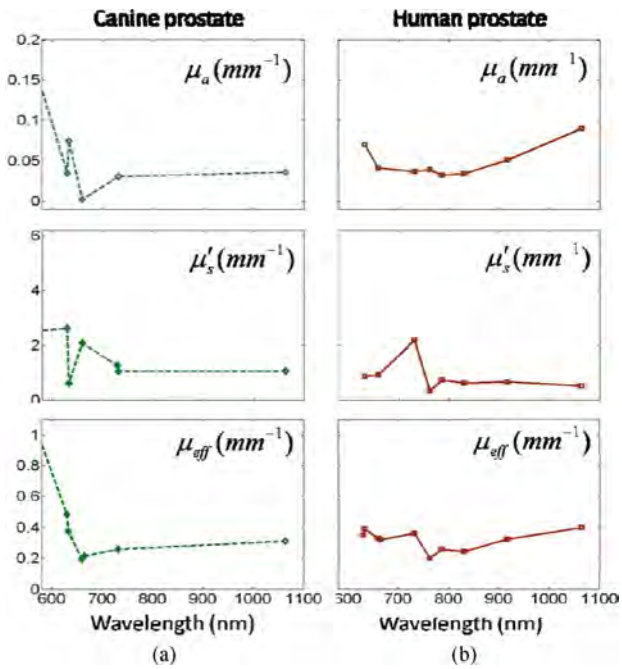

Fig. 2. Optical properties, including absorption, reduced scattering, and effective attenuation coefficients, averaged for existing studies at available spectral band for (a) canine and (b) human. The canine data are of normal tissue only, but the human data are of benign and malignant tissues.

Dogs have been used in a number of prostate studies because of the similarity between canine and human prostate glands. In [30], we have summarized the studies previous to ours, on optical properties, including absorption coefficient μ_a, reduced scattering coefficient μ_s', and effective attenuation coefficient $\mu_{\rm eff}$ of canine prostate within the spectral range from 355 to 1064 nm. These measurements, all performed invasively, include the following:

1) coefficients μ_a, μ_s', and $\mu_{\rm eff}$ of normal canine prostate tissue *in vitro* at 355, 532, and 1064 nm, respectively, using optoacoustic measurements of slab tissue samples [31];
2) coefficients μ_a, μ_s', and $\mu_{\rm eff}$ at 630 nm by interstitial measurements on excised normal prostate [32];
3) *in vitro* μ_a and μ_s' of slab samples of normal canine prostate tissues evaluated at 633 nm by using the standard double-integrating sphere technique [33];
4) coefficient $\mu_{\rm eff}$ at 630, 665, 730, 732 nm by interstitial measurements on normal canine prostate *in vivo* before and after PDT [34]–[37];
5) coefficient $\mu_{\rm eff}$ at 732 nm by reflection measurement upon exposed normal canine prostate *in vivo* [38];
6) transperineal interstitial measurement [35], [36], [39], [40] demonstrating that $\mu_{\rm eff}$ of prostatic urethral regions is statistically higher than that of the prostatic capsular regions.

These measurements together constitute the spectra of the optical properties of normal canine prostate [30], as replotted in Fig. 2(a), after averaging at each band.

TABLE I
LEGEND INDICATING THE MEASUREMENT METHODS USED IN TABLE II

				
Integrating sphere on slab tissue	Interstitial on excised prostate	Interstitial trans-perineally on prostate	Steady-state fluence rate measurement	Time-resolved fluence rate measurement

TABLE II
CURRENT "INVASIVE" KNOWLEDGE OF THE OPTICAL PROPERTIES OF HUMAN PROSTATE (EXPANDED UPON THE TEMPLATE IN [41])

Study	Year	Sample	Path	N	Method	Photon	λ (nm)	μ_a (mm^{-1})	μ_s' (mm^{-1})	μ_{eff} (mm^{-1})
Lee [48]	1999	*In vivo*	PCa	7			630			0.35±0.07 (0.22-0.44)
Pantelides [42]	1990	*Ex vivo*	Normal	3			633	0.07±0.02	0.86±0.05	0.43±0.05
Whitehurst [46]	1994	*In vivo*	BPH PCa	11			633			0.35±0.02 0.36±0.02
Lee [47]	1995	*In vivo*	BPH PCa	11			633			0.39±0.05 (0.24-0.42)
Wei [43]	2008	*In vitro*	BPH	?			640	0.44~0.96	1.12~1.66	2.09±0.54
Svensson [41]	2007	*In vivo*	PCa	9			660	0.05±0.01	0.87±0.19	0.36±0.08
Svensson [52]	2008	*In vivo*	PCa	1			660	~0.032	~0.5-1.4	0.23-0.37
Lee [47]	1995	*In vivo*	BPH UT PCa	11			665			0.32±0.05 (0.24-0.42)
Zhu [49]	2005	*In vivo*	*RC PCa*	13			732	0.037±0.024 (0.007—0.162)	1.40±1.10 (0.11—4.4)	0.29±0.07 (0.091—0.67)
Zhu [50]	2005	*In vivo*	*RC PCa*	2			732	0.011—0.16	0.12—4.0	0.019—0.63
Li [53]	2008	*In vivo*	*RC PCa*	1			732	2-D map 0.01—0.1	2-D map 0.5—4.5	0.65±0.37
Wang [54]	2009	*In vivo*	*RC PCa*	1			732	3-D map 0.01—0.07	3-D map 0.1—5.5	0.19-0.41
Weersink [51]	2005	*In vivo*	*RC PCa*	22			762	0.039±0.018	0.34±0.16	0.20±0.06
Svensson [41]	2007	*In vivo*	PCa	9			786	0.04±0.01	0.71±0.16	0.29±0.07
Svensson [52]	2008	*In vivo*	PCa	1			786	0.025	0.35-1.2	0.17-0.30
Svensson [52]	2008	*In vivo*	PCa	1			830	0.034	0.25-1.0	0.17-0.32
Svensson [41]	2007	*In vivo*	PCa	9			916	0.06±0.01	0.77±0.18	0.38±0.08
Svensson [52]	2008	*In vivo*	PCa	1			916	0.042	0.24-0.9	0.19-0.34
Essebpreis [44]	1992	*Ex vivo*	Normal	?			1064	0.15±0.02	0.64	0.60
Roggan [45]	1995	*Ex vivo*	Normal	?			1064	0.03	0.4	0.2

UT: untreated and RC: recurrent.

Following [30], the published values on optical properties of human prostate, all acquired invasively, as illustrated in Table I, are summarized in Table II, which enriched the template given in [41] with latest studies. The studies summarized in Table II include the following:

1) *ex vivo* steady-state measurements of $\mu_{\rm eff}$ and $\mu_t' = \mu_a + \mu_s'$ at 633 nm in three whole, nonmalignant human prostates [42];
2) three postmortem studies estimating prostate optical properties (μ_a, scattering coefficient μ_s, scattering anisotropy g, and μ_s') at 640 [benign prostatic hyperplasia (BPH)] [43] and 1064 nm (normal prostate) [44], [45] by measuring through thin prostate slices;
3) coefficient $\mu_{\rm eff}$ of prostate *in vivo* diagnosed with BPH or PCa estimated at 633 nm by steady-state interstitial measurements [46], [47] that indicated similar $\mu_{\rm eff}$ between benign and malignant prostate tissues;
4) at wavelengths of 630, 665, 732, 762 nm, transperineal interstitial steady-state measurements on prostate *in vivo* with untreated BPH, untreated PCa, and recurrent PCa conducted before and after PDT [47]–[51] to determine $\mu_{\rm eff}$ or both μ_a and μ_s';
5) coefficients μ_a, μ_s', and $\mu_{\rm eff}$ of untreated PCa *in vivo* at 660, 786, 830 and 916 nm, respectively, using time-resolved fluence rate measurements [41], [52];
6) a few studies on hemoglobin and oxygen saturation [41], [50], [51] indicating relatively small variations of oxygen saturation, but large variations on total hemoglobin concentration within the same gland or different subjects.

Recently, interstitially measured 2-D or 3-D distribution of μ_a and μ_s', in human prostate, are reported [53], [54] for PDT dosimetry.

Studies [49], [51] have indicated that the optical properties of canine prostate and human prostate may be substantially different, specifically the absorption properties. It is noted that the studies of canine prostate optical properties have been performed on all normal glands, but that of human include both normal, benign hyperplastic, and malignant prostate tissues. It is also noted that these studies are conducted at different wavelengths, using different methods, on *ex vivo* or *in vivo* samples. Direct wavelength-specific and tissue-specific comparisons of the canine and human prostate optical properties are, thereby, difficult, but nonetheless, the spectra of the optical properties of canine and human prostates may reveal useful information. To facilitate spectral comparison, for those original measurements of human prostate shown in Table II that have only the absorption and reduced scattering coefficients available, the effective attenuation coefficient is calculated following the method in our previous study [30]. Fig. 2(b) illustrates the spectra of μ_a, μ_s', and μ_{eff} of human prostates that are averaged for existing data at a specific wavelength. The distributions of the optical properties of both canine and human prostates are substantially large, as seen in [30] and Table II, and are not plotted in Fig. 2.

The spectra shown in Fig. 2 are the invasively characterized optical properties of normal canine prostates and mostly malignant human prostates. The similarity or dissimilarity between canine and human prostate optical properties is difficult to draw as the optical properties of malignant canine prostate tissue were previously unavailable; however, previous studies that are summarized in [30] and Table II, and seen in Fig. 2, have important implications to optical interrogation of the prostate in the following aspects.

1) The reduced scattering coefficient of prostate is approximately an order higher than the absorption coefficient of prostate. As this has been confirmed by time-resolved measurements, the prostate can be treated as a scattering-dominant tissue, thereby diffuse optical methods can be applied to modeling the photon propagation as in PDT and image reconstruction in transrectal imaging of the prostate.
2) There are noticeable intersubject and intraorgan heterogeneities in optical properties of prostate. The intraorgan heterogeneity poses a substantial challenge to differentiating malignant tissue from normal tissue, since the optical contrast of the malignant tissue over the normal tissue must be greater than the background heterogeneity for the malignant lesion to be resolved. The intraorgan heterogeneity may also partially contribute to the previous finding that the effective attenuation coefficients of benign and malignant human prostate tissues were similar. It is noted that none of the previous measurements of prostate optical heterogeneities have been examined on intact prostate *in vivo*. Our approach of transrectal NIR diffuse optical tomography, which aims at imaging the intact prostate in its real-time *in vivo* condition, shall demonstrate if and which type of intrinsic optical property contrasts are available for differentiating the malignant prostatic tissue from benign tissue.

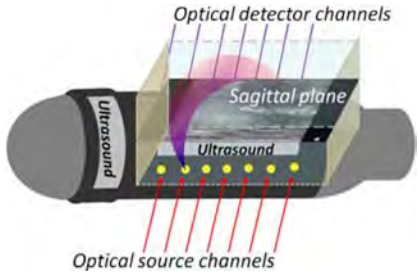

Fig. 3. Geometry of transrectal NIR imaging probe coupled to the sagittal US transducer of a biplane prostate-imaging TRUS probe.

IV. Methods and Materials

A. Transrectal NIR Imaging Probe

Due to the limitation of spatial resolution and the time needed for image formation in diffuse optical tomography, it is imperative to give transrectal NIR prostate imaging a real-time positioning guidance, which most conveniently can be rendered by TRUS. The need of dual-modality endorectal application leaves limited options as to what can be done to the NIR applicator designs. There has to be a clear window for the TRUS transducer, and there has to be a relatively longitudinal NIR array to allow co-parallel imaging into deeper tissue. The NIR probe design is shown in Fig. 3. The longitudinal NIR source array and detector array are placed lateral to the sagittal TRUS transducer of a biplane TRUS probe [55]. This NIR array geometry allows imaging a tissue volume that is dissected by the sagittal TRUS imaging plane. As the NIR array has a dimension of 60 mm $\times$ 20 mm (longitudinal $\times$ lateral), the NIR image reconstruction is performed in 3-D in a volume of 80 mm $\times$ 70 mm $\times$ 50 mm (longitudinal $\times$ lateral $\times$ depth). Since the sagittal US performs only 2-D imaging, obtaining a 3-D morphological profile of the prostate from US becomes unreliable using single sagittal US image. Therefore, no spatial *a priori* information has been implemented in the transrectal NIR tomography image reconstruction, which utilizes a mesh of uniform density. The NIR wavelength is chosen at 840 nm.

B. Image Reconstruction

As the transrectal NIR optical tomography system takes continuous-wave measurement [55], the forward computation is based upon the steady-state photon diffusion equation

$$\nabla\kappa(\vec{r})\nabla\Phi(\vec{r}) - \mu_a(\vec{r})\Phi(\vec{r}) = -q(\vec{r}) \tag{1}$$

where κ is the diffusion coefficient that is equal to $1/[3(\mu_a + \mu_s')]$, Φ is the photon fluence rate at position $\vec{r}$, and q is the source at $\vec{r}$.

The probe–tissue boundary is represented by an index-mismatched type-III condition (also known as the Robin boundary condition), in which the photon fluence existing at the edge

of the tissue does not return [56], [57]. This boundary condition is described by

$$\Phi(\vec{r}_\Omega) + 2A\kappa\,\hat{n}\cdot\nabla\Phi(\vec{r}_\Omega) = 0 \tag{2}$$

where $\vec{r}_\Omega$ corresponds to the point on the boundary, $\hat{n}$ is a unit vector pointing outward (from the tissue to probe) and normal to the tissue–probe interface, and A is determined by the relative refractive index mismatch between the tissue domain and the probe (air) domain. Specifically

$$A = \frac{(2/(1-R_0)) - 1 + |\cos\,\theta_c|^3}{1 - |\cos\,\theta_c|^2} \tag{3}$$

$$R_0 = \frac{((n_{\text{tissue}}/n_{\text{air}}) - 1)^2}{((n_{\text{tissue}}/n_{\text{air}}) + 1)^{-2}} \tag{4}$$

$$\theta_c = \arcsin\left(\frac{n_{\text{air}}}{n_{\text{tissue}}}\right) \tag{5}$$

where n_{tissue} is the refractive index of tissue (chosen as 1.33) and n_{air} is the refractive index of the probe/air (chosen as 1.0).

Equation (1) is solved by finite-element method (FEM) formulated as [1]

$$[K(\kappa) + C(\mu_a) + \xi F]\,\Phi = Q_0 \tag{6}$$

where $\xi = (2A)^{-1}$ is a constant to implement the boundary condition in (2). For each element of the FEM mesh

$$K^e_{ij} = \int_\Omega \kappa(r)\nabla u_i(r)\cdot\nabla u_j(r)d\Omega \tag{7}$$

$$C^e_{ij} = \int_\Omega \mu_a(r)u_i(r)u_j(r)d\Omega \tag{8}$$

$$F^e_{ij} = \oint_{\partial\Omega} u_i(r)u_j(r)d\Lambda \tag{9}$$

$$Q^e_{0i} = \int_\Omega u_i(r)q_0(r)d\Omega \tag{10}$$

where $u = a + bx + cy + dz$ is a linear shape function for each nodes, *K*, *C*, and *Q* are the volume integrals of each element, and *F* is the surface integral of the boundary element. Following the FEM routine of matrix assembly and fluence rate calculation, the boundary measurements are interpolated as weighted averages of the fluence rates of the nodes adjacent to the measurement points.

The inverse problem involves Levernberg–Marquardt algorithm implemented as

$$x_{k+1} = x_k + \alpha[J^T(x_k)J(x_k) + \lambda I]^{-1}J^T(x_k)\Delta v(x_k) \tag{11}$$

where *x* is the optical properties to be reconstructed, Δv is the forward projection error, λ is a regularization term, *J* is the Jacobian or the weight matrix containing the first-order derivative of the measurements with respect to the changes of optical properties, and α is a damping factor in the range of (0, 1) used for preventing over-adjustment of optical properties and rendering stable convergence [58]. The iteration stops when the projection error changes less than 1% or negative values in *x* occur.

The Jacobian in (11) is calculated by an adjoint method [1] based on the following equations with the basis matrix of FEM:

$$J^\kappa_{i,j} = \frac{\Psi^{*T}_j V(\kappa)\Phi_i}{v_{i,j}} \tag{12}$$

$$J^{\mu_a}_{i,j} = \frac{\Psi^{*T}_j V(\mu)\Phi_i}{v_{i,j}} \tag{13}$$

where Φ_i is the fluence rate at each node in the FEM mesh generated by the *i*th source, Ψ_j is the fluence rate generated by assuming an adjoint source at the position of the *j*th detector, $v_{i,j}$ is the computed measurements at the *j*th detector for the *i*th source. $V(\kappa)$ and $V(\mu)$ are the finite-element system basis of

$$V^e_{ij}(\kappa) = \int_\Omega \nabla u_i(r)\cdot\nabla u_j(r)d\Omega \tag{14}$$

$$V^e_{ij}(\mu_a) = \int_\Omega u_i(r)u_j(r)d\Omega \tag{15}$$

The assembled Jacobian in (11) contains two parts as

$$[\,J^{\mu_a}_{i,j} \quad J^\kappa_{i,j}\,] = \left[\,\frac{\partial I_{i,j}}{\partial\mu_a} \quad \frac{\partial I_{i,j}}{\partial\kappa}\,\right] \tag{16}$$

where i is the sequence number of the source and j is the sequence number of the detector. A mesh of 8881 nodes is used for the forward computation, and the inverse reconstruction basis contains a mesh of 832 nodes. After the μ_a and κ are reconstructed, μ_s' is computed as $[(1/3\kappa) - \mu_a]$, and μ_{eff} is estimated by $\sqrt{\mu_a/\kappa}$.

C. Animal Models

The studies were conducted at Oklahoma State University under protocols approved by the University's Institutional Animal Care and Use Committee, and approved by the US Army Medical Research and Material Command after an on-site inspection. For this study, the prostate of a 12-kg sexually intact adult purpose-bred Beagle dog, estimated to be approximately 4 years of age, was injected with canine TVT cells [59]. The TVT cell line was propagated *in vivo* in the subcutis of nonobese-diabetic (NOD)/severe-combined-immunodeficiency (SCID) mice. When the subcutaneous tumor reached an appropriate volume, the neoplastic cells were recovered and homogenized for injection into the canine prostate gland. With the dog under general anesthesia, approximately 3 cc of TVT cells were aseptically injected transperineally into the right lobe of the prostate using a 6-in-16-gauge hypodermic spinal needle under TRUS visualization. The spinal needle was retracted without inserting the inner stylet; therefore, it was assumed that TVT cells could potentially leak from the prostate injection site and be "seeded" along the needle insertion tract. The dog underwent monitoring in 2, 5, 6, and 7 weeks postinjection, and was then humanly euthanized for necropsy and histological examinations at 8 weeks postinjection.

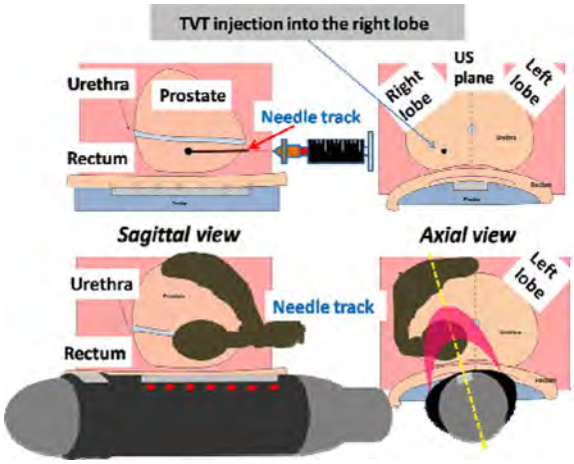

Fig. 4. (Top) Injection of canine TVT cells to the right lobe of a dog prostate. (Bottom) Growth pattern of the tumor revealed by later necropsy and histological examinations.

V. Results

During the first two-week evaluation after TVT injection, there was no evidence of tumor growth on TRUS and rectal examination. The TRUS examination at 5 weeks postinjection showed hypoechoic masses in the prostatic parenchyma, periprostatically around the right lobe of the prostate, and perirectally along the injection track.

A. NIR Absorption Imaging

The NIR absorption images taken prior to TVT injection, at 2-weeks, and at 5 weeks postinjection are displayed in Fig. 5. The sagittal TRUS image and the sagittal NIR image, to which it coupled, are identified in Fig. 5. The axial TRUS images were acquired in week-5 only, therefore, comparison of the axial NIR with axial TRUS images could not be made for results obtained at either preinjection or at week-2 post-injection.

The US and NIR images are displayed with the same dimension of 60 mm $\times$ 30 mm (cranial–caudal $\times$ dorsal–ventral) for sagittal, 40 mm $\times$ 30 mm (right lateral–left lateral $\times$ dorsal–ventral) for axial, and 60 mm $\times$ 40 mm (cranial–caudal $\times$ right lateral–left lateral) for coronal views, respectively. The sagittal transrectal US images were taken at the middle portion of the right lobe (see Fig. 4, bottom right for the imaging view). For week-5 US images, the hypoechoic region L1 indicates an intraprostatic mass. The large hypoechoic region L2 indicates a mass ventral and caudal to the prostate that may have connection with L1. The NT on the US image denotes the needle trajectory for introducing the TVT cells. Longitudinal hypoechoic regions including L3 are seen along the NT. The hyperabsorptive regions on sagittal NIR images correspond to L1, L2, and L3 on sagittal US image. The 10-mm-medial NIR image displays the absorptive masses at reduced NIR contrast, and the 10-mm-lateral NIR image reveals connected strong absorptive masses.

The three axial TRUS images were taken at the cranial edge of the prostate at a plane crossing L1, the caudal edge of the prostate at a plane crossing L2, and the perirectal region at a plane crossing L3, using the axial TRUS transducer. The axial US images show a small hypoechoic intraprostatic mass at the cranial aspect of the prostate, the distortion of the right lobe boundary, and the extension of L2 over the prostate midline. These correlate with the findings on other sagittal US performed at midline, and the imaging of a large perirectal hypoechoic mass cranial to the perineum. The locations of axial NIR images are comparable to those of the axial transrectal US. The axial NIR image A2 should contain L1, and the axial NIR image A5 should contain L3. The coronal NIR images are reconstructed at planes of 5, 10, and 15 mm ventral to the rectum. On coronal images, the hyperabsorptive mass, indicative of L1, is seen medial to the hyperabsorptive masses indicative of L2 and L3. The masses indicative of L2 and L3 are seem to align longitudinally, a feature corresponding to tumors developed along the needle track running parallel to the rectum or the transrectal probe surface.

At the week-2 NIR absorption images, hyperabsorptive regions were found intraprostatically in the right lobe and dorsal to the pelvic bone. The longitudinal locations of these hyperabsorptive regions correlated well with those of the US hypoechoic and NIR hyperabsorptive regions found in week-5. The change of the hyperabsorptive regions from week-2 to week-5 implied tumor growing in the right lobe and potentially extending toward the middle line of the prostate. The growth of the tumor was indicated earlier by the NIR absorption images than by the TRUS, and combining the information of NIR and TRUS could lead to earlier and more accurate findings of tumor growth than with TRUS alone.

B. NIR-Reduced Scattering and Effective Attenuation Imaging

The NIR-reduced scattering and effective attenuation images, with timeline and geometry identical to those of NIR absorption in Fig. 5, are displayed in Figs. 6 and 7, respectively.

The hyperabsorptive masses presumed to be TVTs in NIR absorption images are shown with different contrast patterns for the reduced scattering and effective attenuation coefficients. In both the NIR-reduced scattering and effective attenuation images of week-5, the indications of masses corresponding to L1, L2, and L3 are not as profound, as in NIR absorption images, whereas L3 has much higher contrast than do the masses corresponding to L1 and L2. The contrast elsewhere is also more heterogeneous compared with that in the absorption image at the given color scales.

On the NIR-reduced scattering and effective attenuation coefficient images of week-2, it is difficult to find regions with elevated contrast that could correlate with the hyperabsorptive regions in the NIR absorption images that were located intraprostatically in the right lobe and dorsal to the pelvic bone.

C. Overall Changes of Optical Properties of the Three Tumor Regions Identified in Week-5

From the three hyperabsorptive regions on week-5 images that have longitudinal position correlation with the US hypoechoic tumor-suspecting regions, three circular regions are defined, as

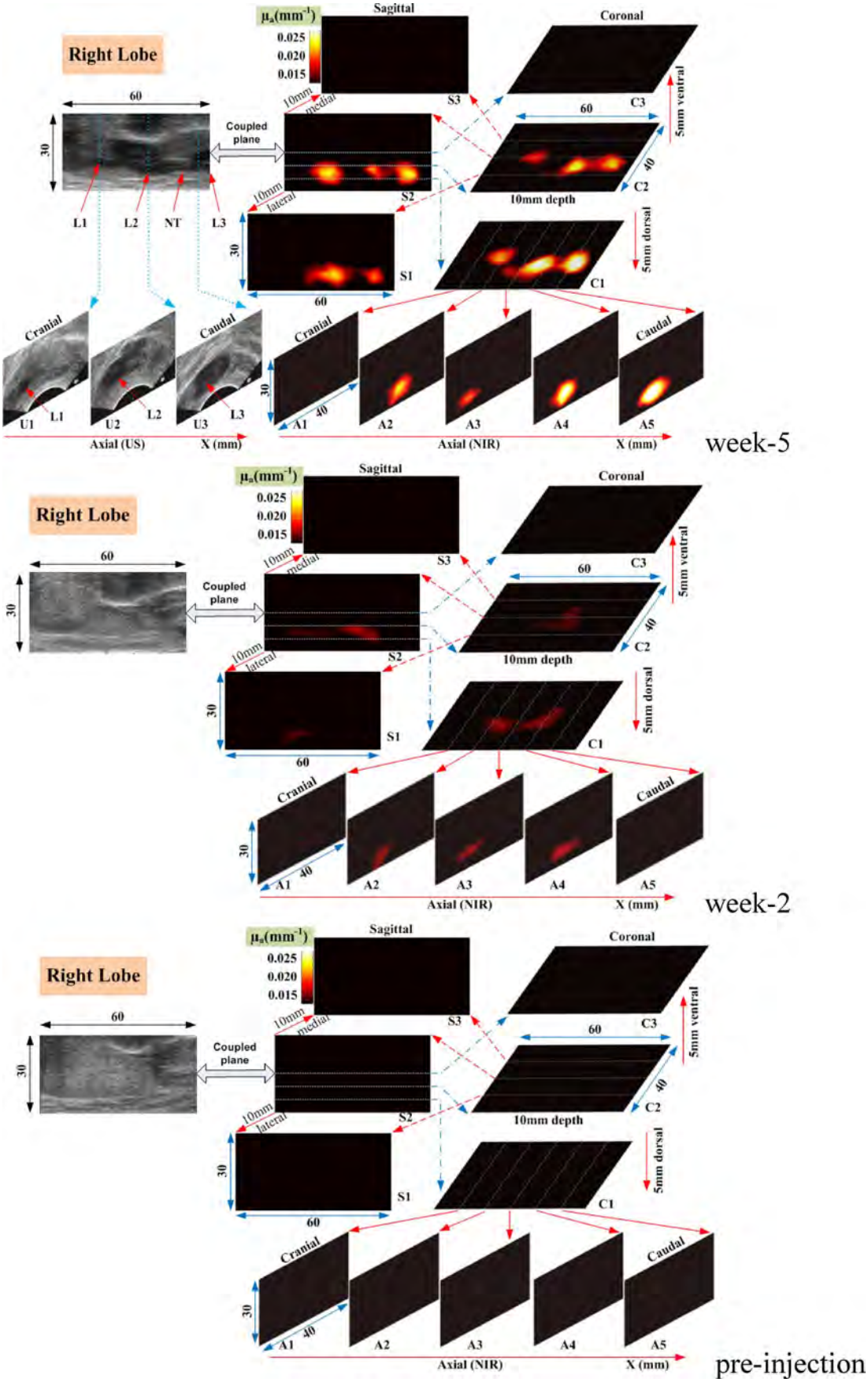

Fig. 5. Transrectal NIR optical tomography of canine TVT tumor images of absorption coefficient.

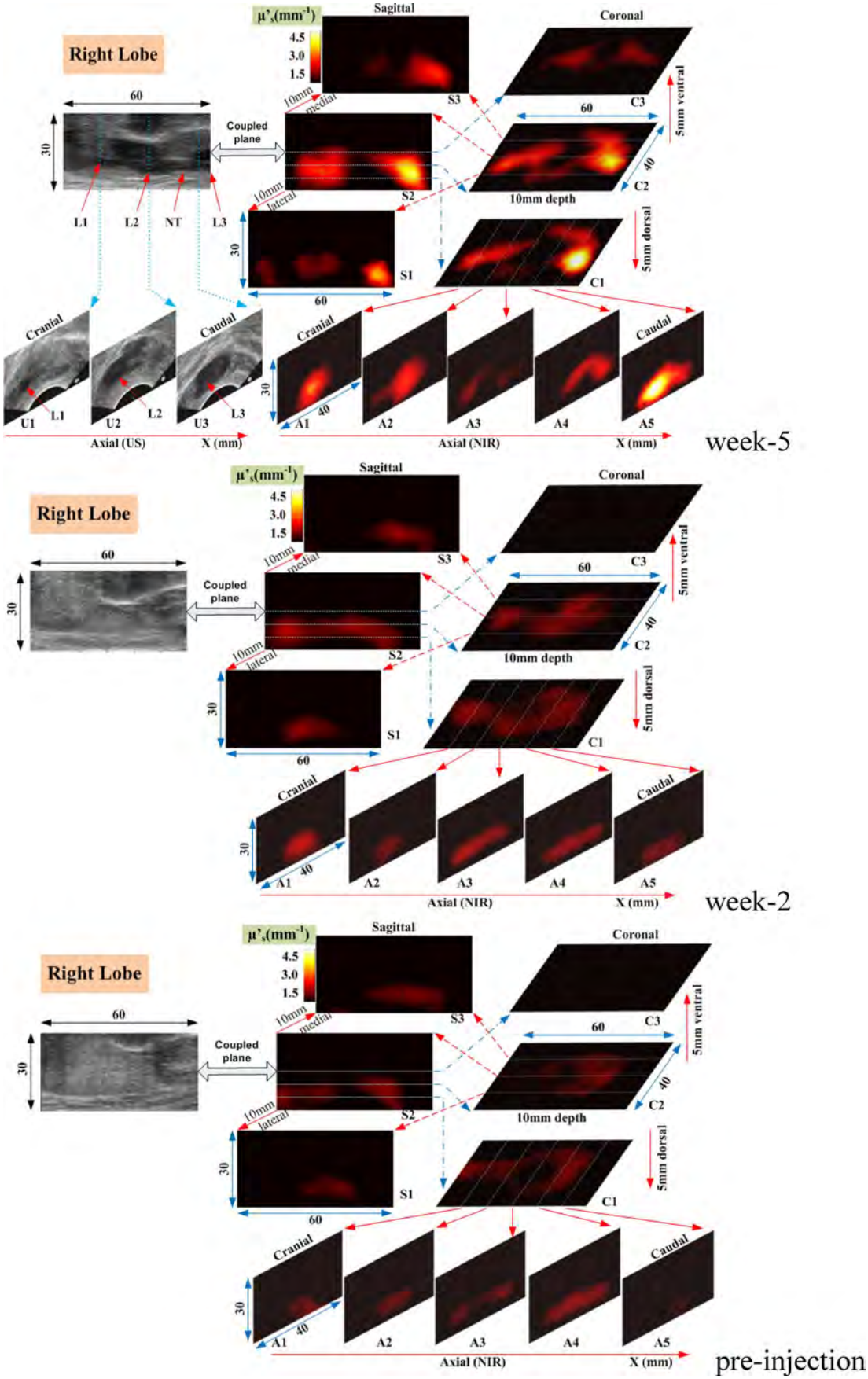

Fig. 6. Transrectal NIR optical tomography of canine TVT tumor images of reduced scattering coefficient.

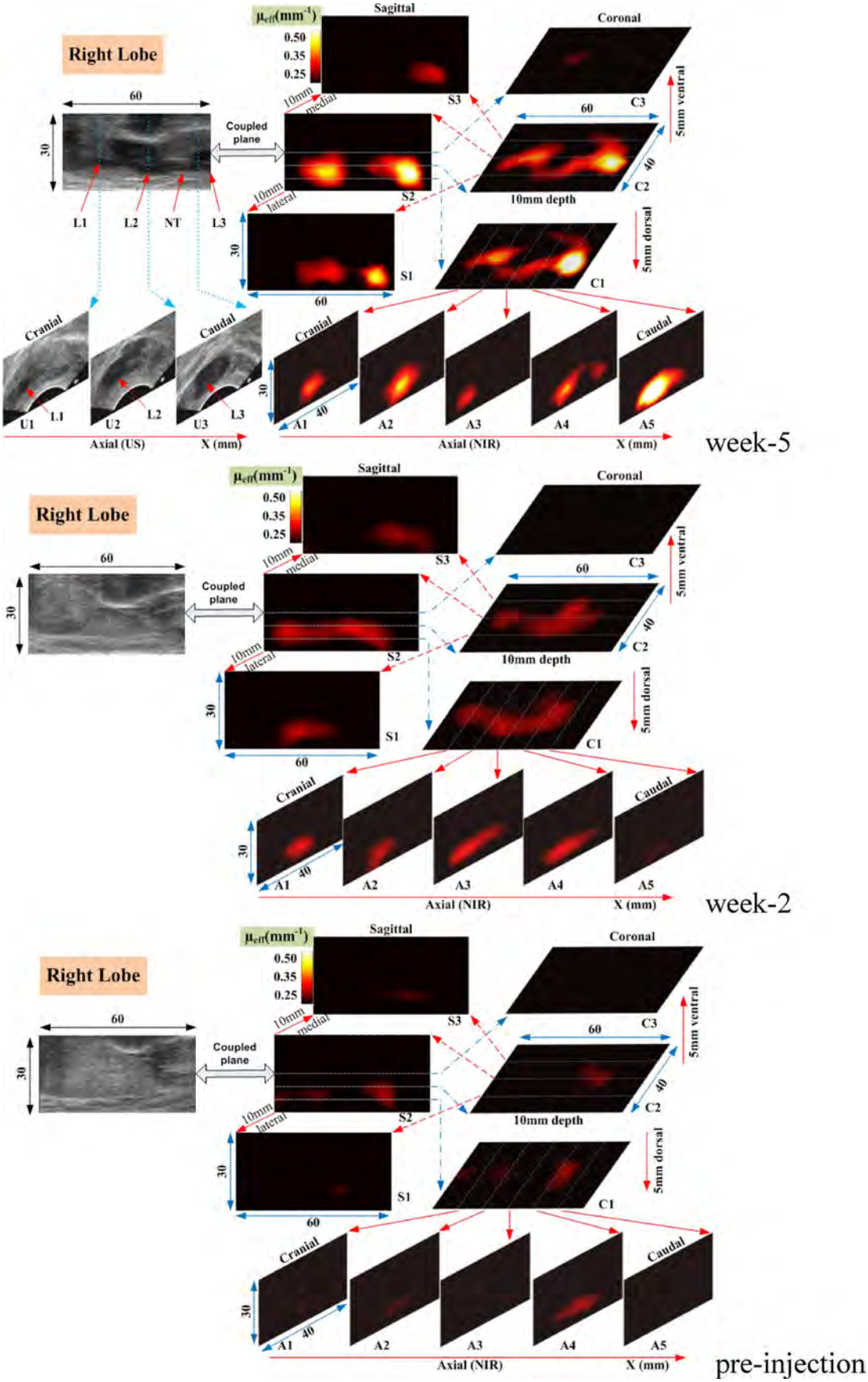

Fig. 7. Transrectal NIR optical tomography of canine TVT tumor images of effective attenuation coefficient.

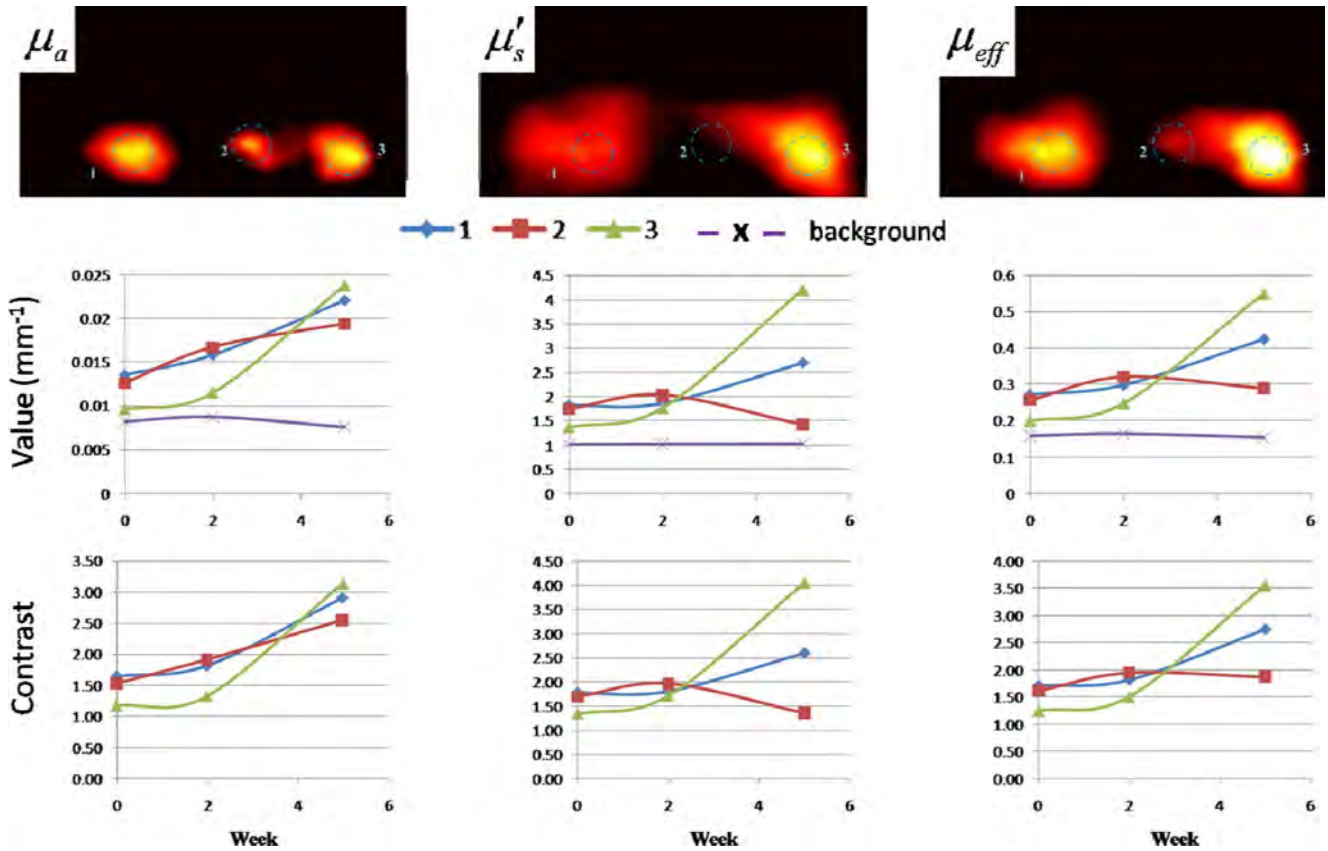

Fig. 8. Changes of the reconstructed optical properties at the three circular regions corresponding to L1, L2, and L3 in Figs. 5, 6, and 7, respectively. (Top) NIR absorption, reduced scattering, and effective attenuation acquired at the middle of the right lobe in week-5, corresponding to those in Figs. 5, 6, and 7 that are "coupled with" the single sagittal US image. (Middle) Absolute values of the mean optical properties in the three circular regions. (Bottom) Contrast of these optical properties with respect to the background values calculated by averaging after excluding the three circular regions.

seen in Fig. 8. The changes of the reconstructed optical properties at the three regions with respect to the background value (averaged on the sagittal plane with the three circular regions excluded) over the 5-week time line are shown in Fig. 8. The absorption coefficients at all the three regions show moderate increase at week-2 and substantial increase in week-5. However, the increase of the reduced scattering and effective attenuation coefficients are seen for regions 1 and 3 only, and at week-5, but not at week-2.

D. Confirmation of the Tumor Growth

The gross and histological findings confirmed intra- and periprostatic neoplastic infiltrates with masses also located along the pelvic urethra and perirectal tissue; the latter related to dissemination along the needle track, as the needle was withdrawn following TVT inoculation in the prostate. Histologically, all masses consisted of diffuse sheets of a monomorphic population of neoplastic round cells dissecting through preexisting fibrovascular stroma. The neoplastic cells have large hyperchromatic nuclei, single conspicuous nucleoli, and moderate amounts of featureless cytoplasm—features histologically consistent with canine TVT.

VI. Discussions

It is noted that the NIR probe consists of a linear source array and a liner detector array separated 20 mm laterally and symmetrically parallel to the TRUS imaging plane. The NIR lateral detection sensitivity is thereby peaked at the midline plane [30]. As the 6-cm-long NIR array performs side-way imaging, the detection sensitivity is optimal at approximately 1.5 cm from the probe surface. In the transrectal NIR image reconstruction, a uniform meshing throughout the entire imaging volume is implemented, therefore, the target located at regions with higher detection sensitivity may be recovered successfully, but targets located at regions with much lower detection sensitivity may not be fully resolved. This accounts for the lack of visualized lesions on the 15-mm coronal plane and those extending $\geq$15 mm lateral to the midline plane. Improvement in the recovery of the lesions at deeper region and more lateral aspect may be achieved by advanced reconstruction approaches, such as applying accurate spatial prostate profile information to the reconstruction process, which nonetheless requires 3-D TRUS capability for this study.

The advanced TVT tumors developed in the canine prostate and elsewhere in the pelvic canal are shown as highly absorbing and more scattering, thereby more attenuating, over the peripheral tissues. However, it seems that the TVT tumor development induced a detectable NIR absorption contrast much earlier than the detectable reduced scattering and effective attenuation contrasts. Previous studies revealed similar effective attenuation properties between benign and malignant prostatic tissues, which are in agreement with this study for the

measurements made at the earlier stage of tumor development. However as the tumor becomes much advanced, the effective attenuation contrast of the tumor becomes elevated substantially over the background.

The TVT is a round cell tumor that has characteristics such as distinct tumor boundary, higher and homogenous cell density, large hyperchromatic nuclei, single conspicuous nucleoli, etc. All these characteristics could contribute to the elevation of optical properties as revealed by transrectal NIR optical tomography. The higher cell density and large hyperchromatic nuclei could increase both the absorption cross-section and scattering cross-section of the NIR light being used. The distinct tumor boundary may introduce specular light reflection at the tumor boundary, as the refractive indexes will highly likely have an abrupt change between the normal tissue and the high-density tumor. The specular reflection, if it occurs, may be reconstructed as elevated absorption, as seen distinct to the TVT nodules. As the specular reflection scatters more light into the tissue peripheral to the tumor, the "true" scattering of the peripheral tissues may be reconstructed with artifacts that may reduce the overall scattering contrast of the tumor over its peripheral tissues, as may have been shown in the figures.

We recognize that since the cellular and subcellular structures of the TVT tumor are distinctly different from those of prostate adenocarcinoma, the absorption, scattering, as well as effective attenuation features of the prostate adenocarcinoma may become much different from those of TVT, as seen in this study. If the PCa develops into larger cells, the absorption and scattering cross sections may be decreased, but the malignant irregular cellular structures may increase the scattering, and the onset of angiogenesis may increase the absorption. As the PCa typically does not have a distinct boundary as the TVT tumor does, the influence of specular reflection may be minimized under light interrogation; thereby, the PCa may be presented with its more unaltered absorption contrast if imaged by NIR light. There are limited studies on the contrast of the optical properties of PCa versus benign tissue from which controversial observations are often implicated. The introduction of this transrectal optical tomography, which aims to spatially resolve the optical properties of intact prostate, may help to first discover which type of optical contrast exists between the adenocarcinoma and benign tissues in prostate at the intact real-time status. If the TRUS of the prostate can be augmented by such fundamental "optical" signatures for PCa, the likelihood that the biopsy of PCa will be image-targeted is greatly improved. The knowledge of intact optical properties of adenocarcinoma and benign tissues may also improve the pretreatment light dosimetry in phototherapy applications.

VII. Conclusion

This paper presented an overview of the current alternative technologies for prostate imaging, and demonstrated a transrectal dual-modality NIR diffuse optical tomography and ultrasonography-integrated method of detecting PCa. The technology of endorectally applied NIR diffuse optical tomography in combination with the conventional TRUS aims to characterize the spatially resolved optical properties of the *intact* prostate that are known to have intraorgan and intersubject heterogeneities. A canine model of PCa using canine TVT was used to demonstrate the utility of this technology in detecting PCa. The tumors in the pelvic canal, including the prostate were found detectable at 2-week post-injection based upon the NIR absorption contrast, which was earlier than using NIR-reduced scattering and effective attenuation contrasts and US. Transrectal NIR tomography can potentially render pathogonomic "optical" contrast information to the standard US of the prostate.

References

[1] American Cancer Society, *Cancer Facts & Figures 2009*. Atlanta: American Cancer Society, 2009.

[2] H. Hricak, P. L. Choyke, S. C. Eberhardt, S. A. Leibel, and P. T. Scardino, "Imaging prostate cancer: A multidisciplinary perspective," *Radiology*, vol. 243, no. 1, pp. 28–53, 2007.

[3] J. H. Pinthus, D. Pacik, and J. Ramon, "Diagnosis of prostate cancer," *Recent Results Cancer Res*, vol. 175, pp. 83–99, 2007.

[4] J. L. Colli and C. L. Amling, "Exploring causes for declining prostate cancer mortality rates in the United States," *Urol. Oncol.*, vol. 26, no. 6, pp. 627–633, Nov./Dec. 2008.

[5] S. M. Collin, R. M. Martin, C. Metcalfe, D. Gunnell, P. C. Albertsen, D. Neal, F. Hamdy, P. Stephens, J. A. Lane, R. Moore, and J. Donovan, "Prostate-cancer mortality in the USA and UK, in 1975–2004: An ecological study," *Lancet Oncol.*, vol. 9, no. 5, pp. 445–452, May 2008.

[6] AUA, *The Management of Localized Prostate Cancer*. Orlando, FL: American Urologic Association, 2008.

[7] H. B. Carter, "PSA scores: Should we use a lower threshold?," *Johns Hopkins Med. Lett. Health After 50*, vol. 17, no. 8, p. 6, 2004.

[8] C. R. Porter, "Does the number of prostate biopsies performed affect the nature of the cancer identified?," *Nat. Clin. Pract. Urol.*, vol. 4, pp. 132–133, 2007.

[9] R. Narayanan, P. N. Werahera, A. Barqawi, E. D. Crawford, K. Shinohara, A. R. Simoneau, and J. S. Suri, "Adaptation of a 3-D prostate cancer atlas for transrectal ultrasound guided target-specific biopsy," *Phys. Med. Biol.*, vol. 53, no. 20, pp. N397–N406, Oct. 2008.

[10] The man, the gland, the dilemmas (2009, Mar. 31). *Wall Street J.* [Online]. Available: http://online.wsj.com/article/SB123845699393571631.html

[11] A. C. Loch, A. Bannowsky, L. Baeurle, B. Grabski, B. König, G. Flier, O. Schmitz-Krause, U. Paul, and T. Loch, "Technical and anatomical essentials for transrectal ultrasound of the prostate," *World J. Urol.*, vol. 25, pp. 361–366, 2007.

[12] A. M. Wise, T. A. Stamey, J. E. McNeal, and J. L. Clayton, "Morphologic and clinical significance of multifocal prostate cancers in radical prostatectomy specimens," *Urology*, vol. 60, pp. 264–269, 2002.

[13] C. M. Coley, M. J. Barry, C. Fleming, and A. G. Mulley, "Early detection of prostate cancer. Part I: Prior probability and effectiveness of tests," *Amer. College Phys. Ann. Intern. Med.*, vol. 126, no. 5, pp. 394–406, 1997.

[14] C. M. Moore, D. Pendse, and M. E. Medscape, "Photodynamic therapy for prostate cancer—A review of current status and future promise," *Nat. Clin. Pract. Urol.*, vol. 6, no. 1, pp. 18–30, 2009.

[15] S. R. Davidson, R. A. Weersink, M. A. Haider, M. R. Gertner, A. Bogaards, D. Giewercer, A. Scherz, M. D. Sherar, M. Elhilali, J. L. Chin, J. Trachtenberg, and B. C. Wilson, "Treatment planning and dose analysis for interstitial photodynamic therapy of prostate cancer," *Phys. Med. Biol.*, vol. 54, no. 8, pp. 2293–2313, 2009.

[16] M. Atri, M. R. Gertner, M. A. Haider, R. A. Weersink, and J. Trachtenberg, "Contrast-enhanced ultrasonography for real-time monitoring of interstitial laser thermal therapy in the focal treatment of prostate cancer," *Can. Urol. Assoc. J.*, vol. 3, no. 2, pp. 125–130, 2009.

[17] R. Weiss, V. Egorov, S. Ayrapetyan, N. Sarvazyan, and A. Sarvazyan, "Prostate mechanical imaging: A new method for prostate assessment," *Urology*, vol. 71, no. 3, pp. 425–429, 2008.

[18] V. Egorov, S. Ayrapetyan, and A. Sarvazyan, "Prostate mechanical imaging: 3-D image composition and feature calculations," *IEEE Trans. Med. Imag.*, vol. 25, no. 10, pp. 1329–1340, Oct. 2006.

[19] K. Koenig, U. Scheipers, A. Pesavento, A. Lorenz, H. Ermert, and T. Senge, "Initial experiences with real time elastography guided biopsies of the prostate," *J. Urol.*, vol. 174, no. 1, pp. 115–117, 2005.

[20] F. G. Mitri, B. J. Davis, M. W. Urban, A. Alizad, J. F. Greenleaf, G. H. Lischer, T. M. Wilson, and M. Fatemi, "Vibro-acoustography imaging of permanent prostate brachytherapy seeds in an excised human prostate—Preliminary results and technical feasibility," *Ultrasonics*, vol. 49, no. 3, pp. 389–394, 2009.

[21] L. Zhai, V. Mouraviev, J. F. Madden, T. J. Polascik, and K. Nightingale, "Acoustic radiation force impulse (ARFI) imaging of human prostate in vivo," presented at the Focal Ther. Imag. Prostate Kidney Cancer, Amsterdam, Jun. 10–13, 2009, 2010.

[22] A. Borsic, R. Halter, Y. Wan, A. Hartov, and K. D. Paulsen, "Sensitivity study and optimization of a 3-D electric impedance tomography prostate probe," *Physiol. Meas.*, vol. 30, no. 6, p. S1-S18, 2009.

[23] R. J. Halter, A. Schned, J. Heaney, A. Hartov, S. Schutz, and K. D. Paulsen, "Electrical impedance spectroscopy of benign and malignant prostatic tissues," *J. Urol.*, vol. 179, no. 4, pp. 1580–1586, 2008.

[24] J. Jossinet, E. Marry, and A. Matias, "Electrical impedance endotomography," *Phys. Med. Biol.*, vol. 47, no. 13, pp. 2189–202, 2002.

[25] M. A. Yaseen, H. P. F. Brecht, S. A. Ermilov, R. R. Gharieb, A. Conjusteau, and A. A. Oraevsky, "Hybrid optoacoustic and ultrasonic imaging system for detection of prostate malignancies," *Proc. SPIE*, vol. 6856, pp. 68560T-1–68560T-11, 2008.

[26] V. G. Andreev, A. E. Ponomarev, P. M. Henrichs, M. Motamedi, E. Orihuela, E. Eyzaguirre, and A. A. Oraevsky, "Detection of prostate cancer with optoacoustic tomography," *Proc. SPIE*, vol. 4960, pp. 45–47, 2003.

[27] A. Agarwal, S. W. Huang, M. O'Donnell, K. C. Day, M. Day, N. Kotov, and S. Ashkenazi, "Targeted gold nanorod contrast agent for prostate cancer detection by photoacoustic imaging," *J. Appl. Phys.*, vol. 102, pp. 064701-1–064701-4, 2007.

[28] Y. Pu, W. B. Wang, B. B. Das, S. Achilefu, and R. R. Alfano, "Time-resolved fluorescence polarization dynamics and optical imaging of Cytate: A prostate cancer receptor-targeted contrast agent," *Appl. Opt.*, vol. 47, no. 13, pp. 2281–2289, 2008.

[29] J. Boutet, L. Guyon, M. Debourdeau, J. M. Dinten, D. Vray, and P. Rizo, "Advances in bi-modal optical and ultrasound detection of prostate cancer diagnosis," *Proc. SPIE*, vol. 7171, pp. 71710E-1–71710E-6, 2009.

[30] D. Piao, Z. Jiang, K. E. Bartels, G. R. Holyoak, J. W. Ritchey, G. Xu, C. F. Bunting, and G. Slobodov, "In vivo trans-rectal ultrasound-coupled near-infrared optical tomography of intact normal canine prostate," *J. Innovative Opt. Health Sci.*, vol. 2, no. 3, pp. 215–225, 2009.

[31] A. A. Oraevsky, S. L. Jacques, and F. K. Tittel, "Measurement of tissue optical properties by time-resolved detection of laser-induced transient stress," *Appl. Opt.*, vol. 36, pp. 402–415, 1997.

[32] Q. Chen, B. C. Wilson, S. D. Shetty, M. S. Patterson, J. C. Cerny, and F. W. Hetzel, "Changes in in vivo optical properties and light distributions in normal canine prostate during photodynamic therapy," *Radiat. Res.*, vol. 147, pp. 86–91, 1997.

[33] W. H. Nau, R. J. Roselli, and D. F. Milam, "Measurement of thermal effects on the optical properties of prostate tissue at wavelengths of 1,064 and 633 nm," *Lasers Surg. Med.*, vol. 24, pp. 38–47, 1999.

[34] L. K. Lee, C. Whitehurst, Q. Chen, M. L. Pantelides, F. W. Hetzel, and J. V. Moore, "Interstitial photodynamic therapy in the canine prostate," *Brit. J. Urol.*, vol. 80, pp. 898–902, 1997.

[35] J. Jankun, L. Lilge, A. Douplik, R. W. Keck, M. Pestka, M. Szkudlarek, P. J. Stevens, R. J. Lee, and S. H. Selman, "Optical characteristics of the canine prostate at 665 nm sensitized with tin etiopurpurin dichloride: Need for real-time monitoring of photodynamic therapy," *J. Urol.*, vol. 172, pp. 739–743, 2004.

[36] J. Jankun, R. W. Keck, E. Skrzypczak-Jankun, L. Lilge, and S. H. Selman, "Diverse optical characteristic of the prostate and light delivery system: Implications for computer modelling of prostatic photodynamic therapy," *Brit. J. Urol.*, vol. 95, pp. 1237–1244, 2005.

[37] T. C. Zhu, S. M. Hahn, A. S. Kapatkin, A. Dimofte, C. E. Rodriguez, T. G. Vulcan, E. Glatstein, and R. A. Hsi, "In vivo optical properties of normal canine prostate at 732 nm using motexafin lutetium-mediated photodynamic therapy," *Photochem. Photobiol.*, vol. 77, pp. 81–88, 2003.

[38] M. Solonenko, R. Cheung, T. M. Busch, A. Kachur, G. M. Griffin, T. Vulcan, T. C. Zhu, H. W. Wang, S. M. Hahn, and A. G. Yodh, "In vivo reflectance measurement of optical properties, blood oxygenation, and motexafin lutetium uptake in canine large bowels, kidneys, and prostates," *Phys. Med. Biol.*, vol. 47, pp. 857–873, 2002.

[39] R. A. Weersink, A. Bogaards, M. Gertner, S. Davidson, K. Zhang, G. Netchev, D. J. Giewercer, J. Trachtenberg, and B. C. Wilson, "Optical delivery and monitoring of photodynamic therapy of prostate cancer," *Proc. SPIE*, vol. 5578, pp. 117–127, 2004.

[40] L. Lilge, N. Pomerleau-Dalcourt, A. Douplik, S. H. Selman, R. W. Keck, M. Szkudlarek, M. Pestka, and J. Jankun, "Transperineal in vivo fluence-rate dosimetry in the canine prostate during SnET2-mediated PDT," *Phys. Med. Biol.*, vol. 49, pp. 3209–3225, 2004.

[41] T. Svensson, S. Andersson-Engels, M. Einarsdóttír, and K. Svanberg, "In vivo optical characterization of human prostate tissue using near-infrared time-resolved spectroscopy," *J. Biomed. Opt.*, vol. 12, pp. 014022-1–014022-10, 2007.

[42] M. L. Pantelides, C. Whitehurst, J. V. Moore, T. A. King, and N. J. Blacklock, "Photodynamic therapy for localized prostatic cancer—Light penetration in the human prostate gland," *J. Urol. (Baltimore)*, vol. 143, no. 2, pp. 398–401, 1990.

[43] H. J. Wei, D. Xing, B. H. He, R. H. Wu, H. M. Gu, G. Y. Wu, and X. M. Chen, "Absorption and scattering characteristics of human benign prostatic hyperplasia tissue with Ti: Sapphire laser irradiation in vitro," *(in Chinese), Guang Pu Xue Yu Guang Pu Fen Xi*, vol. 28, no. 1, pp. 10–13, 2008.

[44] M. Essenpreis, "Thermally induced changes in optical properties of biological tissues," Ph.D. thesis, Univ. College London, London, 1992.

[45] A. Roggan, K. Dörschel, O. Minet, D. Wolff, and G. Müller, "The optical properties of biological tissue in the near infrared wavelength range—review and measurements," in *Laser-induced Interstitial Thermotherapy Thermotherapy*, G. Müller and A. Roggan, Eds.: Washington: SPIE Optical Engineering Press, 1995, pp. 10–44.

[46] C. Whitehurst, M. L. Pantelides, J. V. Moore, P. J. C. Brooman, and N. J. Blacklock, "In vivo laser-light distribution in human prostaticcarcinoma," *J. Urol. (Baltimore)*, vol. 151, no. 5, pp. 1411–1415, 1994.

[47] L. K. Lee, C. Whitehurst, M. L. Pantelides, and J. V. Moore, "In situ comparison of 665 nm and 633 nm wavelength light penetration in the human prostate gland," *Photochem. Photobiol.*, vol. 62, no. 5, pp. 882–886, 1995.

[48] L. K. Lee, C. Whitehurst, M. L. Pantelides, and J. V. Moore, "An interstitial light assembly for photodynamic therapy in prostatic carcinoma," *BJU Int.*, vol. 84, no. 7, pp. 821–826, 1999.

[49] T. C. Zhu, A. Dimofte, J. C. Finlay, D. Stripp, T. Busch, J. Miles, R. Whittington, S. B. Malkowicz, Z. Tochner, E. Glatstein, and S. M. Hahn, "Optical properties of human prostate at 732 nm measured in mediated photodynamic therapy," *Photochem. Photobiol.*, vol. 81, no. 1, pp. 96–105, 2005.

[50] T. C. Zhu, J. C. Finlay, and S. M. Hahn, "Determination of the distribution of light, optical properties, drug concentration, and tissue oxygenation in vivo in human prostate during motexafin lutetiummediated photodynamic therapy," *J. Photochem. Photobiol. B*, vol. 79, no. 3, pp. 231–241, 2005.

[51] R. A. Weersink, A. Bogaards, M. Gertner, S. R. H. Davidson, K. Zhang, G. Netchev, J. Trachtenberg, and B. C. Wilson, "Techniques for delivery and monitoring of TOOKAD _WST09_-mediated photodynamic therapy of the prostate: Clinical experience and practicalities," *J. Photochem. Photobiol. B*, vol. 79, no. 3, pp. 211–222, 2005.

[52] T. Svensson, E. Alerstam, M. Einarsdóttír, K. Svanberg, and S. Andersson-Engels, "Towards accurate in vivo spectroscopy of the human prostate," *J. Biophoton.*, vol. 1, pp. 200–203, 2008.

[53] J. Li and T. C. Zhu, "Determination of in vivo light fluence distribution in a heterogeneous prostate during photodynamic therapy," *Phys. Med. Biol.*, vol. 53, no. 8, pp. 2103–2114, Apr. 2008.

[54] K. K. Wang and T. C. Zhu, "Reconstruction of in-vivo optical properties for human prostate using interstitial diffuse optical tomography," *Opt. Exp.*, vol. 17, no. 14, pp. 11665–11672, 2009.

[55] Z. Jiang, D. Piao, G. Xu, J. W. Ritchey, G. R. Holyoak, K. E. Bartels, C. F. Bunting, G. Slobodov, and J. S. Krasinski, "Trans-rectal ultrasound-coupled near-infrared optical tomography of the prostate. Part II: Experimental demonstration," *Opt. Exp.*, vol. 16, no. 22, pp. 17505–17520, 2008.

[56] M. Schweiger, S. R. Arridge, M. Hiroaka, and D. T. Delpy, "The finite element model for the propagation of light in scattering media: Boundary and source conditions," *Med. Phys.*, vol. 22, pp. 1779–1792, 1995.

[57] H. Dehghani, B. Brooksby, K. Vishwanath, B. W. Pogue, and K. D. Paulsen, "The effects of internal refractive index variation in near infrared optical tomography: A finite element modeling approach," *Phys. Med. Biol.*, vol. 48, pp. 2713–2727, 2003.

[58] X. Yu, G. Chen, and S. Cheng, "Dynamic learning rate optimization of the backpropagation algorithm," *IEEE Trans. Neural Netw.*, vol. 6, no. 3, pp. 669–677, May 1995.

[59] B. Rivera, K. Ahrar, M. M. Kangasniemi, J. D. Hazle, and R. E. Price, "Canine transmissible venereal tumor: A large animal transplantable tumor model," *Comp. Med.*, vol. 55, no. 4, pp. 335–343, 2005.

Daqing Piao (S'00–M'03) received the B.Sc. degree in physics from Tsinghua University, Beijing, China, in 1990, the M.Sc. and Ph.D. degrees in biomedical engineering from the University of Connecticut, Storrs, in 2001 and 2003, respectively.

From 1990 to 1994, he was with the Guandong Weida Medical Apparatus Group Corporation, Jiexi, China, where he was engaged in magnetic resonance imaging instrumentation. From 1994 to 1999, he was with Shanghai Kanglian Medical Engineering Corporation, Ltd., Shanghai, China, where he was engaged in biomedical applications of radio frequency and millimeter wave. He is currently an Assistant Professor of bioengineering with the School of Electrical and Computer Engineering, Oklahoma State University, Stillwater. His research interests include transrectal optical tomography for prostate cancer detection, investigating endoscopic tomography of hemodynamics, and developing alternating magnetic field device for magnetically activated nanothermal cancer therapy, which were funded by the Department of Defense Army Medical Research and Material Command, the Oklahoma Center for the Advancement of Science and Technology, and the National Institutes of Health, respectively. He has authored or coauthored around 30 papers published in various journals, and authored a chapter in the book *Translational Multimodality Optical Imaging* (Norwood, MA: Artech House, 2008).

Prof. Piao is the Member of the Optical Society of America and the International Society of Optical Engineering. He received the FY2002 Predoctoral Traineeship Award from the Department of Defense (DOD) Breast Cancer Research Program and the FY2006 New investigator Award from the DOD Prostate Cancer Research Program.

Kenneth E. Bartels received the M.Sc. degree in veterinary surgery from Colorado State University, Fort Collins, in 1977, and D.V.M degree from the College of Veterinary Medicine, Iowa State University, Iowa City, in 1973.

He is currently a Professor with the Department of Veterinary Clinical Sciences, Center for Veterinary Health Sciences, Oklahoma State University, Stillwater, where he is also the Director of the Biomedical Laser Laboratory and the McCasland Foundation Laser Surgery Professor. He is the Kerr Foundation Chair, where he is engaged in providing extended support for the Veterinary Center's Laser Laboratories. His research interests include lasers in veterinary surgery, laser/tissue interactions, and comparative medicine and surgery. He has authored or coauthored more than 75 peer-reviewed articles, seven book chapters, and edited one book involving surgery and the use of lasers in both humans and animals. He was with the U.S. Army Veterinary Corps for two years. He was with Army Reserve for 27 years, before retiring recently as a Colonel and Deputy Commander of the U.S. Army Veterinary Command.

Prof. Bartels is a Fellow of the American Society for Laser Medicine and Surgery.

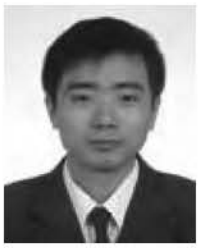

Zhen Jiang received the B.Sc. degree in electronics and information technology and the M.Sc. degree in electromagnetism and microwave engineering from Southeast University, Nanjing, China, in 1998 and 2005, respectively. He is currently working toward a Ph.D. degree with the School of Electrical and Computer Engineering, Oklahoma State University, Stillwater.

From 1998 to 2005, he worked in a number of R&D projects in the telecommunication network and wireless fields. His current research interests include the instrumentation and application of transrectal near-infrared optical tomography in detecting prostate cancer. He has authored or coauthored six journal papers.

Mr. Jiang is a Student Member of Optical Society of America and the International Society of Optical Engineering.

Gilbert Reed Holyoak received the B.Sc. degree in animal science, the M.Sc. degree in animal reproduction from Brigham Young University, Salt Lake City, in 1983 and 1984, respectively, the D.V.M. degree in veterinary medicine from Washington State University, Pullman, in 1988, and the Ph.D. degree in veterinary science from the University of Kentucky, Lexington, in 1992.

From 1992 to 1999, he was a Research Assistant Professor and Assistant Professor in Department of Animal, Dairy, and Veterinary Sciences, Utah State University, Logan. Since 1999, he has been an Assistant Professor, an Associate Professor, and a Professor with the Department of Veterinary Clinical Sciences, Oklahoma State University, Stillwater. He has authored or coauthored more than 45 peer-reviewed articles, and written seven book chapters.

Prof. Holyoak is a Diplomat of American College of Theriogenologists.

Jerry W. Ritchey received the B.Sc. degree in microbiology and the Doctor of Veterinary Medicine degree from Oklahoma State University, Stillwater, in 1987 and 1991, respectively, and the Ph.D. degree in immunology from North Carolina State University, Raleigh, in 1997.

From 1991 to 1993, he was a Resident in anatomic pathology with the College of Veterinary Medicine, North Carolina State University. Since 1997, he has been a Faculty member in the Department of Veterinary Pathobiology, Oklahoma State University, Stillwater, where he is currently a Professor. He has authored or coauthored more than 48 peer-reviewed articles.

Dr. Ritchey is a Diplomat of American College of Veterinary Pathologists, a Member of the American Veterinary Medical Association, Phi Zeta, Sigma Xi, and has been twice recognized as a Regents' Distinguished Teacher.

Guan Xu received the B.Sc. degree in electrical engineering from Hebei University of Technology, Tianjin, China, in 2006. He is currently working toward the Ph.D. degree with the School of Electrical and Computer Engineering, Oklahoma State University, Stillwater, OK.

His current research interests include the algorithms and simulations of transrectal near-infrared optical tomography for prostate imaging. He has authored or coauthored four journal papers.

Mr. Xu is a Student Member of Optical Society of America and the International Society of Optical Engineering.

Charles F. Bunting (S'89–M'94)

He received the A.A.S. degree in electronics technology from Tidewater Community College, Virginia Beach, in 1985, and the B.S. degree in engineering technology from Old Dominion University, Norfolk, VA, in 1989, the M.S. and Ph.D. degrees in electrical engineering from Virginia Polytechnic Institute and State University (Virginia Tech), Blacksburg, in 1992 and 1994, respectively.

From 1994 to 2001, he was an Assistant/Associate Professor with the Department of Engineering Technology, Old Dominion University, where he worked with the NASA Langley Research Center on electromagnetic field penetration in aircraft structures and reverberation chamber simulation using finite-element techniques. In 2001, he was an Associate Professor in Oklahoma State University. He is currently the Director of the Robust Electromagnetics and Field Testing and Simulation Laboratory, School of Electrical and Computer Engineering, Oklahoma State University, Stillwater. His current research interests include emphasis on statistical electromagnetics, electromagnetic characterization and application of reverberation chambers, characterization of electromagnetic compatibility of telecommunications, electronics systems in aircraft and shipboard environments, computational electromagnetics as applied to biological sensors, and applied research in engineering education.

Gennady Slobodov received the B.Sc. degree in chemical engineering from the University of Oklahoma, Norman, OK, in 1996, and the M.D. degree from the University of Oklahoma Health Sciences Center, Oklahoma City, in 2000.

Since 2005, he has been an Assistant Professor with the Department of Urology, University of Oklahoma Health Sciences Center, where he was a resident in Urologic Surgery from 2000 to 2005. He has authored or coauthored six peer-reviewed papers in the *Journal of Biomedical Optics*, the *Journal of Innovative Optical Health Sciences*, the *Journal of Urology and Molecular Cancer*, is an invited lecturer, and has had numerous abstracts accepted and presented at National meetings. He has been a subinvestigator in seven National research studies.

Prof. Slobodov is board certified by the American Board of Urology and is a Member of the American Medical Association, the American Urological Association, the Southwest Oncology Group, the American Urogynecologic Society, the American Association of Clinical Urologists, the Endourological Society, the National Cancer Institute, the Oklahoma State Medical Association, the Oklahoma State Urological Association, the Society of Laparoendoscopic Surgeons, the South Central Section of the American Urological Association, the International Society for the Study of Women's Sexual Health, and the International Continence Society. He has been the recipient of numerous awards including National Institutes of Health Intramural Research Fellowship, the Engineering Undergraduate Research Fellowship, the Outstanding Sophomore in Chemical Engineering, the Golden Key National Honor Society, the National Engineering Honor Society, the Chemical Engineering Program of Excellence, the Boyd Gunning Scholar, the Alpha Lambda Delta Honor Society, and the President's Honor Roll.

Photon diffusion in a homogeneous medium bounded externally or internally by an infinitely long circular cylindrical applicator. I. Steady-state theory

Anqi Zhang,[1] Daqing Piao,[1,*] Charles F. Bunting,[1] and Brian W. Pogue[2]

[1]*School of Electrical and Computer Engineering, Oklahoma State University, Stillwater, Oklahoma 74078, USA*
[2]*Thayer School of Engineering, Dartmouth College, Hanover, New Hampshire, 03755, USA*
**Corresponding author: daqing.piao@okstate.edu*

Received October 5, 2009; revised January 13, 2010; accepted January 14, 2010;
posted January 15, 2010 (Doc. ID 118134); published February 26, 2010

This work presents an analytic treatment for photon diffusion in a homogeneous medium bounded externally or internally by an infinitely long circular cylindrical applicator. Focusing initially on the steady-state condition, the photon diffusion in these two geometries is solved in cylindrical coordinates by using modified Bessel functions and by applying the extrapolated boundary condition. For large cylinder diameter, the analytic solutions may be simplified to a format employing the physical source and its image source with respect to a semi-infinite geometry and a radius-dependent term to account for the shape and dimension of the cylinder. The analytic solutions and their approximations are evaluated numerically to demonstrate qualitatively the effect of the applicator curvature—either concave or convex—and the radius on the photon fluence rate as a function of the source–detector distance, in comparison with that in the semi-infinite geometry. This work is subjected to quantitative examination in a coming second part and possible extension to time-resolved analysis.

OCIS codes: 170.3660, 170.5280, 170.6960.

1. INTRODUCTION

Using near-infrared (NIR) light to image large or deep tissue volumes non-invasively has largely been based on transport modeling with the diffusion approximation to the radiative transport equation [1]. Non-invasive diffuse optical imaging is always involved with some kind of applicator–tissue interface or air–tissue interface, because the light has to be delivered and detected at the surface of the tissue. For any specific applicator or imaging geometry, the analytic model predicting the photon fluence rate to be measured at the applicator–tissue interface dictates the accuracy of calibrating the system using a known homogeneous medium and recovering unknown optical properties of a heterogeneous medium. The analytic solutions to photon diffusion in an infinite homogeneous medium are the least complicated approach, and are solved straightforwardly in spherical coordinates. For a homogeneous medium bounded by an infinite plane edge, which conventionally is referred to as the semi-infinite geometry, the analytic solution to photon diffusion is also well-studied [2] and has been applied widely to analyze raw data measured from surface tissue applicators and for image reconstruction.

When NIR light diffusion is utilized for imaging of the breast, neonatal brain, joints, rodents, etc., the geometry of the applicator often has a planar or concave (with respect to the direction of source illumination) boundary. When a medium is enclosed by a ring-shaped applicator, the photon diffusion within the medium has been modeled as in an infinite medium for a ring applicator of considerable size [3]. For this type of ring applicator, the photon intensity measured at a site on the applicator interface and 180° to the source may resemble that measured in an infinite medium; however, the photon intensity measured at a site on the applicator interface but closer to the source should resemble more that measured in a semi-infinite medium. This inconsistency implies the inaccuracy of modeling the photon diffusion for a ring applicator based on either infinite or semi-infinite geometry. Accurate treatment of the circular concave boundary, as for a ring applicator, requires analysis in cylindrical coordinates. The model of photon diffusion in a medium bounded externally by a circular cylindrical applicator has been investigated previously in several elegant studies. Arridge *et al.* [4] used a boundary condition of zero fluence at the applicator interface to derive the time-domain and frequency-domain solutions for finite and infinite cylinders using Bessel functions and modified Bessel functions. The more accurate extrapolated boundary condition [5,6] was applied to similar concave applicator geometry by Pogue and Patterson [7] for a finite cylinder and Sassaroli *et al.* [8] for an infinite cylinder to express the time-domain solutions by use of Bessel functions. These studies provided important insight into photon diffusion in a medium bounded by a concave applicator, which mostly applies to diffuse optical imaging of the breast. Sassaroli *et al.* [8] also studied the effect of a concave boundary with diameters of 30–50 mm, in comparison with the semi-infinite plan boundary in the perspective of an inverse problem. The time-domain results for a

concave applicator have been applied to the frequency domain by Fourier transformation as in [7], and can be extended to the steady state by temporal integration.

Recently work by our group [9,10] as well as others [11,12] has investigated different aspects of applying diffuse optical tomography to imaging internal organs such as the prostate using an endo-rectal probe. This type of imaging geometry requires a convex-shaped applicator. The analytic model of photon diffusion in compliance with such convex geometry, simplified by a diffusive medium bounded internally by a cylindrical applicator, has not been derived previously. Accurate modeling of photon propagation in a specific convex geometry could certainly be rendered by Monte Carlo methods [8]. The finite-element solution of photon diffusion [10,11] in such convex geometry may also prove sufficiently accurate in the diffusion regime. Given the availability of numerical means, finding the analytic model of photon diffusion is still imperative and important, as it ultimately is beneficial to calibrating measurement data and improving reconstruction accuracy. What and how accurately such diffusion-based model could predict at the smaller scale of the convex geometry for applications such as endo-rectal imaging is especially interesting.

In this work the photon diffusion is analyzed in both external and internal imaging geometries, in which the medium being interrogated is bounded either externally or internally by an infinitely long circular cylindrical applicator. These two geometries resemble imaging the breast using a ring-shaped applicator and imaging the prostate using an endo-rectal probe, respectively. These studies are conducted initially for steady-state photon diffusion only, which is nonetheless adequate in terms of assessing the effect of the cylindrical interface on photon fluence rate when compared with a semi-infinite boundary. The initial works are to be presented in two papers. In this the first part, the Green's function of the photon diffusion equation in an infinite medium geometry is first expanded in cylindrical coordinates to a closed form expressed by modified Bessel functions. Then the extrapolated boundary condition is employed to apply the image–source method to the geometries of a "concave" cylindrical applicator and a "convex" cylindrical applicator, respectively. The analytic solutions are then simplified to a format, valid for large cylinder diameters, that includes the physical source and its image source with respect to the associated semi-infinite geometry and a radius-dependent term to account for the shape and dimension of the cylinder. The simplified format reveals that, as the radius of the cylinder increases, the analytic solution of the photon diffusion for it approaches the well-known semi-infinite result. The analytic solutions and their simplified formats are then evaluated numerically for two specific geometries, one having the source and the detector on the surface positioned only along the azimuthal direction and the other along the longitudinal direction. Placing the source–detector either azimuthally or longitudinally demonstrates explicitly the effect of the applicator curvature, either concave or convex, and the radius of the applicator curvature on the decay of photon fluence rate as a function of the source–detector distance in comparison with that in the semi-infinite geometry. As the radius of the cylindrical applicator increases, the numerically evaluated photon diffusion for it asymptotically approaches that for a semi-infinite geometry, as expected. The features of steady-state photon diffusion for cylindrical concave and convex applicators analyzed theoretically and evaluated qualitatively in this first part will be examined quantitatively in the second part. The study may also be extended to time-resolved analysis in the future.

2. ANALYTIC APPROACH AND GEOMETRIES EXAMINED

A. Steady-State Photon Diffusion in an Infinite Medium: Solution in Cylindrical Coordinates

The steady-state photon diffusion equation is expressed by [2–6]

$$\nabla^2\Psi(\vec{r}) - \frac{\mu_a}{D}\Psi(\vec{r}) = -\frac{S(\vec{r})}{D}, \tag{2.1.1}$$

where Ψ is the photon fluence rate at position $\vec{r}$, μ_a is the absorption coefficient, $D=[3(\mu_a+\mu_s')]^{-1}$ is the diffusion coefficient with μ_s' being the reduced scattering coefficient, and S is the source. Considering a source at $\vec{r}'$ of (ρ',φ',z') and a detector at $\vec{r}$ of (ρ,φ,z) in cylindrical coordinates, the equation for the Green's function of Eq. (2.1.1) is

$$\nabla^2 G(\vec{r},\vec{r}') - k_0^2 G(\vec{r},\vec{r}') = -\delta(\vec{r}-\vec{r}'), \tag{2.1.2}$$

where $k_0=\sqrt{\mu_a/D}$ is the effective attenuation coefficient. The Dirac delta function in Eq. (2.1.2) is

$$\delta(\vec{r}-\vec{r}') = (1/\rho)\delta(\rho-\rho')\delta(\varphi-\varphi')\delta(z-z'), \tag{2.1.3}$$

where the delta functions for φ and z can be written in terms of inverse Fourier series and inverse Fourier transform, respectively, by

$$\delta(\varphi-\varphi') = \frac{1}{2\pi}\sum_{m=-\infty}^{\infty} e^{im(\varphi-\varphi')} \tag{2.1.4}$$

and

$$\delta(z-z') = \frac{1}{2\pi}\int_0^\infty dk e^{ik(z-z')} = \frac{1}{\pi}\int_0^\infty dk\,\cos[k(z-z')]. \tag{2.1.5}$$

Substituting Eqs. (2.1.3)–(2.1.5) into Eq. (2.1.2) and expanding ∇^2 in Eq. (2.1.2) in cylindrical coordinates lead to

$$\frac{1}{\rho}\frac{\partial}{\partial\rho}\left(\rho\frac{\partial G(\vec{r},\vec{r}')}{\partial\rho}\right) + \frac{1}{\rho^2}\frac{\partial^2 G(\vec{r},\vec{r}')}{\partial\varphi^2} + \frac{\partial^2 G(\vec{r},\vec{r}')}{\partial z^2} - k_0^2 G(\vec{r},\vec{r}') = -\frac{1}{2\pi^2\rho}\delta(\rho-\rho')\sum_{m=-\infty}^{\infty}\int_0^\infty dk e^{im(\varphi-\varphi')}\cos[k(z-z')]. \tag{2.1.6}$$

The Green's function can be expanded to a form similar to the right-hand side of Eq. (2.1.6) as

$$G(\vec{r},\vec{r}') = \frac{1}{2\pi^2}\sum_{m=-\infty}^{\infty}\int_0^{\infty} dk \cdot g_m(k,\rho,\rho') \cdot e^{im(\varphi-\varphi')} \times\cos[k(z-z')], \tag{2.1.7}$$

where $g_m(k,\rho,\rho')$ is the radial Green's function to be solved. Substituting Eq. (2.1.7) into Eq. (2.1.6) leads to

$$\frac{1}{\rho}\frac{\partial}{\partial\rho}\left(\rho\frac{\partial g_m(k,\rho,\rho')}{\partial\rho}\right) - \left(k^2 + k_0^2 + \frac{m^2}{\rho^2}\right)g_m(k,\rho,\rho') = -\frac{1}{\rho}\delta(\rho-\rho'). \tag{2.1.8}$$

We define

$$k_{eff}^2 = k^2 + k_0^2 \quad \text{or} \quad k_{eff} = \sqrt{k^2+k_0^2}. \tag{2.1.9}$$

Then Eq. (2.1.8) becomes

$$\frac{1}{\rho}\frac{\partial}{\partial\rho}\left(\rho\frac{\partial g_m(k,\rho,\rho')}{\partial\rho}\right) - \left(k_{eff}^2 + \frac{m^2}{\rho^2}\right)g_m(k,\rho,\rho') = -\frac{1}{\rho}\delta(\rho-\rho'). \tag{2.1.10}$$

Solutions to the Helmholtz Eq. (2.1.10) can be derived by following Jackson's approach of solving Poisson's equation [13] and using the asymptotic approximations of modified Bessel functions [14]. The solution details are given in Appendix A. With the solution for $g_m(k,\rho,\rho')$, we have

$$G(\vec{r},\vec{r}') = \frac{1}{2\pi^2}\int_0^{\infty} dk \cdot \left\{\sum_{m=0}^{\infty}\epsilon_m I_m(k_{eff}\rho_<)K_m(k_{eff}\rho_>) \times\cos[m(\varphi-\varphi')]\right\}\cdot\cos[k(z-z')], \tag{2.1.11}$$

where $\rho_<$ and $\rho_>$ indicate the smaller and larger radial coordinates of the source and the detector, and

$$\epsilon_m = \begin{cases} 2, & m \neq 0 \\ 1, & m = 0 \end{cases}. \tag{2.1.12}$$

Convolving the Green's function with the source term in Eq. (2.1.1) and assuming a point source renders the cylindrical-coordinate solution to the steady-state photon diffusion in an infinite homogeneous medium as

$$\Psi(\vec{r},\vec{r}') = \frac{S}{2\pi^2 D}\int_0^{\infty} dk \cdot \left\{\sum_{m=0}^{\infty}\epsilon_m I_m(k_{eff}\rho_<)K_m(k_{eff}\rho_>) \times\cos[m(\varphi-\varphi')]\right\}\cdot\cos[k(z-z')]. \tag{2.1.13}$$

B. Steady-State Photon Diffusion in an Infinite Homogeneous Medium: Solution in Spherical Coordinates

The solution to Eq. (2.1.1) in spherical coordinates is well-known as

$$\Psi(\vec{r},\vec{r}') = \frac{S}{4\pi D|\vec{r}-\vec{r}'|}e^{-k_0|\vec{r}-\vec{r}'|}. \tag{2.2.1}$$

If the distance between a source and a detector is denoted by d, Eq. (2.2.1) is readily converted to

$$\ln(\Psi\cdot d) = -k_0 d + \ln\left(\frac{S}{4\pi D}\right). \tag{2.2.2}$$

Equation (2.2.2) indicates a linear relationship between the natural logarithm of the product of the fluence rate and the source–detector distance with respect to the source–detector distance, a characteristics useful for calibration with a homogeneous medium when an isotropic point source can be assumed. For the same homogeneous medium and source–detector geometry, the solutions given by Eqs. (2.2.1) and (2.1.13) will be identical to each other, which will be numerically validated in Section 4.

C. Steady-State Photon Diffusion in a Semi-infinite Medium: Solutions in Spherical Coordinates

The effect of an applicator boundary on photon diffusion has been rigorously modeled by the index-mismatched Robin-type (or Type III) boundary condition of

$$\Psi - 2AD\,\nabla\Psi\cdot\vec{n} = 0, \tag{2.3.1}$$

where $A=(1+R_{eff})/(1-R_{eff})$ and R_{eff} is the effective reflection coefficient [3] representing the percentage of the outgoing radiance integrated over all directions pointing toward the ambient medium that is converted to incoming radiance integrated over all directions pointing toward the scattering medium [15]. The Type III boundary condition (2.3.1), which is evaluated on the physical boundary, can be surrogated by an almost equally accurate but more convenient approach by use of a Type I boundary condition that is being evaluated on an "imaginary" boundary. The "imaginary" boundary, referred to as the "extrapolated" boundary [5,6], is located $2AD$ from the physical boundary and away from the medium. It is with respect to this extrapolated boundary that the negative "image" [16] of the source is introduced to set zero the fluence rate on this boundary.

We follow the notations introduced by Fantini *et al.* [2] for the semi-infinite geometry having a directional source and an isotropic detector located on a planar boundary, as illustrated in Fig. 1(a). The directional source is modeled as an isotropic source placed one reduced scattering distance into the medium. Then, based on the extrapolated boundary approach, the steady-state photon fluence rate reaching the detector located on the physical boundary is determined by the equivalent "real" isotropic source and its image source with respect to the extrapolated boundary in spherical coordinates as

$$\Psi = \Psi_{real} - \Psi_{imag} = \frac{S}{4\pi D l_{real}}e^{-k_0 l_{real}} - \frac{S}{4\pi D l_{imag}}e^{-k_0 l_{imag}}, \tag{2.3.2}$$

where

$$l_{real} = \sqrt{d^2+R_a^2}, \qquad R_a = 1/\mu_s'; \tag{2.3.3}$$

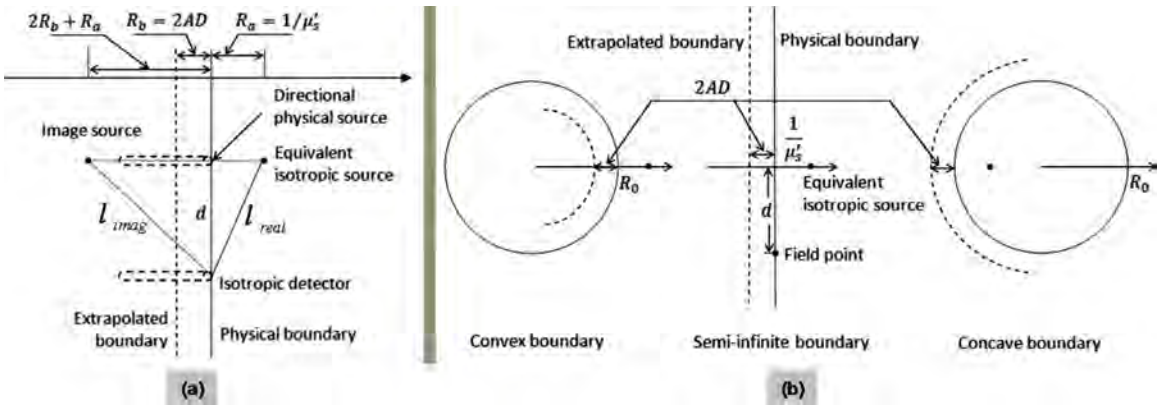

Fig. 1. (Color online) (a) Semi-infinite geometry [2]. The diffuse medium is to the right of the physical boundary, and the light is incident from the left. (b) The two cylindrical geometries in comparison with the semi-infinite geometry. The convex boundary represents that of a cylindrical applicator enclosed by the diffuse medium (e.g., imaging the prostate by a trans-rectal probe), and the concave boundary represents that of a cylindrical applicator enclosing the diffuse medium (e.g., imaging the breast by a ring probe).

$$l_{imag} = \sqrt{d^2 + (2R_b + R_a)^2}, \qquad R_b = 2AD. \tag{2.3.4}$$

The d in relations (2.3.3) and (2.3.4) is the distance between the physical directional source and the detector, both located at the physical boundary, as in Eq. (2.2.2). For $d \gg R_a, R_b$, Eq. (2.3.2) converts [17] to

$$\ln(\Psi \cdot d^2) = -k_0 \cdot d + \ln\left(\frac{s}{2\pi D} \cdot k_0 R_b (R_a + R_b)\right), \tag{2.3.5}$$

which is the model-basis for calibrating in a semi-infinite homogeneous medium.

D. Cylindrical Interface Geometries Being Investigated in this Study

In this work, the "concave" geometry is defined as having the diffusive medium *enclosed* by an infinitely long cylindrical applicator, and the "convex" geometry as having the diffusive medium *enclosing* an infinitely long cylindrical applicator. The physical directional source is always modeled as an isotropic source placed one reduced scattering distance into the medium, as shown in Fig. 1(b). Usually, the extrapolated boundary condition is applicable when a diffusive medium bonds with a non-scattering region—a valid representation of either an external-imaging or an internal-imaging optical applicator. Since the distance of the extrapolated boundary from the physical boundary, $R_b = 2AD$ as in the semi-infinite geometry, is derived from the general expression of the boundary condition in Eq. (2.3.1), this distance will be considered as geometry-independent; therefore in the concave or convex geometry the extrapolated boundary will also be located at a radial distance $R_b = 2AD$ from the physical boundary and away from the diffusive medium. Obviously, as the radius reaches infinity both concave and convex geometries approach the semi-infinite geometry. This feature serves as both the qualitative and quantitative measure of the analytic solutions derived for the concave and convex probe geometries.

3. STEADY-STATE PHOTON DIFFUSION ASSOCIATED WITH CONCAVE OR CONVEX INFINITE CYLINDRICAL APPLICATOR

This section derives the cylindrical-coordinate solutions to steady-state photon diffusion in the concave and convex cylinder geometries. The same analytic principles apply to both the concave and convex geometries; however, the detailed analytic derivations of the two geometries are separately listed for completeness and for facilitating qualitative comparison between them.

A. External "Concave" Boundary; Analytic Solution

The concave geometry for a medium bounded externally by an infinitely long circular cylindrical applicator with

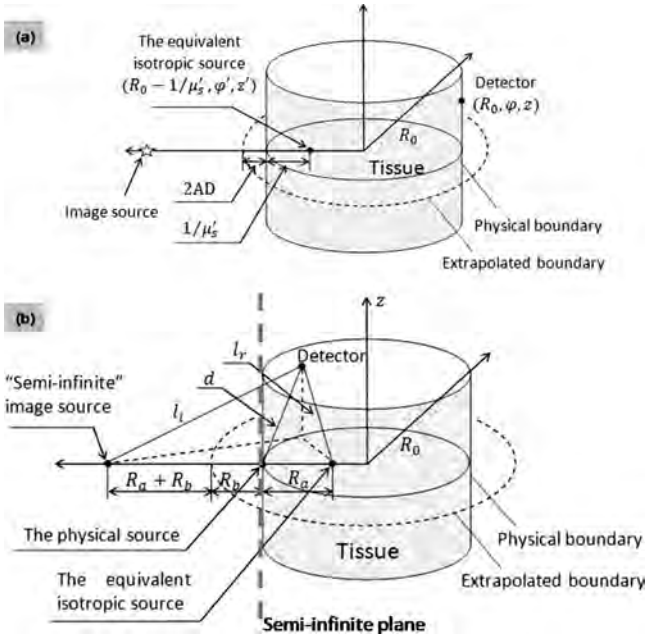

Fig. 2. (a) Details of the concave geometry indicating the equivalent isotropic source and the extrapolated boundary. The image source of the isotropic source with respect to the extrapolated boundary is located along the radial direction of the isotropic source due to symmetry. (b) The concave geometry and the "semi-infinite" image source that is the image source of the isotropic source with respect to a planar boundary tangential to the concave boundary at the location of the physical source.

radius R_0 is illustrated in Fig. 2(a). The physical source is located at (R_0,φ',z') and the detector is located at (R_0,φ,z), both on the physical boundary.

1. Photon Diffusion under the Extrapolated Boundary Condition

As shown in Fig. 2(a), the equivalent "real" isotropic source must be located at (R_0-R_a,φ',z') based on the symmetry of the geometry, and the extrapolated boundary will be located at a radial distance of $R_b=2AD$ outside the physical boundary. Based on the symmetry of the geometry, the image source of the "real" isotropic source with respect to the extrapolated boundary must also be located along the radial direction of the "real" isotropic or the physical source. This image source and the "real" isotropic source collectively set zero the photon fluence rate on the extrapolated boundary.

Based on Eq. (2.1.13), the photon fluence rate associated with the "real" isotropic source and evaluated on the extrapolated boundary, for which the source is located at $\rho_{r<}=R_0-R_a$ and the detector is located at $\rho_{r>}=R_0+R_b$, is

$$\Psi_{real}|_{extr}=\frac{1}{2\pi^2D}\int_0^\infty dk\cdot\cos[k(z-z')]\cdot\left\{\sum_{m=0}^{\infty}\epsilon_m SI_m[k_{eff}(R_0-R_a)]K_m[k_{eff}(R_0+R_b)]\times\cos[m(\varphi-\varphi')]\right\},\tag{3.1.1}$$

where the notation "$_{left}|_{right}$" indicates evaluating the "left" as a source on the "right" as a boundary. Similarly, the photon fluence rate associated with the image source and evaluated on the extrapolated boundary for which the source is located at an unknown or yet-to-decide $\rho_{i>}$ but the detector is located at $\rho_{i<}=R_0+R_b$, is

$$\Psi_{imag}|_{extr}=\frac{1}{2\pi^2D}\int_0^\infty dk\cdot\left\{\sum_{m=0}^{\infty}\epsilon_m S_m^* I_m[k_{eff}(R_0+R_b)]K_m[k_{eff}\rho_{i>}]\times\cos[m(\varphi-\varphi')]\right\}\cdot\cos[k(z-z')].\tag{3.1.2}$$

In Eq. (3.1.2), the S_m^* terms are also unknown or yet-to-decide, besides $\rho_{i>}$. Based on the essential concept of "image–source" [16,18], the two unknown terms S_m^* and $\rho_{i>}$ associated with the mth order "image" source (the K_m component) can be expressed by a single unknown term of S_m associated with the same-order "real" source (the I_m component); that is,

$$S_m^*K_m(k_{eff}\rho_{i>})=S_mI_m[k_{eff}\rho_{r<}]=S_mI_m[k_{eff}(R_0-R_a)].\tag{3.1.3}$$

Applying Eq. (3.1.3) to the extrapolated boundary condition of $\Psi_{real}|_{extr}-\Psi_{imag}|_{extr}=0$, we have

$$S_m=S\frac{K_m[k_{eff}(R_0+R_b)]}{I_m[k_{eff}(R_0+R_b)]},\qquad m=0,1,2,\cdots.\tag{3.1.4}$$

Now for the "real" isotropic source but evaluated at the physical boundary, the source is still located at $\rho_{r<}=R_0-R_a$, but the detector is located at $\rho_{r>}=R_0$. For the "image" source, also evaluated at the physical boundary, the detector is located at $\rho_{i<}=R_0$, and the source terms are known through Eqs. (3.1.3) and (3.1.4). Collectively the photon fluence rate sensed by a detector at the physical boundary becomes

$$\Psi=\Psi_{real}|_{phys}-\Psi_{imag}|_{phys}=\frac{S}{2\pi^2D}\int_0^\infty dk\left\{\cos[k(z-z')]\cdot\sum_{m=0}^{\infty}\epsilon_m I_m[k_{eff}(R_0-R_a)]K_m(k_{eff}R_0)\cdot\left\langle 1-\frac{I_m(k_{eff}R_0)}{K_m(k_{eff}R_0)}\frac{K_m[k_{eff}(R_0+R_b)]}{I_m[k_{eff}(R_0+R_b)]}\right\rangle\cos[m(\varphi-\varphi')]\right\}.\tag{3.1.5}$$

2. Concave Geometry with a Large Cylinder Diameter: Approaching the Semi-infinite Geometry

As shown in Fig. 2(b), if a plane tangential to the cylinder at the physical source position is considered an imaginary semi-infinite planar boundary, then the "real" isotropic source in this semi-infinite geometry is still located at (R_0-R_a,φ',z'), but the image source of the "real" isotropic source with respect to this semi-infinite boundary will be at $(R_0+R_a+2R_b,\varphi',z')$.

According to Eq. (2.1.13) the photon fluence rate sensed by a detector on the cylinder boundary due to the image source of the "real" isotropic source associated with the semi-infinite boundary is

$$\Psi_{imag}^{semi}|_{phys}=\frac{S}{2\pi^2D}\int_0^\infty dk\cos[k(z-z')]\cdot\sum_{m=0}^{\infty}\epsilon_m I_m(k_{eff}R_0)K_m[k_{eff}(R_0+R_a+2R_b)]\times\cos[m(\varphi-\varphi')].\tag{3.1.6}$$

The photon fluence rate sensed by a detector on the cylinder boundary due to the image source of the "real" isotropic source associated with the cylinder boundary as seen in Eq. (3.1.5) can be rewritten to

$$\Psi_{imag}|_{phys}=\frac{S}{2\pi^2D}\int_0^\infty dk\cos[k(z-z')]\cdot\sum_{m=0}^{\infty}\epsilon_m I_m(k_{eff}R_0)K_m[k_{eff}(R_0+R_a+2R_b)]\cdot\eta_m\cos[m(\varphi-\varphi')],\tag{3.1.7}$$

where

$$\eta_m = \frac{I_m[k_{eff}(R_0 - R_a)]}{I_m[k_{eff}(R_0 + R_b)]} \frac{K_m[k_{eff}(R_0 + R_b)]}{K_m[k_{eff}(R_0 + R_a + 2R_b)]}. \tag{3.1.8}$$

If the cylinder diameter is sufficiently large, the modified Bessel functions in Eq. (3.1.8) can be simplified by their asymptotic expressions [14]; then Eq. (3.1.8) becomes

$$\eta_m = \sqrt{\frac{R_0 + R_a + 2R_b}{R_0 - R_a}}. \tag{3.1.9}$$

Substituting Eq. (3.1.9) into Eq. (3.1.7) and comparing with Eq. (3.1.6) we have

$$\Psi_{imag}|_{phys} = \Psi^{semi}_{imag}|_{phys} \cdot \sqrt{\frac{R_0 + R_a + 2R_b}{R_0 - R_a}}. \tag{3.1.10}$$

Hence, for the cylinder of sufficiently large diameter, Eq. (3.1.5) approximates to

$$\Psi = \Psi_{real}|_{phys} - \Psi_{imag}|_{phys} = \Psi_{real}|_{phys} - \Psi^{semi}_{imag}|_{phys} \cdot \sqrt{\frac{R_0 + R_a + 2R_b}{R_0 - R_a}}. \tag{3.1.11}$$

As $R_0 \to \infty$, the $\Psi_{real}|_{phys}$ of Eq. (3.1.11) essentially becomes the Ψ_{real} in Eq. (2.3.2), $\sqrt{(R_0+R_a+2R_b)/(R_0-R_a)} \to 1$, and the $\Psi^{semi}_{imag}|_{phys}$ of Eq. (3.1.11) becomes the Ψ_{imag} in Eq. (2.3.2) because the detector located at (R_0, φ, z) reaches the imaginary semi-infinite boundary. This agrees with the physical aspect that an infinitely long concave cylindrical boundary becomes a semi-infinite boundary as the radius of the cylinder becomes infinity. By using the spherical-coordinate expression of the photon fluence rate given in Eq. (2.2.1), we can rewrite Eq. (3.1.11) as

$$\Psi = \frac{S}{4\pi D} \frac{e^{-k_0 l_r}}{l_r} - \frac{S}{4\pi D} \frac{e^{-k_0 l_i}}{l_i} \sqrt{\frac{R_0 + R_a + 2R_b}{R_0 - R_a}}. \tag{3.1.12}$$

B. Internal "Convex" Boundary; Analytic Solution

The convex geometry for a medium bounded internally by an infinitely long circular cylindrical applicator with radius R_0 is illustrated in Fig. 3(a). The physical source is located at (R_0, φ', z') and the detector is located at (R_0, φ, z), both on the physical boundary.

1. Photon Diffusion under the Extrapolated Boundary Condition

As shown in Fig. 3(a), the equivalent "real" isotropic source must be located at (R_0+R_a, φ', z') based on the symmetry of the geometry, and the extrapolated boundary will be located at a radial distance $R_b = 2AD$ inside the physical boundary. Based on the symmetry of the geometry, the image source of the "real" isotropic source with respect to the extrapolated boundary must also be located along the radial direction of the "real" isotropic or the physical source. This image source and the "real" isotropic source collectively set zero the photon fluence rate on the extrapolated boundary.

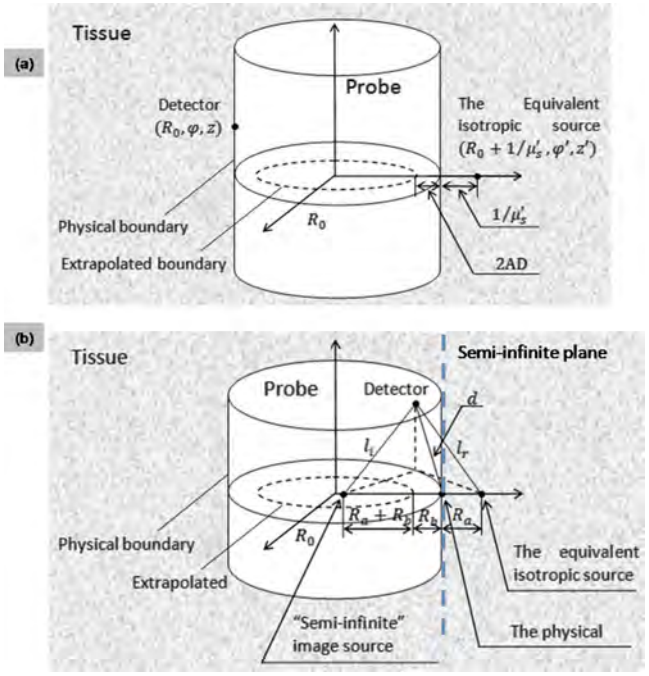

Fig. 3. (Color online) (a) Details of the convex geometry indicating the equivalent isotropic source and the extrapolated boundary. (b) The convex geometry and the "semi-infinite" image source that is the image source of the isotropic source with respect to a planar boundary tangential to the concave boundary at the location of the physical source.

On the basis of Eq. (2.1.13), the photon fluence rate associated with the "real" isotropic source and evaluated on the extrapolated boundary, for which the source is located at $\rho_{r<} = R_0 - R_b$ and the detector is located at $\rho_{r>} = R_0 + R_a$, is

$$\Psi_{real}|_{extr} = \frac{1}{2\pi^2 D} \int_0^\infty dk \cdot \cos[k(z - z')] \cdot \left\{ \sum_{m=0}^{\infty} \epsilon_m S I_m[k_{eff}(R_0 - R_b)] K_m[k_{eff}(R_0 + R_a)] \times \cos[m(\varphi - \varphi')] \right\}, \tag{3.2.1}$$

where we use the same notation "$_{left}|_{right}$" as in Eq. (3.1.1). Similarly, the photon fluence rate associated with the image source and evaluated on the extrapolated boundary, for which the source is located at an unknown or yet-to-decide $\rho_{i<}$ but the detector is located at $\rho_{i>} = R_0 - R_b$, is

$$\Psi_{imag}|_{extr} = \frac{1}{2\pi^2 D} \int_0^\infty dk \cdot \left\{ \sum_{m=0}^{\infty} \epsilon_m S^*_m I_m[k_{eff}\rho_{i<}] K_m[k_{eff}(R_0 - R_b)] \times \cos[m(\varphi - \varphi')] \right\} \cdot \cos[k(z - z')]. \tag{3.2.2}$$

In Eq. (3.2.2), the S_m^* terms are also unknown or yet-to-decide, besides $\rho_{i<}$. Following the approach of [16,18] as in Eq. (3.1.3), we have

$$S_m^* I_m(k_{eff}\rho_{i<}) = S_m K_m[k_{eff}\rho_{r>}] = S_m K_m[k_{eff}(R_0+R_a)], \tag{3.2.3}$$

which expresses the two unknown terms S_m^* and $\rho_{i<}$ associated with the mth order "image" source (the I_m component) by a single unknown term of S_m associated with the same-order "real" source (the K_m component). Applying Eq. (3.2.3) to the extrapolated boundary condition of $\Psi_{real}|_{extr} - \Psi_{imag}|_{extr} = 0$ gives

$$S_m = S\frac{I_m[k_{eff}(R_0-R_b)]}{K_m[k_{eff}(R_0-R_b)]} \quad m = 0,1,2,\cdots. \tag{3.2.4}$$

Now for the "real" isotropic source but evaluated at the physical boundary, the source is still located at $\rho_{r>}=R_0+R_a$, but the detector is located at $\rho_{r<}=R_0$. For the "image" source also evaluated at the physical boundary, the detector is located at $\rho_{i>}=R_0$, and the source terms are known through Eqs. (3.2.3) and (3.2.4). Collectively the photon fluence rate sensed by a detector at the physical boundary becomes

$$\Psi = \Psi_{real}|_{phys} - \Psi_{imag}|_{phys} = \frac{S}{2\pi^2 D}\int_0^\infty dk \Bigg\{ \cos[k(z-z')] \cdot \sum_{m=0}^{\infty} \epsilon_m I_m(k_{eff}R_0) K_m[k_{eff}(R_0+R_a)] \cdot \left\langle 1 - \frac{K_m(k_{eff}R_0)}{I_m(k_{eff}R_0)} \frac{I_m[k_{eff}(R_0-R_b)]}{K_m[k_{eff}(R_0-R_b)]} \right\rangle \cos[m(\varphi-\varphi')] \Bigg\}. \tag{3.2.5}$$

2. Convex Geometry with a Large Cylinder Diameter: Approaching the Semi-infinite Geometry

As shown in Fig. 3(b), if a plane tangential to the cylinder at the physical source position is considered an imaginary semi-infinite planar boundary, then the "real" isotropic source in this semi-infinite geometry is still located at (R_0+R_a,φ',z'), but the "image" source of the "real" isotropic source with respect to this semi-infinite boundary will be at $(R_0-R_a-2R_b,\varphi',z')$.

According to Eq. (2.1.13) the photon fluence rate sensed by a detector on the cylinder boundary due to the image source of the "real" isotropic source associated with the semi-infinite boundary is

$$\Psi_{imag}^{semi}|_{phys} = \frac{S}{2\pi^2 D}\int_0^\infty dk \cos[k(z-z')] \cdot \sum_{m=0}^{\infty} \epsilon_m I_m[k_{eff}(R_0-R_a-2R_b)] K_m(k_{eff}R_0) \times \cos[m(\varphi-\varphi')]. \tag{3.2.6}$$

The photon fluence rate sensed by a detector on the cylinder boundary due to the image source of the "real" isotropic source associated with the cylinder boundary, as seen in Eq. (3.2.5), can be rewritten to

$$\Psi_{imag}|_{phys} = \frac{S}{2\pi^2 D}\int_0^\infty dk \cos[k(z-z')] \cdot \sum_{m=0}^{\infty} \epsilon_m I_m[k_{eff}(R_0-R_a-2R_b)] K_m(k_{eff}R_0) \cdot \eta_m \cos[m(\varphi-\varphi')], \tag{3.2.7}$$

where

$$\eta_m = \frac{I_m[k_{eff}(R_0-R_b)]}{I_m[k_{eff}(R_0-R_a-2R_b)]} \frac{K_m[k_{eff}(R_0+R_a)]}{K_m[k_{eff}(R_0-R_b)]}. \tag{3.2.8}$$

If the cylinder diameter is sufficiently large, the modified Bessel functions in Eq. (3.2.8) can be simplified by their asymptotic expressions [14]; then Eq. (3.2.8) becomes

$$\eta_m = \sqrt{\frac{R_0-R_a-2R_b}{R_0+R_a}}. \tag{3.2.9}$$

Substituting Eq. (3.2.9) into Eq. (3.2.7) and comparing with Eq. (3.2.6) we have

$$\Psi_{imag}|_{phys} = \Psi_{imag}^{semi}|_{phys} \cdot \sqrt{\frac{R_0-R_a-2R_b}{R_0+R_a}}. \tag{3.2.10}$$

Hence, for the cylinder of sufficiently large diameter, Eq. (3.2.5) approximates to

$$\Psi = \Psi_{real}|_{phys} - \Psi_{imag}|_{phys} = \Psi_{real}|_{phys} - \Psi_{imag}^{semi}|_{phys} \cdot \sqrt{\frac{R_0-R_a-2R_b}{R_0+R_a}}. \tag{3.2.11}$$

As $R_0 \to \infty$, the $\Psi_{real}|_{phys}$ of Eq. (3.2.11) essentially becomes Ψ_{real} in Eq. (2.3.2), $\sqrt{(R_0-R_a-2R_b)/(R_0+R_a)} \to 1$, and the $\Psi_{imag}^{semi}|_{phys}$ of Eq. (3.2.11) becomes the Ψ_{imag} in Eq. (2.3.2) because the detector located at (R_0,φ,z) reaches the imaginary semi-infinite boundary. This agrees with the physical aspect that an infinitely long convex cylindrical boundary becomes a semi-infinite boundary as the radius of the cylinder becomes infinity. By using the spherical coordinate expression of the photon fluence rate given in Eq. (2.2.1), we can rewrite Eq. (3.2.11) as

$$\Psi = \frac{S}{4\pi D}\frac{e^{-k_0 l_r}}{l_r} - \frac{S}{4\pi D}\frac{e^{-k_0 l_i}}{l_i}\sqrt{\frac{R_0-R_a-2R_b}{R_0+R_a}}. \tag{3.2.12}$$

C. Summary of the Solutions in Cylindrical Coordinates

In cylindrical coordinates, the steady-state photon fluence rate in an infinite homogeneous medium is

$$\Psi = \frac{S}{2\pi^2 D}\int_0^\infty dk\,\cos[k(z-z')] \cdot \sum_{m=0}^{\infty} \epsilon_m I_m(k_{eff}\rho_<)K_m(k_{eff}\rho_>)\cos[m(\varphi-\varphi')]. \tag{3.3.1}$$

The steady-state photon fluence rate in a concave geometry imposed by an infinitely long circular cylindrical applicator for interrogating the medium internal to the applicator (e.g., breast imaging) is

$$\Psi = \frac{S}{2\pi^2 D}\int_0^\infty dk \left\{ \cos[k(z-z')] \cdot \sum_{m=0}^{\infty} \epsilon_m I_m[k_{eff}(R_0-R_a)]K_m(k_{eff}R_0) \cdot \left\langle 1 - \frac{I_m(k_{eff}R_0)}{K_m(k_{eff}R_0)}\frac{K_m[k_{eff}(R_0+R_b)]}{I_m[k_{eff}(R_0+R_b)]} \right\rangle \cos[m(\varphi-\varphi')] \right\}, \tag{3.3.2conC}$$

where "conC" stands for "concave" and "conV" for "convex" (below).

The steady-state photon fluence rate in a convex geometry imposed by an infinitely long circular cylindrical applicator for interrogating the medium external to the applicator (e.g., prostate imaging) is

$$\Psi = \frac{S}{2\pi^2 D}\int_0^\infty dk \left\{ \cos[k(z-z')] \cdot \sum_{m=0}^{\infty} \epsilon_m I_m[k_{eff}R_0]K_m[k_{eff}(R_0+R_a)] \cdot \left\langle 1 - \frac{K_m(k_{eff}R_0)}{I_m(k_{eff}R_0)}\frac{I_m[k_{eff}(R_0-R_b)]}{K_m[k_{eff}(R_0-R_b)]} \right\rangle \cos[m(\varphi-\varphi')] \right\}. \tag{3.3.2conV}$$

If the concave or convex geometry has a large radial dimension, the photon fluence rate expressed by Eqs. (3.3.2conC and 3.3.2conV) can be approximated to

$$\Psi = \frac{S}{4\pi D}\frac{e^{-k_0 l_r}}{l_r} - \frac{S}{4\pi D}\frac{e^{-k_0 l_i}}{l_i}\sqrt{\frac{R_0+R_a+2R_b}{R_0-R_a}}, \tag{3.3.3conC}$$

$$\Psi = \frac{S}{4\pi D}\frac{e^{-k_0 l_r}}{l_r} - \frac{S}{4\pi D}\frac{e^{-k_0 l_i}}{l_i}\sqrt{\frac{R_0-R_a-2R_b}{R_0+R_a}}, \tag{3.3.3conV}$$

where l_r is defined as the distance from the detector to the "real" isotropic source and l_i as the distance from the detector to the image source of the "real" isotropic source associated with the semi-infinite geometry that is tangential to the concave or convex geometry on the physical source point.

4. STEADY-STATE PHOTON DIFFUSION IN THE INFINITE GEOMETRY: NUMERICAL VERIFICATION OF THE CYLINDRICAL-COORDINATE SOLUTION

This section validates the cylindrical-coordinate solution (2.1.13) of the steady-state photon diffusion in a homogeneous infinite medium, since Eq. (2.1.13) sets the foundation for the analytic derivations thereafter. As evaluating entities like Eq. (2.1.13) involves half-sided integration and summation to infinity, the numerical approaches must provide sufficient accuracy within the framework imposed by the precision of the computer and the algorithm arithmetic.

For an infinite medium it is practical to define a source point arbitrarily at (0,0,0) and a field point at $(\rho,0,0)$. Then the spherical-coordinate solution (2.2.1) can be rewritten as

$$\Psi = (S/4\pi D d)e^{-k_0 d}, \tag{4.1}$$

where d is the source–detector distance. Equation (4.1) can be implemented in terms of the linear relationship between $\ln(\Psi d)$ and d as indicated in Eq. (2.2.2). Similarly the cylindrical-coordinate solution (3.3.1) in the same homogeneous infinite medium becomes

$$\Psi(\rho,\varphi) = \frac{S}{2\pi^2 D}\int_0^\infty dk \sum_{m=0}^{\infty} \epsilon_m I_m(0)K_m(k_{eff}\rho_>). \tag{4.2}$$

The adaptive Gauss–Kronrod quadrature in MATLAB (Mathworks Inc, Natick, Massachusetts) is used to calculate the integrations in Eq. (4.2) as well as all the integrations appearing later. To effectively implement the integration and the infinite-summation terms in Eq. (4.2), it is necessary to evaluate the range for the integration or the summation to be executed. Based on the asymptotic expression of the modified Bessel functions for large argument [14], we have that for sufficiently large k, hence large k_{eff},

$$I(k_{eff}\rho_<)K(k_{eff}\rho_>) = \frac{1}{2k_{eff}\sqrt{\rho_<\rho_>}}e^{-k_{eff}(\rho_>-\rho_<)}, \tag{4.3}$$

which asymptotically and quasi-exponentially reaches zero as k increases. Therefore for a given accuracy Eq. (4.2) can be numerically implemented with an upper limit of k, because it also sets the upper limit of the integration. The contributions of higher k to the integration in Eq. (4.2) are evaluated in Fig. 4(a) for the first m term of $m=0$ using realistic optical and geometry parameters, including $\mu_a = 0.01\ \mathrm{cm}^{-1}$, $\mu_s' = 10\ \mathrm{cm}^{-1}$, $\varphi = 0$, and $d = 0.5-10$ cm. The use of $\ln(\Psi d)$ versus d is necessary for evaluating Eq. (4.2) with respect to Eq. (4.1). The difference of setting the upper limit of k at 50 or 100 is indistinguishable for a source–detector distance greater than 1 mm, at the scale shown. The integration in Eq. (4.2) is therefore executed for $k=50$, as the source–detector distance practically is much greater than 1 mm.

To evaluate the choice of m, we first check the following terms in Eq. (4.2) and denote them Ω:

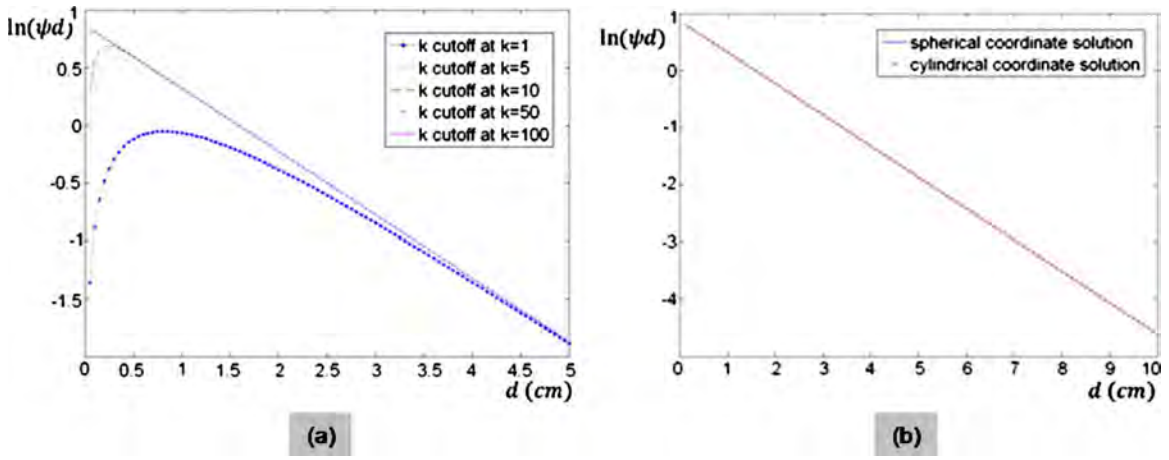

Fig. 4. (Color online) (a) Comparison of the contributions of the k terms when evaluating the cylindrical-coordinate solution to the steady-state photon diffusion in the homogeneous infinite medium. (b) Comparison between the solutions in spherical coordinates and cylindrical coordinates to the steady-state photon diffusion in the homogeneous infinite medium.

$$\Omega = \sum_{m=0}^{\infty} \epsilon_m I_m(0) K_m(k_{eff}\rho_>). \tag{4.4}$$

In Eq. (4.4), $I_m(0)$ will be nonzero only when $m=0$. Hence, only the first m term need be summed. Overall, Eq. (4.2) can be evaluated by integrating up to $k=50$ and summing the first m terms.

Figure 4(b) evaluates Eq. (4.2) with respect to Eq. (4.1) for the parameters of $\mu_a=0.01$ cm^{-1}, $\mu_s'=10$ cm^{-1}, $\varphi=0$, and $\rho=0.5-10$ cm as in Fig. 4(a), and integrating k up to 100 for $m=0$. Figure 4(b) demonstrates that Eq. (4.2) is identical to Eq. (4.1) within the precision of the MATLAB arithmetic.

5. STEADY-STATE PHOTON DIFFUSION IN THE "CONCAVE" AND "CONVEX" GEOMETRIES: NUMERICAL EVALUATION OF THE CYLINDRICAL-COORDINATE SOLUTIONS

This section numerically evaluates the general solutions in Eq. (3.3.2) for geometries having smaller cylinder radius and their approximations in Eq. (3.3.3) for geometries having very large cylinder radius. These evaluations, for simplicity, are limited to two cases: (1) the source and detector are located at the same azimuth plane; (2) the source and detector are located longitudinally with the same azimuthal angle. The results will indicate how the circular boundary affects the photon fluence rate with respect to a semi-infinite boundary, and justify qualitatively these analytic solutions and their approximations.

A. Specific Geometry: Source and Detector Located at the Same Azimuth Plane

The geometries shown in Fig. 5 are chosen to study the effect of concave or convex boundary shape on photon diffusion for the source and detector located at the same azimuth plane. Then the "chord" distance between the source and the detector is considered in a range from 0.5 cm (assuring diffusion treatment) to $2R_0$ for optical properties set at $\mu_a=0.01$ cm^{-1}, $\mu_s'=10$ cm^{-1}, $A=1$, and $S=1$ (these parameters are used throughout the rest of the studies).

1. Numerical Approaches

In this case, both the source and detector are on the same azimuthal plane, that is $z=z'$; therefore Eqs. (3.3.2conC and 3.3.2conV)can be rewritten as

$$\Psi = \frac{S}{2\pi^2 D}\int_0^{\infty} dk \left\{ \sum_{m=0}^{\infty} \epsilon_m I_m[k_{eff}(R_0-R_a)] K_m(k_{eff}R_0) \cdot \left\langle 1 - \frac{I_m(k_{eff}R_0)}{K_m(k_{eff}R_0)} \frac{K_m[k_{eff}(R_0+R_b)]}{I_m[k_{eff}(R_0+R_b)]} \right\rangle \cos[m(\varphi-\varphi')] \right\}, \tag{5.1.1conC}$$

$$\Psi = \frac{S}{2\pi^2 D}\int_0^{\infty} dk \left\{ \sum_{m=0}^{\infty} \epsilon_m I_m(k_{eff}R_0) K_m[k_{eff}(R_0+R_a)] \cdot \left\langle 1 - \frac{K_m(k_{eff}R_0)}{I_m(k_{eff}R_0)} \frac{I_m[k_{eff}(R_0-R_b)]}{K_m[k_{eff}(R_0-R_b)]} \right\rangle \cos[m(\varphi-\varphi')] \right\}. \tag{5.1.1conV}$$

For large k, hence large k_{eff}, the integrands of Eqs. (5.1.1conC and 5.1.1conV) become the following [14]:

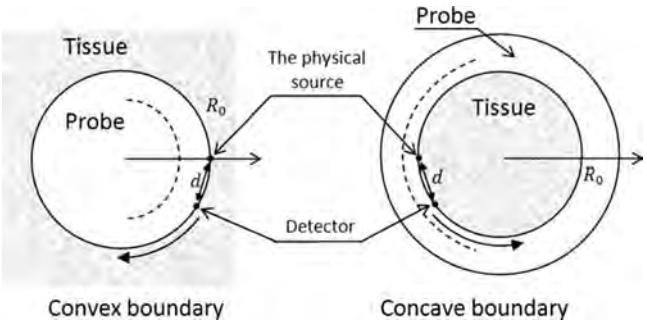

Fig. 5. Concave and convex geometries with the source and the detector located at the same azimuthal plane.

$$I_m[k_{eff}(R_0-R_a)]K_m(k_{eff}R_0)\times\left\langle 1-\frac{I_m(k_{eff}R_0)}{K_m(k_{eff}R_0)}\frac{K_m[k_{eff}(R_0+R_b)]}{I_m[k_{eff}(R_0+R_b)]}\right\rangle = \frac{e^{-k_{eff}R_a}}{2k_{eff}\sqrt{R_0(R_0-R_a)}}(1-e^{-2k_{eff}R_b}), \quad (5.1.2\text{conC})$$

$$I_m(k_{eff}R_0)K_m[k_{eff}(R_0+R_a)]\times\left\langle 1-\frac{K_m(k_{eff}R_0)}{I_m(k_{eff}R_0)}\frac{I_m[k_{eff}(R_0-R_b)]}{K_m[k_{eff}(R_0-R_b)]}\right\rangle = \frac{e^{-k_{eff}R_a}}{2k_{eff}\sqrt{R_0(R_0+R_a)}}(1-e^{-2k_{eff}R_b}). \quad (5.1.2\text{conV})$$

It is again noted that as k_{eff} becomes sufficiently large both Eqs. (5.1.2conC and 5.1.2conV) asymptotically and quasi-exponentially approach zero. Therefore in Eqs. (5.1.1conC and 5.1.1conV) the contribution of the integrands associated with k greater than a certain limit can be neglected. However, according to the IEEE standard for floating-point arithmetic [19], there is a limit for the largest number and the smallest number to be stored. In MATLAB the criterion [20] for overflow is 1.7977×10^{308} in decimal, and for underflow is 2.2251×10^{-308}. In Eqs. (5.1.1conC and 5.1.1conV), the modified Bessel functions of the first and second kinds are exponentially growing and decaying functions, for which overflow will readily occur for a large order m and underflow for a large argument k. To evaluate source and detector at the same azimuthal plane a larger order of m is necessary, and to evaluate the source and detector located longitudinally with the same azimuthal angle a large argument k also becomes crucial. In both Eqs. (5.1.1conC and 5.1.1conV), since all the modified Bessel functions of the first and second kinds appear in pairs in the same order when multiplying with each other, a strategy of "pre-enlarge" and "pre-reduce" is implemented to ease the numerical manipulation. The principle is that instead of evaluating each modified Bessel function individually, the modified Bessel function of the first kind can be "pre-reduced" for large order m and the modified Bessel function of the second kind can be "pre-enlarged" by the same degree, by which the product of each pair will remain unchanged. The outcome of this pre-enlarge and pre-reduce manipulation is demonstrated in Fig. 6(a) for a convex boundary of $R_0=2$ cm, d changing from 0.1 cm to 4 cm, k cutoff at 70, $\mu_a=0.01$ cm^{-1}, $\mu_s'=10$ cm^{-1}, $A=1$, and $S=1$. The m is summed from 0 to 150 (the dotted curve with ripples), which was the limit to avoid overflow and underflow without applying the pre-enlarge and pre-reduce approach. After pre-enlarge and pre-reduce, the summation can be made for m up to 500. Figure 6(a) indicates that this method of pre-enlarge and pre-reduce enables summing modified Bessel functions up to a large order of m by eliminating the ripples or noise seen when no such manipulation is employed.

Additionally, it is also found for Eqs. (5.1.1conC and 5.1.1conV) that the radius R_0 has a great effect on the evaluation outcome. For instance, when R_0 is as large as 8 cm in Eq. (5.1.1conC), for $k=40$, the integration does not converge sufficiently even for summing m up to 500 [the optical parameters are the same as used for Fig. 6(a)], but for a smaller radius $R_0=1$ cm the same integrand converges quickly at $m=100$. A method of "repeated averaging" is thus employed to improve the convergence. The principle is to first examine if there is an oscillating pattern. If there is, the envelope of the maxima and minima of the oscillation is implemented to form a finite converging alternative series, and the last maxima and minima are averaged to become the value of the integrand. If an oscillating pattern is not formed, the last result is chosen as the value of the integrand. The results of applying such "repeated averaging" when evaluating Eq. (5.1.1conC) are shown in Fig. 6(b), in which m is summed up to 540 for $R_0=8$ cm.

Based on these specific approaches of improving the outcome of numerical evaluations, the upper limits of k and m are evaluated individually for each set of computations conducted. For example, at a parameter setting of m terms up to 150, the effects of a finite k cutoff value when evaluating Eq. (5.1.1) are shown in Fig. 7(a) for the concave boundary and Fig. 7(b) for the convex boundary. The difference between integrating k from 0 to 50 and from 0 to 100 is indistinguishable at the given scale, for both con-

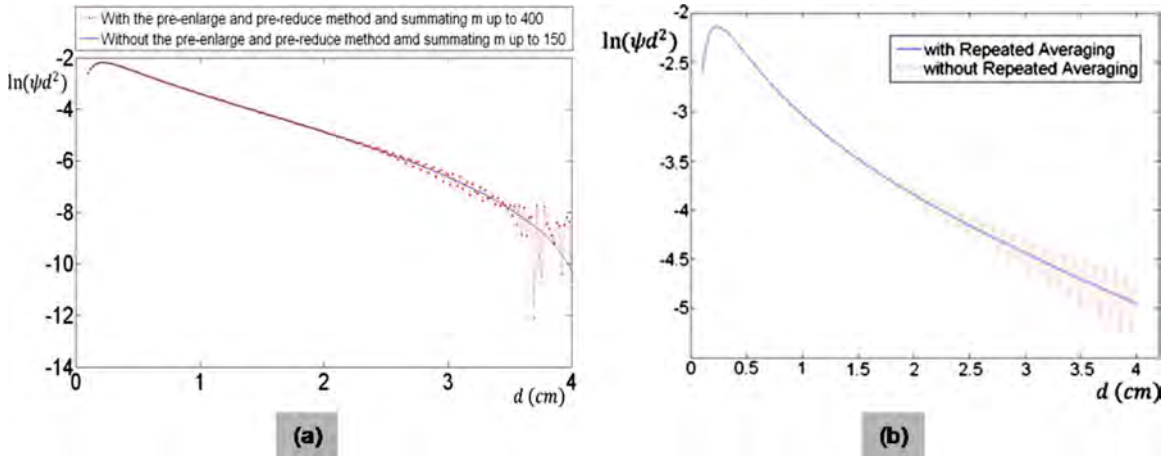

Fig. 6. (Color online) (a) Outcome of applying pre-enlarge and pre-reduce methods for $R_0=2$ cm in convex geometry. (b) Outcome of applying "repeated averaging" for $R_0=8$ cm in concave geometry.

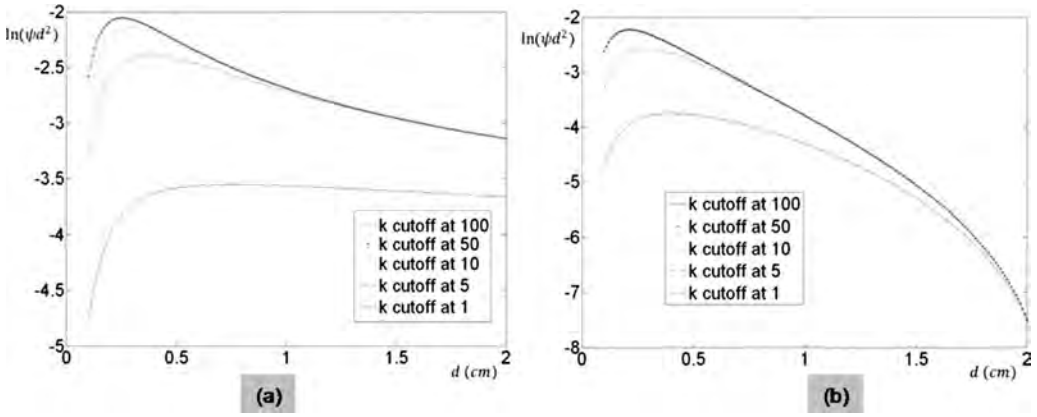

Fig. 7. (Color online) Comparison of the contributions of k terms in the solution for source and detector located in the same azimuthal plane: (a) concave geometry; (b) convex geometry.

cave and convex boundaries. Therefore the cutoff value for k is set at 50 for this set of evaluations.

2. Numerical Evaluation of the General Solutions for a Cylinder Applicator of Radius up to 10 Cm

The general solutions (5.1.1conC and 5.1.1conV) are evaluated numerically with respect to a semi-infinite geometry in Fig. 8(a). The radius R_0 is chosen as 0.5, 1, 2, 5, and 10 cm. The figure is plotted for $\ln(\Psi d^2)$ versus d as this is the linear relationship implied by Eq. (2.3.5) of semi-infinite geometry. It is noted again that d is assigned as the chord distance between the physical source and the detector points on the circular boundary. Therefore the maximum d for a radius of 0.5 cm is 1 cm, of 1 cm is 2 cm, etc., and d is set to change from 0.1 to 4 cm for the remaining radii. On the azimuthal plane, the photon fluence rate associated with a given source–detector distance in a concave geometry is greater than that in a planar geometry for the same source–detector distance, and in a convex geometry it is smaller than that in a planar geometry. The overall qualitative feature, as anticipated, is that as the radius of the cylinder geometry increases, the photon fluence rate for the concave and convex boundaries asymptotically approaches that for a semi-infinite boundary.

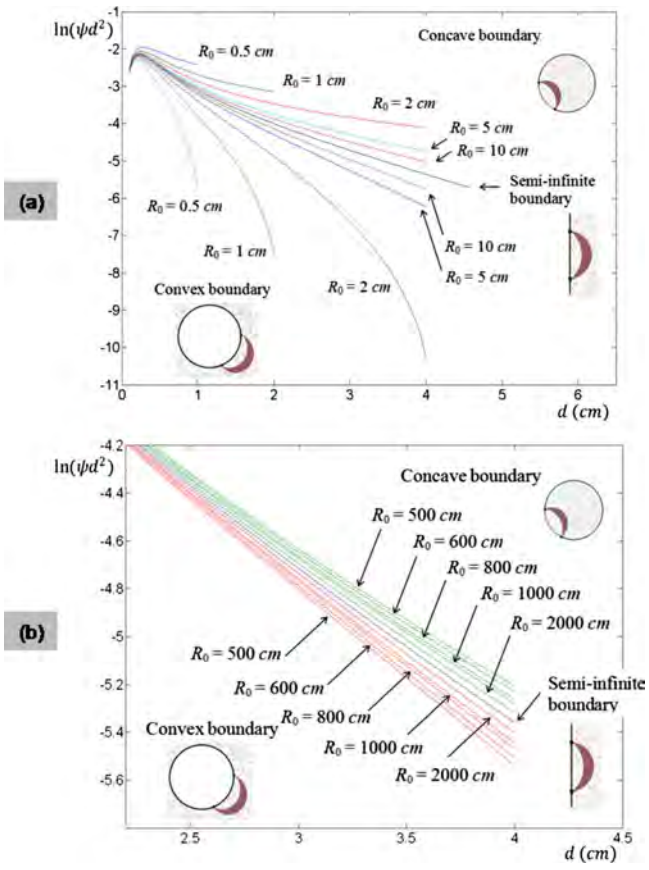

Fig. 8. (Color online) (a) Comparison of the solutions for concave and convex geometries with respect to the semi-infinite geometry, for source and detector located at the same azimuthal plane. (b) Comparison of the solutions for concave and convex geometries having large cylinder radius with respect to the semi-infinite geometry for source and detector located at the same azimuthal plane.

3. Numerical Evaluation of the Solutions Approximated for a Cylindrical Applicator of Very Large Radius

For the azimuthal geometry with large cylinder diameter, the distance terms in Eqs. (3.3.3conC and 3.3.3conV) can be expressed by

$$l_r = [R_a^2 + d^2 - (R_a d^2/R_0)]^{1/2}, \qquad (5.1.4\text{conC})$$

$$l_i = [(R_a + 2R_b)^2 + d^2 + (R_a + 2R_b)(d^2/R_0)]^{1/2} \qquad (5.1.5\text{conC})$$

for concave boundary, and

$$l_r = [R_a^2 + d^2 + (R_a d^2/R_0)]^{1/2}, \qquad (5.1.4\text{conV})$$

$$l_i = [(R_a + 2R_b)^2 + d^2 - (R_a + 2R_b)(d^2/R_0)]^{1/2} \qquad (5.1.5\text{conV})$$

for convex boundary. The comparison of the two azimuthal geometries with respect to the semi-infinite geometry is given in Fig. 8(b), where the radius R_0 is chosen as 500, 600, 800, 1000, and 2000 cm. The results are shown only for d from 2.2 to 4 cm to illustrate that both the concave and convex boundary asymptotically approach the "linear" feature of the planar boundary for $\ln(\psi d^2)$ and d, but with radius-dependent differences in the slope and

potentially in the intersection, both of which clearly will vanish as the radius becomes infinity.

B. Specific Geometry: Source and Detector Located Longitudinally with the Same Azimuthal Angle

The geometries shown in Fig. 9 are chosen to study the effect of concave or convex shape on photon diffusion for the source and detector located longitudinally with the same azimuth angle.

1. Numerical Approaches

For $\varphi=\varphi'$, we rewrite Eqs. (3.3.2conC and 3.3.2conV) as

$$\Psi = \frac{S}{2\pi^2 D}\int_0^\infty dk\left\{\cos[k(z-z')]\cdot\sum_{m=0}^{\infty}\epsilon_m I_m[k_{eff}(R_0-R_a)]K_m(k_{eff}R_0)\cdot\left\langle 1-\frac{I_m(k_{eff}R_0)}{K_m(k_{eff}R_0)}\frac{K_m[k_{eff}(R_0+R_b)]}{I_m[k_{eff}(R_0+R_b)]}\right\rangle\right\}, \tag{5.2.1conC}$$

$$\Psi = \frac{S}{2\pi^2 D}\int_0^\infty dk\left\{\cos[k(z-z')]\cdot\sum_{m=0}^{\infty}\epsilon_m I_m(k_{eff}R_0)K_m[k_{eff}(R_0+R_a)]\cdot\left\langle 1-\frac{K_m(k_{eff}R_0)}{I_m(k_{eff}R_0)}\frac{I_m[k_{eff}(R_0-R_b)]}{K_m[k_{eff}(R_0-R_b)]}\right\rangle\right\}. \tag{5.2.1conV}$$

The previous analysis given for numerical evaluation of Eqs. (5.1.2conC and 5.1.2conV) still holds here; therefore the contribution due to large k, hence large k_{eff}, is neglected.

The numerical manipulation methods of pre-enlarge and pre-reduce as well as repeated averaging discussed in Subsection 5.A are also applied here. The settings of k values are shown in Fig. 10(a) for concave boundary and Fig. 10(b) for convex boundary, where the parameters used are $R_0=1$ cm with d ranging from 0.5 cm to 2 cm and m summing from 0 to 100. It is observed that the plots for k cutoff at 100 and 200 are indistinguishable at the given scale. For this set of computations the upper limit for k is then set at 100. This upper limit of k is higher than that used for evaluating the azimuthal plane. It is also found that the upper limit for m can be chosen much lower than that used for evaluating the azimuthal plane. Again the upper limits of k and m are evaluated individually for each set of computations.

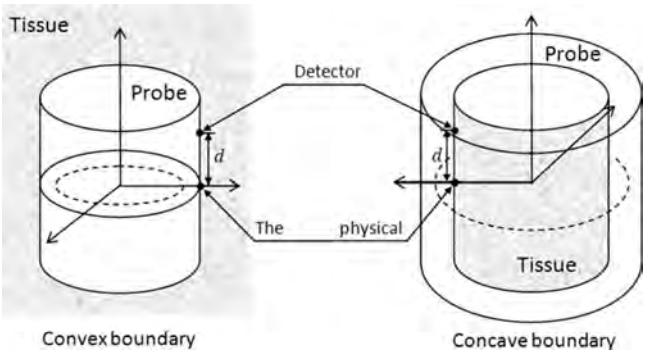

Fig. 9. Concave and convex geometries with source and detector located longitudinally with the same azimuthal angle.

2. Numerical Evaluation of the General Solutions for a Cylindrical Applicator of Radius up to 6 Cm

The general solutions (5.2.1conC and 5.2.1conV) are evaluated numerically with respect to semi-infinite geometry in Fig. 11(a). The radius R_0 is chosen as 1, 2, 3, and 6 cm. The figure is again plotted for $\ln(\Psi d^2)$ versus d, as it is the linear relationship implied by Eq. (2.3.5) for a semi-infinite geometry, and d is the longitudinal distance between the physical source and the detector points on the circular boundary. The d in this geometry is not limited in range, but a range from 0.1 to 4 cm is chosen for comparison with the azimuthal geometry of Fig. 8. Along the longitudinal direction, the photon fluence rate associated with a given source–detector distance in a concave geometry is smaller than that in a planar geometry for the same source–detector distance, and in a convex geometry it is greater than that in a planar geometry. The overall qualitative feature, as anticipated, is that as the radius of the cylinder geometry increases, the photon fluence rate for the concave and convex boundaries asymptotically approaches that for a semi-infinite geometry.

3. Numerical Evaluation of the Solutions for a Cylinder Applicator of Very Large Radius

For the longitudinal geometry with larger cylinder diameter, the distance terms in Eqs. (3.3.3conC and 3.3.3conV) can be expressed by

$$l_r = (R_a^2 + d^2)^{1/2}, \tag{5.2.2}$$

$$l_i = [(R_a + 2R_b)^2 + d^2 +]^{1/2} \tag{5.2.3}$$

for both concave and convex geometries. The comparison of the two longitudinal geometries with respect to the semi-infinite geometry is given in Fig. 11(b) with the rest of the parameters the same as in Fig. 8(b). Again, both the concave and convex geometry asymptotically approach the "linear" feature of the planar boundary for $\ln(\Psi d^2)$ and d, but with radius-dependent differences in the slope and potentially in the intersection, both of which clearly will vanish as the radius becomes infinity.

Finally in terms of the computation time, for each single curve in Fig. 8 or Fig. 11 that includes on average 300 data points, it takes approximately 5 min to formulate on a 2.8 GHz CPU with 1.0 GB of memory.

6. DISCUSSION

The solution to photon diffusion in an infinite homogeneous medium derived in cylindrical coordinates likely will involve two Bessel functions. The solution could have different expressions, depending on the type (normal or modified, the first kind, or the second kind) of Bessel functions used and the way these functions are integrated into

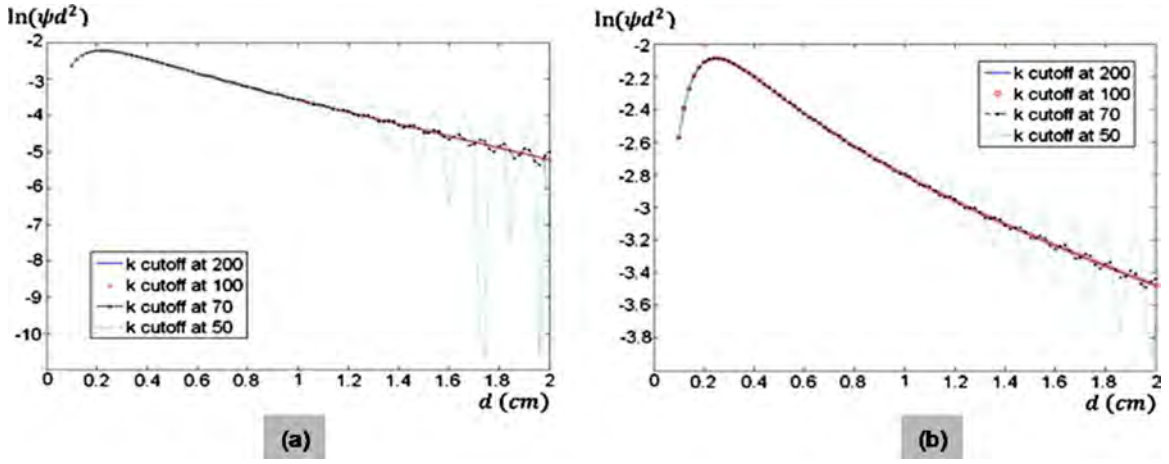

Fig. 10. (Color online) Comparison of the contributions of k terms in the solution for source and detector located longitudinally with the same azimuthal angle: (a) concave boundary; (b) convex boundary.

the solution. In Eq. (3.3.1), we have expressed the solution using the modified Bessel functions. The integration part of Eq. (3.3.1) is identical to that of the solution to the Poisson equation in cylindrical coordinates given in [13], except that the argument contains k_{eff} instead of k as in [13]. This solution may be advantageous as it demonstrates clearly the different roles of the source and the field points in the solution by differentiating the radial coordinates of the source and field points into the arguments specific to different kinds of the modified Bessel functions, such that both of the modified Bessel functions will become valid in the geometry of interest.

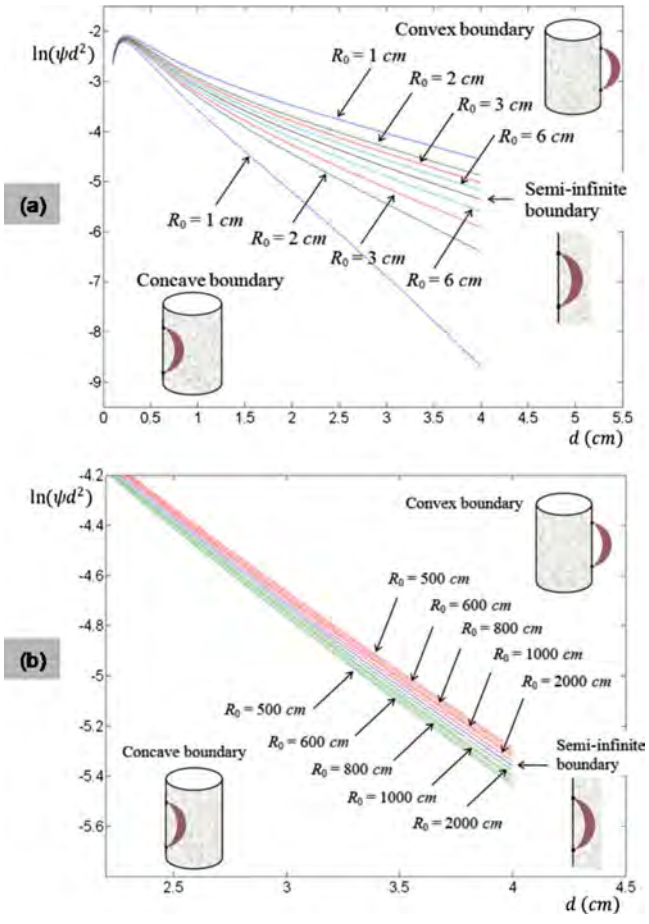

Fig. 11. (Color online) (a) Comparison of the solutions for concave and convex geometries with respect to the semi-infinite geometry for source and detector located longitudinally with the same azimuthal angle. (b) Comparison of the solutions for concave and convex geometries having large cylinder diameter with respect to the semi-infinite geometry for source and detector located longitudinally with the same azimuthal angle.

Applying the solution in Eq. (3.3.1) leads to physically explicit interpretation in the two equations of (3.3.2) for a medium involving an external or internal cylindrical boundary. These equations in (3.3.2) are composed of two parts in the curly brackets: the first part is associated with the "real" isotropic source, and the second part is the contribution of the "image" source term that is represented by the "real" source term scaled by a factor. The scaling factor is related to the radius of the cylinder and the reflective index mismatch of the cylinder–medium interface that determines where the extrapolated boundary will be placed. The equations in (3.3.3), which are derived for large-radius concave and convex boundaries, are given in a format similar to that for semi-infinite geometry but with a shape-curvature-associated term that approaches unity as the radius of the cylinder approaches infinity.

The numerical evaluations in Section 5 demonstrate the qualitative correctness of the analytic solutions in Eqs. (3.3.2) for the two circular cylindrical geometries, within the limits of the current computer arithmetic. It is clearly shown that the solutions given in the two Eqs. (3.3.2) asymptotically approach the semi-infinite medium solution as the applicator radius reaches infinity. For the specific case of having the source and detector located azimuthally on the same axial plane, the photon fluence rate is greater than the semi-infinite geometry for the concave boundary and smaller for the convex boundary given the same source–detector distance. This can be explained by noting that, for the same source–detector distance, more near-field photons from the source could scatter and reach the detector in the concave geometry than in the semi-infinite geometry, but in the convex geometry they do the opposite. For the specific case of having the source and detector located longitudinally on the same azimuthal angle, the photon fluence rate is smaller than the semi-infinite geometry for the concave boundary and greater

for the convex boundary given the same source–detector distance. This again can be explained by noting that, for the same source–detector distance, fewer near-field photons from the source could scatter and reach the detector in the concave geometry than in the semi-infinite geometry, but in the convex geometry the opposite is true.

7. CONCLUSIONS

The steady-state photon diffusion in a homogeneous medium bounded externally or internally by an infinitely long circular cylindrical applicator has been analyzed. The geometry of a diffusive medium bounded externally by a cylindrical applicator resembles that of imaging externally accessible biological tissue such as the breast using a ring-type array. The geometry of a diffusive medium bounded internally by a cylindrical applicator resembles that of imaging internally accessible biological tissue such as the prostate using a trans-rectal probe. Solutions to steady-state photon diffusion in these two geometries are derived in cylindrical coordinates by applying the extrapolated boundary condition and are expressed in modified Bessel functions of the first and second kinds. Approximate solutions for large cylinder radius are also derived in the format close to that for semi-infinite geometry by including a shape-radius-associated term. Numerical evaluations are provided for the cases of having the source and the detector positioned only along the azimuthal or longitudinal directions. The results demonstrate that compared with a semi-infinite boundary, the concave boundary has smaller photon fluence decay in the azimuth direction but greater photon fluence decay along the longitudinal direction compared with a semi-infinite geometry having the same source–detector distance. On the other hand, the convex boundary has greater photon fluence decay in the azimuth direction but smaller photon fluence decay along the longitudinal direction. As the radius of the concave or convex circular applicator becomes infinitely large, the results for these specific geometries reach the well-known condition for a semi-infinite medium, as expected. This theory and "qualitative" numerical evaluation constitute the first part of this work, which will be quantitatively examined in the second part and potentially extended to time-resolved analysis in future studies.

APPENDIX A: SOLUTION TO EQ. (2.1.10) FOLLOWING JACKSON'S APPROACH IN [13]

Equation (2.1.10) is rewritten here:

$$\frac{1}{\rho}\frac{\partial}{\partial\rho}\left(\rho\frac{\partial g_m(k,\rho,\rho')}{\partial\rho}\right)-\left(k_{eff}^2+\frac{m^2}{\rho^2}\right)g_m(k,\rho,\rho')=-\frac{1}{\rho}\delta(\rho-\rho'). \tag{A.1}$$

For $\rho\neq\rho'$, Eq. (A.1) is the equation for the modified Bessel functions $I_m(k_{eff}\rho)$ and $K_m(k_{eff}\rho)$. According to Jackson [13], assume that $\psi_1(k_{eff}\rho)$ is some linear combination of I_m and K_m satisfying the boundary conditions for $\rho<\rho'$, and $\psi_2(k_{eff}\rho)$ is a linearly independent combination of I_m and K_m satisfying the boundary conditions for $\rho>\rho'$; then the symmetry of the Green's function in ρ and ρ' requires that

$$g_m(k,\rho,\rho')=\psi_1(k_{eff}\rho_<)\psi_2(k_{eff}\rho_>), \tag{A.2}$$

where $\rho_<$ and $\rho_>$ indicate the smaller and larger radial coordinates of the source and the detector.

The normalization of the product $\psi_1(k_{eff}\rho_<)\cdot\psi_2(k_{eff}\rho_>)$ requires that $g_m(k,\rho,\rho')$ satisfy the discontinuity in slope implied by the delta function in Eq. (A.1):

$$\left.\frac{dg_m}{d\rho}\right|_+-\left.\frac{dg_m}{d\rho}\right|_-=-\frac{1}{\rho'}, \tag{A.3}$$

where $|_\pm$ means "evaluated at $\rho=\rho'\pm\epsilon$." Then we have

$$\left.\frac{dg_m}{d\rho}\right|_+-\left.\frac{dg_m}{d\rho}\right|_-=k_{eff}(\psi_1\psi_2'-\psi_2\psi_1')=k_{eff}W[\psi_1,\psi_2], \tag{A.4}$$

where $W[\psi_1,\psi_2]$ is the Wronskian of ψ_1 and ψ_2. Equation (A.1) is of the Sturm–Liouville type

$$\frac{d}{dx}\left[p(x)\frac{dy}{dx}\right]+g(x)y=0, \tag{A.5}$$

and it is known that the Wronskian of two linearly independent solutions of such an equation is proportional to $[1/p(x)]$. Hence the possibility of $g_m(k,\rho,\rho')$ satisfying Eq. (A.3) for all values of ρ' is assured, so it requires that the Wronskian has the value

$$W[\psi_1(x),\psi_2(x)]=-\frac{1}{x}, \tag{A.6}$$

which normalizes $\psi_1(k_{eff}\rho_<)\cdot\psi_2(k_{eff}\rho_>)$. If there is no boundary surface, $g_m(k,\rho,\rho')$ must be finite at $\rho=0$ and vanish at $\rho\to\infty$. Consequently we can define

$$\psi_1(k_{eff}\rho_<)=\Omega I_m(k_{eff}\rho_<)\quad\text{and}\quad\psi_2(k_{eff}\rho_>)=k_m(k_{eff}\rho_>), \tag{A.7}$$

where the constant Ω is to be determined from the normalization requirement of Eq. (A.6). Substituting Eq. (A.7) into Eq. (A.6) by changing the argument $k_{eff}\rho\to x$ we have

$$\Omega\cdot W[I_m(x),K_m(x)]=-\frac{1}{x}, \tag{A.8}$$

which can be evaluated at any value of x. Based on the asymptotic expressions for the modified Bessel functions [14], we have for either small x or large x

$$W[I_m(x),K_m(x)]=-\frac{1}{x}, \tag{A.9}$$

which leads to $\Omega=1$ in Eq. (A.8); thereby Eq. (A.2) changes to

$$g_m(k,\rho,\rho')=I_m(k_{eff}\rho_<)K_m(k_{eff}\rho_>). \tag{A.10}$$

Substituting Eq. (A.10) into Eq. (2.1.7) gives the Green's function of Eq. (2.1.3) in cylindrical coordinates as

$$G(\vec{r},\vec{r}') = \frac{1}{2\pi^2}\sum_{m=-\infty}^{\infty}\int_0^{\infty} dk e^{im(\varphi-\varphi')} \times [I_m(k_{eff}\rho_<)K_m(k_{eff}\rho_>)]\cdot\cos[k(z-z')]. \quad (A.11)$$

Writing in terms of the real function:

$$G(\vec{r},\vec{r}') = \frac{1}{2\pi^2}\int_0^{\infty} dk\cdot\left\{\sum_{m=0}^{\infty}\epsilon_m I_m(k_{eff}\rho_<)K_m(k_{eff}\rho_>) \times\cos[m(\varphi-\varphi')]\right\}\cdot\cos[k(z-z')], \quad (A.12)$$

where $$\epsilon_m = \begin{cases} 2, & m \neq 0 \\ 1, & m = 0 \end{cases}. \quad (A.13)$$

ACKNOWLEDGMENTS

This work has been supported in part by a research grant HR06-171 from the Oklahoma Center for the Advancement of Science and Technology (OCAST), a Big-XII faculty fellowship awarded to Daqing Piao, and the Prostate Cancer Research Program of the Department of Defense through grant #W81XWH-07-1-0247. We also thank Prof. Gang Yao in the University of Missouri, Columbia, for insightful comments.

REFERENCES

1. A. Ishimaru, "Diffusion of light in turbid material," Appl. Opt. **28**, 2210–2215 (1989).
2. S. Fantini, M. A. Franceschini, and E. Gratton, "Semi-infinite-geometry boundary problem for light migration in highly scattering media: a frequency-domain study in the diffusion approximation," J. Opt. Soc. Am. B **11**, 2128–2138 (1994).
3. S. Srinivasan, B. W. Pogue, C. Carpenter, S. Jiang, W. A. Wells, S. P. Poplack, P. A. Kaufman, and K. D. Paulsen, "Developments in quantitative oxygen-saturation imaging of breast tissue in vivo using multispectral near-infrared tomography," Antioxid. Redox. Signal. **9**, 1143–1156 (2007) (review).
4. S. R. Arridge, M. Cope, and D. T. Delpy, "The theoretical basis for the determination of optical pathlengths in tissue: temporal and frequency analysis," Phys. Med. Biol. **37**, 1531–1560 (1992).
5. R. C. Haskell, L. O. Svaasand, T. Tsay, T. Feng, M. S. McAdams, and B. J. Tromberg, "Boundary conditions for the diffusion equation in radiative transfer," J. Opt. Soc. Am. A **11**, 2727–2741 (1994).
6. D. Contini, F. Martelli, and G. Zaccanti, "Photon migration through a turbid slab described by a model based on diffusion approximation. I. Theory," Appl. Opt. **36**, 4587–4599 (1997).
7. B. W. Pogue and M. S. Patterson, "Frequency-domain optical absorption spectroscopy of finite tissue volumes using diffusion theory," Phys. Med. Biol. **39**, 1157–1180 (1994).
8. A. Sassaroli, F. Martelli, G. Zaccanti, and Y. Yamada, "Performance of fitting procedures in curved geometry for retrieval of the optical properties of tissue from time-resolved measurements," Appl. Opt. **40**, 185–197 (2001).
9. D. Piao, H. Xie, W. Zhang, J. S. Kransinski, G. Zhang, H. Dehghani, and B. W. Pogue, "Endoscopic, rapid near-infrared optical tomography," Opt. Lett. **31**, 2876–2878 (2006).
10. D. Piao, Z. Jiang, K. E. Bartels, G. R. Holyoak, J. W. Ritchey, G. Xu, C. F. Bunting, and G. Slobodov, "In vivo trans-rectal ultrasound-coupled near-infrared optical tomography of intact normal canine prostate," J. Innovative Opt. Health Sciences **2**, 215–225 (2009).
11. C. Li, R. Liengsawangwong, H. Choi, and R. Cheung, "Using a priori structural information from magnetic resonance imaging to investigate the feasibility of prostate diffuse optical tomography and spectroscopy: a simulation study," Med. Phys. **34**, 266–274 (2007).
12. J. Boutet, L. Herve, M. Debourdeau, L. Guyon, P. Peltie, J.-M. Dinten, L. Saroul, F. Duboeuf, and D. Vray, "Bimodal ultrasound and fluorescence approach for prostate cancer diagnosis," J. Biomed. Opt. **14**, 064001 (2009).
13. J. D. Jackson, "Expansion of Green functions in cylindrical coordinates," in *Classical Electrodynamics*, 3rd ed. (Wiley, 1998), pp. 125–126.
14. G. B. Arfken and H. J. Weber, *Mathematical Methods for Physicists*, 6th ed. (Harcourt, 2005).
15. L. V. Wang and H. Wu, *Biomedical Optics, Principles and Imaging* (Wiley, 2007).
16. K. S. Fine and C. F. Driscoll, "The finite length diocotron mode," Phys. Plasmas **5**, 601–607 (1998).
17. V. Ntziachristos, "Concurrent diffuse optical tomography, spectroscopy and magnetic resonance imaging of breast cancer," Ph.D. dissertation (University of Pennsylvania, Philadelphia, Pennsylvania, 2000).
18. S. T. Cui, "Electrostatic potential in cylindrical dielectric media using the image charge method," Mol. Phys. **104**, 2993–3001 (2006).
19. IEEE 754-2008 Standard for Floating-Point Arithmetic (IEEE, 2008).
20. C. Moler, "Floating points: IEEE standard unifies arithmetic model," Cleve's Corner, The MathWorks, Inc., 1996.

Photon diffusion in a homogeneous medium bounded externally or internally by an infinitely long circular cylindrical applicator. II. Quantitative examinations of the steady-state theory

Anqi Zhang,[1] Guan Xu,[1] Chathuri Daluwatte,[2] Gang Yao,[2] Charles F. Bunting,[1] Brian W. Pogue,[3] and Daqing Piao[1,*]

[1]*School of Electrical and Computer Engineering, Oklahoma State University, Stillwater, Oklahoma 74078-5032, USA*
[2]*Department of Biological Engineering, University of Missouri, Columbia, Missouri 65211, USA*
[3]*Thayer School of Engineering, Dartmouth College, Hanover, New Hampshire 03755-8000, USA*
**Corresponding author: daqing.piao@okstate.edu*

Received August 31, 2010; revised October 27, 2010; accepted October 29, 2010; posted November 3, 2010 (Doc. ID 134287); published January 5, 2011

This is Part II of the work that examines photon diffusion in a homogenous medium *enclosed by* a concave circular cylindrical applicator or *enclosing* a convex circular cylindrical applicator. Part I of this work [J. Opt. Soc. Am. A **27**, 648 (2010)] analytically examined the steady-state photon diffusion between a source and a detector for two specific cases: (1) the detector is placed only azimuthally with respect to the source, and (2) the detector is placed only longitudinally with respect to the source, in the infinitely long concave and convex applicator geometries. For the first case, it was predicted that the decay rate of photon fluence would become smaller in the concave geometry and greater in the convex geometry than that in the semi-infinite geometry for the same source–detector distance. For the second case, it was projected that the decay rate of photon fluence would be greater in the concave geometry and smaller in the convex geometry than that in the semi-infinite geometry for the same source–detector distance. This Part II of the work quantitatively examines these predictions from Part I through several approaches, including (a) the finite-element method, (b) the Monte Carlo simulation, and (c) experimental measurement. Despite that the quantitative examinations have to be conducted for finite cylinder applicators with large length-to-radius ratio to approximate the infinite-length condition modeled in Part I, the results obtained by these quantitative methods for two concave and three convex applicator dimensions validated the qualitative trend predicted by Part I and verified the quantitative accuracy of the analytic treatment of Part I in the diffusion regime of the measurement, at a given set of absorption and reduced scattering coefficients of the medium.

OCIS codes: 170.3660, 170.5280, 170.6960.

1. INTRODUCTION

This is a continuation of the work that examines the photon diffusion in a homogenous medium that is either *enclosed by* or *enclosing* an infinitely long circular cylindrical applicator. The geometry of imaging a medium enclosed by an infinitely long circular cylindrical applicator resembles approximately that of imaging externally accessible tissue, such as breast or arm, using a ring-shaped applicator and is referred to as a concave geometry in this work. The geometry of imaging a medium enclosing a circular cylindrical applicator resembles closely that of imaging internally accessible tissue, such as prostate or rectum, using an endorectal applicator, and is referred to as a convex geometry in this work. In Part I [1] of this work, the solutions to the steady-state photon diffusion associated with concave and convex geometries were derived by employing the extrapolated boundary condition [2,3] and expressed in closed forms using the modified Bessel functions. The validity of the approach in [1], which has to our knowledge for the first time unified the analytic treatments of photon diffusion in both concave and convex geometries, was examined qualitatively for the case wherein the radial dimension of the tissue–applicator interface would reach infinity. As is expected, the decay rate of photon fluence for the case of applicator radius approaching infinity was found to asymptotically reach that for a planar interface case or the semi-infinite geometry. The analytic approach was then applied to the concave and convex geometries with the radial dimensions of the tissue–applicator interfaces comparable to those found in practical applications. For these practical geometries, the work in [1] further examined two specific configurations: (1) the source and the detector have the same longitudinal coordinate and are placed along the azimuth direction on the boundary, and (2) the source and the detector have the same azimuth angle and are placed along the longitudinal direction on the boundary. For case (1), which is called "*case-azi*" in this work, it was predicted that the decay rate of photon fluence would become smaller in the concave geometry and greater in the convex geometry than that in a semi-infinite geometry for the same source–detector distance. For case (2), which is called "*case-longi*" in this work, it was projected that the decay rate of photon fluence would be greater in the concave geometry and smaller in the convex geometry than that in a semi-infinite geometry for the same source–detector distance.

This Part II of the work examines the predictions given in Part I for steady-state photon diffusion in the *case-azi* and

case-longi configurations within the concave and convex geometries by the following quantitative methods: (a) the finite-element method (FEM), (b) the Monte Carlo (MC) simulation, and (c) experimental measurement. The predictions for *case-azi* and *case-longi* configurations in Part I, which were based upon solving the equation of photon diffusion analytically in the studied geometries, is to be first examined by solving the same equation of photon diffusion numerically in the same geometries using the widely validated FEM solver. It is expected that the FEM-based results will support the analytic solution that has been proposed, but as both the FEM and analytical solutions are based upon the model of photon diffusion, the expected model-data match between these two does not necessarily substantiate the validity of the analytic approach. The ultimate verification of any analytic approach of photon propagation requires examining it against experimental measurement or the gold standard numerical method of MC. Among the three quantitative methods of the FEM, the MC, and experimental measurement employed in this work, the experimental examination apparently has the least flexibility in the study design; therefore, it becomes rational to conduct the FEM and MC examinations by employing as many available parameters as possible for the experimental measurements. It is noted that the infinitely long cylindrical applicator modeled in Part I cannot be reproduced in any of the three methods of the FEM, the MC, and experimental examination, but it can be approximated by one cylindrical applicator whose longitudinal dimension is much greater than its radial dimension, e.g., with a large length-to-radius ratio.

The rest of this Part II work is structured into the following sections. Section 2 reprints the analytic results derived in Part I that are relevant to the predictions for *case-azi* and *case-longi* configurations. Section 3 details the configurations of the FEM, MC, and the experimental examinations. Section 4 evaluates the effect of the measurement errors associated with the positioning of the source and detector due to the limitations of the experimental study, and discusses the rationale of minimizing the error-induced data-model deviation when the experimental measurements are grouped with the FEM and the MC for examining the analytic predictions. Section 5 examines the analytic predictions of *case-azi* and *case-longi* configurations in two concave and three convex applicator dimensions against the FEM, MC, and experimental results, for a given set of medium optical properties.

2. RELEVANT ANALYTIC RESULTS DERIVED IN PART I

The following notations have been used in [1]: $\vec{r}_0 = (R_0, \varphi', z')$ is the position of the source, $\vec{r} = (R_0, \varphi, z)$ is the position of the field or the detector, S is the intensity of the source, Ψ is the photon fluence rate at the field/detector position, μ_a is the absorption coefficient, μ_s' is the reduced or transport scattering coefficient, $D = [3(\mu_a + \mu_s')]^{-1}$ is the diffusion coefficient, $R_a = 1/\mu_s'$ is the mean path length for the photon to lose its history of incident direction and is used for modeling the directional source as an isotropic source placed into the medium, $R_b = 2AD$ is the distance from the extrapolated boundary to the physical boundary wherein A is a parameter determined by the refractive index mismatch across the tissue–applicator interface.

The steady-state photon fluence rate Ψ associated with a concave geometry of radius R_0 is

$$\Psi = \frac{S}{2\pi^2 D}\int_0^\infty \mathrm{d}k \Bigg\{ \cos[k(z-z')] \times \sum_{m=0}^{\infty} \varepsilon_m I_m[k_{\mathrm{eff}}(R_0 - R_a)] K_m(k_{\mathrm{eff}} R_0) \cdot \left\langle 1 - \frac{I_m(k_{\mathrm{eff}}R_0)}{K_m(k_{\mathrm{eff}}R_0)} \frac{K_m[k_{\mathrm{eff}}(R_0+R_b)]}{I_m[k_{\mathrm{eff}}(R_0+R_b)]} \right\rangle \times \cos[m(\varphi-\varphi')] \Bigg\}, \tag{2.1conC}$$

where I_m and K_m are the modified Bessel functions of the first and second kind at order m, respectively. Similarly, the steady-state photon fluence rate Ψ associated with a convex geometry of radius R_0 is

$$\Psi = \frac{S}{2\pi^2 D}\int_0^\infty \mathrm{d}k \Bigg\{ \cos[k(z-z')] \sum_{m=0}^{\infty} \varepsilon_m I_m(k_{\mathrm{eff}} R_0) \times K_m[k_{\mathrm{eff}}(R_0 + R_a)] \cdot \left\langle 1 - \frac{K_m(k_{\mathrm{eff}}R_0)}{I_m(k_{\mathrm{eff}}R_0)} \frac{I_m[k_{\mathrm{eff}}(R_0-R_b)]}{K_m[k_{\mathrm{eff}}(R_0-R_b)]} \right\rangle \times \cos[m(\varphi-\varphi')] \Bigg\}. \tag{2.1conV}$$

For equations in (2.1), if the source and the detector locate at the same azimuth plane, e.g., in *case-azi* configuration, we have

$$\Psi = \frac{S}{2\pi^2 D}\int_0^\infty \mathrm{d}k \Bigg\{ \sum_{m=0}^{\infty} \varepsilon_m I_m[k_{\mathrm{eff}}(R_0 - R_a)] K_m(k_{\mathrm{eff}} R_0) \left\langle 1 - \frac{I_m(k_{\mathrm{eff}}R_0)}{K_m(k_{\mathrm{eff}}R_0)} \frac{K_m[k_{\mathrm{eff}}(R_0+R_b)]}{I_m[k_{\mathrm{eff}}(R_0+R_b)]} \right\rangle \cos[m(\varphi-\varphi')] \Bigg\}, \tag{2.2conC}$$

$$\Psi = \frac{S}{2\pi^2 D}\int_0^\infty \mathrm{d}k \Bigg\{ \sum_{m=0}^{\infty} \varepsilon_m I_m(k_{\mathrm{eff}} R_0) K_m[k_{\mathrm{eff}}(R_0 + R_a)] \left\langle 1 - \frac{K_m(k_{\mathrm{eff}}R_0)}{I_m(k_{\mathrm{eff}}R_0)} \frac{I_m[k_{\mathrm{eff}}(R_0-R_b)]}{K_m[k_{\mathrm{eff}}(R_0-R_b)]} \right\rangle \cos[m(\varphi-\varphi')] \Bigg\}, \tag{2.2conV}$$

and if the source and the detector locate longitudinally with the same azimuth angle, e.g., in *case-longi* configuration, we have

$$\Psi = \frac{S}{2\pi^2 D}\int_0^\infty \mathrm{d}k \Bigg\{ \cos[k(z-z')] \sum_{m=0}^{\infty} \varepsilon_m I_m[k_{\mathrm{eff}}(R_0 - R_a)] K_m(k_{\mathrm{eff}} R_0) \left\langle 1 - \frac{I_m(k_{\mathrm{eff}}R_0)}{K_m(k_{\mathrm{eff}}R_0)} \frac{K_m[k_{\mathrm{eff}}(R_0+R_b)]}{I_m[k_{\mathrm{eff}}(R_0+R_b)]} \right\rangle \Bigg\}, \tag{2.3conC}$$

$$\Psi = \frac{S}{2\pi^2 D}\int_0^\infty \mathrm{d}k\left\{\cos[k(z-z')]\sum_{m=0}^{\infty}\varepsilon_m I_m(k_{\mathrm{eff}}R_0)K_m[k_{\mathrm{eff}}(R_0 + R_a)]\left\langle 1 - \frac{K_m(k_{\mathrm{eff}}R_0)}{I_m(k_{\mathrm{eff}}R_0)}\frac{I_m[k_{\mathrm{eff}}(R_0-R_b)]}{K_m[k_{\mathrm{eff}}(R_0-R_b)]}\right\rangle\right\}. \quad (2.3\mathrm{conV})$$

3. CONFIGURATIONS OF THE QUANTITATIVE EXAMINATIONS

A. Configuration of the FEM Solver to the Equation of Photon Diffusion

The FEM-based computation [4,5] of photon diffusion is based on our work [6] of solving the equation of steady-state photon diffusion under a Robin-type boundary condition using NIRFAST [7]. It is noted that the source term in the FEM is often defined as a distributed, Gaussian source, matching the intensity profile at the tip of the optical fiber, and the source may therefore be defined over more than one element [7]. The source term in the FEM is thus different from the basis of Green's function in analytic treatment. This difference is expected to cause a mismatch between the FEM and analytical results as the source–detector distance becomes comparable to the spatial dimension of the Gaussian source even though both methods are based on the same model of photon propagation. The finite-element meshes for the *case-azi* and *case-longi* configurations of the concave geometry are shown in Figs. 1(a) and 1(b), respectively. Two sets of the concave geometry are considered: one has a radius of 0.95 cm and a length of 40 cm, and the other has a radius of 2.53 cm and a length of 40 cm. The radii of the two concave-geometry sets are chosen the same as those used in the experiments, but the length-to-radius ratios of the two geometry sets are 2.62 times those used in the experimental study. The larger length-to-radius ratio is necessary for bridging between the model prediction based on an infinitely long concave geometry and the experimental data obtained from a long yet finite concave applicator. For the *case-azi* geometry, denser meshes are placed along the midazimuth plane on the boundary for evaluating the solution along the azimuth direction. Similarly, for the *case-longi* geometry, denser meshes are placed along the longitudinal direction on the boundary for evaluating the solution along the longitudinal direction. The domain of FEM modeling with a radius of 2.53 cm is discretized into a mesh of 22,182 tetrahedral elements and 4988 nodes. The domain of FEM modeling with a radius of 0.95 cm is discretized into mesh of the same density as that in the radius of 2.53 cm. For the convex geometry, the FEM volumes used for both *case-azi* and *case-longi* configurations are illustrated in Fig. 1(c). Three sets of the convex geometry are considered: all have a longitudinal dimension of 40 cm and an outer radius of 15 cm, and the inner radii are 1.27 cm, 2.41 cm, and 5.07 cm. The radii of the three convex geometry sets are chosen the same as those found in the experiments, but the length-to-radius ratios of the three geometry sets are also 2.62 times those employed in the experimental study as that in the concave geometry. The discretized domain of the convex geometry is illustrated in Fig. 1(d), which shows only the *case-azi* configuration and does not visualize the meshes at the outer surfaces for the purpose of clarification. The domain of FEM modeling with an inner radius of 1.27 cm is discretized into a mesh of 90,856 tetrahedral elements and 17,545 nodes. The domains of FEM modeling with inner radii of 2.31 cm and 5.07 cm are discretized into meshes of the same density as that in the radius of 1.27 cm. The value of A is experimentally determined (detailed in Subsection 3.D) as being 1.86 for the interface between the tissue/medium and the applicator.

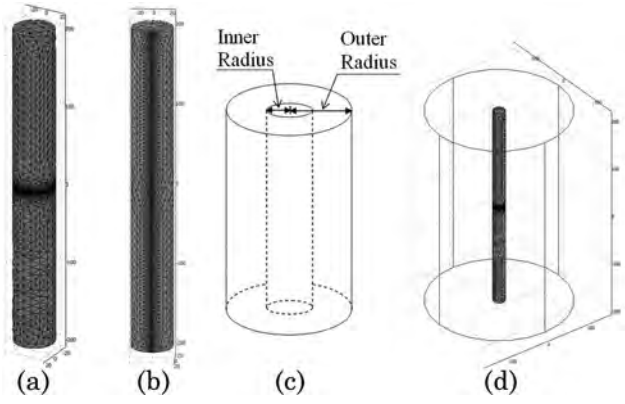

Fig. 1. Three-dimensional rendering of the finite-element mesh of the cylindrical applicator: (a) concave geometry for the *case-azi* configuration shown with denser mesh along the azimuth direction at the outer surface of the cylinder domain, (b) concave geometry for the *case-longi* configuration shown with denser mesh along the longitudinal direction at the outer surface of the cylinder domain, (c) convex geometry for both *case-azi* and *case-longi* configurations, (d) discretization of the convex imaging volume for the *case-azi* configuration shown with denser mesh along the azimuth direction at the inner surface of the cylinder domain.

B. Configuration of the Monte Carlo Simulation

The MC model was adapted from a program previously developed for simulating photon migration in cylindrical blood vessels [8]. The concave and convex geometries for MC simulation are illustrated in Fig. 2, with Figs. 2(a) and 2(c) for the *case-azi* configurations, and Figs. 2(b) and 2(d) for the *case-longi* configurations. For both *case-azi* and *case-longi* configurations, two sets of the concave applicator dimensions are considered: one has a radius of 0.95 cm and a length of 40 cm, and the other has a radius of 2.53 cm and a length of 40 cm; three sets of the convex applicator dimensions are considered: all have a longitudinal dimension of 40 cm and an outer radius of 15 cm, and the inner radii are 1.27 cm, 2.41 cm and 5.07 cm. The dimensions of these geometries are identical to those used for FEM evaluations. A single-point "pencil beam" source and a set of isotropic detectors (1 mm in diameter) were positioned at the tissue–applicator interface, as shown in Fig. 2, based on the *case-azi* or *case-longi* configuration.

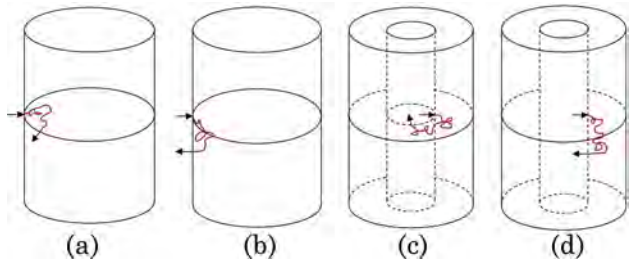

Fig. 2. (Color online) Geometry of the MC simulation: (a) concave geometry for *case-azi* configuration, (b) concave geometry for *case-longi* configuration, (c) convex geometry for *case-azi* configuration, (d) convex geometry for *case-longi* configuration..

The experimentally determined value of $A = 1.86$ on the tissue–applicator interface is implemented in the MC as a 30% probability of photon re-entering the modeled tissue domain after reaching the applicator boundary. The number of incident photons ranged from 5×10^7 for convex geometry with a small radius to 2×10^8 for the concave geometry. All recordings had a smaller than 10% error (the ratio of the standard deviation to the mean).

C. Configuration of the Experimental Study

1. Dimensions of the Applicators in Concave and Convex Geometries

Five pieces of cylindrical applicators, shown schematically in Fig. 3(a) and photographed in Fig. 3(b), were fabricated from presorted 6 in. long (15.24 cm in length, compared to the 40 cm long imaging domain used for the FEM and the MC simulation) raw black acetal materials. These cylindrical pieces could be used for both concave and convex imaging geometries; however, due to the difficulty of fabricating both the external and internal surfaces of the same cylindrical applicator under identical machining processes to make the boundary conditions consistent, each piece was used for either the concave or convex imaging geometry, but not for both. Two applicator pieces with inner radii of 0.95 cm and 2.53 cm were used as the concave imaging geometry whereat the measurement was made along the inner surface [the dashed line on the two pieces at the lower row of Fig. 3(a)] enclosing the tissue medium, and three applicator pieces with outer radii of 1.27 cm, 2.41 cm, and 5.07 cm were used as the convex imaging geometry whereat the measurement was made along the outer surface [the solid line on the three pieces at the upper row of Fig. 3(a)] enclosed by the tissue medium. Therefore, for each group of *case-azi* or *case-longi* measurements, the results contained two sets from the concave geometries with different radii and three sets from the convex geometries with different radii.

2. Configuration of the Measurement Assembly Using the Cylindrical Applicator

The analytic treatments in [1] utilized a well-known important approach of modeling a directional illumination (from a fiber) as an isotropic source placed into the medium at a distance of $1/\mu_s'$ from the directional incident point. The FEM solver adopted this approach of modeling a fiber illumination by simply placing an equivalent isotropic source at the $1/\mu_s'$ distance into the medium. In the MC simulation, since the incident photon is strictly forward launched (pencil beam), the condition of an equivalent isotropic source at the $1/\mu_s'$ distance is also satisfied. In the experimental study, placing the facet of an illumination fiber evenly on the applicator–tissue interface can mimic the condition of an equivalent isotropic source; however, the accuracy of the setup was limited by the variable practicability among the different applicator pieces employed and would not be as desirable as those in the FEM and MC studies. The examination of the analytic predictions for *case-azi* and *case-longi* configurations also was in need of continuously translating either the source or the detector fiber azimuthally or longitudinally, which further discouraged the experimental implementation that involved inserting a fiber in the wall of the applicator piece unless it was the only feasible choice. It has been argued that the measurement of a diffuse photon is insensitive to the orientation of the detector fiber [9]; nevertheless, using an isotropic detector shall provide measurement of the photon diffusion that is minimally affected by the orientation of the detector fiber. In light of all these restrictions, the experimental design physically placed a fiber with an isotropic diffuser tip as the source in the medium at a distance of $1/\mu_s'$ from the tissue–applicator boundary, instead of inserting a regular fiber through the applicator wall, and used a fiber with isotropic sensing tip as the detector.

A diffuser (Medlight SD200) with a spherical tip of 2 mm in diameter was used as the isotropic source, and an isotropic probe (Medlight IP159) with a spherical tip of 1.59 mm in diameter was used for detection of the diffuse photon. The 785 nm light from a laser diode (Thorlabs, model HL7851G) operating at constant power mode was fiber-coupled to the spherical diffuser. The isotropic detector probe was coupled to a spectrometer (Princeton Instruments, SpectraPro 2300i, not necessary for the measurement but kept for system integrity and convenience of use) for readout of the detected photon intensity by a 16 bit CCD camera (Photometrics Cascade 512F).

The source and the detector fibers were fixed individually in stainless tubes [except for the detection fiber shown in the configuration in Fig. 6(a) only], which were then fixated to the positioning structure. The stainless tube for housing the source fiber had a diameter of 4.76 mm (3/16 in.) and the one for fixing the detector fiber had a diameter of 3.18 mm (1/8 in.). Figure 4 is an exemplary photograph of the complete setup for measurement of the *case-azi* configuration in the convex geometry, wherein the source and detector fibers were placed azimuthally and outside of the cylindrical

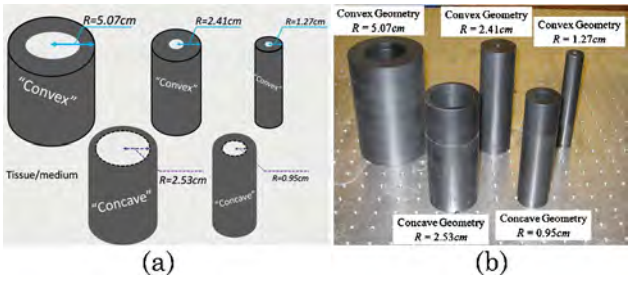

Fig. 3. (Color online) Five cylindrical applicators made from the same black acetal material, shown by the (a) sketch and (b) photograph. The lower front two with radii of 0.95 cm and 2.53 cm were used for the concave geometry, and the upper rear three with radii of 1.27 cm, 2.41 cm, and 5.07 cm were used for the convex geometry..

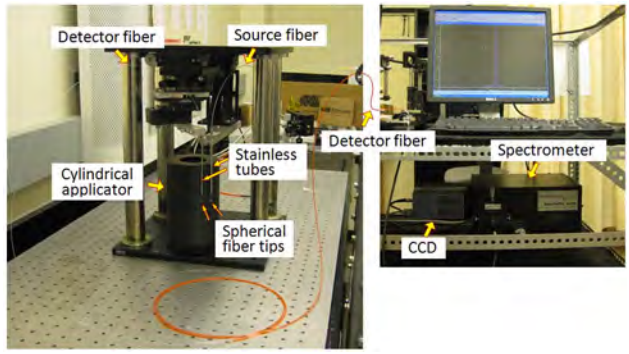

Fig. 4. (Color online) Photographs of the experimental setup for the *case-azi* configuration in the convex geometry. The tank that housed the Intralipid solution for immersing the setup is not shown..

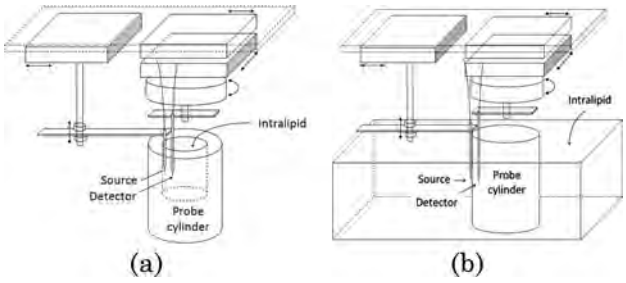

Fig. 5. Illustration of the experimental setup for the *case-azi* configurations: (a) concave geometry with the source and the detector placed azimuthally in proximity to the inner surface of the cylinder applicator, (b) convex geometry with the source and the detector placed azimuthally in proximity to the outer surface of the cylinder applicator.

applicator at the same longitudinal coordinate. The entire positioning assembly as shown on the breadboard was then immersed in a large tank filled with bulk Intralipid solution as the homogenous medium.

3. Control of the Source–Detector Distance for Measurement in the Case-Azi Configuration

For the *case-azi* configuration in concave geometry as shown in Fig. 5(a), the isotropic detector was fixed at the inner surface of the cylindrical applicator, and the isotropic source was placed at a distance of $1/\mu_s'$ inward from the inner surface. The isotropic source rotated isoazimuthally with respect to the isotropic detector and the center of the applicator curvature. The Intralipid solution filled the inside of the cylindrical applicator. For the *case-azi* configuration in convex geometry as shown in Fig. 5(b), both the isotropic source and detector were placed at the outer surface of the cylinder applicator, with the source placed at a distance of $1/\mu_s'$ outward from the outer surface. The isotropic source rotated isoazimuthally with respect to the isotropic detector and the center of the applicator curvature. The Intralipid solution filled up the tank that housed the cylinder applicator. The azimuth plane that contains the source and the detector was halfway along the longitudinal working range of the cylinder applicator to minimize the effect of the finite length of the applicator. The chord distance d between the positions of the modeled directional source and the detector on the applicator surface was calculated by $d = 2R\sin(\theta/2)$, where the angle θ between the azimuth coordinates of the source and the detector was directly read out from the rotational stage controlling the source position.

4. Control of the Source–Detector Distance for Measurement in the Case-Longi Configuration

For the *case-longi* configuration in concave geometry, as shown in Fig. 6(a), the isotropic detector fiber without the stainless tube passed through the wall of the cylindrical applicator and was fixed at the inner surface of the applicator. The isotropic source was placed at a distance of $1/\mu_s'$ inward from the inner surface of the applicator and translated longitudinally. The Intralipid solution filled the inside of the cylindrical applicator. For the *case-longi* configuration in convex geometry, as shown in Fig. 6(b), the cylindrical applicator was placed horizontally. The isotropic detector housed by the stainless tube was placed on the outer surface of the applicator. The isotropic source was placed at a distance of $1/\mu_s'$ outward from the outer surface and translated longitudinally with

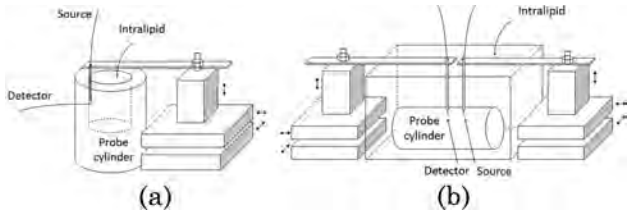

Fig. 6. Illustration of the experimental setup for the *case-longi* configurations: (a) concave geometry with the detector penetrating the cylinder wall and the source placed longitudinally in proximity to the inner surface of the cylinder applicator, (b) convex geometry with the source and the detector placed longitudinally in proximity to the outer surface of the cylinder applicator.

respect to the isotropic detector. The Intralipid solution filled the tank that housed the cylindrical applicator and most parts of the fiber-holding stainless tubes.

In the experimental study, all measurements were based on a bulk Intralipid solution of 0.5% concentration. This concentration of Intralipid solution gave $\mu_s' = 5\,\mathrm{cm}^{-1}$ at 785 nm [10], with which $1/\mu_s' = 2\,\mathrm{mm}$, so there was sufficient space to place the 1 mm radius spherical diffuser source away from the applicator surface, and the scattering-dominant condition was also satisfied as $\mu_a = 0.025\,\mathrm{cm}^{-1}$ [11]. Using a single concentration of the Intralipid solution undoubtedly limited the experimental examinations to a single set of μ_a and μ_s' of the medium properties; however, if the analytical treatment had been incorrect, none of the predictions made could have matched with the experimental results.

D. Experimental Determination of the *A* Value

In the experimental examinations, all of the parameters appearing in Eqs. (2.2conC), (2.2conV), (2.3conC), and (2.3conV) were known, except for the A value appearing in $R_b = 2AD$. A is determined by the refractive index mismatch between an applicator material and the diffuse medium, usually based on the assumption of a tissue–air interface, even though that does not accurately represent the tissue–applicator interface. In this study, the A value must be experimentally determined in order to assure the accuracy of model-data examination.

The determination of the A value involved two steps. In the first step, the same set of isotropic diffuser source and detector as that used for the studies in Subsection 3.C were immerged in the same 0.5% Intralipid solution to form an infinite-medium geometry. The measurement of photon diffusion in this infinite-medium geometry was specified by the well-known formula [1] of

$$\ln(\Psi \cdot d) = -\sqrt{\frac{\mu_a}{D}}d + \ln\left(\frac{S}{4\pi D}\right), \tag{3.1}$$

where d is the source–detector distance. The source term $S/4\pi D$ or the intercept term $\ln(S/4\pi D)$ was found by fitting the experimental data to the linear relationship between $\ln(\Psi \cdot d)$ and d. In the second step, a semi-infinite geometry was constructed using a large plate of black acetal, which was materially the same as that used for the studies in Subsection 3.C. The measurement of photon diffusion in this semi-infinite-medium geometry was specified by the formulas [1,12] of

$$\Psi = \frac{S}{4\pi D l_{\mathrm{real}}} e^{-k_0 l_{\mathrm{real}}} - \frac{S}{4\pi D l_{\mathrm{imag}}} e^{-k_0 l_{\mathrm{imag}}}, \tag{3.2}$$

where

$$l_{\text{real}} = \sqrt{d^2 + R_a^2}, \qquad R_a = 1/\mu_s', \tag{3.3}$$

$$l_{\text{imag}} = \sqrt{d^2 + (2R_b + R_a)^2}, \qquad R_b = 2AD. \tag{3.4}$$

By substituting the value of $S/4\pi D$ obtained from (3.1) into (3.2) and fitting the experimental data Ψ to different A values, the A value was determined as 1.86 after averaging four sets of measurements ($A = 1.897, 1.806, 1.905, 1.814$).

4. ANALYSIS OF THE MEASUREMENT ERROR ASSOCIATED WITH INACCURATE POSITIONING OF THE SOURCE AND DETECTOR

A. Effect of the Radial Positioning Errors of the Source and the Detector

In the analytic solutions, both the source and the detector are assumed as infinitesimally small, whereas the isotropic source and detector used in the experiments had finite sizes, specifically spherical tips with diameters of 2 mm and 1.59 mm, respectively. In all the experimental setups except the one shown in Fig. 6(a), the source and detector fibers were first fixed in stainless tubes, which were then fixed onto the positioning stages. Thus, the detector might not have been located precisely on the surface of the applicator, and the source might not have been positioned precisely $1/\mu_s'$ from the surface of the applicator. To model how much the measurement could be affected due to the positioning error, Eqs. (2.1conC) and (2.1conV) are rewritten to

$$\Psi = \frac{S}{2\pi^2 D}\int_0^\infty \mathrm{d}k \left\{ \cos[k(z-z')] \sum_{m=0}^{\infty} \varepsilon_m I_m(k_{\text{eff}}\rho_{r<}) K_m(k_{\text{eff}}\rho_{r>}) \cdot \left\langle 1 - \frac{I_m(k_{\text{eff}}\rho_{r>})}{K_m(k_{\text{eff}}\rho_{r>})} \frac{K_m[k_{\text{eff}}(R_0+R_b)]}{I_m[k_{\text{eff}}(R_0+R_b)]} \right\rangle \cos[m(\varphi-\varphi')] \right\}, \tag{4.1conC}$$

$$\Psi = \frac{S}{2\pi^2 D}\int_0^\infty \mathrm{d}k \left\{ \cos[k(z-z')] \sum_{m=0}^{\infty} \varepsilon_m I_m(k_{\text{eff}}\rho_{r<}) K_m(k_{\text{eff}}\rho_{r>}) \cdot \left\langle 1 - \frac{K_m(k_{\text{eff}}\rho_{r<})}{I_m(k_{\text{eff}}\rho_{r<})} \frac{I_m[k_{\text{eff}}(R_0-R_b)]}{K_m[k_{\text{eff}}(R_0-R_b)]} \right\rangle \cos[m(\varphi-\varphi')] \right\}, \tag{4.1conV}$$

where $\rho_{r<}$ and $\rho_{r>}$ indicate the smaller and larger radial coordinates of the source and the detector. For the concave geometry, $\rho_{r<} = R_0 - R_a$ and $\rho_{r>} = R_0$; for the convex geometry, $\rho_{r<} = R_0$ and $\rho_{r>} = R_0 + R_a$ [1]. When there is positioning error for the source or the detector in the azimuth plane, the $\rho_{r<}$ and $\rho_{r>}$ for the concave geometry and convex geometry can be expressed, respectively, as

$$\rho_{r<} = R_0 - R_a - \xi|_{\text{source}}, \qquad \rho_{r>} = R_0 - \xi|_{\text{detector}} \tag{4.2conC}$$

$$\rho_{r<} = R_0 + \xi|_{\text{detector}}, \qquad \rho_{r>} = R_0 + R_a + \xi|_{\text{source}} \tag{4.2conV}$$

where $\xi|_{\text{subscript}}$ denotes the shift of the position of the subscript from the intended location in the azimuth plane. The details of $\rho_{r<}$ and $\rho_{r>}$ in the azimuth plane are shown in Figs. 7(a) and 7(b) for concave and convex geometry, respectively. By using the notations $\rho_{r<}$ and $\rho_{r>}$ defined in (4.2), Eqs. (2.2conC) and (2.2conV) for the *case-azi* configuration can be converted to

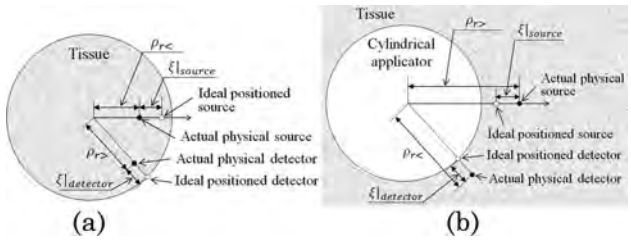

Fig. 7. Details of $\rho_{r<}$ and $\rho_{r>}$ in the azimuth plane: (a) concave geometry, (b) convex geometry.

$$\Psi = \frac{S}{2\pi^2 D}\int_0^\infty \mathrm{d}k \left\{ \sum_{m=0}^{\infty} \varepsilon_m I_m(k_{\text{eff}}\rho_{r<}) K_m(k_{\text{eff}}\rho_{r>}) \left\langle 1 - \frac{I_m(k_{\text{eff}}\rho_{r>})}{K_m(k_{\text{eff}}\rho_{r>})} \frac{K_m[k_{\text{eff}}(R_0+R_b)]}{I_m[k_{\text{eff}}(R_0+R_b)]} \right\rangle \cos[m(\varphi-\varphi')] \right\}, \tag{4.3conC}$$

$$\Psi = \frac{S}{2\pi^2 D}\int_0^\infty \mathrm{d}k \left\{ \sum_{m=0}^{\infty} \varepsilon_m I_m(k_{\text{eff}}\rho_{r<}) K_m(k_{\text{eff}}\rho_{r>}) \left\langle 1 - \frac{K_m(k_{\text{eff}}\rho_{r<})}{I_m(k_{\text{eff}}\rho_{r<})} \frac{I_m[k_{\text{eff}}(R_0-R_b)]}{K_m[k_{\text{eff}}(R_0-R_b)]} \right\rangle \cos[m(\varphi-\varphi')] \right\}, \tag{4.3conV}$$

and Eqs. (2.3conC) and (2.3conV) for the *case-longi* configuration can be converted to

$$\Psi = \frac{S}{2\pi^2 D}\int_0^\infty \mathrm{d}k \left\{ \cos[k(z-z')] \times \sum_{m=0}^{\infty} \varepsilon_m I_m(k_{\text{eff}}\rho_{r<}) K_m(k_{\text{eff}}\rho_{r>}) \left\langle 1 - \frac{I_m(k_{\text{eff}}\rho_{r>})}{K_m(k_{\text{eff}}\rho_{r>})} \frac{K_m[k_{\text{eff}}(R_0+R_b)]}{I_m[k_{\text{eff}}(R_0+R_b)]} \right\rangle \right\}, \tag{4.4conC}$$

$$\Psi = \frac{S}{2\pi^2 D}\int_0^\infty \mathrm{d}k \left\{ \cos[k(z-z')] \times \sum_{m=0}^{\infty} \varepsilon_m I_m(k_{\text{eff}}\rho_{r<}) K_m(k_{\text{eff}}\rho_{r>}) \left\langle 1 - \frac{K_m(k_{\text{eff}}\rho_{r<})}{I_m(k_{\text{eff}}\rho_{r<})} \frac{I_m[k_{\text{eff}}(R_0-R_b)]}{K_m[k_{\text{eff}}(R_0-R_b)]} \right\rangle \right\}. \tag{4.4conV}$$

Equations (4.3conC), (4.3conV), (4.4conC), and (4.4conV) were numerically implemented, by letting $\xi|_{\text{det ector}}$ change from 0 to 1 mm and $\xi|_{source}$ change from –0.5 mm to 0.5 mm, to assess the effect of the positioning errors of the source and the detector in the azimuth plane within 1 mm, based on the set of parameters, including $\mu_a = 0.025\ \text{cm}^{-1}$, $\mu_s' = 5\ \text{cm}^{-1}$, $A = 1.86$, and $S = 1$. The concave geometry dimensions being evaluated had the radii of 0.95 cm and 2.53 cm, and the convex geometry dimensions being evaluated had the radii of 1.27 cm, 2.41 cm and 5.07 cm, as those studies in Section 3. The results for the *case-azi* configuration are shown in Fig. 8. Figure 8(a) presents the results for the source fixed but the detector shifted

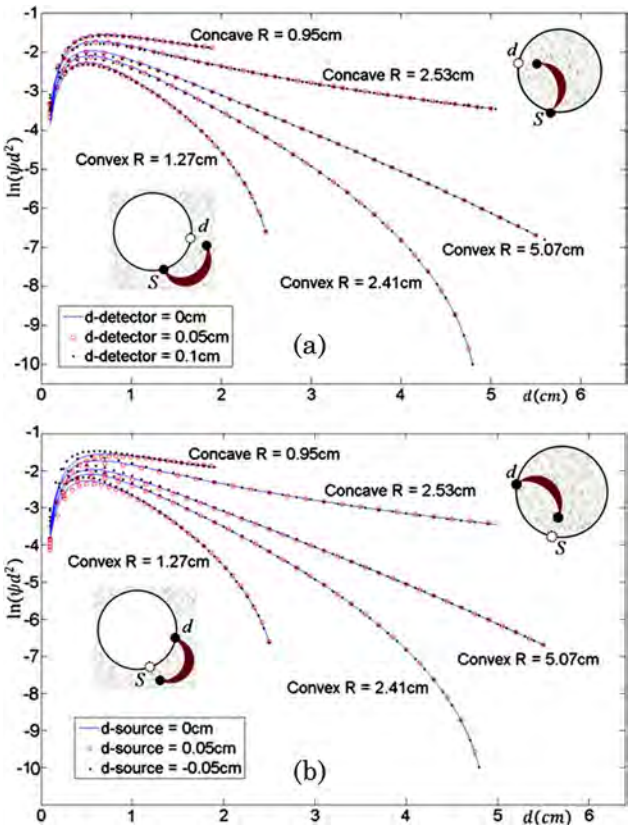

Fig. 8. (Color online) Effect of positioning error of the source or the detector in *case-azi* configurations: (a) source is fixed, but the detector is shifted radially by 0 mm, 0.5 mm and 1 mm, (b) detector is fixed, but the source is shifted radially by −0.5 mm, 0 mm, and 0.5 mm. Conditions for (a) and (b) are not identical due to the requirement of an isotropic source placed $1/\mu_s'$ distance into the medium, whereas the detector is ideally located on the surface..

radially on the same azimuth plane by 0 mm, 0.5 mm, and 1 mm. Figure 8(b) presents the results for the detector fixed but the source shifted radially on the same azimuth plane by −0.5 mm, 0 mm, and 0.5 mm. For the evaluations in Fig. 8, the longitudinal positioning of the source and the detector has been assumed accurate. It is indicated from Figs. 8(a) and 8(b) that, for source–detector distances greater than approximately five times the transport mean free path length ($\geq 5/\mu_s' = 1$ cm in this case), the 1 mm radial positioning error of the source and the detector in the azimuth plane would have negligible effect upon the measurement of photon fluence. The results for the *case-longi* configuration are shown in Fig. 9. Figure 9(a) is for the source fixed but the detector shifted radially on the same azimuth plane by 0 mm, 0.5 mm, and 1 mm. Figure 9(b) is for the detector fixed but the source shifted radially on the same azimuth plane by −0.5 mm, 0 mm, and 0.5 mm. For the evaluations in Fig. 9, the longitudinal positioning of the source and the detector has been assumed accurate. Figures 9(a) and 9(b) again indicate that the 1 mm radial positioning error of the source and the detector has negligible effect to the measurements of photon fluence when the source-detector distance is greater than approximately five transport mean free path lengths ($\geq 5/\mu_s'$). Based on Figs. 8 and 9, it was expected that the experimental measurement in the diffusion regime of the given setup should be insensitive to small inaccuracy of the radial positions of the source and the detector.

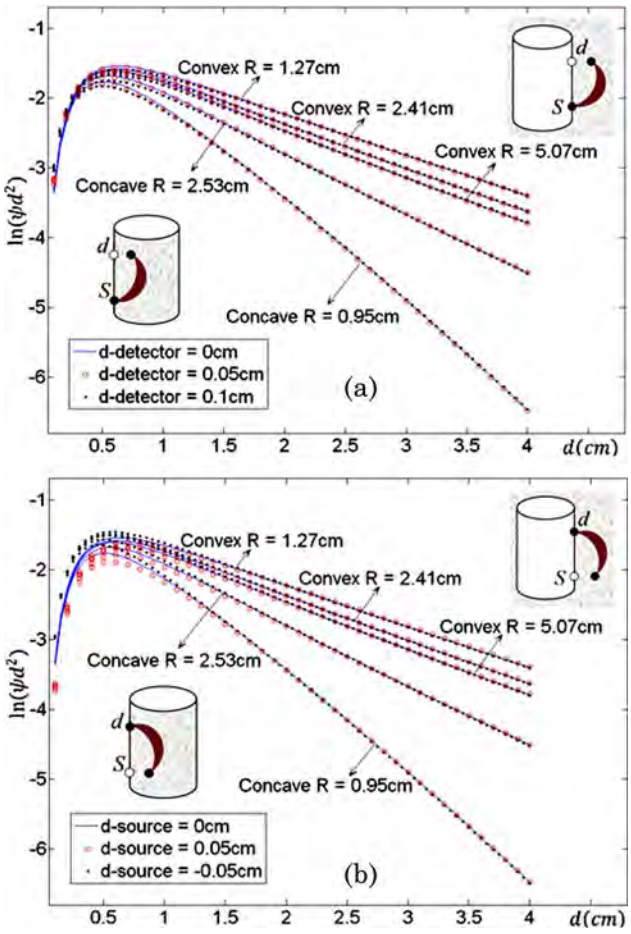

Fig. 9. (Color online) Effect of positioning error of the source or the detector in *case-longi* configurations: (a) source is fixed, but the detector is shifted radially by 0 mm, 0.5 mm, and 1 mm, (b) detector is fixed, but the source is shifted radially by −0.5 mm, 0 mm, and 0.5 mm. Conditions for (a) and (b) are not identical due to the requirement of an isotropic source placed $1/\mu_s'$ distance into the medium, whereas the detector is ideally located on the surface..

B. Effect of the Initial Error of the Source–Detector Distance

In the analytical evaluation, the source–detector distance is precisely determined. In the experimental measurement, either the source or the detector was fixed, and the other was translated continuously starting from an initial value of source–detector distance that was subjected to an error. .The effect due to the error of this initial measurement of source–detector distance is investigated in Figs. 10(a) and 10(b). The evaluations are similar to those in Figs. 8 and 9, with the changes being made from varying the radial position of the source or the detector to instead increasing or decreasing the initial source–detector distances, respectively, by 0.5 mm, 1 mm, and 2 mm.

The curves shown in Figs. 10(a) and 10(b) have been shifted vertically with respect to the one with the defined initial distance to give more direct comparisons. It is indicated from Fig. 10 that, for both the *case-azi* and *case-longi* configurations, the effect of the error of the initial source–detector distance resembles changing the radius of the cylindrical applicator as demonstrated in Fig. 8 for the *case-azi* and Fig. 11 for the *case-longi* configurations in Part I of this work [1]. This agrees with the expectation that the measurement of the

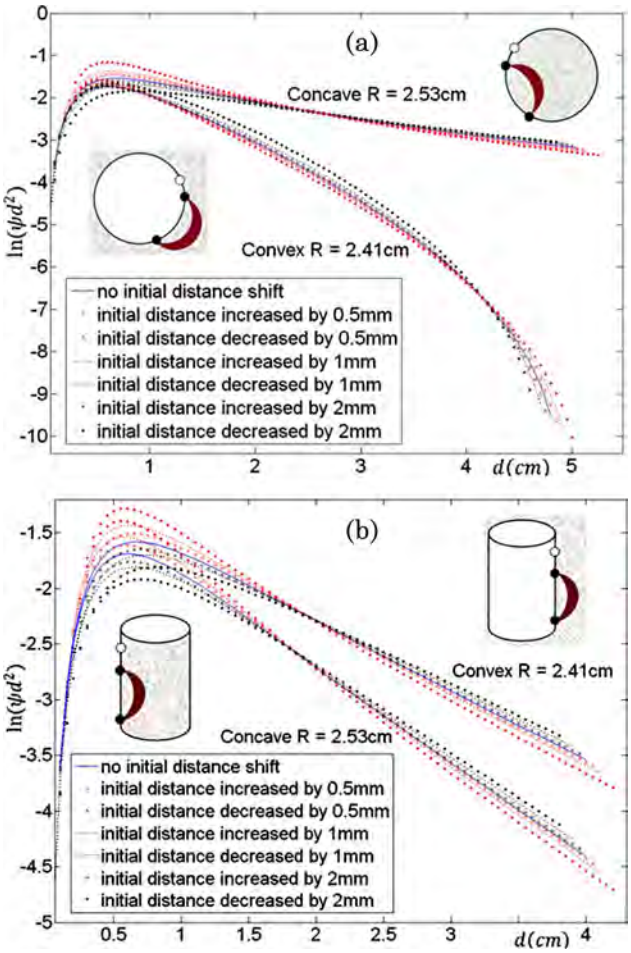

Fig. 10. (Color online) Effect of the measurement error of the initial source–detector distance. Initial source–detector distance is changed +0.5 mm, −0.5 mm, +1 mm, −1 mm, +2 mm, and −2 mmfor (a) *case-azi* configuration and (b) *case-longi* configuration..

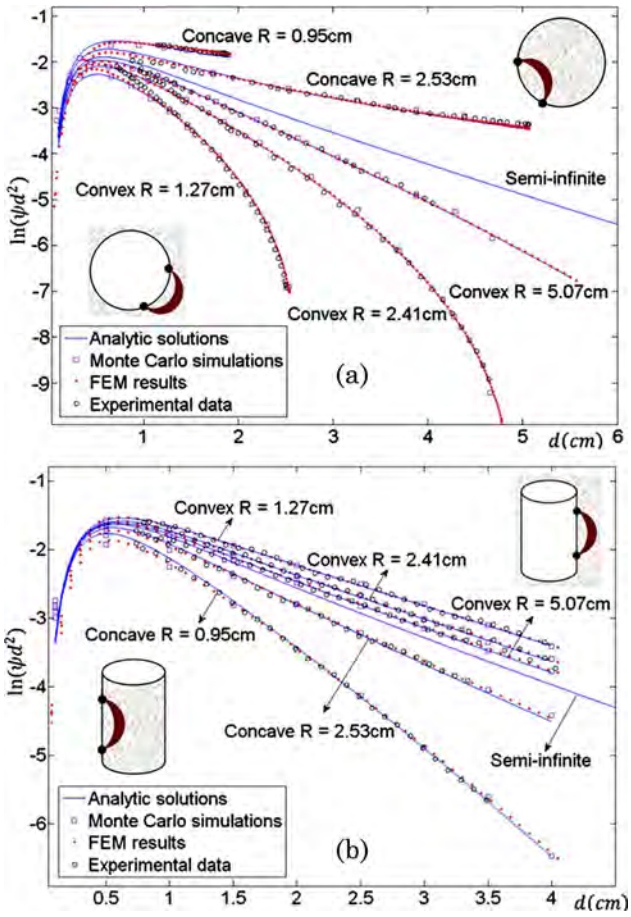

Fig. 11. (Color online) Comparisons of analytic prediction, the FEM simulation, the MC simulation, and experimental results for both concave and convex geometries: (a) *case-azi* configuration, (b) *case-longi* configuration. Optical properties are $\mu_a = 0.025\,\mathrm{cm}^{-1}$, $\mu_s' = 5\,\mathrm{cm}^{-1}$, $A = 1.86$, and $S = 1$..

photon fluence decay will be sensitive to the initial source–detector distance, but it also implies that experimental measurements with an uncertainty of the initial source–detector distance is justifiable using analytical predictions by slightly varying the radius parameter in the computation.

5. RESULTS OF QUANTITATIVE EXAMINATION

This section compares the analytic predictions made for the *case-azi* and *case-longi* configurations with respect to the results obtained from the FEM, the MC, and the experimental examinations. The differences in the source intensity settings in all of these quantitative measurements were compensated by a vertical shift for each of them in Fig. 11 in order to compare with the analytic predictions. The results for the *case-azi* configuration are given in Fig. 11(a). The shortest source–detector distance implemented in the analytic predictions, the FEM, and the MC simulations were seen as at or below 0.1 cm, but that in the experimental examinations had been at approximately 1 cm. This was due to the consideration of maximizing the measurement consistency, because each set of data corresponding to the available range of source–detector distance was acquired by setting the source power and CCD gain as fixed, rather than as variable to only accommodate a larger dynamic range. As indicated previously, the measurement of the initial source–detector distance was subjected to an error due to the spherical diffuser tips as well as other experimental limitations, but the error was controlled to be within 0.9 mm for the *case-azi* and 0.5 mm for the *case-longi* configurations.

The decay rate of photon fluence for the *case-azi* configuration made by analytic predictions was compared with those by the FEM, the MC, and the experimental examinations in Fig. 11(a). The data are plotted for $\ln(\psi d^2)$ as a function of d to verify the different trends of photon fluence decay expected for the concave and convex geometries, with respect to that for a semi-infinite medium, which is largely linear over the entire range of source–detector distance. It was predicted analytically that the decay rate of photon fluence of the *case-azi* configuration in concave geometry would be smaller than that in the semi-infinite medium, which was expected as the decreasing magnitude of the curve's slope toward longer source–detector distance, e.g., the curve becoming upward bended. It had also been predicted analytically that the decay rate of photon fluence of the *case-azi* configuration in convex geometry would be greater than that in the semi-infinite medium, which was expected as the increasing magnitude of the curve's slope toward longer source–detector distance, e.g., the curve becoming downward bended. For the *case-azi*

configurations of concave geometry and convex geometry that have the same radius parameter, it has also been predicted that the deviation of the upward-bending curve of concave geometry from the semi-infinite line (e.g., the magnitude of the slope difference between them) is smaller than that of the downward-bending curve of convex geometry from the semi-infinite line. The comparison for the decay rate of photon fluence for the *case-longi* configuration is shown in Fig. 11(b). Contrary to that in the *case-azi* configuration, in the concave geometry, the decay rate of photon fluence is larger than that in the semi-infinite medium, and in the convex geometry, the decay rate of photon fluence is smaller than that in the semi-infinite medium. However, for both the concave and convex geometries, the slope of the curve in either concave or convex geometry tends to be largely constant, with the slope of concave geometry greater in magnitude than that of semi-infinite medium and the slope of convex geometry smaller in magnitude than that of semi-infinite medium.

It was observed that the analytical, the FEM, the MC, and the experimental measurements agree with each other qualitatively, in terms of the pattern of deviation from the semi-infinite geometry, for the entire range of source–detector distances investigated for both *case-azi* and *case-longi* configurations. For source–detector distances greater than approximately five times of the transport mean free path, the results from the four methods agree quantitatively with each other.

6. DISCUSSION

Numerous studies have demonstrated that the assumption of a spherically isotropic source in the diffusion model accurately reflects experimental data when the source is centered one transport scattering distance within the medium from the boundary. This type of equivalent representation of a directional source by an inwardly displaced isotropic source can well quantify the fluence rate at distances greater than 3–5 transport scattering lengths from the source [13]. The agreement shown in this work among the four methods, for a considerable range of source–detector separations as long as they are greater than approximately five transport scattering lengths, is again supportive of the diffusion treatment of directional source using a spherically isotropic source placed one transport scattering distance into the medium, even for concave or convex geometries with a considerably small radius. At the subdiffusion regime, a disagreement is expected between diffusion model and experimental result, which in this work has been carried out by the MC simulation, as physical measurement for the given geometries became impractical at source–detector distances shorter than approximately five transport scattering lengths. Between the diffusion-based analytical quantification and the FEM simulation for the subdiffusion regime, however, the analytical result is slightly closer to the MC results than the FEM simulation is. This is largely due to the fact that, for the given spatial dimension, the spatial impulse source employed in the analytical solution is physically analogous to the launching of strictly forward-directional photons at a single point in the MC simulation, whereas the size effect of the spatially distributed Gaussian source profile implemented in the FEM is manifested at shorter distances from the source. Besides, our treatment of boundary effect, e.g., the probability of a boundary-reaching photon returning to the medium, in the MC simulation was based on the experimental measurements by use of extrapolated boundary condition as in the analytical model, whereas a Robin-type boundary condition was used by the FEM. The subtle difference in the boundary conditions could have been amplified at the subdiffusion regime.

The analytic model investigated in [1] and utilized in this work assumes that the cylindrical applicator is infinitely long, whereas the one tested in our experiments has finite length. For the *case-azi* configurations shown in Fig. 11(a), all experimental measurements have been confined in an azimuth plane that is several centimeters away from the edge of the applicator. The results in Fig. 11(a) show no noticeable edge effect, which is specified as the degree of the model-data mismatch being proportional to the radius of the applicator. For the *case-longi* configuration shown in Fig. 11(b), either the source or detector has been translated 4 cm from the middle of the applicator toward the edge, and the edge effect may be perceived as a slightly larger deviation of the experimental data from the analytical predictions for a larger applicator radius that gives smaller length-to-radius ratio. .The effect of the finite length of the applicator may be accounted for by considering the effects of two additional image sources of the physical source, with respect to the two longitudinal boundary facets, or modeled rigorously by deriving the Green's function specific to the geometry of a finite cylindrical applicator. In fact, Liemert and Kienle[14] have had extensive analysis of photon diffusion in finite concave cylindrical applicator geometry for time-domain and frequency-domain measurements. Their derivation of the Green's function for the time-domain or frequency-domain photon diffusion in the finite concave geometry used the cosine transform and Hankel transform, which can be readily extended to finite convex applicator geometry to understand time-domain or frequency-domain photon diffusion in a geometry similar to that investigated in our experiments. Our analytic approach in [1] has been for the steady-state photon diffusion only by expanding the Green's function in Fourier series and Fourier transform; however, our approach provides the first insights for the models of photon diffusion in both concave and convex geometries. The analytic treatment in [1] involved a real k in the solution of steady-state photon diffusion. By implementing a complex k in the analytic process, the approach may be extended to frequency-domain analysis for both concave and convex geometries, but for time-domain analysis, the method of Liemert and Kienle [14] may be the method to follow. .The approaches by Liemert and Kienle [14] and that demonstrated in [1] are complimentary and when combined may render analytic solutions to more geometries and measurement conditions.

Our unified modeling of both concave and convex geometries has given us the opportunity of observing some previously less-known patterns of photon diffusion associated with a cylindrical applicator. Figure 11 verified that, for the specific case of having the source and detector located azimuthally on the same axial plane, the decay rate of photon fluence is smaller in the concave geometry and greater in the convex geometry than that in the semi-infinite geometry for the same source–detector distance. For the specific case of having the source and detector located longitudinally with the same azimuth angle, the decay rate of photon fluence is greater in the concave geometry and smaller in the convex geometry than that in the semi-infinite geometry for the same source–detector

distance. These interesting findings imply the existence of a potentially spiral direction on the surface of both the concave cylindrical applicator and the convex cylindrical applicator, along which the decay rate of photon fluence could be equivalent to that in a planar surface or a semi-infinite geometry. This interesting phenomenon of photon diffusion that may associate with a cylindrical applicator is predicted as "spiral-planar equivalence." If the existence of such a planar-equivalent spiral direction inside or outside a cylindrical applicator is verified, for certain translumenal sensing or imaging applications, the semi-infinite geometry may be implemented for greatly simplified modeling and rapid recovery of tissue optical properties. Work is ongoing to investigate the validity of the hypothesis of a spiral-planar equivalence phenomenon.

7. CONCLUSION

Part I of this work analytically examined the steady-state photon diffusion along the azimuth direction or the *case-azi* configuration and the longitudinal direction or *case-longi* configuration, in the infinitely long concave and convex applicator geometries. This Part II of the work quantitatively examined the predictions of Part I for the *case-azi* configuration that the decay rate of photon fluence would become smaller in the concave geometry and greater in the convex geometry than that in the semi-infinite geometry for the same source–detector distance. This Part II work also examined predictions of Part I for the *case-longi* configuration, which suggested that the decay rate of photon fluence would be greater in the concave geometry and smaller in the convex geometry than that in the semi-infinite geometry for the same source–detector distance. The results of three quantitative examination approaches, including (a) the FEM, (b) the MC simulation, and (c) experimental measurement on finite cylindrical-applicator geometries with large a length-to-radius ratio, validated the qualitative trend predicted by Part I and verified the quantitative accuracy of the analytic treatment of Part I in the diffusion regime of the measurement, at a given set of absorption and reduced scattering coefficients of the medium.

ACKNOWLEDGMENTS

This work has been supported in part by research grant HR06-171 from the Oklahoma Center for the Advancement of Science and Technology (OCAST), a Big XII Faculty Fellowship award from Oklahoma State University, research award W81XWH-07-1-0247 from the Prostate Cancer Research Program of Department of Defense, and Oklahoma IDeA Network of Biomedical Research Excellence (INBRE).

REFERENCES

1. A. Zhang, D. Piao, C. F. Bunting, and B. W. Pogue, "Photon diffusion in a homogeneous medium bounded externally or internally by an infinitely long circular cylindrical applicator. I. Steady-state theory," J. Opt. Soc. Am. A **27**, 648–662 (2010).
2. R. C. Haskell, L. O. Svaasand, T. Tsay, T. Feng, M. S. McAdams, and B. J. Tromberg, "Boundary conditions for the diffusion equation in radiative transfer," J. Opt. Soc. Am. A **11**, 2727–2741 (1994).
3. D. Contini, F. Martelli, and G. Zaccanti, "Photon migration through a turbid slab described by a model based on diffusion approximation. I. Theory," Appl. Opt. **36**, 4587–4599 (1997).
4. M. Huang, T. Xie, N. Chen, and Q. Zhu, "Simultaneous reconstruction of absorption and scattering maps with ultrasound localization: feasibility study using transmission geometry," Appl. Opt. **42**, 4102–4114 (2003).
5. X. Zhou and T. C. Zhu, "Interstitial diffuse optical tomography using an adjoint model with linear sources," Proc. SPIE **6845**, 68450C (2008).
6. C. Musgrove, C. F. Bunting, H. Dehghani, B. W. Pogue, and D. Piao, "Computational aspects of endoscopic near-infrared optical tomography: initial investigations," Proc. SPIE **6434**, 643409 (2007).
7. .H. Dehghani, M. E. Eames, P. K. Yalavarthy, S. C. Davis, S. Srinivasan, C. M. Carpenter, B. W. Pogue, and K. D. Paulsen, "Near infrared optical tomography using NIRFAST: algorithm for numerical model and image reconstruction," Commun. Numer. Methods Eng. **25**, 711–732 (2009).
8. G. Yao and M. A. Haidekker, "Transillumination optical tomography of tissue engineered blood vessels: a Monte-Carlo simulation," Appl. Opt. **44**, 4265–4271 (2005).
9. A. Ya. Polishchuk, J. Dolne, F. Liu, and R. R. Alfano, "Average and most-probable photon paths in random media," Opt. Lett. **22**, 430–432 (1997).
10. R. Michels, F. Foschum, and A. Kienle, "Optical properties of fat emulsions," Opt. Express **16**, 5907–5925 (2008).
11. I. Driver, J. W. Feather, P. R. King, and J. B. Dawson, "The optical properties of aqueous suspensions of Intralipid, a fat emulsion," Phys. Med. Biol. **34** (12), 1927–1930 (1989).
12. S. Fantini, M. A. Franceschini, and E. Gratton, "Semiinfinite-geometry boundary problem for light migration in highly scattering media: a frequency-domain study in the diffusion approximation," J. Opt. Soc. Am. B **11**, 2128–2138 (1994).
13. T. J. Farrell, M. S. Patterson, and B. C. Wilson, "A diffusion theory model of spatially resolved, steady-state diffuse reflectance for the noninvasive determination of tissue optical properties," Med. Phys. **19**, 879–888 (1992).
14. A. Liemert and A. Kienle, "Light diffusion in a turbid cylinder. I. Homogeneous case," Opt. Express **18**, 9456–9473 (2010).

Trans-rectal Ultrasound–coupled Spectral Optical Tomography of Total Hemoglobin Concentration Enhances Assessment of the Laterality and Progression of a Transmissible Venereal Tumor in Canine Prostate

Zhen Jiang, D. Piao, G. R. Holyoak, J. W. Ritchey, K. E. Bartels, G. Slobodov, C. F. Bunting, and J. S. Krasinski

OBJECTIVES To evaluate whether trans-rectal spectral optical tomography of total hemoglobin concentration (HbT) can image longitudinal and lateral developments of a canine transmissible venereal tumor (TVT) in a canine prostate.

METHODS A near-infrared (NIR) applicator was integrated with a trans-rectal ultrasound (TRUS) transducer to perform ultrasound (US)–coupled optical tomography of the canine prostate. Spectral detection at 785 and 830 nm enabled quantitation of HbT. Canine TVT cells were injected into the right lobe of a dog's prostate gland. Longitudinal imaging assessment of the post-injection prostate was performed by coupled US/NIR imaging over a 45-day duration.

RESULTS By day 7, NIR indicated TVT infiltration in the noninjected left prostatic lobe with the gray-scale US indistinct. By day 31, both NIR and gray-scale US revealed more widespread TVT involvement in the left than in the right lobe, as well as an extensive TVT mass in the caudal aspect of the gland, of which the peak HbT increased 3-fold and the mass volume grew exponentially over the 45-day duration. Increased blood supply to the mass was also observed on Doppler US.

CONCLUSIONS TRUS-coupled spectral optical tomography enhances assessment of the laterality and progression of prostate tumor compared with using gray-scale and Doppler TRUS. UROLOGY xx: xxx, xxxx.

Carcinoma of the prostate is a leading cause of death by cancer in American men.[1] The diagnosis of prostate cancer is based on trans-rectal ultrasound (TRUS)–guided systematic core biopsy of the gland, when a suspicion of cancer is indicated by screening methods such as serum prostate-specific antigen (PSA) test and digital rectal examination (DRE).[2,3] However, the ultrasonographic finding of classic hypoechoic peripheral zone lesion has a sensitivity of ~85%, a specificity of ~28%, a positive predictive value of ~29%, a negative predictive value of ~85%, and an overall accuracy of ~43%,[4] for prostate cancer detection. The prevalence of isoechoic or nearly invisible prostate cancer on ultrasonography ranges from 25% to 42%.[5] Because prostatic cancer usually has multifocal involvement,[6] sampling the prostate with multiple needle cores is necessary; however, TRUS is not reliable for guiding focal biopsy as well as assessing the laterality of prostate cancer[7] before pathologic evaluation. Ultrasonography needs to be supplemented by a pathognomonic indicator of prostate cancer.

There is strong evidence to suggest that the vascular supply to malignant prostate tissue differs from the vascular anatomy of normal prostate tissue.[8] Doppler sonography, as an adjunct to gray-scale sonography, is used to identify increased blood flow to assist in the identification of suspicious lesions within the prostate. Studies of microvessel density within the prostate demonstrated a clear association of increased microvessel density with the presence of cancer.[9] Doppler imaging is able to detect signals from small vessels such as those feeding vessels to the microvascular bed; however, because of its sensitivity dependence upon motion, it is limited in visualizing the microcirculation.[10,11]

From the School of Electrical and Computer Engineering, Oklahoma State University, Stillwater, Oklahoma; Department of Veterinary Clinical Sciences, Oklahoma State University, Stillwater, Oklahoma; Department of Veterinary Pathobiology, Oklahoma State University, Stillwater, Oklahoma; and Department of Urology, University of Oklahoma Health Sciences Center, Oklahoma City, Oklahoma

Correspondence to D. Piao, School of Electrical and Computer Engineering, 202 Engineering South, Oklahoma State University, Stillwater, OK 74078; e-mail: daqing.piao@okstate.edu (D. Piao)

Submitted: February 18, 2010, accepted (with revisions): June 9, 2010

0090-4295/xx/$34.00
doi:10.1016/j.urology.2010.06.017

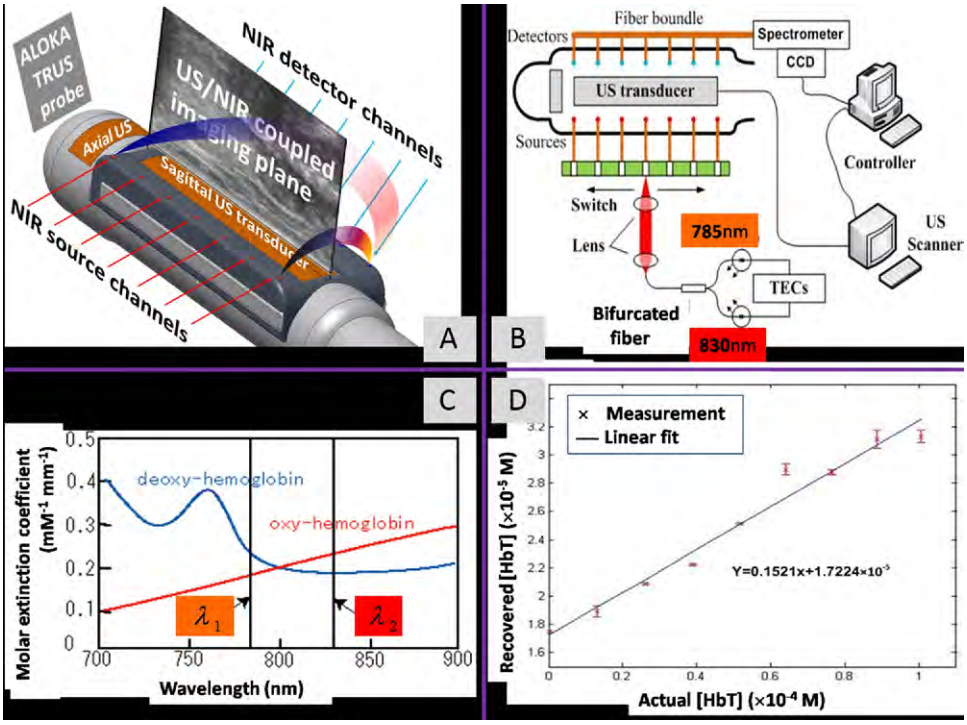

Figure 1. **(A)** Three-dimensional rendering of coupled US/NIR imaging. **(B)** Schematic diagram of NIR imager. **(C)** Dual-band of NIR imaging. **(D)** HbT calibration results.

In the near-infrared (NIR) band, light interacts with tissue at the microscopic level, largely by two mechanisms: strong scattering by subcellular organelles and the dominant absorption by chromophores such as hemoglobin. It has been recognized in breast studies[12] that increased total hemoglobin concentration (HbT) due to angiogenesis causes an elevation of NIR absorption. For a sonographically suspicious lesion in the breast, NIR imaging of HbT in the lesion is shown to improve the specificity of cancer detection.[13] These findings suggest that augmenting TRUS, in gray-scale or Doppler, with the NIR measurement of HbT in prostate will likely improve detection accuracy. Recently we have demonstrated that combining ultrasonography and NIR absorption measurement of prostatic tissue at 840 nm detected development of a rapidly growing transmissible venereal tumor (TVT) in canine prostate at least 1 week earlier than by using gray-scale TRUS alone.[14] This study, by using spectral NIR measurements at 785 and 830 nm to extract the HbT information, demonstrates that combining ultrasonography with NIR measurement of HbT enhances detection of the laterality and progression of TVT in the canine prostate.

MATERIALS AND METHODS

Transrectal US–Coupled Spectral Optical Tomography System

The trans-rectal NIR/US applicator based on ALOKA UST 672-5/7.5 biplane prostate probe[15] is illustrated in Fig. 1a. The NIR channels are placed laterally symmetric to the sagittal US transducer and perform volumetric imaging,[16] of which the mid-sagittal NIR is position-correlated with the sagittal US. The imager illustrated in Fig. 1b combines the outputs of two laser diodes (785 and 830 nm) for sequential delivery to the optical source channels via a fiber switch. The dual-band signals are separated by a spectrometer and acquired by a CCD detector. The data acquisition for one set takes 3 s. The dual-band absorption coefficients ($\mu_a^{\lambda_1}$ and $\mu_a^{\lambda_2}$) are reconstructed first, then used to calculate oxygenated and deoxygenated hemoglobin concentrations by $[HbO] = [\mu_a^{\lambda_1} \cdot e_{Hb}^{\lambda_2} - \mu_a^{\lambda_2} e_{Hb}^{\lambda_1}] / [e_{HbO}^{\lambda_1} \cdot e_{Hb}^{\lambda_2} - e_{HbO}^{\lambda_2} \cdot e_{Hb}^{\lambda_1}]$ and $[Hb] = [\mu_a^{\lambda_1} \cdot e_{HbO}^{\lambda_2} - \mu_a^{\lambda_1} \cdot e_{HbO}^{\lambda_2}] / [e_{Hb}^{\lambda_1} \cdot e_{HbO}^{\lambda_2} - e_{Hb}^{\lambda_2} \cdot e_{HbO}^{\lambda_1}]$, respectively, where e^{λ} denotes the molar extinction coefficient as shown in Fig. 1c. Summing HbO and Hb gives HbT. Fresh bovine blood[17,18] was used to calibrate the HbT measurement as shown in Fig. 1d.

Animal Model and Imaging Protocol

This study was approved by the Animal Care and Use Committee of Oklahoma State University, and inspected on-site by the U.S. Army Medical Research and Material Command. An adult 20-kg, intact male, foxhound estimated to be 6 years of age was used. The canine TVT cells were propagated in NOD/SCID mice and recovered/homogenized for injection into the canine prostate gland without immune suppression. Under general anesthesia, ~3 cc of TVT cells were aseptically injected transperineally into the right lobe of the prostate using a 6-inch, 16-gauge hypodermic needle (Fig. 2a), via US visualization (Fig. 2b) using an Aloka UST-9132I convex-array multi-frequency (3.75-10 MHz) finger-grip transducer. The TVT cells were confined within the right prostatic lobe during the injection in two locations, the first near the cranial aspect and the second slightly caudal to the mid-point of the right lobe as the needle was withdrawn. The dog then was closely monitored, which included rectal digital palpation, and transrectal gray-

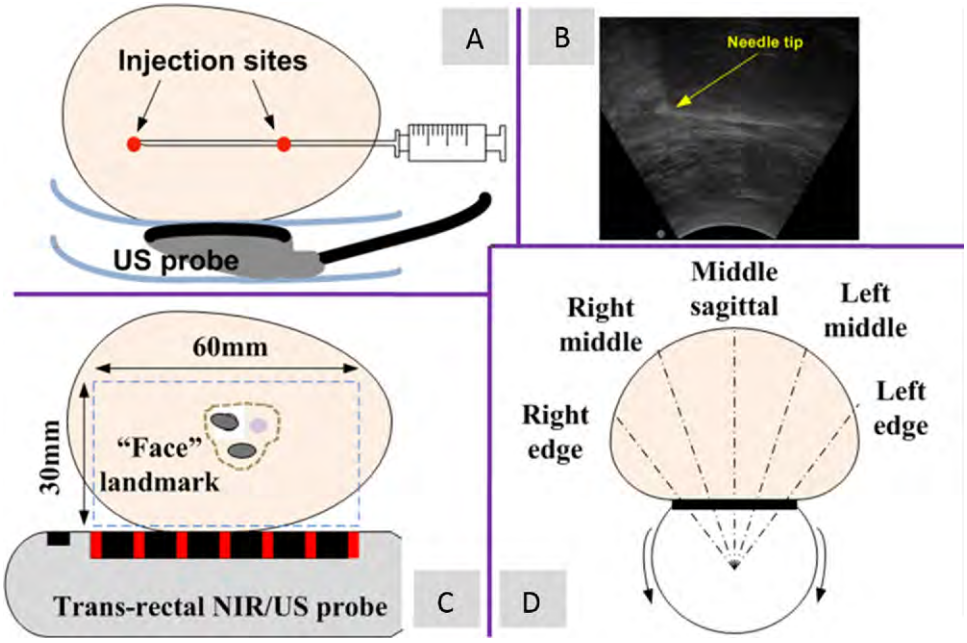

Figure 2. **(A)** The two TVT injection sites. **(B)** Needle visualization. **(C)** The "face" landmark. **(D)** The five quasi-sagittal planes of NIR imaging.

scale TRUS and NIR, at 7, 14, 21, 31, 38, and 45 days post-injection. Doppler US evaluations were performed at day 38 and day 45.

The baseline US indicated a prostate measuring 6 cm cranial to caudal. A cluster of cysts in the right aspect of the gland resembling a "face" was used as a landmark (Fig. 2c) to facilitate multiple images taken in the same relative location during the length of the study. TRUS-coupled optical tomography was performed on five quasi-sagittal planes (Fig. 2d), including the middle-sagittal, half-way to the right lateral edge, the right lateral edge, half-way to the left lateral edge, and the left lateral edge of the prostate gland. On each of the 5 quasi-sagittal planes the imaging was performed at 3 longitudinal positions for cross-validation.

Pathological Assessment

On day 55, the dog was humanely euthanized with a barbiturate overdose. A complete necropsy was performed, which included a thorough gross inspection and excision of the prostate gland and urinary bladder. The prostate was serially sectioned using a freehand technique in the conventional transverse planes. Routine histology with hematoxylin and eosin stain for light microscopy was performed on specimens selectively sampled from the sectioned prostate, each of which contained tissues that were grossly expected to be normal, cystic, or neoplastic.

RESULTS

Two sets of images on day 7 and day 31, each taken at two longitudinal positions as indicated by the ~25 mm shift of the "face" landmark, are presented in Fig. 3. On US, the "face" landmark was clearly visible by day 7 but distorted significantly by day 31. The day 7 images revealed a hyper-HbT and hypo-echoic region near the cranial injection site in the right lobe. That region disappeared in images taken on day 14 and after; therefore, it was thought to be related to hemorrhage and subsequent inflammation resulting from the injection.

The day 31 US images revealed a cluster of hypoechoic masses with irregular boundaries in the caudal aspect of both right and left lobes, with an overall greater volume of the hypoechoic masses located in the left lobe than in the right lobe. The spatial content of the hyper-HbT regions generally agree with that of the hypo-echoic regions in the caudal-to-middle-left aspect, but presented a different pattern in the cranial-to-right aspect of the gland. The US presented a large heteroechoic mass dorsal-cranial to the pelvic bone and extending predominantly into the left lobe but also included right-lobe involvement. Near that location a corresponding NIR image revealed a cluster of hyper-HbT regions, the center of which seemed displaced slightly cranial with respect to that of hypo-echoic mass. Retrospectively, on the day 7 NIR images a smaller hyper-HbT region was found near that location. In addition, on day 7 US images, a substantially smaller hypoechoic region was weakly distinguishable near that same location. Again on day 7 images, the smaller hyper-HbT region was also displaced slightly cranial with respect to the marked hypoechoic mass, which, developing much more rapidly than other masses, presented marked enhancement of peripheral blood flow on Doppler US on day 38 and after.

Figure 4a displays 3 sets of images of the middle-aspect of the right lobe at baseline, day 21 (week 3) and day 45 (week 6). The hypoechoic mass grown caudal to the prostate was shown clearly on week 6, and approximately a 3-fold HbT change was observed in the marked 10 mm-diameter region from baseline to week 6. The HbT values are within previously reported ranges.[19] The vol-

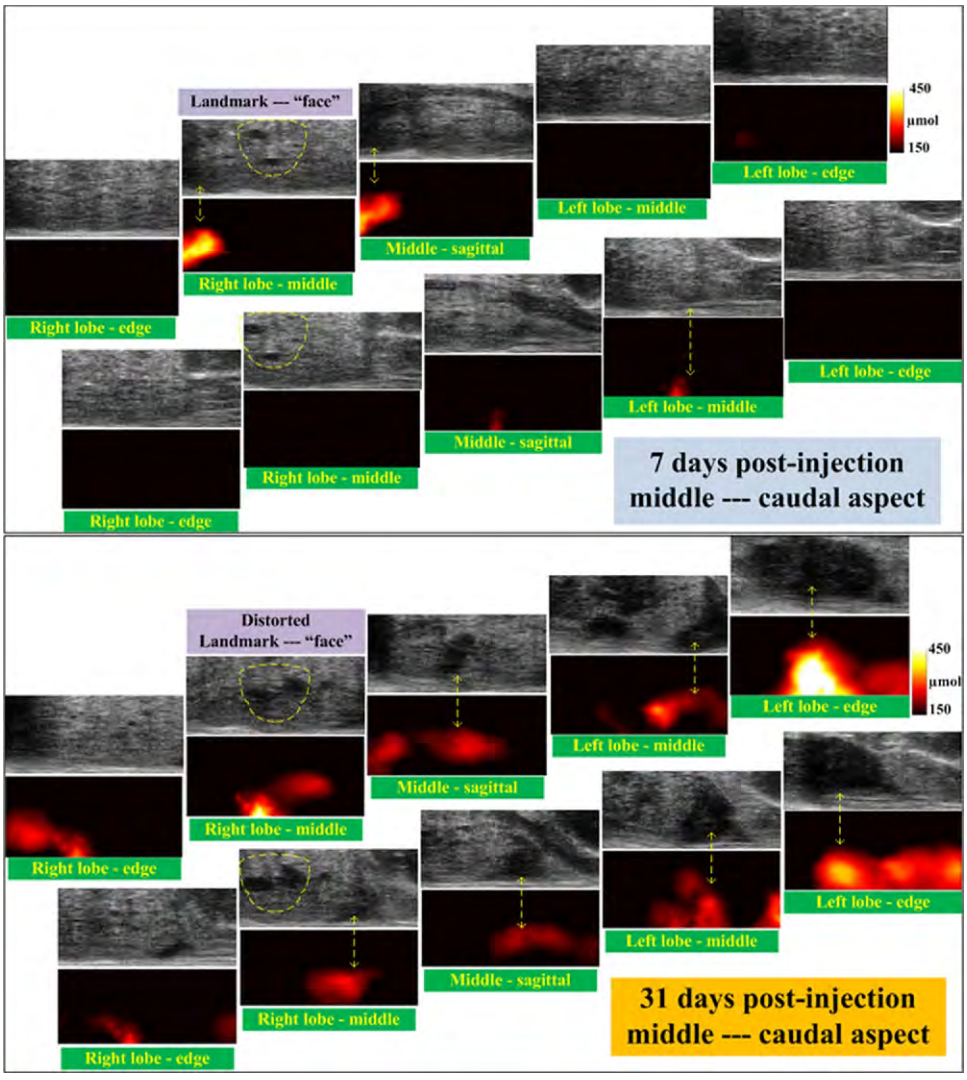

Figure 3. Image dimension 60 × 30 mm^2 (cranial-caudal × dorsal-ventral). At day 7, NIR detected a mass in the cranial injection site, which later disappeared. The day 7 NIR image also provided the earliest sign of tumor growth in the left lobe. Both NIR and gray-scale US revealed larger volumes of tumor mass in the left lobe than in the right lobe.

ume of HbT ≥ 150 μM, within the caudal-aspect of the right lobe corresponding to the week 6 hypoechoic mass, was estimated from volumetric NIR reconstruction. The post-injection volumetric change followed an exponential growth pattern,[20] as shown in Fig. 4c.

The excised prostate (Fig 4d) was approximately 10 × 5 × 5 cm^3. The prostate was serially sectioned in the conventional transverse orientation in ~1.5-cm slices. The gross examination confirmed multiple coalescing foci of TVT in the caudal aspect of the gland, and significant infiltration of the tumor from right to the left lobes. After fixation in 10% buffered formalin, the prostatic sections were again closely examined. On slice 6 corresponding to the left-caudal-aspect of the gland, a small pocket (indicated by a 10-mm circle) of normal prostatic tissue surrounded by multi-foci TVT was noted. Indication of similar morphology can also be seen as demarcated by the line in Fig. 4e on the sagittal NIR image of day 38 as a region of baseline HbT enclosed by heterogeneous hyper-HbT masses. The simultaneous sagittal Doppler US of day 38 revealed substantially enhanced blood supply ventral to the heterogeneously hypoechoic mass.

DISCUSSION

Some NIR images obtained in this study were inconsistent with US because of motion that occurred between US frame and completion of the NIR data acquisition. Using the images that were consistent, when comparing peripheral vascularity enhancement shown on Doppler US with NIR, we found the elevation of HbT on NIR was generally distributed in the entire hypoechoic TVT-indicating region. Angiogenesis is essential for tumor growth and metastasis. Recent longitudinal studies of the prostate cancer developmental phase suggested that neoangiogenesis or tumor-associated neovascularity must increase before rapid growth of tumor.[21] Because NIR at-

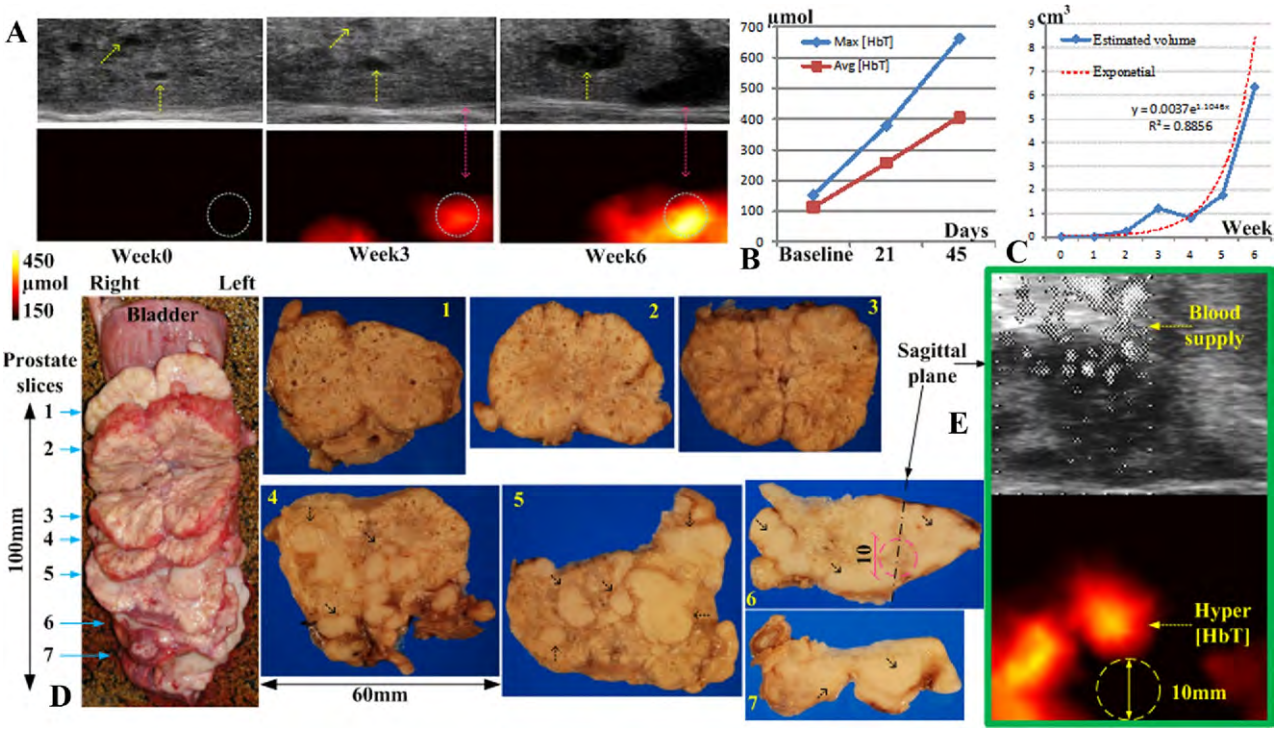

Figure 4. **(A)** Sagittal images of the right lobe in the middle-caudal aspect at baseline, day 21 (week 3), and day 45 (week 6). **(B)** Changes in HbT in the 10-mm-diameter region of interest over the 6-week duration. **(C)** Estimated tumor volume changes from week 1 to week 6. **(D)** Gross examination of the canine prostate on necropsy. After fixation in 10% buffered formalin, 7 slices of the prostate gland were sectioned from cranial to caudal, at an interval of approximately 15 mm. **(E)** Doppler US and optical images of the sagittal plane were taken approximately across the line marked on slice 6.

tenuation is mainly related to HbT, NIR imaging has the potential of early detection of the onset of the neovasculature. Combining NIR imaging with gray-scale and Doppler US may enhance the assessment of prostatic tumor growth and involvement. However, this approach needs to be examined by blinded animal studies or human clinical trials.

Even though it is possible to extract oxygenation information using the two NIR bands, results appeared to be inconsistent in this study. An ongoing investigation has implemented 3 NIR bands, which enhanced quantification of tumor oxygenation. In addition, in this study, the optical reconstruction is performed with no prior information of the suspected mass, which impairs the overall quantitative accuracy of the NIR imaging, specifically of the deeper prostatic tissue. One of the future directions is to extract the ultrasonically-indicated morphology as a spatial *priori* to improve NIR spectral characterization of the tumor-suspicious lesion; however, the effectiveness will be limited by US resolution parameters in visualizing hypoechoic lesions in prostate cancer.

CONCLUSION

This study demonstrated noninvasive optical measurement of HbT changes associated with development of a rapidly growing tumor in the canine prostate. TRUS-coupled spectral optical tomography was shown to enhance the detection of the progression and lateral involvement of the prostatic tumor compared to using TRUS alone. Systematic complementary use of gray-scale US, Doppler US, and NIR optical measurement may provide more accurate evaluation of prostatic malignancies.

Acknowledgment. The authors acknowledge a FY2006 New Investigator Award (PC060814) from the DoD Prostate Cancer Research Program (to D.P.) and an endowment fund from the Kerr Foundation, Oklahoma City, OK (to K.E.B.).

References

1. Jemal A, Siegel R, Ward E, et al. Cancer statistics, 2009. *CA Cancer J Clin.* 2009;59:225-249.
2. Hodge KK, McNeal JE, Stamey TA. Ultrasound guided transrectal core biopsies of the palpably abnormal prostate. *J Urol.* 1989;142:66-70.
3. Garber SJ, Goldenberg SL, Cooperberg PL, et al. Systematic transrectal ultrasound-guided biopsy of the prostate. *Can Assoc Radiol J.* 1994;45:387-390.
4. Downs TM, Grossfield GD, Shinohara K, et al. Transrectal ultrasound-guided prostate biopsy. In: D'Amico AV, Loefler JS, Harris, et al., eds. *Image-Guided Diagnosis and Treatment of Cancer*. Totowa, NJ: Humana Press Inc.; 2003.
5. Ellis WJ, Brawer MK. The significance of isoechoic prostate carcinoma. *J Urol.* 1994;152:2304-2307.
6. Wise AM, Stamey TA, McNeal JE, et al. Morphologic and clinical significance of multifocal prostate cancers in radical prostatectomy specimens. *Urology.* 2002;60:264-269.

7. Mouraviev V, Mayes JM, Madden JF, et al. Analysis of laterality and percentage of tumor involvement in 1386 prostatectomized specimens for selection of unilateral focal cryotherapy. *Technol Cancer Res Treat*. 2007;6:91-95.
8. Newman JS, Bree RL, Rubin JM. Prostate cancer: diagnosis with color Doppler sonography with histologic correlation of each biopsy site. *Radiology*. 1993;195:86-90.
9. Bigler SA, Deering RE, Brawer MK. Comparison of microscopic vascularity in benign and malignant prostate tissue. *Hum Pathol*. 1993;24:220-226.
10. Cosgrove D. Angiogenesis imaging—ultrasound. *Br J Radiol*. 2003; 76:S43-S49.
11. Halpern EJ. Color and power Doppler evaluation of prostate cancer. In: Halpern EJ, Cochlin DL, Goldberg BB, eds. Imaging of the Prostate. London, England: Martin Dunitz; 2002.
12. Tromberg BJ, Pogue BW, Paulsen KD, et al. Assessing the future of diffuse optical imaging technologies for breast cancer management. *Med Phys*. 2008;35:2443-2451.
13. Zhu Q, Cronin EB, Currier AA, et al. Benign versus malignant breast masses: optical differentiation with US-guided optical imaging reconstruction. *Radiology*. 2005;237:57-66.
14. Jiang Z, Holyoak GR, Bartels KE, et al. In vivo trans-rectal ultrasound coupled near-infrared optical tomography of a transmissible venereal tumor model in the canine pelvic canal. *J Biomed Opt Lett*. 2009;14:030506.
15. Piao D, Jiang Z, Bartels KE, et al. In vivo trans-rectal ultrasound-coupled near-infrared optical tomography of intact normal canine prostate. *J Innov Opt Heal Sci*. 2009;2:215-225.
16. Piao D, Bartels KE, Jiang Z, et al. Alternative trans-rectal prostate imaging: A diffuse optical tomography method. *IEEE J Select Top Quant Electron*. 2010;16:715-729.
17. McCay CM. The hemoglobin and total phosphorus in the blood of cows and bulls *J Dairy Sci*. 1931;14:373-378.
18. Hayes MD, Vanzant ES, Stombaugh TS, et al. Comparison of bovine blood absorption coefficients to human curves. *Livestock Environ VIII Proc*. 2008;PN:701P0408; 981-985.
19. Svensson T, Andersson-Engels S, Einarsdóttír M, Svanberg K. (2007) In vivo optical characterization of human prostate tissue using near-infrared time-resolved spectroscopy. *J Biomed Opt*. 2007; 12:0140221–014022-10.
20. Guiot C, Degiorgis PG, Delsanto PP, Gabriele P, Deisboeck TS. Does tumor growth follow a universal law? *J Theor Biol*. 2003;225: 147-151.
21. Xuan JW, Bygrave M, Jiang H, et al. Functional neoangiogenesis imaging of genetically engineered mouse prostate cancer using three-dimensional power Doppler ultrasound. *Cancer Res*. 2007;67: 2830-2839.

CHAPTER 4

Diffuse Optical Techniques: Instrumentation

Daqing Piao

4.1 Introduction: Deterministic "Diffuse" Detection of Probabilistic Photon Propagation

The term *diffuse optical technique* refers to the use of photons undergoing many scattering events to obtain the measurement of optical properties in deep tissue volumes for the ultimate purpose of investigating tissue physiology [1–5]. When depth-resolved cross-sectional image is the endpoint of visualization, it is specified as diffuse optical tomography (DOT) [6–10]. DOT is becoming increasingly interesting and important for functional imaging in biological tissues [11]. DOT relies on noninvasive or minimally invasive administration of light in the near-infrared (NIR) spectral window. The diagnostic premises of NIR light have been established from at least three physical pieces of evidence. First, the relatively weak NIR absorption in water allows photon propagation into deep tissue volumes. Second, the stronger NIR absorption of hemoglobin as compared to other tissue constituents such as water provides intrinsic contrast between blood and parenchymal tissues [12–24]. Third, the distinct crossover feature of NIR absorption by hemoglobin between oxygenated and deoxygenated states enables direct quantification of tissue oxygenation [25–27]. The integrative outcome of utilizing NIR light is thus directed to obtaining optically expressed physiological contrasts, such as differences in microvessel density and tissue oxygenation, in deep tissue volumes by nonionizing optical interrogation. Such physiological contrasts offer specific and often sensitive indications of tissue metabolic changes and malignancies at both macroscopic and microscopic scales.

Although biological tissue is a weak absorber of NIR light due to the large water content, it is a strong NIR scatterer owing predominantly to the micrometer-scale intracellular organelles. NIR light becomes essentially diffuse a few millimeters away from the point of a directional launching in typical soft biological tissue where a single scattering event may occur at a scale of 100 μm or less [28]. The NIR diffuse propagation makes it feasible to interrogate tissue volume that is much wider than the direct geometric sensing region between light illumination and collection positions and much deeper than the depth achieved by optical imaging methods where

coherent photons are utilized, as in optical coherence tomography [29] and low-coherence enhanced backscattering [30].

Although DOT is not a choice of whole-body imaging for human due to NIR's limited penetration of several centimeters in soft tissue and strong attenuation by bone, in many cases it can perform relatively large-scale imaging for tissues or organs comparable to the size of breast. When compared with imaging modalities wherein ballistic illumination-detection path is employed for organ-level imaging, such as X-ray CT, DOT requires fewer illumination and measurement channels in order to measure the same volume of tissue. However, due to the loss of intrinsic information in DOT related to where the photon was launched when it is detected, the sensing of a photon that transpasses or originates from a specific spatial location becomes a probabilistic matter. The direct information that DOT measurement seeks to acquire is the tissue optical property, such as the absorption coefficient and reduced scattering coefficient upon which the relevant contrast of physiological parameters may be retrieved. Since these optical properties are coupled with probabilistic propagation of NIR light in the imaging volume, the deterministic detection of the trajectory of diffuse photons becomes one of the preeminent issues in DOT techniques.

The aims of DOT instrumentation in performing deterministic "diffuse" detection of probabilistic photon propagation may be specified into the flowing three categories: (1) to identify the position of where the photon is launched from, (2) to determine the path along which the photon is diffused, and (3) to locate the target by which the photon is perturbed. These three objectives are resolved in principle by individual or combined solutions of following tasks: (1) encoding source-detector pairs for signal discrimination among many channels, (2) separating absorption and scattering contributions to the photon attenuation, and (3) obtaining tomographic image reconstruction of the heterogeneity in optical properties without or with prior information. The advancement in these three tasks may foster new DOT applications; at the same time, the drive to apply NIR methods to new imaging regimes may prompt novel approaches in DOT techniques, in particular instrumentation. The first part of this chapter is intended to provide a brief overview of some fundamental technological issues of DOT that have evolved over the time. Detailed discussion covering these technological advances in more breadth and depth can be found in many outstanding review papers [7–11, 28]. The second part of this chapter introduces in detail some of the latest unconventional approaches in DOT instrumentation for the aim of extending DOT to previously unattempted or difficult applications. These unconventional approaches may also infer potential future directions of DOT instrumentation.

4.2 Methods for Differentiating the Origin of Diffuse Photons

NIR imaging uses diffused photons as measured through transmission of significant volumes of tissue and after they have undergone many scattering events. The intrinsic information related to where the photon was launched from is thus lost when it is detected. NIR DOT as a tomographic imaging modality requires measurements from multiple source and detector channels; therefore, a mechanism of differentiat-

ing the signals corresponding to specific source and detector pairs must be implemented.

4.2.1 The Source-Encoding Requirement in DOT

The measurements by multiple detectors when multiple sources are launched may be expressed by the following equation (it is derived by assuming a linear model for simplicity; however, the derivation can also be applied to a nonlinear model):

$$D_{M\times 1} = \Psi_{M\times N} S_{N\times 1} \tag{4.1}$$

where D denotes the assembly of detector outputs, M is the number of detector channels, S represents the assembly of source inputs, N is the number of source channels, and Ψ is the weight matrix governed by the imaging geometry and the medium optical property. The output of the individual detector is then represented by

$$d_m = \sum_{n=1}^{N} \psi_{mn} s_n, \quad m = 1, 2, \ldots, M, n = 1, 2, \ldots, N \tag{4.2}$$

which indicates that the output of each single detector contains a mixture of signals originating from all source channels. The separation of individual source-detector signals of diffuse photon propagation as a requirement of DOT image formation can only be implemented through encoding of the source-detector channels at the source side and proper decoding of the channels at the measurement. This may not be as explicit as it seems without the analysis of two simplified configurations. When considering the geometry of an imaging array with only one source and multiple detectors, the detector outputs are

$$D_{M\times 1} = \Psi_{M\times 1} S_{1\times 1} \tag{4.3}$$

or

$$d_m = \psi_m s \tag{4.4}$$

where it is clear that there is a unique correspondence of the signal from the single source to each detector by $1 \rightarrow m$. For the other geometry with multiple sources and only one detector, the detector output becomes

$$D_{1\times 1} = \Psi_{1\times N} S_{N\times 1} \tag{4.5}$$

or

$$d = \sum_{n=1}^{N} \psi_{1n} s_n \tag{4.6}$$

where the multiple-source information is coupled in the output of the single detector. Equation (4.6) implies that the source origination of diffuse photons cannot be

tracked unless the photons are differentiated prior to launching into the medium, or, in other words, unless the source channels are properly encoded.

When the sources in DOT are properly encoded, the discriminated signals corresponding to all source-detector pairs can be described intuitively by

$$D_{M\times N} = \Psi_{M\times N} E_{N\times 1} S_{1\times N} \tag{4.7}$$

where $E = \langle encod \rangle$ represents the encoding operation applied to the source channels:

$$\langle encod_i \rangle\ s_j = \begin{cases} \langle s_j \rangle & i = j \\ 0 & i \neq j \end{cases} \tag{4.8}$$

Substituting (4.8) into (4.7) for E gives

$$\begin{bmatrix} d_{11} & d_{12} & \cdots & d_{1N} \\ d_{21} & d_{22} & \cdots & d_{2N} \\ \vdots & \vdots & \cdots & \vdots \\ d_{M1} & d_{M2} & \cdots & d_{MN} \end{bmatrix} = \begin{bmatrix} \langle \psi_{11} s_1 \rangle & \langle \psi_{12} s_2 \rangle & \cdots & \langle \psi_{1N} s_N \rangle \\ \langle \psi_{11} s_1 \rangle & \langle \psi_{22} s_2 \rangle & \cdots & \langle \psi_{2N} s_N \rangle \\ \vdots & \vdots & \cdots & \vdots \\ \langle \psi_{11} s_1 \rangle & \langle \psi_{M2} s_2 \rangle & \cdots & \langle \psi_{MN} s_N \rangle \end{bmatrix} \tag{4.9}$$

Equation (4.9) indicates that under a proper detector decoding that matches with the source-encoding method, the signals corresponding to all source-detector pairs can be discriminated thoroughly.

4.2.2 Methods of Source Encoding and Detector Decoding for Diffuse Optical Tomography

Many source-encoding and detector-decoding methods have been demonstrated [31]. These methods fall into one or a combination of the following three categories.

4.2.2.1 Time-Based Multiplexing

Perhaps the most straightforward method of source encoding is sequentially turning on the sources, or time-series multiplexing [32, 33]. This time-based multiplexing is valid if the multiplexing interval is much greater than the time of photon flight, which is obviously obeyed for all biological tissues of finite size. This encoding technique can be described based on (4.7) as

$$D^{\tau}_{M\times N} = \Psi_{M\times N} T_{N\times 1} S_{1\times N} \tag{4.10}$$

The $T_{N\times 1}$ in (4.10) is an operator representing the time-based multiplexing of

$$T_{N\times 1} = \begin{bmatrix} \langle \delta(\tau - 1) \rangle \\ \langle \delta(\tau - 2) \rangle \\ \vdots \\ \langle \delta(\tau - N) \rangle \end{bmatrix} \tag{4.11}$$

where the discrete time impulse function δ is used to denote the turning-on sequencing of the source from 1 to N. The output of each detector at each multiplexing sequence is then

$$d_{mn} = \sum_{\tau=1}^{N} \psi_{m\tau} s_\tau \delta(\tau - n) = \psi_{mn} s_n \tag{4.12}$$

Equation (4.12) gives the decoded signal for a specific source-detector pair $n \rightarrow m$, which also means that the time-based multiplexing operation performs both source encoding and detector decoding instantaneously. The advantage of this time-based multiplexing technique for source encoding and detector decoding is that at any instance of source sequencing, each detector receives only the signal illuminated from one source; therefore, the maximum dynamic range of each photodetector (denoted by $I_{\max}$) is devoted exclusively to the detection of signals from a single source-detector pair. The disadvantage of this encoding/decoding technique is the potentially lengthy data acquisition for entire source-detector pairs at a total period of $(N-1) \cdot \Delta t_0$, where Δt_0 is the multiplexing timing for each step, under the condition that the signal-to-noise ratio integrated over the time of Δt_0 is sufficient. The vast majority of all optical tomography methods use this approach either to deliver light of single-band to multiple-source channels or to distribute light of multiple bands to single source channels.

4.2.2.2 Frequency-Based Multiplexing

Modulation frequency-based multiplexing is another commonly used source-encoding method [34–37]. In frequency-based multiplexing, the source intensities are modulated at different frequencies of $\omega_n = \omega_0 + \delta\omega_n$ upon the same base band of ω_0, under the valid assumption that the intensity modulation frequency does not vary when propagating through diffuse medium.

Similar to (4.10), the frequency-encoded signal at the detector output can be expressed by

$$D^{\omega}_{M\times N} = \Psi_{M\times N} F_{N\times 1} S_{1\times N} \tag{4.13}$$

where $F_{N\times 1}$ is an operator representing the frequency multiplexing of

$$F_{N\times 1} = \begin{bmatrix} <\cos\left[(\omega_0 + \delta\omega_1)t\right]> \\ <\cos\left[(\omega_0 + \delta\omega_2)t\right]> \\ \vdots \\ <\cos\left[(\omega_0 + \delta\omega_N)t\right]> \end{bmatrix} \tag{4.14}$$

and the output of each detector is approximately

$$d_m = \sum_{n=1}^{N} \psi_{mn} s_n \cos\left[(\omega_0 + \delta\omega_n)t\right] + k_{nm} \tag{4.15}$$

Note that the exact signal is not precisely a pure cosine wave for the response of the laser, and the detector to modulation is not entirely linear with the applied current. Here $\psi_{mn}s_n$ is the modulation depth and k_{nm} is the dc bias offset due to the fact that the laser must operate with a positive output. For frequency-based source encoding, the detector decoding of source-detector pair $n \rightarrow m$ is obtained by demodulation of d_m at ω_0 and bandpass filtering at $\delta\omega_n$, that is

$$d_{mn} = \psi_{mn} s_n \cos\left[\delta\omega_n t\right] \tag{4.16}$$

The advantage of source encoding and detector decoding by frequency multiplexing/demultiplexing is the gain in sampling speed by simultaneous measurement of signals from all source-detector pairs as a result of parallel light delivery. However, the frequency-encoded source signals must be directed to the same photodetector for photoelectronic conversion prior to applying any demodulation operation for signal decoding. When one detector collects signals from N source channels in parallel, the average dynamic range corresponding to one source-detector pair reduces to

$$I_{n\rightarrow m} = \frac{\sum_{n=1}^{N}\left(\psi_{mn} s_n\right)^2}{N} = \frac{I_{\max}}{N} \tag{4.17}$$

Therefore the average dynamic range available for each source-detector signal is linearly reduced with more sources adding on, and the lowest-level signals are potentially buried under the noise present in the higher-intensity signals. This is particularly problematic if the tissue volume being imaged is large, the absorption of the tissue is strong, and the distances between optodes have big variations. To fully understand the limiting factors in this type of system, an analysis of signal to noise would be required where the limiting contribution to noise in the ideal case is shot noise.

4.2.2.3 Wavelength-Based Multiplexing or Spectral Encoding

A wavelength-based multiplexing method for source encoding was introduced in 2005 [38, 39]. This method for source encoding refers to operating the sources at different wavelengths. The encoded signal after transmitting through the medium thus becomes

$$D^{\lambda}_{M\times N} = \Psi_{M\times N}\Gamma_{N\times 1} S_{1\times N} \tag{4.18}$$

where $\Gamma_{N\times N}$ is the wavelength-multiplexing or spectral-encoding operator having the structure of

$$\Gamma_{N\times 1} = \begin{bmatrix} <\lambda_1> \\ <\lambda_2> \\ \vdots \\ <\lambda_N> \end{bmatrix} \tag{4.19}$$

with $<\lambda_n>$, $n = 1, 2, \ldots, N$ representing the operating wavelength of the source. When a spectrometer is used at the detection side, the spectrally encoded signals can be spatially spread or decoded to provide measurement of

$$d_{mn} = \psi_{mn} s_n(\lambda_n) \tag{4.20}$$

for a source-detector pair $n \rightarrow m$. If the orientation of the detector array is set orthogonal to the spectral-spread direction, all source-detector pairs can be decoded completely in a two-dimensional pattern and acquired simultaneously by parallel photodetectors such as CCD. This approach performs decoding of all source-detector pairs prior to the photoelectronic conversion as compared with either time-based multiplexing or frequency-based multiplexing where the photoelectronic detection is performed along with or prior to the decoding. This feature of parallel light delivery renders the principle that adding on more sources will not cause reduction in the signal dynamic range of an individual source-detector channel. This is valid so long as the source spectra can be differentiated by the spectrometer and the number of photoelectronic conversion channels in the detector is greater than that of source channels. This configuration ensures that different photoelectronic detector elements sense different signals, and each detector's full dynamic range is maintained.

The major advantage of this wavelength-based source-encoding and detector-decoding method is the data-acquisition speed it could potentially reach without compromising the dynamic range of each detection channel. However, attention should be paid to the overall wavelength range used for source encoding. Contrary to time-based and frequency-based multiplexing methods, where all source channels are detected at a single wavelength, the source channels in wavelength-based multiplexing experiences potentially wavelength-dependent light propagation. This is due to the fact that in the NIR band of 650 to 900 nm, the absorption of hemoglobin is stronger and more wavelength variant in comparison to the water, even though the scattering may not be as wavelength-dependent for both hemoglobin and water. Therefore, in the spectral-encoding approach, the overall source wavelength band should be maintained at a small range, ideally less than 5 nm, in order to maintain relatively uniform tissue absorption among different source channels. This poses a limitation on source channels that can be encoded within the spectrometer resolution.

4.3 Techniques for Decoupling the Absorption and Scattering Contributions to the Photon Remission

Source encoding and detector decoding assure the discrimination of photons transported from a specific source to a detector. Microscopically, the photons could take any path from the source to the detector due to the strong scattering of NIR photons in biological tissue. Yet, statistical analyses demonstrate that macroscopically the highest probability of photon propagation takes a banana-shaped path connecting the source and the detector [40]. The banana shape gives a rough estimation of the path length of the majority of the photons arriving at the detector. The optical prop-

erties that DOT expects to retrieve contain both absorption and reduced- or transport-scattering coefficients. This requires knowledge not only of actual photon path length but also of the method of differentiating absorption and scattering contributions to the photon loss, both being evaluated by surface measurement of remitted photons. Theoretical breakthroughs and instrumentation advancements have demonstrated that time-resolved or time-domain detection and frequency-domain detection methods are capable of determining the photon path length and differentiating or decoupling absorption and reduced-scattering properties of the medium.

4.3.1 Time-Domain Detection

When a short light pulse (typically 2 to 5 ps for NIR DOT) is delivered to a purely absorptive tissue, the pulse detected after propagation will change in only the amplitude due to the attenuation, as depicted in Figure 4.1(a). When the same pulse is

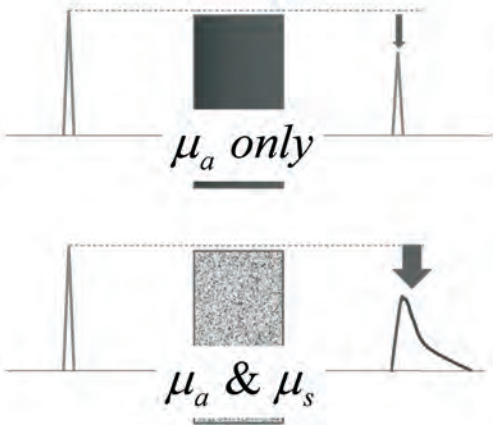

(a)

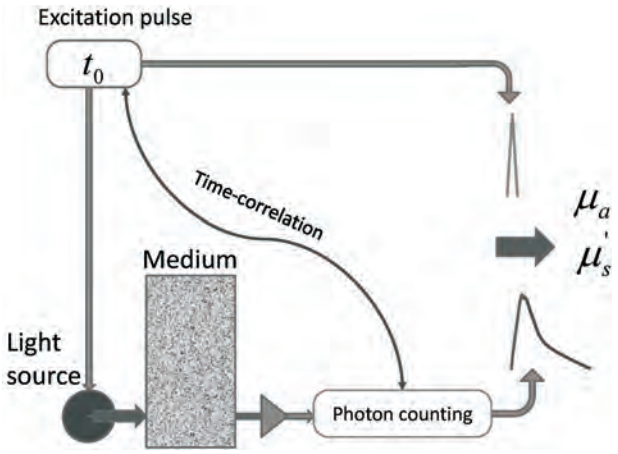

(b)

Figure 4.1 Time-domain DOT technique: (a) pulse width alteration by scattering medium compared with pulse attenuation by purely absorptive medium, and (b) schematic illustration of time-domain detection of light pulse propagating through a turbid medium.

delivered to an absorptive and highly scattering tissue, the family of photon paths produced by scattering leads to broadening of the pulse in addition to the amplitude attenuation of the pulse. The time $< t >$ of the temporal point spread function (TPSF) at which the maximum detected intensity occurs relative to the input pulse is the mean arrival time of photons, and this may be used, together with velocity of light c in tissue to calculate a mean optical path length of $< ct >$ [28]. Use of the measurement of time gives the method its alternative name, *time-resolved* or *time-of-flight detection*.

When the diffusion approximation is incorporated into the radiative transport equation, the time-domain photon-diffusion equation may be written as [41]

$$\frac{1}{c}\frac{\partial}{\partial t}\phi(\vec{r},t) = \vec{\nabla}\cdot\left(D\vec{\nabla}\phi(\vec{r},t)\right) - \mu_a\phi(\vec{r},t) + S(\vec{r},t) \tag{4.21}$$

where $\phi(\vec{r},t)$ is the diffuse photon fluence rate, c is the speed of light in the tissue, D is the diffusion coefficient,

$$D = \frac{1}{3\left[\mu_a + (1-g)\mu_s\right]} \tag{4.22}$$

μ_a is the absorption coefficient, μ_s is the scattering coefficient, g is the mean cosine of the scattering angle, and $S(\vec{r},t)$ is the photon source. The term $(1 - g)\mu_s$ is often denoted by a reduced scattering coefficient of μ_s' to represent the assembled equivalent isotropic scattering property of tissue even though each scattering event is anisotropic.

For a short pulse from a point source, $S(\vec{r}, t) = \delta(0, 0)$, it may be shown that the mean photon path length for a tissue slab of thickness d is [28]

$$<ct> = \left(4\pi_a D\right)^{-1/2}\frac{(d-z_0)\exp\left(2z_0\sqrt{\mu_a/D}\right) - (d+z_0)}{\exp\left(2z_0\sqrt{\mu_a/D} - 1\right)} \tag{4.23}$$

where $z_0 = [(1 - g)\mu_s]^{-1}$ is the depth between the actual source location of initial directional launching and the position of an imaginary point from which the photons can be considered to be becoming isotropic. Equation (4.23) indicates the feasibility of determining the absorption μ_a and diffusion coefficient D (predominantly the reduced scattering) by multiple measurements of mean photon path length or by fitting to the single measurement data using "time-of-flight" estimation.

Figure 4.1(b) gives the simplified instrumentation scheme for a time-domain DOT measurement. Two fundamental requirements of the instrumentation are generation of short-pulse light and time-correlated measurement of the pulse width and amplitude after tissue propagation. Fast-streaking camera or other slower single-photon counting devices may be used for the detection. It is acknowledged that time-domain measurement leads to the richest or the most accurate information about the tissue optical properties; however, the instrumentation is typically expensive and difficult [42, 43].

4.3.2 Frequency-Domain Detection

When a light of amplitude modulation (typically 100 MHz to 1 GHz for NIR DOT) is delivered to purely absorptive tissue, both the dc and ac levels of the light after detection will be attenuated with no alteration of its phase, as depicted in Figure 4.2(a). When the same light is delivered to an absorptive and highly scattering tissue, the multiple photon scattering leads to a delay of the modulation phase in addition to the attenuation of dc and ac levels. The phase delay and ac/dc attenuation rate can also be used to calculate the mean optical path length of photons for calculation of absorption and the scattering contribution to the diffuse photon propagation [44].

The Fourier transform of time-domain diffusion (4.21) will lead to the frequency-domain diffusion equation of [43, 44]

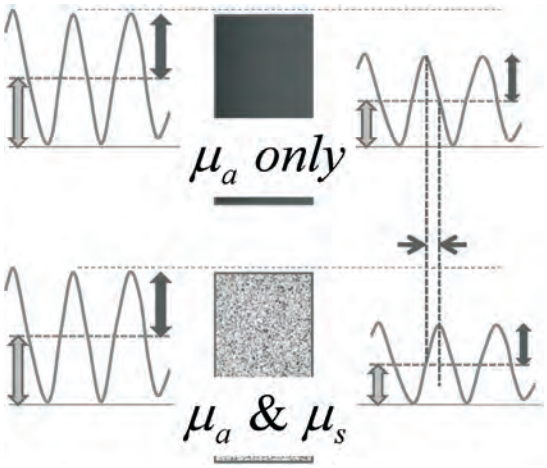

(a)

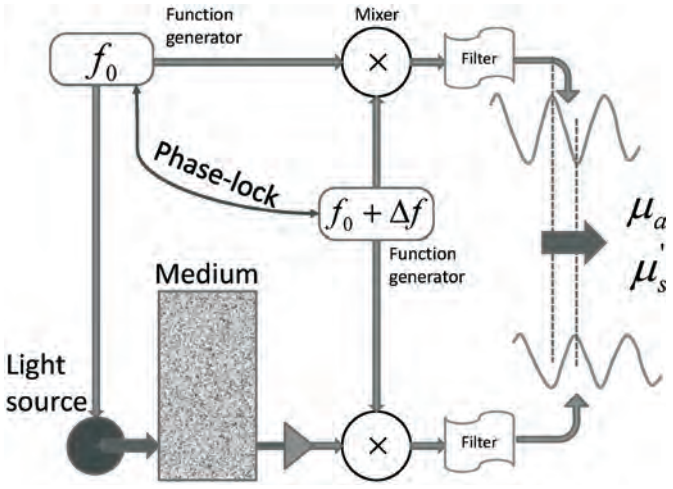

(b)

Figure 4.2 Frequency-domain DOT technique: (a) modulation phase delay by scattering medium compared with modulation amplitude attenuation by purely absorptive medium, and (b) schematic illustration of frequency-domain detection of light propagating through a turbid medium.

$$\frac{1}{c}\frac{\partial}{\partial t}\phi(\vec{r},\omega) = \vec{\nabla}\cdot\left(D\vec{\nabla}\phi(\vec{r},\omega)\right) - \left(\mu_a + i\frac{\omega}{c}\right)\phi(\vec{r},\omega) + S(\vec{r},\omega) \tag{4.24}$$

where ω is the angular frequency of the light modulation. For infinite medium and an amplitude modulation of the light at

$$I = I_{dc} + I_{ac}\sin(\omega t - \Phi) = I_{dc} + I_{ac}\sin(2\pi\nu t - \Phi) \tag{4.25}$$

it is found that the detector measurement of steady-state photon density, the amplitude of photon-density modulation, and the phase shift of the photon-density modulation can be expressed by [28]

$$U_{dc} = \frac{S}{4\pi D}\frac{\exp\left[-r\left(\frac{\mu_a}{D}\right)^{1/2}\right]}{r} \tag{4.26}$$

$$U_{ac} = \frac{S\frac{I_{ac}}{I_{dc}}}{4\pi\nu D}\frac{\exp\left[r\,\mathrm{Re}(k)\right]}{r} \tag{4.27}$$

$$\Phi = r\,\mathrm{Im}(k) + \Phi_s \tag{4.28}$$

where

$$k = -\left(\frac{\mu_a - i2\pi\nu}{D}\right)^{1/2} \tag{4.29}$$

and r is the source-detector separation. More complicated expression of similar measurements for a semiinfinite medium can be found in [44–46]. By single measurement of the changes in both the phase and modulation, the absorption and reduced-scattering properties of the bulk tissue can be retrieved.

Frequency-domain instrumentation involves amplitude modulation of the light at frequencies on the order of hundreds of megahertz, wherein the phase change of photon density caused by tissue scattering over several centimeters of tissue volume may be resolved. In practice, the frequency-domain measurement is usually done by downshifting the frequency to the kilohertz or tens-of-kilohertz range to take advantage of much-reduced sampling requirements. This requires demodulation of the light propagating through the medium by a phase-locked local oscillator signal. The downshifted signal passing through the scattering medium is compared with a reference signal that is demodulated directly from the source modulation frequency to retrieve the phase shift and ac/dc attenuation. The light source used for frequency-domain detection is usually laser diode, which can be conveniently modulated, and the photodetector is most frequently chosen between photomultiplier tube (PMT) and avalanche photodiode (APD). PMT is known to have excellent sensitivity and gain, while APD generally has better performance in terms of dynamic range.

4.3.3 Continuous-Wave Detection

The continuous-wave DOT detection method can be considered the extreme case of time-domain measurement in (4.21) when $t \to \infty$; therefore, the photon density becomes time invariant. The continuous-wave DOT method can also be considered the special case of frequency-domain measurement in (4.24) when $\omega \to 0$; thus, the photon density contains only the dc component. Instrumentation for continuous-wave DOT measurement is the simplest since it needs only source and detector running at steady state or at low-frequency kilohertz range modulation [36, 47–49].

At one time, it was generally argued that CW measurement provides limited information regarding tissue optical properties and cannot reliably recover the absolute values of absorption and reduced-scattering properties of the tissue even with very careful calibration due to lack of phase information which is critical to the determination of photon path length. However, recent studies have demonstrated that when a complicated image-reconstruction method is used, the absorption and reduced-scattering properties may be reconstructed separately from continuous-wave measurement [50, 51].

4.4 Principles for Determining the Heterogeneity of Optical Properties

When the launching position and path of the photons can be determined, the global optical properties along the photon trajectory may be quantified. However, without a tomographic visualization of the optical properties of the tissue volume, the physiological information that diffuse photon detection can provide is limited since the potential existence of optical heterogeneity within a bulky tissue volume is not localized; therefore, correlating the abnormal optical properties with physiological malfunctions tends to be inexplicit.

4.4.1 Tomographic Image Reconstruction and Prior Utilization

Tomographic imaging or cross-sectional mapping of optical heterogeneity in DOT can be achieved by integration of projection measurements at multiple angles as illustrated in Figure 4.3. The image reconstruction may be conducted by assuming linear projection of the measurement data as in X-ray tomography [52] or by use of a model-based iterative approach [6, 8, 9]. Model-based DOT image reconstruction involves solving the photon-diffusion equation with numerical methods such as the finite-element method and iteratively minimizing the error between the measurement and the model prediction to recover the piecewise optical properties within a given imaging volume [53–55]. The flow chart of a typical model-based image-reconstruction routine is sketched in Figure 4.4(a).

The forward estimation task based on the light-propagation model is known to be sensitive to small perturbations in the light measurements (which is the basis of superior contrast in DOT imaging), not all of which are caused by the heterogeneity changes in tissue optical properties. The ill-posed and underdetermined features of the DOT inverse problem, coupled with this ill-conditioning, imply that the accuracy of retrieving optical heterogeneity (including location, size, and contrast) inside the tissue volume is dependent upon many issues such as the stability of surface mea-

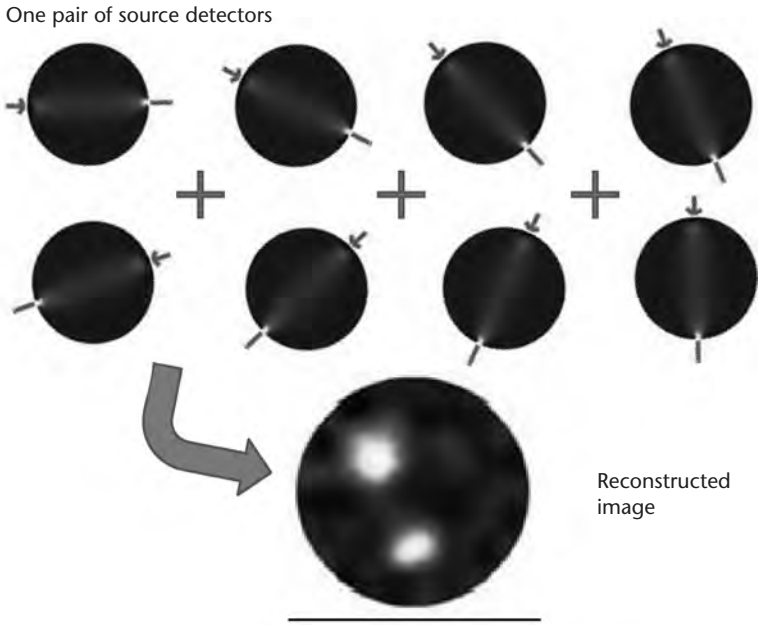

Figure 4.3 Illustration of image reconstruction in DOT where integration of the multiple-angle projection measurements leads to the localization of optical heterogeneity in the imaging volume, similar to back-projection in CT. (Courtesy of Brian W. Pogue.)

surement and the number of iterations. Investigations demonstrated that significant improvement in the stability and accuracy of the reconstruction process can be obtained by including prior information in the iterative minimization process [56–61]. Studies have shown that anatomical information from other modalities, such as ultrasound, MRI, or CT, when used in the reconstruction procedure, can improve the stability of the reconstruction and result in faster convergence, better localization, more accurate optical properties, and higher spatial resolution [62–65].

The spatial (also known as structural or anatomic) prior information can be utilized within the NIR DOT image-reconstruction scheme in two forms. The hard prior illustrated in Figure 4.4(b), also known as region-based (or parameter-reduction) reconstruction, utilizes the prior anatomic regions information to reduce the large number of unknown parameters into a few unknown parameters by assuming that the optical distribution within each region is constant [61]. Since the number of the unknowns is dramatically reduced, the computation becomes efficient. In the soft prior, the spatial information is instead incorporated within the image-reconstruction algorithm in a form of regularization [see Figure 4.4(b)]. This type of a priori information in effect relates the recovery of each unknown parameter within the reconstruction to other unknowns within the same defined region [61].

Another type of prior for DOT reconstruction when multispectral measurement is performed incorporates the known spectral behavior of tissue chromophores and Mie scattering theory as constraints. This type of prior-guided NIR image reconstruction uses multiwavelength measurements simultaneously to compute images of constituent parameters without intermediate recovery of optical properties. Simula-

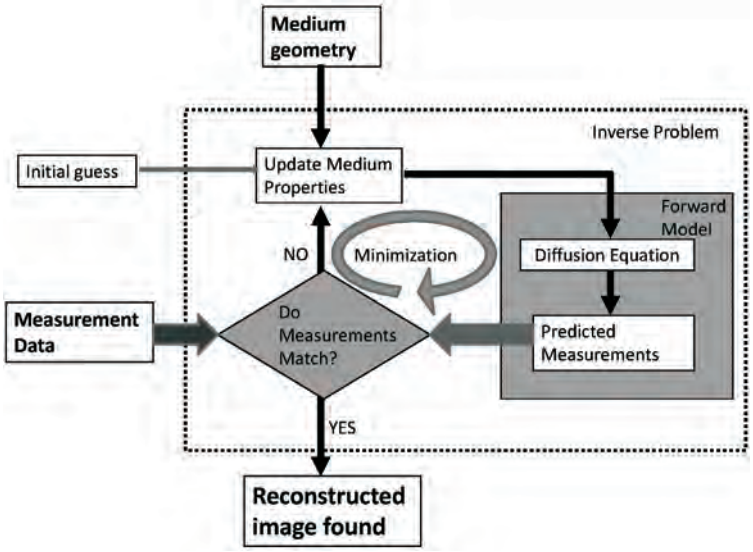

(a)

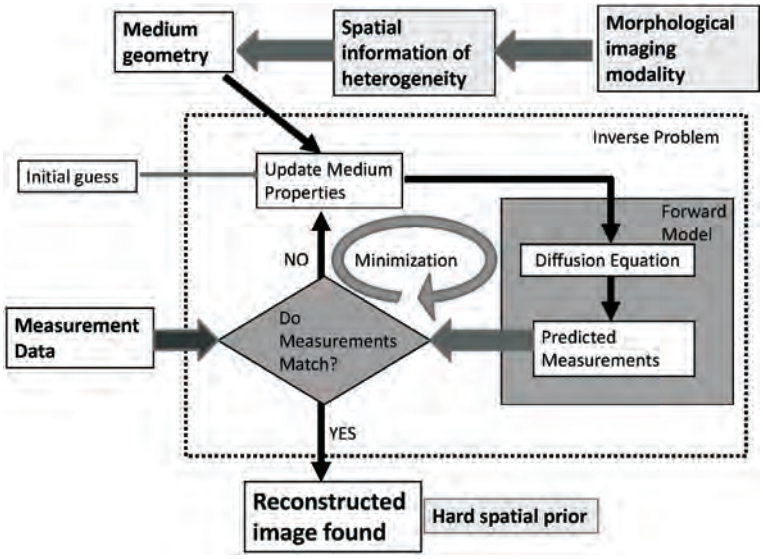

(b)

Figure 4.4 Model-based NIR image reconstructions: (a) typical iterative image reconstruction based on photon propagation model, (b) NIR image reconstruction by use of hard spatial prior, (c) NIR image reconstruction by use of soft spatial prior, and (d) NIR image reconstruction by use of spectral prior.

tion studies have shown that the combination of spatial and spectral priors improves the accuracy and quality of NIR images [49, 66]. The spectral prior obtained by including the intrinsic behavior of tissue chromophores and scattering plays a more important role in preserving quantitative functional parameter estimates by DOT. It has been demonstrated that a synergy between these two priors yields the most accu-

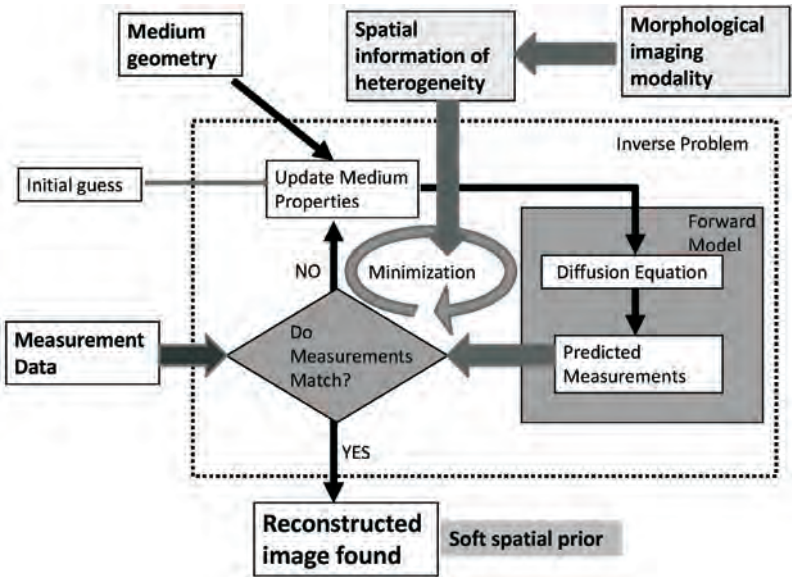

(c)

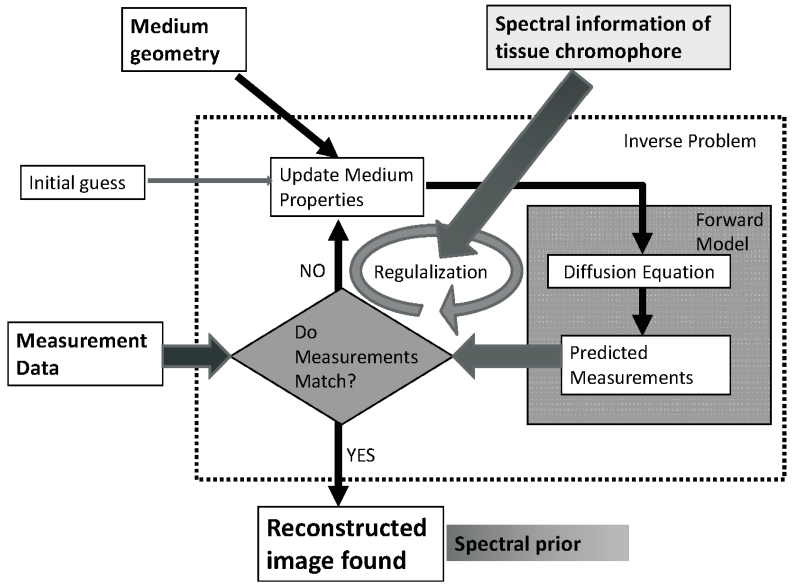

(d)

Figure 4.4 (continued)

rate characterization of absolute tissue optical properties currently available [49, 67, 68].

4.4.2 Diffuse Optical Tomography Imager in the Context of Multimodality Imaging

The functional or spectroscopic information of near-infrared DOT is often compromised by the limitations inherent to the ill-posed iterative image reconstruction

required for diffuse photon detection. Combining DOT with other imaging modalities that are anatomically accurate can not only correlate the DOT functional contrast with the spatial anatomy of the lesion but also use the structural delineation of the lesion to guide and constrain the DOT image reconstruction. In terms of the morphological imaging modalities that can be cohesively integrated with DOT for complimentary imaging as well as the prior DOT reconstruction, there have been a few choices out of some standard techniques mainly used for anatomic imaging, but arguably the most-successful modalities are US [69–73] and MRI [59, 63–65, 74–76]. The following section briefly reviews the instrumentations leading to the integration of DOT with US and MRI for breast cancer imaging, which are the representative examples of the DOT instrumentation advancement and growing impact of DOT technology in multimodality clinical imaging.

4.4.2.1 Diffuse Optical Tomography Integrated with Ultrasound

Ultrasound imaging is frequently used as an adjunct tool to mammography in differentiating cysts from solid lesions. Ultrasound also plays an important role in guiding interventional procedures such as needle aspiration, core needle biopsy, and prebiopsy needle localization [69].

Several studies have been reported on the instrumentation technology of combining DOT with US [69–72]. The system developed at the University of Connecticut is implemented by simultaneously deploying optical sensors and a commercial US transducer mounted on a handheld probe and utilizing coregistered lesion structure information provided by US to improve the inverse optical imaging reconstruction. The handheld hybrid probe consists of a commercial US transducer located in the center and the NIR source-detector fibers distributed at the periphery [see Figure 4.5(a)]. The NIR imager consists of 12 pairs of dual-wavelength (780 and 830 nm) laser diodes and eight photomultiplier tubes (PMTs) for detection. The laser diodes' outputs were amplitude modulated at 140 MHz, and the detector outputs were demodulated to 20 kHz. The demodulated signals were further amplified and bandpass filtered at 20 kHz. A reference signal of 20 kHz was also generated by directly mixing the detected radiofrequency (RF) signals with the RF signal generated from the oscillator.

The NIR reconstruction takes advantages of US localization of lesions and segments the imaging volume into a finer grid in lesion region L and a coarser grid in nonlesion background region B [see Figure 4.5(b)]. A modified Born approximation is used to relate the scattered field measured at each source and detector pair to total absorption variations at wavelength in each volume element of two regions within the sample. The absorption distribution at each wavelength is obtained by dividing total absorption distribution changes of lesion and background regions, respectively, by different voxel sizes in lesion and background tissue regions. This dual-mesh scheme results in well-conditioned inversion and convergence of the image reconstruction in a few iterations [69, 71, 73].

An example of a DOT/US image is given in Figure 4.5(c, d) for an early-stage invasive ductal carcinoma [69]. US showed a nodular mass with internal echoes, and the lesion was considered suspicious. The estimated lesion diameter measured from the US image was 8 mm. US-guided core needle biopsy revealed intraductal and

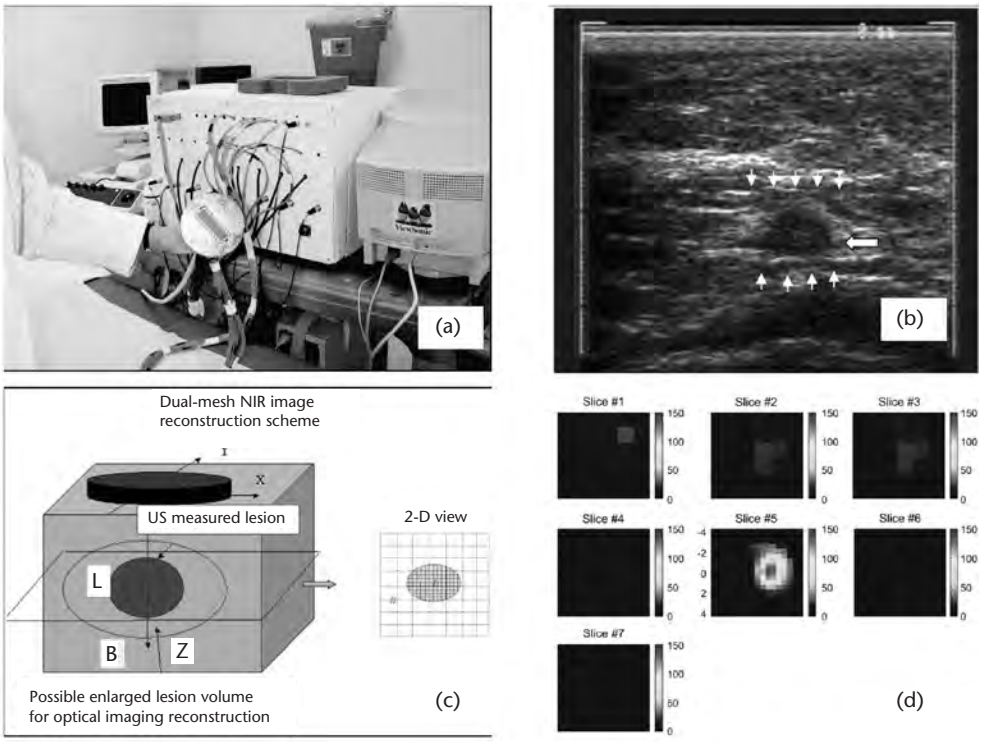

Figure 4.5 (a) Prototype of the handheld combined NIR/US imager developed at the University of Connecticut is shown. (b) The entire imaging volume is segmented into lesion (L) and background (B) regions. The fine imaging grid is used for the lesion region, and the coarse grid is used for the background. (c) NIR/US images of a nonpalpable lesion in a 55-year-old woman are shown. US showed a nodular mass with internal echoes, and the lesion was considered suspicious. The maps of total hemoglobin concentration distribution correspond to slices from 0.7 cm underneath the skin surface to the chest wall, with 0.5 cm spacing. The lesion is well resolved in slice 5. (*From:* [69]. © 1998 Elsevier. Reprinted with permission.)

infiltrating ductal carcinoma. The total hemoglobin concentration distribution computed from optical absorption maps at 780 and 830 nm wavelengths are shown, with the first slice 0.7 cm deep into the breast tissue from the skin surface and the last slice closer to the chest wall at slice spacing of 0.5 cm. The horizontal and vertical axes of each slice are spatial x and y optical probe dimensions of 9 cm. The lesion is well resolved in slice 5, and the measured maximum total hemoglobin concentration for the lesion is 122 mmol/L, the average measured within full width and half maximum (FWHM) is 91 mmol/L, and the measured average background hemoglobin concentration is 14 mmol/L.

4.4.2.2 Diffuse Optical Tomography Integrated with Magnetic Resonance Imaging

The NIR/MRI imaging system [Color Plate 9(a)] developed at Dartmouth College [74] consisted of six laser diodes (660 to 850 nm), which were amplitude modulated at 100 MHz. The bank of laser tubes was mounted on a linear translation stage that

sequentially coupled the activated source into 16 bifurcated optical-fiber bundles. The central seven fibers delivered the source light, while the remaining fibers collected transmitted light and were coupled to photomultiplier tube (PMT) detectors. For each source, measurements of the amplitude and phase shift of the 100 MHz signal were acquired from 15 locations around the breast. The fibers extended 13m [Color Plate 9(b)] into a 1.5-T whole-body MRI (GE Medical Systems), and the two data streams (i.e., NIR and MRI) were acquired simultaneously. The open architecture breast array coil (Invivo, Orlando, Florida) houses the MR-compatible fiber-positioning system [Color Plate 9(c)]. Two fiber-breast interface prototypes were constructed. The first, pictured in Color Plate 9(d), allows each of the 16 fibers to move independently in a radial direction, and tissue contact is enforced with bronze compression springs. The second, shown in Color Plate 9(e), maintains a circular breast circumference and allows more user control.

One set of MRI-guided NIR reconstruction images is shown in Color Plate 9(f). The MRI images are axial and coronal T1-weighted slices of a breast. Reconstructed images of chromophores and scatter parameters from simultaneously acquired NIR measurements (left to right) are as follows: total hemoglobin concentration ([HbT], μM), hemoglobin oxygen saturation (S_tO_2, %), water fraction (H_2O, %), scattering amplitude (A), and scattering power. Interestingly, the spatial distributions in the NIR images do not exactly match the segmented MRI regions in all cases, and some heterogeneity occurs, although the predominant effect is the significant change in optical properties that results between the adipose and fibroglandular boundaries. The technique provides high-resolution images of both tissue structure through MRI and tissue function through NIR contrast.

The combined NIR/US and NIR/MRI modalities demonstrated the increasing probability that DOT will provide high sensitivity and specificity values to diagnostics when combined with other imaging systems.

4.5 Novel Approaches in Instrumentation of Diffuse Optical Tomography: Source Spectral Encoding

4.5.1 Discrete Spectral Encoding by Use of Multiple Laser Diodes

The principle of parallel source delivery based on wavelength multiplexing or spectral encoding is initially demonstrated by use of multiple laser diodes (LDs) [38, 39]. In this approach, each LD operates at a unique wavelength as shown in Color Plate 10 and Figure 4.6(a, b). The unique wavelength corresponds to $<\lambda_n>$ ($n = 1, 2, \ldots, N$) in (4.19). It is imperative to maintain small wavelength separation among the source channels as discussed previously. Actually, the LDs can be spectrally encoded at close wavelength separation, simply and effectively, by use of a number of single-mode diodes manufactured for the same spectral band whose emission wavelengths can be varied slightly by adjusting the laser operating temperature. The wavelength of the LD is a function of both operating temperature and driving current. The wavelength stability of the LD against temperature and current may be expressed by

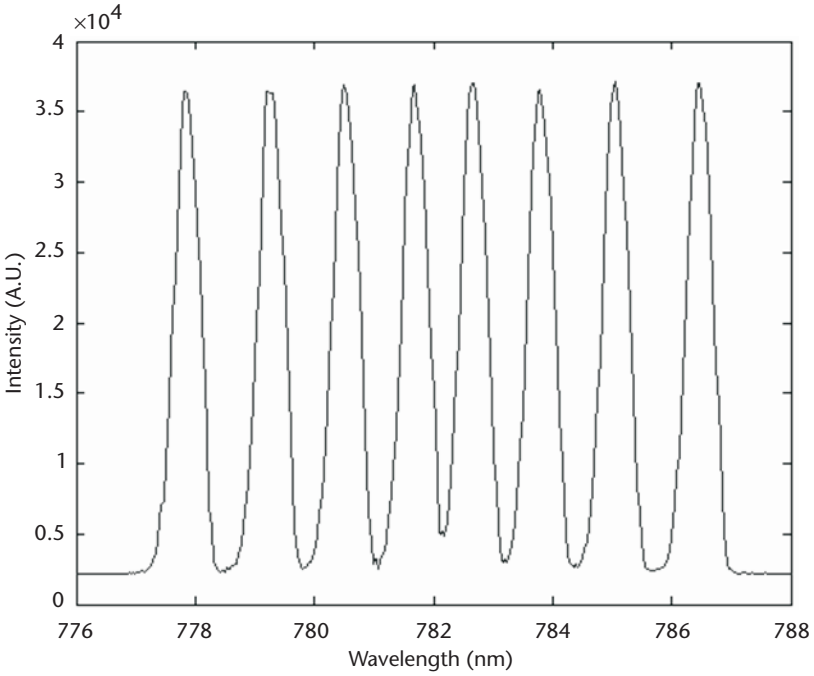

(a)

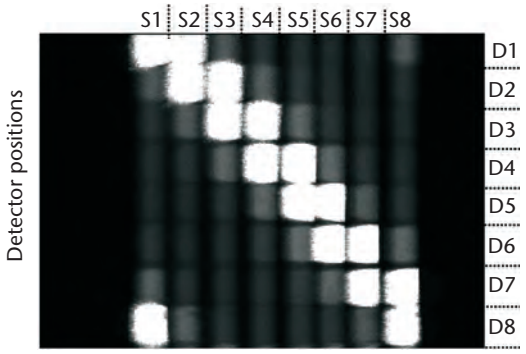

(b)

Figure 4.6 The spectral-encoding NIR tomography system developed by Dartmouth NIR imaging group: (a) the source spectral-encoding profile, where the emission wavelengths of eight laser diodes are operated at approximately 1.25 nm separation, and (b) the completely decoded signals acquired by CCD after spectrometer corresponding to eight sources and eight detectors in Color Plate 10.

$$\frac{d\lambda}{dT} = a_1 - \frac{a_2}{T_0} \tag{4.30}$$

where a_1 corresponds to a red shift in wavelength with temperature at constant current, and a_2 corresponds to a blue shift in wavelength with current at constant temperature. By operating the LD in constant current mode and adjusting the LD temperature, the emission wavelength can be adjusted with a typical tuning sensitivity of 0.1 to 0.3 nm/°C [77]. In this LD-based spectral-encoding system, a source

spectral separation of 1.25 nm is achieved among eight source channels. The source spectral separation can be reduced if the precision of LD temperature control is improved and mode hopping of LD can be suppressed.

The parallel source illumination and complete decoding of all source-detector pairs allow rapid acquisition of the DOT data by imaging devices like CCD. Figure 4.6(c) shows the data pattern of parallel source-detector decoding that is available for CCD detection. This LD-based spectral-encoding system has achieved a 35-Hz frame rate of data acquisition in a medium of 27 mm in diameter, which is believed as the first DOT system of performing video-rate sampling.

4.5.2 Imaging Examples of Spectral-Encoding Rapid NIR Tomography

Video-rate NIR imaging allows real-time sampling of transient changes in tissue optical properties that may be linked to fast physiological responses such as tissue permeability variation. One example is given in Figure 4.7, where the images were taken when diluted ink as an optical absorber was continuously injected to Intralipid solution contained within a hole of solid tissue phantom. The instantaneous absorption coefficients of the solution over 10 seconds are plotted with the inset showing the images of the phantom at six discrete timings. Slow ink injection started after 2 seconds and stopped at 9 seconds. A total of 350 frames were taken over 10 seconds. The gradual increasing of the absorption coefficient after the ink injection and the reaching of a plateau before stopping the ink injection are very

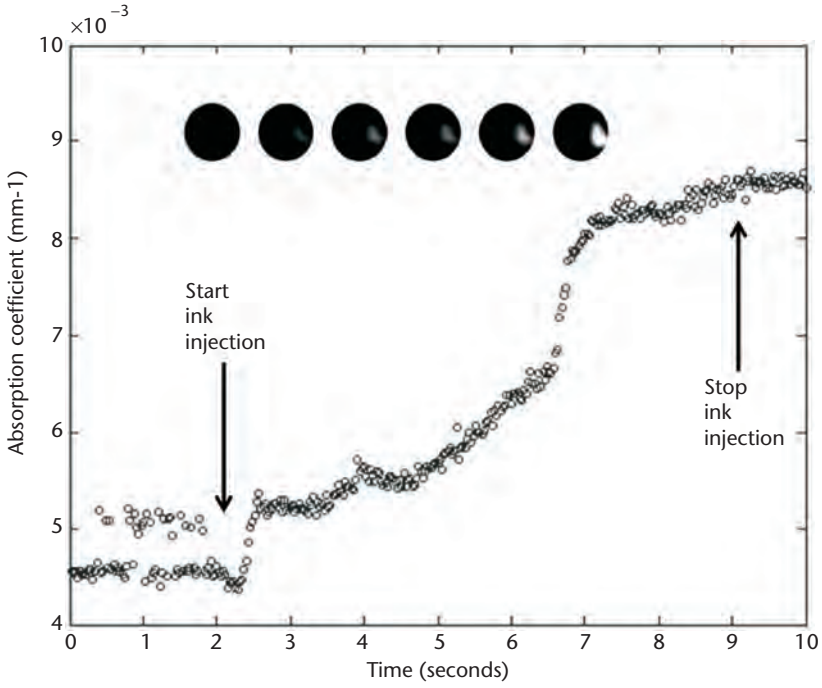

Figure 4.7 Examples of video-rate NIR tomography imaging. Images of diluted-ink injection into the Intralipid solution held in a hole of a solid phantom. Continuous changes of the light absorption during ink injection have been successfully captured. The inset shows the images at 2, 3, 4, 5, 6, and 7 seconds.

clearly captured. Such "snapshot" capturing of spatial absorption variations and time-resolved measurements of localized transient absorption changes is critical for dynamic imaging of rapid perfusion changes in biological tissues by DOT.

Figure 4.8 shows in vivo imaging of tumor and hemodynamic responses by this video-rate NIR system. A tumor-bearing rat leg was imaged in Figure 4.8(a), where the bigger and brighter spot at the bottom was the implanted solid prostate tumor, and the smaller spot at the top was the tail. The implanted tumor has clear elevated contrast compared with the normal tissue. In Figure 4.8(b), a mouse leg was utilized to image the blood pulsation in the muscle. Both legs were imaged successively, with one leg having compromised blood flow due to blockage of the iliac artery, while the other leg had normal blood flow. The tomographic images of these legs are shown in Figure 4.8(b), with each pair of images being one of a sequence of images at 1/35th of a second. The blood flow pulsation in the left leg can be seen between images 3 and 4 as a successive decrease in overall intensity, whereas the intensity of pulsation is significantly less in the right leg [78].

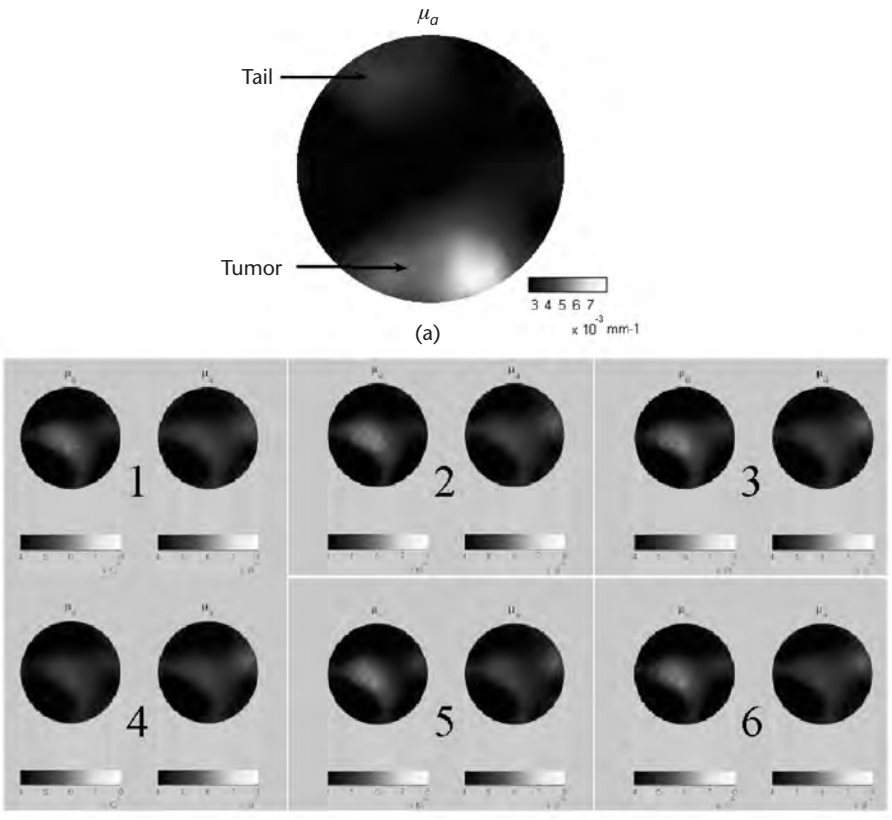

Figure 4.8 In vivo images taken with this spectral-encoding video-rate NIR system. (a) Image of rat tumor. The tumor was at the lower half of the FOV, and the tail was at the top. (b) Tomographic images of the two legs of a mouse at successive time points, with one frame every 1/35th of a second. The leg at left in each pair of frames was normal, and the leg at right in each pair of images had the iliac artery blocked. The lower overall absorption coefficient is apparent in the leg at right, and the pulsation in the leg at left is more apparent between frames 3, 4, and 5. This pulsation is due to blood flow.

4.5.3 Spread Spectral Encoding by Use of Single Wideband Light Source

Alternately, spectral encoding can be implemented by use of a low-coherence (implying a finite or wide-bandwidth) light source. The spectrum of a wideband light source can be dispersed by optical components, such as a grating, and collimated thereafter to form a one-dimensional spatial spectral distribution (see Color Plate 11). The linear spatial distribution of dispersed spectral components can be coupled to a fiber bundle wherein the light delivered to each fiber has a small wavelength offset from the neighboring ones. This configuration gives a spread spectral encoding of the source channels in comparison to the discrete spectral encoding from multiple LDs. In spread spectral encoding, the dimension of the collimated beam strip at the fiber bundle facet plane is determined by

$$L_{FWHM} = 2f\tan(\Delta\beta) \approx \frac{f \cdot \Delta\lambda_{FWHM}}{p\sqrt{1-(\lambda_0/p-\sin\alpha)^2}} \tag{4.31}$$

where f is the focal length of the collimating lens following the grating dispersion, $\Delta\beta$ is the half of the angular dispersion of the low-coherence source by the grating, $\Delta\lambda_{FWHM}$ is the FWHM spectral bandwidth of the source, λ_0 is the center wavelength of the source, p is the grating period, and α is the beam incident angle with respect to the grating normal. For a linear fiber bundle consisting of N fibers aligned side by side, the total spectral band coupled to the fiber bundle is

$$\Delta\lambda_{bundle} = N \cdot \Delta\lambda_{fiber} = N \cdot \frac{d_{fiber}}{L_{FWHM}} \cdot \Delta\lambda_{FWHM} = N\frac{d_{fiber}}{f} p\sqrt{1-(\lambda_0/p-\sin\alpha)^2} \tag{4.32}$$

where $\Delta\lambda_{fiber}$ is the bandwidth coupled to each fiber, and d_{fiber} is the diameter of one fiber. The spread-spectral-encoding operator can be expressed by (4.19) with argument $<\lambda_n>$ being represented by

$$<\lambda_n> = <\lambda_0 + \left[n - \frac{N+1}{2}\right] \cdot \Delta\lambda_{fiber}> \tag{4.33}$$

where the total number of the bundled fibers N is assumed to be even, and the overall spectral band coupled to the fiber bundle is assumed to be centered at λ_0.

The use of a low-coherence source gives a "spread" spectral encoding among the fibers for parallel illumination unto the tissue. A single light source is used to couple to all these channels; therefore, a potential trade-off exists between the number of channels and the power coupled to each channel. On the other hand, the use of a single light source for spread spectral encoding provides several unique characteristics in comparison to the LD-based spectral-encoding approach. First, the wavelength difference between the neighboring channels is generated by the grating dispersion of a single light source; therefore, the spectral encoding coupled to the fibers is always constant, and none of the coupled bands will cross over to the neighboring ones, which may happen in LD based spectral encoding due to spontaneous mode hopping of each individual LD. The spread spectral encoding is thus a shift-free configu-

ration that ensures the decoding of the source-detector signal at all times. Second, the interchannel intensity profile always follows the source power spectrum; therefore, the spontaneous channel-to-channel intensity fluctuation can be minimized compared with LD-based configuration, wherein the intensity of each LD is spontaneously fluctuating. This may lead to substantially confined or reduced reconstruction uncertainty. Third, the linear fiber bundle used for source coupling can be fabricated with bare or thinly coated fibers, which makes it feasible to arrange the fibers into a circular array inside a small probe for endoscopic interrogation that extends NIR tomography to imaging of internal organs [79]. The implementation of NIR optical tomography to endoscopic mode would have been difficult with conventional methods, including the LD-based spectral-encoding technique, because the separate coupling of each LD to a connector-terminated fiber or light guide is rather bulky, and integrating many channels of such jacketed fibers inside an endoscopic probe is difficult.

4.5.4 Light Sources for Spread Spectral Encoding

There are at least three parameters to consider for the use of a low-coherence or wideband source in spread spectral encoding: (1) the center wavelength, (2) the spectral bandwidth, and (3) the power. A center wavelength around 800 nm is required as NIR tomography operates in the neighborhood of this band. A narrow bandwidth of less than10 nm is preferred for coupling to the fiber bundle to minimize the wavelength-dependent absorption variation that would occur among the source channels. A high power of tens of milliwatts is needed to provide sufficient illumination to each channel following the segmentation of the light power among fibers by spectral encoding. A number of low-coherence sources are available on the market. Among these sources, the light-emitting diode (LED) can provide hundreds of milliwatts in a narrow bandwidth of several nanometers, but the collimation and coupling of LED emission into a fiber for grating illumination is rather difficult. A white-light source like a tungsten or halogen lamp provides tens of watts across hundreds of nanometers; however, coupling such a source into small fibers is always highly problematic. A fiber-based stimulated-emission-amplifier source may provide high power for low-coherent light illumination; nevertheless, this type of source is mostly centered around 1,300 or 1,550 nm. A pulsed-light source like the femtosecond Ti:sapphire laser is perhaps the most powerful within a narrow bandwidth, but this type of source is still currently quite expensive or bulky, although future generations may be more attractive.

Superluminescent diode (SLD) [or superluminescent LED (SLED)], is a light-emitting diode in which there is stimulated emission with amplification but insufficient feedback for oscillations to build up to achieve lasing action [80]. SLDs have similar geometry to LDs but no built-in optical feedback mechanism as required by an LD to achieve lasing action for amplification of narrow modes. SLDs have structural features similar to the edge-emitting LED (ELED) that suppresses lasing action by reducing the reflectivity of the facets. An SLD is essentially a combination of LD and ELED [81, 82].

An idealized LED emits incoherent spontaneous emission over a wide spectral range into a large solid angle. The unamplified light emerges in one pass from a depth limited by the material absorption. The LED output is unpolarized and increases linearly with input current. An idealized LD emits coherent stimulated emission (and negligible spontaneous emission) over a narrow spectral range and solid angle. The light emerges after many passes over an extended length with intermediate partial mirror reflections. The LD output is usually polarized and increases abruptly at a threshold current that provides just enough stimulated gain to overcome losses along the round-trip path and at the mirrors. In an idealized SLD, however, the spontaneous emission experiences stimulated gain over an extended path and, possibly, one mirror reflection, but no feedback is provided. The output is low coherent compared with an LD due to the spontaneous emission; on the other hand, it is at high power with respect to an LED because of the stimulated gain. The SLD output, which may be polarized, increases superlinearly versus current with a knee occurring when a significant net positive gain is achieved [83].

In the last decade, SLDs at several wavelength options have been implemented extensively in low-coherence interferometry [84–89] and optical coherence tomography techniques [29, 90–93] owing to its relatively high power available on the order of 10 mW and a bandwidth of tens of nanometers that corresponds to a low temporal coherence on the order of 10 μm. The spread-spectral-encoding method presented in this work demonstrates that SLD sources are also applicable to NIR diffuse optical tomography.

4.5.5 Characteristics of Spread Spectral Encoding

4.5.5.1 The Spectral Band and Power Coupled into the Linear Fiber Bundle

Because single source is used, the spectral bandwidth and power coupled to the fibers are associated. Consider an SLD source with a Gaussian spectrum profile of

$$S_0(\lambda) = \frac{2\sqrt{\ln 2/\pi}}{\Delta\lambda_{FWHM}} \exp\left[-4\ln 2\left(\frac{\lambda-\lambda_0}{\Delta\lambda_{FWHM}}\right)^2\right] \tag{4.34}$$

and assume that only the middle portion of the dispersed beam is coupled to the fiber bundle and that the coupled spectrum profile is essentially a Gaussian spectrum truncated on both sides. The percentage of the spectrum power remaining in this truncated Gaussian spectrum with respect to the SLD source power is determined by

$$\frac{P_{bundle}}{P_{source}} = erf\left(\sqrt{\ln 2}\cdot\frac{\Delta\lambda_{bundle}}{\Delta\lambda_{FWHM}}\right) \tag{4.35}$$

where *erf* is the error function defined as

$$erf(\lambda) = \frac{2}{\sqrt{\pi}}\int_0^{\lambda}\exp\left(-x^2\right)dx \tag{4.36}$$

Equation (4.35) indicates that reducing the bandwidth coupling to the fiber bundle to further minimize the wavelength-dependent absorption among the source channels would cause a major reduction in the total power delivered to the tissue. This, however, can be improved if a source with higher power concentrated at a narrower bandwidth can be employed.

4.5.5.2 The Shift-Free Encoding and Minimized Reconstruction Uncertainty

In the LD-based discrete-spectral-encoding system, the instantaneous wavelength-intensity fluctuation of each channel was independent of the others. In the SLD-based spread-spectral-encoding system, the spectral encoding was from the single source; therefore, the instantaneous intensity change of each coupled channel was always correlated with those of other channels. Moreover, the use of dispersion to create spectral encoding also prevented the coupling profile from wavelength shifting. These two features imply a more stable NIR tomography measurement.

The use of multiple LDs for spectral encoding introduced an average of 1.0% and 1.2% signal intensity fluctuation over 1-minute and 30-minute periods, respectively [39]. The average wavelength shift observed for the LD-based system in a well-controlled situation was 0.027 and 0.21 nm over 1- and 30-minute periods, respectively. The long-term wavelength shift over the course of 30 minutes is greater than the spectrometer resolution of 0.1 nm, and a 1.2% standard deviation in the intensity fluctuation over this period introduced a 4.8% standard deviation in the reconstructed absorption coefficient value over the time. Quantitative measurements similar to those for an LD-based discrete-spectral-encoding system have been conducted for an SLD-based spread-spectral-encoding system. It is found that the short-term and long-term wavelength shifts of the SLD-based system were on the order of 0.02 nm, or about one-fifth of the spectrometer resolution. This subresolution shift more likely resulted from the digitization of the signal rather than the occurrence of actual wavelength shift. Compared with the LD-based system where the long-term wavelength shift was substantially higher than the short-term shift, there is no meaningful difference between the long-term and short-term wavelength shifts in this SLD-based measurement. This validates that the use of a single wideband source via dispersion provides virtually shift-free spectral encoding among the channels. The interchannel intensity fluctuation of this system was less than, yet close to, that of the LD-based system. The variation of the reconstructed μ_a value in the 300 frames acquired in 30 minutes is calculated. Compared with the similar experiments in the LD-based system, however, the measurement is less clustered, and the uncertainly of the μ_a value was 1.49% standard deviation, a value less than one-third of that observed in the LD-based system. Considering that the intensity fluctuation was a perturbation to the image reconstruction, the uncertainty of reconstructed μ_a values appears to be an amplification of the data uncertainty. In the LD-based system, the 1.2% perturbation caused a fourfold amplification of 4.8% in the reconstructed absorption coefficient value, whereas in this SLD-based system, the 0.86% perturbation ended up with only 1.49% of uncertainty in reconstruction, an amplification factor less than 2. The significantly reduced amplification of the intensity fluctuation in the SLD-based system implies

that the intensity fluctuation in this configuration might be due to the measurement noise rather than any systematic factor and validates the notion that a more accurate and stable measurement could be made. The relatively small 1.49% reconstruction standard deviation of this rapid NIR tomography system constructed based on a single wideband source indicated that there was good feasibility of discerning subtle and rapid absorption variations in biological tissues.

4.5.6 Hemodynamic Imaging by Spread-Spectral-Encoding NIR Tomography

A 5 Hz frame-rate NIR DOT system based on the spread spectral encoding of a single SLD source was constructed at Oklahoma State University. The typical resting heart rate (HR) of an adult is between about 60 and 100 beats per minute (bpm); therefore, the 5 Hz NIR tomography should be sufficient for measuring the absorption changes when induced by normal heart rate pulsation in the capillaries, as measured by pulse oximetry. An example is given in Figure 4.9 to evaluate the feasibility of imaging hemodynamic responses with this system. A male volunteer with resting HR of 72 bpm was imaged. The volunteer positioned his little finger against the lower-left surface of the imaging array and practiced voluntary breath holding, starting from when the image acquisition begun, to provide a hemoglobin variation signal that was not contaminated by breathing variation and motion artifact. A total of 50 frames were acquired in 10 seconds. One frame of the reconstructed image is

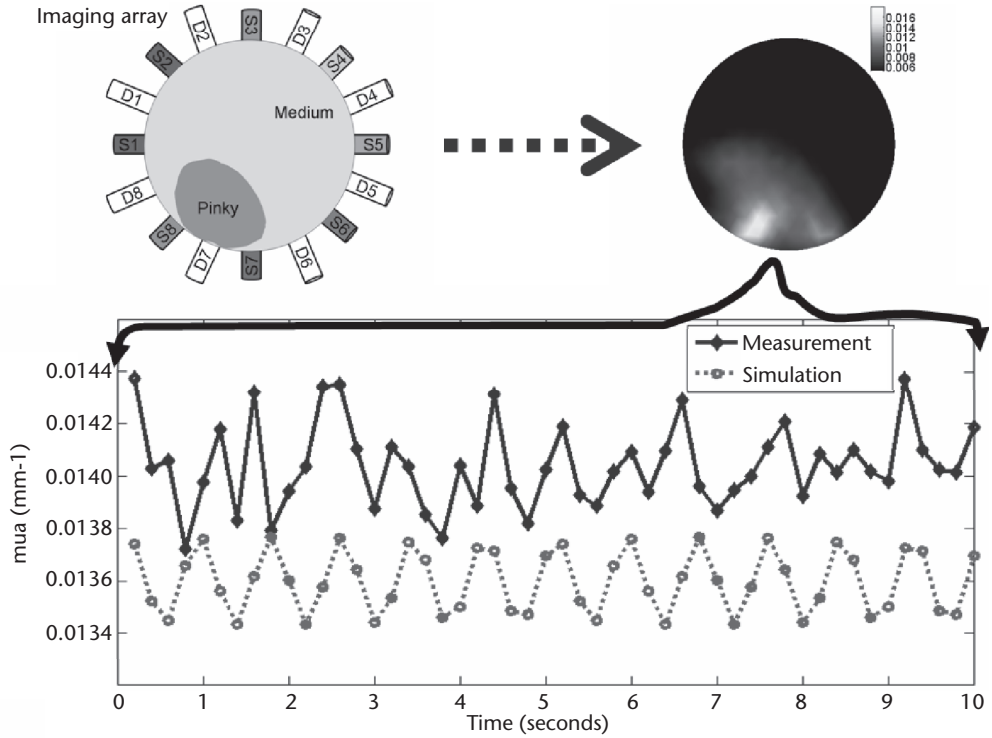

Figure 4.9 Imaging of finger during 10 seconds of breath holding. The curve shows near-periodic variation of the global absorption value of the finger, and it is correlated to the heart rate of the subject. The global absorption variation is 5.0% at the beginning of the acquisition and reduces to 2.9% at the end of the 10 second imaging period.

displayed. The cross section of the imaged finger was approximately 13 mm, which corresponds well with the higher absorption area in the image. In order to assess the time-resolved absorption changes of the finger, the absorption coefficients within 15% difference from the peak value were averaged for each frame. The global absorption changes in 50 frames of acquisition were compared with a simple simulated response by assuming 12 pulsations in 10 seconds. The simulation curve was placed under the curve of measurement to assess if there was a periodic variation of the responses; therefore, the absolute value of the simulated curve is chosen arbitrarily. It is interesting to notice that the variance of the global absorption values follows the simulated periodic pattern quite well except for the jittering between about 1 and 2 seconds. The mean value of the global absorption coefficient was 0.014 mm^{-1}, which is close to the expected value for human tissue [94]. The variance of the global absorption coefficient at the beginning of the breath holding was 5.0% and reduced gradually to 2.9% during the 10 seconds of breath holding. Both are above the measured system reconstruction uncertainly of 1.5%.

4.6 Novel Approaches in Instrumentation of Diffuse Optical Tomography: Transrectal Applicator

Near-infrared DOT has been shown to be particularly useful over the past decades for functional imaging of biological tissues where scattering of the photons dominates and where NIR contrast based on intrinsic chromophore content or exogenous probe can be linked to tissue physiology such as angiogenesis, oxygen deprivation, or overexpression of specific biomarkers. Despite the considerably promising outcome of NIR optical tomography in the diagnosis of breast cancer, the understanding of cortex response [11], and the characterization of rheumatologic dysfunction [95–97], where all the tissues under imaging are interrogated externally by noninvasive methods, there is limited information regarding the practice of NIR tomography in internal imaging regimes. Since similar physiological conditions may be found valuable for diagnostics in internal organs, an extension of DOT to imaging internally applicable tissue/organs becomes imperative. Interstitial measurement by use of diffuse or near-diffuse photons has been employed for monitoring photodynamic responses in organs such as the prostate [98]. From the diagnostic perspective, the most appealing feature of NIR tomography may arguably be its unique functional contrast that is obtained noninvasively. It is thereby not surprising to see that significant interest has developed recently in understanding the challenges and benefits of noninvasive NIR optical tomography of internal organs, particularly imaging the prostate [99, 100].

There is evidence that prostate cancer development is associated with angiogenesis [101], and NIR imaging may provide noninvasive assessment of prostate cancer. Noninvasive prostate imaging by optical means will enable the study of prostate optical properties and augment current diagnostics if the optical properties of prostate cancer are found to have substantial contrast with respect to those of normal prostate tissues. In this section, the instrumentation involved in developing an internal or endoscopic applicator array for DOT of the prostate or potentially other internal organs is presented.

4.6.1 Transrectal Applicator for Transverse DOT Imaging

Although the principle of near-infrared tomography of internal organs, specifically the prostate, is similar to that of breast, noninvasive internal DOT imaging faces unique challenges. In NIR optical tomography of breast, either planar-shaped or ring-type applicators of minimum restriction in size can be applied at either reflection or transmission geometry. In prostate imaging, there is only limited space inside the rectum for transrectal probing of deep tissue volumes. Special consideration must be incorporated into the design of the internal applicator. Figure 4.10 shows the schematic diagram of the first approach to the internal transverse (axial) imaging NIR probe. It utilizes the above-mentioned spread spectral encoding, where the spectrum of a broadband source is dispersed and coupled to a linear fiber bundle. The linear fiber bundle coupling the source light is rearranged to circular geometry at the distal end of the endoscope probe, and a conic lens is used to deflect the light circumferentially. The detector fibers are cocentric to and interspersed with the source fibers, and the proximal end of the detector fiber is linearly aligned to adapt to the spectrometer entrance slit. This outward-imaging geometry gave the first DOT image in endoscopic view [79].

Figure 4.11 shows a transverse-imaging NIR probe having a 20-mm diameter. This probe consists of 16 fibers of 1.0 mm in core diameter evenly spaced with interspersing source and detector channels. Each fiber is parallel to the longitudinal axis of the probe and is aligned to a 45° rod lens 2 mm in diameter. The beam is deflected transversely for side firing. A 2 mm drum lens is then used to provide a sealed optical

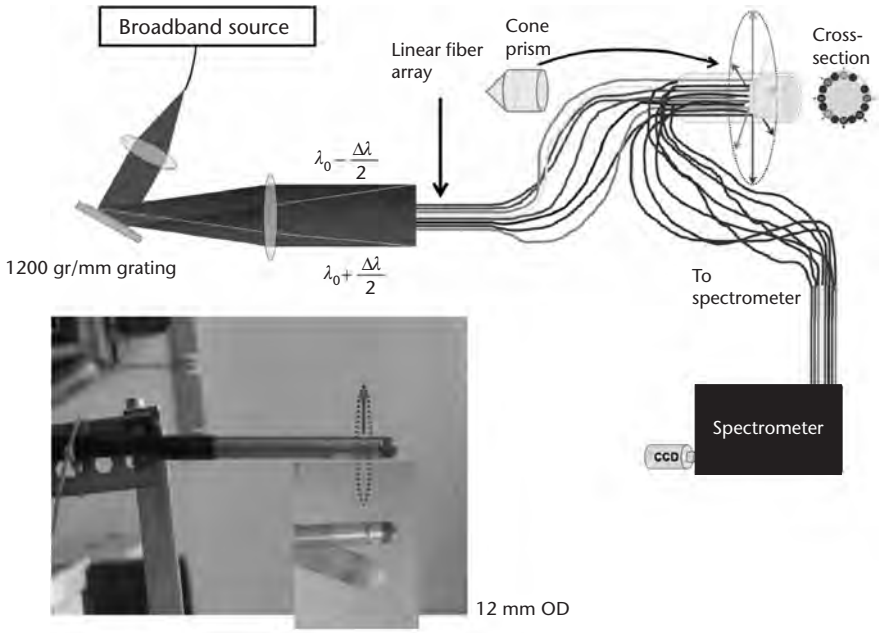

Figure 4.10 The first endoscopic applicator array for NIR tomography imaging of internal organs. A direct comparison with Figure 4.8 shows that the fiber bundle consisting of bare fibers can be integrated into a circular array inside the endoscopic probe. Circumferential illumination and detection is done by using a conic lens. The inset is the photograph of a 12 mm diameter endosocpic NIR tomography probe having eight source channels and eight detector channels.

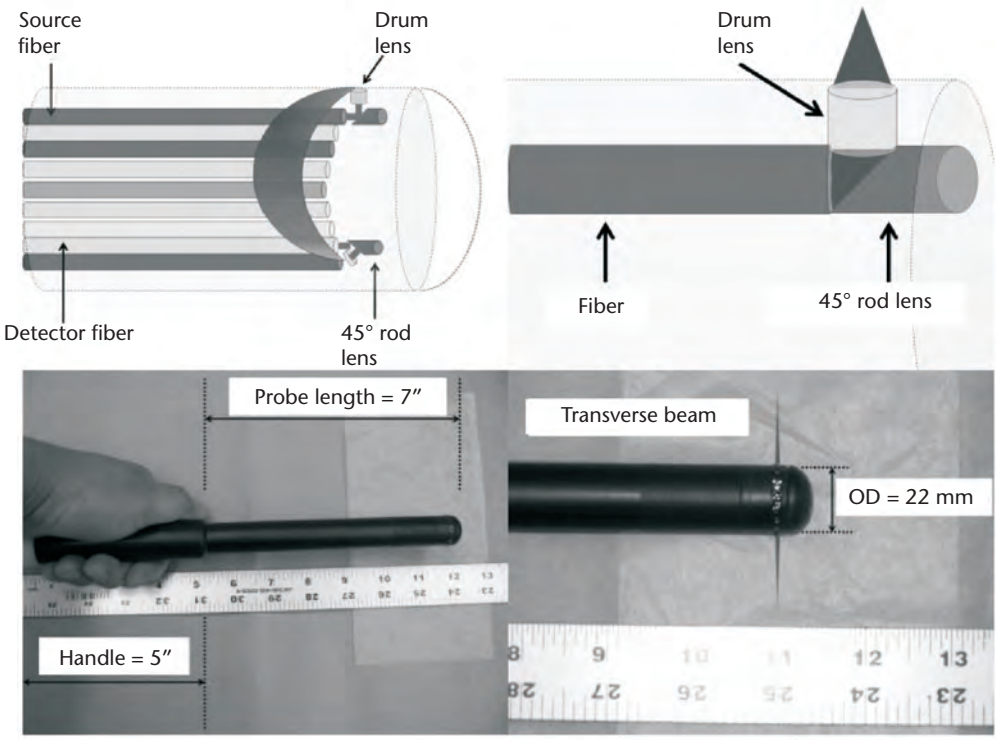

Figure 4.11 The transverse-imaging transrectal NIR tomography probe of 20 mm diameter. Each source/detector channel consists of a 1 mm fiber; a 2 mm, 45° rod lens; and a 2 mm drum lens. The light beam is delivered and focused transversely. Photograph of the probe shows the dimensions of 20 mm in diameter, 7″ in probing length, 5″ handle, and the two fiber bundles 3m long for source and detector coupling.

aperture for illumination as well as beam focusing. All eight source and eight detector channels have used the same light-delivering configuration. The eight source fibers and eight detector fibers are aligned to form a linear source fiber bundle and detector fiber bundle. The illumination light is coupled to the source fiber bundle by the spread-spectral-encoding technique, and the detector fiber bundle is adapted to the spectrometer for acquisition of NIR surface-measurement data.

The internal-application NIR tomography images taken by this 20 mm transverse-imaging NIR probe are given in Figure 4.12. The imaging geometry is now opposite to what is done for most NIR imaging of breast, as the optodes are distributed noninvasively and internally to the tissue volume. We incorporated the outward imaging finite-element mesh as shown to reconstruct the NIR tomography images. The annular image is taken from a highly absorptive phantom over an intralipid background medium by use of the 20 mm transverse-imaging probe. The semiannular image was taken from a sample of avian rectum tissue with injected NIR absorption contrast by use of the 12 mm transverse-imaging NIR probe shown in Figure 4.10. Both sets of images demonstrate that NIR contrast of heterogeneous targets can be acquired successfully by these probes at internal-imaging geometry.

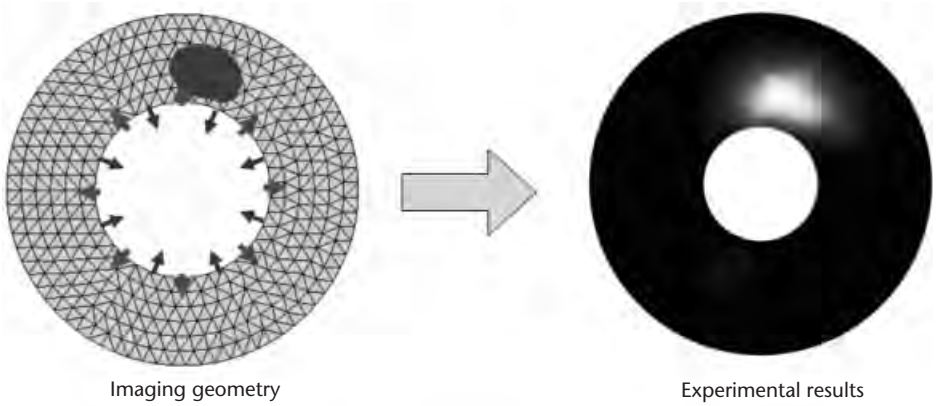

(a)

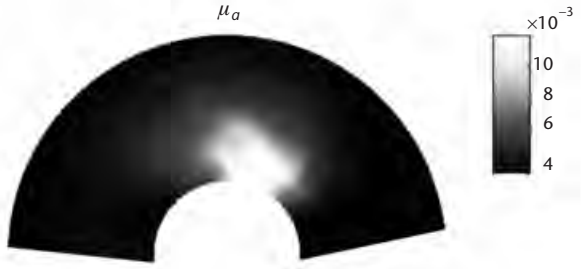

In vitro imaging of avian rectum with exogenous contrast
(b)

Figure 4.12 The transverse-imaging examples by transrectal NIR probe. (a) The top row demonstrates the relative positions of optodes in the imaging volume as well as the reconstructed images of a contrast occlusion embedded in background Intralipid medium. (b) The bottom image was taken by transrectal imaging of an avian rectum sample with connecting tissues, where the contrast was from a small amount of diluted ink to introduce exogenous contrast to the homogenous rectal tissue.

4.6.2 Transrectal Applicator for Sagittal DOT Imaging

We have lately developed a sagittal-imaging NIR probe to attach to a commercial biplane TRUS transducer for multimodality imaging [102]. The NIR applicator can perform stand-alone DOT imaging or utilize the spatial prior information from ultrasound. The design, dimension, and completed probe are detailed in Figure 4.13. This probe is capable of acquiring sagittal NIR images concurrently with TRUS. The source/detector channels are placed at 1 cm separation, and the source array is placed 2 cm from the detector array. The array dimension of 60×20 mm is designed to couple to the 60×10 mm TRUS transducer performing sagittal imaging at the middle plane of the NIR array.

4.6.2.1 Simulation for the Sagittal Transrectal DOT Applicator

Simulations for the sagittal NIR probe are given in Figure 4.14 for a 10 mm diameter inclusion located at middle plane and 5 mm longitudinal shift from the center of the probe. The transrectal NIR probe is placed at the bottom of the imaging volume,

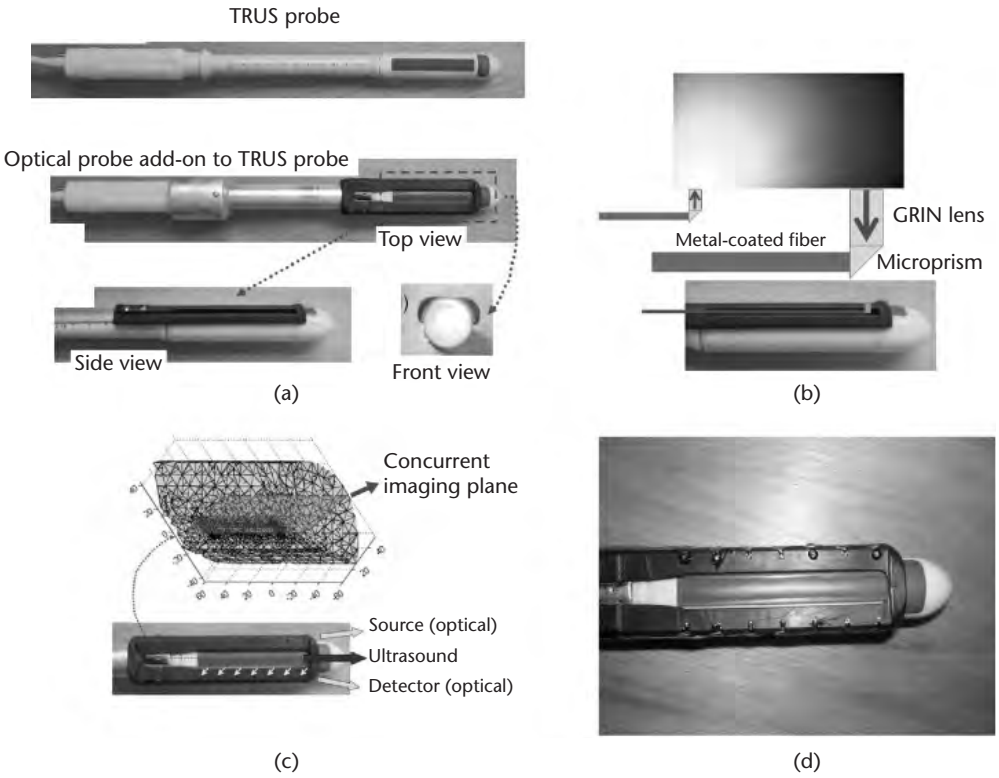

Figure 4.13 The sagittal-imaging transrectal NIR tomography probe for coupling with TRUS. (a) The overall assembly of transrectal NIR attached to TRUS is shown. (b) The probe has one source array and one detector array, each having seven channels. Each channel consists of a 600 μm metal-coated fiber coupled to a 1 mm coated microprism for 90° deflection and a 1 mm gradient-index (GRIN) lens for coupling to and from the tissue surface. (c) The NIR imaging reconstruction is taken at the middle sagittal plane of source and detector arrays, which falls identically with the sagittal TRUS. (d) Photograph of completed transrectal NIR probe attached to TRUS is shown.

and the depth is counted upward. Homogenous background is set at $\mu_a = 0.002$ mm^{-1}, $\mu_s' = 0.8$ mm^{-1}, and the target has $\mu_a = 0.025$ mm^{-1}, $\mu_s' = 1.0$ mm^{-1}. A noise level of 1% has been added to the forward calculation.

The NIR-only reconstruction (uniform mesh density throughout the imaging volume) is conducted for the target at depths of 1, 2, and 3 cm. The second row of Figure 4.14 shows that the target is reconstructed accurately for 1 cm depth and closer to the probe surface for 2 cm depth. This is expected due to the sensitivity degrading along with the depth. The third row of Figure 4.14 gives the images reconstructed with spatial prior information that will be available from TRUS using a denser mesh in the target location and at a size double that of the target [103]. The images reconstructed with this guided-reconstruction approach locate the lesion correctly. The accuracy of recovering lesions in the longitudinal dimension is given in Figure 4.15 for a lesion of 2cm depth that is placed at 2, 4, and 6 cm in axial dimension. Their positions are correctly reconstructed.

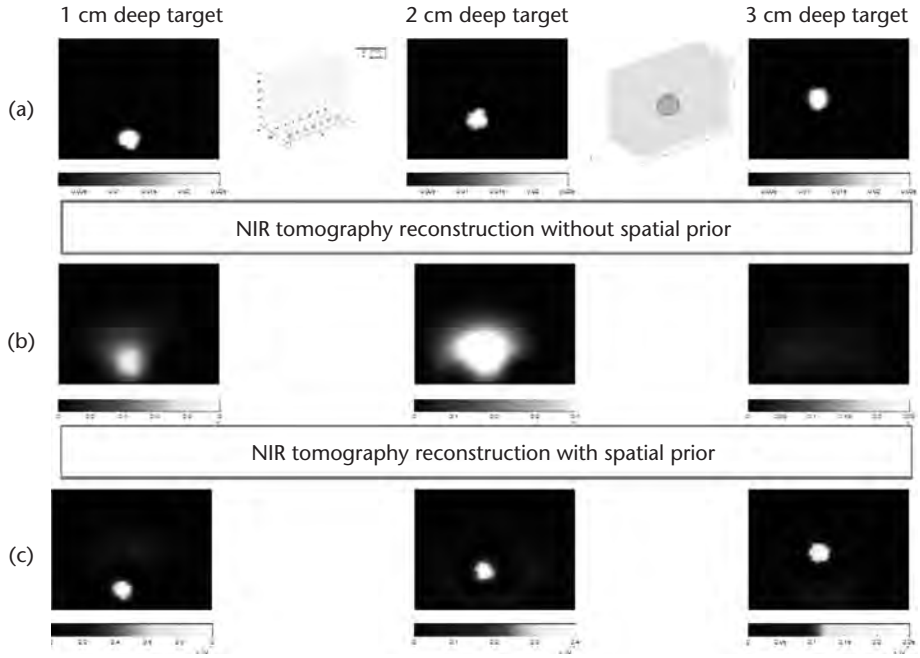

Figure 4.14 Reconstruction of (a) targets with (b) NIR only and with (c) spatial prior.

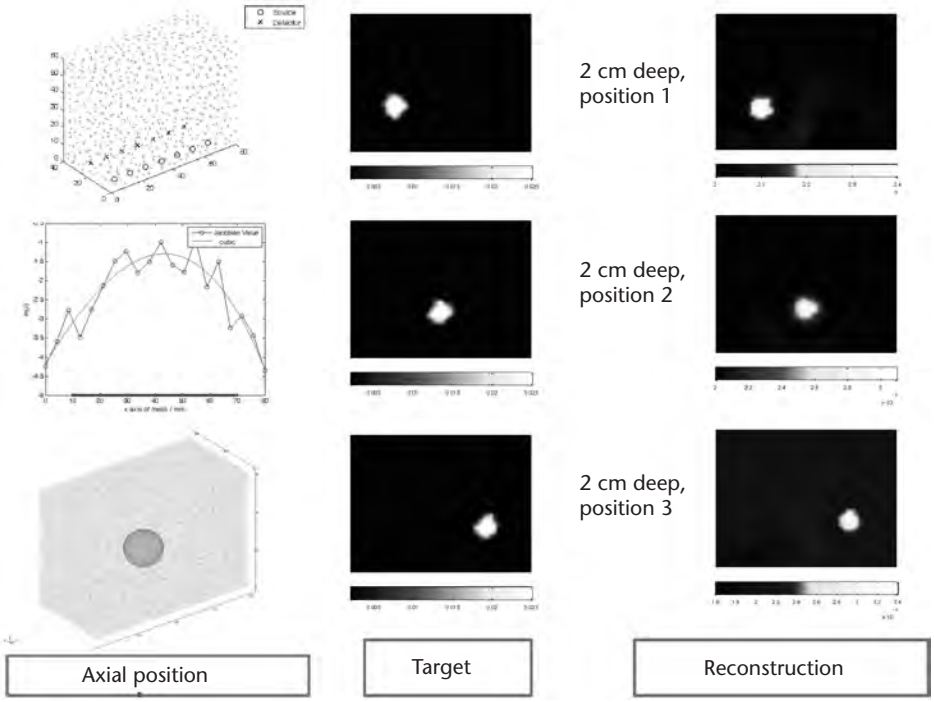

Figure 4.15 Accuracy of localization for reconstruction in the longitudinal direction.

4.6.2.2 Experimental Results of the Sagittal Transrectal DOT Applicator

Figure 4.16 gives the images reconstructed from experimental data for a highly absorbing cylindrical occlusion positioned at the left side, middle, and right side. The bottom of the cylinder is roughly 7 mm away from the probe surface, giving a 15-mm depth of the occlusion. The left column is reconstructed with NIR information only, and the right column is reconstructed by knowing the location and approximate size of the occlusion as the hard spatial prior. The images reconstructed with priori information show the occlusion closer to true positions. The image for the occlusion at the right end of the probe is quite interesting, where the two-blob artifact shown for NIR-only image reconstruction is corrected when the reconstruction is guided by prior information.

Color Plate 12 presents the images reconstructed from experimental data using chicken breast tissue as the background medium and an inclusion. The inclusion is a cylinder 15 mm in diameter and 15 mm in height made of black plastic material to simulate an absorption target. The TRUS image obtained in Color Plate12(a) has a field of view of 5×5 cm. Using the information of target location and approximate size, dual-mesh NIR tomography reconstruction is performed with a sagittal field of view of 8×6 cm, where the size of denser mesh for the target doubles the approximate size of the target shown on TRUS. The reconstructed sagittal NIR image is displayed at a field of view of 6×3 cm, and the active US transducer of 5 cm long is indicated underneath for comparison. The NIR image with TRUS guidance clearly reconstructs the target identified by TRUS. In Color Plate 12(b), no inclusion is embedded in the chicken breast medium; yet, the dual-mesh identical to that in

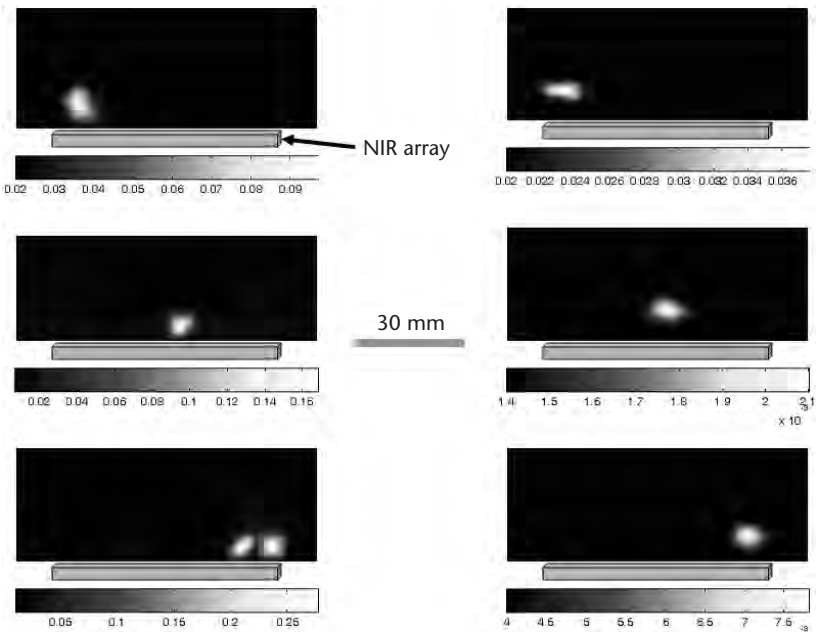

Figure 4.16 Image reconstructed from experimental data without and with a priori location information.

Color Plate 12(a) is used. The reconstructed NIR image does not show a target in the denser mesh region, which demonstrates that NIR measurement of the target amid the background medium is reliable. In Color Plate 12(c), the target is shifted longitudinally, and in Color Plate 12(d), the target is moved approximately 5 mm deeper. In both cases, the NIR image reconstruction gives satisfactory results.

Figure 4.17 presents a very interesting result. In the left column, the background medium is chicken breast only; therefore, a homogenous mesh is used for NIR image reconstruction since there is no spatial prior information for any target available from TRUS. The reconstructed NIR image does not show a target. In the right column, a cube of chicken breast tissue was immerged in absorbing solution (diluted ink) for 20 minutes and then embedded in the middle of the tissue at a depth of approximately 1.5 cm. The TRUS image does not identify a target in the manipulated region. NIR reconstruction is again performed by use of homogenous mesh, assuming that no spatial prior from TRUS is available. The target shows up in NIR image at the correct longitudinal position but shallower depth. The shallower depth is caused by the reduced sensitivity along the depth as indicated previously when only NIR information is used for reconstruction. This example demonstrates that transrectal NIR is capable of detecting target that is nonsensitive to TRUS. The clinical outcome of integrating transrectal NIR and TRUS is mainly directed at providing optical contrast for the lesions that are suspicious to US; nevertheless, this example proved that transrectal NIR tomography could localize lesions to which US is blind. This is potentially very important for biopsy guidance and diagnostics since

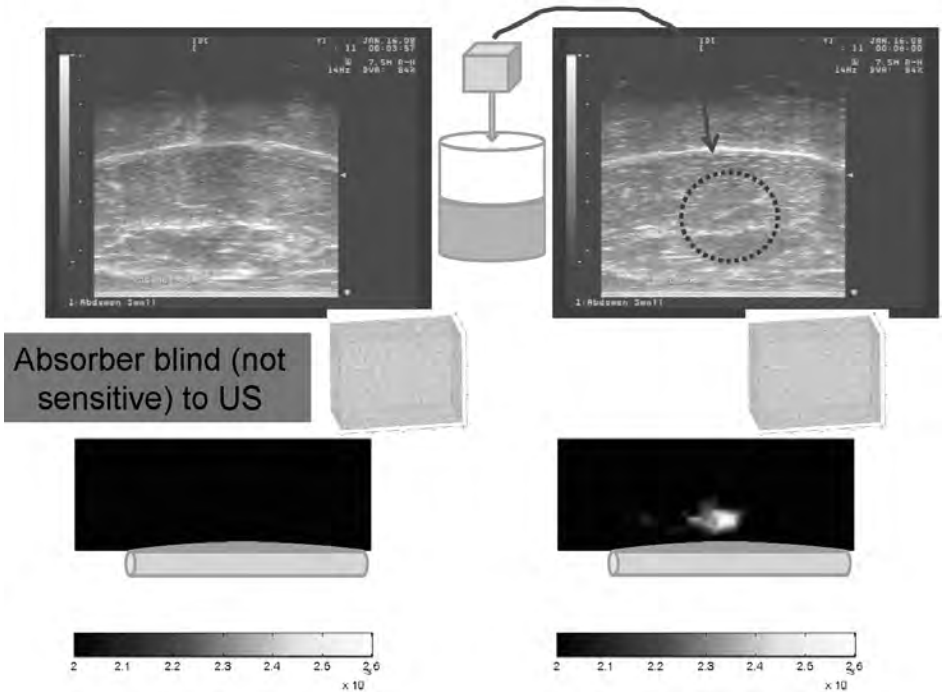

Figure 4.17 Concurrent sagittal transrectal NIR/US images of chicken breast tissue: (a) chicken breast tissue only, and (b) a cube of chicken breast immerged in diluted ink for approximately 20 minutes, then embedded in the medium. The absorptive surface of the tissue cube is insensitive to US. NIR image reconstruction without prior information located the target.

a malignant lesion that may be missed by TRUS can be identified by transrectal NIR.

4.7 Potential Directions of Instrumentation for Diffuse Optical Measurements

The advancement of biomedical-oriented optical imaging technology, including diffuse optical techniques, is dependent largely upon the progress in photonics instruments, including a variety of coherent, low-coherent, or incoherent light sources and high-speed, high-sensitivity, high-dynamic range detectors. Meanwhile, the special need of optical imaging application, such as optical coherence tomography, has been a driving force behind some important advancement in photonic devices. It is certain that novel applications and advancements in optical imaging and optical instrumentation will foster each other over the foreseeable period.

The applicator array for external imaging in DOT has evolved from rigid single modality to flexible modality [11], from rigid multimodality [62] to adaptive multimodality [74]. Recently, the applicator array for internal imaging has evolved from rigid single modality [100] to rigid multimodality for prostate imaging [102]. If there comes the demand of applying DOT techniques to internal organs other than the prostate, flexible internal applicator array may be necessary for single-modality or multimodality imaging.

So far, the varieties of sources used for diffuse optical imaging include noncoherent source like tungsten light [51], coherent source like laser diode [62], and low-coherent sources like superluminescenet diode and the mode-locked Ti:sapphire laser [79]. The mode-locked pulsed-laser source is particularly interesting for DOT. First, it may be used for time-domain measurement by taking advantage of its short pulse operation. Second, it has been used in spread-spectral-encoding-based DOT systems for its low coherence or wideband feature. Third, it may also be used in frequency-domain measurement if the repetition timing can serve as the modulation base frequency. Other light sources like swept laser have found exciting applications in OCT [104], and it is anticipated that swept source may find novel application in DOT if the wavelength band is appropriate.

Applying DOT to noninvasive imaging of internal organs presents unprecedented benefits and challenges. For external imaging of DOT, no matter whether for breast, brain, or joints, there isn't much limitation for placing the bulky source and detector fibers, except for some multimodality imaging requirements. Internal imaging in small spaces is, however, different. A small-diameter fiber, such as a single-mode fiber, is sufficient for delivering tens of milliwatts of light power to the tissue for a point-source illumination. For detection, however, although the orientation of the fiber is not important, the dimension of the fiber detection aperture is critical for collecting sufficient photons. If the small-diameter fiber needs to be implemented, it is likely that the fiber tip will need microoptics to improve the total detection power. Another option may be fabricating microphotosensors directly to the applicator if the interference of electrical signals can be resolved. Direct multimodality sensing on the applicator may also be performed if a monolithic multimodality sensor/detector can be engineered.

4.8 Conclusions

The diffuse optical technique is continuously evolving as a viable biomedical imaging modality owing to its unique spectroscopic functional contrast. Near-infrared light probes tissue absorption as well as scattering properties by means of diffuse photon measurement. Although the spatial resolution of diffuse optical detection is limited due to indefinite photon path when compared with other imaging modalities such as MRI and CT, DOT provides access to a variety of physiological parameters that are otherwise not accessible [9]. Other appealing features of DOT include noninvasive or minimally invasive imaging; nonionizing radiation, eliminating the concern of repeated dose; and compactness, relatively low cost, and appropriateness for continuous use in office or at the bedside [9]. The exciting applications of DOT in diagnostics over the past decades have been led by several key advancements in instrumentation techniques that are briefly reviewed in this chapter. The emerging interest in DOT for coupling with other diagnostic modalities as well as application to different organ levels presents new challenges for DOT instrumentation principles as well as device techniques.

Acknowledgments

This work has been supported in part by the Prostate Cancer Research Program of the U.S. Army Medical Research Acquisition Activity (USAMRAA), 820 Chandler Street, Fort Detrick, MD, 21702-5014, through grant W81XWH-07-1-0247, and the Health Research Program of the Oklahoma Center for the Advancement of Science and Technology (OCAST) through grant HR06-171. The content of the information does not necessarily reflect the position or policy of the USAMRAA or OCAST, and no official endorsement should be inferred.

The graduate students who contributed to this work include Zhen Jiang, Guan Xu, Cameron H. Musgrove, and Hao Xie. I acknowledge collaborations with Drs. Charles F. Bunting, Jerzy S. Kransiski, and Weili Zhang in my department. Drs. Kenneth E. Bartels, Jerry Ritchey, and G. Reed Holyoak from Oklahoma State University Vet-Med College, Dr. Gennady Slobodov of the University of Oklahoma Health Sciences Center, and Dr. Sreenivas Vemulapalli of Tri-Valley Urology are acknowledged for their suggestions. Finally, this work would not have been possible without the encouragement of many experts in the DOT field, including Drs. Brian W. Pogue, Quing Zhu, and Bruce J. Tromberg.

References

[1] Yodh, A. G., and B. Chance, "Spectroscopy and imaging with diffusing light," *Phys. Today* 48(3) (1995): 34–40.

[2] Benaron, D. A., G. Müller, and B. Chance, "Medical perspective at the threshold of clinical optical tomography," in G. Müller, et al., (eds.), *Medial Optical Tomography: Functional Imaging and Monitoring*, 3–9, Bellingham, WA: SPIE—International Society for Optical Engineering, 1993.

[3] Tromberg, B., A. Yodh, E. Sevick, and D. Pine, "Diffusing photons in turbid media: introduction to the feature," *Appl. Opt.* 36(1) (1997): 9–9.

[4] Boas, D. A., et al., "Imaging the body with diffuse optical tomography," *IEEE Sign. Process. Mag.* 18(6) (2001): 57–85.

[5] Miller, E., "Focus issue: diffuse optical tomography—introduction," *Opt. Exp.* 7(13) (2000): 461–461.

[6] Pogue, B. W., et al., "Image analysis methods for diffuse optical tomography," *J. Biomed. Opt.* 11(3) (2006): 033001–033001-16.

[7] Gibson, A. P., J. C. Hebden, and S. R. Arridge, "Recent advances in diffuse optical imaging," *Phys. Med. Biol.* 50(4) (2005): R1–R43.

[8] Hielscher, A. H., "Optical tomographic imaging of small animals," *Curr. Opin. Biotechnol.* 16(1) (2005): 79–88.

[9] Hielscher, A. H., et al., "Near-infrared diffuse optical tomography," *Dis. Mark.* 18, Nos. 5–6 (2002): 313–337.

[10] Ntziachristos, V., and B. Chance, "Probing physiology and molecular function using optical imaging: applications to breast cancer," *Breast Canc. Res.* 3(1) (2001): 41–46.

[11] Hillman, E. M., "Optical brain imaging in vivo: techniques and applications from animal to man," *J. Biomed. Opt.* 12(5) (2007): 051402–051402-28.

[12] Hebden, J. C., and T. Austin, "Optical tomography of the neonatal brain," *Eur. Radiol.* 17(11) (2007): 2926–2933.

[13] Zhang, X., V. Toronov, and A. Webb, "Spatial and temporal hemodynamic study of human primary visual cortex using simultaneous functional MRI and diffuse optical tomography," *Proc. 27th Ann. Conf. IEEE Eng. Med. Biol. Soc.*, Shanghai, China, September 1–4, 2005, 727–730.

[14] Wang, X., et al., "Imaging of joints with laser-based photoacoustic tomography: an animal study," *Med. Phys.* 33(8) (2006): 2691–2697.

[15] Srinivasan, S., et al., "In vivo hemoglobin and water concentrations, oxygen saturation, and scattering estimates from near-infrared breast tomography using spectral reconstruction," *Acad. Radiol.* 13(2) (2006): 195–202.

[16] Diamond, S. G., et al., "Dynamic physiological modeling for functional diffuse optical tomography," *NeuroImage* 30(1) (2006): 88–101.

[17] Rinneberg, H., et al., "Scanning time-domain optical mammography: detection and characterization of breast tumors in vivo," *Technol. Canc. Res. Treat.* 4(5) (2005): 483–496.

[18] Zhao, H., et al., "Time-resolved diffuse optical tomographic imaging for the provision of both anatomical and functional information about biological tissue," *Appl. Opt.* 44(10) (2005): 1905–1916.

[19] Taga, G., et al., "Brain imaging in awake infants by near-infrared optical topography," *Proc. Natl. Acad. Sci. USA* 100(19) (2003): 10722–10727.

[20] Durduran, T., et al., "Bulk optical properties of healthy female breast tissue," *Phys. Med. Biol.* 47(16) (2002): 2847–2861.

[21] Barbour, R. L., et al., "Optical tomographic imaging of dynamic features of dense-scattering media," *J. Opt. Soc. Am. A* 18(12) (2001): 3018–3036.

[22] Hintz, S. R., et al., "Bedside functional imaging of the premature infant brain during passive motor activation," *J. Perinat. Med.* 29(4) (2001): 335–343.

[23] Boas, D. A., et al., "The accuracy of near infrared spectroscopy and imaging during focal changes in cerebral hemodynamics," *NeuroImage* 13(1) (2001): 76–90.

[24] Van Houten, J. P., D. A. Benaron, S. Spilman, and D. K. Stevenson, "Imaging brain injury using time-resolved near infrared light scanning," *Pediat. Res.* 39(3) (1996): 470–476.

[25] Srinivasan, S., et al., "Interpreting hemoglobin and water concentration, oxygen saturation, and scattering measured in vivo by near-infrared breast tomography," *Proc. Natl. Acad. Sci. USA* 100(21) (2003): 12349–12354.

[26] Heffer, E., et al., "Near-infrared imaging of the human breast: complementing hemoglobin concentration maps with oxygenation images," *J. Biomed. Opt.* 9(6) (2004): 1152–1160.

[27] Zhu, Q., S. Tannenbaum, and S. H. Kurtzman, "Optical tomography with ultrasound localization for breast cancer diagnosis and treatment monitoring," *Surg. Oncol. Clin. N. Am.* 16(2) (2007): 307–321.

[28] Rolfe, P., "In vivo near-infrared spectroscopy," *Ann. Rev. Biomed. Eng.* 2 (2000): 715–754.

[29] Huang, D., et al., "Optical coherence tomography," *Science* 254(5035) (1991): 1178–1181.

[30] Kim, Y. L., et al., "Low-coherence enhanced backscattering: review of principles and applications for colon cancer screening," *J. Biomed. Opt.* 11(4) (2006): 041125–041125–10.

[31] Yodh, A. G., and D. A. Boas, "Functional imaging with diffusing light," in T. Vo-Dinh (ed.), *Biomedical Photonics Handbook*, 21–21–45, Boca Raton, FL: CRC Press, 2003.

[32] Schmitz, C. H., et al., "Instrumentation for fast functional optical tomography," *Rev. Sci. Instr.* 73(2) (2002): 429–439.

[33] Nissilä, I., et al., "Instrumentation and calibration methods for the multichannel measurement of phase and amplitude in optical tomography," *Rev. Sci. Instr.* 76(4) (2005): 044302–044302-10.

[34] Fantini, S., et al., "Frequency-domain optical mammography: edge effects correction," *Med. Phys.* 23(1) (1996): 149–157.

[35] Franceschini, M. A., et al., "Frequency-domain techniques enhance optical mammography: initial clinical results," *Proc. Natl. Acad. Sci. USA* 94(12) (1997): 6468–6473.

[36] Siegel, A. M., J. J. A. Marota, and D. A. Boas, "Design and evaluation of a continuous-wave diffuse optical tomography system," *Opt. Exp.* 4(8) (1999): 287–298.

[37] Cerussi, A. E., and B. J. Tromberg, "Photon migration spectroscopy frequency-domain techniques," in T. Vo-Dinh (ed.), *Biomedical Photonics Handbook*, 22–22–17**<AQ: page span correct?>**, Boca Raton, FL: CRC Press, 2003.

[38] Piao, D., et al., "Video-Rate Near-Infrared Optical Tomography Using Spectrally Encoded Parallel Light Delivery," *Opt. Lett.* 30(19) (2005): 2593–2595.

[39] Piao, D., et al., "Instrumentation for video-rate near-infrared diffuse optical tomography," *Rev. Sci. Instr.* 76(12) (2005): 124301–124301-13.

[40] Hillman, E. M. C., *Experimental and Theoretical Investigations of Near-Infrared Tomographic Imaging Methods and Clinical Applications*, Ph.D. Dissertation, University College London, UK, 2002, 15–26.

[41] Patterson, M. S., B. Chance, and B. C. Wilson, "Time resolved reflectance and transmittance for the noninvasive measurement of tissue optical properties," *Appl. Opt.* 28(12) (1989): 2331–2336.

[42] Grosenick, D., et al., "Development of a time-domain optical mammograph and first in vivo applications," *Appl. Opt.* 38(13) (1999): 2927–2943.

[43] Hawrysz, D. J., and E. M. Sevick-Muraca, "Developments toward diagnostic breast cancer imaging using near-infrared optical measurements and fluorescent contrast agents," *Neoplasia* 2(5) (2000): 388–417.

[44] Fantini, S., and M. A. Franceschini, "Frequency-domain techniques for tissue spectroscopy and imaging," in V. T. Tuchin (ed.), *Handbook of Optical Biomedical Diagnostics*, 405–453, Bellingham, WA: SPIE Press, 2002.

[45] Pogue, B. W., et al., "Instrumentation and design of a frequency-domain diffuse optical tomography imager for breast cancer detection," *Opt. Exp.* 1(13) (1997): 391–403.

[46] Fantini, S., M. A. Franceschini, and E. Gratton, "Semi-infinite geometry boundary problem for light migration in highly scattering media: a frequency-domain study in the diffusion approximation," *J. Opt. Soc. Am. B* 11(10) (1994): 2128–2138.

[47] Intes, X., et al., "In Vivo Continuous-Wave Optical Breast Imaging Enhanced with Indocyanine Green," *Med. Phys.* 30(6) (2003): 1039–1047.

[48] Su, J., H. Shan, H. Liu, and M. V. Klibanov, "Reconstruction method with data from a multiple-site continuous-wave source for three-dimensional optical tomography," *J. Opt. Soc. Am. A* 23(10) (2006): 2388–2395.

[49] Corlu, A., et al., "Uniqueness and wavelength optimization in continuous-wave multispectral diffuse optical tomography," *Opt. Lett.* 28(23) (2003): 2339–2341.

[50] Jiang, H., Y. Xu, and N. Iftimia, "Experimental three-dimensional optical image reconstruction of heterogeneous turbid media from continuous-wave data," *Opt. Exp.* 7(5) (2000): 204–209.

[51] Xu, H., *MRI-Coupled Broadband Near-Infrared Tomography for Small Animal Brain Studies*, Ph.D. Dissertation, Dartmouth College, Hanover, NH, 2005, 36–36.

[52] Walker, S. A., S. Fantini, and E. Gratton, "Image reconstruction using back-projection from frequency-domain optical measurements in highly scattering media," *Appl. Opt.* 36(1) (1997): 170–179.

[53] Arridge, S. R., and M. A. Schweiger, "A Gradient-Based Optimisation Scheme for Optical Tomography," *Opt. Exp.* 2(6) (1998): 213–226.

[54] Saquib, S. S., K. M. Hanson, and G. S. Cunningham, "Model-Based Image Reconstruction from Time-Resolved Diffusion Data," *Proc. SPIE* 3034 (1997): 369–380.

[55] Hielscher, A. H., A. D. Klose, and K. M. Hanson, "Gradient-based iterative image reconstruction scheme for time resolved optical tomography," *IEEE Trans. Med. Imag.* 18(3) (1999): 262–271.

[56] Brooksby, B., et al., "Combining near infrared tomography and magnetic resonance imaging to study in vivo breast tissue: implementation of a Laplacian-type regularization to incorporate magnetic resonance structure," *J. Biomed. Opt.* 10(5) (2005): 051504–051504-10.

[57] Arridge, S. R., and M. Schweiger, "Sensitivity to prior knowledge in optical tomographic reconstruction," *Proc. SPIE* 2389 (1995): 378–388.

[58] Brooksby, B., et al., "Magnetic resonance-guided near-infrared tomography of the breast," *Rev. Sci. Instr.* 75(12) (2004): 5262–5270.

[59] Ntziachristos, V., X. H. Ma, and B. Chance, "Time-correlated single photon counting imager for simultaneous magnetic resonance and near-infrared mammography," *Rev. Sci. Instr.* 69(12) (1998): 4221–4233.

[60] Dehghani, H., et al., "Three-dimensional optical tomography: resolution in small object imaging," *Appl. Opt.* 42(16) (2003): 3117–3128.

[61] Dehghani, H., et al., "Structural a Priori Information in Near-Infrared Optical Tomography," *Proc. SPIE* 6431 (2007): 64310B–64310B-7.

[62] Zhu, Q., "Optical tomography with ultrasound localization: initial clinical results and technical challenges," *Technol. Canc. Res. Treat.* 4(3) (2005): 235–244.

[63] Ntziachristos, V., A. G. Yodh, M. Schnall, and B. Chance, "Concurrent MRI and diffuse optical tomography of breast after indocyanine green enhancement," *Proc. Natl. Acad. Sci. USA* 97(6) (2000): 2767–2772.

[64] Gulsen, G., et al., "Congruent MRI and near-infrared spectroscopy for functional and structural imaging of tumors," *Technol. Canc. Res. Treat.* 1(6) (2002): 497–505.

[65] Strangman, G., J. P. Culver, J. H. Thompson, and D. A. Boas, "A quantitative comparison of simultaneous BOLD fMRI and NIRS recordings during functional brain activation," *NeuroImage* 17(2) (2002): 719–731.

[66] Li, A., et al., "Reconstructing chromosphere concentration images directly by continuous-wave diffuse optical tomography," *Opt. Lett.* 29(3) (2004): 256–258.

[67] Brooksby, B., et al., "Spectral priors improve near-infrared diffuse tomography more than spatial priors," *Opt. Lett.* 30(15) (2005): 1968–1970.

[68] Corlu, A., et al., "Diffuse optical tomography with spectral constraints and wavelength optimization," *Appl. Opt.* 44(11) (2005): 2082–2093.

[69] Zhu, Q., S. Tannenbaum, and S. H. Kurtzman, "Optical Tomography with ultrasound localization for breast cancer diagnosis and treatment monitoring," *Surg. Oncol. Clin. N. Am.* 16(2) (2007): 307–321.

[70] Zhu, Q., et al., "Benign versus malignant breast masses: optical differentiation with US-guided optical imaging reconstruction," *Radiology* 237(1) (2005): 57–66.

[71] Zhu. Q., et al., "Utilizing optical tomography with ultrasound localization to image heterogeneous hemoglobin distribution in large breast cancers," *Neoplasia* 7(3) (2005): 263–270.

[72] Holboke, M. J., et al., "Three-dimensional diffuse optical mammography with ultrasound localization in a human subject," *J. Biomed. Opt.* 5(2) (2000): 237–247.

[73] Zhu, Q., et al., "Ultrasound-guided optical tomographic imaging of malignant and benign breast lesions," *Neoplasia* 5(5) (2003): 379–388.

[74] Brooksby, B., et al., "Imaging breast adipose and fibroglandular tissue molecular signatures by using hybrid MRI-guided near-infrared spectral tomography," *Proc. Natl. Acad. Sci. USA* 103(23) (2006): 8828–8833.

[75] Shah, N., et al., "Combined diffuse optical spectroscopy and contrast-enhanced magnetic resonance imaging for monitoring breast cancer neoadjuvant chemotherapy: a case study," *J. Biomed. Opt.* 10(5) (2005): 051503–051503–9.

[76] Huppert, T. J., et al., "Quantitative spatial comparison of diffuse optical imaging with blood oxygen level–dependent and arterial spin labeling–based functional magnetic resonance imaging," *J. Biomed. Opt.* 11(6) (2006): 064018–064018-16.

[77] Kondow, M., T. Kitatani, K. Nakahara, and T. Tanaka, "Temperature dependence of lasing wavelength in a GaInNAs laser diode," *IEEE Photon. Technol. Lett.* 12(7) (2000): 777–779.

[78] Pogue, B. W., D. Piao, H. Dehghani, and K. D. Paulsen, "Demonstration of video-rate diffuse optical tomography in phantoms and tissues," *Proc. 2006 IEEE Int. Symp. Biomed. Imag.*, Arlington, VA, April 6–9, 2006, 1196–1199.

[79] Piao, D., et al., "Endoscopic, rapid near-infrared optical tomography," *Opt. Lett.* 31(19) (2006): 2876–2878.

[80] Shidlovski, V., "Superluminescent diodes: short overview of device operation principles and performance parameters," 2004, www.superlumdiodes.com/pdf/sld_overview.pdf (accessed February 2008).

[81] Holtmann, C., P. A. Besse, and H. Melchior, "High-power superluminescent diodes for 1.3 μm," *Electron. Lett.* 32(18) (1996): 1705–1706.

[82] Li, L. H., et al., "Wide emission spectrum from superluminescent diodes with chirped quantum dot multilayers," *Electron. Lett.* 41(1) (2005): 41–42.

[83] Kaminow, I. P., G. Eisenstein, L. W. Stulz, and A. G. Dentai, "Lateral confinement InGaAsP superluminescent diode at 1.3 μm," *IEEE J. Quant. Electron.* QE-19(1) (1983): 78–82.

[84] Youngquist, R. C., S. Carr, and D. E. N. Davies, "Optical coherence domain reflectometry: a new optical evaluation technique," *Opt. Lett.* 12(3) (1987): 158–160.

[85] Swanson, E. A., et al., "High-resolution optical coherence domain reflectometry," *Opt. Lett.* 17(2) (1992): 151–153.

[86] Chiang, H. P., W. S. Chang, and J. Wang, "Imaging through random scattering media by using CW broadband interferometry," *Opt. Lett.* 18(7) (1993): 546–548.

[87] Wang, X. J., et al., "Characterization of human scalp hairs by optical low-coherence reflectometry," *Opt. Lett.* 20(6) (1995): 524–526.

[88] Podoleanu, A. G., G. M. Dobre, D. J. Webb, and D. A. Jackson, "Simultaneous en-face**<AQ: enface?>** imaging of two layers in the human retina by low-coherence reflectometry," *Opt. Lett.* 22(13) (1997): 1039–1041.

[89] Choi, H. S., H. F. Taylor, and C. E. Lee, "High-performance fiber-optic temperature sensor using low-coherence interferometry," *Opt. Lett.* 22(23) (1997): 1814–1816.

[90] Tearney, G. J., et al., "Determination of the refractive index of highly scattering human tissue by optical coherence tomography," *Opt. Lett.* 20(21) (1995): 2258–2260.

[91] de Boer, J. F., T. E. Milner, M. J. C. can Gemert, and J. S. Nelson, "Two-dimensional birefringence imaging in biological tissue by polarization-sensitive optical coherence tomography," *Opt. Lett.* 22(12) (1997): 934–936.

[92] Everett, M. J., K. Schoenenberger, B. W. Colston Jr., and L. B. Da Silva, "Birefringence characterization of biological tissue by use of optical coherence tomography," *Opt. Lett.* 23(3) (1998): 228–230.

[93] Jiao, S., and L. V. Wang, "Two-dimensional depth-resolved Mueller matrix of biological tissue measured with double-beam polarization sensitive optical coherence tomography," *Opt. Lett.* 27(2) (2002): 101–103.

[94] Cheong, W. F., S. A. Prahl, and A. J. Welch, "A review of the optical properties of biological tissues," *IEEE J. Quant. Electron.* 26(12) (1990): 2166–2185.

[95] Scheel, A. K., et al., "First clinical evaluation of Sagittal laser optical tomography for detection of synovitis in arthritic finger joints," *Ann. Rheum. Dis.* 64(2) (2005): 239–245.

[96] Yuan, Z., Q. Zhang, E. Sobel, and H. Jiang, "Three-dimensional diffuse optical tomography of osteoarthritis: initial results in the finger joints," *J. Biomed. Opt.* 12(3) (2007): 034001–034001-11.

[97] Xu, Y., et al., "Three-dimensional diffuse optical tomography of bones and joints," *J. Biomed. Opt.* 7(1) (2002): 88–92.

[98] Yu, G., et al., "Real-time in situ monitoring of human prostate photodynamic therapy with diffuse light," *Photochem. Photobiol.* 82(5) (2006): 1279–1284.

[99] Li, C., R. Liengsawangwong, H. Choi, and R. Cheung, "Using a priori structural information from magnetic resonance imaging to investigate the feasibility of prostate diffuse optical tomography and spectroscopy: a simulation study," *Med. Phys.* 34(1) (2007): 266–274.

[100] Piao, D., et al., "Near-infrared optical tomography: endoscopic imaging approach," *Proc. SPIE* 6431 (2007): 643103–643101-100.

[101] Padhani, A. R., C. J. Harvey, and D. O. Cosgrove, "Angiogenesis imaging in the management of prostate cancer," *Nat. Clin. Prac., Urol.* 2(12) (2005): 596–607.

[102] Piao, D., et al., "Approach on trans-rectal optical tomography probing for the imaging of prostate with trans-rectal ultrasound correlation," *Proc. SPIE* 6850 (2008): # 68500E–68500E-14.

[103] Huang, M, and Q. Zhu, "Dual-mesh optical tomography reconstruction method with a depth correction that uses a priori ultrasound information," *Appl. Opt.* 43(8) (2004): 1654–1662.

[104] Choma, M., M. Sarunic, C. Yang, and J. Izatt, "Sensitivity advantage of swept source and Fourier domain optical coherence tomography," *Opt. Exp.* 11(18) (2003): 2183–2189.

Approach of trans-rectal NIR optical tomography probing for the imaging of prostate with trans-rectal ultrasound correlation

Daqing Piao, Zhen Jiang, Guan Xu, Cameron Musgrove, Charles F. Bunting
School of Electrical & Computer Engineering
Oklahoma State University, Stillwater, OK 74078
daqing.piao@okstate.edu

Abstract:
The trans-rectal implementation of NIR optical tomography makes it possible to assess functional status like hemoglobin concentration and oxygen saturation in prostate non-invasively. Trans-rectal NIR tomography may provide tissue-specific functional contrast that is potentially valuable for differentiation of cancerous lesions from normal tissues. Such information will help to determine if a prostate biopsy is needed or can be excluded for an otherwise ambiguous lesion. The relatively low spatial resolution due to the diffuse light detection in trans-rectal NIR tomography, however, limits the accuracy of localizing a suspicious tissue volume. Trans-rectal ultrasound (TRUS) is the clinical standard for guiding the positioning of biopsy needle owing to its resolution and convenience; nevertheless, TRUS lacks the pathognomic specificity to guide biopsy to only the suspicious lesions. The combination of trans-rectal NIR tomography with TRUS could potentially give better differentiation of cancerous tissue from normal background and to accurately localize the cancer-suspicious contrast obtained from NIR tomography. This paper will demonstrate the design and initial evaluation of a trans-rectal NIR tomography probe that can conveniently integrate with a commercial TRUS transducer. The trans-rectal NIR tomography obtained from this probe is concurrent with TRUS at matching sagittal imaging plane. This design provides the flexibility of simple correlation of trans-rectal NIR with TRUS, and using TRUS anatomic information as spatial prior for NIR image reconstruction.

Keywords:
Near-infrared optical tomography, trans-rectal, prostate, trans-rectal ultrasound

1. Introduction

Near-infrared (NIR) optical tomography is shown particularly useful for functional imaging of biological tissues where scattering of the photons dominates [1] and where NIR contrast based on intrinsic chromorphore content or exogenous probe can be linked to tissue physiology such as angiogenesis, oxygen deprivation or over-expression of specific biomarkers. Despite the considerable promising outcome of NIR optical tomography in diagnosis of breast cancer [2], understanding of cortex response [3], and characterization of rheumatologic dysfunction [4] where all the tissues under imaging are interrogated externally by non-invasive method, there is limited information regarding the practice of NIR tomography in internal imaging regime. Interstitial measurement by use of diffuse or near-diffuse photons has been employed for monitoring of photodynamic responses in organs such as prostate [5]. From the diagnostic perspective, the most appealing feature of NIR tomography may be arguably its unique functional contrast that is obtained *non-invasively*. It is thereby not surprising to see significant interest developed recently toward understanding the challenges and benefits of non-invasive NIR optical tomography of internal organs, in particular imaging the prostate [6, 7].

The translation of NIR optical tomography toward prostate imaging application may be prompted by the inadequate diagnostic modalities for prostate cancer. Prostate cancer may not be as lethal as breast cancer, however, the occurrence of prostate cancer among US men (1/6 life-time risk) is higher than that of breast cancer, making it the 2nd common cancer in US. The adoption of serum prostate specific antigen (PSA) test has significantly improved the chances of finding prostate cancer development at early stages. However, PSA is not a specific marker of prostate cancer, and PSA level as the single decision criterion could miss as many as 30% of prostate cancers [8].

In addition to PSA test, physical examination by digital rectal palpation can identify solid tumors in prostate; however, digital rectal examination (DRE) is not sensitive to small tumors. The suspicion of prostate cancer indicated by PSA, DRE, or its combination will prompt the use of prostate biopsy before evaluation of any treatment options. Prostate biopsy is guided by trans-rectal ultrasound (TRUS) as a clinical standard; however, the utility of TRUS in imaging prostate has been questionable except for directing the needle trajectory due to its lack of pathogonomic information of

Multimodal Biomedical Imaging III, edited by Fred S. Azar, Xavier Intes,
Proc. of SPIE Vol. 6850, 68500E, (2008)
1605-7422/08/$18 · doi: 10.1117/12.778329

the tissue. Systematic random biopsy is thus conducted in prostate with 6-24 samples of prostate tissue removed for pathology analysis [9].

There is evidence that prostate cancer development is associated with angiogenesis as in breast cancer [10], and NIR imaging may provide non-invasive assessment of prostate cancer. However, unlike the breast cancer, prostate cancer is thought to be more diffuse, even though the occurrence of it is mainly in the peripheral zone of the organ. Little has known to the optical properties of intact prostate tissue due to lack of optical modality that can image the prostate non-invasively. Capability of non-invasive prostate imaging by optical means will enable the study of prostate optical properties, and augment current diagnostics if the optical properties of prostate cancer are found to have substantial contrast with respect to those of normal prostate tissues.

Recently, a few simulative studies have been reported for trans-rectal NIR optical tomography of prostate, either by single NIR imaging modality [11], or a combination with MRI [6] to obtain the *a prior* spatial information. Experimental techniques for trans-rectal optical tomography at phantom or in vivo settings are also demonstrated [7]. NIR optical tomography is considerably stand-alone when used for imaging external organs owing to the ability of continuously and accurately monitoring the position of applicator array. The multi-modality approach also adds the morphological prior to substantially increase the reconstruction accuracy. The unique prostate anatomy of lying deep in pelvic compartment makes it difficult if not impossible to monitor the location and orientation of the probe without a real-time imaging of the relative anatomy of the prostate during optical interrogation. This difficulty certainly necessities the integration NIR optical tomography which is relatively slow and lack of spatial resolution to integrate with other fast and morphological imaging modalities. Integration of trans-rectal optical tomography with current morphological imaging modality comes with a few options: TRUS, MRI or endorectal MRI, and CT. Optical imaging as a non-invasive and potentially low-cost imaging modality will likely to play role for a broader population, which indicates the choice toward combining with the most commonly used imaging modality in urology---TRUS.

In this paper, we report the approach of developing a trans-rectal NIR tomography probe and system that can integrate with commercial TRUS. The trans-rectal NIR probe can add-on to TRUS probe, and the NIR tomography and TRUS data can be obtained concurrently in precisely aligned sagittal plane. The instrumentation of this add-on TR-NIR probe is confronted with some unprecedented fabrication challenges in NIR tomography. The fabrication approaches are reported, and the simulative studies on reconstructing trans-rectal NIR tomography is introduced. Initial investigation of using spatial a prior information for trans-rectal NIR reconstruction is also presented.

2. Design of sagittal-imaging combined trans-rectal NIR/US probe

The combined trans-rectal NIR/US probe is constructed with a commercial bi-plane TRUS probe. The TRUS probe has a 5MHz transverse imaging transducer and a 7.5MHz sagittal imaging transducer. The trans-rectal NIR probe is designed to take images in sagittal plane for coupling with sagittal TRUS. The choice of sagittal imaging NIR tomography is supported by the fact that prostate biopsy is mostly taken in sagittal view and sagittal NIR may reach deeper targets as there is more room to arrange NIR optodes in longitudinal direction. The TRUS probe has a circular cross-section profile of 20mm in diameter; however, the straightforward design of a co-centric circular NIR probe that can slide-fit with TRUS is abandoned. There are two issues preventing the use of this slide-fit design. Firstly a co-centric circular NIR probe will likely to increase the combined NIR/US transducer over 25mm in diameter, a dimension not well tolerable for insertion in clinical setting. Secondly the distal end of this TRUS probe which is transverse imaging transducer has larger diameter than the sagittal imaging transducer as well as the connection part between handle and the transducer, therefore the axial sliding will leave NIR array and sagittal TRUS transducer in loose contact. We thus incorporated a top-capping option to couple NIR array closely to the sagittal TRUS transducer.

As shown in Fig. 1, the sagittal NIR array attaches to the top of TRUS, which is better illustrated in side and front views. The NIR probe consists of one source array and one detector array running parallel, each with 7 channels. The source/detector channels are placed at 1cm separation, and the source array is placed 2cm from the detector array. The array dimension of 60mm×20mm will be used to couple the 60mm×10mm sagittal TRUS transducer that is exposed in the open window between NIR source and detector arrays. The minimum source-detector distance of 20mm in this sagittal geometry validates the use of diffusion approximation to the radiative transfer equation for image reconstruction. Since the detection depth of a NIR probe is roughly 1/3-1/2 of the probe dimension, the imaging depth is expected to reach approximately 30mm from the probe surface. This depth may be sufficient for imaging of prostate peripheral zone where most of prostate cancers are found.

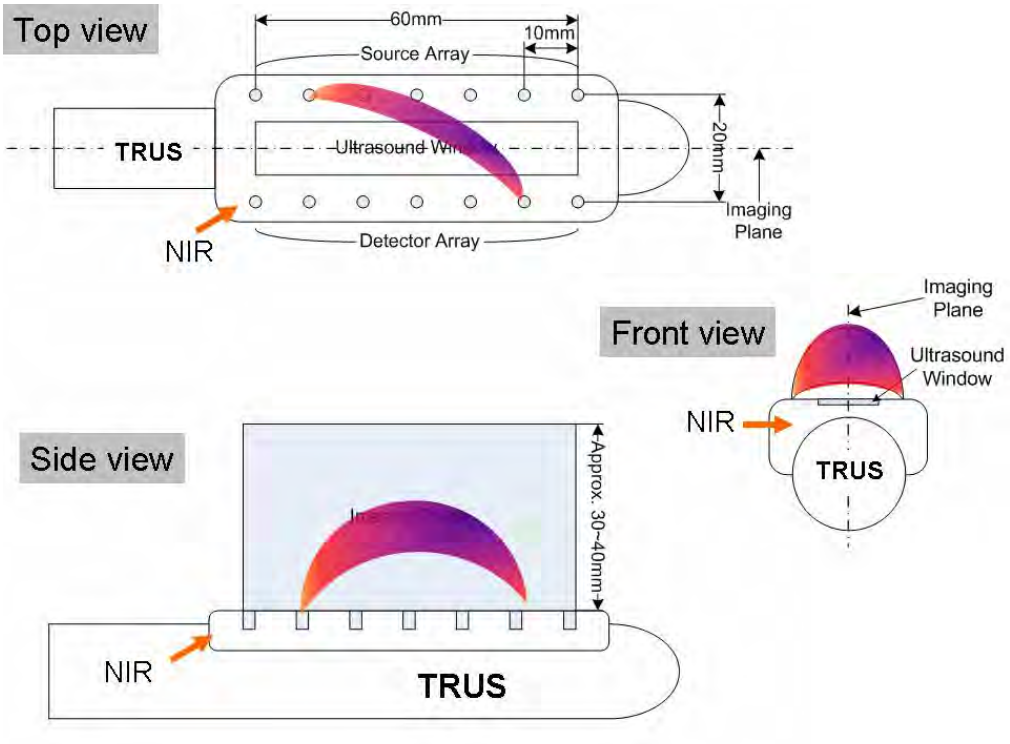

Fig. 1 Geometry of sagittal NIR optical tomography array for coupling to sagittal TRUS transducer

3. Simulative study for sagittal trans-rectal NIR optical tomography

3.1 Forward model

Prostate and peripheral tissues are shown to have scattering dormant in near-infrared spectral region [12]. Diffusion theory is thus considered as an accurate description of photon propagation in prostate tissue. The minimum source-detector distance of 20mm in this sagittal imaging geometry justifies the use of diffusion approximation to the radiative transfer equation.

In the forward model, a frequency domain diffusion equation is used [13]:

$$-\nabla\cdot\kappa(r)\nabla\Phi(r,\omega)+\left(\mu_a+\frac{i\omega}{c}\right)\Phi(r,\omega)=q_0(r,\omega) \qquad (1)$$

where $\Phi(r,\omega)$ is the photon fluence rate at position *r*, μ_a is the absorption coefficient, c is the speed of light in tissue, $q_0(r,\omega)$ is the source term, and κ is the diffusion coefficient defined as:

$$\kappa=\frac{1}{3(\mu_a+\mu_s')} \qquad (2)$$

where μ_s' is the reduced scattering coefficient.

Equation (1) is solved by finite-element method. The geometry of this sagittal NIR imaging probe attached to TRUS is inherently a 3-D imaging problem because the image will be reconstructed in a single plan intersecting the source and detector arrays. A 3-D mesh is thus needed for the defined imaging volume of 80mm×40mm× 60mm (length×width×depth when seeing longitudinally). The finite element mesh of this imaging volume is generated in COMSOL Multiphysics package (see Fig.2a). A total of approximately 9000 nodes and 50000 tetrahedron elements are included in this FEM mesh. The mesh is then embedded to a diffuse optical tomography modeling package NIRFAST (see Fig. 2b) developed in Dartmouth College [13].

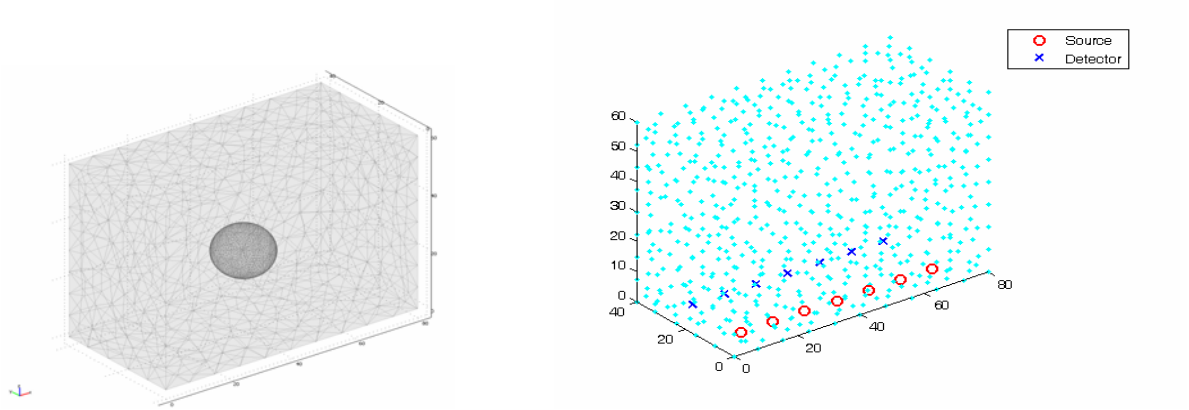

(a)Mesh Generated with COMSOL (b)Mesh converted to be used in NIRFAST

Fig. 2 Mesh generated for forward model

3.2 Sensitivity profile

The Jacobian matrix derived from equation 1 contains four categories of elements: $\frac{\partial I_{ij}}{\partial \mu_{an}}, \frac{\partial \theta_{ij}}{\partial \mu_{an}}, \frac{\partial I_{ij}}{\partial \kappa_n}$ and $\frac{\partial \theta_{ij}}{\partial \kappa_n}$, where I and θ are the intensity and phase of the surface measurement of the photon fluence, i is the source number, j is the detector number, n is the node number. The value of $\frac{\partial I_{ij}}{\partial \mu_{an}}$ part is plotted in Fig.3 as a measure of diction sensitivity of the system. The plot is obtained by first adding terms with the same subscript n value as shown below:

$$\left[\sum_{i=1,j=1}^{7,7} \frac{\partial I_{ij}}{\partial \mu_{a1}}, \sum_{i=1,j=1}^{7,7} \frac{\partial I_{ij}}{\partial \mu_{a2}}, \ldots\ldots, \sum_{i=1,j=1}^{7,7} \frac{\partial I_{ij}}{\partial \mu_{a8000}} \right] \quad (3)$$

which reflects the total effects of the μ_a at each node on the photon density flux intensity at the detectors. The Jacobian values for the nodes along a straight line (x=40mm, y=20mm for Fig. 3.2) are then calculated afterward with respect to the z coordinates. The Jacobian plot in the middle plane of the imaging volume in Fig. 3.2 demonstrates that imaging sensitivity rapidly degrades as the depth increases, indicating the tendency of reconstructing deep lesions in shallower location. The plot in Fig. (b) indicates the profile of higher sensitivity toward the middle region of the probe. It is thus expected that the anatomic information obtained from TRUS may improve the lesion localization in both depth and longitudinal directions.

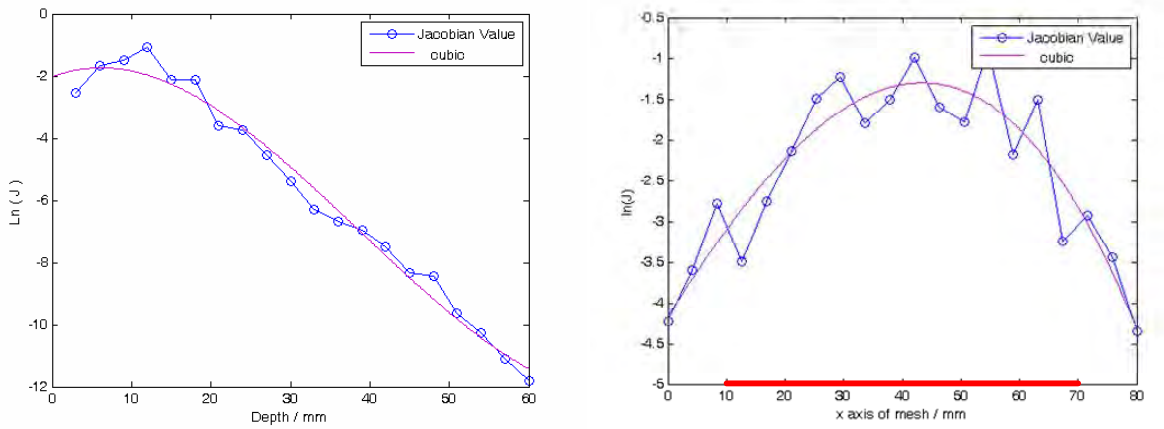

(a) Sensitivity along the depth (b) Sensitivity along the longitudinal direction (probe marked red)

Fig. 3 Sensitivity analysis

3.3 Image reconstruction

3.3.1 NIR image reconstruction

Image reconstruction routine based on NIRFAST is used for the inverse computation. The reconstruction is based on the non-linear searching of the minimum sum-squared error equivalent to solving the equation:

$$S(\mu_a,\kappa)=\sum[f_{simulated}(\mu_a,\kappa)-f_{measured}]^2=0 \quad (4)$$

where $f_{measured}$ is the experimental measurement and $f_{simulated}$ is the calculated forward data based on initial guess of μ_a and κ.

Newton-Raphoson method is used to iteratively solve equation (4) by approximation of:

$$S(\mu_a+\Delta\mu_a,\kappa+\Delta\kappa)=S(\mu_a,\kappa)+J(\mu_a,\kappa)\cdot(\Delta\mu_a,\Delta\kappa) \quad (5)$$

where $\Delta\mu_a$ and $\Delta\kappa$ are very small values as being used in finite difference method, *J* is the first order partial derivative of the $f_{simulated}$ function. Move the $S(\mu_a,\kappa)$ term to the left of the equation and differentiate both sides, the following equation can be derived:

$$J(\mu_a,\kappa)^T[f_{simulated}(\mu_a+\Delta\mu_a,\kappa+\Delta\kappa)-f_{neasured}]=J(\mu_a,\kappa)^T J(\mu_a,\kappa)\cdot(\Delta\mu_a,\Delta\kappa) \quad (6)$$

Since the solving of (μ_a,κ) involves the calculation of the inverse of $J(\mu_a,\kappa)^T J(\mu_a,\kappa)$, which might induce singularity, a normalization factor ρI is added to avoid singularity:

$$J(\mu_a,\kappa)^T[f_{simulated}(\mu_a+\Delta\mu_a,\kappa+\Delta\kappa)-f_{neasured}]=[J^T J(\mu_a,\kappa)+\rho I]\cdot(\Delta\mu_a,\Delta\kappa) \quad (7)$$

Therefore the updating value of (μ_a,κ) can be calculated by:

$$(\Delta\mu_a,\Delta\kappa)=J(\mu_a,\kappa)^T[J^T J(\mu_a,\kappa)+\rho I]^{-1}[f_{simulated}(\mu_a+\Delta\mu_a,\kappa+\Delta\kappa)-f_{neasured}] \quad (8)$$

In NIRFAST, the actual updating equation is as follows:

$$(\mu_a,\kappa)_{new}=(\mu_a,\kappa)_{old}-J^T(JJ^T+\rho I)^{-1}[f_{measured}-f((\mu_a,\kappa)_{old})] \quad (9)$$

3.3.2 NIR image reconstruction with prior target information

Trans-rectal NIR tomography reconstruction is first achieved without any prior information. A 80mm×40mm× 60mm mesh similar to that in is Fig. 2a is used, where a 5mm radius spherical inclusion located at (35,20,20) has similar mesh density as the background but within with optical contrast. The background is set at $\mu_a=0.002mm^{-1},\mu_s'=0.8mm^{-1}$ and the occlusion at $\mu_a=0.025mm^{-1},\mu_s'=1.0mm^{-1}$. These parameters are used throught out the rest of simulation in this paper.

As is shown in Fig. 4 for a target located 2cm in depth, the images reconstructed without any prior structural information shift the occlusion toward the source-detector plane. This is expected from Fig.3.

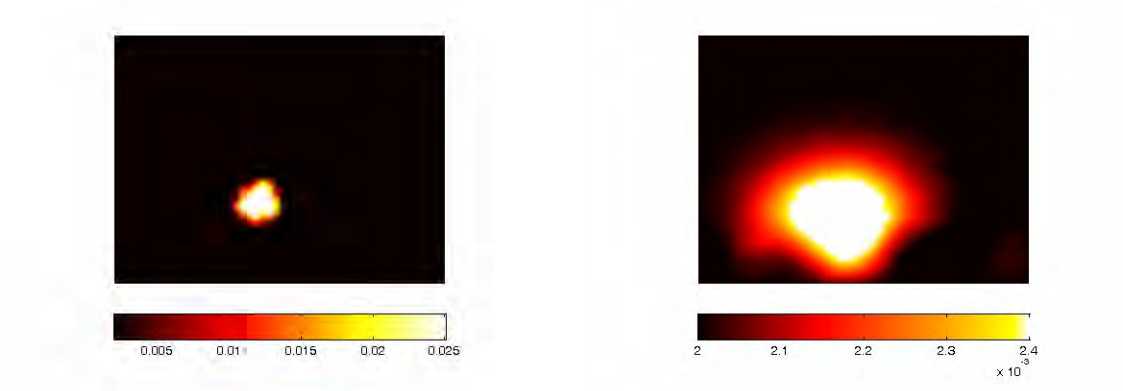

(a) Simulated Lesion Position (b) Reconstructed Image

Fig. 4 Blind NIRFAST Reconstruction without a priori information

When a priori structural information can be included, a denser element area with 10mm radius (twice the size of that of the simulated lesion) in the forward mesh is generated. In addition a Jacobian weighing method is used to intentionally elevate the sensitivity in the suspicious region [14]. By dividing the imaging volume to 12 layers of depth, the weight for each layer is determined by: $W_i = \{\max[J(layer_i)]/\max[J(layer_1)]\}^{-1}$, and the Jacobian value of each layer is updated by : $J_{i\_new} = J_{i\_old} \cdot W_i$, $i \in$ layeri . Images of this approach are shown in Fig. 5 where the localization accuracy is improved but it comes with ring-type artifacts.

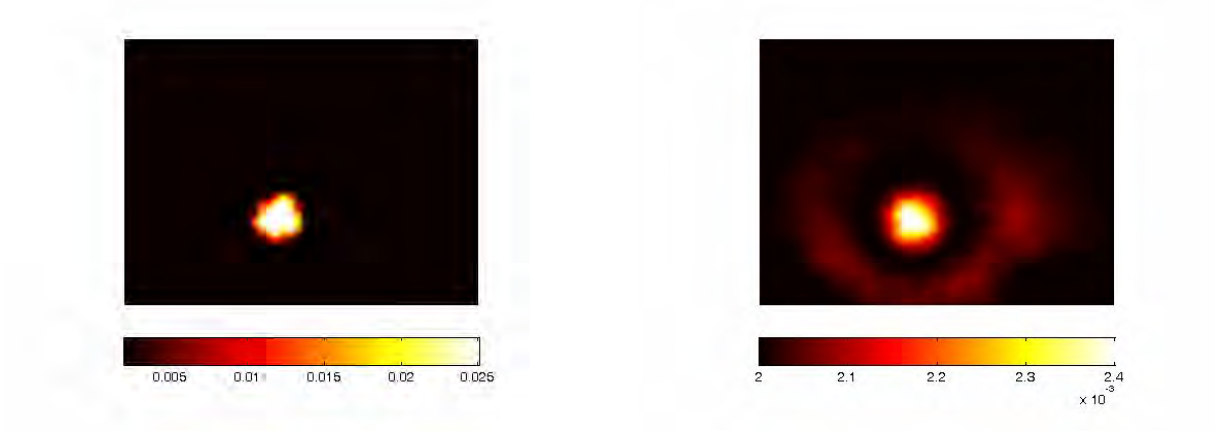

(a) Simulated Lesion Position (b) Reconstructed Image

Fig. 5 Jacobian-weighted reconstruction with spatial a priori information

3.3.3 Direct validation of Jacobian weighing method

The Jacobian weighing method leading to Fig. 5 is performed by weighing only at the suspicious lesion area. The validity of this approach is examined by a simple case as shown in Fig. 6. In this test two inclusions are created at (40,20,20) and (40,20,30), and a 5mm radius lesion with absorption contrast is added only to the deeper occlusion. Although Jacobin weighting is performed to both occlusions, the reconstruction reveals only one occlusion with the optical contrast at the preset location. The Jacobin-weighting method is thus considered robust and adequate.

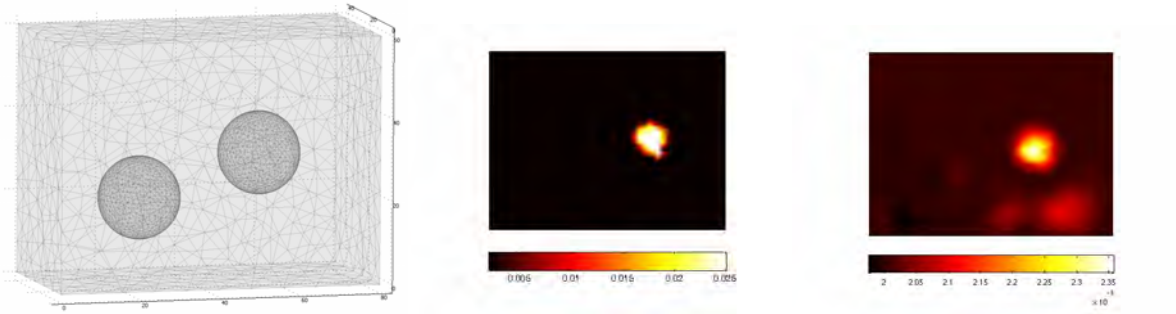

(a) mesh (b) forward contrast (c) reconstruction

Fig. 6 A Simple case to validate Jacobian weighing method

4. Instrumentation for combined trans-rectal NIR/US imaging probe

4.1 Add-on NIR probe design and fabrication

The geometry of bi-plane TRUS probe with NIR array attached is shown in Fig. 7(a). The NIR array is fabricated out of black polycarbonate material to suffice absorptive boundary condition. The array is connected to a handle by an aluminum brace structure, and this NIR handle is clamped to TRUS handle by another bottom piece. Neither of the connecting brace or the handle is shown in this picture. The imaging view of TRUS which is the middle plane of the transducer falls in the center of the total volume of tissue interrogated by trans-rectal NIR array (the 3-D volume mesh shown in the figure).

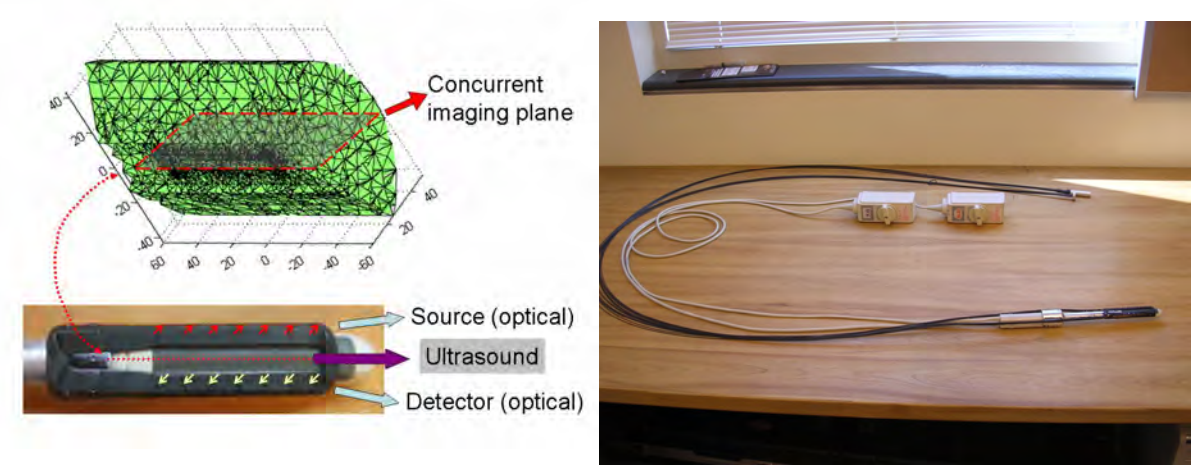

(a) (b)

Figure 7 (a) Concurrent trans-rectal NIR/US geometry (b) The NIR/US transducer with cable/fiber

This trans-rectal NIR probe consists of 14 channels of fibers, 7 for sources and 7 for detectors. The source array at the probe surface is 20mm away from the detector array. In each array the 7 sources or the 7 detectors are separated 10mm with each other. The side firing arrangement requires the source/detector channels be directed laterally. The detection of diffuse photons for large source-detector separation requires the use of large detection aperture, whereas the compact space in the probe prohibits virtually any attempt of bending the fiber for lateral illumination.

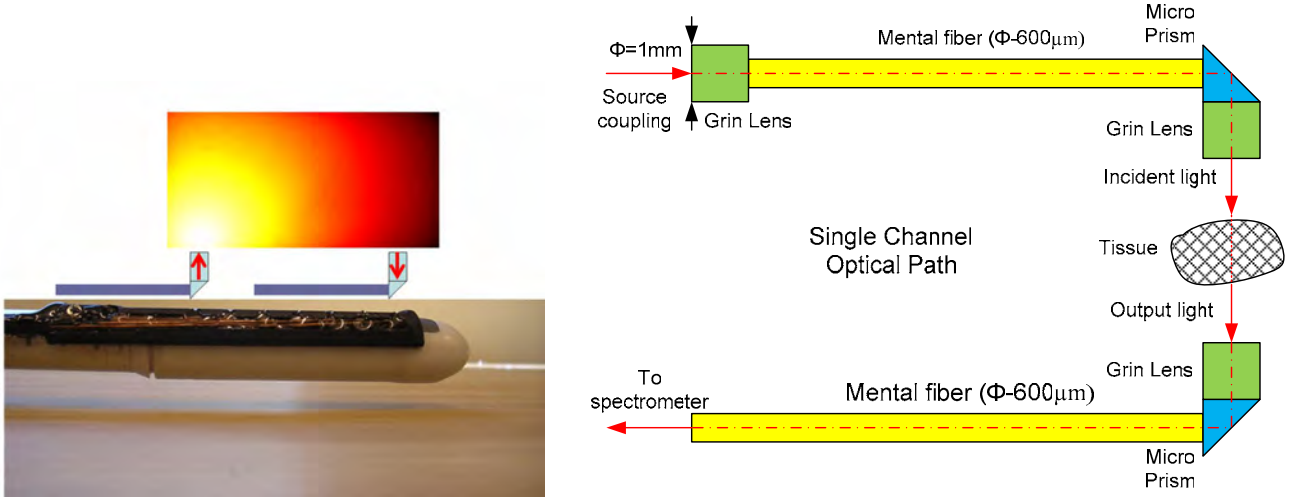

(a) (b)

Figure 8 (a) Photograph of the completed probe single showing the packaging of 7 fibers. (b) Single channel optical path between source and detector.

The micro-optics-based 90 deg deflection approach that is commonly used in side-firing optical coherence tomography endoscope design is implemented in this trans-rectal NIR array fabrication. This configuration is illustrated in Fig. 8, where the photon fluence from a side-firing source fiber is plotted and the returning path to detector is depicted. The photograph is the completed probe with 7 fiber channels assembled in the small groove of the NIR probe at each side. There are total of 49 source-detector pairs, and the optical path for each source-detector is shown in Fig. 8(b). The source fiber and the detector fiber, both of 600 μm metal-coated, are polished and attached to a 1mm right angle micro-prism to deflect light 90 degree inside the probe. A 0.25pitch Φ-1mm gradient-index (GRIN) lens having N.A. of 0.46 is attached to the micro-prism for illumination and detection at the probe surface. The proximal end of the source fiber is epoxyed to another GRIN lens to improve the coupling of the light power. It is found that the fiber (600μm-core diameter) with GRIN lens gives 5%~10% higher coupling efficiency than using the fiber only. The micro-prism has

~80% deflection at 830nm for collimated beam. The overall coupling efficiency of the entire assembly including two GRIN lenses, 3m fiber and one micro prism is approximately 50%, so each single channel from the proximal coupling point to the detector will experience ~6dB attenuation of the signal in addition to the absorption and scattering loss.

4.2 Distribution of the source channel, SLD source spectrum and the coupled spectrum.
The spread-spectral-encoding technique based on a single broad-band light source is implemented for simultaneous sampling of all 7 source channels at all 7 detector locations with a single 16 bit CCD camera [15]. Under the condition of a source with power uniformly distributed across a spectral band, the signal dynamic range will only be determined by the medium optical properties and the distance between source-detector pairs. The CCD camera used in the system has 16 bit resolution corresponding to maximum of 48dB. This dynamic range may not be sufficient to handle a large imaging volume when shorter and longer source-detector distances are used. This is made worse since the source spectrum is actually Gaussian shape, so the power distributed to different source channels will be different. To alleviate this issue, higher power of the source spectrum is coupled to sources at the side, and weaker power to the sources in the middle. This is illustrated in Fig. 9. The source is a superluminescent diode having FWHM spectrum band of 14nm. It is coupled to 7 source fibers at the sequence of 4 3 2 1 7 6 5 from shorter wavelength to longer one. Source channel 1 and 7 thereby couple more power than the other source channels. In the pervious coupling configuration, the spectrally-decoded signals corresponding to all source-detector pairs forms a diagonally brightest pattern as shown in Fig. 10(a), where the fibers of 1 to 8 couple the source spectrum from shorter to longer wavelength sequentially. The current signal intensity patterns are shown in Fig. 10(b) where the sequences of the source coupling are marked on top. The intensity pattern is then post-configured to retrieve the signal for corresponding source-detector channels before data calibration and image reconstruction.

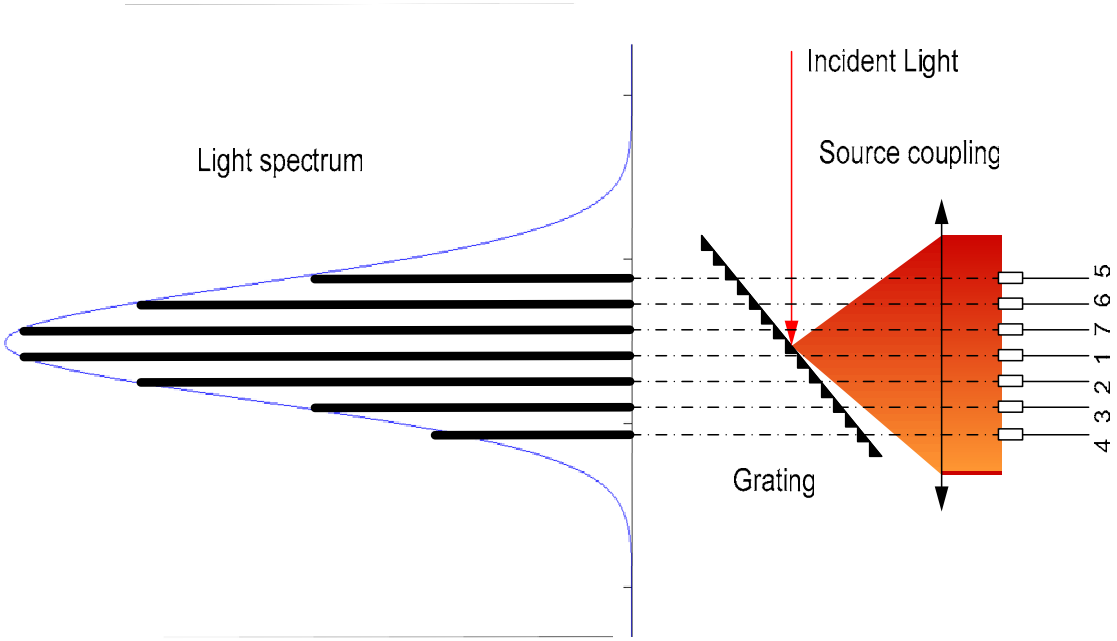

Figure 9. Coupling of dispersed Gaussian beam to source fibers.

4.3 Calibration of signal based on semi-infinite boundary condition
A semi-infinite boundary condition [16] employed for this sagittal imaging NIR probe gives the following equation:

$$Ln\left(\rho^2 I\right) = a \cdot \rho + b \tag{10}$$

where ρ is the distance between the each source-detector pair, I is the intensity of the surface signal, a and b are coefficients determined by tissue optical properties and light modulation frequency. Figure 11 (a) shows the simulation result of the relation between the distance and the intensity for semi-infinite modal, which fits the linear model quite

well. The experiment data shown in figure 11 (b) only fit the line well in the distance shorter than 50mm, when the distance between the source and detector goes up to 55mm or longer, the relation between those two parameters does not follow the linear model anymore. This is potentially caused by either limited CCD dynamic range or lack of source power for further source-detector pairs. There are 7 data sets for each source or detector; however, we use only the first fifth data-sets to reconstruct the image. The non-uniformity of the data from source up to detector is first corrected by fitting the data of homogenous medium to the linear pattern predicted by semi-infinite model, then the non-uniformity correction matrix for all source-detector pairs is used to correct the data acquired from medium with occlusion. A typical complete intensity profile after compensating chanel non-uniformity is shown in Fig. 12. The intensity compensated data is then fed to 'NIRFAST' package for image reconstruction. There is no phase information obtained by our CCD-based system, therefore only the intensity part of the NIRFAST reconstruction is actually implemented by mapping the CW data to a 100MHz modulation domain where the scattering properties are presumed to be known [17].

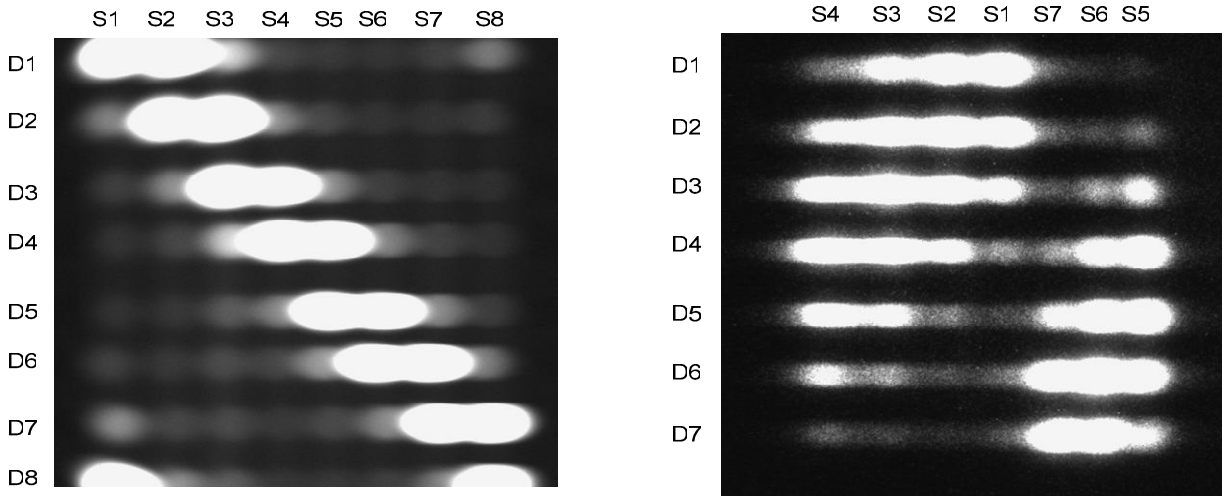

(a) Previous sequential source coupling (b) Current non-sequential source coupling

Fig. 10 Patterns of the spectrally-decoded pattern

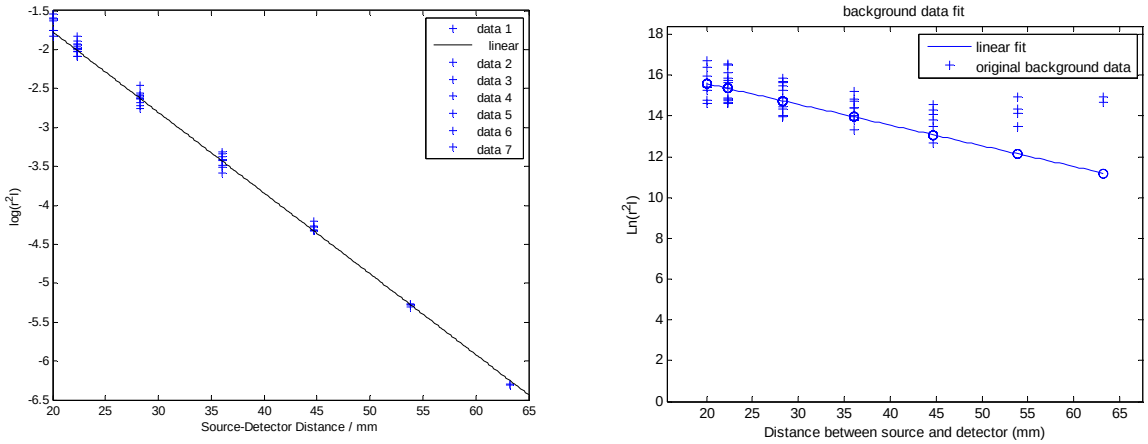

(a) (b)

Figure 11. Data calibration using semi-infinite model (a) simulation shows that the signal intensity follows the pattern in semi infinite model. (b) Using the linearity pattern of semi-infinite model to calibrate the experimental data.

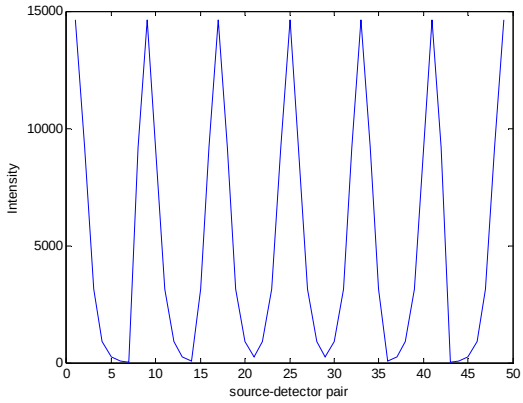

Figure 12. Calibrated homogenous background signal

5. Initial results of sagittal NIR optical imaging with a prior information

5.1 Experimental setup

Fig. 13 shows our initial experimental setup. In the experiment, the probe is positioned on one side of the container that has 45 deg angle to the tabe surface. The 1% Intralipid solution is used as background of having $\mu_a = 0.002mm^{-1}$ and $\mu_s' = 1.0mm^{-1}$. The occlusion is cylinder with 15mm in diameter and 15mm in height that can move parallel or perpendicular to the probe surface by 45 deg mounted translation stages. The occlusion is made of black plastic to simulate very high absorption contrast. The intralipid surface is high enough above the probe to for removing the boundary effect of upper surface.

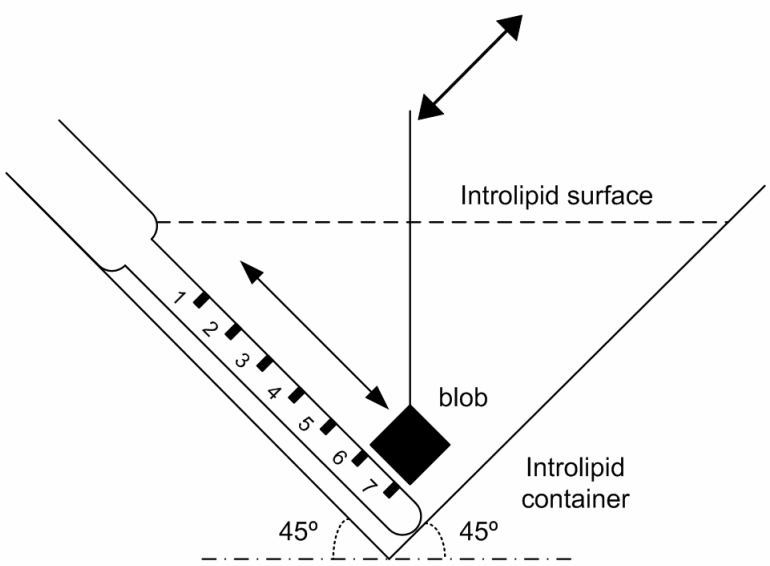

Fig. 13 Experimental setup for combined TR-NIR/US imaging of occlusion in homogenous medium

5.2 NIR image reconstruction from experimental data.

Figure 14 shows the images reconstructed from experimental data for the occlusion positioned at left side (closest to source/detector 1), middle, and right side (closest to source/detector 7). The bottom of the cylinder is roughly 7mm away from the probe surface, giving a 15mm depth of the occlusion. The left column is reconstructed with NIR information

only, and the right column is reconstructed by knowing the location and approximate size of the occlusion, as described in Section 3.3. The information of occlusion location and size is assumed to be known from TRUS. TRUS images were actually unavailable when the images were taken due to an outstanding system configuration problem. In Figure 14, the images reconstructed with a prior information has the occlusion displayed at the correct depth as expected. The image for the occlusion in the right end of the probe is quite interesting, where the two-blob artifact shown for only NIR reconstruction is removed when the reconstruction is guided by a prior information.

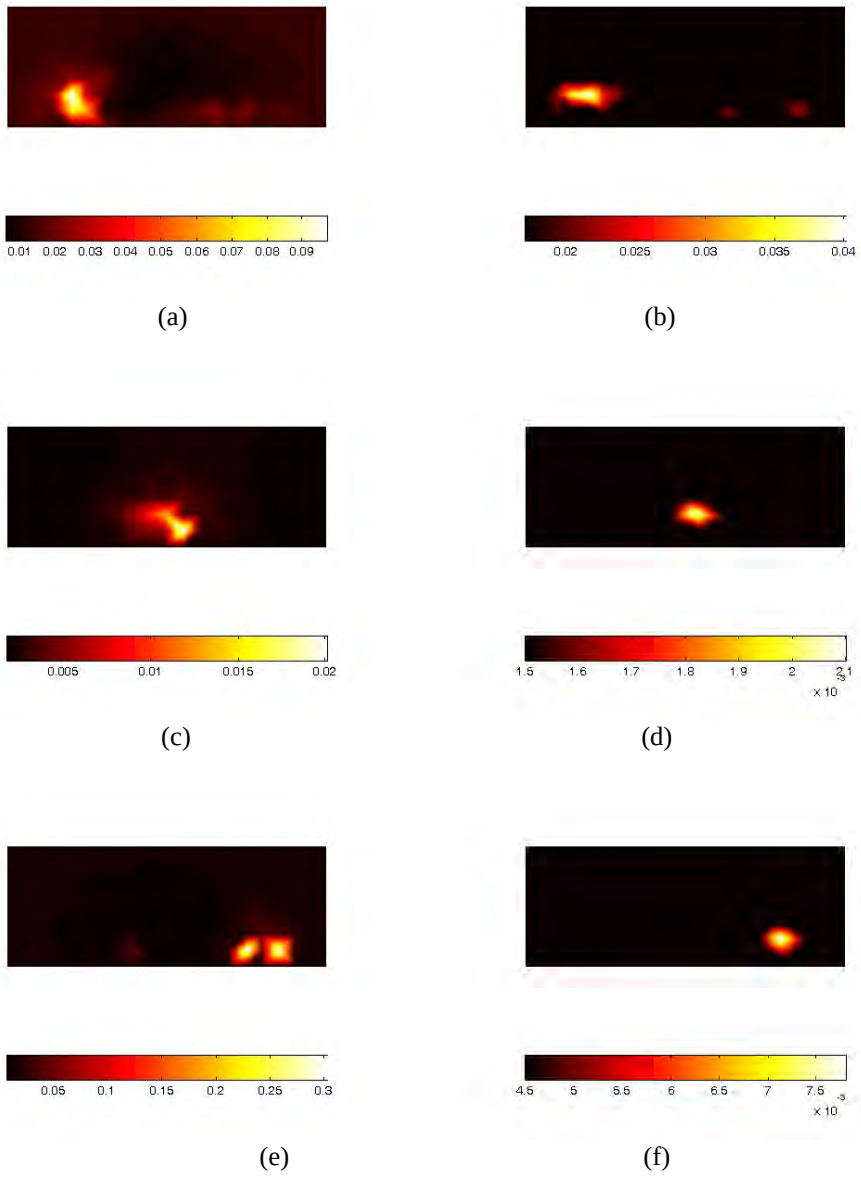

Figure 14. Image reconstructed from experimental data without and with a prior location information

The 1-D profiles of the occlusion are further depicted in Fig. 15 for the reconstruction without and with location information. Figure 15 (a) is the longitudinal profile across the occlusion when it is in the middle of the probe. There is no significant change of longitudinal location as expected. Figure 15 (b) is the depth-resolved profile across the

occlusion when it is in the middle of the probe. It is clearly shown that the center of the blob is localized deeper into the medium with a prior information, however, it does not reach the actual 15mm location.

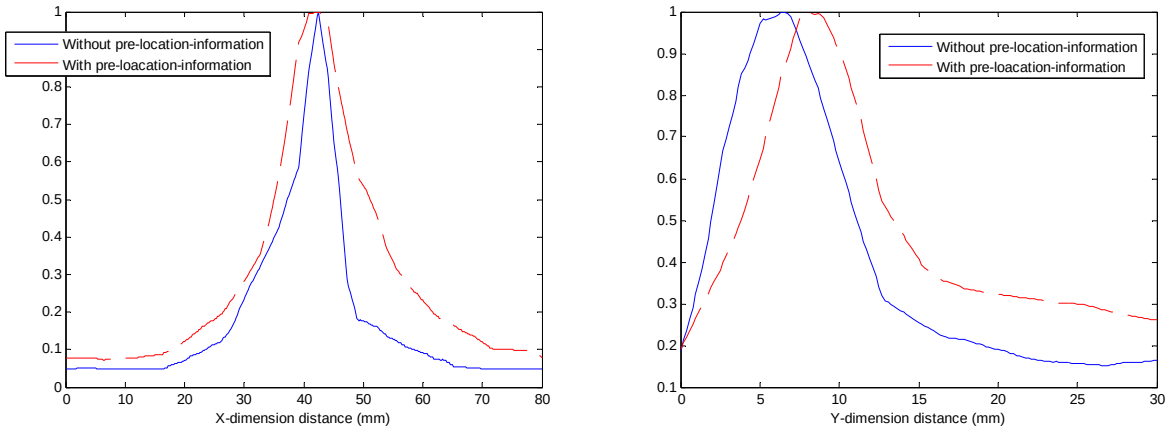

(a) (b)

Figure 15. 1-D profiles across the occlusion located in the middle of the probe at 10mm depth. (a) longitudinal dimension, (b) along the depth from the probe surface

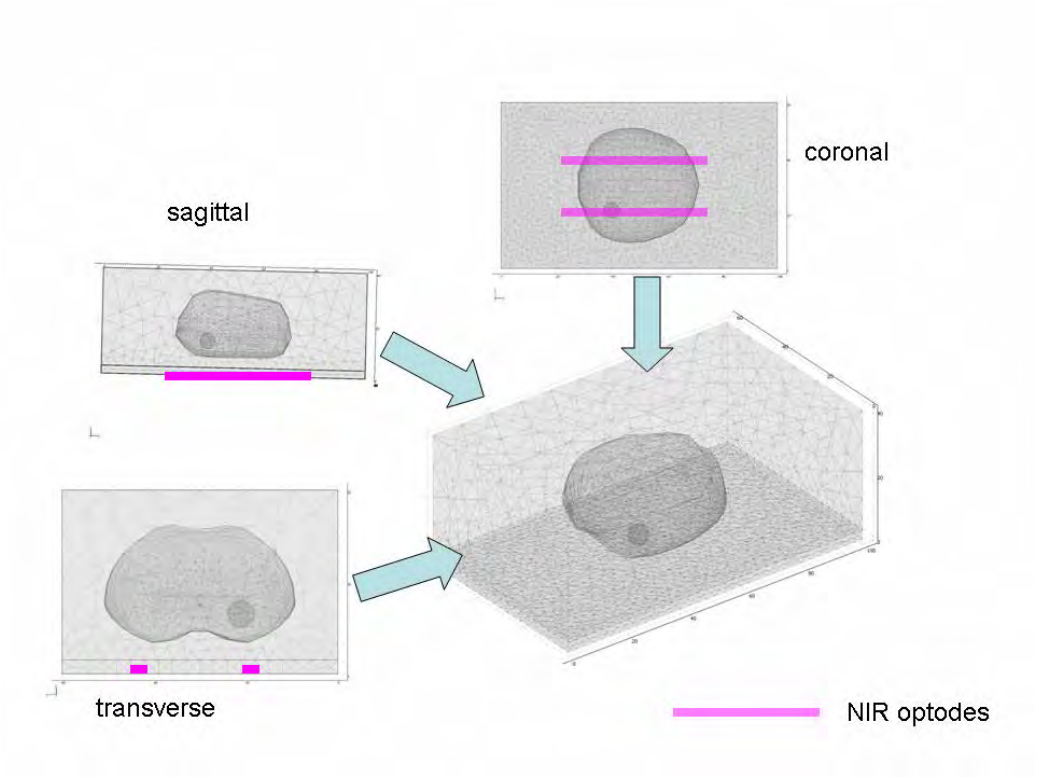

Figure 16. 3-D synthetic prostate model under development to account for prostate anatomy

6. Discussions and future works

What is presented in this paper is very preliminary results of simulation and experiments based on a sagittal-imaging trans-rectal NIR probe and system. The prostate anatomy is much more complicated than Fig. 2. An immediate task will

be to construct a synthetic prostate model that accounts for the anatomy of prostate and takes the rectal wall thickness into consideration. A 3-D prostate model is under development as shown in Fig. 15. This mesh is first generated in 3Ds MAX (Trial Version) for the surface profile, then converted to 3D solid volume with AUTOCAD 2008, and finally imported into COMSOL Multi-physics. Works are going on to make this mesh compatible for our existing reconstruction methods. Such a model will be used to quantitatively investigate the imaging performance of the developed system, primarily the contrast resolution and depth resolution, as well as validating if the source-detector channels are sufficient to reconstruct reasonably accurate optical properties for a frequency-domain setup.

Adding a prior location information in simulation does give correct reconstruction of the occlusion target, however, the experiments so far are not successful as much as in simulation. We anticipate that this is mainly related to the calibration of the experimental data acquired from the CCD camera. Future investigations will be conducted to optimize the data libration method.

In this work, the a prior structural information incorporated so far is actually by assumption, not from actual US image. Taking the structural information from TRUS image will be underway by investigating the segmentation technique needed to robustly extract the needed structural information not limited to location, dimension, and number of suspicious occlusions. Extensive simulative studies are required to understand the optimum way of using TRUS a prior information in NIR tomography. It is expected that NIR tomography of prostate may deal with multiple occlusions due to the potentially diffuse distribution of prostate cancer. NIR tomography of prostate may therefore become more complicated than NIR imaging of breast, not only because of the unique anatomy, bit also due to the different cancer problem.

Acknowledgement

This work has been supported by Army Medical Research and Material Command through grant W81XWH-07-1-0247.

References

[1] Hillman EM. “Optical brain imaging in vivo: techniques and applications from animal to man.” J Biomed Opt. 2007 Sep-Oct;12(5):051402.
[2]. B.W. Pogue, S.P. Poplack, T.O. McBride, W. A. Wells, K.S. Osterman, U.L. Osterberg, and K.D. Paulsen, “Quantitative hemoglobin tomography with diffuse near-infrared spectroscopy: pilot results in the breast,” Radiology, 218: 261-266 (2001).
[3]. S.G. Diamond, T.J. Huppert, V. Kolehmainen, M.A. Franceschini, J.P. Kaipio, S.R. Arridge, D.A. Boas, “Dynamic physiological modeling for functional diffuse optical tomography,” Neuroimage. 30(1):88-101 (2006).
[4]. JM Lasker, CJ Fong, DT Ginat, E Dwyer, AH Hielscher, “Dynamic optical imaging of vascular and metabolic reactivity in rheumatoid joints,” J Biomed Opt. 2007 Sep-Oct;12(5):052001.
[5] G Yu, T Durduran, C Zhou, TC Zhu, JC Finlay, TM Busch, SB Malkowicz, SM Hahn, AG Yodh, “Real-time in situ monitoring of human prostate photodynamic therapy with diffuse light,” Photochem Photobiol. 2006 Sep-Oct;82(5):1279-84.
[6] C. Li, R. Liengsawangwong, H. Choi, R. Cheung, “Using a priori structural information from magnetic resonance imaging to investigate the feasibility of prostate diffuse optical tomography and spectroscopy: a simulation study,” Med Phys. 2007 Jan;34(1):266-74.
[7] D Piao, H Xie, W Zhang, G Zhang, C Musgrove, CF Bunting, H Dehghani, BW Pogue, SN Vemulapalli, “Near-infrared optical tomography: endoscopic imaging approach” Proceedings of SPIE, 6431-02 (invited paper), San Jose, CA, January 20-25, 2007
[8] L Boccon-Gibod. “Rising PSA with a negative biopsy,” Eur Urol. 2001;40 Suppl 2:3-8. Review.
[9] GD Grossfeld, PR Carroll, “Prostate cancer early detection: a clinical perspective,” Epidemiol Rev. 2001;23(1):173-80. Review.
[10] AR Padhani, CJ Harvey, DO Cosgrove, “Angiogenesis imaging in the management of prostate cancer.” Nat Clin Pract Urol. 2005 Dec;2(12):596-607. Review.
[11] C Musgrove, CF Bunting, H Dehghani, BW Pogue, D Piao, “Computationa aspects of endoscopic near-infrared optical tomography: initial investigations” Proceedings of SPIE, 6434-09, San Jose, CA, January 20-25, 2007
[12] M Solonenko, R Cheung, TM Busch, A Kachur, GM Griffin, T Vulcan, TC Zhu, HW Wang, SM Hahn, AG Yodh, “In vivo reflectance measurement of optical properties, blood oxygenation and motexafin lutetium uptake in canine large bowels, kidneys and prostates,” Phys Med Biol. 2002 Mar 21;47(6):857-73.

[13] H Dehghani, BW. Pogue, SP. Poplack, and KD. Paulsen, “Multiwavelength three-dimensional near-infrared tomography of the breast: initial simulation, phantom, and clinical results”, Applied Optics Vol. 42, No. 1, 135-145(2003).
[14] M. Huang and Q. Zhu, “Dual-mesh optical tomography reconstruction method with a depth correction that uses a priori ultrasound information,” Applied Optics 43, 1654-1662 (2004)
[15] D Piao, BW Pogue, “Rapid near-infrared tomography for hemodynamic imaging using a low coherence wideband light source”, Journal of Biomedical Optics, (12): 014016 (2007).
[16] Q Zhu, NG Chen, D Piao, P Guo, X Ding, “Design of Near-Infrared Imaging Probe with the Assistance of Ultrasound Localization,” Applied Optics, Vol. 40 Issue 19, pp.3288-3303 (2001)
[17] H Xu, “MRI-coupled Broadband Near-infrared Tomography for Small Animal Brain Studies (4.43 Mbytes) “ PhD thesis, Dartmouth College, 2005.

Development of a continuous-wave dual-band trans-rectal optical tomography system for concurrent sagittal imaging with trans-rectal ultrasound

Zhen Jiang, Hao Xie, Daqing Piao, Jerzy S. Krasinski
School of Electrical and Computer Engineering, Oklahoma State University, Stillwater, OK 74078
[*]*Corresponding author: daqing.piao@okstate.edu*

ABSTRACT

A dual-band trans-rectal optical tomography system is constructed based on an endo-rectal near-infrared/ultrasound applicator that has been developed previously in our laboratory. The endo-rectal NIR/US applicator consists of a commercial bi-plane ultrasound and a NIR probe attached to the sagittal ultrasound transducer. The NIR probe consists of 7 illumination & 7 detection channels that are distributed in parallel to and aside the sagittal TRUS transducer. The emissions from a 780nm and an 830nm light sources are combined and delivered sequentially to the 7 NIR source channels of the endo-rectal NIR/US probe. The 7 NIR detection channels are coupled to a spectrometer for separation of the signals at two wavelengths illuminated from single source channel. The dual-band signals from all source channels are acquired sequentially by a CCD camera synchronized with the source switching. The acquisition of dual-band trans-rectal optical tomography data is accompanied by position-correlated concurrent trans-rectal ultrasound imaging. The reconstruction of a target at dual-wavelength illumination is guided by *a priori* spatial information provided by the sagittal trans-rectal ultrasound. Liquid phantoms with different hemoglobin concentration and oxygen saturation are used to test the feasibility of dual-band trans-rectal optical tomography.

Keywords: Near-infrared tomography, oxygen saturation, trans-rectal ultrasound

1. INTRODUCTION

The utility of non-invasive imaging of the tissue oxygenation by multi-band near-infrared (NIR) light has been recognized for decades. The distinctly different spectra of hemoglobin absorption of the NIR light when being oxygenated and deoxygenated have enabled finding lesions of angiogenesis or altered oxygenation indicating malignant changes [1-2]. Studies on prostate cancer have found a correlation between the cancer and increased micro-vessel density [3]. Changes of the local oxygen saturation were also observed during the prostate photodynamic therapy under interstitial NIR measurement [4]. Tissue oxygenation status is also an important prognostic indicator for androgen-deprivation therapy of newly diagnosed metastatic prostate cancer [5]. There is increasing evidence that the ability of quantifying the hemoglobin concentration and oxygen saturation in prostate is important for the diagnosis, prognosis, and treatment monitoring.

Encouraged by the applications of multi-band NIR light in breast cancer imaging [6-7], researchers recently start to develop NIR tomography techniques for trans-rectal imaging of the prostate [8-10]. In this work we report the progress on the instrumentation of dual-band trans-rectal NIR imaging. The dual-band trans-rectal NIR tomography is to be combined with trans-rectal ultrasound (TRUS) to take advantage of real-time positioning information and further the anatomic information of US to guide the NIR image reconstruction.

2. METHODS AND MATERIALS

A total of three endo-rectal imaging NIR applicators have been historically developed in our laboratory to investigate dual-band trans-rectal NIR tomography that may be coupled with TRUS. The first one was an axial-imaging probe of 13mm in diameter [11]. The second one was an axial-imaging probe of 20mm in diameter [8] which is comparable in

Multimodal Biomedical Imaging IV, edited by Fred S. Azar, Xavier Intes, Proc. of SPIE Vol. 7171,
71710G · © 2009 SPIE · CCC code: 1605-7422/09/$18 · doi: 10.1117/12.808232

size to the trans-rectal ultrasound transducer. The third probe was for sagittal imaging and could couple directly to a sagittal TRUS transducer for concurrent NIR/US imaging [10].

2.1 The 13mm-diamter axial-imaging endo-rectal NIR probe

Figure 1 illustrates the 13mm-diamter axial imaging NIR tomography probe. It consists of 16 optical channels including 8 for sources and 8 for detectors. Those source and detector channels were interlaced evenly on the circle. The diameter of each optical fiber is 600μm. A 10mm-diameter cone lens was used for deflecting the light circumferentially for axial-imaging. The fibers and cone-lens were mounted together in a 13mm diameter black sleeve and sealed with transparent optical epoxy. A total of 16 sealed transparent apertures were made at the axial-plane of the probe for the light-path.

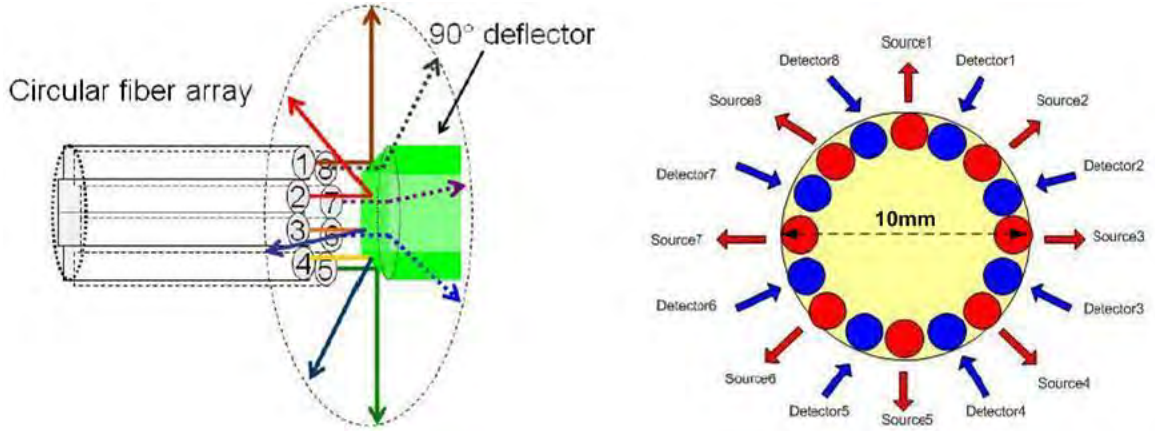

Figure 1. Geometry of the 13mm axial-imaging NIR tomography probe

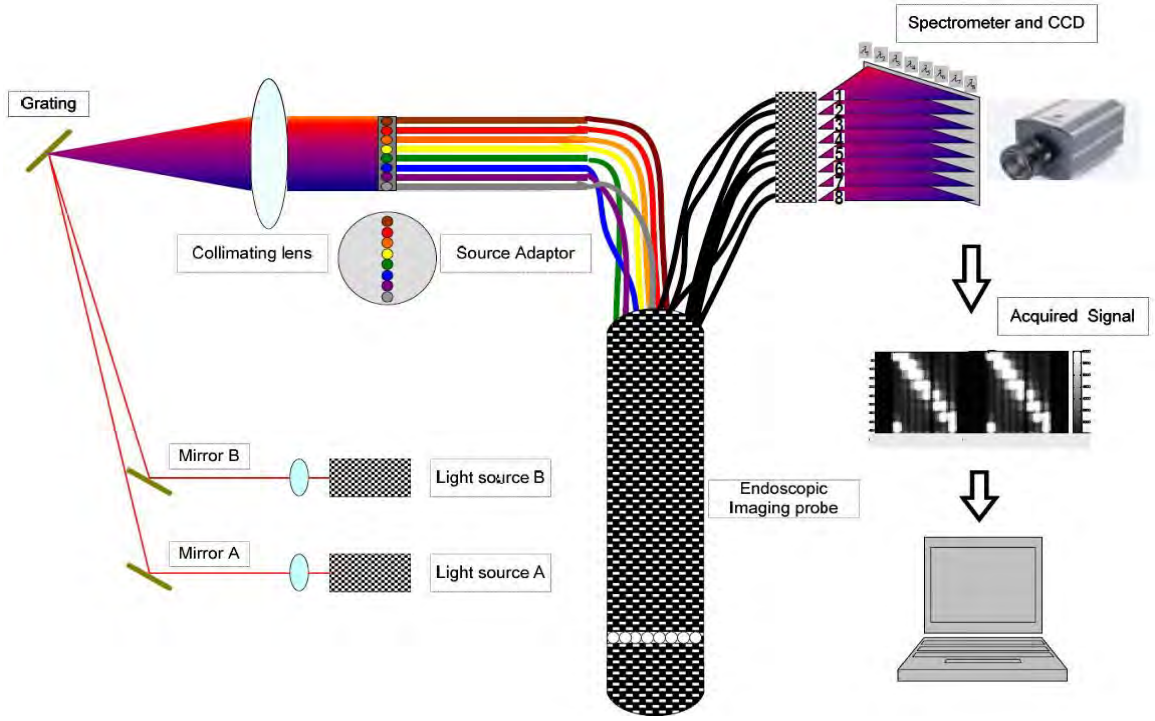

Figure 2. Spread-spectral-encoding based dual-wavelength NIR imaging system

For this probe the dual-wavelength NIR imaging was configured in spread-spectral-encoding mode. Shown in Fig. 2, two broadband (~14nm bandwidth) superluminescent diode (SLD) light sources (780nm and 830nm) pigtailed to single mode fibers were used in the system. Each SLD delivers 14mW of power. The SLD outputs were collimated at

different angles to a 1200 groves/mm grating and the dispersed beams of both bands overlap. The dual-wavelength dispersed beam was collimated by a planar-convex lens with a focal length of 300mm, and then coupled onto 8 linearly aligned source fibers. Each source channel coupled ~1.5nm bandwidth out of each SLD bands for illumination to the medium, and the dual-band light was collected by detection fibers coupled to a spectrometer where the dual-band signals were differentiated by a 300 grooves/mm grating to two groups, each containing a complete set of measurements for all source and detector channels for each wavelength band. The complete set of the dual-band data, shown in Fig. 3 which was acquired by a 16-bit CCD camera, was calibrated based on photon diffusion equation and underwent image-reconstruction using the NIRFAST algorithm developed by Dartmouth NIR imaging group. The use of photon-dissuion equation for this 13mm probe may not be accurate owing to the smaller size of the probe with respect to the mean scattering distance; however, the reconstructed dual-band images of the hemoglobin and oxygenation were qualitatively correct as a result of likely canceling out of the inaccuracy from both bands.

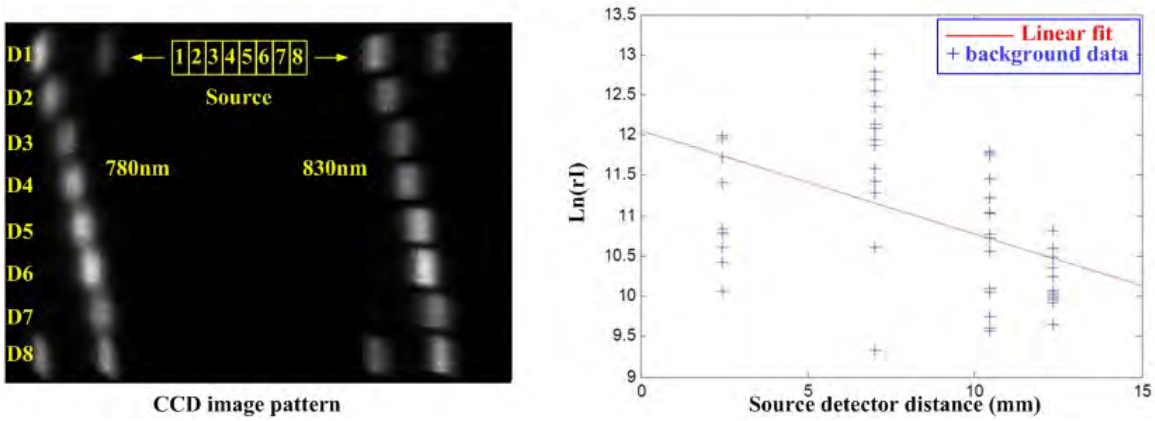

Figure 3. CCD image and raw data of 13mm-probe

2.2 The 20mm axial-imaging endo-rectal NIR probe

Figure 4 illustrates the configuration of the 20mm axial-imaging endo-rectal NIR probe. Similar to the previous 13mm-imaging probe, there are 8 source and 8 detector optical channels spaced circularly. Each optical channel was constructed with a 1.0mm core diameter fiber and aligned to a 45º rod lens of 2mm diameter to deflect the beam transversely for side-firing. A 2mm drum lens was attached for illumination and beam focusing. The length of the probe is 7” which was comparable to a standard TRUS probe.

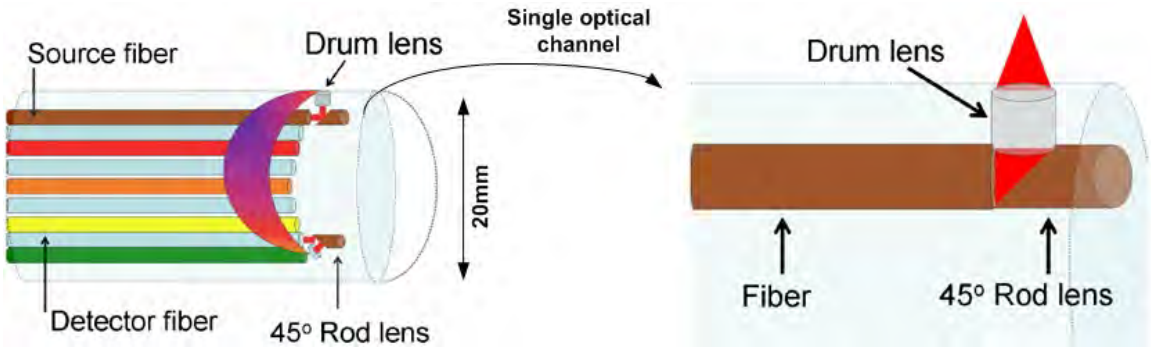

Figure 4. Diagram of 20mm endoscope NIR tomography transverse imaging probe

This 20mm diameter probe was connected to a time-multiplexing light delivery setup for dual-band NIR tomography as shown in Fig. 5. The ~100mW outputs from two laser diodes (LDs) at 785nm and 850nm were coupled by a bifurcated fiber to a fiber switch that was home-made using a linear motorized translation stage (Zaber Technologies). The switching of the light upon 8 source channels was synchronized with the CCD acquisition of the corresponding signals received by all detectors.

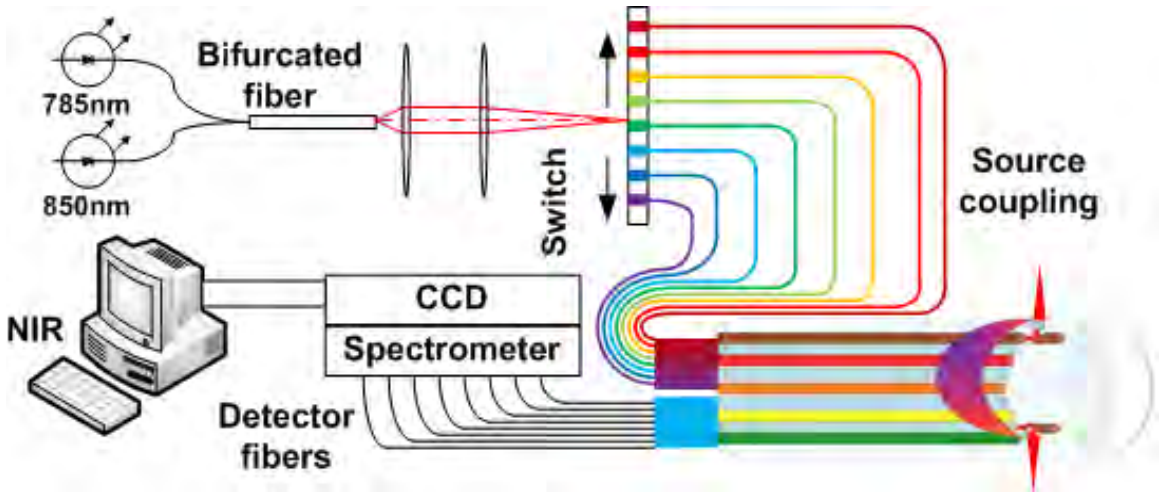

Figure 5. Dual wavelength NIR tomography system for 20mm-probe

Each complete set of the data consists of 8 frames corresponding to each source channel being turned on by the fiber switch. Fig. 6 is the one frame data when the source 3 is switched on. Because of the longer distance between the source and detector, the total 64 data sets follow a better linear fitting curve than the previous data sets for the 13mm probe in Fig. 3. The use of fiber switching also minimized the cross-talk among the adjacent source channels. The weakest signal however may submerge in the background noise owing to the limited dynamic range of the CCD.

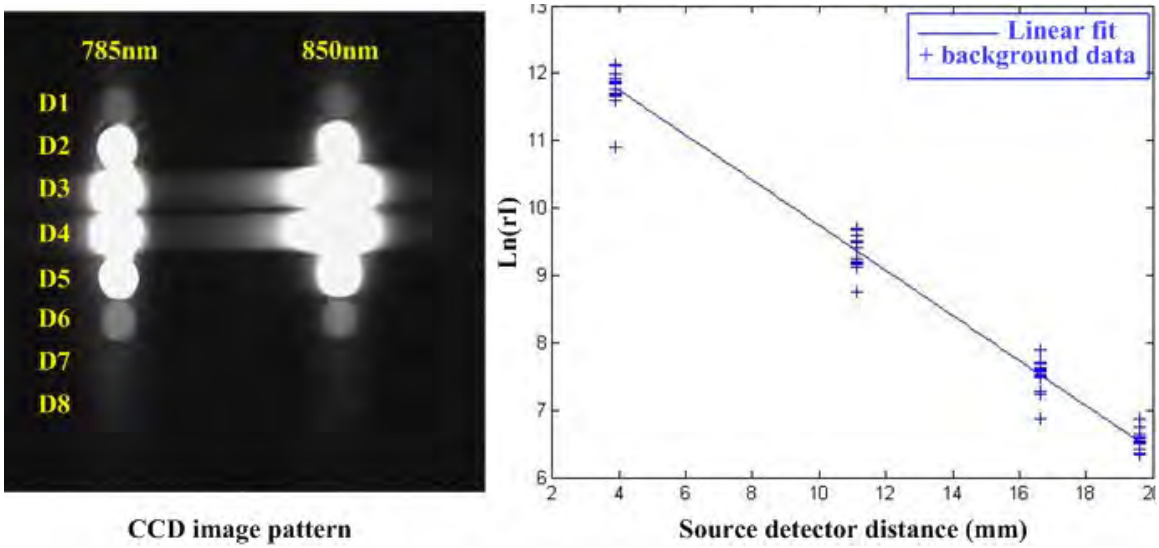

Figure 6. CCD image and raw data of 20mm probe

2.3 Combined trans-rectal NIR and ultrasound imaging probe

A sagittal trans-rectal NIR imaging probe was developed for coupling with the TRUS and to improve the imaging depth as in sagittal view the optodes can occupy larger array for deeper interrogation. The integrated sagittal-imaging trans-rectal NIR/US applicator consists of a custom-built NIR probe and a commercial sagittal TRUS transducer operating at 7.5MHz, as shown in Fig. 7. The sagittal TRUS transducer occupies a space of 60mm×10mm. The NIR applicator was fabricated from a black polycarbonate material and built to a cap-shape to attach to the TRUS probe. A slot of 60mm×10mm was opened up in the NIR applicator to expose the sagittal TRUS transducer.

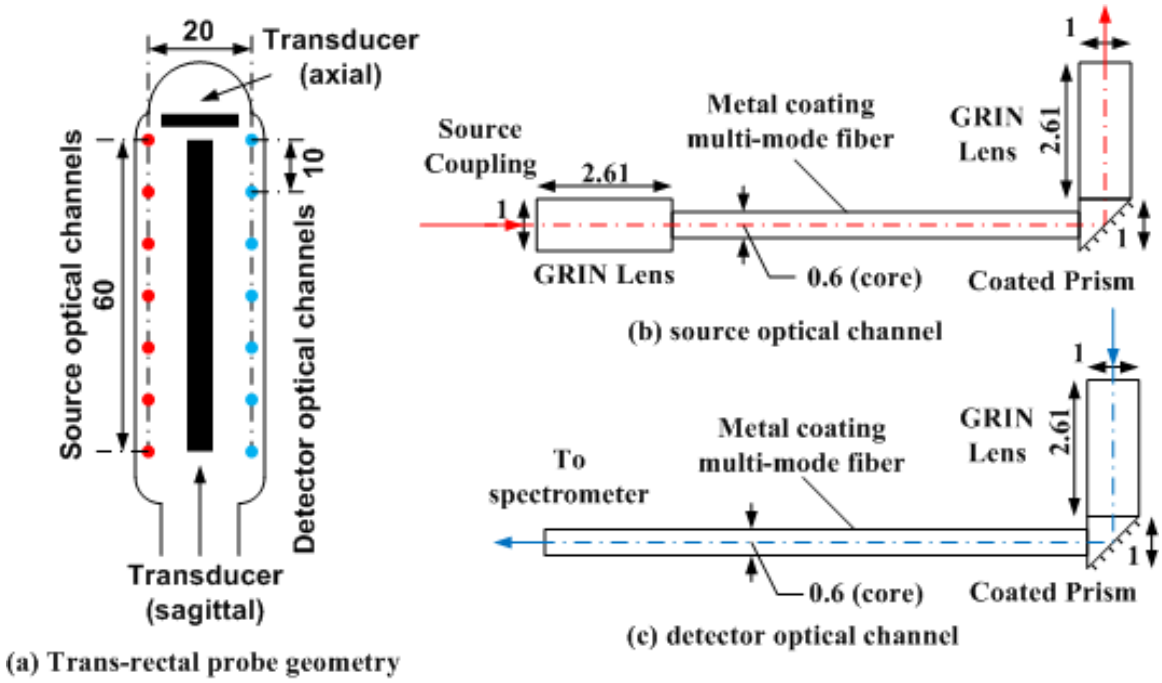

Figure 7. Combined trans-rectal NIR/US imaging probe geometry (unit: mm)

The source array and the detector array, separated 20mm laterally, each has 7 channels spaced at 10mm. A metal-coated 600μm-core diameter fiber (Oxford Electronics) was chosen for each optical channel. As shown in Fig. 7, each source channel includes 2 gradient-index (GRIN) lenses and 1 prism attached to the fiber while each detector channel has 1 GRIN lens and 1 prism attached to the fiber. The GRIN lens (Newport Corporation) has a pitch of 0.25, a diameter of 1mm, a length of 2.61mm, and a numerical aperture of 0.46. The prism is a coated 1mm right angle micro-prism (Tower Optics). Each fiber was polished and epoxied to a prism and a GRIN lens was attached to the other side of the micro-prism for illumination and detection at the probe surface. Each source channel has one GRIN lens attached to the proximal end of the fiber for coupling the emission from the light source.

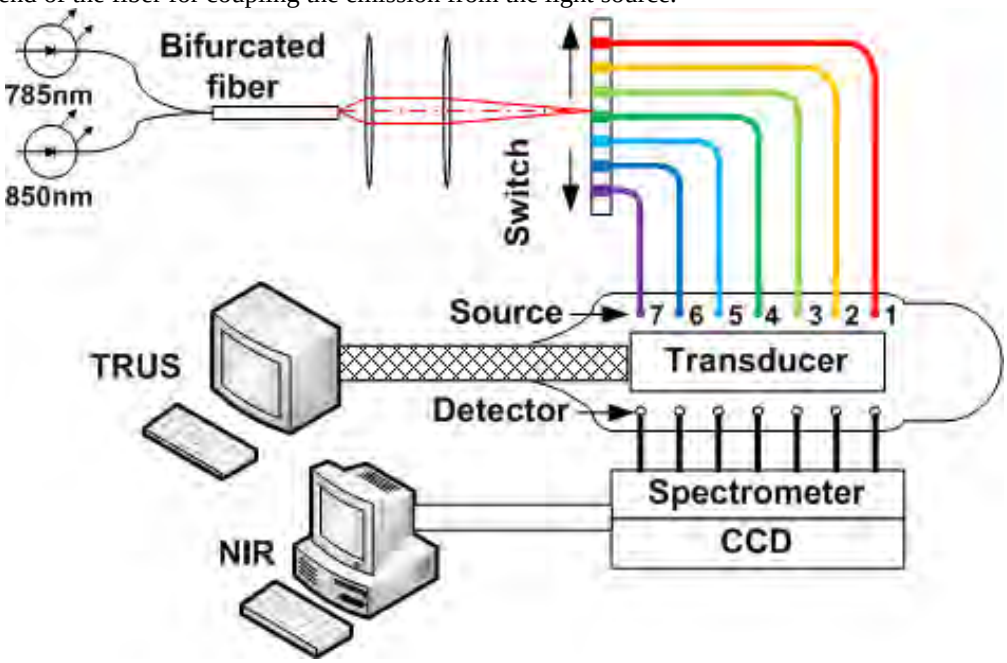

Figure 8. Dual wavelength system setup for combined trans-rectal NIR/US probe

The combined NIR/US system for dual-band trans-rectal mode imaging is shown schematically in Fig. 8. The US scanner was an Aloka SSD-900V portable machine. The US images were transferred to the main computer of the combined imager by a PCI image acquisition card (National Instruments PCI-1405). The source switching is by the time-multiplexing setup described in Fig. 5. This system takes 7 frames to acquire a complete set of data. One example of the single-frame image for the fiber switch being turned to source channel 4 is depicted in Fig. 9. The signals have less dynamic range than do in Fig. 6 because of the configurations of the optodes.

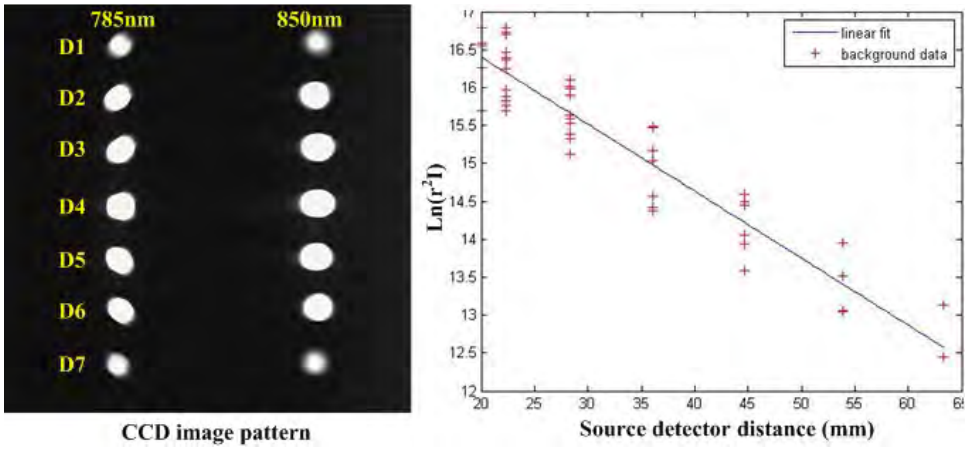

Figure 9. CCD image and raw data for trans-rectal NIR/US imaging probe

2.4 Setup for measurements of hemoglobin concentration and oxygen saturation.

A setup shown in Fig. 10 was built for measuring the blood hemoglobin concentration and oxygen saturation. Oxygen and Nitrogen gases were introduced to the fresh sheep blood (300mL) in a tank to administer the level of blood oxygen saturation (StO_2) which was monitored by an oxi-meter. A pump delivered the blood from the tank to a cylindrical container placed 2.5mm away from the endo-rectal NIR probe. Test started from the lowest StO_2 level in the blood and stopped when it became saturated.

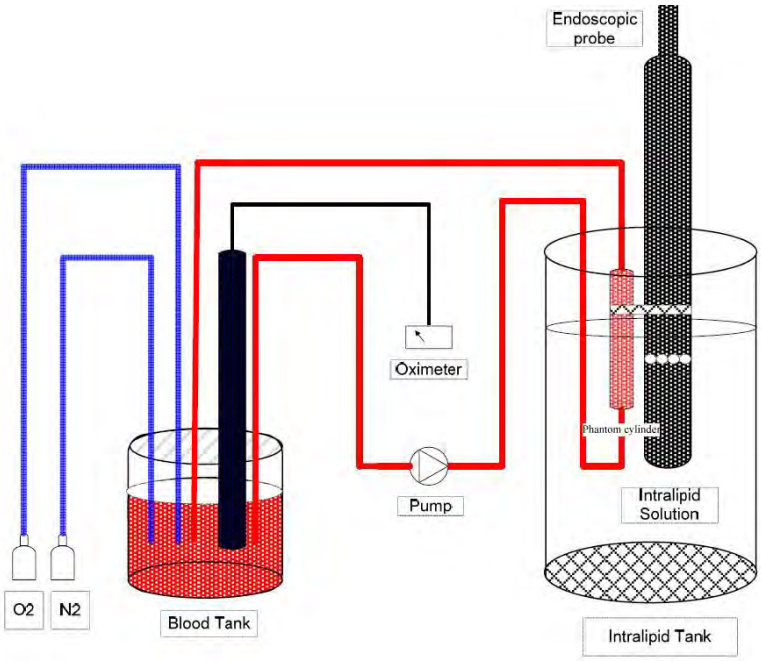

Figure 10. Diagram of blood circulation system for measurements of StO_2

3. PRELIMINARY RESTULS

3.1 Dual-band absorption measurements by the 13mm axial-imaging endo-rectal NIR probe.

Calibration of the system at both wavelengths was carried out using homogenous medium with different concentrations of diluted India ink (concentration 0.005%~0.5%). A container was made into cylinder shape (10mm inner diameter) from a solid phantom (0.0056mm^{-1} of absorption and 1.03mm^{-1} of reduced scattering). The container was fixed close to the probe (2.5mm away from container surface to probe surface) in a 1% intralipid background (0.0023mm^{-1} in absorption and 1.0mm^{-1} in reduced scattering). Another 2ml 1% intralipid was poured into the cylindrical container. The container wall was thinner than 1mm. The total volume of this cylindrical container was 3ml. The change of the absorption of adding one drop (0.02ml) of the diluted ink (0.5%) into the intralipid medium was previously calibrated by use of transmission measurements and Beer's law. One frame data was taken after adding each drop of ink up to 10 drops. The reconstructed absorption of the diluted ink in the container was shown in Fig. 11 where a linear relationship is found comparing with the true values.

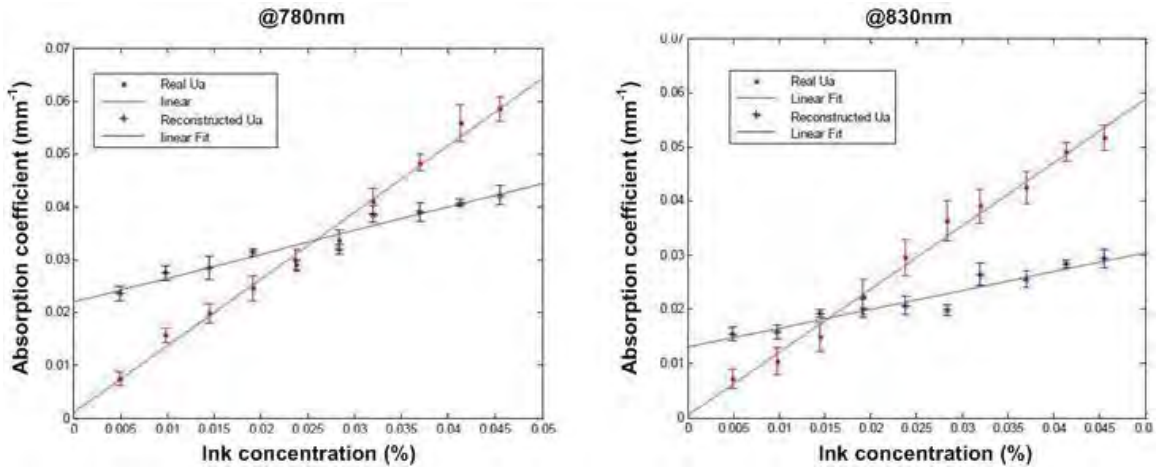

Figure 11. True absorption coefficient and reconstructed absorption coefficient of diluted ink

3.2 Dual-band measurements of blood oxygenation by the 13mm axial-imaging endo-rectal NIR probe.

By using the imaging system configured in Fig. 10 and the calibration results in Fig. 11, the reconstructed absorption coefficients of the sheep blood when the oxygen saturation level changed were illustrated in Fig. 12. Due to the fluctuation of oxygen and nitrogen flowing in the blood and some other aspects including temperature control, leakage of gas from the blood tank, the blood could not be fully oxygenated. However, the tendencies of decreasing and increasing absorption values with respect to the increasing oxygenation at the two wavelength bands were correct.

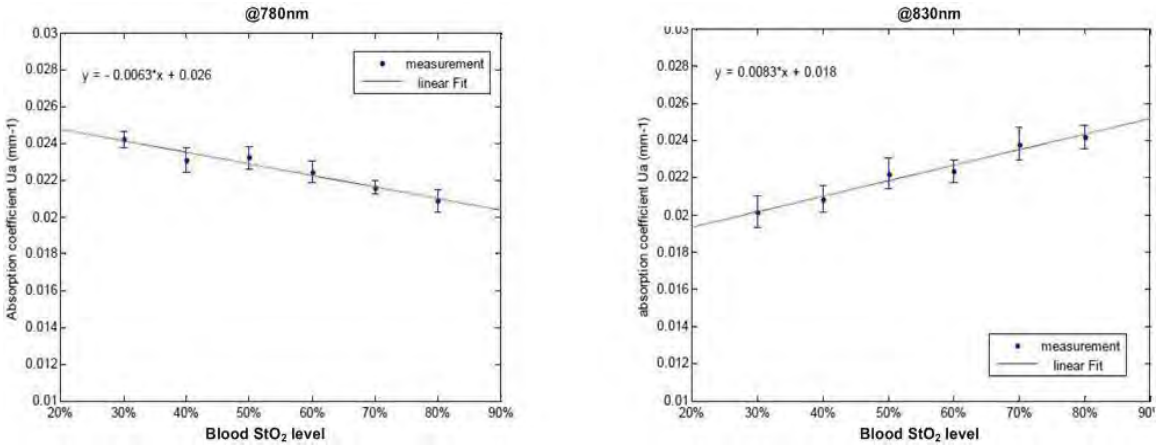

Figure 12. Variation of the hemoglobin absorption coefficient along with the StO_2 changes

The reconstructed total hemoglobin concentration of the sheep blood circulated to the cylinder container aside the 13mm probe is illustrated in Fig. 13. Constant level of the total hemoglobin concentration was correctly imaged. The reconstructed oxygen saturation of the sheep blood circulated to the cylinder container is illustrated in Fig. 14. The images show correct trend of increased StO_2 levels.

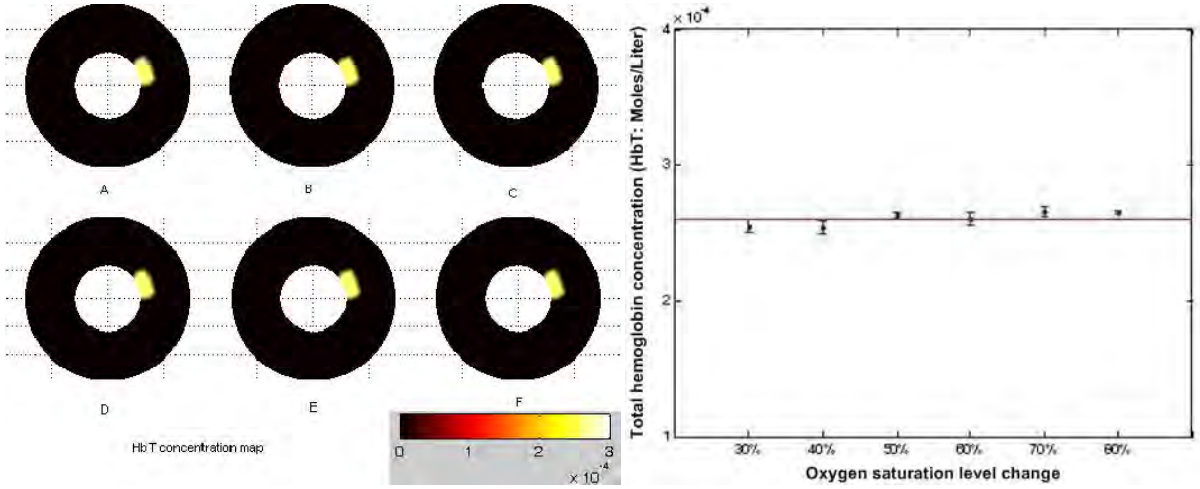

Figure 13. Reconstructed map (left) and the level (right) of the total hemoglobin concentration vs. oxygenation change.

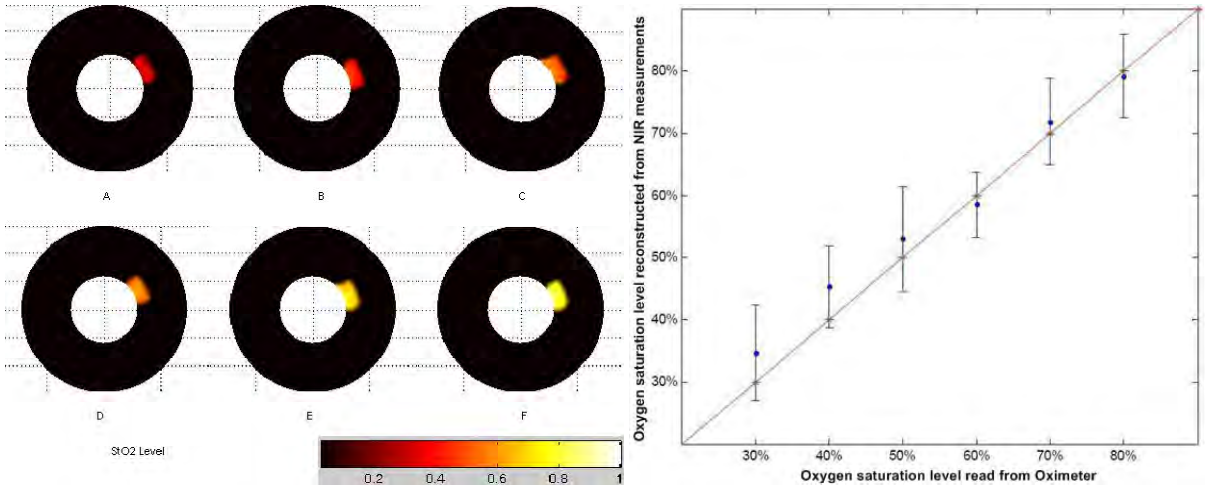

Figure 14. Reconstructed map (left) and the level (right) of the oxygen saturation vs. the true oxygenation change

3.3 Dual-band absorption measurements by the 20mm axial—imaging endo-rectal NIR probe.

In the previous measurement by use of the 13mm probe, the 2.5mm separation of the target from the probe surface was too small to be differentiated by the NIR tomography. This is not only related to the relatively low resolution of the NIR tomography, but also to the non-uniform sensitivity of the axial imaging probe along the radial depth [12] as well as the use of photon-diffusion equation without accounting for the circular curvature. Further test on the 20mm axial-imaging probe confirmed that the depth of a target is severely compromised at this axial-imaging geometry without proper analytic treatment of the boundary curvature, as indicated in Fig. 15. A solid cylinder shape phantom (10mm in diameter and 16mm in length) was put into a homogeneous background of 1% solution intralipid. The phantom was put 10mm away (center) from the 20mm probe surface. The solid phantom has the optical properties of μ_a =0.0064mm^{-1}, μ_s' =0.91mm^{-1}. The high absorption regions reconstructed at two wavelengths are consistent, but at a position close to the probe surface. Improving the depth localization of the axial-imaging NIR tomography may be rendered by incorporating spatial information of the target. Yet, the curvature of the axial-imaging geometry may limit the depth of target being detected.

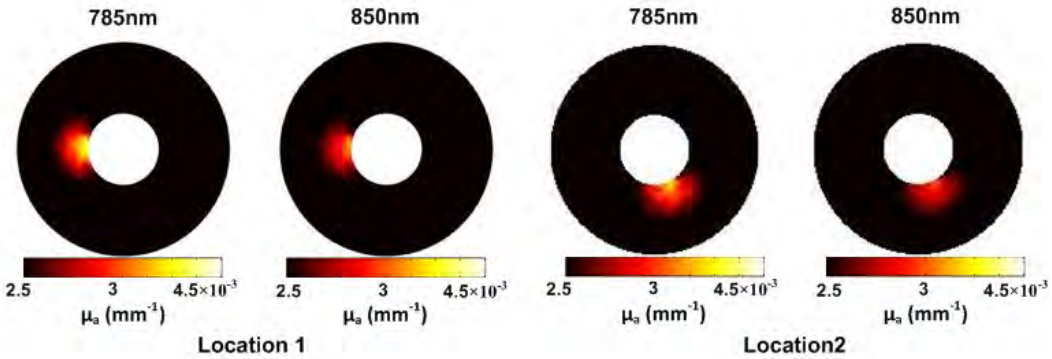

Figure 15. Stand-alone optical reconstruction of transverse images

3.4 Dual-band absorption measurements by the sagittal-imaging concurrent NIR/US probe.

The dual-band measurements of absorption based on the sagittal-imaging NIR probe are shown in Fig. 16. A solid phantom target (μ_a =0.0056mm^{-1}, μ_s' =1.03mm^{-1}) was put in the middle-sagittal plane of the probe at a depth of 10mm and 15mm, respectively, in a homogeneous background (1% solution intralipid). Both targets appear at the same depth of 10mm by NIR only reconstruction. This target depth corresponds to the maximum depth sensitivity of the probe. The absorption value of the target is also underestimated. Figure 17 shows the dual-band reconstruction after incorporating the spatial information of the target available from the TRUS. The target spatial information is used to develop a mesh representing a target at the correct location and the background. The *prior*-guided NIR reconstruction at both bands gives more accurate recovery of the absorption coefficient of the target.

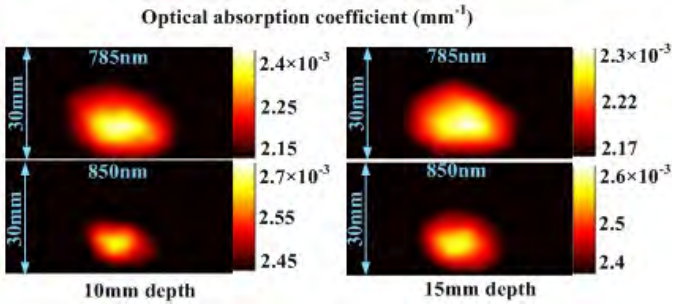

Figure 16. Stand-alone optical reconstruction for sagittal images

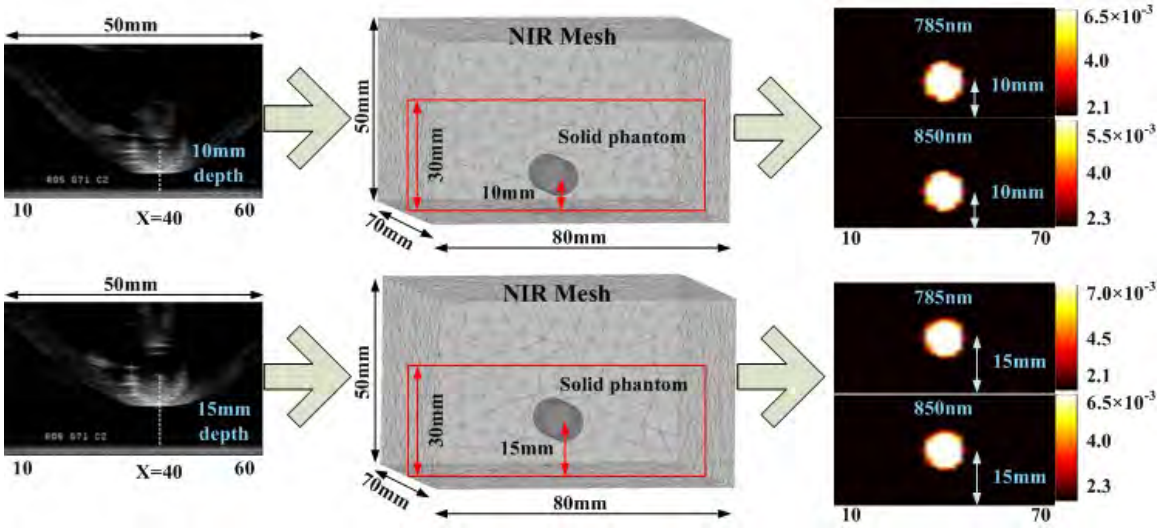

Figure 17. Sagittal images of combined trans-rectal NIR/US probe in different depth

4. SUMMARY

We described the development of three NIR imaging probes intended for dual-band endo-rectal imaging of the prostate and ultimately coupling with TRUS for ultrasound-guided NIR image reconstruction. We have demonstrated that oxygenation changes of blood can be quantified by the axial-imaging probe being developed. Work is ongoing to validate the dual-band imaging of the oxygenation in blood samples and with the sagittal-imaging NIR probe, as well as conduct n vivo testing with cancer models developed in canine prostate.

5. ACKNOWLEDGEMENT

This work has been supported by the Prostate Cancer Research Program of the U.S. Army Medical Research Acquisition Activity (USAMRAA), 820 Chandler Street, Fort Detrick MD, 21702-5014, through grant #W81XWH-07-1-0247. Comments and questions may be directed to Daqing Piao whose e-mail address is daqing.piao@okstate.edu.

REFERENCES

[1] Srinivasan, S., Pogue, B.W., Carpenter C., Jiang, S., Wells, W.A., Poplack, S.P., Kaufman P.A. and Paulsen, K.D., "Developments in Quantitative Oxygen-Saturation Imaging of Breast Tissue In Vivo Using Multispectral Near-Infrared Tomography", Antioxidants & Redox Signaling, 9(8): 1143-56 (2007).

[2] Chance B., Nika S., Zhang J., Conant E.F., Hwang E., Briest S., Orel S.G., Schnall M.D., and Czerniecki B.J., "Breast cancer detection based on incremental biochemical and physiological properties of breast cancers: a six-year, two-site study", Acad Radiol., 12: 925-933 (2005).

[3] Vollmer, R.T., Kantoff, P.W., Dawson, N.A. and Vogelzang, N.J., "Importance of Serum Hemoglobin in Hormone Refractory Prostate Cancer", Clinical Cancer Research, 8: 1049-1053 (2002).

[4] Yu, G., Durduran, T., Zhou, C., Zhu, T.C., Finlay, J.C., Busch, T.M., Malkowicz, S.B., Hahn, S.M. and Yodh, A.G., "Real-time In situ Monitoring of Human Prostate Photodynamic Therapy with Diffuse Light", Photochemistry and Photobiology, 82: 1279-1284 (2006).

[5] Beer, T.M., Tangen, C.M., Bland, L.B., Hussain, M., Goldman, B.H., DeLoughery, T.G. and Crawford, E.D., "The prognostic value of Hemoglobin change after initiating Androgen-Deprivation therapy for newly diagnosed metastatic prostate cancer", Cancer, 107(3):489-96 (2006).

[6] Kondepati, V.R., Heise, H. M. and Backhaus, J., "Recent application of near-infrared spectroscopy in cancer diagnosis and therapy," Anal Bioanal Chem, 390:125-139 (2008).

[7] Pogue, B.W., Jiang, S., Dehghani, H., Kogel, C., Soho, S., Srinivasan, S., Song, X., Tosteson, T.D., Poplack, S.P. and Paulsen, K.D., "characterization of hemoglobin, water and NIR scattering inbreast tissue:analysis of intersubject variability and menstrual cycle changes," Journal of Biomedical Optics, 9(3): 541-552 (2004).

[8] Piao, D., Jiang, Z., Xu, G., Musgrove, C.H. and Bunting, C.F., "Approach of trans-rectal NIR optical tomography probing for the imaging of prostate with trans-rectal ultrasound correlation", Proc. SPIE, 6850: 68500E-1 (2008).

[9] Xu, G. Piao, D., Musgrove, C.H., Bunting, C.F. and Dehghani H., "Trans-rectal ultrasound-coupled near-infrared optical tomography of the prostate, Part I: Simulation", Optics Express, 16(22): 17484–17504 (2008).

[10] Jiang, Z., Piao D., Xu, G., Ritchey, J.W., Holyoak, G.R., Bartels, K.E., Bunting, C.F., Slobodov, G. and Krasinki, J.S., "Trans-rectal ultrasound-coupled near-infrared optical tomography of the prostate Part II: Experimental demonstration," Optics Express, 16(22): 17505–17520 (2008).

[11] Xie, H., "Dual-spectral endoscopic near-infrared optical tomography for assessment of hemoglobin concentration and oxygen saturation", Oklahoma State University, Master thesis, (2008).

[12] Musgrove, C., Bunting, C.F., Dehghani, H., Pogue, B.W. and Piao, D., "Computational Aspects of Endoscopic (Trans-rectal) Near-infrared Optical Tomography: Initial Investigations", Proc. SPIE, 6434, 643409 (2007).

A hierarchical spatial *prior* approach for prostate image reconstruction in trans-rectal optical tomography

Guan Xu,[1] Charles F. Bunting, [1] Hamid Dehghani,[2] Daqing Piao [1]
1 School of Electrical and Computer Engineering, Oklahoma State University, Stillwater, OK, 74078-5032
2 School of Physics, University of Exeter, Exeter, UK, EX4 4QL

ABSTRACT

An approach of hierarchically implementing the spatial *prior* information in trans-rectal optical tomography is introduced. Trans-rectal optical imaging of the prostate deals with photon propagation through the rectum wall, the peri-prostate tissue and the prostate. Reconstructing a lesion in the prostate is challenging due to the structural complexity as well as the optical heterogeneity. Incorporating spatial "hard" *a priori* information available from complementary imaging modalities such as trans-rectal ultrasound could in principle improve the accuracy of trans-rectal optical tomography reconstruction. However, the reconstruction is potentially subject to the local-minimum sensitivity if the values of all regional optical properties are to be initialized simultaneously. We propose a hierarchical spatial *prior* approach for trans-rectal optical tomography reconstruction. Instead of assigning the initial values to all sub-regions at once, a region is initially assumed homogenous, and the reconstructed optical properties are used as the initial guess for the region as a background when a sub-region is included in the next step. This approach translates to a 3-step iteration routine whereby the first step reconstructs the entire imaging volume as a single region, the second step uses these results as the initial guess of peri-prostate tissue to reconstruct the prostate and the rectum wall, and the third step assigns the updated results as the initial values of 3 existing regions to reconstruct a lesion inside the prostate. This approach, validated by simulation and applied to experimental measurements, is more reliable in global convergence, robust in imaging of single or multiple targets, and accurate for the recovering of optical properties.

Keywords: Prostate, optical tomography, trans-rectal, image reconstruction, near-infrared.

1. INTRODUCTION

Among the men in USA, prostate cancer is the most common cancer that is only second to skin cancer[1]. Prostate cancer screening is performed by measurement of serum prostate-specific antigen (PSA), digital rectal examination (DRE), and a combination of these tests[2]. When the suspicion of prostate cancer is raised by abnormal PSA and/or DRE, the diagnosis is made by biopsy, most often performed under trans-rectal ultrasound (TRUS) guidance, to confirm the neoplastic lesions and to determine their clinical significance for treatment planning[3,4]. It is known that most times prostate cancer presents as being multi-focal[5, 6], thereby tissue sampling at multiple sites within the prostate gland is necessary.

The most common appearance for prostate cancer on TRUS is a hypoechoic lesion in the peripheral zone. With PSA based screening enabling earlier cancer detection, fewer overt abnormal sonographic findings are being detected at the time of TRUS guided biopsy[7]. The sonographic finding of the classic hypoechoic peripheral zone lesion has a sensitivity of cancer detection of 85.5%, specificity of 28.4%, positive predictive value of 29%, negative predictive value of 85.2% and overall accuracy of 43%. The prevalence of isoechoic or nearly invisible prostate cancers on TRUS ranges from 25 to 42%. To date, no biologic differences have been noted between isoechoic and hypoechoic prostate cancers[8,9]. The notably high rates of iso-echoic cancers on TRUS imaging leads to increasing the number of biopsy cores to improve the probability of detecting the prostate cancer. However, the current prostate

Multimodal Biomedical Imaging IV, edited by Fred S. Azar, Xavier Intes, Proc. of SPIE Vol. 7171, 71710S · © 2009 SPIE · CCC code: 1605-7422/09/$18 · doi: 10.1117/12.808208

biopsy strategy of "systematic sampling" results in large number of negative diagnosis performed for initial biopsy evaluations.

TRUS is widely received as a standard imaging modality in performing the prostate biopsy owing to its real-time utility, patient-and-physician friendly features as well as cost-effectiveness. The prostate anatomy and needle track are visualized accurately with TRUS enabling accurate localization of the tissue sites being sampled. TRUS will maintain as the primary imaging guidance for prostate biopsy in the future, thereby the quest of reducing the numbers of unnecessary biopsies demands the specificity of TRUS be improved. Doppler ultrasonography, contrast-enhanced gray-scale ultrasonography, 2^{nd}-harmonic imaging, etc. are among the approaches being investigated to improve the outcome of TRUS imaging[10]. A more effective approach of improving the outcome of TRUS prostate imaging is, perhaps, to augment the TRUS with a complimentary modality being more specific to the tumor malignancy.

It has been recognized during the past decades that near-infrared (NIR) tomography, being non-ionizing and non-or-minimally-invasive similar to TRUS, has the potential of providing a functional or "surrogate" markers of prostate tumors. Near-infrared measurements of attenuation through tissue have demonstrated significant contrast gradients between blood and parenchymal tissue that is otherwise difficult to obtain[11-16]. The alteration of vascularity or the hemoglobin content in the tumor provides, often very high, intrinsic optical contrast between the tumor and benign tissues which has been well demonstrated in breast cancer imaging. When multi-spectral detection is engaged, NIR imaging is also capable of directly quantifying the chromorphore concentrations important for determining the local tissue malignancy[11-16]. In prostate, studies have shown vascular density gradient in malignant versus benign tissue specimens[17], and different water concentrations in cancerous and benign tissues *in vitro*[18]. Invasive NIR measurements of prostate have been conducted for experimental prostate tumors[19] and human prostate[20, 21]. Surface measurements of implanted prostate tumor have also been reported[22, 23]. All these studies demonstrate the potential of using NIR to detect and characterize prostate cancer. NIR diffuse optical measurement, performed interstitially, is also becoming an important tool for monitoring of the photodynamic therapy in prostate [20, 21, 24]. Prostate NIR imaging via trans-urethral probing had been analyzed and tested[25]. Recently, trans-rectal prostate NIR imaging has been investigated in simulation in the context of assisting MRI for treatment decision[26]. NIR optical tomography, when carried out trans-rectally and performed concurrently with TRUS, will improve the specificity of TRUS imaging.

The implementation of trans-rectal NIR tomography for imaging the prostate, similar to other NIR tomography applications, will be benefited by knowing the structural properties of tissue volume being imaged. The tissue volume interrogated by trans-rectal NIR imaging constitutes a nested-domain including a thin layer of rectum wall, a large volume of peri-prostate tissue, a relatively absorbing prostate, and the lesion within the prostate. These nested imaging domains may be further complicated by the pelvic bone, the bladder if not completely voided and other peri-prostatic anatomic structures, that could interfere with the light propagation in the prostate. Previous investigations have discussed the issue of recovering the shapes and optical properties of regions with optical contrast inside non-nested or nested domains[27-31], where the shapes of the regions-of-interest (ROIs) were derived from optical information when no spatial *prior* is available from other complementary imaging modalities. These methods have shown sufficient robustness in recovering the shapes and optical properties of the ROIs, yet the problem of stability and/or slow convergence was noticed in such approaches dealing with nested-domains. In trans-rectal NIR tomography reconstruction the spatial information from TRUS may be implemented by assigning homogenous optical properties within each ROIs of the imaging domain. However, the convergence and the accuracy of reconstruction for trans-rectal NIR tomography of the prostate will likely be more dependent upon the initial guess, given sufficient accuracy of the spatial *prior* information, due to the possible multiple combinations of optical properties in the nested-structures. The image reconstruction in trans-rectal optical tomography is further complicated by the non-consensus regarding the optical contrast that the prostate tumor has with respect to the benign prostate tissue. All these features, as shown in this paper, will complicate and thereby reduce the accuracy of the reconstruction in trans-rectal NIR tomography even with the structural information from TRUS.

In this work, we propose a hierarchical reconstruction scheme that may be more robust and accurate for structural *prior* guided NIR tomography reconstruction of the prostate. This hierarchical method improves both the stability of the convergence and the convergence to the global minimum for the iterative inverse solver. The improvement and robustness of the hierarchical reconstruction approach are demonstrated via simulations and experimental investigations.

2. SIMULATION CONFIGURATIONS

2.1 Geometry of TRUS coupled trans-rectal NIR imaging of the prostate

We have designed and developed a trans-rectal NIR probe that is directly coupled to a bi-plane TRUS probe (Aloka UST-672-5/7.5). Having more NIR channels in the trans-rectal probe would certainly render more advantageous imaging features, however, the probe dimension and fabrication challenges posed limitation to integrate only 7 source and 7 detector channels to the NIR applicator. The NIR optodes are set laterally aside the sagittal TRUS transducer spanning 60mm×10mm. On each lateral side of the TRUS transducer, the 7 sources or detectors are spaced at 10mm thereby covering a total length of 60mm. The source array and detector array are laterally spaced at 20mm. The geometry of the trans-rectal NIR probe and TRUS transducer with respect to the prostate imaging domain is schematically shown in Fig. 1.

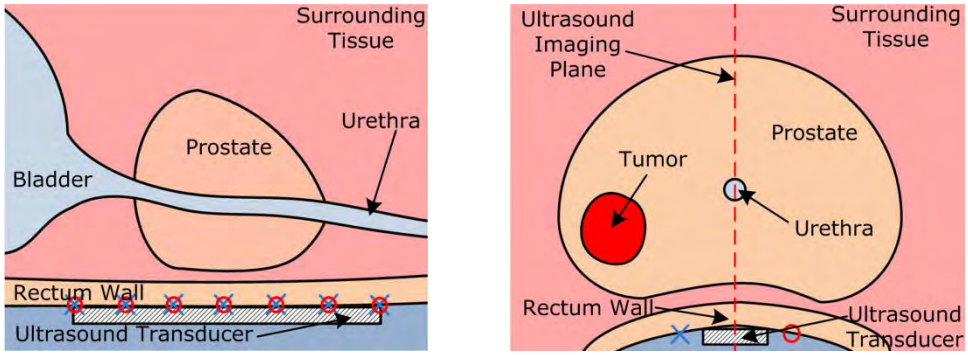

Fig. 1 Illustration of the TRUS coupled trans-rectal NIR imaging of the prostate: (a) sagittal view, (b) transverse view. The middle plane of the sagittal TRUS is marked with a red dash line. The red circles denote NIR sources and the blue crosses denote the NIR detectors.

2.2 Model-based trans-rectal optical tomography reconstruction

The prostate and peripheral tissues[18-21] are scattering-dominant that justifies describing the light propagation in them by use of the diffusion approximation to the radiative transport equation. We use the frequency-domain photon diffusion equation[32]:

$$-\nabla \cdot D(\vec{r})\nabla U(\vec{r},\omega) + (\mu_a + \frac{i\omega}{c})U(\vec{r},\omega) = q_0(\vec{r},\omega) \quad (1)$$

where $U(\vec{r},\omega)$ is the photon density at position $\vec{r}$, $q_0(\vec{r},\omega)$ is the source term, ω is the source modulation frequency, c is the speed of light in medium, μ_a is the absorption coefficient, and $D = \left[3(\mu_a + \mu_s')\right]^{-1}$ is the diffusion coefficient with μ_s' being the reduced or transport scattering coefficient.

Equ. (1) is solved under the Type-III boundary condition[32] by use of finite-element method[33] The imaging volume to be reconstructed in trans-rectal optical tomography can be divided approximately to, as previously described, 4 domains or ROIs: the rectum wall, the peri-prostate tissue, the prostate, and the prostate tumor. When concurrent TRUS image is available, the thickness of the rectum wall, the size/shape of the prostate, and the approximate spatial extent of the prostate lesion can be defined to guide trans-rectal optical tomography reconstruction. We utilize the TRUS structural information by the "hard" *a priori* method[34-36]. The "hard" *a priori* method treats each ROI as homogenous, thereby in our reconstruction 8 parameters are to be recovered as μ_a and μ_s' of the four ROIs. The Jacobian values are calculated for each ROI instead of for each node in every ROI and has the form of:

$$\begin{bmatrix} \dfrac{I_{i,j}}{\mu_{a\_ROI\_k}} & \dfrac{I_{i,j}}{D_{ROI\_k}} \\ \dfrac{\phi_{i,j}}{\mu_{a\_ROI\_k}} & \dfrac{\phi_{i,j}}{D_{ROI\_k}} \end{bmatrix} \tag{2}$$

where I_{ij} $(i, j = 1,2,...,7)$ and ϕ_{ij} $(i, j = 1,2,...,7)$ are the intensity and phase terms of $U(\vec{r}, \omega)$, respectively. In (2), k=1, 2, 3, 4 denote "rectum wall", "peri-prostate tissue", "prostate", and "prostate lesion", which are the four ROIs, respectively. The optical properties are iteratively recovered by use of the well-known Levenberg-Marquart (LM) algorithm wherein the ROI-specific values of μ_a and *D* are updated according to

$$x_{k+1} = x_k + \alpha \cdot [J^T(x_k)J(x_k) + \lambda I]^{-1} J^T(x_k)\Delta v(x_k) \tag{3}$$

where *x* is the array of parameters to be optimized, *J* is the Jacobian matrix defined by Equ. (2), Δv is the forward projection error, λ is a penalty or regularization term. In the iteration a small damping factor α in the range of (0, 1) is used to stabilize the convergence[37].

2.3 TRUS prior assisted finite-element mesh for trans-rectal NIR tomography reconstruction

Utilizing TRUS structural information to guide trans-rectal NIR tomography reconstruction could be performed by using the location and size of a suspected lesion to directly generate a mesh that contains two ROIs to represent the lesion with a dense mesh and the background tissue with a coarse mesh[35, 36]. For trans-rectal prostate imaging a mesh is needed to represent regions including the rectum wall, the peri-prostate tissue, the prostate, and the tumor within the prostate.

The TRUS image (available in open source) was imported into a software 3ds-MAX [Autodesk Inc] for primary 3-D model generation. The finalized 3-D mesh of the prostate is converted to COMSOL Multiphysics [COMSOL AB] compatible format with MeshToSolid [Syncode Inc]. The absorption and reduced scattering coefficients of rectum, peri-prostate tissue, and prostate are assumed homogenous in each individual ROI and assigned based on[26]. A spherical shape is adopted for the prostate tumor. Figure 2 illustrates one completed NIR FEM-mesh. The prostate in Fig. 2 has a walnut shape of ~50×40×30 mm^3 in the maximum extensions. The rectum wall has a thickness of 4mm and a curvature radius of 80 mm. The completed mesh similar to that shown in Fig. 2 contains approximately 4000 nodes and 20000 elements.

The source-modulation frequency ω in Equ. (1) is set at 100MHz, and 1% Gaussian noise is added to all forward calculations to form the measurement data. In all the figures presented thereafter, the unit of the length is millimeter, x is the longitudinal coordinate in the range of [0, 80], y is the lateral coordinate in the range of [0, 80], and z is the depth coordinate in the range of [0, 80].

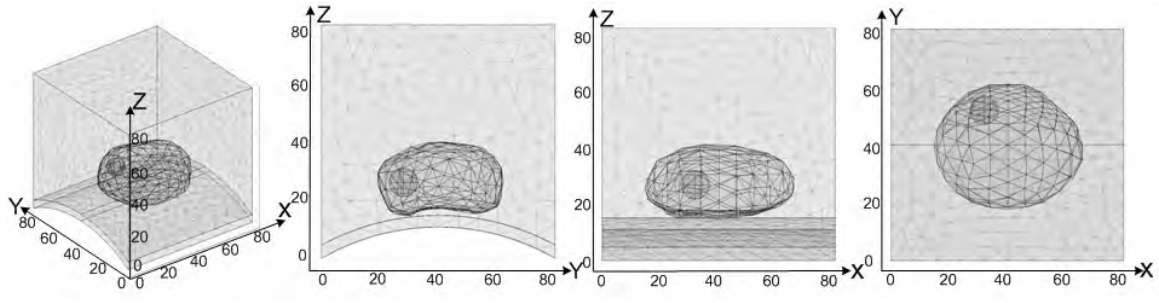

(a) Perspective view *(b)Axial view* *(b)Sagittal view* *(c) Coronal view*

Fig. 2 FEM mesh of the NIR imaging volume generated based on TRUS image

3. A HIERARCHICAL SPATIAL *PRIOR* APPROACH FOR NIR TOMOGRAPHY RECONSTRUCTION

3.1 Trans-rectal NIR imaging reconstruction without *a priori* information

The performance of recovering a tumor target by trans-rectal NIR tomography without structural *prior* is first examined. With the accurate forward measurement being calculated by the TRUS-defined geometry as shown in Fig. 2, the iterative image reconstruction is conducted using mesh of homogenous element density throughout the entire volume. The optical properties of a 10mm diameter tumor target is assigned as $\mu_a = 0.02mm^{-1}$ and $\mu_s^{'} = 1.6mm^{-1}$, with the parameters of other regions the same as those in Fig. 2 and listed in Table 1 coming later in the text. The reconstruction results are given in Fig. 3 for the tumor target being placed at left, middle, and right locations inside the prostate. The (a) is for μ_a and (b) is for $\mu_s^{'}$ respectively. The 1-dimensional profile across the tumor and parallel to the probe surface indicates the quantitative comparison between the set and reconstructed values. It is observed that the existence of a heterogeneous structure in the prostate region is rendered, but the spatial characterization of the heterogeneity is poor. Further, a tumor with negative absorption contrast is difficult to be recovered when the spatial *prior* is not implemented.

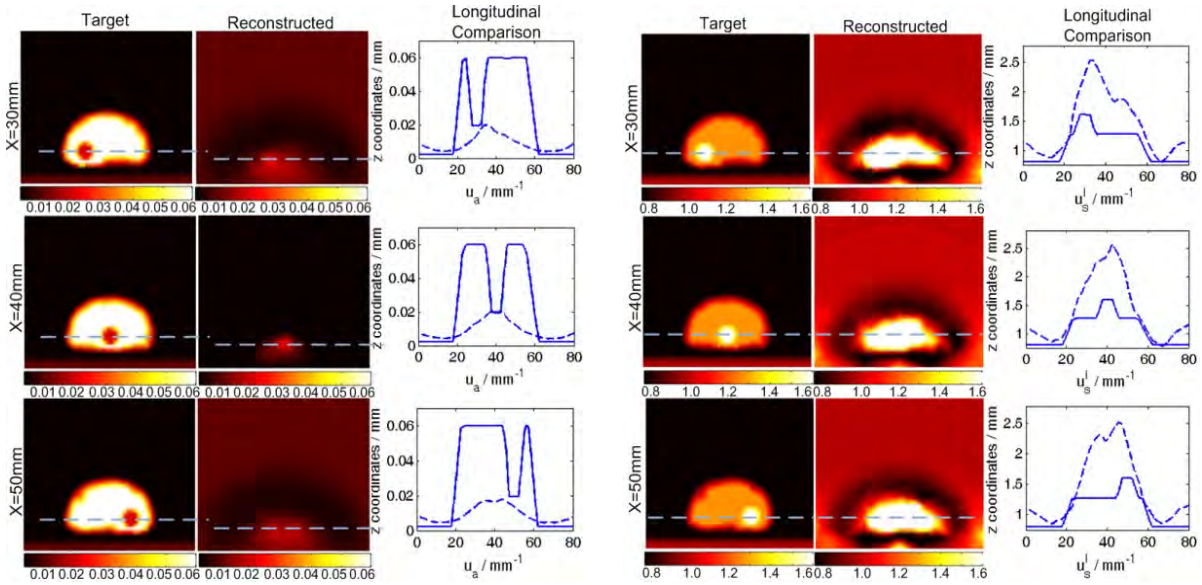

(a) (b)

Fig. 3 NIR-only reconstruction for target in varying longitudinal locations. Optical properties are plotted to along line y=40mm, z=26mm (actual depth is 15.1mm because of the bottom curvature of the mesh) for both the target and the reconstructed images (a) Recovery of μ_a . μ_a values are intentionally plotted along the line going through the center of the reconstructed blobs (~ y=40mm, z=26mm, actual depth is approximately 15.1mm because of the bottom curvature of the mesh), which is shallower because the non-uniform sensitivity has dragged the reconstructed target closer to the NIR array. (b) Recovery of $\mu_s^{'}$ for the target locations identical to those in (a).

3.2 Spatial *prior* guided trans-rectal NIR reconstruction-----simultaneous updating of all ROIs

The trans-rectal prostate imaging domain constitutes nested-structures including a thin layer of rectum wall in the vicinity of NIR array, a large and under-defined volume of peri-prostate tissue owing to the one-sided NIR array, a relatively absorbing prostate, and the lesion within the prostate. In our approach of coupling trans-rectal NIR with TRUS, the shapes of the ROIs for trans-rectal optical tomography reconstruction could be defined directly from TRUS. The simplest approach of implementing the TRUS *a priori* information may be assigning homogenous optical properties within each ROIs of the imaging domain. However the convergence and the accuracy of reconstruction will still be dependent on the initial guess. This can be attributed to the gradient based solver for which the local minimum feature would likely be exaggerated in prostate imaging in which the multiple combinations of optical properties of the nested-structures in the imaging volume could give multiple combinations

of optical properties that may fit with the measurements, in which case the projection error of the reconstruction routine could converge to a very small value but the recovered optical properties may be far from the desired ones, as is shown in Fig. 4(c). The local-minimum problem makes the reconstruction sensitive to the initial guess of optical properties. In trans-rectal optical tomography finding the global minimum for the iterations to converge may become particularly intriguing.

When TRUS *prior* is available, a conventional way of utilizing the TRUS spatial information would be the "hard" *a priori* method in which the optical properties of each ROIs are set homogenous and updated simultaneously at each iteration. However, we have found that this conventional approach may not lead to reliable convergence for prostate imaging, which is believed due to the local-minimum problem. One example is given in Table 1 where the calculation is taken for the NIR array in Fig. 1(c), the prostate model in Fig. 2, and a target of 10mm in diameter located at a coordinate setting of (40, 40, 26) that is 15.1 mm from the rectal surface. When the four ROIs including the rectum, the peri-prostate tissue, the prostate, and the prostate tumor are updated simultaneously from the same initial guess of μ_a =0.01mm^{-1} and μ_s' =1.0mm^{-1}, the iteration stops after 1 round due to the negative μ_a value obtained for the rectum wall. This is due largely to the effect that the iteration has fallen into local minimums which were the minimum values locally but not globally.

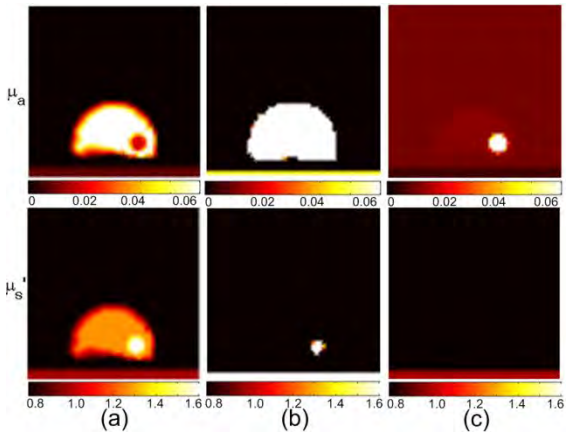

Fig. 4 Local-minimum issue in reconstruction. The forward calculation is based on (a). (b) Reconstruction results with the initial values of all regions as μ_a =0.1mm^{-1} and μ_s' =2mm^{-1}, the iterations stopped with projection error of 123.0100. (c) Reconstruction results with the initial values of all regions as μ_a =0.002mm^{-1} and μ_s' =0.5mm^{-1}, the final projection error of the iterations is 0.8329.

Table 1 Results of simultaneously updating the 4 ROIs from the same initial guess

	μ_a (mm^{-1})				μ_s' (mm^{-1})			
Regions	Surrounding Tissue	Rectum Wall	Prostate	Tumor	Surrounding Tissue	Rectum Wall	Prostate	Tumor
Set value	0.002	0.01	0.06	0.02	0.8	1	1.27	1.6
Simultaneous Update	0.1216	**-0.008**	0.026	0.0215	1.1482	2.3602	0.6173	0.7073

3.3 Spatial-prior guided trans-rectal NIR reconstruction-----hierarchical updating of the ROIs

The local minimum problem may be mitigated by a hierarchical spatial *prior* approach that may allow more steady and global convergence of the iteration. The fundamental idea of this method is to first reconstruct the global optical properties of the entire volume, then to reconstruct the optical properties of prostate and rectum wall, and last to reconstruct the tumor lesion area. The 2nd and 3rd steps use the value obtained in the previous step as the initial guess

of that specific ROI. Therefore at each step, the perturbation by a relatively smaller region is less influential and convergence of iteration is better warranted. The detailed steps are shown in Fig. 5 and described in below:

(a) The first iterations assume an entirely homogenous imaging volume. In this round the initial projection errors will be large and the converging process is most likely to be affected by the global minimum. Therefore, a single set of optimum values of μ_a and μ_s' are determined with LM algorithm and will be used as the initial guess in the second step.

(b) The second iterations consider three regions of rectum wall, peri-prostate tissue, and prostate within the imaging volume. The iterations of optical properties of these three ROIs start at the same initial guess provided in step (a) and converge at different values.

(c) The values obtained from step (b) are used as the initial guess for the same three ROIs but with a tumor added to the prostate. The tumor and the prostate take the same initial values resulted from the previous step. Now each of the four ROIs (rectum wall, peri-prostate tissue, prostate, and tumor) converges to different end values.

The comparison of the optical properties reconstructed at each step is shown in Fig. 5(d). The change of the overall projection error for the three steps is plotted in Fig. 5(e). Rapid and reliable convergence can be observed.

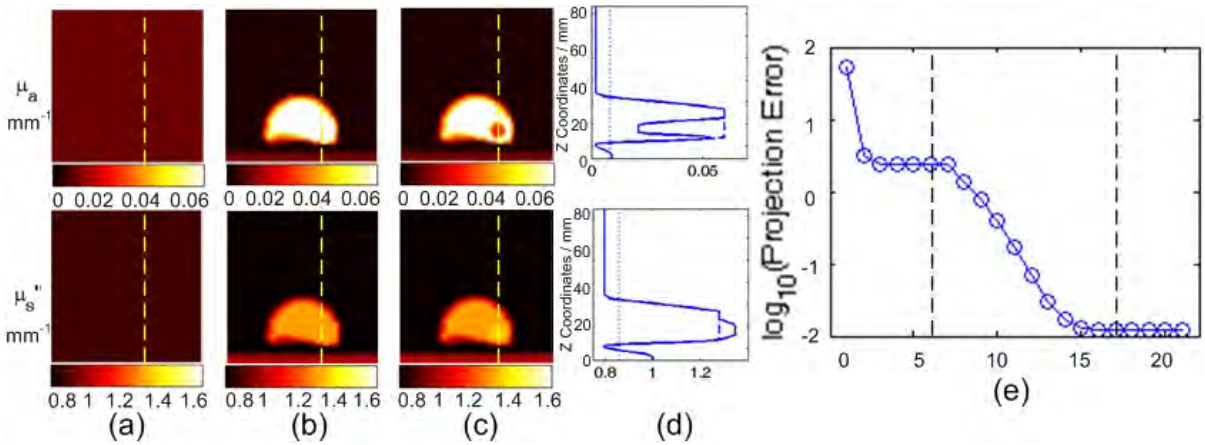

Fig. 5. The 3-step hierarchical reconstruction method (a) Step 1—one ROI for the entire volume; (b) step 2—three ROIs representing rectum wall, peri-prostate tissue, prostate; (c) step 3—four ROIs representing rectum wall, peri-prostate tissue, prostate, tumor; (d) The recovered optical properties along the z direction at x=40mm, y=50mm. The dot line denotes the step 1, the dash line the step 2 and the solid line the step 3; (e) changes of the projection error, where the dash lines separate the converging of the three steps in (a)—(c).

4. Validation of the hierarchical spatial *prior* method

4.1 Simulation geometry

Recently, Li et al. reported simulation results for trans-rectal optical tomography reconstruction in the context of using MRI anatomic information[26]. Their work is referred as "NIR/MRI" in the following text. We have tested the performance of our hierarchical spatial *prior* method using the probe geometry (shown in Fig. 6) and the optical properties presented in the NIR/MRI work.

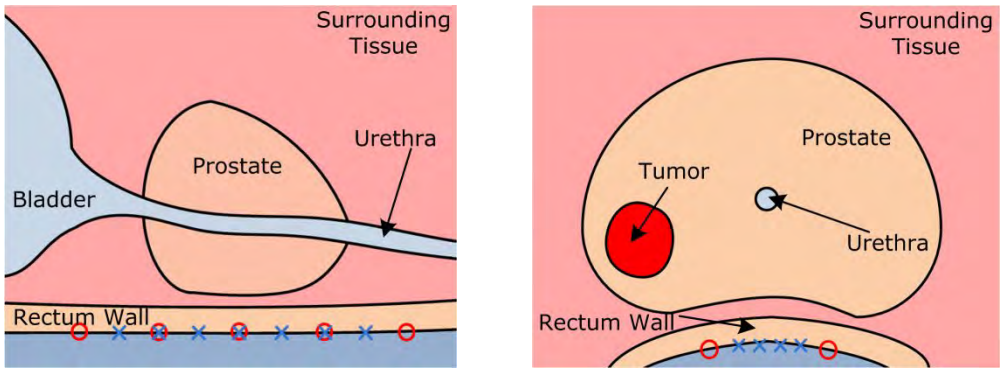

(a) (b)

Fig. 6 The imaging geometry used in the NIR/MRI paper[26]. Two source arrays are distributed laterally with 20mm distance. Each array has 5 sources with 10mm gaps, as denoted by red circles. 28 detectors are evenly distributed within a 15mm by 30mm area, as denoted by blue crosses. (a) Sagittal view of the distribution of the optodes. (b) Transversal view of the distribution of the optodes.

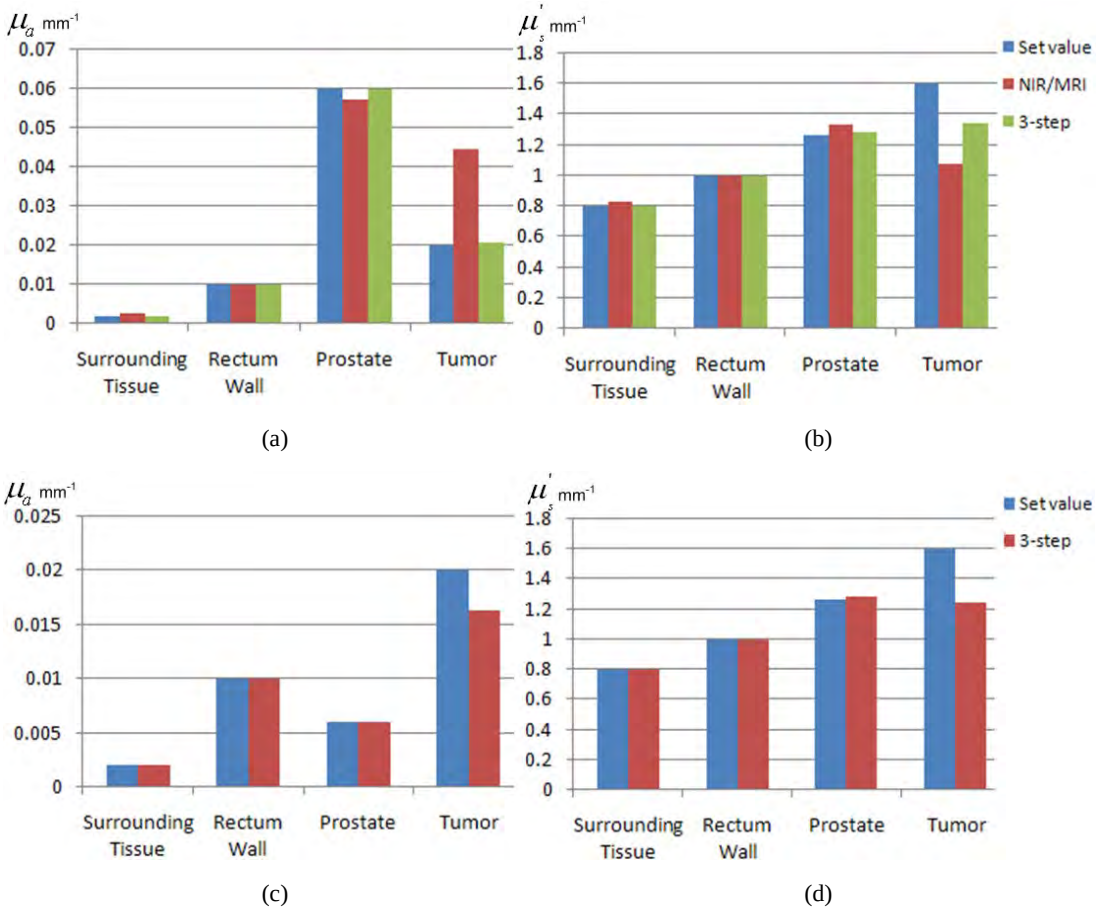

(a) (b)

(c) (d)

Fig. 7 Comparison of the reconstruction values: (a) & (b) the tumor has a negative absorption contrast with respect to the prostate, (c) & (d) the tumor has a positive absorption contrast with respect to the prostate. The "3-step" refers to the hierarchical image reconstruction method.

With the 1% noise added to the forward simulation data as is indicated in the NIR/MRI paper, the performance of our hierarchical spatial *prior* method with respect to the NIR/MRI one is given in Fig. 7 (a) & (b) for a prostate lesion of negative absorption contrast. It is observed that our hierarchical method (listed as "3-step" in the

table), as expected, slightly outperforms the NIR/MRI method in terms of the accuracy of recovering optical properties. We have also tested recovering a target of positive absorption contrast in Fig. 7(c) & (d) using the NIR/MRI probe geometry and our 3-step method. Since no results were given in the NIR/MRI work for target of positive absorption contrast, only the recovered properties based on our method are presented for comparison with the set values. In (c) & (d) the absorption coefficient of prostate is set much lower than that in (a) & (b) but the tumor optical properties are kept the same as those in (a) & (b). If the absorption of prostate in (c) & (d) is kept the same as in (a) & (b), the positive absorption target is hardly reconstructed at the set location. The choice of lower prostate absorption is for testing our hierarchical method, but it does not necessarily disagree with the actual value of prostate absorption. As a matter of fact, the absorption properties of prostate has shown large variation in literatures where the measurement are either taken from *in vitro* tissue or may be interfered by bleeding of *in vivo* tissue under invasive measurement. The absorption coefficient of non-exposed prostate measured *in situ* & *in vivo* is unavailable so far, and if available, is likely lower than the values reported in literatures for non-intact prostate. The results in Fig. 7 demonstrate the robustness of our hierarchical spatial *prior* method in reconstructing prostate lesion with either negative or positive absorption contrast.

4.2 Experimental validations of the hierarchical reconstruction

Two sets of experimental data acquired with continuous-wave NIR imaging system were employed to evaluate the hierarchical reconstruction scheme. The samples were administrated mostly with absorption contrast; therefore results of only absorption reconstruction are displayed in the following figures.

Case I: Internal imaging of avian tissues

As shown in Fig. 8(a), the empty abdomen of a whole chicken was filled with chicken breast tissue and a piece of chicken liver was embedded within the breast tissue. The embedded liver shows up as the hypo-echoic region circled in Fig. 8(b). A two-ROI FEM mesh is generated to simulate the experiment setup, as is shown in Fig. 8(d).

Since there are only two ROI in this experimental case, when implementing the hierarchical reconstruction scheme, only a two-step reconstruction is performed. The results are shown in Fig. 8(e) & (f), respectively. It can be observed that the absorption values are reconstructed quite close to the true values of a liver tissue indicated by literature findings. Comparing the NIR images reconstructed without structural *prior* in Fig. 8(c) and reconstructed with hierarchical method in Fig. 8(f), the utility of the hierarchical reconstruction method is demonstrated.

Case II: Trans-rectal optical tomography of canine prostate in situ

The second experiment is conducted on a canine cadaver. The prostate was exposed and approximately 0.33ml of homogenized foal liver was injected ventral-dorsally, paramedian in the left lobe of the prostate. The prostate was then enclosed in thick layers of peri-prostate tissues. On the TRUS image of Fig. 9(a) the injected liver tissue is visible by the mass proximal to the center of the prostate and the vertical hyper-echoic strip at the ventral side of the prostate. The large hypo-echoic region at the upper half was due to absorption by thick layers of muscle, skin and exposal to the air. The mesh is according generated in Fig. 9(b). The rectum wall was not outlined in the mesh because of its close proximity to the US transducer due to the small size of this canine cadaver. The finalized mesh in Fig. 9(b) shows nested-domains including the prostate and a target region in the prostate. The NIR images in Fig. 9(c), (d), and (e) show the absorption distribution reconstructed at each step of the hierarchical reconstruction method. A highly absorptive mass is clearly recovered corresponding to the injected liver tissue. The absorption coefficient of the foal liver tissue in Fig. 9(a) is lower than that of the avian liver tissue in Fig. 8(b); nevertheless both values are at the order of $0.1mm^{-1}$, indicating high absorption by both tissues.

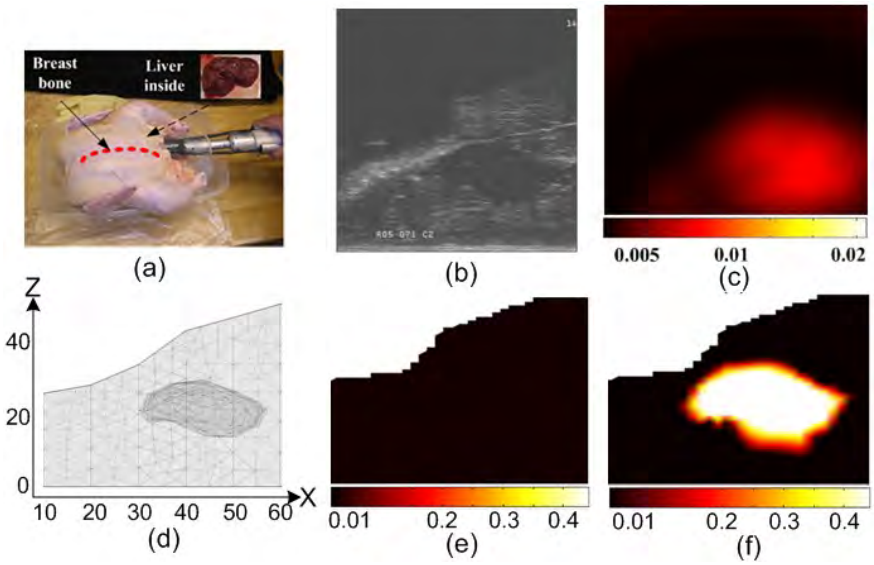

Fig. 8 Experiment I: Internal imaging of avian tissues. (a) Tissue phantom. (b) Ultrasound imaging. (c) NIR-only reconstruction. (d) FEM mesh. (e) Reconstruction step 1: background. (f) Reconstruction step 2 with the target structure

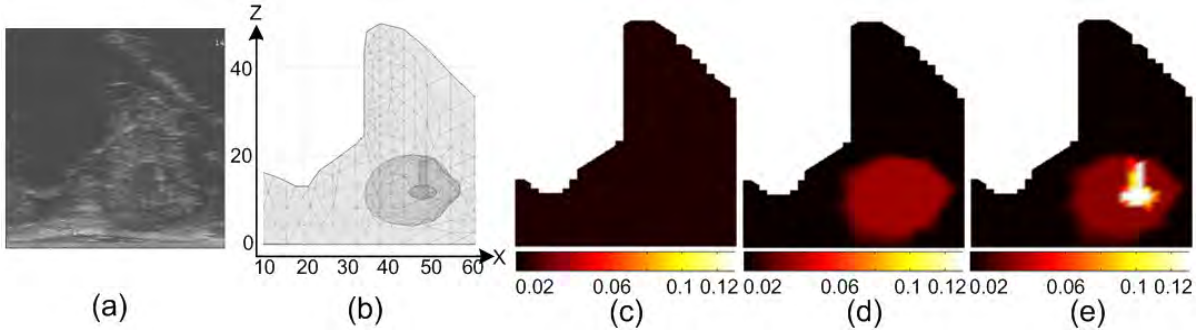

Fig. 9 Experiment II: Imaging on canine cadaver. (a) TRUS imaging (b) FEM mesh. (c), (d), (e) the 3 steps of hierarchical reconstruction

5. DISCUSSION AND SUMMARY

In this paper, a structural *prior* guided hierarchical NIR tomography reconstruction scheme aimed at improving the reconstruction accuracy of trans-rectal optical tomography of the prostate is presented. The method is developed under the framework of utilizing the trans-rectal ultrasound information as the structural *prior*. Nevertheless, the hierarchical method could be extended to implementing other high-resolution imaging modalities such as MRI to guide NIR tomography and to applying NIR tomography in other complicated tissue domains. The accuracy of the hierarchical reconstruction method, as indicated by the simulation and experimental investigations, relies on explicit demarcation of the inner structure of the imaging volume to form the region-resolved FEM mesh. In prostate a large amount of the cancer may be shown iso-echoic on TRUS. Thereby the utility or accuracy of this hierarchical imaging approach is hindered when TRUS images do not specify a suspicious region. Under such circumstance, the third step of recovering the tumor lesion in the prostate may proceed by reconstructing the optical properties on every element within the prostate but the overall accuracy of the reconstruction must be compromised.

In summary, an approach of hierarchically implementing the spatial *prior* information in trans-rectal optical tomography is introduced. Trans-rectal optical imaging of the prostate is challenging due to the structural complexity as well as the optical heterogeneity. Incorporating spatial “hard” *a priori* information available from complementary imaging modalities such as trans-rectal ultrasound is potentially subject to the local-minimum

sensitivity if the values of all regional optical properties are to be initialized simultaneously. A hierarchical spatial *prior* approach for trans-rectal optical tomography reconstruction does not assign the initial values to all sub-regions at once, instead a region is initially assumed homogenous, and the reconstructed optical properties are used as the initial guess for the region as a background when a sub-region is included in the next step. This approach translates to a 3-step iteration routine whereby the first step reconstructs the entire imaging volume as a single region, the second step uses these results as the initial guess of peri-prostate tissue to reconstruct the prostate and the rectum wall, and the third step assigns the updated results as the initial values of 3 existing regions to reconstruct a lesion inside the prostate. The robustness of this approach is demonstrated in both simulations and experiments.

ACKNOWLEDGEMENT

This work has been supported by the Prostate Cancer Research Program of the U.S. Army Medical Research Acquisition Activity (USAMRAA), 820 Chandler Street, Fort Detrick MD, 21702-5014, through grant #W81XWH-07-1-0247.

REFERENCES

[1] Jemal, A., Siegel, R., Ward, E., Murray, T., Xu, J., and Thun, M. J., "Cancer statistics, 2007," CA Cancer J. Clin. 57, 43-66 (2007).
[2] Polascik, T. J., Oesterling, J. E., and Partin, A. W., "Prostate specific antigen: a decade of discovery—what we have learned and where we are going," J. Urol. 162, 293-306 (1999).
[3] Grossfeld, G. D. and Carroll, P. R., "Prostate cancer early detection: a clinical perspective," Epidemiol Rev. 23, 173-80 (2001).
[4] Loch, A. C., Bannowsky, A., Baeurle, L., Grabski, B., König, B., Flier, G., Schmitz-Krause, O., Paul, U., and Loch, T., "Technical and anatomical essentials for transrectal ultrasound of the prostate," World J. Urol. 25, 361-366 (2007).
[5] Wise, A. M., Stamey, T. A., McNeal, J. E., and Clayton, J. L., "Morphologic and clinical significance of multifocal prostate cancers in radical prostatectomy specimens," Urology 60, 264-9 (2002).
[6] Miller, G. J. and Cygan, J. M., "Morphology of prostate cancer: the effects of multifocality on histological grade, tumor volume and capsule penetration," J. Urol., 152, 1709-13 (1994).
[7] Purohit, R.S., Shinohara, K., Meng, N.V., Carroll, P.R., "Imaging clinically localized prostate cancer," Urol. Clin. North Am., 30(2),279-93. Review (2003).
[8] Shinohara, K., Wheeler, T., and Scardino, P., "The appearance of prostate cancer on transrectal ultrasonography: correlation of imaging and pathological examinations," J. Urol, 142, 76 (1989).
[9] Tang, J., Yang, J.C., Li, Y., Li, J., Shi, H., "Peripheral zone hypoechoic lesions of the prostate: evaluation with contrast-enhanced gray scale transrectal ultrasonography," J Ultrasound Med, 26(12), 1671-9(2007).
[10] Linden, R.A., and Halpem, E..J., "Advances in transrectal ultrasound imaging of the prostate," Semin Ultrasound CT MR, 28(4), 249-57 (2007).
[11] Tromberg, B., Coquoz, J., Fishkin, O., Pham, J. B., Anderson, T., Butler, E. R., Cahn, J., Gross, M., Venugopalan, J. D., and Pham, D., "Non-invasive measurements of breast tissue optical properties using frequency-domain photon migration," Phil. Trans. R. Soc. Lond. B 352, 661-668 (1997).
[12] Pogue, B. W., Poplack, S. P., McBride, T.O., Wells, W. A., Osterman, K. S., Osterberg, U. L., and Paulsen, K. D.," Quantitative hemoglobin tomography with diffuse near-infrared spectroscopy: pilot results in the breast," Radiology 218, 261-266 (2001).
[13] Ntziachristos, V. and Chance, B., "Probing physiology and molecular function using optical imaging: applications to breast cancer," Breast Cancer Res. 3, 41-46 (2001).
[14] Choe, R., Corlu, A., K. Lee, Durduran, T., Konecky, S. D., Grosicka-Koptyra, M., Arridge, S. R., Czerniecki, B. J., Fraker, D. L., DeMichele, A., Chance, B., Rosen, M. A., and Yodh, A. G., "Diffuse optical tomography of breast cancer during neoadjuvant chemotherapy: a case study with comparison to MRI," Med. Phys. 32, 1128-1139 (2005).
[15] Franceschini, M. A., Moesta, K. T., Fantini, S., Gaida, G., Gratton, E., Jess, H., Mantulin, W. W., Seeber, M., Schlag, P. M., and Kaschke, M., "Frequency-domain techniques enhance optical mammography: initial clinical results," Proc. Nat. Acad. Sci. USA 94, 6468-6473 (1997).
[16] Zhu, Q., Cronin, E. B., Currier, A. A., Vine, H. S., Huang, M., Chen, N., and Xu, C., "Benign versus malignant breast masses: optical differentiation with US-guided optical imaging reconstruction," Radiology 237, 57-66 (2005).
[17] Bigler, S. A., Deering, R. E., and Brawer, M. K., "Comparison of microscopic vascularity in benign and malignant prostate tissue," Hum. Pathol. 24, 220-226 (1993).
[18] Ali, J. H., Wang, W. B., Zevallos, M., and Alfano, R. R. , "Near infrared spectroscopy and imaging to probe differences in water content in normal and cancer human prostate tissues," Technol. Cancer Res. Treat. 3, 491-497 (2004).
[19] Arnfield, M. R., Chapman, J. D., Tulip, J., Fenning, M. C., and McPhee, M. S., "Optical properties of experimental prostate tumors in vivo," Photochem. Photobiol. 57, 306-311 (1993).
[20] Zhu, T. C., Dimofte, A., Finlay, J. C., et al. "Optical properties of human prostate at 732 nm measured in mediated photodynamic therapy," Photochem. Photobiol. 81, 96-105 (2005).
[21] Svensson, T., Andersson-Engels, S., Einarsdóttír, M., and Svanberg, K., "In vivo optical characterization of human prostate tissue using near-infrared time-resolved spectroscopy," J. Biomed. Opt. 12, 014022 (2007).
[22] Goel, M., Radhakrishnan, H., Liu, H., et al. "Application of near infrared multi-spectral CCD imager system to determine the hemodynamic changes in prostate tumor," in *OSA Biomedical Topical Meetings* (Optical Society of America, 2006), paper SH10.
[23] Liu, H., Song, Y., Worden, K. L., Jiang, X., Constantinescu, A., and Mason, R. P., "Noninvasive investigation of blood oxygenation dynamics of tumors by near-infrared spectroscopy," Appl. Opt. 39, 5231-43 (2000).
[24] Zhou, X. and Zhu, T. C., "Image reconstruction of continuous wave diffuse optical tomography (DOT) of human prostate," in *Proceedings of the COMSOL Users Conference, n/a,* (2006).

[25] Jacques, S. L. and Motamedi, M., “Tomographic needles and catheters for optical imaging of prostatic cancer,” Proc. SPIE 2395, 111-118 (1995).
[26] Li, C., Liengsawangwong, R., Choi, H., and Cheung, R., "Using *a priori* structural information from magnetic resonance imaging to investigate the feasibility of prostate diffuse optical tomography and spectroscopy: a simulation study," Med. Phys. 34, 266-274 (2007).
[27] Schweiger, M., Arridge, S. R., Dorn, O., Zacharopoulos, A., and Kolehmainen, V., “Reconstructing absorption and diffusion shape profiles in optical tomography using a level set technique,” Opt. Lett. 31, 471-473 (2006).
[28] Kolehmainen, V., Arridge, S. R., Lionheart, W. R. B., Vauhkonen, M., and Kaipio, J. P., “Recovery of region boundaries of piecewise constant coefficients of an elliptic PDE from boundary data,” Inverse Probl. 15, 1375-1391 (1999).
[29] Kolehmainen, V., Vauhkonen, M., Kaipio, J. P., and Arridge, S. R., “Recovery of piecewise constant coefficients in optical diffusion tomography,” Opt. Express 7, 468-480 (2000).
[30] Kolehmainen, V., Arridge, S. R., Vauhkonen, M., and Kaipio, J. P., “Simultaneous reconstruction of internal tissue region boundaries and coefficients in optical diffusion tomography,” Phys. Med. Biol. 45, 3267-3284 (2000).
[31] Srinivasan, S., Pogue, B. W., Dehghani, H., Jiang, S., Song, X., and Paulsen, K. D., ”Improved quantification of small objects in near-infrared diffuse optical tomography,” J. Biomed. Opt. 9, 1161-1171 (2004).
[32] Pogue, B. W., Geimer, S., McBride, T. O., Jiang, S., Osterberg, U. L., and Paulsen, K. D., “Three-dimensional simulation of near-infrared diffusion in tissue: boundary condition and geometry analysis for finiteelement image reconstruction,” Appl. Opt. 40, 588-600 (2001).
[33] Schweiger, M., Arridge, S. R., and Delpy, D. T., “Application of the finite-element method for the forward and inverse models in optical tomography,” J. Math. Imag. Vision 3, 263-283 (1993).
[34] Dehghani, H., Carpenter, C. M., Yalavarthy, P. K., Pogue, B. W., and Culver, J. P., “Structural *a priori* information in near-infrared optical tomography,” Proc. SPIE 6431, 64310B1 (2007).
[35] Zhu, Q., Durduran, T., Ntziachristos, V., Holboke, M., and Yodh, A. G., “Imager that combines near-infrared diffusive light and ultrasound,” Opt. Lett. 24, 1050-1052 (1999).
[36] Holboke, M. J., Tromberg, B. J., Li, X., Shah, N., Fishkin, J., Kidney, D., Butler, J., Chance, B., and Yodh, A. G., “Three-dimensional diffuse optical mammography with ultrasound localization in a human subject,” J. Biomed. Opt., 5, 237-47 (2000).
[37] Yu, X., Chen, G., and Cheng, S., “Dynamic learning rate optimization of the backpropagation algorithm,” IEEE Trans. Neural Netw. 6, 669-677 (1995).

In vivo trans-rectal ultrasound coupled trans-rectal near-infrared optical tomography of canine prostate bearing transmissible venereal tumor

Zhen Jiang,[1] G. Reed Holyoak,[2] Kenneth E. Bartels,[2] Jerry W. Ritchey,[3]
Guan Xu,[1] Charles F. Bunting,[1] Gennady Slobodov,[4] Jerzy S. Krasinski,[1] Daqing Piao [1*]

[1] *School of Electrical and Computer Engineering, Oklahoma State University, Stillwater, OK 74078 USA*
[2] *Department of Veterinary Clinical Sciences, Oklahoma State University, Stillwater, OK 74078 USA*
[3] *Department of Veterinary Pathobiology, Oklahoma State University, Stillwater, OK 74078 USA*
[4] *Department of Urology, University of Oklahoma Health Science Center, Oklahoma City, OK 73104 USA*
[*] *E-mail: daqing.piao@okstate.edu*

Abstract: *In vivo* trans-rectal near-infrared (NIR) optical tomography is conducted on a tumor-bearing canine prostate with the assistance of trans-rectal ultrasound (TRUS). The canine prostate tumor model is made possible by a unique round cell neoplasm of dogs, transmissible venereal tumor (TVT) that can be transferred from dog to dog regardless of histocompatibility. A characterized TVT cell line was homogenized and passed twice in subcutaneous tissue of NOD/SCID mice. Following the second passage, the tumor was recovered, homogenized and then inoculated by ultrasound guidance into the prostate gland of a healthy dog. The dog was then imaged with a combined trans-rectal NIR and TRUS imager using an integrated trans-rectal NIR/US applicator. The image was taken by NIR and US modalities concurrently, both in sagittal view. The trans-rectal NIR imager is a continuous-wave system that illuminates 7 source channels sequentially by a fiber switch to deliver sufficient light power to the relatively more absorbing prostate tissue and samples 7 detection channels simultaneously by a gated intensified high-resolution CCD camera. This work tests the feasibility of detecting prostate tumor by trans-rectal NIR optical tomography and the benefit of augmenting TRUS with trans-rectal NIR imaging.

Keywords: Prostate; near-infrared optical tomography; trans-rectal; ultrasound; transmissible venereal tumor.

1. INTRODUCTION

Prostate cancer is prevalent in the men in the U.S. and in the industrialized countries [1]. Most of the prostate cancers are diagnosed at earlier stage now with the use of the sensitive prostate-specific antigen (PSA) test [2] aided by the digital rectal exam (DRE). Prostate biopsy, guided by trans-rectal ultrasound (TRUS), is performed when the pathological evidence is needed to confirm or rule out the onset of carcinoma in prostate [3].

The real-time utility and the excellent morphological information of TRUS make it ideal for visualizing the needle trajectory during the biopsy. TRUS had been utilized to assess the malignant changes in prostate tissue [4], unfortunately, the lack of specificity has limited the value of TRUS in diagnostic imaging of the prostate cancer and transformed the role of TRUS to becoming primarily an imaging tool for placing the biopsy needle. The accuracy of TRUS imaging may be improved by augmenting it with a functional contrast, thereby reducing unnecessary biopsies and more accurately targeting the malignant areas for biopsy. The near-infrared (NIR) light is known to reveal significant functional contrasts between a tumor and normal tissue originated from the angiogenic and hypoxic changes of the malignancy [5-11]. However, using NIR alone is less viable for prostate imaging due to its low spatial resolution and non-real time image reconstruction. An appealing approach is to combine NIR and TRUS to take advantage of the complementary features of NIR and TRUS.

In vivo imaging of NIR tomography of the prostate to augment TRUS is confronted with difficulties uncommon to the previous application of NIR tomography in cancer imaging. First of all, the prostate lies deep inside the pelvic compartment wherein the imaging by trans-rectal probing may be the optimal choice. In trans-rectal probing the NIR light will be attenuated by the condom (required when using TRUS) first, then the rectum wall, and the peri-rectum

Optical Tomography and Spectroscopy of Tissue VIII, edited by Bruce J. Tromberg, Arjun G. Yodh, Mamoru Tamura, Eva M. Sevick-Muraca, Robert R. Alfano, Proc. of SPIE Vol. 7174
71741U · © 2009 SPIE · CCC code: 1605-7422/09/$18 · doi: 10.1117/12.807990

tissue before reaching the prostate. As the light reaches the prostate, reflection on the prostate capsule and the potentially strong absorption by the peripheral vascular structures may limit the amount of light interrogating the deep prostate tissues. Secondly there is considerable challenge of fabricating an endo-rectal NIR applicator which should contain a number of source and detector channels if spatially-resolved imaging of large tissue volumes of the prostate is intended. The challenge becomes more pronounced when the NIR is to be combined with TRUS [12].

Recently we have constructed a trans-rectal NIR/US probe and validated the utility of the combined trans-rectal NIR/US imaging in a cadaver canine prostate *in situ* [13]. In this paper, we demonstrate the *in vivo* utility of the trans-rectal NIR/US imaging by use of a canine prostate bearing transmissible venereal tumor (TVT). TVT has an anechoic response that makes it visible on the TRUS. The TVT is known to have a higher cell density that tends to absorb and potentially scatter more NIR light than does the normal prostate tissue. In this work, the TVTs in the prostate and peri-prostatatic tissue were located by TRUS, then imaged by NIR tomography in situ. The TVTs are shown as strong hyper-absorptive and moderately hyper-scattering on NIR tomography images being reconstructed without any prior.

2. METHODS AND MATERIALS

2.1 Sagittal-imaging trans-rectal NIR/US system

The details of the integrated sagittal-imaging trans-rectal NIR/US applicator and system are described elsewhere [13]. Briefly, this combined imaging applicator consists of a custom-built NIR probe and a commercial bi-plane TRUS transducer. The 7.5MHz sagittal-imaging transducer of the TRUS probe is used to couple with the NIR. The NIR applicator was fabricated to a cap-shape and attached to the TRUS probe on the top with a slot opened to expose the sagittal US transducer. The NIR array substrate was fabricated from a black polycarbonate material to satisfy the absorptive boundary condition. The NIR probe consists of two linear arrays, one for the source and the other for the detector, separated by 20mm and placed on each side of the sagittal TRUS transducer of 60mm in length. Each linear-array consists of 7 channels spaced 10mm apart and covering a total length of 60mm. Each NIR channel consists of a metal-coated fiber epoxied to a gradient-index lens and a prism to deflect the light to and from the probe surface.

The geometric relation between the imaging probe and the prostate is depicted in Fig. 1 where the optical channels are seen arranged cranial-caudally from 1 to 7. The NIR light illuminates through the condom, the rectum, and propagates into the prostate.

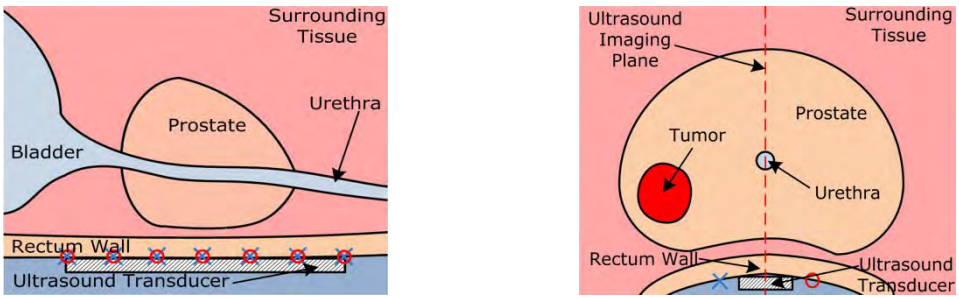

(a) Sagittal view (b) axial view

Fig. 1 Illustration of the TRUS coupled trans-rectal NIR imaging of the prostate. The TRUS middle-sagittal plane is marked by a red dash-line. The red circles denote NIR sources and the blue crosses denote the NIR detectors.

The TRUS probe is connected to an Aloka-3500 scanner. The US images were transferred to the main computer of the combined NIR/US imager by a PCI image acquisition card (National Instruments PCI-1405). The NIR imager uses a custom-designed superluminescent diode (SLD) (Superlumdiodes Inc.) that is pigtailed to a multi-mode fiber and delivers 100mW of 840nm NIR light with 14.2nm FWHM bandwidth. The SLD output beam is focused and delivered sequentially onto 7 source fibers of the NIR applicator by a translating fiber multiplexer. The entire NIR bandwidth is coupled to each fiber at a time. The remitted NIR light is collected by 7 detection fibers coupled to a spectrometer (Acton Research). A 16-bit intensified CCD camera (Princeton Instruments) acquires the 7 optical signals corresponding to one source simultaneously, and a complete set of data for all 7 source channels is taken within 5 seconds.

2.2 Animal model

Dogs have been previously used for prostate tumor model studies because of the similarity between canine and human prostate glands [14-16]. For this study, the prostate of a mature dog was injected with canine TVT cells with the purpose

of developing an *in vivo* prostate tumor model for NIR/US imaging. The unique canine TVT is a round cell tumor of dogs that mainly affects the external genitalia and can be transmitted from animal to animal during copulation, regardless of histocompatibility. The neoplastic cells are generally thought to be of histiocytic origin [17]. TVT cells can be propagated in immunocompromised (SCID) mice and transferred to different tissues (such as the prostate gland) of the dog to result in a neoplastic mass effect useful for imaging studies [16].

The experiments were conducted in the Center for Veterinary Health Sciences at Oklahoma State University under a protocol approved by the university's Institutional Animal Care and Use Committee. The protocol was also approved and underwent an on-site inspection by the US Army Medical Research and Material Command. For these studies, an existing TVT cell line was obtained as cryopreserved tissue from MD Anderson Cancer Center (Houston, TX). The tumor tissue was quick-thawed, homogenized and inoculated into the subcutis of a NOD/SCID mouse. After approximately 12 weeks, the tumor reached an appropriate volume (4.0-4.5cm^3) for recovery and were processed and inoculated into a second NOD/SCID mouse. Following growth in the second mouse (8 weeks), the neoplastic cells were recovered and homogenized for inoculation into the canine prostate gland.

A 12 kg sexually intact adult Beagle dog estimated to be approximately 4 years of age was housed single in a inside run and given free access to water and food. For TVT cell injection, the dog was anesthetized using an intravenous injection of propofol (8mg/kg) followed by intubation and halothane/oxygen inhalation anesthetic maintenance. The animal was placed in left lateral recumbency for bowel preparation and physical examination of the prostate. The perineum was aseptically prepared for injection and under TRUS visualization, a 6-inch 16 gauge hypodermic needle was inserted transperineally into the right lobe of the prostate where 3 cc of the prepared TVT cells were injected. During retraction of the injection needle, it was considered unavoidable that TVT cells would leak from the prostate injection site and be "seeded" along the needle insertion tract.

The dog was examined weekly by TRUS using a condom-covered combined NIR/US probe. For all TRUS and NIR follow-on imaging sessions, the dog underwent general anesthesia using a similar protocol used for TVT cell injection. During the first two weeks following TVT cell injection there was no evidence of tumor growth. The next TRUS examination occurred 5 weeks post-injection when hypoechoic masses were observed both in the prostatic parenchyma and peri-prostatically around the right lobe of the prostate. The dog underwent weekly monitoring for 2 more weeks, and was then humanly euthanized 8 weeks after the initial TVT cell injection. A complete necropsy was performed with the prostate and peri-prostatic structures submitted for histological examination.

3. SYSTEM PERFORMENCE

The combined NIR/US probe & system enables concurrent acquisition of trans-rectal NIR tomography and TRUS images on the same sagittal plane. Our previous studies have validated that incorporating TRUS *a priori* information allows trans-rectal NIR tomography to recover an absorption target accurately. We have also demonstrated that trans-rectal NIR imaging could recover an absorptive target with no spatial prior. In this paper, the TRUS is used to locate a suspected TVT target, and NIR image reconstruction is performed without *prior* information in order to examine if the TVT shows inherent NIR contrast. As our trans-rectal NIR probe allows 3-dimensional imaging, the system performance is evaluated for recovering targets located on or off the sagittal plane when using only the NIR information.

3.1 Reconstruction of a target on the mid-sagittal plane----------Simulation

The performance of reconstructing absorptive targets in the sagital-plane using continuous-wave measurement has been investigated previously [13]. As the optical scattering properties of the prostate cancer and the benign tissue may be different, simulation is performed to investigate reconstruction of the reduced scattering property of a target using continuous-wave measurements. Figure 2 lists the results simulated for a single target having both absorption and scattering contrasts over the background. The homogeneous background (for all the simulations conducted in this work) is set at μ_a (absorption coefficient) of 0.002mm^{-1} and μ_s' (reduced scattering coefficient) of 1.0mm^{-1}. The μ_a of the target is set at 0.004mm^{-1} and 0.02mm^{-1}; the μ_s' of the target is set at 2.0mm^{-1} and 10mm^{-1}. The target is a sphere of 10mm in diameter and located along the middle-sagittal plane (the TRUS imaging plane) at a depth of 10mm. Figure 2(a) shows the results for the target at a depth of 10mm and placed 20 mm longitudinally from the mid-line of the sagittal plane. Figure 2(b) shows the results when the target is at the mid-line of the sagittal plane. The sagittal and coronal locations of the target are correctly reconstructed. Cross-coupling between the absorption and scattering reconstructions out of the continuous-wave data is not observed, however, the optical properties are underestimated.

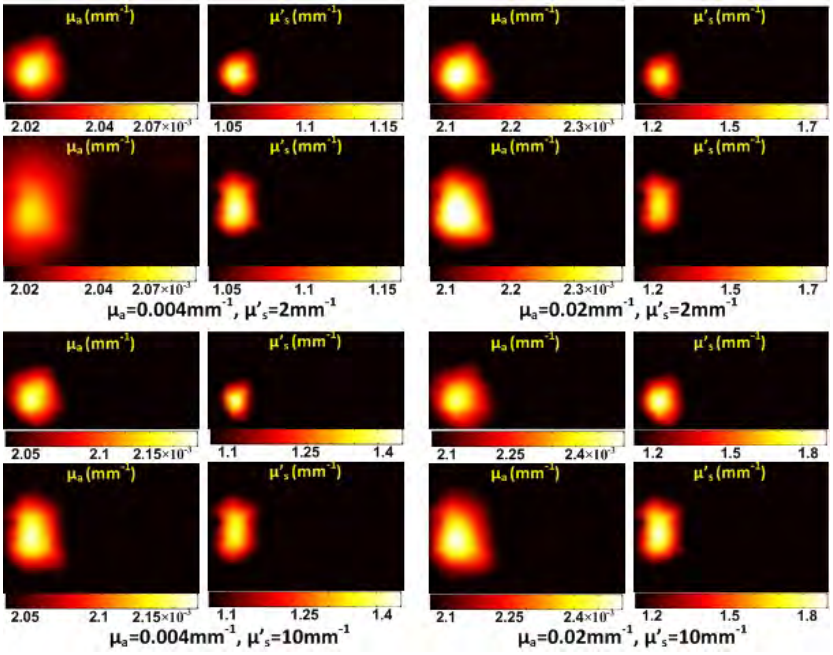

(a) Target shift 20mm longitudinally from the mid-point

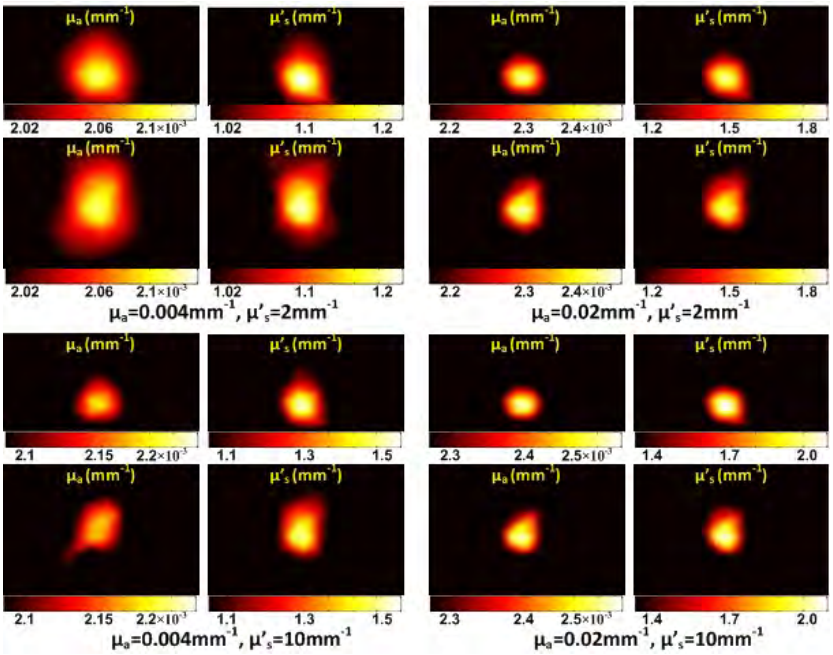

(b) Target at the mid-point

Figure 2 Reconstruction of the absorption and reduced scattering of a target located in the sagittal plane based on continuous-wave data. For each set of 4-image, the top row corresponds to the sagittal view, and the bottom row corresponds to the coronal view.

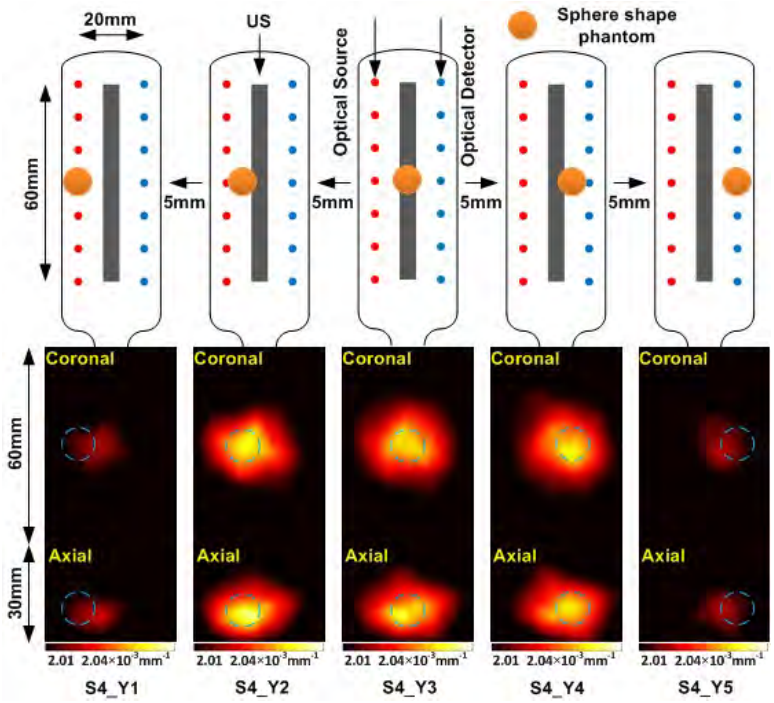

(a) Simulation for a sphere target

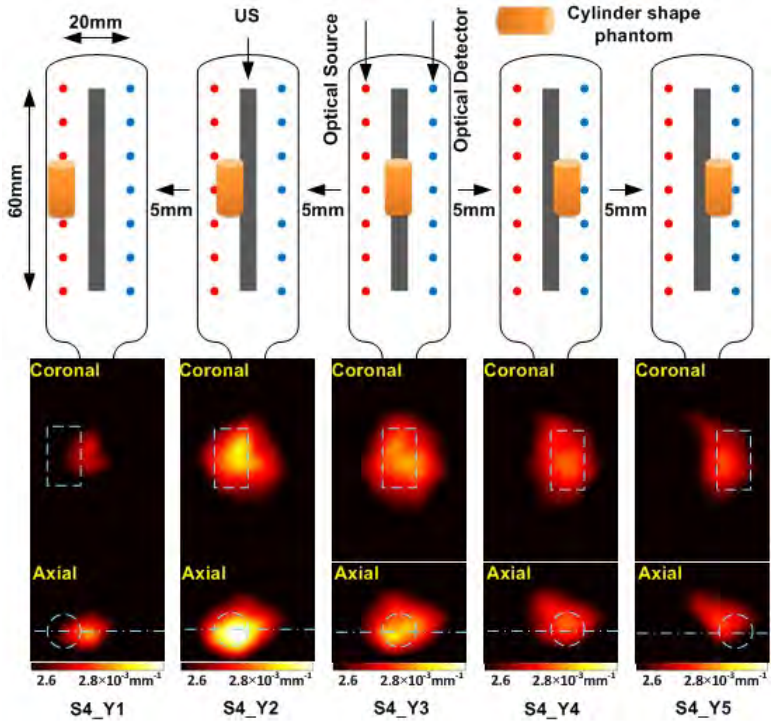

(b) Experimental results for a cylinder target

Figure 4. Recovering of a target at different lateral positions.

3.2 Reconstruction of a target off the mid-sagittal plane-----Simulation and experimental results

The geometry of the trans-rectal NIR applicator allows 3-dimensional imaging. The reconstruction of a target located off the middle-sagittal plane is illustrated in Fig. 4. Figure 4 (a) shows the target being displaced from left-lateral to right-

lateral at 5mm per step. The target is a sphere of 10mm in diameter with μ_a of 0.0056mm^{-1} and μ_s' of 1.03mm^{-1}. The experiment results are shown as Fig. 4(b) for a target of cylinder shape (10mm in diameter and 16mm in length) having the same optical properties of the target in simulation of (a). Both the simulation and the experimental results indicated that a target off the middle-sagittal plane may be recovered by NIR only, but at slightly displaced spatial location.

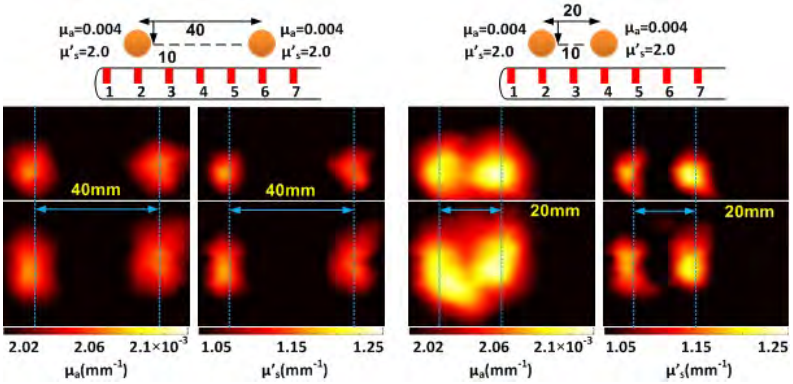

(a) Multiple targets with the same absorption and scattering coefficients

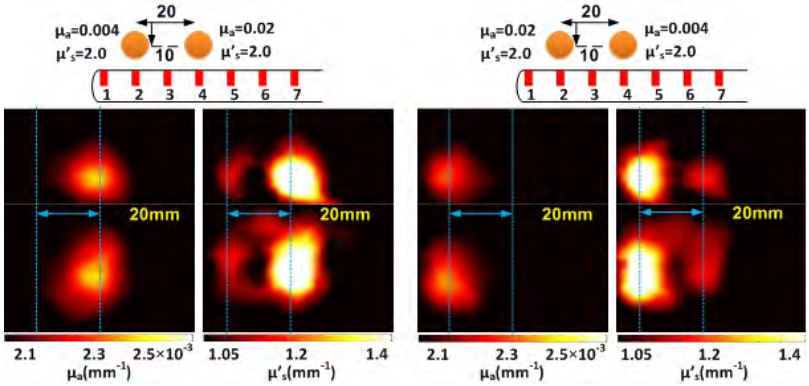

(b) Multiple targets with different absorption but same scattering coefficients

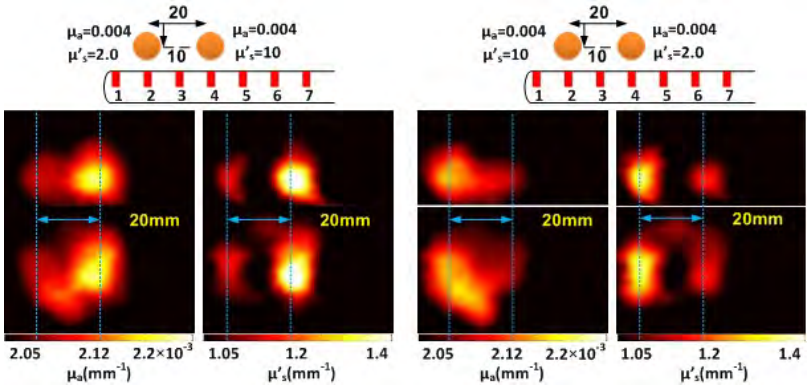

(c) Multiple targets with same absorption but different scattering coefficients

Figure 1. Reconstruction of multiple targets

3.3 Reconstruction of multiple targets on the mid-sagittal plane-----Simulation

The performance of differentiating multiple targets on the mid-sagittal plane is evaluated by simulation. The simulation is performed for two sphere targets of 10mm in diameter. In (a) the two targets have the same $\mu_a = 0.004\text{mm}^{-1}$ and

$\mu_s' = 2.0\text{mm}^{-1}$. At 40mm longitudinal separation, the targets can be separated on both μ_a and μ_s' images. At closer separation, overlapping of the two targets is seen on μ_a before on μ_s'. In (b), the two targets are 20mm apart, the μ_s' of both is 2.0mm^{-1}, and the μ_a values are set at 0.004mm^{-1} and 0.02mm^{-1} respectively. In the μ_a image, only the higher contrast target is recovered. While in the μ_s' image, the lower contrast target is recovered but with cross-coupling from the higher contrast target. In (c), the μ_a is 0.004mm^{-1} for both, and the μ_s' is set at 2.0mm^{-1} and 10mm^{-1} for the two targets. The two targets are recovered on μ_s' image, but barely separated on the μ_a image. The above simulation and experimental results demonstrate the utility of reconstructing both μ_a and μ_s' based on continuous-wave measurement even though the recovery of the target is not satisfactory for all conditions.

4. IN VIVO RESULTS

The results of in vivo trans-rectal NIR tomography and TRUS of the canine are presented in Fig. 6 for the NIR absorption images and Fig. 7 for the NIR reduced scattering images. All NIR images are displayed with consistent color scales for both μ_a and μ_s'. The dimensions of US and NIR images are 60mm (cranial-caudal)×30mm (posterior-anterior) for sagittal, 40mm (right lateral –left lateral)×30mm (posterior-anterior) for axial, and 60mm (cranial-caudal)×40mm (right lateral –left lateral) for coronal views, respectively.

4.1 Hyper-absorptive indication of the TVT on NIR image

The three sagittal TRUS images (Fig. 6) were taken at the mid-line of the prostate, the middle portion of the right lobe of the prostate, and the right lateral edge of the prostate. The hypo-echoic region L1 indicates an abnormal intra-prostatic mass. The large hypo-echoic region L2 indicates an abnormal mass anterior and caudal to the prostate that may have connection with L1. The NT on the right lobe US image denotes the needle trajectory for introducing the TVT cells. Longitudinal hypo-echoic regions including L3 are seen along the NT. The three sagittal NIR images correspond to the US taken at the middle portion of the right lobe, 10mm medial to it and 10mm lateral to it, respectively. Hyper-absorptive regions on sagittal NIR images correspond to L1, L2, and L3 on sagittal US images. The 10mm-medial NIR image shows reduced contrast for the absorptive masses, and the 10mm-lateral NIR reveals connected strong absorptive masses. The bladder is seen as slightly hypo-echoic at the 2 more medial sagittal US images; however, no hyper-absorptive mass is presented at the left-most region of the sagittal NIR images.

The three axial TRUS images were taken at the cranial edge of the prostate crossing L1, the caudal edge of the prostate crossing L2, and the peri-rectal region crossing L3. The axial US images show a small hypo-echoic intra-prostatic mass at cranial side of the prostate, the bulging of the right lobe and extending of the L2 over the prostate mid-line that correlates with the findings on mid-line sagittal US, and large peri-rectal hypo-echoic mass cranial to the perineum. Of the five axial NIR images, the longitudinal positions are 10mm apart from cranial to caudal. The axial NIR image A2 should contain L1, and the axial NIR image A5 should contain L3.

The coronal NIR images correspond to 5mm, 10mm, and 15mm anterior to the anterior edge of the rectal lumen. The hyper-absorptive mass indicative of L1 is seen medial to the hyper-absorptive masses indicative of L2 and L3. The anatomies of the hyper-absorptive masses on the NIR images in 3-views agree with the hypo-echoic regions on the US images in 2-views.

The US and NIR imaging were also performed at the middle-line of the left lobe where no abnormal features were found on the US, and globally homogenous and low absorption was seen in the NIR images.

4.2 Hyper-scattering indication of the TVT on NIR image

The hyper-absorptive masses in Fig.6 being suspicious of TVTs are shown in Fig. 7 with different patterns of the reduced scattering contrast, indicating minimum cross-coupling between the reconstructions of μ_a and μ_s' from the in vivo continuous-wave measurement. In the scattering NIR images, L3 has much higher contrast than do the other masses corresponding to L1 and L2. The contrast elsewhere is also slightly more homogenous compared with that in the absorption image.

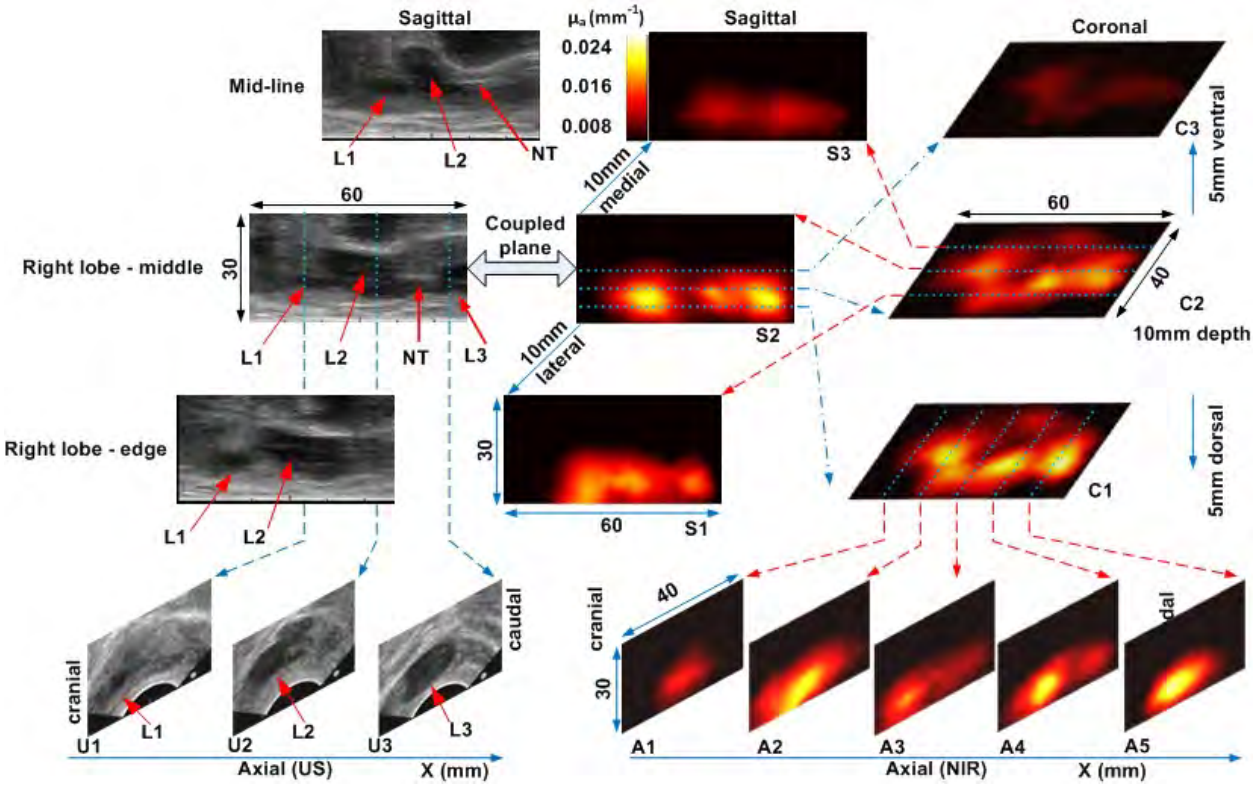

Figure 2. Trans-rectal NIR imaging (absorption) in 3-views vs TRUS imaging in 2-views

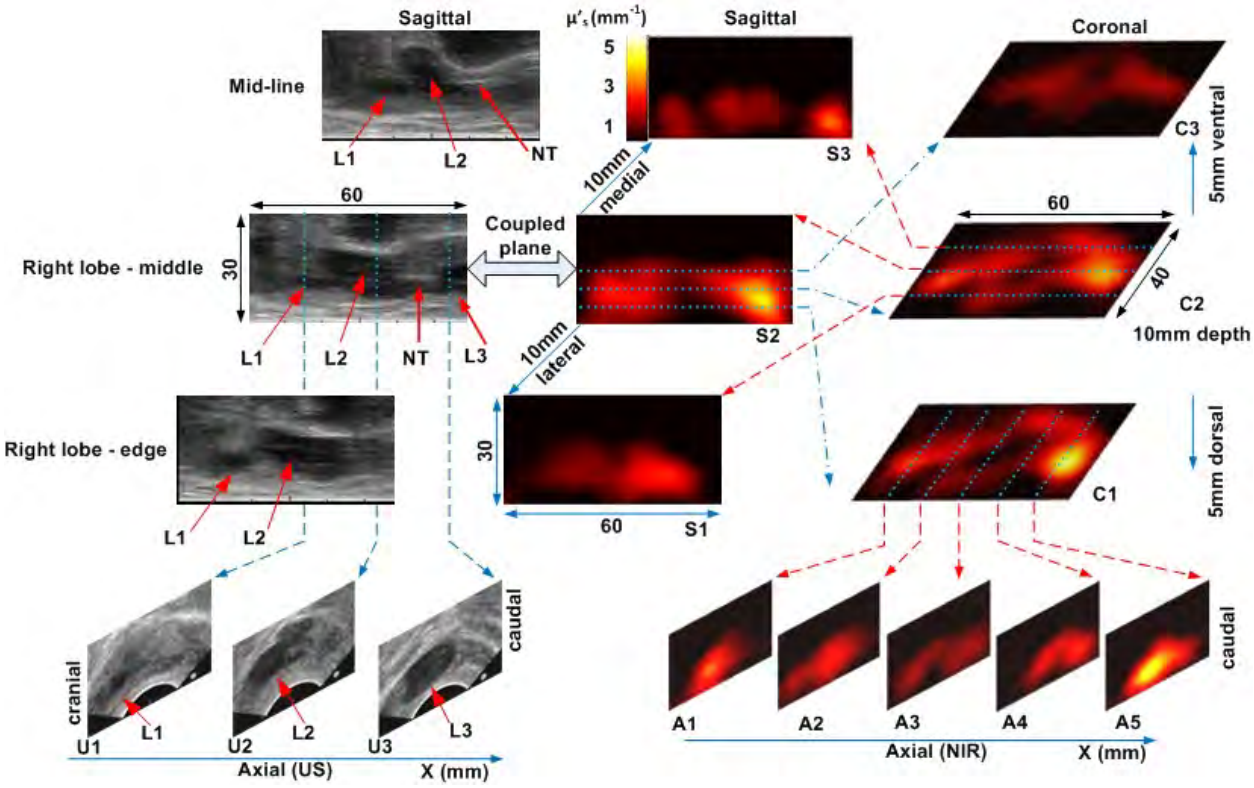

Figure 7. Trans-rectal NIR imaging (reduced scattering) in 3-views vs TRUS imaging in 2-views

4.3 Confirmation of the TVT growth

The mass L3 indicated by the US and NIR correlates with a large peri-prostatic nodule along the needle track site determined by digital rectal examination prior to imaging. Necropsy confirmed that L3 was a peri-rectal nodule along the needle track. The necropsy also confirmed a large nodule, corresponding to L2, anterior to the prostate at the caudal side of the prostate that extended from the right-lateral aspect of the prostate to the middle-line of the prostate. Exposing the interior of the prostate also confirmed a nodule at the right lobe of the prostate that corresponds to the mass L1. Histological examination confirmed all nodules to be TVT.

5. DISCUSSIONS AND CONCLUSIONS

Among the hypo-echoic masses shown on the US, L1 was intra-prostatic, L2 was largely anterior to the prostate, and L3 was caudal to the prostate. These 3 masses are however shown at similar depths on NIR images. This is attributed to the un-even NIR sensitivity profile along the posterior-anterior direction [12]. It is however noted that the existence of TVT nodules have been recovered by use of only the NIR information. If the anatomic location of the TVT available from the US can be utilized as the spatial prior for NIR image reconstruction, the localization of the TVT nodules on NIR images will certainly be more accurate.

It is known that most of the prostate cancers are presented as multi-focal [18, 19]. It must be noted that the intraprostatic TVT tumors were initiated and developed during this project in a non-immunosuppressed canine model. The subject in this study developed multiple TVT nodules intra-prostatically and peri-prostatically. Although the sites of the TVT tumors were not totally confined to the prostate, the successful imaging of multiple TVT tumor nodules by trans-rectal NIR tomography implies the feasibility of recovering multiple intra-prostatic TVT tumors. All of the TVT tumor nodules developed in this subject were shown strongly hypo-echoic on the US, which correlates with the strongly hyper-absorptive and moderately hyper-scattering findings on NIR imaging. The bladder, on the other hand, shows hypo-echoic on the ultrasound; however it is not shown as hyper-absorptive or hyper-scattering on the NIR images. This confirms that trans-rectal NIR tomography has higher specificity of imaging the regions hypo-echoic to TRUS.

It has been well-demonstrated that cancers in organs like breast are presented in NIR tomography as having increased absorption and different reduced scattering contrast over the normal tissues when imaged intact, in situ and in vivo. However, there was previously no information on the optical contrast of prostate cancer compared to normal prostatic or peri-prostatic tissue taken at intact prostate *in situ* and *in vivo*. Our work presents a new paradigm for prostate imaging that shows promises of improving the specificity of TRUS imaging by augmenting it with trans-rectal NIR tomography.

In conclusion, this work reported in vivo imaging of TVT tumors in the canine prostate and pelvic canal by trans-rectal NIR tomography coupled with TRUS. The TVT tumor nodules show strong NIR absorption and moderate scattering contrasts over the normal prostatic and peri-prostatic tissues. Correlation of the TVT locations is found between trans-rectal NIR and TRUS results.

6. ACKNOWLEDGEMENT

This work has been supported by the Prostate Cancer Research Program of the U.S. Army Medical Research Acquisition Activity (USAMRAA), 820 Chandler Street, Fort Detrick MD, 21702-5014, through grant #W81XWH-07-1-0247.

References:

1. A. Jemal, R. Siegel, E. Ward, T. Murray, J. Xu, and M. J. Thun, "Cancer statistics, 2007," CA Cancer J. Clin. **57**, 43-66 (2007).
2. T. J. Polascik, J. E. Oesterling, and A. W. Partin, "Prostate specific antigen: a decade of discovery--what we have learned and where we are going," J. Urol. **162**, 293-306 (1999).
3. A. C. Loch, A. Bannowsky, L. Baeurle, B. Grabski, B. König, G. Flier, O. Schmitz-Krause, U. Paul, and T. Loch, "Technical and anatomical essentials for transrectal ultrasound of the prostate," World J. Urol. **25**, 361-366 (2007).
4. B. Spajic, H. Eupic, D. Tomas, G. Stimac, B. Kruslin, and O. Kraus, "The incidence of hyperechoic prostate cancer in transrectal ultrasound-guided biopsy specimens," Urology **70**, 734-737 (2007).
5. B. Tromberg, J. Coquoz, O. Fishkin, J. B. Pham, T. Anderson, E. R. Butler, J. Cahn, M. Gross, J. D. Venugopalan, and D. Pham, "Non-invasive measurements of breast tissue optical properties using frequency-domain photon migration," Phil. Trans. R. Soc. Lond. B **352**, 661-668 (1997).
6. B. W. Pogue, S. P. Poplack, T.O. McBride, W. A. Wells, K. S. Osterman, U. L. Osterberg, and K. D. Paulsen," Quantitative hemoglobin tomography with diffuse near-infrared spectroscopy: pilot results in the breast," Radiology **218**, 261-266 (2001).
7. V. Ntziachristos and B. Chance, "Probing physiology and molecular function using optical imaging: applications to breast cancer," Breast Cancer Res. **3**, 41-46 (2001).

8. R. Choe, A. Corlu, K. Lee, T. Durduran, S. D. Konecky, M. Grosicka-Koptyra, S. R. Arridge, B. J. Czerniecki, D. L. Fraker, A. DeMichele, B. Chance, M. A. Rosen, and A. G. Yodh, "Diffuse optical tomography of breast cancer during neoadjuvant chemotherapy: a case study with comparison to MRI," Med. Phys. **32**, 1128-1139 (2005).
9. M. A. Franceschini, K. T. Moesta, S. Fantini, G. Gaida, E. Gratton, H. Jess, W. W. Mantulin, M. Seeber, P. M. Schlag, and M. Kaschke, "Frequency-domain techniques enhance optical mammography: initial clinical results," Proc. Nat. Acad. Sci. USA **94**, 6468-6473 (1997).
10. Q. Zhu, E. B. Cronin, A. A. Currier, H. S. Vine, M. Huang, N. Chen, and C. Xu, "Benign versus malignant breast masses: optical differentiation with US-guided optical imaging reconstruction," Radiology **237**, 57-66 (2005).
11. S. A. Bigler, R. E. Deering, and M. K. Brawer, "Comparison of microscopic vascularity in benign and malignant prostate tissue," Hum. Pathol. **24**, 220-226 (1993).
12. G. Xu, D. Piao, C.H. Musgrove, C.F. Bunting, H. Dehghani, "Trans-rectal ultrasound-coupled near-infrared optical tomography of the prostate Part I: Simulation," Optics Express, 16(22), 17484–17504 (2008).
13. Z. Jiang, D. Piao, G. Xu, J.W. Ritchey, G.R. Holyoak, K.E. Bartels, C.F. Bunting, G. Slobodov, J.S. Krasinski, "Trans-rectal ultrasound-coupled near-infrared optical tomography of the prostate Part II: Experimental demonstration," Optics Express, 16(22), 17505–17520 (2008).
14. J.D. Hazle, C.J. Diederich, M. Kangasniemi, R.E. Price, L.E. Olsson, and R.J. Stafford, "MRI-guided thermal therapy of transplanted tumors in the canine prostate using a directional transurethral ultrasound applicator," J Magn Reson Imaging., 15(4), 409-17 (2002).
15. F. Forsberg, D.K. Johnson, D.A. Merton, J.B. Li, P.E. Losco, E.K. Hagen, and B.B. Goldberg, "Contrast-enhanced transrectal ultrasonography of a novel canine prostate cancer model," J Ultrasound Med., 21(9), 1003-13 (2002).
16. B. Rivera, K. Ahrar, M.M Kangasniemi, J.D. Hazle, R.E. Price, "Canine transmissible venereal tumor: a large-animal transplantable tumor model," Comp Med., 55(4), 335-43 (2005).
17. E. Mozos, A. Mendez, J.C. Gomez-Villamandos, J.M. De Las Mulas, J. Perez, "Immunohistochemical characterization of canine transmissible venereal tumor," Vet Pathol., 33, 257-263 (1996).
18. A. M. Wise, T. A. Stamey, J. E. McNeal, and J. L. Clayton, "Morphologic and clinical significance of multifocal prostate cancers in radical prostatectomy specimens," Urology **60,** 264-9 (2002).
19. G. J. Miller and J. M. Cygan, "Morphology of prostate cancer: the effects of multifocality on histological grade, tumor volume and capsule penetration," J. Urol. 152(5 Pt 2), 1709-13 (1994).

FPGA-Assisted Strategy toward Efficient Reconstruction (FAStER) in Diffuse Optical Tomography

Yuanyuan Jiang, Sovanlal Mukherjee, James E. Stine, Charles F. Bunting, Daqing Piao*
School of Electrical and Computer Engineering, Oklahoma State University, Stillwater, OK, 74078, USA
Corresponding author: daqing.piao@okstate.edu

Abstract: The finite-element computation of photon fluence and adjoint photon fluence necessary to image reconstruction in steady-state DOT has been implemented on field-programmable-gate-array (FPGA). Preliminary results encourage further exploration toward efficient DOT image reconstruction using FPGA.

OCIS codes: (170.6960) Tomography; (170.3010) Image reconstruction techniques.

1. INTRODUCTION

Diffuse optical tomography (DOT) utilizes near-infrared (NIR) light to interrogate biological tissues at a depth up to several centimeters to recover the distribution of internal optical properties based on boundary measurements. The image reconstruction of DOT is most often rendered by diffusion-model-based forward computation and iterative non-linear optimization [1], which is inevitably computationally expensive. Consequently, using application-specific computer architecture to accelerate the DOT computation becomes attractive. A number of computer architectures useful for accelerating the data acquisition and processing in optical imaging have been demonstrated recently. Examples include using field-programmable gate array (FPGA) technology to accelerate raw data processing in optical imaging [2, 3], using FPGAs or graphic processing units (GPUs) to accelerate Monte Carlo computation of photon migration [4-6], using FPGAs to solve partial differential equations (PDEs) governing heat transfer [7] or wave propagation [8], and using GPU to perform finite-element-method (FEM) computation [9].

In this work the FEM solution to photon diffusion in biological tissue is implemented using an FPGA. The FPGA executes conjugate gradient (CG) solver of 12 linear equations formulated in an FEM framework, which are associated with 6 sources and 6 detectors, for computing the photon fluence rate and the adjoint fluence rate. Preliminary results demonstrate that a lower-end FPGA outperforms a higher-end PC in CG-based solution of the 12 linear equations, thereby encouraging further exploration toward efficient DOT image reconstruction using FPGA.

2. METHOD AND MATERIALS

2.1 Development of an open-code FEM-based forward solver for steady-state diffuse optical tomography

Implementing the DOT image reconstruction routine in FPGA requires an algorithm architecture that is transparent to FPGA. An open-code forward FEM solver for steady-state DOT reconstruction is developed. The solver is based on the steady-state photon diffusion equation [1] $\nabla\cdot\kappa(\vec{r})\nabla\Phi(\vec{r})-\mu_a(\vec{r})\cdot\Phi(\vec{r})=-q(\vec{r})$ (where μ_a is the absorption coefficient, κ is the diffusion coefficient, Φ is the photon fluence rate at position $\vec{r}$, and q is the source at $\vec{r}$), and the boundary condition [1] of $\Phi(\vec{r}_\Omega)+2A\kappa\,\hat{n}\cdot\nabla\Phi(\vec{r}_\Omega)=0$ (where $\vec{r}_\Omega$ corresponds the point on the boundary, $\hat{n}$ is a unit vector pointing outward (from the tissue to probe) and normal to the tissue-probe interface, and A is the boundary mismatch factor determined by the relative refractive indices of the tissue domain and the probe (air) domain). These equations formulate into the FEM framework $[K(\kappa)+C(\mu_a)+B/(2A)]\Phi=Q_0$, where the K, C and Q are volume integrals of each element with regard to κ, μ_a and q, and B is the surface integral of the boundary element. The FEM forward solver results in a set of linear equations containing sparse matrices. The inverse problem performs a non-linear optimization of the objective function of $b=\left\|\Phi_{measurement}-\Phi_{estimation}\right\|$ by updating the pixel or voxel-wise values of κ and μ_a. The inverse solver requires finding $\partial\Phi/\partial\kappa$ and $\partial\Phi/\partial\mu_a$, which are integrated into the forward computation process by using the adjoint method of deriving the Green's function associated with an impulse source at the detector position, as shown in Fig. 1(a) (b). Therefore, the number of sources, s, and the number of detectors, s generate $2s$ sets of linear equations for solving by the CG method.

Our open-code FEM-solver is developed in MATLAB (Mathworks, Inc. Natick, MA) platform. A comparison of our solver with the NIRFAST package [10] is given in Fig. 1(c), where the target has an absorption coefficient of 0.02 mm^{-1} and a reduced scattering coefficient of 1.2 mm^{-1}, in a background of 0.002 mm^{-1} absorption and 0.8 mm^{-1} reduced scattering. The performance of our solver is comparable to that of NIRFAST, at the same 1% noise-level.

2.2 Implementation of the conjugate gradient solution of the linear equations in FPGA

The FPGA implementation of the linear equations for DOT forward computation is composed of four modules. The calculation module, which includes two floating point adders and two floating point multipliers, is capable of two simultaneous floating point vector operations with an approximately throughput of four floating point operations per clock cycle. The memory modules utilize on-chip block memory. And the sparse FEM matrix is stored by compressed row storage (CRS) [11]. The DOT sources are considered Gaussian and the adjoint sources are impulse, which also lead to sparse structure.

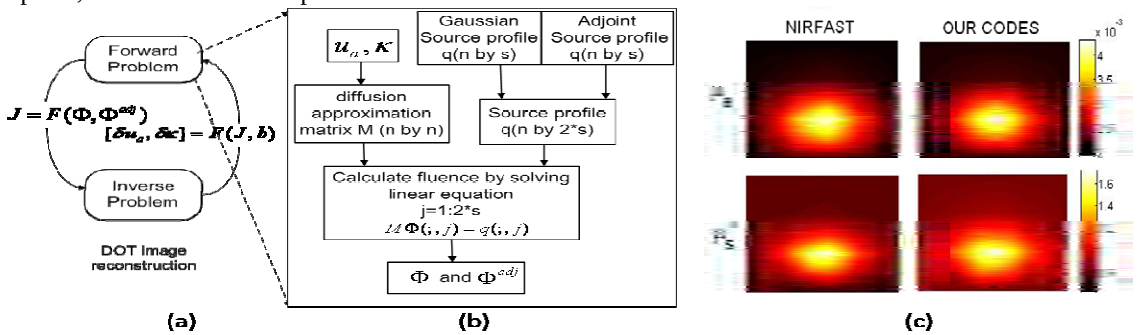

Fig.1 (a) Flow chart for DOT reconstruction (b) Forward problem (c) DOT image reconstructed by NIRFAST and our codes

We have temporarily used the RS232 protocol for the data transfer between the FPGA and PC (shown in Fig. 2). We have also temporarily implemented only the forward computation in FPGA, and performed the inverse solver algorithm on a PC. The control module, which is a finite state machine (FSM), controls the data flow in forward computation, as shown in Fig. 3. The data flow starts from loading FEM matrix from PC and then clears all the intermediate memories. The source profile is restored as originally vector sequence according to the address offset and address index. At the same time, the initial calculation of residual norm, or α_0, which is out of the CG loop, is calculated. Then it enters the CG iteration and three states, updates α, β, and Φ, runs iteratively until α_0 is below a threshold. Then the FSM jumps out of the CG iteration, sends the computed fluence to PC, clears the state, and loads the next source or adjoint source profiles. The complete fluence data set are transferred to PC for running the inverse solver that leads to a new set of FEM matrices for being transferred to FPGA for the next iteration.

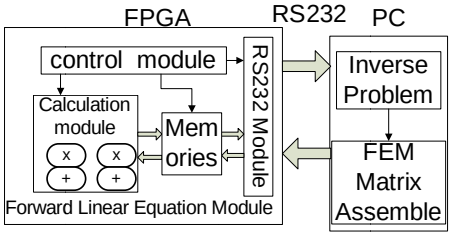

Fig.2. System sketch

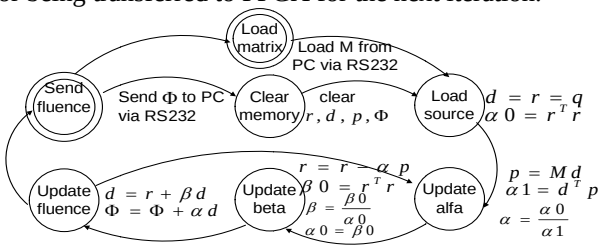

Fig.3 Control flow (finite state machine)

3. RESULTS AND DISCUSSIONS

The FEM solver is implemented on PC only and on FPGA-PC unit as specified above for comparison of the speed. On PC, the FEM-solver is executed on an Intel® quad-core *2.33* GHz processor. The linear equation is solved by using "bicgstab" function in Matlab with the FEM matrix being specified as sparse, which means the nonzeros in the matrix are stored together in main memory and the low spacial-locality caused by the zeros in sparse matrix is solved. A 2-D mesh with 1,705 nodes and *11,593* non-zeros in the corresponding FEM matrix, for an imaging dimension of 54mm×30 mm with 6 sources and 6 detectors on the boundary, is generated for DOT image reconstruction. The background is set at absorption coefficient of 0.01mm^{-1} and reduced scattering of 1mm^{-1}, with a target of 0.025mm^{-1} absorption and 1.75mm^{-1} reduced scattering. A Xilinx VirtexII Pro FPGA (XC2VP30 Package ff896 Speed Grade -7) is used, which contains 30,816 logic cells, 136 18×18 multipliers and 2,448 Kbits of Block RAM [12] with maximum clock frequency of 150MHz (the actual clock frequency being used is 100MHz). The execution speeds of PC-only and FPGA-PC unit, both in IEEE 754R double precision, are given in Fig. 4 (red and blue bars). The bars #1 and #2 correspond to CG algorithms with 50 and 100 iterations, respectively, for a 1705×1705 matrix. The bars #3 correspond to solving one above-mentioned FEM-associated linear equation. The bars #4 correspond to one complete forward computation of solving 12 linear equations. For each group of the bars, there are two FPGA-runtime settings. The "one-instance" corresponds to using 32 out of 136 on-board DSP modules that is necessary to computing the linear equation one by one, and the "two-instances" corresponds to using 64 out

of 136 on-board DSP modules to compute two linear equations simultaneously. Compared with PC running time, there is a 1.8 folds and 3.6 folds of speed improvements with the "1-instance" and "2-instances", respectively. The 136 DSP modules ideally allow simultaneous computation of 4 linear equations that could lead to 7.2 folds of speed improvement at the given clock frequency, but the insufficient on-chip memory has limited implementing more than 64 DSP modules for this study. The images reconstructed by PC only and by FPGA-PC unit are compared in Fig. 5.

It is noted that the FPGA used in this study is a low-end sample unit with limited on-board resources. Using high-end FPGAs with more on-board resources could further speed up the above computations. Higher-end FPGAs such as Virtex 5 and Virtex 6 families has more DSP resources which accommodate 25×18 instead of 18×18 multipliers, thereby could further improve the speed. Table 1 lists the performance improvement that could be expected, with the present study listed as the first one, by using the existing higher-end FPGAs.

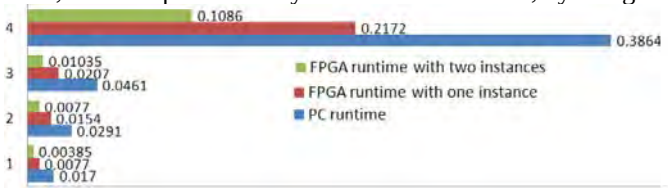

Fig.4. Runtime comparison between FPGA and PC

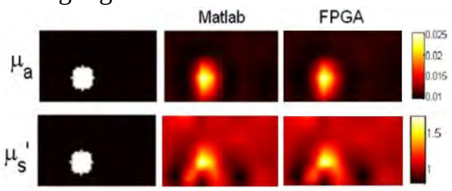

Figure 5. Images reconstructed by PC and using FPGA

Table 1 FPGA performance improvement achieved by different FPGA

FPGA	VirtexII Pro XC2VP30 (136 18×18 DSPs)		VirtexII Pro XC2VP100 (444 18×18 DSPs) 150M 12 instances	Virtex 5 XC5VSX240T (1056 25×18 DSPs) 150M 40 instances	Virtex6 VSX475T (2016 25×18 DSPs) 150M 76 instances
	100M, 1 instance	150M,4instances			
Speedup	1.8 folds	10.8 folds	32.4 folds*(1)	108 folds*(2)	205.2 folds*(3)

*(1) the maximum speed improvement for system employs 6 detectors and 6 sources
*(2) the expected speed improvement for a DOT geometry with 20 detectors and 20 sources
*(3) the expected speed improvement for a DOT geometry with 38 detectors and 38 sources

The use of RS232 protocol in this initial study has resulted in overall slower DOT iteration due to the initial and final data transmissions between the FPGA and PC. There are a number of approaches to improve the overall performance, including implementing a real-time data transmission protocol such as USB or Ethernet, developing a stand-alone on-board operating system, and performing both the forward and inverse solver algorithms on the FPGA.

4. CONCLUSION AND FUTURE DIRECTION

In summary, FPGA implementation of FEM based forward computation for steady-state DOT is demonstrated. For a system employing 6 sources and 6 detectors with a mesh having *1,705* nodes, forward computations involving *12* linear equations solved by CG method are performed by FPGA. The preliminary results, even though hindered by the slow RS232 data transfer protocol and limited resources on the FPGA, encourage implementing complete forward and inverse iteration on FPGA for efficient reconstruction.

Acknowledgement: This work has been supported by Oklahoma Center for the Advancement of Science and Technology (OCAST) (HR06-171), and DOD Prostate Cancer Research Program (#W81XWH-07-1-0247).

REFERENCES

[1] Arridge SR, "Optical tomography in medical imaging," Invers. Prob. 15, R41-R93 (1999).
[2] Browne TA, Condell JV, Prasad g, McGinnity TM, "An investigation into optical flow computation on FPGA hardware," Proc. Inter. Machine Vis. Image Process. Conf., pp.176-181 (2008).
[3] Watt D, Harmon K, Srivastava A, Faris GW, "High speed processing of frequency domain images," in Biomedical Optics, OSA Technical Digest (CD) (Optical Society of America, 2008), page BWG3.
[4] Lo WC, Redmond K, Luu J, Chow P, Rose J, Lilge L, "Hardware acceleration of a Monte Carlo simulation for photodynamic therapy treatment planning," J. Biomed. Opt., 14(1), 014019 (2009).
[5] Alerstam E, Svensson T, Andersson-Engels S, "GPU-Based Monte Carlo Simulations of Photon Migration in Heterogenous Materials," European Conf. Biomed. Opt., pp. 14-18 (2009).
[6] Fang Q, Boas DA, "Monte Carlo Simulation of Photon Migration in 3D Turbid Media Accelerated by Graphics Processing Units." Opt. Express, 17(22), pp. 20178-20190 (2009).
[7] Pardo E, Lopez R, Cabello D, Balsi M, "FPGA finite difference time domain solver for thermal simulation," Inter. Conf. Field Program. Logic Appl., pp. 721-722 (2005).
[8] Gibbons JA, Howard DM, Tyrrell AM, "FPGA implementation of 1D wave equation for real-time audio synthesis," IEE proceedings: Comp. Digital Tech., 152, pp. 619-631 (2005).
[9] Goddeke D, "Accelerating Double Precision FEM simulations with GPUs," Simul. Tech. 18th Sympos. (ASIM), 139-144(2005).
[10] Dehghani H, Eames ME, Yalavarthy PK, Davis SC, Srinivasan S, Carpenter CM, Pogue BW, Paulsen KD, "Near infrared optical tomography using NIRFAST: Algorithms for numerical model and image reconstruction algorithms," Commun. Num. Meth. Engi., DOI: 10.1002/cnm.1162 (2008)
[11] DeLorimier M, DeHon A, "Floating-point sparse matrix-vector multiply for FPGAs," Proc. Inter. Symp. FPGA, 75-78 (2005).
[12] Xilinx, Xilinx University Program Virtex-II Pro Development System: Hardware Reference Manual, March, 2005.

Photon Diffusion Associated with a Cylindrical Applicator Boundary for Axial Trans-lumenal Optical Tomography: Experimental Examination of the Steady-State Theory

Anqi Zhang,[1] Daqing Piao,[1*] Gang Yao, [2] Brian W. Pogue [3]
[1]*School of Electrical and Computer Engineering, Oklahoma State University, Stillwater, OK 74078, USA*
[2]*Department of Biological Engineering, University of Missouri, Columbia, MO, 65211, USA*
[3]*Thayer School of Engineering, Dartmouth College, Hanover, NH, 03755, USA*
**Corresponding Author: daqing.piao@okstate.edu*

Abstract: A new approach for steady-state photon diffusion modeling associated with a cylindrical applicator boundary for trans-luminal optical tomography was evaluated numerically and experimentally. In the diffusion regime the theoretical predictions agree well with experimental findings.

OCIS codes: (170.3660) Light propagation in tissues; (170.5280) Photon migration; (170.6960) Tomography

1. Introduction

Using near-infrared (NIR) light to image deep tissue volumes non-invasively has largely been based upon transport modeling with the diffusion approximation to the radiative transport equation [1]. The photon diffusion in a medium enclosed by a circular cylindrical applicator has been analyzed previously in two elegant studies [2, 3]. The analytic results of these studies, however, were not in an explicit format that could guide the data calibration, and it has also been difficult to assess from these results how much the circular applicator boundary affects the photon diffusion when compared with the more studied semi-infinite boundary. Recent work by our group [4] has investigated the photon diffusion theory as applied to the geometries corresponding to an external ring-structure applicator or an internal cylinder probe, which leads to analytic solutions of the photon diffusion in a homogenous medium bounded externally or internally by an infinitely long circular cylindrical applicator. These analytic solutions can be further developed into the form that includes an isotropic "physical" source & its image source, with respect to a semi-infinite boundary that is tangential to the circular boundary at the location of directional physical source. As well, there is a radial-dependent term that approaches unity as the circular cylindrical geometry reaches semi-infinite case. Given that this theory qualitatively makes sense, the current paper attempts to confirm that the theory matches experimental data. Initial experimental work was conducted along the azimuthal plane of the cylindrical boundary, corresponding to a "convex" axial-imaging application, like that used in trans-lumenal diffuse optical tomography.

2. Analytic Approach and Its Numerical Evaluations

Using the modified Bessel functions of the 1st and 2nd kind, the cylindrical-coordinate solution of the steady-state photon fluence rate in a concave geometry for an infinitely long circular cylindrical applicator with radius R_0, is [4]:

$$\Psi = \frac{S}{2\pi^2 D}\int_0^\infty dk \left\{ \cos\left[k(z-z')\right] \sum_{m=0}^{\infty} \varepsilon_m I_m\left[k_{eff}(R_0 - R_a)\right] K_m\left(k_{eff} R_0\right) \left\langle 1 - \frac{I_m\left(k_{eff} R_0\right)}{K_m\left(k_{eff} R_0\right)} \frac{K_m\left[k_{eff}(R_0 + R_b)\right]}{I_m\left[k_{eff}(R_0 + R_b)\right]} \right\rangle \cos\left[m(\varphi - \varphi')\right] \right\} \quad \text{(1-conc)}$$

This latter geometry is commonly seen when the sources and detectors are on the exterior of the cylindrical volume. Similarly, the cylindrical-coordinates solution of the steady state photon fluence rate in a convex geometry imposed by an infinitely long circular cylindrical applicator with radius R_0, as seen in trans-rectal prostate imaging, is [4]:

$$\Psi = \frac{S}{2\pi^2 D}\int_0^\infty dk \left\{ \cos\left[k(z-z')\right] \sum_{m=0}^{\infty} \varepsilon_m I_m\left(k_{eff} R_0\right) K_m\left[k_{eff}(R_0 + R_a)\right] \left\langle 1 - \frac{K_m\left(k_{eff} R_0\right)}{I_m\left(k_{eff} R_0\right)} \frac{I_m\left[k_{eff}(R_0 - R_b)\right]}{K_m\left[k_{eff}(R_0 - R_b)\right]} \right\rangle \cos\left[m(\varphi - \varphi')\right] \right\} \quad \text{(1-conv)}$$

where in both (1-conc) and (1-conv) Ψ is the photon fluence rate at position (R_0, φ', z') with source at (R_0, φ, z), $D = [3(\mu_a + \mu_s')]^{-1}$ is the diffusion coefficient with μ_s' being the reduced or transport scattering coefficient, μ_a is the absorption coefficient, S is the source term, $R_b = 2AD$, $R_a = 1/\mu_s'$ and A is a constant depending on the relative refractive index mismatch between cylindrical applicator and tissue.

For a cylindrical applicator, a virtual "semi-infinite" image source can be introduced, as shown in Fig. 1(a) for "concave" geometry and in Fig. 1(b) for "convex" geometry. The virtual "semi-infinite" image source is defined as the image of the equivalent isotropic source of the physical source with respect to the semi-infinite boundary that is tangential to the circular boundary at the location of the physical source. Using the asymptotic expressions of the

modified Besel functions, one can have $\Psi_{imag}^{ph} = \Psi_{imag}^{semi} \cdot \sqrt{(R_0 + R_a + 2R_b)/(R_0 - R_a)}$ for concave geometry and $\Psi_{imag}^{ph} = \Psi_{imag}^{semi} \cdot \sqrt{(R_0 - R_a - 2R_b)/(R_0 + R_a)}$ for convex geometry, where Ψ_{imag}^{ph} is the fluence rate associated with the image of the isotropic source with respect to the actual circular boundary, and Ψ_{imag}^{semi} is the fluence rate associated with the virtual "semi-infinite" image source. Then for a source-detector separation of l, (1-conc) and (1-conv) can be converted to the spherical-coordinate forms, given as:

$$\Psi = \frac{S}{4\pi D}\frac{e^{-k_0 l_r}}{l_r} - \frac{S}{4\pi D}\frac{e^{-k_0 l_i}}{l_i}\sqrt{\frac{R_0 + R_a + 2R_b}{R_0 - R_a}} \qquad \Psi = \frac{S}{4\pi D}\frac{e^{-k_0 l_r}}{l_r} - \frac{S}{4\pi D}\frac{e^{-k_0 l_i}}{l_i}\sqrt{\frac{R_0 - R_a - 2R_b}{R_0 + R_a}} \qquad (2)$$

both of which asymptotically approach the solution for a semi-infinite boundary as the radius of the applicator R_0 becomes infinity

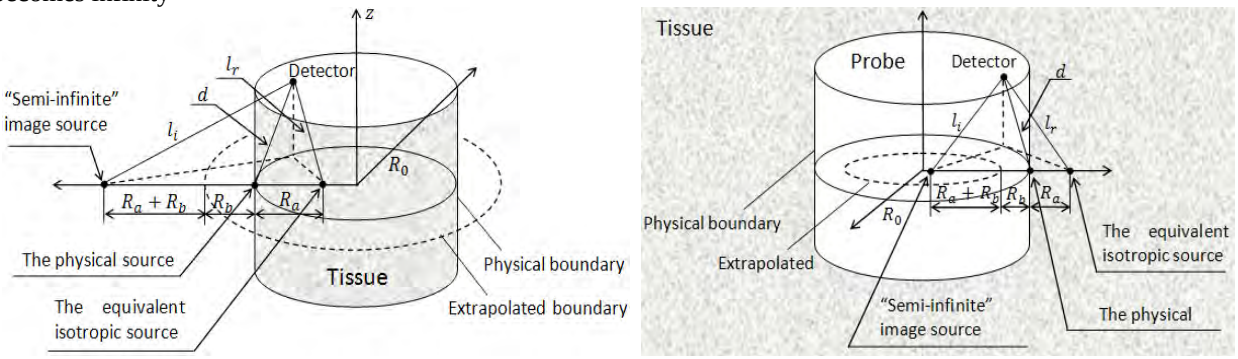

(a) (b)

Figure 1. Details of the cylindrical boundary geometry indicating the equivalent isotropic source, the extrapolated boundary, and the virtual "semi-infinite" image source. (a) Concave geometry (b) Convex geometry.

The original form of the analytic solution in (1-conc) and (1-conv) are evaluated numerically for the specific geometries of having the source and the detector on the surface positioned only along the azimuthal or the longitudinal directions. Placing the source-detector either azimuthally or longitudinally helps demonstrate explicitly the effect of the applicator curvature shape, either concave or convex, and the radius of the applicator curvature on the decay of photon fluence rate as a function of the source-detector distance, in comparison to that in the semi-infinite geometry. In both (1-conc) and (1-conv), for sufficiently large *k*, hence large k_{eff} [4], the modified Bessel functions in the integrands approach their asymptotic expressions which drop to zero. Therefore the contribution of the integrands associated with *k* greater than a certain limit can be neglected. According to the IEEE standard for floating-point arithmetic [5], there is a limit for the biggest number and the smallest number to be stored in computer. In Matlab the criterion [6] for overflow is 1.7977×10^{308} in decimal, and for underflow is 2.2251×10^{-308}. In (1-conc) and (1-conv), the modified Bessel function of the 1st and 2nd kinds are exponentially growing and decaying functions, respectively, for which overflow will readily occur for a large order *m* and underflow for a large argument *k*. A strategy of "pre-enlarge" and "pre-reduce" is implemented, based on the principle that before evaluating each modified Bessel function individually, the modified Bessel function of the 1st kind is "pre-reduced" for large order *m* and the modified Bessel function of the 2nd kind is "pre-enlarged" by the same degree, by which the product of each pair remains unchanged. Additionally, it is also found in (1-conc) and (1-conv) that the radius R_0 has a great effect on the evaluation outcome. When R_0 is as large as 8*cm* as an instance in (1-conc), for $k = 40$, the integrand does not converge sufficiently even for summating *m* up to 500, but for a smaller radius $R_0 = 1cm$, the same integrand converges quickly at $m = 100$. A method of "repeated averaging" is thus employed to improve the convergence when computing the integrand. The principle is to first examine if the integrand presents an oscillating pattern. If there is an oscillation, the envelop-profile of the maxima and minima of the oscillation is implemented to form a finite converging alternative series, and the last series of maxima and minima are averaged to get the value of the integrand. If not, the last result is chosen as the value of the integrand.

These numerical techniques were implemented to evaluate the analytic solutions given in (1), to examine if the theoretical predictions agree with experimental findings.

3. Experimental Examination

The initial experimental examinations were conducted for the "convex" cylinder geometry only. The experimental setup is shown in Fig. 2(a). A 0.5% bulk Intralipid solution was used as the diffusive medium. The cylinder probe was made of black acetal. In terms of the *A* parameter in diffusion approximation, a value of 2.82 is often assigned for a tissue-air interface [7][8], which is less-likely to be true for the cylinder probe material and the probing

geometry used in this study. To determine the *A* value associated with the cylinder material, we used both an infinite geometry to determine the optical properties of the Intralipid medium and a semi-infinite geometry using a material identical to that of the cylinder probe to determine A, based on the well-known semi-infinite theory. It was found that $A = 1.86$.

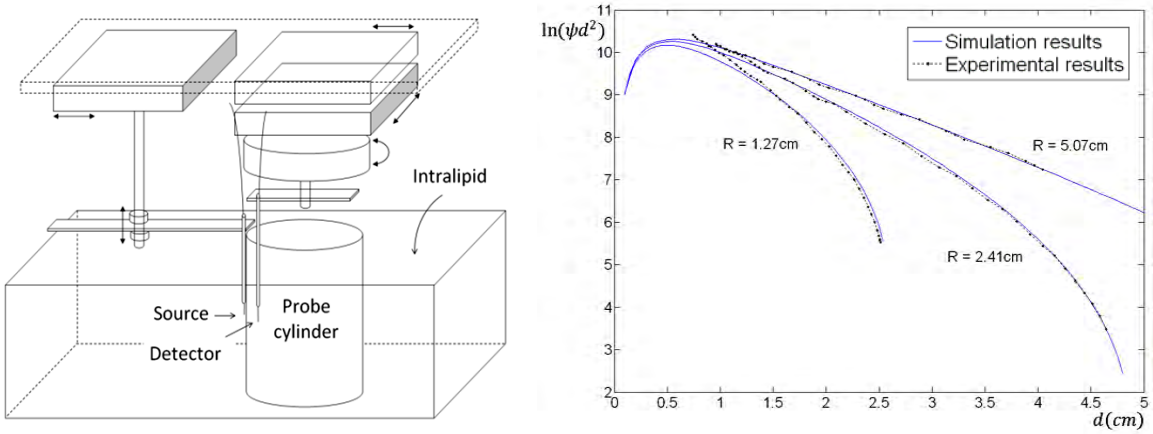

(a) (b)

Figure 2. System diagram for the convex geometry experiments (a) and the experimental results (b)

The experimental data were compared in Fig. 2(b) with the numerical evaluations based on (1-conv), which corresponded to photon diffusion in a homogenous medium bounded internally by a cylindrical probe that was infinitely long, not as the finite-length probe used in experiments. The optical properties of the medium were $\mu_a = 0.025cm^{-1}$, $\mu_s' = 5cm^{-1}$ and $A = 1.86$. The results in Fig. 2 (b) indicated that: (1) As the radius R increases, the photon diffusion gradually reached that in a semi-infinite medium (a straight-line in Fig. 2(b)); (2) At larger source-detector separation that renders valid diffusion process, the theory accurately predicted the change of the photon fluence rate versus the source-detector distance and versus the boundary radius; (3) At smaller source-detector separation, which shall be in non-diffuse regime, the theoretical prediction was inaccurate as expected.

4. Discussions and Future Work

Experimental work were conducted to examine the predictions based on the theory derived for photon diffusion associated with an infinitely-long cylindrical applicator for axial trans-lumenal optical tomography. For finite-length applicator, the theory could be improved by considering the effects of two longitudinal boundaries. The experimental results, however, demonstrate that the current theory may be sufficiently accurate in the diffusion regime. Our future plans include experimental examinations with a "concave" cylinder probe applicable to external imaging, to further simplify the theory into a closer form to the well-known logarithm-form of the semi-infinite geometry, and to amend the experimental examinations with Monte Carlo methods.

Acknowledgement: This work has been supported in part by a research grant HR06-171 from the Oklahoma Center for the Advancement of Science and Technology (OCAST), a Big-XII Faculty fellowship awarded to Daqing Piao, and the Prostate Cancer Research Program of Department of Defense through a grant #W81XWH-07-1-0247.

References

1. A. Ishimaru, "Diffusion of light in turbid material," Appl. Opt., 28, 2210—2215 (1989).
2. S.R. Arridge, M. Cope, D.T. Delpy, "The theoretical basis for the determination of optical pathlengths in tissue: temporal and frequency analysis," Phys Med Biol., 37(7):1531-60 (1992).
3. B.W. Pogue, and M.S. Patterson, "Frequency-domain optical absorption spectroscopy of finite tissue volumes using diffusion theory," Phys Med Biol., 39(7):1157-80 (1994).
4. Zhang A, Piao D, Yao G, Bunting CF, Krasinski JS, Pogue BW, "Forward modeling of axial trans-lumenal diffuse optical imaging with a cylindrical applicator using continuous-wave photon-illumination," International Symposium on Biomedical Optics, San Jose, CA, Jan. 24-29, 2009. Proceedings of SPIE, Vol. 7174, Paper #717404.
5. IEEE 754-2008 Standard for Floating-Point Arithmetic, IEEE, Aug 2008
6. Moler, C., "Floating points: IEEE Standard unifies arithmetic model." Cleve's Corner, The MathWorks, Inc., 1996.
7. B. W. Pogue, S. Geimer, T. O. McBride, S. Jiang, U. L. Osterberg, and K. D. Paulsen, "Three-dimensional simulation of near-infrared diffusion in tissue: boundary condition and geometry analysis for finiteelement image reconstruction," Appl. Opt. 40, 588-600 (2001).
8. Xu G, Piao D, Musgrove CH, Bunting CF, Dehghani H, "Trans-rectal ultrasound-coupled near-infrared optical tomography of the prostate Part I: Simulation," Optics Express, Vol. 16, Iss. 22, pp. 17484–17504 (2008).

The pain and gain of DC-based diffuse optical tomography reconstruction---New insights into an old-like problem

Guan Xu,[1] Daqing Piao,[1*] Charles F. Bunting, [1] Hamid Dehghani [2]
[1] *School of Electrical and Computer Engineering, Oklahoma State University*
Stillwater, OK, 74078-5032, USA
[2] *University of Birmingham, Birmingham, UK*
**Corresponding Author: daqing.piao@okstate.edu*

Abstract: For diffuse optical tomography reconstruction, DC-based method outperforms frequency-domain method in background artifacts, at the known cost of increased coupling between absorption and scattering. The differences of these methods diminish when spatial *priors* are available.

OCIS codes: (170.3880) Medical and biological imaging; (170.3010) Image reconstruction techniques; (170.6960) Tomography; (170.5270) Photon density waves

1. Introduction

Diffuse optical tomography quantifies the spatial heterogeneities of NIR absorbing chromophors and scattering particles by measurement of light diffused through biological tissue. Steady-state and frequency-domain (FD) measurements are most commonly utilized to reconstruct the tissue absorbance and scattering distributions. Steady-state system only measures the attenuation of the direct-current (DC) amplitude of the photon while frequency domain system ideally acquires the same DC, the amplitude of the modulated light intensity (AC), and the phase of the modulation of the light intensity (referred to as "Phs" in this paper). The role of DC component in FD reconstruction has yet to be comprehensively analyzed and the confidence level of reconstruction with only the DC information available has yet to be clearly understood.

This paper compares the image reconstructions using three sets of measurements, which are DC only, AC/Phs and DC/AC/Phs, to evaluate the role of DC information in diffuse optical tomography reconstruction. It is found that, DC-based method outperforms FD method in background artifacts, at the known cost of increased coupling between absorption and scattering, and the differences of the methods diminish when spatial *prior* can be implemented.

2 Theory

Under the assumption of accurate forward computational model to describe the light propagation, it is necessary to consider two factors when evaluating the overall performance of the reconstruction: First, the assembled measurement error that could be mapped to the uncertainty in image reconstruction; Second, the determinacy of the inverse problem.

2.1 Analyses of the parameter recovery uncertainty caused by assembled measurement error (PRUAME)

The measurements for both FD and CW systems are typically governed by the diffusion approximation to the radiative transfer equation[1]. For the simplest case of recovering the optical properties of an infinite homogeneous medium, the photon densities for DC and FD measured at a position $\vec{r}'$ that has a distance of d from a source at $\vec{r}'$ are:

$$U_{DC}(\vec{r},0)=\frac{S_{DC}(\vec{r}',0)}{4\pi vDd}\exp(-\sqrt{\frac{\mu_a}{D}}d) \tag{1}$$

$$U_{AC}(\vec{r},\omega)=\frac{S_{AC}(\vec{r}',\omega)}{4\pi vDd}\exp(-d\sqrt{\frac{\mu_a}{2D}\left(\sqrt{1+\frac{\omega^2}{v^2{\mu_a}^2}}+1\right)})\cdot\exp(id\sqrt{\frac{\mu_a}{2D}\left(\sqrt{1+\frac{\omega^2}{v^2{\mu_a}^2}}-1\right)}) \tag{2}$$

Therefore the measurements made at source-detector separations of d_1 and $d_2=d_1+\rho$, respectively, may results in the following parameters: δ --attenuation of steady state light intensity (DC); α --attenuation of the amplitude of the modulated light intensity (AC); ϕ --phase shift of the modulation of the light intensity (Phs), as

$$\delta=\ln\frac{(d_2|U_{DC}(d_2)|)}{(d_1|U_{DC}(d_1)|)}=-\rho\cdot\sqrt{\frac{\mu_a}{D}};\ \alpha=\ln\frac{(d_2|U_{AC}(d_2)|)}{(d_1|U_{AC}(d_1)|)}=-\rho\cdot\sqrt{\frac{\mu_a}{2D}\left(\sqrt{1+\frac{\omega^2}{v^2{\mu_a}^2}}+1\right)};\ \phi=\Phi(d_2)-\Phi(d_1)=\rho\cdot\sqrt{\frac{\mu_a}{2D}\left(\sqrt{1+\frac{\omega^2}{v^2{\mu_a}^2}}-1\right)} \tag{3}$$

For small variations of the source-detector distance among different source-detector pairs, the signal variations may actually be sensed as the "assembled measurement error" [2]. Suggested by [2], the "**parameter recovery uncertainty caused by assembled measurement error"** (PRUAME) is derived for the reconstruction methods of DC, AC/PHs, and DC/AC/Phs, with respect to each unknown quantities, as shown in Table 1.

Table 1 PRUAME expressions.

	$\sigma_{\mu a}/\mu_a$		σ_D/D	$\sigma_{\mu s'}/\mu_s'$
DC	$2\cdot\left(\frac{\sigma_\delta^2}{\delta^2}\right)^{1/2}$ [2]		$2\cdot\left(\frac{\sigma_\delta^2}{\delta^2}\right)^{1/2}$	$\left[\left(\frac{1}{3D}\right)^2+\mu_a^2\right]^{1/2}\cdot 2\left(\frac{\sigma_\delta^2}{\delta^2}\right)^{1/2}\cdot\left[\frac{1}{3D}-\mu_a\right]^{-1}$
	Est. Val.	2	2	2
AC/ Phs	$\frac{\alpha^2+\phi^2}{\alpha^2-\phi^2}\left(\frac{\sigma_\phi^2}{\phi^2}+\frac{\sigma_\alpha^2}{\alpha^2}\right)^{1/2}$ [2]		$\left(\frac{\sigma_\alpha^2}{\alpha^2}+\frac{\sigma_\phi^2}{\phi^2}\right)^{1/2}$	$\left[\left(\frac{1}{3D}\right)^2\left(\frac{\sigma_\alpha^2}{\alpha^2}+\frac{\sigma_\phi^2}{\phi^2}\right)\cdot+\mu_a^2\cdot\left(\frac{\alpha^2+\phi^2}{\alpha^2-\phi^2}\right)^2\cdot\left(\frac{\sigma_\alpha^2}{\alpha^2}+\frac{\sigma_\phi^2}{\phi^2}\right)\right]^{1/2}\cdot\left[\frac{1}{3D}-\mu_a\right]^{-1}$
	Est. Val.	1.6189	1.4142	~1.4142
AC/ DC/ Phs	$\left(\frac{\sigma_\phi^2}{\phi^2}+\frac{\sigma_\alpha^2}{\alpha^2}+4\frac{\sigma_\delta^2}{\delta^2}\right)^{1/2}$		$\left(\frac{\sigma_\alpha^2}{\alpha^2}+\frac{\sigma_\phi^2}{\phi^2}\right)^{1/2}$	$\left[\left(\frac{1}{3D}\right)^2\left(\frac{\sigma_\alpha^2}{\alpha^2}+\frac{\sigma_\phi^2}{\phi^2}\right)\cdot+\mu_a^2\cdot\left(4\frac{\sigma_\delta^2}{\delta^2}+\frac{\sigma_\alpha^2}{\alpha^2}+\frac{\sigma_\phi^2}{\phi^2}\right)\right]^{1/2}\cdot\left[\frac{1}{3D}-\mu_a\right]^{-1}$
	Est. Val.	2.4495	1.4142	~1.4142

To quantitatively compare the magnitude of the expressions, optical properties close to those of actual tissue, μ_a=0.005mm^{-1}, μ_s'=1mm^{-1}, and source-detector separation of ρ=10mm are substituted into the previous equations. Further assumptions are made by the assumption that the error magnitudes are the same for all the measurements ($\frac{\sigma_\delta^2}{\delta^2}\cong\frac{\sigma_\alpha^2}{\alpha^2}\cong\frac{\sigma_\phi^2}{\phi^2}$) as indicated in [2]. By normalizing the values along column 2 and 3 with $\frac{\sigma_\delta}{\delta}$ and column 4 with $\frac{\sigma_\delta}{\delta}\cdot\left[\frac{1}{3D}-\mu_a\right]^{-1}$, the reconstruction uncertainties are given in Table 1 as the "estimated value".

Comparison in Table 1 indicates that from only the PRUAME perspective, AC/Phs possesses the least overall reconstruction uncertainty, followed by AC/DC/Phs and DC only.

With ref [3,4], the above analyses for the PRUAME comparisons based on infinite medium can be extended to semi-infinite medium and reaches qualitatively similar estimations.

2.2 Inverse problem determinacy

The inverse problem includes two scenarios. When the spatial *prior* is unavailable, more independent measurements are desired to reduce the under-determinacy condition of piecewise reconstruction. Under such consideration, DC/AC/Phs measurement could be the most deterministic measurement combination, although DC components are sometimes ignored in the sense that it may be redundant to the AC components. However, by comparing the 2nd and 3rd sub-equations in equ. (3), it can be concluded that the AC attenuation usually is not linearly proportional to the DC attenuation. Therefore DC information may be necessary for complete recovery of tissue properties.

When a complementary imaging modality is available to provide hard *a prior* to the image reconstruction [5], the inverse problem becomes over-determined. Under such condition, it is imperative to know how well DC-based image reconstruction performs as compared to the cases of having FD information available.

3 Simulations

Numerical simulations are conducted to investigate the validity of the above theoretical analyses. The forward model is formulated with finite element method based on diffusion approximation and Robin type boundary condition [6]. The sensitivity matrices (Jacobian) are structured as the one in below, for each measurement category in Fig. 1&2

$$J=\left[\frac{\partial\ln I_{AC}}{\partial\mu_a}\quad\frac{\partial\ln I_{AC}}{\partial D};\quad\frac{\partial\phi}{\partial\mu_a}\quad\frac{\partial\phi}{\partial D};\quad\frac{\partial\ln I_{DC}}{\partial\mu_a}\quad\frac{\partial\ln I_{DC}}{\partial D}\right] \tag{4}$$

The DC/AC/Phs combination utilizes all the measurements so it contains all terms shown in equ. (4); while for CW method, only the last two terms in equ (4) are used and the first four terms are retained for AC/Phs method. The Levernberg-Marquardt algorithm is integrated as the inverse solver for the simulative evaluations.

3.1 Piece-wise simulation

The simulation is to solve for the optical properties at 2760 nodes in FEM mesh 240 (16×15), the location and maximum optical properties (shown on the bar chart) within each target region are shown in Fig.1. For the target

profile and optical property recovery, DC only reconstruction demonstrates lowest accuracy and most significant crosstalk. DC/AC/Phs outperforms AC/Phs in most cases, especially for the μ_a contour of target 3 and μ_s'/D value recovery of target 2. However, the background variations (σ^2 value of each reconstructed image) indicate that DC only reconstruction presents the best background homogeneity, followed by DC/AC/Phs and AC/Phs. The background homogenity in image reconstruction is espacially important for DOT of prostate cancer, because the cancer target is to be resolved within the optically heterogeous prostatic tissue.

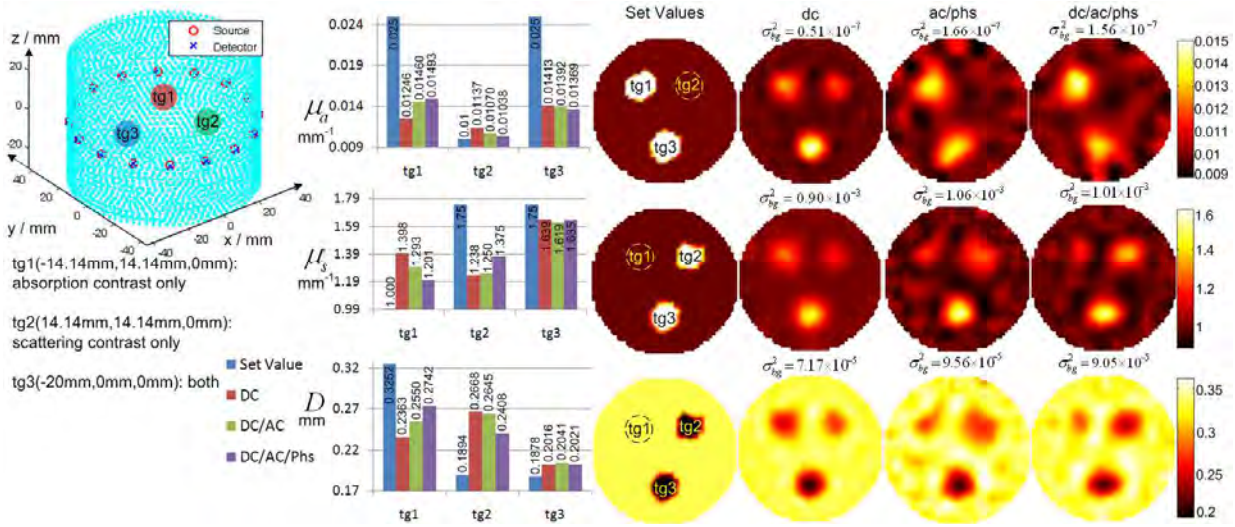

Fig.1 Piece-wise reconstruction

3.2 Region-wise simulation

With the same setup as the piecewise simulation and the assumption that the target region can be accurately segmented, region-wise reconstructions found that the DC only method, having less measurements, performs equivalently to the two methods with the FD information included.

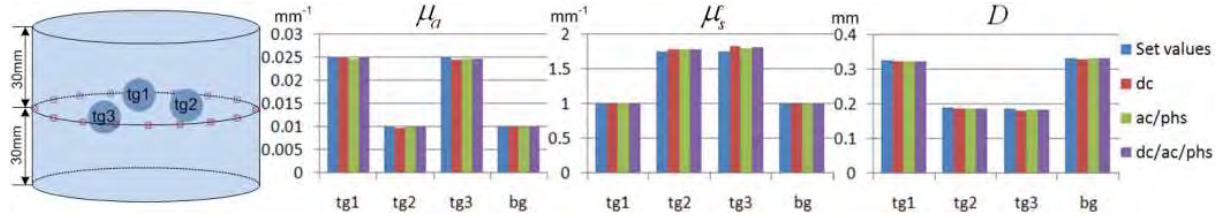

Fig.2 Region-wise reconstruction

4 Conclusions

The theoretical analysis and numerical studies have several implications to make: (1) DC-only piece-wise reconstruction outperforms other methods in background artifacts reduction but its performance on the target recovery accuracy and cross coupling suppression is less desirable; (2) DC/AC/Phs approach shows superiority over AC/Phs in piecewise reconstruction; (3) DC only region-wise reconstruction is equivalent to that based on FD system when the spatial *a priori* constraint is available.

Acknowledgment

This work has been supported in part by DOD Prostate Cancer Research Program through a grant #W81XWH-07-1-0247, and Oklahoma Center for the Advancement of Science and Technology (OCAST) through a grant HR06-171.

References

[1] S. R. Arridge, "Optical tomography in medical imaging," Inverse Probl. 15, R41–R93(1999).
[2] S. Fantini, M. A. Franceschini, J. B. Fishkin, B. Barbieriand, and E. Gratton, "Quantitative determination of the absorption spectra of chromophores in strongly scattering media: a light-emitting-diode based technique," Appl. Opt. 33, 5204-5213 (1994).
[3] K. K. Wang and T. C. Zhu, "Reconstruction of in-vivo optical properties for human prostate using interstitial diffuse optical tomography," Opt. Exp. 17, 11665-11672 (2009).
[4] S. Fantini, M. A. Franceschini, and E. Gratton, "Semi-infinite-geometry boundary problem for light migration in highly scattering media: a frequency-domain study in the diffusion approximation," J. Opt. Soc. Am. B 11, 2128-2138 (1994).
[5] G. Xu, D. Piao, C. H. Musgrove, C. F. Bunting, and H. Dehghani, "Trans-rectal ultrasound-coupled near-infrared optical tomography of the prostate Part I: Simulation," Opt. Exp. 16, 17484–17504 (2008).
[6] Z. Yuan and H. Jiang, "Image reconstruction scheme that combines modified Newton method and efficient initial guess estimation for optical tomography of finger joints," Appl. Opt. 46, 2757-2768 (2007).

Trans-rectal ultrasound-coupled spectral optical tomography at 785nm and 830nm detects elevation of total hemoglobin concentration in canine prostate associated with the development of transmissible venereal tumors

Zhen Jiang,[1] Kenneth E. Bartels,[2] G. Reed Holyoak,[2] Jerry W. Ritchey,[3] Jerzy S. Krasinski,[1] Charles F. Bunting,[1] Gennady Slobodov,[4] Daqing Piao[1*]

1. School of Electrical and Computer Engineering, Oklahoma State University, Stillwater, Oklahoma, U.S.A.
2. Department of Veterinary Clinical Sciences, Oklahoma state University, Stillwater, Oklahoma, U.S.A.
3.Department of Veterinary Pathobiology, Oklahoma state University, Stillwater, Oklahoma, U.S.A.
4.Department of Urology, University of Oklahoma Health Sciences Center, Oklahoma City, Oklahoma, U.S.A.
** Correspondence: Email: daqing.piao@okstate.edu*

Abstract: Spectral trans-rectal ultrasound-coupled optical tomography at 785nm and 830nm has revealed non-invasively longitudinal elevation of total hemoglobin concentration associated with development of transmissible venereal tumors in canine prostate over a 6-week time-course.

OCIS codes: (170.3880) Medical and biological imaging; (170.6960) Tomography; (170.7230) Urology; (170.1610) Clinical applications.

1. Introduction

Prostate cancer is the leading cause of death in American men. Since its introduction [1, 2], trans-rectal ultrasound (TRUS) guided biopsy has evolved to become a standard procedure used in prostate cancer diagnosis when indicated by elevated serum prostate-specific antigen (PSA) levels or abnormal digital rectal examination (DRE). However, TRUS of the prostate has limitations. The ultrasonographic finding of the classic hypoechoic peripheral zone lesion has a sensitivity of 85.5%, specificity of 28.4%, positive predictive value of 29%, negative predictive value of 85.2% and overall accuracy of 43% [3] in prostate cancer detection. The prevalence of isoechoic or nearly invisible prostate cancers visualized with TRUS ranges from 25 to 42% [4]. As a result, the overall cancer detection rates for patients undergoing repeat prostate needle biopsy with various biopsy templates range from 10% - 38% [5]. Improving the cancer detection rate using TRUS-guided biopsy requires TRUS imaging be augmented or aided with a potentially pathognomonic indicator of prostate cancer development that can be detected non-invasively.

Recently there have been several approaches utilizing endogenous [6] or exogenous [7] near-infrared (NIR) absorption of the tissue to assist detecting prostate cancer. We have developed a TRUS-coupled NIR optical tomography probe, and with which the development of a transmissible venereal tumor (TVT) within the canine prostate was detected *in vivo* [8]. In that study, the optical information aiding TRUS was the NIR absorption and reduced scattering of the prostatic tissue at a single wavelength of 840nm. The tumor progression was associated with significant elevation of the NIR absorption earlier in the tumor development, and heterogeneous/moderate elevation of NIR reduced scattering that was resolved later than the NIR absorption at that wavelength. The significant elevation of NIR attenuation, as a result of combined absorption and reduced scattering elevations, in the tumor has been attributed partially to substantially denser cellular structure and morphology changes at sub-cellular level that could increase the NIR attenuation cross-sections. However, as the tumor aggression is associated with angiogenesis [9], the elevation of the total hemoglobin concentration ([HbT]) could have been observed in that study if we had had the capability of spectral optical tomography in a band covering the isosbestic point of hemoglobin.

Based on this hypothesis, we have upgraded our trans-rectal NIR tomography system to spectroscopic detection, at dual-bands of 785nm and 830nm only. Although it is theoretically feasible to quantify both hemoglobin concentration and oxygen saturation using these two bands, providing that the absorptions by other chromophores could be neglected in these bands, it has been reported that the accuracy of oxygen saturation based on only these two bands or in their vicinity is limited [10]. We therefore have focused on quantifying the [HbT] only, in the prostatic tissue. This study is the first demonstration of non-invasive optical tomographic detection of [HbT] in the canine prostate *in vivo*, which reveals significant increase of the [HbT] at the cancer foci in a time-course of 6-weeks of tumor development. Such non-invasively acquired information of the hemoglobin contrast of prostate cancer over that of benign prostatic tissue, which shall be a result of tumor vasculature change, may improve the overall accuracy of prostate cancer detection by coupling the ultrasonography with NIR tomography.

2. Materials and Methods

The system is upgraded from our previously demonstrated integrated trans-rectal NIR/US sagittal-imaging system [11]. The outputs from one 785nm and one 830nm laser diodes (Thorlabs Inc.) are combined by a bifurcated fiber (FiberTech Optica Inc.,), as shown in Fig. 1 (a), and sequentially delivered to the 7 source channels of NIR applicator via a fiber switch made with a linear translation stage (Zaber Technology Inc.). The 7 detection channels are coupled to a 300mm focal-length spectrometer (Acton Research) for separating the two bands of remitted light. The acquisition of the spectrally separated light by a 16-bit intensified CCD camera (Princeton Instruments) is synchronized with the sequential source illumination. The acquisition time for one set of data was 3 seconds.

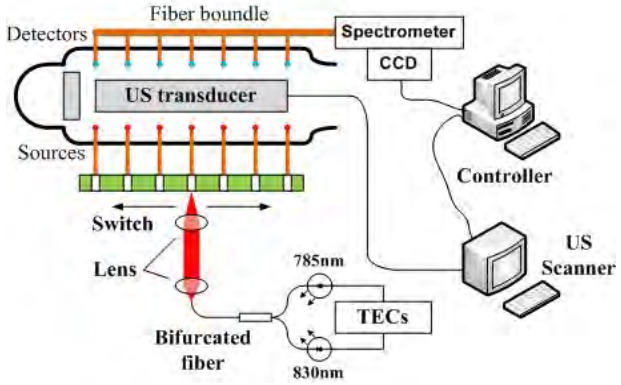

Fig. 1 (a) Dual-band trans-rectal NIR/US imaging system

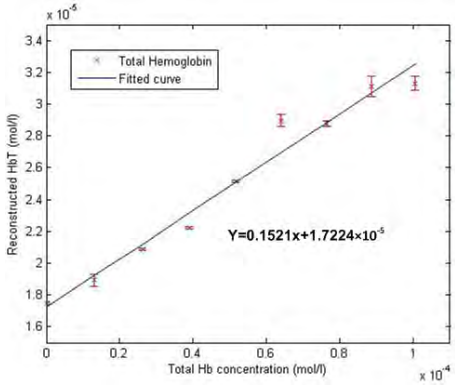

Fig.1 (b) System calibration with bovine blood

The calibration of the measurement of [HbT] was conducted with fresh bovine blood, whose optical absorption spectra in 600-850nm are very close to that of human blood [12]. The blood was held in a cylinder-container with μ_a=0.006mm^{-1} and μ_s'=1.0mm^{-1}, which was embedded in a 1% bulk Intralipid solution (μ_a=0.0023mm^{-1} and μ_s'=1.0mm^{-1}). The blood was diluted with an isotonic saline solution to establish a hemoglobin concentration gradient. The [HbT] of the fresh bovine blood is 12.8±0.8 grams per 100cc [13]. The absorption coefficients at the two bands were reconstructed without spatial *prior* information of the cylinder, then the [HbT] was calculated by:

$$[HbT]=[HbO_{(Oxygenized)}]+[Hb_{(Deoxygenized)}]=\frac{\mu_a^{\lambda_1}\cdot e_{Hb}^{\lambda_2}-\mu_a^{\lambda_2}e_{Hb}^{\lambda_1}}{e_{HbO}^{\lambda_1}\cdot e_{Hb}^{\lambda_2}-e_{HbO}^{\lambda_2}\cdot e_{Hb}^{\lambda_1}}+\frac{\mu_a^{\lambda_1}\cdot e_{HbO}^{\lambda_2}-\mu_a^{\lambda_1}\cdot e_{HbO}^{\lambda_2}}{e_{Hb}^{\lambda_1}\cdot e_{HbO}^{\lambda_2}-e_{Hb}^{\lambda_2}\cdot e_{HbO}^{\lambda_1}} \quad (1)$$

where "*e*" denotes the extinction coefficient. The measurements given in Fig. 1(b) reveal a residue error in the reconstructed [HbT] when no blood was present, albert it indicates a linear relationship between the reconstructed [HbT] above that residue value and the actual [HbT], which thereafter was applied to calibrating the *in vivo* results.

The animal protocols were approved by the Institutional Animal Care and Use Committee of Oklahoma State University. The canine protocol was also approved after an on-site inspection by the U.S. Army Medical Research and Material Command. For this study, the prostate of a 20-kg sexually intact mix-bred Beagle dog estimated to be approximately six years of age was used. The TVT cell line was propagated in non-obese-diabetic/severe combined-immunodeficiency (NOD/SCID) mice. The neoplastic TVT cells were recovered and homogenized for injection into the canine prostate gland. Approximately 3 cc of TVT cells were aseptically injected transperineally into the right lobe of the prostate using a 6-in. 16-gauge hypodermic needle via TRUS visualization. The TVT cells were confined within the right prostatic lobe during the injection in two locations, one near the cranial aspect, and the second slightly caudal to the mid-point of the right lobe as the needle was withdrawn. The dog underwent weekly monitoring, including physical rectal examination, TRUS, and trans-rectal NIR tomography, for 7 weeks and was then humanly euthanized for necropsy and histological examinations. Color and power Doppler TRUS evaluations performed at and after 5-weeks revealed blood circulating to the clearly hypo-echoic tumor masses.

3. Results

The sagittal TRUS/NIR imaging view taken across the right lobe of the prostate is given in Fig. 2 (a), and the NIR [HbT] images are presented in Fig. 3. The image dimension is 60mm×30mm (cranial-caudal×dorsal-ventral) for both US and NIR. A cluster of prostatic cysts looking like a "face" were used as a landmark to facilitate multiple images to be taken in the same relative areas over time throughout the course of the imaging study. Week 0 was the baseline images measured before the TVT cell injection. The base-line [HbT] is approximately 150uMol, that is in the lower range of the values of human prostate obtained by invasive time-resolved method [14]. At week 3, the tumor in the right lobe became visible in NIR images with a higher contrast while it was ambiguous in US images. The TVT continued to expand and became a large, infiltrative mass by week 6. Post mortem examination confirmed multiple coalescing foci of TVT in the caudal aspect of the prostate, and significant infiltration of the tumor from the

right lobe to the left lobe that was also indicated earlier by other NIR images. Histological examination of prostate sections confirmed TVT. Fig. 2(b) depicts the changes of the peak and averaged [HbT] in a 10mm-diameter region-of-interest specified in Fig. 3. Approximately 300% increase of the [HbT] has been indicated.

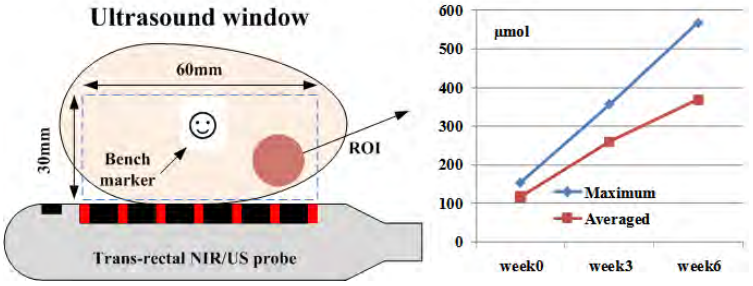

Fig. 2 (a). The view of sagittal US/NIR of the right lobe; (b) The changes of [HbT] at the region specified in Fig. 3, in week 0, 3 and 6

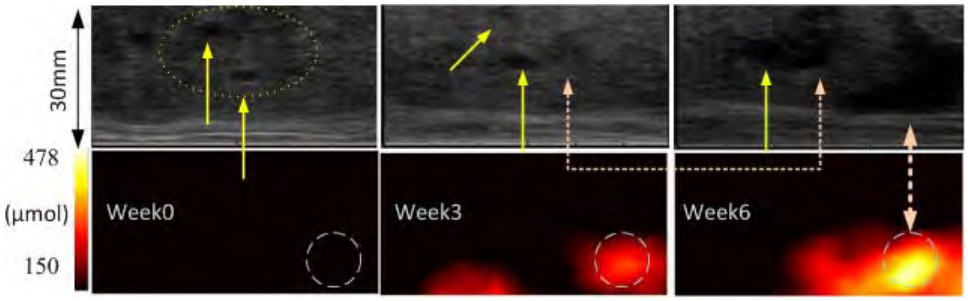

Fig. 3 The US and NIR images acquired at the right lobe, longitudinally in the middle-point and the caudal side, from week 0 to 6.

4. Discussions and Conclusions

This study reveals the first time non-invasive optical measurement of [HbT] changes associated with tumor development in the canine prostate. If spectral trans-rectal optical tomography can be implemented with an improved arrangement of the dual-bands or with more wavelength bands, the changes of oxygen saturation associated with tumor progression may be detected along with the elevations of [HbT], thereby providing another dimension of information for non-invasively characterizing the prostate cancer.

5. Acknowledgement

The study has been supported by DOD Prostate Cancer Research Program through a New Investigator Award to Piao (PC060814), and an endowment fund to Bartels from the Kerr Foundation, Oklahoma City, Oklahoma.

6. Reference

[1] Wild J, Reid J, "Echographic tissue diagnosis," Fourth Annual Conference on Ultrasound Therapy, Philadelphia, PA, 1955
[2]. Watanabe H, Kaiho J, Tanaka M, Terasawa Y, "Diagnostic application of ultrasonography of the prostate." Invest Urol.; **8**:548-559 (1971).
[3]. Brawer M. Chetner M. "Ultrasonography of the prostate biopsy," in Campbell's Urology, Walsh P, Retick A, Vaughna EJ, Wein A, eds., W.B. Saunders Company, Philadelphia, pp. 2506-2518 (1998).
[4] Ellis WJ, Brawer MK, "The significance of isoechoic prostate carcinoma," J. Urol,; **152**: 2304-2307 (1994).
[5]. Loch AC, Bannowsky A, Baeurle L, Grabski B, König B, Flier G, Schmitz-Krause O, Paul U, Loch T, "Technical and anatomical essentials for transrectal ultrasound of the prostate," World J. Urol. **25**, 361-366 (2007).
[6]. Yaseen MA, Brecht HPF, Ermilov SA, Gharieb RR, Conjusteau A, Oraevsky AA, "Hybrid optoacoustic and ultrasonic imaging system for detection of prostate malignancies," Proc. SPIE, **6856**, 68560T (2008).
[7]. Boutet J, Herve L, Debourdeau M, Guyon L, Peltie P, Dinten JM, Saroul L, Duboeuf F, Vray D, " Bimodal ultrasound and fluorescence approach for prostate cancer diagnosis**,"** J. Biomed. Opt.; **14**: 064001-1-064001-7 (2009).
[8]. Jiang Z, Holyoak GR, Bartels KE, Ritchey JW, Xu G, Bunting CF, Slobodov G, Piao D, "In vivo trans-rectal ultrasound coupled near-infrared optical tomography of a transmissible venereal tumor model in the canine pelvic canal," J. Biomed. Opt. Lett., **14(3):** 030506-1-030506-3 (2009)
[9]. Bigler SA, Deering RE, and Brawer MK, "Comparison of microscopic vascularity in benign and malignant prostate tissue," Hum Pathol. **24(2):**220-6 (1993).
[10]. Zhu Q, Cronin EB, Currier AA, Vine HS, Huang M, Chen N, Xu C. "Benign versus malignant breast masses: optical differentiation with US-guided optical imaging reconstruction," Radiology; **237(1):**57-66 (2005).
[11]. Jiang Z, Piao D, Xu G, Ritchey JW, Holyoak GR, Bartels KE, Bunting CF, Slobodov G, Krasinski JS, "Trans-rectal ultrasound-coupled near-infrared optical tomography of the prostate Part II: Experimental demonstration," Optics Express, **16(22):** 17505–17520 (2008)
[12]. Hayes MD, Vanzant ES, Stombaugh TS, Gates RS, "Comparison of bovine blood absorption coefficients to human curves," Livestock Environment VIII, Proceedings, 981-985 (2008).
[13]. McCay CM, "The hemoglobin and total phosphorus in the blood of cows and bulls," J. Dairy Sei., **14 (4):** 373-378 (1931).
[14]. Svensson T, Andersson-Engels S, Einarsdóttír M, Svanberg K, "In vivo optical characterization of human prostate tissue using near-infrared time-resolved spectroscopy," J Biomed Opt.;12(1): 014022-1-014022-10 (2007).

"Spectral *a priori*" to "spatial *a posteriori*" in continuous-wave image reconstruction in near-infrared optical tomography

Guan Xu,[a] Daqing Piao,[a]* Hamid Dehghani [b]
[a]School of Electrical and Computer Engineering, Oklahoma State University, Stillwater, OK, USA
[b]University of Birmingham, Birmingham, UK

* School of Electrical and Computer Engineering, Oklahoma State University, Stillwater, OK 74078
(Phone: 405-744-5250; FAX: 405-744-9198; e-mail: daqing.piao@okstate.edu)

ABSTRACT

This work examines the robustness of spectral *prior* to continuous-wave based, with respect to frequency domain based, image reconstruction for unique recovering of chromophores and scattering property distributions. An analytical model for parametric uncertainty in recovering optical property is derived, which afterwards is implemented for optimized selection of wavelengths and quality estimation of the image. Simulation results agree with the theoretical predictions in the following aspects: 1) the proposed analytical model is capable of selecting the optimal set of wavelengths for CW-based spectral reconstruction; 2) with sufficient number of wavelengths, DC-only reconstruction can resolve the concentrations of several important chromophores and scattering parameters, with the accuracy and background artifact level equivalent to those by DC-excluded or DC-included frequency-domain reconstructions; and 3) including DC in frequency-domain reconstruction generally improves reconstruction outcome as compared to when neglecting DC.

Keywords: multi-spectral, optical tomography, image reconstruction

1. INTRODUCTION

The outcome of functional imaging of near-infrared (NIR) optical tomography [1-2] depends upon the information obtained over a spectrum of light. A conventional technique of spectral optical tomography reconstruction is to reconstruct the wavelength-specific absorption and scattering properties first, then to derive the concentrations of tissue chromophores and distributions of the scatterers. An alternative technique of spectral optical tomography reconstruction utilizes *a priori* knowledge of the absorption and scattering spectra of tissue compositions within the NIR range to modify the inverse problem to directly recover the chromophore concentrations and scattering parameters including scattering power and amplitude. Such alternative technique, which is commonly stated as "spectral-*prior*" method, has been demonstrated by a number of studies [1-2]. The most successful demonstration[2] of spectral-*prior* method has been in coupling with *a priori* knowledge of the spatial content of the tissue under frequency-domain imaging, in other words, the *spectral-prior* has been implemented along with *spatial-prior* in frequency-domain measurement.

An interesting question thereby arises, in regards to the outcome of spectral-*prior* without the availability of *spatial-prior*, that what the likelihood of recovering the spatially-resolved spectral information would be, given only continuous-wave measurement. Our study on multi-wavelength optical tomography without *spatial-prior* has shown that implementing the spectral-*prior* in DC measurements often results in spatial information being reconstructed in unexpected level of details. This observation is referred to as "spectral *a priori*" to "spatial *a posteriori*", in other words it is the likelihood of accurately recovering spatially-resolved tissue absorption and scattering distribution from spectral reconstruction without spatial *prior*. The observation that spectrally-resolved measurements in DC lead to accurate spatially-resolved reconstruction, in our opinion, deserves further investigation. This study, as an initial exploration of the underlining mechanism, attempts to justify one derivative issue of such mechanism, specifically the reliability of recovering each unknown spectral variables including chromophore concentrations and scattering contributions under DC-based reconstruction. Based on the analytical approach demonstrated in our previous study [3], the analytical solution for multi-spectral optical tomography and the "parametric reconstruction uncertainty level" (PRUL) of each variable being reconstructed are derived, in a semi-infinite planar medium geometry. Such model provides quantitative means of estimating the relative errors among the parameters subjected to spectral reconstruction, with which the quality of spectral reconstruction may be better understood.

Multimodal Biomedical Imaging VI, edited by Fred S. Azar, Xavier Intes, Proc. of SPIE Vol. 7892,
78920D · © 2011 SPIE · CCC code: 1605-7422/11/$18 · doi: 10.1117/12.873462

In this study the analytical model is first implemented on the optimization of the wavelength sets for the spectral measurements. Studies [1, 4] have demonstrated selection of the optimum wavelengths for reliable recovery of chromophore concentrations and scattering parameters based on statistical investigation, by comparing numerically approximated sensitivity matrices derived from numerous possible wavelength combinations within the NIR spectrum, which is computationally intensive. In this paper, a novel method of optimizing the selection of wavelengths is investigated based on the PRUL model of multi-spectral optical tomography, which is found to be computationally less demanding.

The analytic model introduced in this work also supports the uniqueness of continuous-wave spectral optical tomography, which is an extension of the prediction made in our previous studies for single wavelength optical tomography [3]. The uniqueness of continuous-wave spectral optical tomography substantiated integrating more wavelengths in direct-current measurement to improve spectral reconstruction [1-2, 4-7]. As few studies have investigated the difference in performance between continuous wave and frequency domain spectral optical tomography, this study extends the approach of single-wavelength analysis in [3] to the analysis of spectral-*prior*, on measurement combinations of 1) continuous wave only (DC); 2) frequency domain measurements excluding direct-current components (AC+PHS); and 3) frequency domain measurements including direct-current (DC+AC+PHS), in the outcome of "spatial *a posteriori*" from "spectral *a priori*".

Finally, this study conduct numerical evaluations of synthetic models to examine the effect of "spectral *a priori*" on "spatial *a posterior*". The simulation studies demonstrate that, in agreement with the analytical predictions: 1) the proposed analytical model is capable of selecting the optimum set of wavelengths for spectral reconstruction; 2) with sufficient number of wavelengths for a given set of tissue chromophores, the DC-only reconstruction delivers spatially-resolved chromophore concentrations and scattering parameters with the accuracy and background artifact equivalent to that of AC+PHS and DC+AC+PHS; and 3)including DC in frequency-domain reconstruction generally improves reconstruction outcome more than neglecting DC.

2. THEORY

An earlier study [3] on the parametric-recovery-uncertainty-level (PRUL) has demonstrated an analytic approach of estimating the background artifact level in single-wavelength optical tomography reconstruction. The PRUL analysis in [3] adopted the analytic treatment originally introduced in [8], and in this study this analytic approach is extended to spectral reconstruction. For two field points separated from a source at distances of d_1 and d_2, respectively, in a homogenous diffusive medium, one has:

$$\begin{aligned}
\delta(\lambda) &= \ln\left(\frac{d_2}{d_1}\frac{U_{DC}(d_2,\lambda)}{U_{DC}(d_1,\lambda)}\right) = -\rho\cdot\sqrt{\frac{\mu_a(\lambda)}{D(\lambda)}} \\
\alpha(\lambda) &= \ln\left(\frac{d_2}{d_1}\frac{U_{AC}(d_2,\lambda)}{U_{AC}(d_1,\lambda)}\right) = -\rho\cdot\sqrt{\frac{\mu_a(\lambda)}{2D(\lambda)}\left(\sqrt{1+\frac{\omega^2}{v^2\mu_a^2(\lambda)}}+1\right)} \\
\phi(\lambda) &= \Phi(d_2,\lambda)-\Phi(d_1,\lambda) = \rho\cdot\sqrt{\frac{\mu_a(\lambda)}{2D(\lambda)}\left(\sqrt{1+\frac{\omega^2}{v^2\mu_a^2(\lambda)}}-1\right)}
\end{aligned} \tag{1}$$

where $U_{DC}(d., \lambda)$ $U_{AC}(d., \lambda)$ and $\Phi(d., \lambda)$ are the wavelength-specific amplitude of the direct-current modulated amplitude and phase of the modulation of the intensity measured at distance $d.$ from the source, respectively. In equ.(1) $\delta(\lambda)$ $\alpha(\lambda)$ and $\varphi(\lambda)$ are the attenuation of the direct-current (DC), the attenuation of the amplitude modulation (AC) and the phase shift (PHS) accordingly between two detectors placed d_1 and d_2 from the source, $\rho = |d_1 - d_1|$ is the distance between the two detectors, and ω is the angular modulation frequency. Also

$$\begin{aligned}
\mu_a(\lambda) &= \sum_i \varepsilon_i(\lambda)c_i, \\
\mu_s'(\lambda) &= A\lambda^{-b}, \\
D(\lambda) &= 1/3[\mu_a(\lambda)+\mu_s'(\lambda)]
\end{aligned} \tag{2}$$

are the absorption, scattering and diffusion coefficients of the medium at wavelength λ, respectively, where $\varepsilon_i(\lambda)$ is the extinction coefficient of chromophore i at λ and A is the scattering amplitude and b is the scattering power. The PRUL of

the chromophore concentrations and the scattering amplitude/power can be derived by analysis of the propagation of uncertainty and chain rule of partial derivatives as:

$$\sigma_{x_j} = \sqrt{\left(\frac{\partial x_j}{\partial M(\lambda)}\right)^2 \cdot \sigma^2_{M(\lambda)}} = \left|\frac{\partial x_j}{\partial \mu(\lambda)} \cdot \frac{\partial \mu(\lambda)}{\partial M(\lambda)}\right| \cdot \sigma_{M(\lambda)} = \left|\frac{\partial x_j}{\partial \mu(\lambda)}\right| \cdot \sigma_{\mu(\lambda)} \tag{3}$$

where M represents the set of δ, α and φ for the measurement, and x represents the unknowns including derived concentrations of the chromophores, the scattering amplitude and the scattering power. The μ represents the absorption and scattering coefficients in general. Given the extensive analyses of the PRUL of μ_a and μ_s' in [3], the analytical solution of $\sigma_{\mu(\lambda)}$ given in table 2 and table 4 of [3] are directly integrated into equ. (3), with the $\partial x/\partial \mu$ being newly derived.

Equation (2) transforms to a matrix form of

$$\begin{bmatrix} \mu_a(\lambda) \\ \mu_a(\lambda) \\ \vdots \\ \mu_a(\lambda) \end{bmatrix}_{m\times 1} = \begin{bmatrix} \varepsilon_1(\lambda_1) & \varepsilon_2(\lambda_1) & \cdots & \varepsilon_n(\lambda_1) \\ \varepsilon_1(\lambda_2) & \varepsilon_2(\lambda_2) & \cdots & \varepsilon_n(\lambda_2) \\ \vdots & \vdots & \ddots & \vdots \\ \varepsilon_1(\lambda_m) & \varepsilon_2(\lambda_m) & \cdots & \varepsilon_n(\lambda_m) \end{bmatrix}_{m\times n} \times \begin{bmatrix} c_1 \\ c_2 \\ \vdots \\ c_n \end{bmatrix}_{n\times 1} \tag{4}$$

with which one has

$$\frac{\partial \vec{c}_{n\times 1}}{\partial (\vec{\mu}_a)_{m\times 1}} = [(\vec{\varepsilon}^T)_{n\times m}\vec{\varepsilon}_{m\times n}]^{-1}(\vec{\varepsilon}^T)_{n\times m} = \begin{bmatrix} \frac{\partial c_1}{\partial \mu_a(\lambda_1)} & \frac{\partial c_1}{\partial \mu_a(\lambda_2)} & \cdots & \frac{\partial c_1}{\partial \mu_a(\lambda_m)} \\ \frac{\partial c_2}{\partial \mu_a(\lambda_1)} & \frac{\partial c_2}{\partial \mu_a(\lambda_2)} & \cdots & \frac{\partial c_2}{\partial \mu_a(\lambda_m)} \\ \vdots & \vdots & \ddots & \vdots \\ \frac{\partial c_n}{\partial \mu_a(\lambda_1)} & \frac{\partial c_n}{\partial \mu_a(\lambda_2)} & \cdots & \frac{\partial c_n}{\partial \mu_a(\lambda_m)} \end{bmatrix}_{n\times m} \tag{5}$$

and then for the terms in PRUL of chromophore concentrations we have:

$$(\vec{\sigma}_c)_{n\times 1} = \left|\frac{\partial \vec{c}_{n\times 1}}{\partial (\vec{\mu}_a)_{m\times 1}}\right|_{n\times m} \cdot (\vec{\sigma}_{\mu_a(\lambda)})_{m\times 1} \tag{6}$$

Note that the scattering power and amplitude are not linearly related as the chromophore concentrations are in equ. (2). The PRULs of these two variables are derived by firstly obtaining:

$$\log \mu_s' = \log A + (-b)\log \lambda \tag{7}$$

then converting equ. (7) to a matrix form of:

$$\begin{bmatrix} \log[\mu_s'(\lambda_1)] \\ \log[\mu_s'(\lambda_2)] \\ \ldots \\ \log[\mu_s'(\lambda_m)] \end{bmatrix}_{m\times 1} = \begin{bmatrix} 1 & \log\lambda_1 \\ 1 & \log\lambda_2 \\ \ldots & \ldots \\ 1 & \log\lambda_m \end{bmatrix}_{m\times 2} \times \begin{bmatrix} \log A \\ (-b) \end{bmatrix}_{2\times 1} \tag{8}$$

which gives the following result:

$$\left(\frac{\partial \log A}{\partial \log \mu_s'(\lambda_i)}\right)_{1\times m} = \frac{1}{m\sum_{i=1}^{m}\log^2(\lambda_i) - [\sum_{i=1}^{m}\log(\lambda_i)]^2} \cdot \left(\begin{bmatrix} \sum_{i=1}^{m}\log^2(\lambda_i) - \log(\lambda_1)\sum_{i=1}^{m}\log(\lambda_i) \\ \sum_{i=1}^{m}\log^2(\lambda_i) - \log(\lambda_2)\sum_{i=1}^{m}\log(\lambda_i) \\ \ldots \\ \sum_{i=1}^{m}\log^2(\lambda_i) - \log(\lambda_m)\sum_{i=1}^{m}\log(\lambda_i) \end{bmatrix}^T \right)_{1\times m} \tag{9}$$

$$\left(\frac{\partial b}{\partial \log \mu_s'(\lambda_i)}\right)_{1\times m} = \frac{1}{m\sum_{i=1}^{n}\log^2(\lambda_i) - [\sum_{i=1}^{n}\log(\lambda_i)]^2} \cdot \left(\begin{bmatrix} \sum_{i=1}^{m}\log(\lambda_i) + m\cdot\log(\lambda_1) \\ \sum_{i=1}^{m}\log(\lambda_i) + m\cdot\log(\lambda_2) \\ \cdots \\ \sum_{i=1}^{m}\log(\lambda_i) + m\cdot\log(\lambda_m) \end{bmatrix}^T \right)_{1\times m} \tag{10}$$

The PRULs of scattering amplitude and power are finally expressed as:

$$\sigma_A = \left|\frac{\partial A}{\partial \log A}\cdot\frac{\partial \log A}{\partial \log \mu_s'(\lambda)}\cdot\frac{\partial \log \mu_s'(\lambda)}{\partial \mu_s'(\lambda)}\right|\cdot\sigma_{\mu_s'(\lambda)} = A\cdot\left|\frac{\partial \log A}{\partial \log \mu_s'(\lambda)}\right|\cdot\frac{\sigma_{\mu_s'(\lambda)}}{\mu_s'(\lambda)} \tag{11}$$

$$\sigma_b = \left|\frac{\partial b}{\partial \log \mu_s'(\lambda)}\cdot\frac{\partial \log \mu_s'(\lambda)}{\partial \mu_s'(\lambda)}\right|\cdot\sigma_{\mu_s'(\lambda)} = \left|\frac{\partial b}{\partial \log \mu_s'(\lambda)}\right|\cdot\frac{\sigma_{\mu_s'(\lambda)}}{\mu_s'(\lambda)} \tag{12}$$

Up to here, by substituting expressions in table 2 and 4 in [3] to equ.s (6) (11) and (12), all the PRUL equation for reconstruction variables in multi-spectral optical tomography are derived and a series of comparison and analysis will be conducted to reveal the intrinsic relationships between the reconstruction parameters. It should also be noted that since PRUL analysis is expressed in terms of the standard deviations, all comparisons will neglect common factors and consider only the absolute values of the equations.

Integrating the results of PRUL in the previous study, the uncertainty level of the parameters to be recovered can be quantitatively compared. Note that in equ. (5), the expression does not facilitate the normalization of σ_{μ_a} on the right hand side compared to the ($\sigma_{\mu_s'}/\mu_s'$) terms in equ.s (9) and (10). Multiplication by μ_a values is thereby necessary when utilizing (σ_{μ_a}/μ_a) results.

It is desirable that the uncertainty values can be reduced by correctly selecting the wavelengths used in the system. One approach is to increase absolute value of the determinant of $\varepsilon^T\varepsilon$ in equ. (6) and $m\sum_{i=1}^{m}\log^2(\lambda_i) - [\sum_{i=1}^{m}\log(\lambda_i)]^2$ in equ.s (9) and (10) to reduce the overall absolute value of the PRULs. Several random attempts on the denominator terms will show that the values of $\left|m\sum_{i=1}^{m}\log^2(\lambda_i) - [\sum_{i=1}^{m}\log(\lambda_i)]^2\right|$ stay in a narrow range of [0,1] but the determinant of $\varepsilon^T\varepsilon$ varies in several orders depending on the selection of wavelengths. Such phenomenon is understandable because high similarity between the row vectors of the extinction coefficient matrix could induce rank deficiency, making its determinant close to zero or producing singular values in its pseudo-inverse, which reduces the accuracy of matrix inversion in equ. (4). Previous study [1] has shown such problems and recommended to construct sensitivity matrix with small residual numbers for improving the reliability of the inverse algorithm. From another perspective, the determinant of the matrix geometrically quantifies the volume in the space bounded by the row factors, therefore, larger divergence of the row vectors in extinction coefficients enclosures larger volumes in the vector space, which again supports the hypothesis that larger determinant of the $\varepsilon^T\varepsilon$ matrix ensures more accurate reconstruction.

Further, reference [4] indicates that the uniformity of the sensitivity matrix ($\partial x/\partial M(\lambda)$ in equ. (3)) is also desired for stable and accurate reconstruction. The criteria for wavelengths optimization in this study thereby also include the standard deviation of ($\partial x/\partial M(\lambda)$) for each wavelength set and again the common terms $|\partial\mu(\lambda)/\partial M(\lambda)|\cdot\sigma_{M(\lambda)}$ is neglected in the quantitative evaluation.

This study is conducted for 3 sets of wavelength, each containing 5 wavelengths adopted from a previous literature [1], in the numerical evaluation of the analytical approach for recovering concentrations of oxygenated hemoglobin, deoxygenated hemoglobin, water, scattering power, and scattering amplitude, as is listed in table 1. Although the previous study [1] has shown that the wavelength selection method is capable of determining the optimum wavelength set and validated the method with simulations, it is difficult to rank the performance of the other two sets. In observation of Table 1 as well as the expectation to have larger denominator determinant and smaller variation among the sensitivity values, the performance ranking of the three wavelength sets can be predicted, from best to worst as: 3,1,2, which agrees with the simulations presented in[1]. Validations from more aspects will be shown later in this paper.

For the calculation of the PRULs in this study, the chromophore concentrations and scattering parameters are estimated as: $C_{HbO}=C_{Hb}=0.01$mM, $C_{H_2O}=40\%$ and A=b=1. It is also assumed that for all measurement types the relative uncertainties of the measurements are the same, that is: $\frac{\sigma^2_{\delta(\lambda)}}{\delta^2(\lambda)}=\frac{\sigma^2_{\alpha(\lambda)}}{\alpha^2(\lambda)}=\frac{\sigma^2_{\phi(\lambda)}}{\phi^2(\lambda)}$. Further, with a given set of wavelengths and a modulation frequency, equ.(1) implicitly determined the value of $\frac{\alpha^2(\lambda)+\phi^2(\lambda)}{\alpha^2(\lambda)-\phi^2(\lambda)}$ ($=\sqrt{1+\frac{\omega^2}{v^2\mu_a^2(\lambda)}}$), which is approximately 1 for all cases. With these approximations and preconditions in-place, equ.s (6) (11) and (12) can be evaluated and compared to simulation results later in this paper.

Table 1 Wavelength sets to be examined and comparison of the PRUL evaluation with the analytical solutions

Set	Wavelengths / nm	Absorption component		Scattering component	
		Determinant of denominator: $(\varepsilon^T\varepsilon)^{-1}$	Standard deviation of chromophores dev(ε)	Absolute value of denominator	Sensitivity standard deviation of scattering amplitude and power
1	740,788,866,902,926	8.18×10^{-7}	63.7	0.18	1.03
2	650,700,716,860,890	2.58×10^{-7}	388.0	0.37	0.67
3	650,716,866,914,930	1.30×10^{-5}	63.8	0.53	0.45

3. SIMULATIONS

Simulations are conducted to quantitatively examine the accuracy of the analytically derived predictions. Similar to [3], PRULs of three measurement types: DC, AC+PHS, DC+AC+PHS are calculated and compared.

3.1 Synthetic model

Forward model is carried out with Finite Element Method solution of photon diffusion at each wavelength[9]:

$$\left(-\frac{\mu_a(\vec{r},\lambda)}{D(\vec{r},\lambda)}+\frac{i\omega}{vD(\vec{r},\lambda)}\right)U(\vec{r},\omega,\lambda)+\nabla^2U(\vec{r},\omega,\lambda)=-\frac{S(\vec{r},\omega,\lambda)}{D(\vec{r})} \tag{13}$$

Where $U(\vec{r},\omega,\lambda)$ is the photon fluence of wavelength λ modulated to angular frequency ω (ω=0 for DC) at position $\vec{r}$ in phasor notation. $S(\vec{r},\omega,\lambda)$ is the source term. The Jacobian matrix is constructed according to the measurement type [3] as:

$$J=\begin{bmatrix}DC\\AC\\PHS\end{bmatrix}=\begin{bmatrix}\frac{\partial\ln U_{DC}(\lambda_1)}{\partial x} & \frac{\partial\ln U_{DC}(\lambda_2)}{\partial x} & \cdots & \frac{\partial\ln U_{DC}(\lambda_m)}{\partial x}\\ \frac{\partial\ln|U_{AC}(\lambda_1)|}{\partial x} & \frac{\partial\ln|U_{AC}(\lambda_2)|}{\partial x} & \cdots & \frac{\partial\ln|U_{AC}(\lambda_m)|}{\partial x}\\ \frac{\partial\Phi_{AC}(\lambda_1)}{\partial x} & \frac{\partial\Phi_{AC}(\lambda_2)}{\partial x} & \cdots & \frac{\partial\Phi_{AC}(\lambda_m)}{\partial x}\end{bmatrix} \tag{14}$$

where *x* represents the parameters to be reconstructed, including chromophore concentrations and scattering amplitude and scattering power. The Levernberg-Marquardt algorithm is implemented as the inverse solver.

A 43mm-radius circular geometry with 16 optode channels evenly distributed on its perimeter is used in this study for its relatively uniform sensitivity along the azimuthal direction with respect to the center of the circle. Each channel functions as source channel sequentially while others function as detector simultaneously. Background values of each reconstruction variables are assigned identical to those used in analytical calculation and the contrast of the anomaly are: C_{HbO_anom} =0.0023mM, C_{Hb_anom} = 0.0023mM, $C_{H_2O\_anom}$ =80% A_{anom}=2, and b_{anom}=2. Contrasts of each of the five variables are assigned to a set of five 8mm-radius targets, as is shown in Fig.1 columns Set. The targets locate 25 mm away from the center of the geometry with 0.4π angular separation. 1% randomly distributed noise is added to all forward data to simulate the perturbations in the actual measurement system.

3.2 Results

Fig.1 shows the reconstruction results and Table 2 demonstrates the maximum values of each variable within the target regions and the percentage error of the contrast. Comparisons in Fig. 1 and table 2 infer that the set 3 outperforms the other two in terms of the overall reliability of quantitative reconstruction and the crosstalk among the recovered variables. Next to the set 3 is set 1, which underestimates hemoglobin concentration and has higher level of crosstalk between hemoglobin and scattering parameters in DC reconstruction. The set 2 is the least accurate, producing severe crosstalk between the oxygenated hemoglobin and water concentration. Besides the comparison among the sets of wavelength, it is also noted that for most cases, DC reconstruction demonstrates the most accurate recovery of the targets when the target presents the contrast of only one parameter, and including DC measurement in frequency domain usually improve the estimation precision.

Further, table 3 lists the analytical PRULs and the reconstructed background artifact levels normalized by the absolute variable of the contrast being recovered, which is, in a more explicit way, the inverse of the contrast-noise-ratio. For more clarity in comparison, the noise to contrast (NCR) ratios are normalized by that of the deoxygenated hemoglobin for the absorptive chromophores and by that of the scattering amplitude for the scattering parameters.

Although the analytically estimated values of the noise to contrast ratios always exceed those calculated from the numerical simulations, the data unanimously shows that, $NCR_{c\_Hb} < NCR_{c\_HbO} < NCR_{c\_H_2O}$ for the absorption part and $NCR_A < NCR_b$ for the scattering part, both of which are in agreement with the previous hypotheses. The quantitative inaccuracy could relate to the smoothing effect of the piecewise reconstruction algorithm.

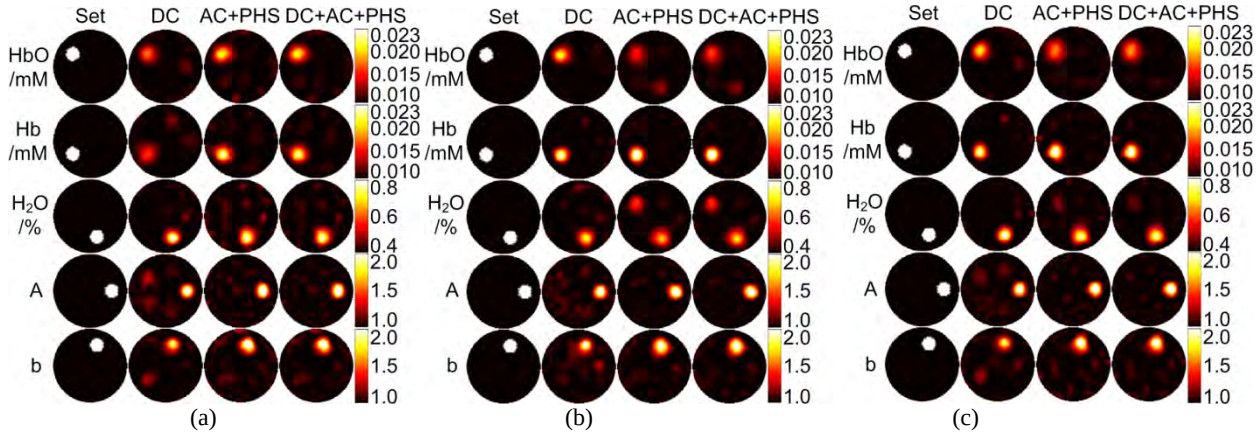

Fig.1Synthetic study on targets with independent contrast

Table 2 Target accuracy comparison

Data		HbO / mM		Hb / mM		H2O / %		A		b	
		Abs.	Err. / %	Abs.	Err. / %	Abs.	Err. / %	Abs.	Err. / %	Abs.	Err. / %
Set Values		2.3E-2		2.3E-2		0.80		2.0		2.0	
(1)	DC	1.7E-2	-46	1.6E-2	-55	0.82	5	2.2	21	1.9	-9
	AC+PHS	2.0E-2	-23	2.3E-2	-2	0.81	2	2.4	39	2.3	30
	DC+AC+PHS	2.0E-2	-24	2.2E-2	-6	0.80	0.4	2.3	34	2.2	23
(2)	DC	2.0E-2	-21	2.4E-2	4	0.72	-21	2.4	40	2.1	7
	AC+PHS	1.6E-2	-56	2.6E-2	24	0.67	-33	2.3	26	2.1	6
	DC+AC+PHS	1.7E-2	-48	2.7E-2	27	0.69	-27	2.2	23	2.1	10
(3)	DC	2.0E-2	-25	2.3E-2	1	0.83	8	2.3	33	1.9	-11
	AC+PHS	1.8E-2	-42	2.5E-2	16	0.78	-6	2.4	45	2.2	19
	DC+AC+PHS	1.8E-2	-39	2.5E-2	18	0.77	-8	2.4	39	2.2	17

Table 3 Comparison between the PRULs and the background artifact levels normalized by variable contrast

Set		Measurement	HbO / mM		Hb / mM		H2O / %		A		b	
			Abs.	Norm.	Abs.	Norm.	Abs.	Norm.	Abs.	Norm.	Abs.	Norm.
(3)	Ana.	DC	5.38	5.40	1.00	1	3.24	3.26	0.79	1	3.10	3.91
		AC+PHS	7.61	5.40	1.41	1	4.59	3.26	1.12	1	4.39	3.91

		DC+AC+PHS	13.17	5.40	2.44	1	7.94	3.26	1.12	1	4.39	3.91
	Sim.	DC	0.0489	1.89	0.0258	1	0.0395	1.53	0.0260	1	0.0381	1.46
		AC+PHS	0.0716	1.62	0.0443	1	0.0466	1.05	0.0242	1	0.0498	2.06
		DC+AC+PHS	0.0521	1.58	0.0328	1	0.0367	1.12	0.0203	1	0.0404	1.99

4. DISCUSSIONS AND CONCLUSION

The predictions made by a novel analytical PRUL model regarding spectral *a priori* leading to spatial *a posteriori* is supported by the results from simulation. The wavelength ranking method shows agreement with previous study, with much less computational intensity. The PRUL values qualitatively estimates the background artifact level of the DC and frequency domain reconstructions, although neglecting DC components in DC+AC+PHS induces explainable aberration. Comparisons on both the multi-spectral tomography reconstruction PRULs and the projected absorption and scattering reconstruction PRULs support the reliability of the model predictions. However, quantitative inaccuracy still exists in the comparisons, which could be attributed to the approximation and smoothing effect of the inverse algorithm.

An interesting observation is that different from the study in [3], the DC reconstruction with spectral *prior* has quite desirable reconstruction outcome. This should relate to the expectation that sufficient wavelength components will impose the outcome as a result of the uniqueness of DC multispectral tomography, with minimized cross-coupling among the parameters to be recover. Moreover, fewer measurement components facilitate less system noise in the inverse problem and thereby generate less background artifacts, improving the overall DC reconstruction quality. As to frequency domain reconstruction, although DC component could contribute to excessive reconstruction uncertainty, its extra information has actually balanced the negative effect and made DC+AC+PHS a better choice.

ACKNOWLEDGEMENT

This work has been supported in part by the Prostate Cancer Research Program of the U.S. Army Medical Research Acquisition Activity (USAMRAA) through grants #W81XWH-07-1-0247 and #W81XWH-10-1-0836.

REFERENCES

[1] Corlu, A., et al., "Diffuse optical tomography with spectral constraints and wavelength optimization," Appl. Opt. 44(11), 2082-2093 (2005)
[2] Srinivasan, S., et al., "Spectrally constrained chromophore and scattering near-infrared tomography provides quantitative and robust reconstruction," Appl. Opt. 44(10), 1858-1869 (2005)
[3] Xu, G., et al., "Direct-current-based image reconstruction versus direct-current included or excluded frequency-domain reconstruction in diffuse optical tomography," Appl. Opt. 49(16), 3059-3070 (2010)
[4] Eames, M.E., et al., "Wavelength band optimization in spectral near-infrared optical tomography improves accuracy while reducing data acquisition and computational burden," Journal of Biomedical Optics 13(5), 054037-9 (2008)
[5] Li, C., et al., "Multispectral diffuse optical tomography with absorption and scattering spectral constraints," Appl. Opt. 46(34), 8229-8236 (2007)
[6] Jones, P.B., et al., "Simultaneous multispectral reflectance imaging and laser speckle flowmetry of cerebral blood flow and oxygen metabolism in focal cerebral ischemia," Journal of Biomedical Optics 13(4), 044007 (2008)
[7] Xu, H., et al., "Magnetic-resonance-imaging-coupled broadband near-infrared tomography system for small animal brain studies," Appl. Opt. 44(11), 2177-2188 (2005)
[8] Fantini, S., et al., "Quantitative determination of the absorption spectra of chromophores in strongly scattering media: a light-emitting-diode based technique," Appl. Opt. 33(22), 5204-5213 (1994)
[9] Dehghani, H., et al., "Near infrared optical tomography using NIRFAST: Algorithm for numerical model and image reconstruction," Communications in Numerical Methods in Engineering 25(6), 711-732 (2009)

Different optical spectral characteristics in a necrotic transmissible venereal tumor and a cystic lesion in the same canine prostate observed by triple-band trans-rectal optical tomography under trans-rectal ultrasound guidance

Zhen Jiang,[1] G. Reed Holyoak,[2] Jerry W. Ritchey,[3] Kenneth E. Bartels,[2] Kendra Rock,[2] Charlotte L. Ownby,[4] Gennady Slobodov,[5] Charles F. Bunting,[1] Daqing Piao,[1*]

1 School of Electrical and Computer Engineering, Oklahoma State University, Stillwater, Oklahoma, U.S.A. Currently Department of Biomedical Engineering, Washington University in St. Louis, St. Louis, MO, U.S.A.
2 Department of Veterinary Clinical Sciences, Oklahoma State University, Stillwater, Oklahoma, U.S.A.
3 Department of Veterinary Pathobiology, Oklahoma State University, Stillwater, Oklahoma, U.S.A.
4 Microscopy Laboratory, Oklahoma State University, Stillwater, Oklahoma, U.S.A.
5 Department of Urology, University of Oklahoma Health Sciences Center, Oklahoma City, Oklahoma, U.S.A.
* Correspondence: School of Electrical and Computer Engineering, 202 Engineering South, Oklahoma State University, Stillwater, OK 74078 (Phone: 405-744-5250; FAX: 405-744-9198; e-mail: daqing.piao@okstate.edu).

Abstract

Different optical spectral characteristics were observed in a necrotic transmissible venereal tumor (TVT) and a cystic lesion in the same canine prostate by triple-wavelength trans-rectal optical tomography under trans-rectal ultrasound (TRUS) guidance. The NIR imager acquiring at 705nm, 785nm and 808nm was used to quantify both the total hemoglobin concentration (HbT) and oxygen saturation (StO2) in the prostate. The TVT tumor in the canine prostate as a model of prostate cancer was induced in a 7-year old, 27 kg dog. A 2 mL suspension of 2.5×10^6 cells/mL of homogenized TVT cells recovered from an *in vivo* subcutaneously propagated TVT tumor in an NOD/SCID mouse were injected in the cranial aspect of the right lobe of the canine prostate. The left lobe of the prostate had a cystic lesion present before TVT inoculation. After the TVT homogenate injection, the prostate was monitored weekly over a 9-week period, using trans-rectal NIR and TRUS in grey-scale and Doppler. A TVT mass within the right lobe developed a necrotic center during the later stages of this study, as the mass presented with substantially increased [HbT] in the periphery, with an area of reduced StO2 less than the area of the mass itself shown on ultrasonography. Conversely, the cystic lesion presented with slightly increased [HbT] in the periphery of the lesion shown on ultrasound with oxygen-reduction inside and in the periphery of the lesion. There was no detectable change of blood flow on Doppler US in the periphery of the cystic lesion. The slightly increased [HbT] in the periphery of the cystic lesion was correlated with intra-lesional hemorrhage upon histopathologic examination.

Keywords: Diffuse optical tomography, transmissible venereal tumor, cyst, hemoglobin, oxygen saturation.

1. INTRODUCTION

Prostate cancer has been the second leading cause of death in American men in recent decades [1]. Digital rectal examination (DRE) and serum testing of prostate specific antigen (PSA)

Multimodal Biomedical Imaging VI, edited by Fred S. Azar, Xavier Intes, Proc. of SPIE Vol. 7892, 78920P · © 2011 SPIE · CCC code: 1605-7422/11/$18 · doi: 10.1117/12.873144

concentrations are the main screening methods in prostate cancer detection. The patients will be referred to prostate biopsy given an abnormal DRE result or PSA level. Trans-rectal ultrasound (TRUS) guided needle biopsy is considered an essential procedure in the definitive diagnosis of prostate cancer [2]. However, low sensitivity and specificity of the TRUS imaging between cancerous lesions and normal tissue leads to an overall accuracy much lower than 50% in prostate cancer detection [2]. Diffuse optical tomography using near-infrared (NIR) light was demonstrated as a non-invasive functional imaging technique on breast cancer [3-5] and has been extended to prostate imaging [6]. A trans-rectal NIR imaging system with concurrent TRUS for visualization guidance was reported on *in-vivo* imaging of canine prostate bearing a transmissible venereal tumor (TVT) [7]. The growth of a TVT tumor in that subject was associated with an increased total hemoglobin concentration [HbT] [8] indicative of angiogenesis, which agrees with the correlation found between the prostate cancer and increased micro-vessel density in another study [9]. There was approximately a 300% increase in [HbT] along a 7-week course of TVT tumor growth [8]. The estimated tumor volume also grew exponentially over the same time period.

In the prostate, changes in local oxygen saturation were observed via interstitial NIR measurement during prostate photodynamic therapy [10]. Tissue oxygenation status is considered an important prognostic indicator for androgen-deprivation therapy of newly diagnosed metastatic prostate cancer [11]. There is evidence that hypoxia exists in the nidus of prostate cancer [12]. The ability of quantifying the hemoglobin concentration and oxygen saturation in prostate tissue is important for the diagnosis, prognosis, and treatment of prostate cancer. Augmented StO2 mapping of prostate is expected to provide more definitive information for cancer diagnosis when combined with [HbT] mapping and Doppler US imaging.

Prostatic cysts are benign lesions in the prostate that are considered congenital or secondary to neoplasia and prostatic hyperplasia/inflammation. Regardless of etiopathogenesis, cysts are typically lined by secretory epithelium. Generally, they are small, well defined structures filled with prostatic fluid, and they can be predisposed for bacterial infection [13]. The appearance of cysts is often an indication of bacterial prostatitis. The ultrasonographic appearance of the prostatic cyst is usually hypo-echoic, remarkably similar in appearance to that of a homogenous cell type tumor. The optical property of an intact prostate cystic lesion, has, to our knowledge, not been previously reported. In breast cancer, some studies showed that cysts could have increased contrast of optical absorption because of the light transmission rather than scattering effects [14]. Recent DOT studies focusing on breast cancer research showed lower imaging contrast of the cyst on both optical absorption and scattering [15]. Also, in several cases cystic lesions were presented with higher contrast of optical absorption and scattering, but the [HbT] and StO2 were reported to be lower than normal tissue [16].

This study reports the difference in the optical contrasts of a solid tumor and a contra-lateral cystic lesion in an intact canine prostate. In this study, a dog with a cystic lesion in prostate was injected with TVT tumor cells and monitored over 9-week duration using a triple-wavelength trans-rectal US-guided optical tomography system. The 3 wavelengths were 705nm, 785nm and 808nm, covering a ~100nm bandwidth. Both [HbT] and StO2 in canine prostate were mapped in situ by optical imaging. Each week the dog was monitored by Doppler US, TRUS and optical imaging. An increased [HbT] associated with the tumor foci was compared with a relatively stable [HbT] in the periphery of the cystic lesion during 9-weeks of tumor development. Differences in StO2 were also found between the tumor and the cyst.

2. MATERIALS AND METHODS

2.1 Triple-band trans-rectal near-infrared optical tomography

Near-infrared light at three wavelengths were applied to a previously demonstrated trans-rectal NIR/US sagittal-imaging system (diagram in Fig. 1-a and photograph in Fig. 1-b) [8]. The NIR source and detector channels were placed laterally, symmetric to the sagittal US transducer to perform volumetric imaging, of which the mid-sagittal NIR plane was co-registered with the sagittal US plane. The outputs from laser diodes of 705nm, 785nm and 808nm (Thorlabs Inc.) were combined by a tri-furcated fiber bundle (FiberTech Optica Inc.,), and sequentially delivered to the 7 source channels of NIR applicator via a fiber switch installed on a linear translation stage (Zaber Technology Inc.). Each of the laser diodes of 785nm/100mw and 808nm/200mw was controlled by one turn-key TEC/driver module LDC3722 (ILX lightwave Inc.). The laser diode of 705nm/50mw was controlled by a turn-key TEC/driver LDC205C (Thorlabs, Inc.). The 7 detection channels were coupled to a spectrometer of 300mm focal-length (Acton Research) which covered around 120nm of bandwidth for separating the three bands of remitted light. The acquisition of the spectrally separated light by a 16-bit intensified CCD camera (Princeton Instruments) was synchronized with the sequential source illumination. The total acquisition time for each data set was about 3 seconds. The trans-rectal NIR/US applicator developed based on ALOKA UST 672-5/7.5 biplane prostate probe is illustrated in Fig. 1-a. In the image formation, the absorption coefficients ($\mu_a^{\lambda_1}$, $\mu_a^{\lambda_2}$ and $\mu_a^{\lambda_3}$) were reconstructed first, then oxygenated and deoxygenated hemoglobin concentrations were derived by

$$[C] = \left([\varepsilon]' [\varepsilon] \right)^{-1} [\varepsilon]' [\mu_a] \tag{1}$$

where [C] indicates a concentration vector of oxygenated [HbO] and deoxygenated [Hb] hemoglobin, and ε denotes the vector of molar absorption coefficient of [HbO] and [Hb].

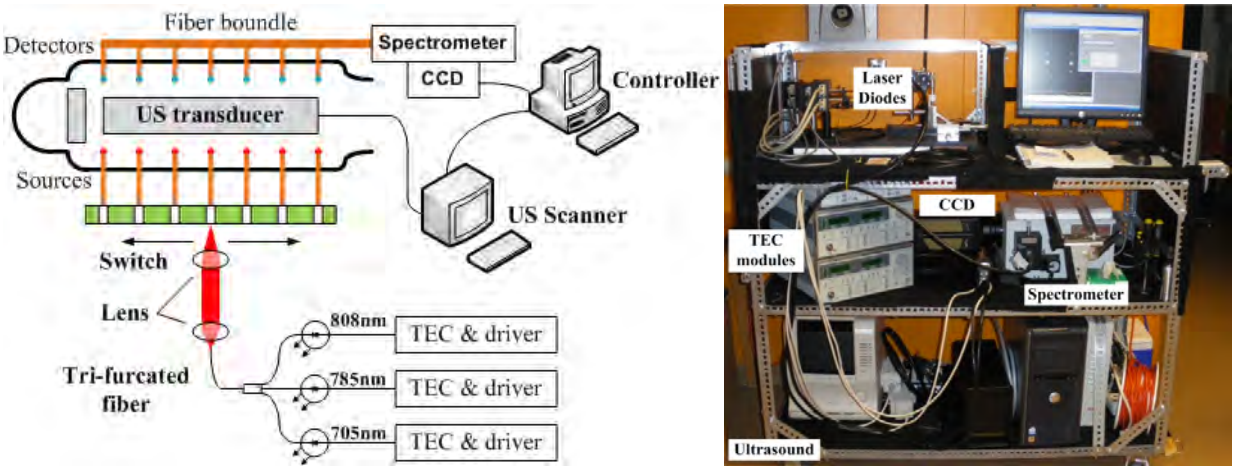

(a) (b)

Figure 1. Triple-band trans-rectal NIR optical tomography system (a) Schematic payout of the system; (b) Photograph of the completed system.

Figure 2 illustrates the results of calibrating the system measurements on [HbT] and StO2. The calibration of [HbT] measurements compensates the underestimation of the [HbT] due to the non-linear reconstruction of diffuse optical tomography [17, 18]. In the calibration process, a tube of

15mm in diameter made of tissue-mimicking phantom material filled with different concentrations of bovine blood was placed in the middle range of the NIR probe-span and on top of the probe. In calibration of the StO2 measurement, sodium dithionite was added to the blood to decrease the oxygenation without destroying the blood cells. The decreased trend of the derived StO2 was recovered linearly, though the range of averaged StO2 values in the region of the blood were much smaller than the actual values estimated from the de-oxygenation model of sodium dithionite [19]. No conversion from the derived StO2 values to the expected ranges was made in this study. Therefore the derived average StO2 level of 60% may correspond to StO2 values as low as 30% due to the variation of the derivation itself, or even lower than 30%.

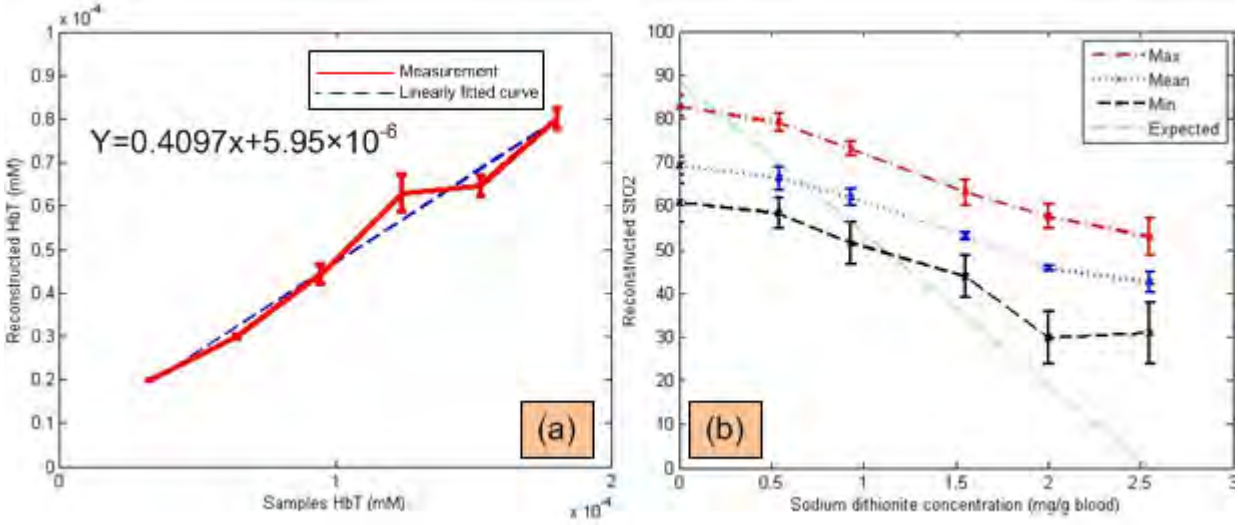

Figure 2 System calibration with different blood concentration and oxygenation

2.2 Animal model and imaging protocol

The animal protocols involving studies on canine and rodent species were approved by the Institutional Animal Care and Use Committee of Oklahoma State University. The canine protocol was also approved after an on-site inspection by the U.S. Army Medical Research and Material Command. For this study a 7 year old, 27-kg sexually intact mixed-bred hound was used. The TVT cell line was propagated in non-obese-diabetic/severe combined-immunodeficiency (NOD/SCID) mice. The neoplastic TVT cells were recovered and homogenized for injection into the canine prostate gland parenchyma. Approximately a 2 cc suspension of 2.5×10^6 cells/mL of homogenized TVT cells were aseptically injected trans-perineally into the right lobe of the prostate using a 6-in. 16-gauge hypodermic needle via TRUS visualization (Fig. 3-a). The TVT cells were confined within the cranial aspect of right prostatic lobe during injection. The dog underwent weekly monitoring, including physical rectal examination, TRUS, Doppler US and trans-rectal NIR tomography, for 9 weeks and was then humanly euthanized for necropsy and histological examinations.

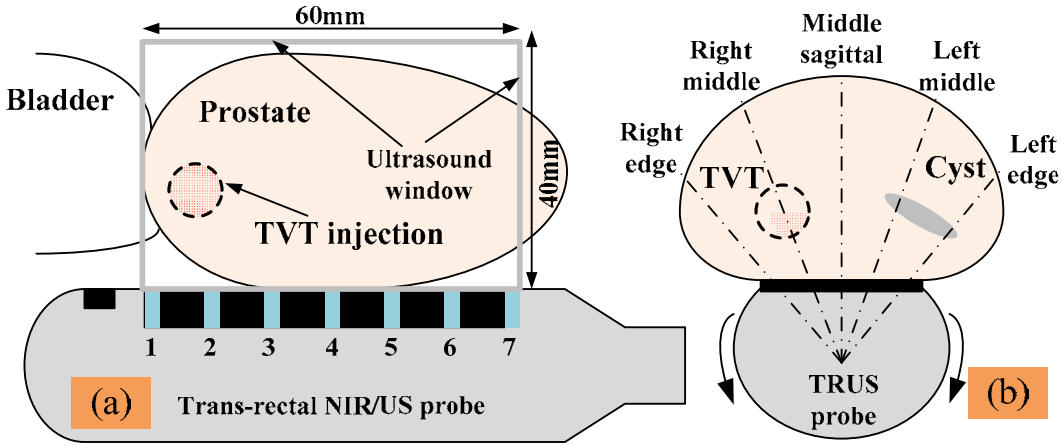

Figure 3 Imaging protocol of trans-rectal NIR and US of canine prostate

3. RESTULS AND DISCUSSIONS

3.1 Development of a transmissible venereal tumor visualized on NIR and TRUS

Shown in Figure 4 are the imaging results, over three weeks, of the right lobe around the site of tumor cell injection. In each column there are Doppler US, TRUS, [HbT] and StO2 images from the top row to bottom row. The optical images of [HbT] and StO2 were set to the same color-bar respectively for comparison. At baseline imaging, there was a hypo-echoic region in TRUS that was suspected as the pelvic lymph node that had a higher [HbT] and a lower StO2 than the prostate. At 7 days post injection, there was an indication of increased blood flow in the periphery of the injection site in the prostate which was consistent in both Doppler US and [HbT]. The region around the infused blood vessel had a higher StO2 than the adjacent prostate region. There was a region of higher [HbT] inside the prostate which was clearly visualized in optical images while unremarkable in TRUS. This region of higher [HbT] became a distinct hypo-echoic region in TRUS image at and after 14 days post injection.

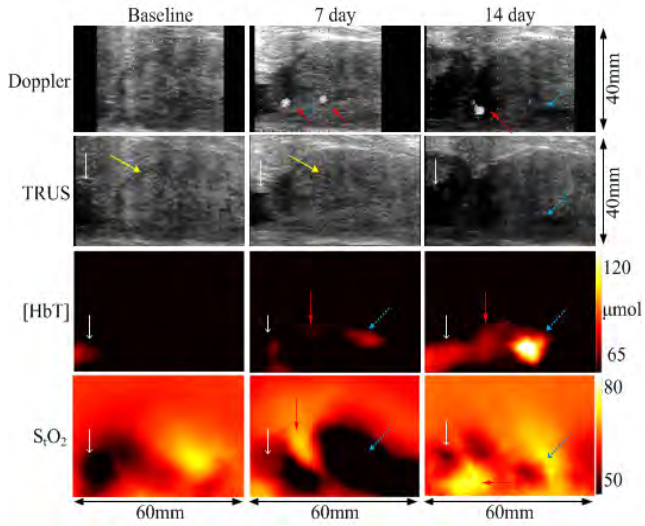

Figure 4 Images of prostate right lobe at baseline, 7 days post-injection and 14 days post-injection.

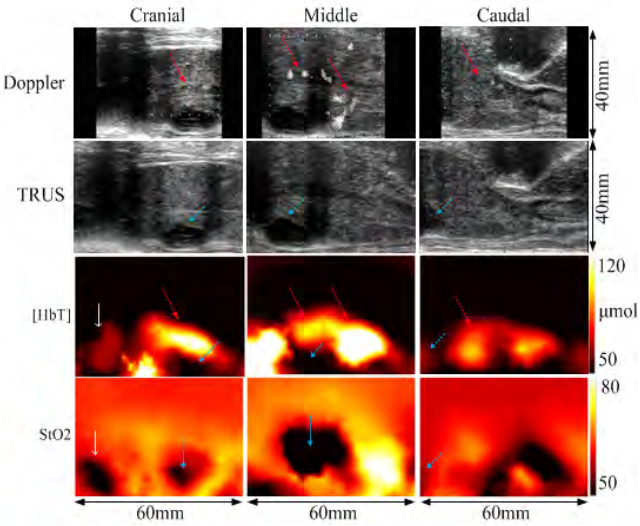

Figure 5 Images of prostate right lobe at 56 days (8-week) post-injection.

At 8 weeks post-injection (Fig. 5), the hypo-echoic region in TRUS images increased in size as a result of the tumor growth. The Doppler ultrasound showed that the blood flow surrounded the tumor, which in optical imaging was presented as a region of high contrast of [HbT] encircling a region of low [HbT], while the StO2 of the region inside the indicated tumor site was low. This pattern of [HbT] and [StO2] indicated that the core of the solid TVT might have become necrotic.

3.2 A contra-lateral native cystic lesion visualized on NIR and TRUS

Figure 6 presents the images of the left lobe of the prostate which was visualized with a cystic region before the inoculation of the TVT cells. Shown in Figure 7 were the images of the cystic lesion taken at the 6th week post-injection. The cyst had consistently shown a moderate [HbT] contrast and significant lower StO2 compared with peripheral normal-appearing prostatic tissue. The region of low StO2 region was slightly greater than the region of higher [HbT] and definitively greater than the region of remarkably hypo-echoic in US.

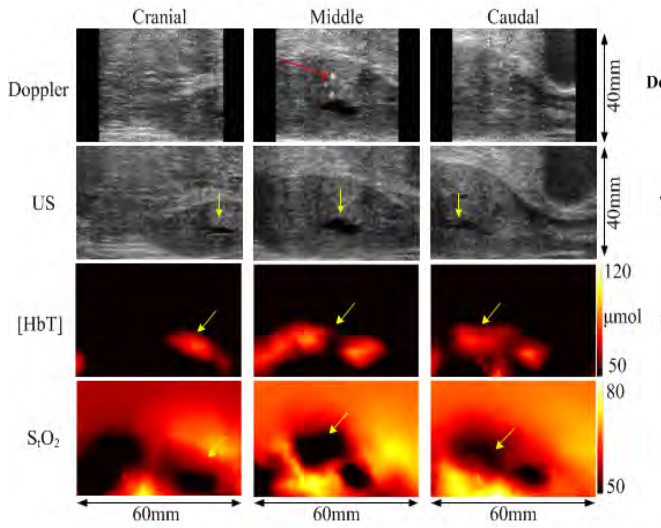

Figure 6 Cysts in the left lobe prostate at three longitudinal locations before tumor cell injection.

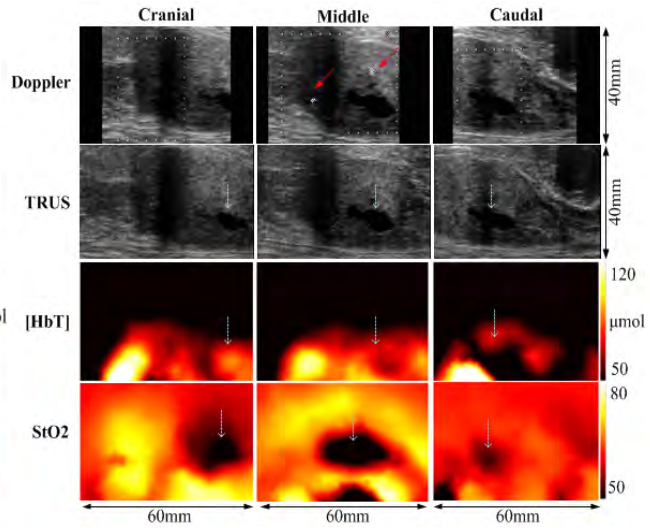

Figure 7 Cysts in the left lobe prostate at three longitudinal locations 42 days after tumor cell injection.

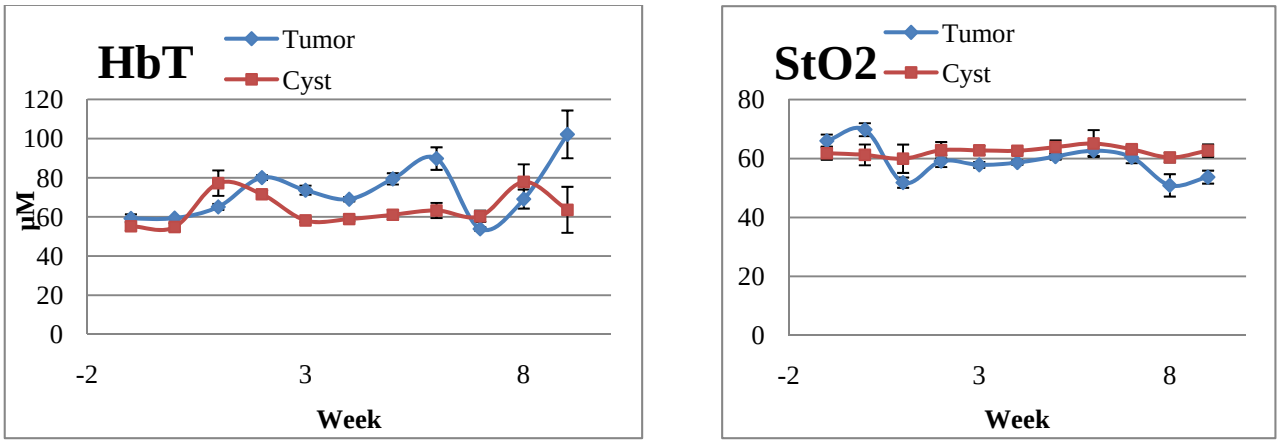

Figure 8 Estimated [HbT] and StO2 in the region of interest of the tumor and cyst.

3.3 Longitudinal changes of hemoglobin and oxygen saturation in regions of tumor and cyst

Average values of [HbT] and StO2 at regions corresponding to the growth of tumor mass and peripheral to the cyst (a circle with 1cm diameter that is approximately 200% of the area of the cyst shown on US) were calculated and compared in Fig. 8. At each weekly measurement, the reconstructed data were evaluated among three longitudinal locations from cranial, middle to caudal sites accordingly to minimize sensitivity issues and artifacts [20]. At the baseline measurement performed over a two week duration before the tumor cell injection, the [HbT] (blue line) indicating the normal prostate tissue had a little higher [HbT] than that indicating the cystic lesion, and also had higher StO2 than that indicating the cystic lesion. After injection of the tumor cells, the [HbT] at both lobes were increased which could have been due to the inflammational response of the prostate.

Around the cystic lesion, the [HbT] increased during the first two weeks after the injection and dropped back to the previous normal level after 4 weeks. In the right lobe at the site of the TVT cell injection, the [HbT] remained high for the following 5 weeks. During week 6 and week 7 the tumor site [HbT] decreased to a value similar to that of the normal tissue. After week 7 the blood supply around the tumor became significantly increased, which was shown as an increased [HbT] in week 8 and week 9 post-injection, while the StO2 decreased during the last four weeks.

3.4 Histological results

The dog was euthanized at 9 weeks post-inoculation of TVT and subjected to thorough gross and histological examination. Metastasis to the regional lymph nodes in the pelvic canal was found. The prostate was excised, and sliced sagittally by free-hand technique at positions approximately the same as those used for in vivo NIR and TRUS monitoring, specifically middle-line, half-way between middle-line and right edge, slightly medial to the right edge, half-way between middle-line and left-edge, and slightly medial to the left edge.

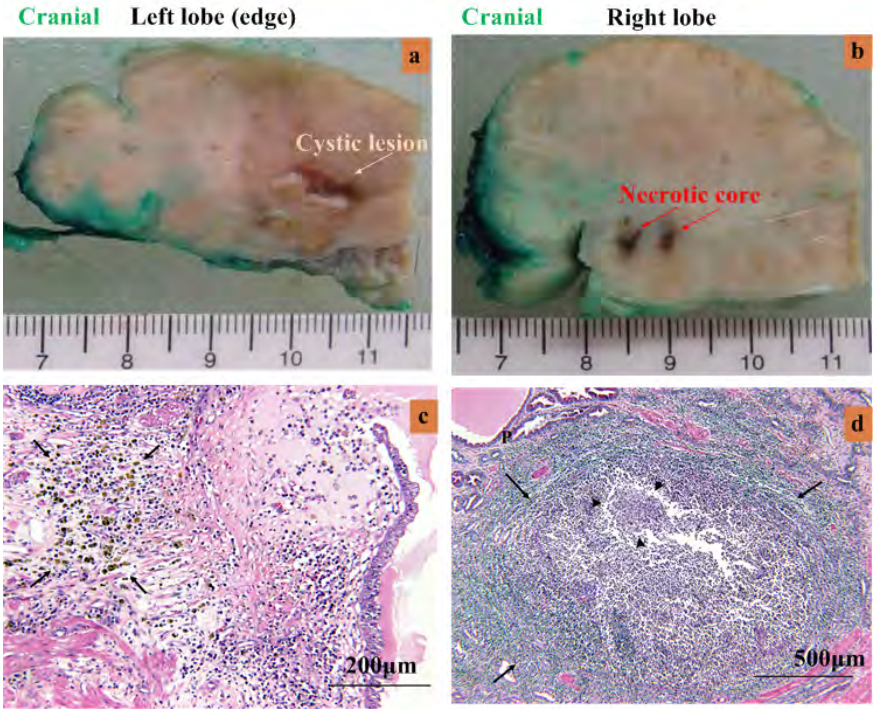

Figure 9 Gross histology and H&E staining results. (a) A cystic lesion confined in the left lobe. (b) The necrotic foci of TVT in the middle aspect of the right lobe. (c) A concentrated infiltrate of hemosiderophages (framed by arrows) indicating old hemorrhage in another region around the prostatic cyst lumen. Bar = 200um. (d) Focus of necrosis within TVT mass in middle of right lobe. Portion of TVT mass outlined by arrows. Central focus of necrosis outlined by arrowheads. Bar = 500um.

A cystic lesion was found in the middle of the left lobe that correlated with a cystic lesion seen during imaging (Fig. 9-a). The right lobe contained primarily TVT tumor masses at dorsal and

slightly cranial regions (Fig.9-b). Histologically, necrotic foci were observed in the solid tumor masses, which supported the minored results of low [HbT] and low [StO2] in the tumor-indicative region in Fig.5. Shown in Fig. 9-c is the H&E image of tissue excised from the periphery of the cystic lesion in Fig. 9-a, wherein a concentrated infiltrate of hemosiderophages (framed by arrows) indicates previous hemorrhage. The necrotic foci of the TVT mass shown in Fig. 9-b were confirmed by H&E staining as illustrated in Fig. 9-d.

SUMMARY

In summary, this work reported the in-vivo optical imaging of both [HbT] and StO2 changes associated with the growth of a TVT tumor in canine prostate during a 9-week time-source, and that associated with a native prostate cystic lesion during the same period of evaluation. This study demonstrated the potential to improve the accuracy of prostate cancer detection by applying multi-wavelength optical spectral measurement to augment the US and Doppler US imaging techniques.

ACKNOWLEDGEMENTS

The study has been supported by DOD Prostate Cancer Research Program through a grant #W81XWH-07-1-0247, and an endowment fund to Bartels from the Kerr Foundation, Oklahoma City, Oklahoma.

REFERENCES

[1] Jemal A, Siegel R, Ward E, Hao YP, Xu JQ, Murray T, Thun MJ, "Cancer Statistics, 2008", CA Cancer J Clin, 58: 71-96 (2008).

[2] A. C. Loch, A. Bannowsky, L. Baeurle, B. Grabski, B. König, G. Flier, O. Schmitz-Krause, U. Paul, and T. Loch, “Technical and anatomical essentials for transrectal ultrasound of the prostate,” World J. Urol.25, 361-366 (2007).

[3] B. W. Pogue, S. P. Poplack, T. O. McBride, W. A. Wells, K. S. Osterman, U. L. Osterberg, and K. D.Paulsen," Quantitative hemoglobin tomography with diffuse near-infrared spectroscopy: pilot results in the breast," Radiology 218, 261-266 (2001).

[4] Tara Yates, Jeremy C Hebden, Adam Gibson, Nick Everdell, Simon R Arridge and Michael Douek, “Optical tomography of the breast using a multi-channel time-resolved imager”, Phys. Med. Biol. 50, 2503–2517 (2005).

[5] S.M.W.Y. van de Ven, W.P.Th.M. Mali, S.G. Elias, A.J. Wiethoff, M. van der Voort, M.B. van der Mark, P. Luijten, “Optical imaging of the breast: clinical research using an experimental Diffuse Optical Tomography system”, MEDICAMUNDI 54/1 (2010).

[6] Jiang Z, Piao D, Xu G, Ritchey JW, Holyoak GR, Bartels KE, Bunting CF, Slobodov G, Krasinski JS, “Trans-rectal ultrasound-coupled near-infrared optical tomography of the prostate Part II: Experimental demonstration,” Optics Express, Vol. 16, Iss. 22, pp. 17505–17520 (2008).

[7] B. Rivera, K. Ahrar, M.M. Kangasniemi, J.D. Hazle and R.E. Price, “Canine Transmissible Venereal Tumor: A Large-Animal Transplantable Tumor Model”, Comparative Medicine, Vol. 55, No. 4 (2005).

[8] Jiang Z, Piao D, Holyoak GR, Ritchey JW, Bartels KE, Slobodov G, Bunting CF, Krasinski JS, "Trans-rectal ultrasound-coupled spectral optical tomography of total hemoglobin concentration enhances assessment of the laterality and progression of a transmissible venereal tumor in canine prostate," Urology, in press.
[9] Bigler SA, Deering RE, Brawer MK, "Comparison of microscopic vascularity in benign and malignant prostate tissue," Hum Pathol.; 24(2):220-6 (1993).
[10] Grant D. Stewart, James A. Ross, Duncan B. Mclaren, Christopher C. Parker, Fouad K. Habib and Antony C.P. Riddick, "The relevance of a hypoxic tumor microenvironment in prostate cancer", BJUI international, 105, 8-13 (2009).
[11] Marie-Fance Penet, Arvind P. Pathak, Venu Raman, Paloma Ballesteros, Dmitri Artemov and Zaver M. Bhujwalla, "Noninvasive Multiparametric Imaging of Metastasis-Permissive Microenvironments in a Human Prostate Cancer Xenograft", Cancer Research; 69-22 (2009).
[12] Venu Raman, Dmitri Artemov, Arvind P. Pathak, Paul T. Winnard, Jr., Stephen Mc Nutt, Anna Yudina, Alexei Bogdanov, Jr., and Zaver M. Bhujwalla, "Characterizing Vascular Parameters in Hypoxic Regions: A combined Magnetic Resonance and Optical Imaging Study of a Human Prostate Cancer Model", Cancer Res 2006; 66-20 (2006).
[13] P. A. Gevenois, M. L. Van Sinoy, S. A. Sintzoff, Jr. B. Stallenberg, I. Salmon, G. Van Regemorter, J. Struyven, "Cysts of the Prostate and Seminal Vesicles: MR Imaging Findings in 11 cases", American Journal of Roentgenology, (1990).
[14] Stephanie van de Ven, Sjoerd Elias, Andrea Wiethoff, Marjolein van der Voort, Anais Leproux, Tim Nielsen, Bernhard Brendel, Leon Bakker, Martin van der Mark, Willem Mali, Peter Luijten, "Diffuse Optical Tomography of the Breast: Initial Validation in Benign Cysts", Mol. Imaging Biol. 11:64Y70 (2009).
[15] Michael Guppy, "The hypoxic core: a possible answer to the cancer paradox", Biochemical and Biophysical Research Communications 299: 676-680 (2002).
[16] Louise C. Enfield, Adam P. Gibson, Nicholas L. Everdell, David T. Delpy, Martin Schweiger, Simon R. Arridge, Caroline Richardson, Mohammad Keshtgar, Michael Douek, and Jeremy C. Hebden, "Three-dimensional time-resolved optical mammography of the uncompressed breast", Applied Optics/Vol. 46, No.17 (2007).
[17] Subhadra Srinivasan, Brian W. Pogue, Hamid Dehghani, Shudong Jiang, Xiaomei Song, Keith D. Paulsen, "Improved quantification of small objects in near-infrared diffuse optical tomography", Journal of Biomedical Optics 9(6), 1161-1171 (2004).
[18] David A. Boas, Anders M. Dale, and Maria Angela Franceschini, "Diffuse optical imaging of brain activation: approaches to optimizing image sensitivity, resolution and accuracy", NeuroImage 23, S275-S288 (2004).
[19] Karen Briley-Saeb and Atle Bj rnerud, "Accurate de-oxygenation of ex vivo whole blood using sodium Dithionite", Proc. Intl. Soc.Mag. Reson. Med. 8 (2000).
[20] Xu G, Piao D, Musgrove CH, Bunting CF, Dehghani H, "Trans-rectal ultrasound-coupled near-infrared optical tomography of the prostate Part I: Simulation," Optics Express, Vol. 16, Iss. 22, pp. 17484–17504 (2008).

Optical Biopsy of the Prostate: Can We TRUST (Trans-Rectal Ultrasound-coupled Spectral Tomography)?

Daqing Piao,[1*] Zhen Jiang, [1#] Kenneth E. Bartels,[2] G. Reed Holyoak,[2] Jerry W. Ritchey,[3] Kendra Rock,[2] Charlotte L. Ownby,[4] Charles F. Bunting,[1] Gennady Slobodov[5]

1 * School of Electrical and Computer Engineering, Oklahoma State University, Stillwater, OK, USA
Department of Biomedical Engineering, Washington University in St. Louis, St. Louis, MS, USA
2. Department of Veterinary Clinical Sciences, Oklahoma State University, Stillwater, OK, USA.
3. Department of Veterinary Pathobiology, Oklahoma State University, Stillwater, OK, USA.
4. Microscopy Laboratory, Oklahoma State University, Stillwater, OK, USA.
5. Department of Urology, University of Oklahoma Health Sciences Center, Oklahoma City, OK, USA.
* Correspondence: School of Electrical and Computer Engineering, 202 Engineering South, Oklahoma State University, Stillwater, OK 74078-5032 (telephone: 405-744-5250; FAX: 405-744-9198; e-mail: daqing.piao@okstate.edu).

Abstract: Needle-based core-biopsy to locate prostate cancer relies heavily upon trans-rectal ultrasound (TRUS) imaging guidance. Ultrasonographic findings of classic hypoechoic peripheral zone lesions have a low specificity of ~28%, a low positive predictive value of ~29%, and an overall accuracy of ~43%, in prostate cancer diagnosis. The prevalence of isoechoic or nearly invisible prostate cancers on ultrasonography ranges from 25 to 42%. As a result, TRUS is useful and convenient to direct the needle trajectory following a systematic biopsy sampling template rather than to target only the potentially malignant lesion for focal-biopsy. To address this deficiency in the first-line of prostate cancer imaging, a trans-rectal ultrasound-coupled spectral tomography (TRUST) approach is being developed to non-invasively resolve the likely optical signatures of prostate malignancy. The approach has evolved from using one NIR wavelength to two NIR bands, and recently to three bands of NIR spectrum information. The concept has been evaluated on one normal canine prostate and three dogs with implanted prostate tumor developed as a model. The initial results implementing TRUST on the canine prostate tumor model includes: (1) quantifying substantially increased total hemoglobin concentration over the time-course of imaging in a rapidly growing prostate tumor; (2) confirming hypoxia in a prostatic cystic lesion; and (3) imaging hypoxic changes of a necrotic prostate tumor. Despite these interesting results, intensive technologic development is necessary for translating the approach to benefiting clinical practice, wherein the ultimate utility is not possibly to eliminate needle-biopsy but to perform focal-biopsy that is only necessary to confirm the cancer, as well as to monitor and predict treatment responses.

I. INTRODUCTION

Prostate cancer has been the second leading cause of cancer death in American men over a decade. In US alone an estimated 190,000 new prostate cancer cases occurred during 2010, and

Optical Biopsy IX, edited by Robert R. Alfano, Stavros G. Demos,
Proc. of SPIE Vol. 7895, 78950I · © 2011 SPIE · CCC code: 1605-7422/11/$18 · doi: 10.1117/12.876527

an estimated 27,000 patients died from prostate cancer in 2010 [1]. The first-line screening of prostate cancer depends upon digital rectal examination (DRE) and prostate specific antigen (PSA) blood test in asymptotic men. The reported sensitivity, specificity, and positive predictive value for PSA were 72.1%, 93.2% and 25.1%, respectively; and for DRE were 53.2%, 83.6% and 17.8%, respectively [2]. Abnormal DRE or PSA test, when raising the suspicion of prostate cancer, is usually followed by an invasive evaluation of the prostatic tissue by trans-rectal ultrasound (TRUS) guided core-needle biopsy. During the biopsy, an 18 gauge needle is directed under TRUS imaging to systematically selected positions, most often 12-18 of them, to extract tissue samples for pathological examination. The need of multi-core needle biopsy in prostate is prompted partially by the diffusiveness and multi-focal appearance of prostate cancer [3], but largely by the inability of TRUS in accurately distinguishing prostate cancer from benign prostatic lesion based on the sonographic features. Ultrasonographic findings of classic hypoechoic peripheral zone lesions have a low specificity of ~28%, a low positive predictive value of ~29%, and an overall accuracy of ~43%, in prostate cancer diagnosis [4-6]. The prevalence of isoechoic or nearly invisible prostate cancers on ultrasonography ranges from 25 to 42% [7]. As a result, TRUS is useful and convenient to direct the needle trajectory following a systematic biopsy sampling template rather than to target only the potentially malignant lesion foci for focal-biopsy.

There is a need to develop a less invasive, ideally non-invasive, imaging technique for detection of prostate cancer that may be utilized in the first-line screening stage for improving the accuracy of focal-biopsy. Non-invasive detection entails identifying the signatures of tissue that can be interrogated noninvasively by specific mechanisms, such as by applying electromagnetic or other type of radiation. One of such signatures may associate with optical interrogations. Native optical signature of tissues is produced by the light scattering and absorption properties of the tissue, due to changes in blood concentration, nuclear size distribution, epithelial thickness, and collagen content [8]. For more than two decades, optical methods, by way of spectroscopy, tomography, or a combination of both, have been widely explored for non-invasive detection of the onset and progression of disease including pre-malignancy and malignancy as well as other pathological conditions [9-12]. These reported studies indicate that optical spectroscopy has potential to improve screening and early detection of cancer. This work discusses the application of diffuse optical spectral tomography, combined with TRUS, in exploring the optical signatures of malignant prostatic tissues.

II. DIFFUSE OPTICAL TOMOGRAPHY FOR PROSTATE IMAGING

A. Diffuse optical tomography in the context of probing the prostatic optical properties

Diffuse optical technique refers to the use of photons undergoing many scattering events to obtain the measurement of optical properties in deep tissue volumes for the ultimate purpose of investigating tissue physiology. When depth-resolved cross-sectional image is the endpoint of visualization, it is specified as diffuse optical tomography (DOT) [9-12]. DOT is becoming increasingly interesting and important for functional imaging in biological tissues [12]. DOT relays on non-invasive or minimally-invasive administration of light in near-infrared (NIR, 650-900nm) spectral window. The relatively weak NIR absorption in water allows photon propagation into deep tissue volumes. The stronger NIR absorption of hemoglobin as compared

to other tissue constituents such as water provides intrinsic contrast between blood and parenchymal tissues [13]. The distinct cross-over feature of NIR absorption by hemoglobin between oxygenated and deoxygenated states enables direct quantification of tissue oxygenation [14] by use of as few as two wavelengths at the both sides of and close to the isosbestic point of hemoglobin. The integrative outcome of utilizing NIR light has been obtaining optically-expressed physiological contrasts, due to differences in micro-vessel density, tissue oxygenation, and changes of water or lipid concentrations, in deep tissue volumes by non-ionizing optical interrogation. Such physiological contrasts offer specific and often sensitive indications of tissue metabolic changes and malignancies at both macroscopic and microscopic scales.

Although biological tissue is a weak absorber of NIR light, it is a strong NIR scatterer owing predominantly to the μm-scale intracellular organelles. NIR light becomes essentially diffuse after a few millimeters away from the point of a directional launching in typical soft biological tissue where single scattering event may occur at a scale of 100 μm or less [15]. The NIR diffuse propagation makes it feasible to interrogate tissue volume that is much wider than the direct geometric sensing region between light illumination and collection positions, and much deeper than the depth achieved by optical imaging methods where coherent photons are utilized as in optical coherence tomography [16] and low-coherence enhanced backscattering [17]. However, DOT is apparently not a choice of whole-body imaging for human due to NIR's limited penetration of several centimeters in soft tissue and strong attenuation by bone. Nonetheless, in many cases DOT can perform relatively large-scale imaging for tissues or organs comparable to the size of breast, including some internal organs such as the prostate. When compared with imaging modalities wherein ballistic illumination-detection path is employed for organ-level imaging such as X-ray CT, DOT requires less number of illumination and measurement channels in order to measure the same volume of tissue. However, due to the loss of precise location information in DOT due to diffusive photon propagation, the direct information that DOT measurement seeks to acquire is the tissue optical property, in low spatial resolution, such as absorption coefficient and reduced scattering coefficient, upon which the relevant contrasts of physiological parameters may be retrieved.

Near-infrared DOT is shown particularly useful over the past decades for functional imaging of biological tissues where scattering of the photons dominates and where NIR contrast based on intrinsic chromophore content or exogenous probe can be linked to tissue physiology such as angiogenesis, oxygen deprivation or over-expression of specific biomarkers. Considerable promising outcomes of NIR optical tomography are reported in diagnosis of breast cancer [10], understanding of cortex response [12], and characterization of rheumatologic dysfunction [18, 19], in which all the tissues under imaging are interrogated externally by non-invasive method. In terms of the utility of NIR tomography in internal imaging regime, there is however limited information available. Interstitial measurement by use of diffuse or near-diffuse photons has been employed for monitoring of photodynamic responses in organs such as prostate [20]. From the diagnostic perspective, the most appealing feature of NIR tomography may be arguably its unique functional contrast that is obtained non-invasively. Recently there are increased interests toward understanding the challenges and benefits of non-invasive NIR optical tomography of internal organs, in particular imaging the prostate [21, 22]. Such increased interest is prompted by the evidence that prostate cancer development is associated with angiogenesis [23] and NIR

imaging may provide non-invasive assessment of prostate cancer. Capability of non-invasive prostate imaging by optical means will likely enable the study of prostate optical properties, and augment current diagnostics if the optical properties of prostate cancer are found to have substantial contrast with respect to those of normal prostate tissues.

B. Diffuse optical tomography in the context of ultrasound-coupled or guided imaging

The spatial information of NIR DOT is compromised by the diffusive photon propagation and the resulted ill-posed iterative image reconstruction. Combining DOT with other imaging modalities that are anatomically accurate has proven effective in firstly correlating the DOT functional contrast with the spatial anatomy of the lesion, and secondly using the structural delineation of the lesion, if the lesion profile can be defined accurately, to guide and constrain the DOT image reconstruction to characterize the optical properties of the lesion for augmenting the diagnosis. In terms of the morphological imaging modalities that can be cohesively integrated with DOT for complimentary imaging, of breast and prostate etc, one excellent choice is ultrasound.

Ultrasound imaging is frequently used as an adjunct tool in cancer detection for differentiating cysts from solid lesions, and it plays an important role in guiding interventional procedures such as needle aspiration and core needle biopsy [24]. Several studies have been reported on the technology of combining DOT with US, for breast cancer detection [24-27]. A system developed in University of Connecticut is implemented by simultaneously deploying optical sensors and a commercial US transducer mounted on a hand-held probe, and utilizing co-registered lesion structure information provided by US to improve the inverse optical imaging reconstruction. The hand-held hybrid probe consists of a commercial US transducer located in the center and the NIR source detector fibers distributed at the periphery. The NIR imager consists of 12 pairs of dual-wavelength (780 and 830 nm) laser diodes for measurement of total hemoglobin and eight photomultiplier tubes (PMTs) for detection. In that system, the NIR reconstruction takes advantages of US localization of lesions and segments the imaging volume into a finer grid in lesion region and a coarser grid in nonlesion background region. A modified Born approximation is used to relate the scattered field measured at each source and detector pair to total absorption variations at wavelength in each volume element of two regions within the sample. The absorption distribution at each wavelength is obtained by dividing total absorption distribution changes of lesion and background regions, respectively, by different voxel sizes in lesion and background tissue regions. This dual-mesh scheme results in well conditioned inversion and convergence of the image reconstruction in a few iterations [28]. The studies of DOT/US of breast have provided strong evidence that NIR DOT's functional imaging capability. For an early-stage invasive ductal carcinoma [24], US showed a nodular mass with internal echoes and the lesion was considered suspicious. The lesion, by DOT imaging, was measured with maximum total hemoglobin concentration of 122 mmol/L. The average measured total hemoglobin concentration within full width and half maximum (FWHM) is 91 mMol/L, and the measured average background hemoglobin concentration is 14 mMol/L.

III. APPROACHES OF TRANSRECTAL ULTRASOUND-COUPLED SPECTRA TOMOGRAPHY (TRUST)

The studies of combined DOT/US in breast cancer imaging have encouraged the development of combined DOT/US for prostate cancer imaging. A trans-rectal spectral NIR/US probe and imager are developed [29] and shown in Fig. 1. The TRUS probe having a bi-plane sector (5MHz for axial imaging) and linear array (7.5MHz for sagittal imaging) transducer is compatible to a portable ALOKA SSD-900V unit and a standard ALOKA SSD-3500 scanner. The NIR applicator was integrated over the 7.5MHz sagittal-imaging transducer. The NIR source and detector array, each having 7 channels, were 60mm in longitudinal dimension, which was identical to the longitudinal length of the sagittal US transducer. The light sources used for NIR tomography in this system have undergone three stages toward improved spectral information in the acquired optical properties. In the first stage, which was used for the imaging of our first and second canine subjects, a super-luminescent diode of 100mW at 840nm was used. In the second stage, which was used for the imaging of our third canine subject, the light sources used were two laser diodes at 785nm and 830nm. In the third stage, which was used for the imaging of our fourth canine subject, three laser diodes were implemented at 705nm, 785nm, and 808nm. The source lights, via single fiber for one source or multiply-branched fiber-bundle for multiple sources, were focused sequentially onto 7 source fibers of the NIR applicator by a home-made translating fiber multiplexer based on a linear motorized translations stage. The spectral NIR remissions collected by the 7 detection fibers were acquired by a 16-bit intensified CCD camera of 12.4x12.4mm^2 in chip-size through a 300mm spectrometer. Acquisition of NIR signals from the 7 source channels took less than 4 seconds after the plane of view of imaging in the prostate was localized by the sagittal US. The absorption and reduced scattering coefficients of the prostate were reconstructed from steady-state measurements, which are then used to derive information such as total hemoglobin and oxygen saturation, as detailed in Table 1.

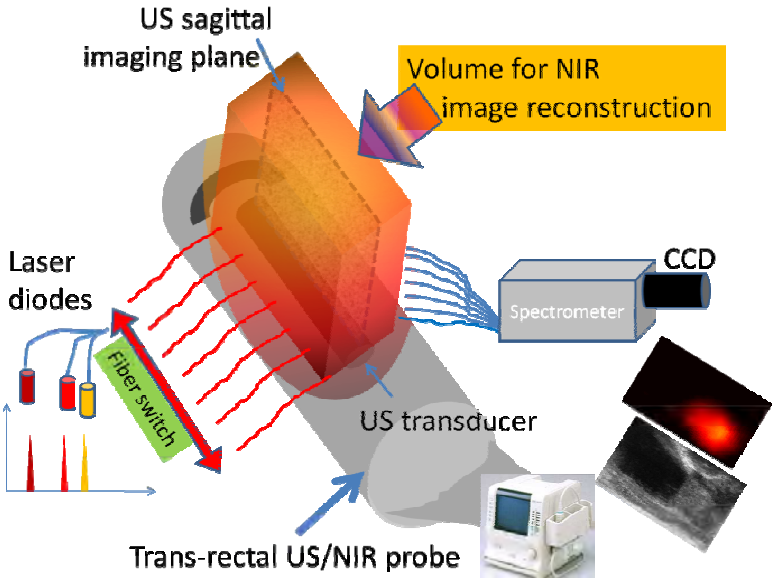

Fig. 1 Schematic configurations of the spectral trans-rectal DOT coupled with TRUS

Table 1. Configurations of the trans-rectal DOT for the studied of four dog subjects.

Configurations of the trans-rectal DOT for the studies of four dogs				
	#1 (Cooper)	**#2 (Spencer)**	**#3 (Buck)**	**#4 (Duke)**
Near-infrared wavelengths utilized	840 nm (14nm FWHM)	840 nm (14nm FWHM)	785 nm 830nm	705 nm 785 nm 808 nm
Light source	MM-coupled Super-luminescent	MM-coupled Super-luminescent	Laser diode	Laser diode
Operation mode	Continuous-wave	Continuous-wave	Continuous-wave	Continuous-wave
Detection method	(Spectrometer)/ intensified CCD	(Spectrometer)/ intensified CCD	Spectrometer/ intensified CCD	Spectrometer/ intensified CCD
Image reconstruction	Based on NIRFAST	Based on NIRFAST	Based on NIRFAST	Based on NIRFAST
Parameters reconstructed	$\mu_a(\lambda)$ $\mu_s'(\lambda)$	$\mu_a(\lambda)$ $\mu_s'(\lambda)$	$\mu_a(\lambda)$ $\mu_s'(\lambda)$	$\mu_a(\lambda)$ $\mu_s'(\lambda)$
Parameters derivable			[HbT] $[S_tO_2]$	[HbT] $[S_tO_2]$ [???]
Measurements calibrated			[HbT]	[HbT] $[S_tO_2]$

IV A DOG MODEL OF PROSTATE CANCER FOR EVALUATING TRANSRECTAL SPECTRAL OPTICAL TOMOGRAPHY

A. Canine transmissible venereal tumor for evaluating prostate imaging

Large animal models for human prostatic studies are limited. Dog is considered an acceptable model as the prostate develops abscesses, cysts, benign hyperplasia, and neoplasia as human prostate do [30]. The neoplasia of dog prostate shares some morphological similarities to that of human prostate. The similarities include metastatic pattern, increased occurrence of adenocarcinoma with age, occurrences in sexually intact males, etc. However, canine prostatic carcinoma cell lines are limited in numbers available. Lines recently derived from canine prostatic carcinoma include DPC-1 [31], CT1258 [32], which were maintained in severe combined-immunodeficiency (SCID) mice or tumergenetic medium.

Canine transplantable or transmissible venereal tumor (TVT) [30] known to have a viral etiology has been specified as effective for evaluating imaging techniques. The unique canine TVT is a round cell tumor of dogs that mainly affects the external genitalia and can be transmitted from animal to animal during copulation, regardless of histocompatibility. It can be propagated in immune-compromised mice and transferred to different tissues of the dog to result in a neoplastic mass effect very useful for imaging studies. Studies have shown development or metastasis of canine TVT in prostate, lung, hepatic lymph node, lumbar paraspinal muscle [30], etc. In canine

prostate, the signal intensity of the TVT in T2-weighted image was similar to that of the normal prostate tissue, resulting in an inability to completely discern tumor boundaries. The signal intensity of the TVT in T1-weighted MR image obtained after gadolinium administration rendered the margin of the tumor partially discernable because the TVT enhanced less than did the surrounding prostatic tissue [30].

Photomicrograph of canine TVT in the prostate has shown tumor groups of individual pleomorphic histiocytic neoplatic round cells. The tumor is shown expansile. The groups of tumor are usually separated by a distinct, reticulated, delicate network of fibrovascular septa. The TVT in morphology is characterized by distinct tumor boundary, higher density than normal tissue, large hyperchromatic nucleus, and single conspicuous nucleoulus. All these features, when being interrogated by NIR light, are expected to generate different NIR absorption and scattering contrasts. However, the optical contrasts obtained from TVT may not necessarily represent those from prostate carcinoma because of the difference between the round-cell tumor and adenocarcinoma. But nonetheless, the canine prostate TVT model would be sufficient for evaluating the imaging characteristics of trans-rectal spectral tomography in distinguishing malignant from benign and normal prostatic tissue.

B. Animal Protocol

The animal protocols implemented in these studies involve canine species for implanting the tumor cells in prostate and rodent species for maintaining the viability of the cell-lines. These animal protocols were approved by the Institutional Animal Care and Use Committee of Oklahoma State University. The canine protocol was also approved after an on-site inspection by the U.S. Army Medical Research and Material Command.

For all studies involving dog species, sexually intact male dogs were used after minimum 2 weeks of baseline monitoring. The TVT cell line was obtained from M.D. Anderson Cancer Center through a biological material transfer agreement. The TVT cell lines were propagated in non-obese-diabetic/severe combined-immunodeficiency (NOD/SCID) mice. The neoplastic TVT cells were recovered and homogenized for injection into the canine prostate gland parenchyma. For each study, 2-3 cc suspension of approximately 2.5×10^6 cells/mL of homogenized TVT cells were aseptically injected trans-perineally into the right lobe of the prostate using a 6-in. 16-gauge hypodermic needle. The injected tumor cells were confirmed by TRUS using the above-mentioned bi-planar transducer. Figure 2 illustrated the harvested TVT tumor before homogenization (a), the homogenized TVT cells housed in syringe (b), the injection of the TVT cells to canine prostate (c), and the TRUS visualization of the injection needle in the prostate (d). In all studies the TVT cells were confined in the right prostatic lobe during injection. Post-injection monitoring, besides trans-rectal NIR tomography, included physical rectal examination, and grey-scale TRUS in all studies, and Doppler US for canine subject 3 and 4. The studies all involved gross necropsy and histological examinations after humanly euthanizing the subject.

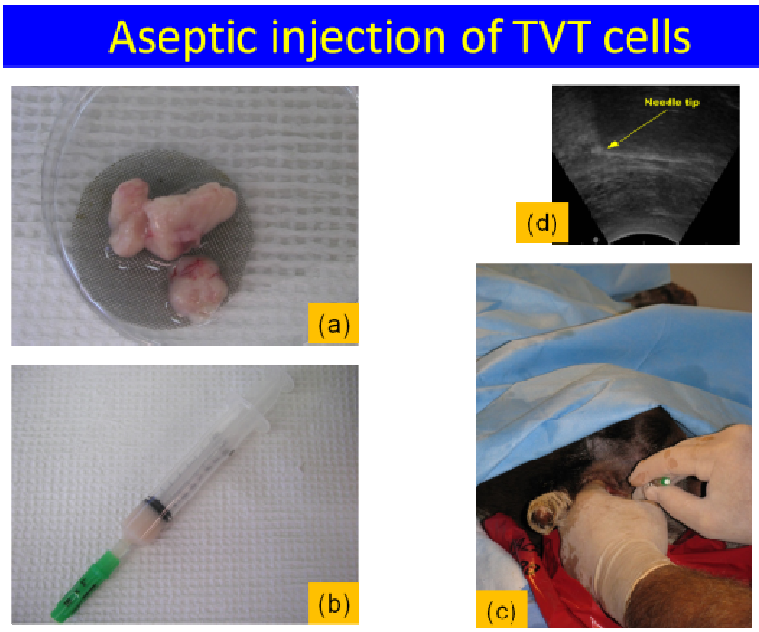

Figure 2. Process of preparing TVT for injection into canine prostate.

Table 2. Configurations of the TRUS and DOT for the studied of four dog subjects.

Configurations of the trans-rectal US and DOT for the studies of four dogs				
	#1 (Cooper)	#2 (Spencer)	#3 (Buck)	#4 (Duke)
TRUS scanner	SSD 900 	SSD 3500 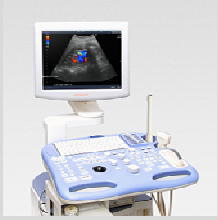	SSD 3500 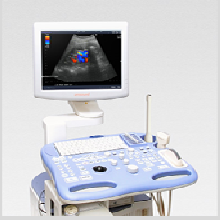	SSD 3500 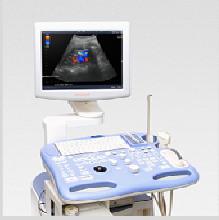
Sagittal field of view	50mm (60mm-long transducer)	60mm (60mm-long transducer)	60mm (60mm-long transducer)	60mm (60mm-long transducer)
US mode	Grey-scale	Grey-scale	Grey-scale Doppler later	Grey-scale & Doppler
DOT reconstruction	$\mu_a(\lambda)$ $\mu_s'(\lambda)$	$\mu_a(\lambda)$ $\mu_s'(\lambda)$	[HbT]	[HbT] $[S_tO_2]$
Trans-rectal DOT wavelengths utilized	840 nm	840 nm	830nm 785 nm	808nm 785nm 705 nm

V. RESULTS

The comparisons of the study designs for the four canine subjects as well as the most prominent differences in the tumor development among the canine subjects are summarized in Table 3.

Subject 1.
The subject 1 underwent TVT injection, however, the TVT growth was not observed, and therefore it became a control. In necropsy at 9-wweks post-injection, the prostate gland exhibited diffuse, symmetrical (and mild) enlargement (4.5cm× 4.5cm×2.5cm). On cross-section, the tissue was grossly normal with the exception of a discrete, 0.5cm in diameter focus of grey/tan tissue located in the region of the right prostatic lobe. Histologically, this focus corresponded to moderate interstitial fibrosis with infiltration by primarily lymphocytic inflammatory cells. The remainder of the prostatic tissue exhibited diffuse slight enlargement of the prostatic epithelium with occasional papillary projections and cystic dilation of prostatic glands consistent with early benign prostatic hyperplasia/hypertrophy. Otherwise, the tissue was histologically unremarkable. The histological results confirmed that the NIR optical contrasts presented in this work are of a normal canine prostate [33].

Subject 2.
The TVT injection to subject 2 differs from the rest in that the TVT cells were seeded along the needle track during needle retraction. The gross and histological findings (8-week post-injection) confirmed intra- and peri-prostatic neoplastic infiltrates with masses also located along the urethra and peri-rectal tissue; the latter related to dissemination along the needle track during TVT inoculation. All masses consist of diffuse sheets of a monomorphic population of neoplastic round cells dissecting through pre-existing fibrovascular stroma. The neoplastic cells have large hyperchromatic nuclei, single conspicuous nucleoli and moderate amounts of featureless cytoplasm. The cytological features are consistent with canine TVT [34].

Subject 3.
The TVT was injected at two locations in the right aspect of the prostate of this dog, one in the cranial aspect, one close to the middle aspect. In necropsy performed 8-weeks post-injection, the excised prostate was approximately 10×5×5cm3 in size. The prostate was serially sectioned in the conventional transverse orientation in ~1.5cm slices. The gross examination confirmed multiple coalescing foci of TVT in the caudal-aspect of the gland, and significant infiltration of the tumor from right to the left lobes. After fixation in 10% buffered formalin, the prostatic sections were again closely examined. On one slice corresponding to the left-caudal-aspect of the gland, a small pocketof normal prostatic tissue surrounded by multi-foci TVT was noted. Indication of similar morphology was seen as demarcated on the sagittal NIR image obtained at similar time as a region of base-line [HbT] enclosed by heterogeneous hyper-[HbT] masses. The simultaneously obtained sagittal Doppler US revealed substantially enhanced blood supply ventral to the heterogeneously hypo-echoic mass [35].

Table 3. Study designs for and the outcomes of the four dog subjects.

Summary of the studies of the four dogs				
	#1 (Cooper)	**#2 (Spencer)**	**#3 (Buck)**	**#4 (Duke)**
	Adult male, sexually intact			
Class	B	A	B	B
Species	German short-hair	Beagle	Foxhound	Foxhound
Age (yrs)	~4	4	~6	~7
Weight (lbs)	22		27	27
	General anesthesia, non-immune suppressed			
Injected amount	2 cc ($5x10^7$ cells)	3 cc	2 cc ($5x10^6$ cells)	2 cc ($2.5x10^6$ cells)
Injection site (right lobe)	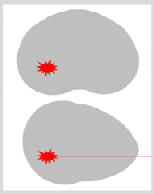	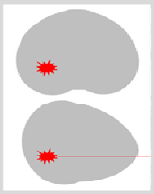	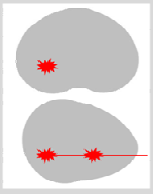	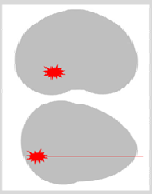
Post-injection study (days)	10, 20, 30, 40	14, 35, 42, 49	7, 14, 21, 31, 38, 45	7, 14, 21, 28, 35, 42, 49, 56, 63
Day of euthanasia	63	56	55	63
Gross examination	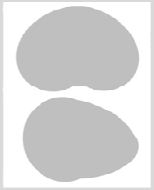	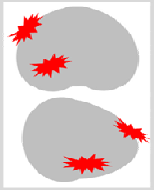	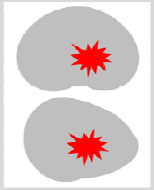	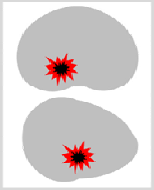
Histology	Unremarkable /benign	Multi-focal masses	Infiltration to the left lobe	Necrosis

Subject 4.

The subject 4 was presented in base-line imaging with a large cystic lesion at the left aspect of the prostate. The study design therefore was benefited from a course-long contra-lateral

comparison of the expected development of the tumor in the right aspect versus any anatomic changes of the cystic lesion in the left aspect. The tumor developed in the right aspect was revealed sonographically after 7-weeks post-injection that the tumor mass reduced indicating regression or necrosis, comparing with a relatively stable volume of the cystic lesion in the left aspect. In spectral DOT, the tumor mass presented with substantially increased [HbT] in the periphery, with an area of reduced StO2 less than the area of the mass itself shown on ultrasonography. Conversely, in spectral DOT, the cystic lesion presented with slightly increased [HbT] in the periphery of the lesion shown on ultrasound with oxygen-reduction inside and in the periphery of the lesion. There was no detectable change of blood flow on Doppler US in the periphery of the cystic lesion. In necropsy performed 9weeks post-injection, the right lobe contained primarily TVT tumor masses at dorsal and slightly cranial regions. Histologically, necrotic foci were observed in the solid tumor masses, which agreed with the monitored results of low [HbT] and low [StO2] in the tumor-indicative region by spectral DOT. The necropsy also confirmed the cystic fluid occupying the region indicative of cyst on ultrasound [36].

VI. SUMMARY

A trans-rectal ultrasound-coupled spectral tomography (TRUST) approach is being developed to non-invasively resolve the likely optical signatures of prostate malignancy. The approach has evolved from using one NIR wavelength for mapping the absorption and scattering heterogeneities in prostate, to two NIR bands for extracting total hemoglobin heterogeneities in prostate, and to three bands of NIR spectrum information that was useful for mapping the oxygen saturation in addition to total hemoglobin concentration. The approach of using spectral optical tomography to discover optical signatures of malignant prostatic tissue has been evaluated on one normal canine prostate and three dogs with implanted TVT tumor in the prostate. Wavelength-specific reconstruction of the absorption and scattering properties demonstrated contrasts in the optical properties of malignant and normal tissue. Absorption properties reconstructed at multiple wavelengths were used to derive the total hemoglobin and oxygen saturation. These information additionally indicated the potential optical signatures of malignant prostatic tissue, as suggested by the findings of trans-rectal spectral DOT include: (1) substantially increased total hemoglobin concentration was observed over the time-course of imaging in a rapidly growing prostate tumor; (2) hypoxia in a prostatic cystic lesion was observed with the region of the reduced oxygenation greater than the area of the cyst-indicative region on ultrasound; and (3) hypoxic core of a necrotic prostate tumor was observed with the region of the reduced oxygenation smaller than the area of the tumor-indicative region on ultrasound.

Despite these interesting results, intensive technologic development is necessary for translating the approach to clinical practice. The challenges lie in reducing the size of the combined NIR/US applicator, incorporating more wavelengths for more spectral information, enabling three dimensional ultrasound for providing accurate spatial reconstruction prior to trans-rectal DOT, accelerating the trans-rectal DOT image formation, discovering the optical signatures of prostate adenocarcinoma, etc. The ultimate utility of this approach of trans-rectal spectral DOT combined or guided with US, is not possibly to eliminate needle-biopsy but to perform focal-biopsy that is only necessary to confirm the cancer, as well as to monitor and predict treatment responses.

ACKNOWLEDGEMENTS

The study has been supported in part by DOD Prostate Cancer Research Program through a grant #W81XWH-07-1-0247, and an endowment fund to Bartels from the Kerr Foundation, Oklahoma City, Oklahoma.

REFERENCES

1. Jemal A, Siegel R, Xu J, and Ward E. "Cancer statistics, 2010," CA Cancer J Clin.; 60(5):277-300 (2010).
2. Mistry K and Cable G, "Meta-analysis of prostate-specific antigen and digital rectal examination as screening tests for prostate carcinoma," J Am Board Fam Pract.; 16(2):95-101 (2003).
3. Hodge KK, McNeal JE, Stamey TA, "Ultrasound guided transrectal core biopsies of the palpably abnormal prostate," J Urol.; 142(1):66-70 (1989).
4. Wise AM, Stamey TA, McNeal JE, and Clayton JL, "Morphologic and clinical significance of multifocal prostate cancers in radical prostatectomy specimens," Urology 60: 264-9 (2002).
5. Garber SJ, Goldenberg SL, Cooperberg PL, Wong AD, Bilby JH, and Mathieson JR, "Systematic transrectal ultrasound-guided biopsy of the prostate," Can Assoc Radiol J.; 45(5):387-90 (1994).
6. Downs TM, Grossfield GD, Shinohara K, and Carroll PR, "Transrectal ultrasound-guided prostate biopsy," in Image-Guided Diagnosis and Treatment of Cancer, edited by D'Amico AV, Loefler JS, Harris JR,Human Press, 2003.
7. Ellis WJ and Brawer MK, "The significance of isoechoic prostate carcinoma," J. Urol,; 152: 2304-2307 (1994).
8. Benaron DA, "The future of cancer imaging," Cancer metastasis Rev.; 2:45-78 (2002).
9. Gibson AP, Hebden JC, and Arridge SR, "Recent advances in diffuse optical imaging," Physics in Medicine and Biology, 50(4): R1-R43 (2005). Review.
10. Hielscher AH, et al., "Near-infrared diffuse optical tomography," Disease Markers, 18: 313-337 (2002). Review.
11. Ntziachristos V, and Chance B, "Probing physiology and molecular function using optical imaging: applications to breast cancer," Breast Cancer Res.; 3(1): 41-46 (2001). Review.
12. Hillman EM, "Optical brain imaging in vivo: Techniques and applications from animal to man," J. Biomed Optics, 12(5): 051402-051402-28 (2007). Review.
13. Yodh AG and Chance B, "Spectroscopy and imaging with diffusing light," Physics Today, 48(3): 34-40 (1995).
14. Heffer E, et al., "Near-infrared imaging of the human breast: complementing hemoglobin concentration maps with oxygenation images," J. Biomed. Opt., 9(6): 1152-1160 (2004).
15. Rolfe P, "In vivo near-infrared spectroscopy," Ann. Rev. Biomed. Eng., 2: 715-754 (2000). Review.
16. Huang D, et al., "Optical coherence tomography," Science, 254: 1178-1181 (1991).
17. Kim YL, et al., "Low-coherence enhanced backscattering: review of principles and applications for colon cancer screening," J. Biomed. Opt., 11: 041125 (2006). Review.

18. Scheel AK, et al., “First clinical evaluation of sagittal laser optical tomography for detection of synovitis in arthritic finger joints,” Annals of the Rheumatic Diseases, 64: 239-245 (2005).
19. Yuan Z, et al., “Three-dimensional diffuse optical tomography of osteoarthritis: initial results in the finger joints,” J. Biomed Opt,, 12: 034001-034001-11 (2007).
20. Yu G, et al, “Real-time in situ monitoring of human prostate photodynamic therapy with diffuse light,” Photochemistry and Photobiology, 82(5): 1279-1284 (2006).
21. Li C et al, “Using a priori structural information from magnetic resonance imaging to investigate the feasibility of prostate diffuse optical tomography and spectroscopy: a simulation study,” Medical Physics, 34(1): 266-274 (2007).
22. Piao D, et al., “Near-infrared optical tomography: endoscopic imaging approach,” Proc. of the SPIE, 6431: 6431-02 (2007).
23. Padhani AR, et al., “Angiogenesis imaging in the management of prostate cancer,” Nature Clinical Practice, Urology, 2(12): 596-607 (2005). Review.
24. Zhu Q, et al, “Optical tomography with ultrasound localization for breast cancer diagnosis and treatment monitoring,” Surg. Onco. Clin. North Amer., 16(2): 307-321 (2007). Review.
25. Zhu Q, et al., “Benign versus malignant breast masses: optical differentiation with US-guided optical imaging reconstruction,” Radiology, 237 (1): 57-66 (2005).
26. Zhu Q, et al., “Utilizing optical tomography with ultrasound localization to image heterogeneous hemoglobin distribution in large breast cancers,” Neoplasia, 7(3): 263-270 (2005).
27. Holboke MJ, et al., “Three-dimensional diffuse optical mammography with ultrasound localization in a human subject,” J. Biomed. Opt., 5(2): 237-247 (2000).
28. Zhu Q,, et al., “Ultrasound-guided optical tomographic imaging of malignant and benign breast lesions,” Neoplasia, 5(5), 379–388 (2003);
29. Jiang Z, Piao D, Xu G, Ritchey JW, Holyoak GR, Bartels KE, Bunting CF, Slobodov G, Krasinski JS, “Trans-rectal ultrasound-coupled near-infrared optical tomography of the prostate Part II: Experimental demonstration,” Optics Express, Vol. 16, Iss. 22, pp. 17505–17520 (2008).
30. Rivera, B, Ahrar, K, Kanasniemi, M, et al, Canine Transmissible Venereal Tumor: A Large Animal Transplantable Tumor Model, Comp. Med., 55(4):335-343 (2005).
31. Anidjar, M, Villette, JM, Devauchelle, P, et al, In Vivo Model Mimicking Natural History of Dog Prostate Cancer Using DPC-1, a New Canine Prostate Cell Line, The Prostate, 46:2-10 (2001)
32. Fork, MA, Escobar, H, Soller, J, Establishing an In Vivo Model of Canine Prostate Carcinoma Using the New Cell Line CT 1258, BMC Cancer, 8:240, 15AUG(2008)
33. Piao D, Jiang Z, Bartels KE, Holyoak GR, Ritchey JW, Xu G, Bunting CF, Slobodov G, “In vivo trans-rectal ultrasound-coupled near-infrared optical tomography of intact normal canine prostate,” J. Innovative Optical Health Sciences, 2(3): 215-225 (2009).
34. Jiang Z, Holyoak GR, Bartels KE, Ritchey JW, Xu G, Bunting CF, Slobodov G, Piao D, “In vivo trans-rectal ultrasound coupled near-infrared optical tomography of a transmissible venereal tumor model in the canine pelvic canal,” J. Biomed. Opt. Letters, 14(3): 030506 (2009).
35. Jiang Z, Piao D, Holyoak GR, Ritchey JW, Bartels KE, Slobodov G, Bunting CF, Krasinski JS, “Trans-rectal ultrasound-coupled spectral optical tomography of total hemoglobin

concentration enhances assessment of the laterality and progression of a transmissible venereal tumor in canine prostate," Urology, 77(1): 237-42 (2011).
36. Jiang Z, Holyoak GR, Ritchey JW, Bartels KE, Rock K, Ownby CL, Slobodov G, Bunting CF, Piao D, "Different optical spectral characteristics in a necrotic transmissible venereal tumor and a cystic lesion in the same canine prostate observed by triple-band transrectal optical tomography under transrectal ultrasound guidance," SPIE International Symposium on Biomedical Optics, Jan. 22-27, 2011, San Francisco, CA. Paper 7892-24.

Feasibility of rapid near-infrared diffuse optical tomography by swept-spectral-encoded sequential light delivery

Guan Xu, Daqing Piao,*
School of Electrical and Computer Engineering, Oklahoma State University, Stillwater, OK, USA, 74078
Daqing.piao@okstate.edu

ABSTRACT

We investigate the feasibility of rapid near infrared diffuse optical tomography by spectrally-encoded sequential light delivery using wavelength-swept source. The wavelength-swept light beam is dispersed by a spectrometer to form "swept-spectral-encoded" light beam which scans linearly across the exit window of the spectrometer and delivers sequential illumination to linearly bundled source fibers. A data acquisition rate of 0.5 frame/second is reached from a 4mW 830nm swept-source and a 20mm-diameter transverse-imaging intra-lumenal applicator with 7 source and 8 detector channels placed in a liquid phantom. Higher rate of data acquisition is achievable with more powerful wavelength-swept source or in a smaller imaging regime. This new configuration is intended for being implemented in rapid fluorescence diffuse optical tomography by enabling sequential source-channel-encoded excitations of fluorophores.

Keywords: biomedical optics, tomography, medical imaging

1. INTRODUCTION

Near-infrared optical tomography has demonstrated high functional contrast in imaging applications for cancer detection [1-3] and assessing disorders of extremity [4-5], functional status of brain [6] and hemodynamics of small animals [7-8]. Compared to other imaging modalities such as X-ray computed tomography and ultrasound imaging, NIR optical tomography usually is implemented at relatively slower rate of data acquisition due to the need of source-encoding in differentiating the origin of light diffused through scattering-dominant biological tissue.

Several methods have been used for source-decoding in NIR optical tomography. One of the method being implemented widely is by mechanically switching the light illumination among the source channels [1-2, 5], which ensures the sole-source illumination necessary to maximizing the signal dynamic range, but it could have potential issues such as reliability and repeatability if high-speed is desired. Frequency-multiplexing can in principle render real-time data acquisition, but the cross-channel suppression of weak signal by stronger signal is difficult to overcome. Recent studies have implemented digitally-controlled source-channeling coupled with frequency-multiplexing [9] to reach higher speed in DOT data acquisition.

One configuration of source-encoding in DOT leading to the first video-rate DOT imaging acquisition has been based upon the principle of spectral-encoding of the source channels. The spectral-encoded DOT has been demonstrated by discrete-spectral-encoding using multiple laser diodes (LD) with individual temperature and current control for each LD [10], and spread-spectral-encoding using a broad-band light source [11]. The configuration using multiple LDs demonstrates higher acquisition rate (approximately 30Hz), but the inter-channel frequency-hopping and uncorrelated channel-wise intensity fluctuation limit the accuracy of the system in resolving smaller dynamic changes of tissue optical properties. The configuration using a broad-band light-source for spread-spectral-encoding overcomes the issues of cross-channel frequency-hopping and intensity fluctuation because of the use of different spectral components from the same source, which resulted in much higher sensitivity to dynamic changes of tissue optical properties. One drawback of spread-spectral-encoding using single broadband light source is the potential overlapping of the spectrum of each source-channel with the neighboring source-channel when using imperfect optics [11], which may require deconvolution to remove the effect of spectral and intensity cross-talk.

Wavelength-swept light source is widely utilized in spectral-domain optical coherent tomography [12], and is recently implemented for spectrally-encoded detection of surface profile of a subject [13]. This work demonstrates the use of wavelength-swept light source in DOT applications by a configuration of swept-spectral-encoded sequential light delivery. Some advantages of this approach over previously demonstrated source-sequencing techniques are

Optical Tomography and Spectroscopy of Tissue IX,
Edited by Bruce J. Tromberg, Arjun G. Yodh, Mamoru Tamura, Eva M. Sevick-Muraca, Robert R. Alfano,
Proc. of SPIE Vol. 7896, 78961W · © 2011 SPIE · CCC code: 1605-7422/11/$18 · doi: 10.1117/12.874349

demonstrated, by phantom experiments, as: 1) the spectrally and temporally encoded source channeling facilitates rapid non-mechanical switching; 2) sole-source illumination eliminatess the cross-coupling problem seen in spectral-encoding based on a broadband light source. Temporally independent source illumination can also couple with CCD gain control to allow adaptive CCD exposure to the range of signals specific to one source-channel.

This paper also applied a recently developed analytic model of endoscopic imaging geometry to the reconstruction process. It is well-known that most of the system calibration in DOT image reconstruction involves fitting the numerically solved light propagation to the experimental measurements. Most of contemporary studies seem to utilize the analytical model for planar semi-infinite photon diffusion [14] during the first step of data calibration. Such approach demonstrates its robustness in many frequency domain systems, in which the gradients of the measurement components are considered in the analytical fitting process. However, as to the continuous wave systems, since multiple optical properties cannot be strictly decoupled by merely utilizing the attenuation of light signal intensity, the accurate fitting to the absolute intensity is also required. Therefore, more accurate analytical model specified for the applicator geometry of each imaging system are desired, which, for the particular case of this study targeted for endo-rectal imaging using a circular cylindrical applicator a new model is derived and validated by Zhang et al[15]. This geometry-specific analytic model is expected to provide more accurate estimation of the optical properties of homogeneous medium during the initial step of data calibration as it improves the data-model match.

This paper discusses the structure of the system and presents experimental results based on phantom for assessment of system performance as well as demonstrating the use of geometry-specific analytic model for data calibration.

2. METHODS AND MATERIALS

2.1 Principles of swept-spectral-encoding

The principle of swept-spectral-encoding is illustrated in Fig. 1(a). As is shown, the source light with swepting wavelengths is dispersed by spectrometer #1 and sequentially coupled to the fiber channels linearly arranged at the output plane of spectrometer #1. Therefore, the sweeping source light appears similar to a broadband light, and a spectral-encoding of the source illumination similar to the one reported in [11] is achieved. At the detection end, spectrometer #2 decodes the light signals for CCD acquisition, as is shown in Fig.1 (b) (with 1200 groove/mm grating) and Fig.1(c) (with 600 groove/mm grating).

The detection signals corresponding to each source channel are acquired independently in time, *per se*, by spectral as well as temporal encoding represented by equ(1):

$$\mathbf{Loop}(t=1{:}m)\mathbf{:}\ \{\boldsymbol{D}(t)_{n\times 1}=(\boldsymbol{W}_{m\times n})^{T}\times\boldsymbol{T}(t)_{m\times m}\times\boldsymbol{Spec}_{m\times m}\times\boldsymbol{S}_{m\times 1}\} \quad (1)$$

where t is the time-slot of wavelength-sweeping controlled by PC; $\boldsymbol{D}(t)$ is the detector signal at time t, $\boldsymbol{W}$ is the weight matrix or sensitivity matrix of the imaging geometry; $\boldsymbol{T}(t)$ is the diagonal matrix representing the time-encoding, $\boldsymbol{T}(t)(i,i)=\begin{cases}1 & i=t\\ 0 & i\neq t\end{cases}$; $\boldsymbol{Spec}=\begin{bmatrix}\lambda_1 & \lambda_2 & \cdots & \lambda_3\\ \lambda_1 & \lambda_2 & \cdots & \lambda_3\\ \vdots & \vdots & \ddots & \vdots\\ \lambda_1 & \lambda_2 & \cdots & \lambda_3\end{bmatrix}$ is the spectral encoding matrix.

The synchronization mechanism between the swept source and CCD is shown in Fig.1(a). Controlled by the PC, the source -sweeping stops when the maximum source power is coupled to designated source channel, followed by the CCD exposure. Therefore, for one imaging cycle, image acquisition number equals to the number of source channels (illustrated in Fig.1(d)). Such design facilities the temporal separation of the light spots at the detection end despite the spatial overlapping.

2.2 System configuration

A Superlum wavelength-swept light source is used. It has 4mW output power and scans in the range of 838nm to 858nm at an increment of 0.05nm. The wavelength stability is ±2.5pm per five hours. The source light is pigtailed by a single-mode fiber and collimated by an aspherical lens of 4.51mm focal length. The collimated source light is coupled to a spectrometer #1 (SpectroPro 500i, Princeton Instrument). The 1200 groove per mm grating and 500mm path length of the spectrometer expands the 20nm spectral range of the source light to approximately 15mm span at the output plane of the spectrometer, where linearly arranged 1mm-diameter fibers deliver the sequentially coupled light to the imaging

applicator. At the detection end, a CCD camera (ACTON PIXIS 512) with 12.3mm×12.3mm imaging area and a 300mm focal-length spectrometer #2 (SpectroPro 2300i, Princeton Instrument) is integrated for signal acquisition. The source-sweeping and CCD data acquisition are synchronized by a data acquisition card (National Instrument) using LabView (National Instrument). Limited by the source power, a minimum exposure time of 170ms is required and an extra 150ms CCD readout time is necessary before sweeping the source light to the next source channel. Therefore for each channel approximately 320ms is required, which is equivalent to 0.5 frames per second. This frame rate can be improved with stronger source.

The experiment validation utilizes a two dimensional circular endoscopic imaging geometry previously studied by our group[16]. As is shown in Fig. 2, the 8 source channels and 8 detector channels are evenly interspersed around the perimeter of the 20mm-diameter probe. However, one source channel (marked in Fig.2(c)) is discarded because of its significantly low coupling efficiency due to fabrication defect. The actual experimental system is shown in Fig.3.

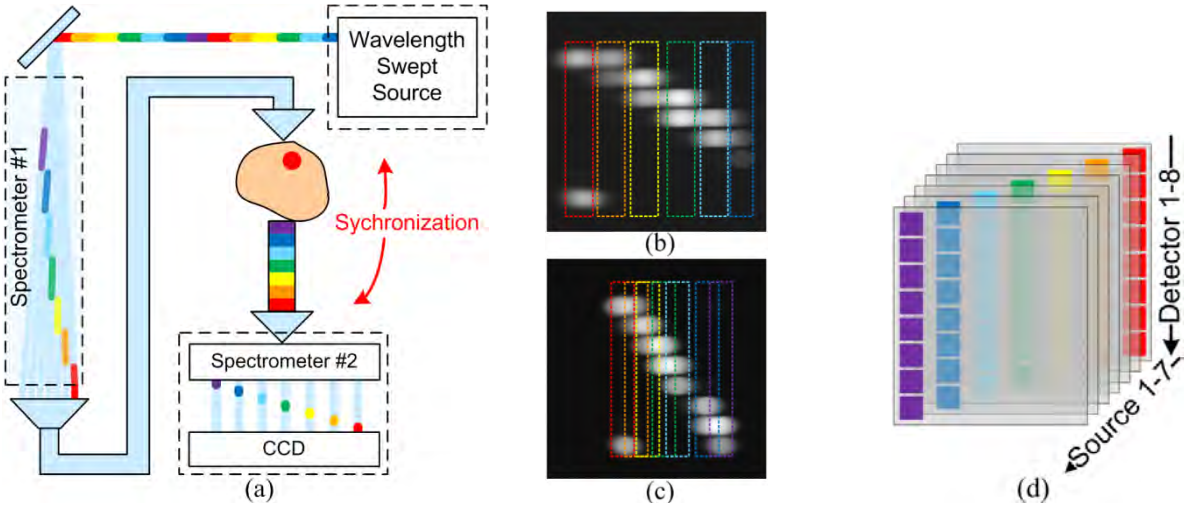

Fig. 1 Principle of swept-spectral-encoding
(a) System schematics (b) Spectral encoding mode 1200 grooves / mm
(c) Spectral encoding mode 600 grooves / mm (d) Spectral and temporal encoding mode

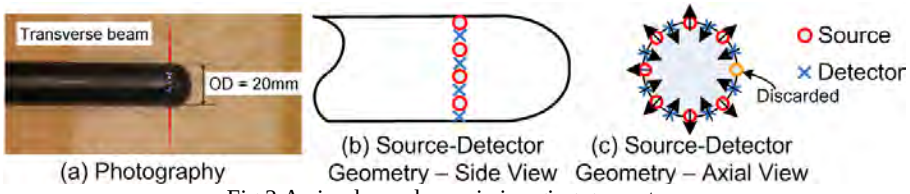

Fig.2 A circular endoscopic imaging geometry

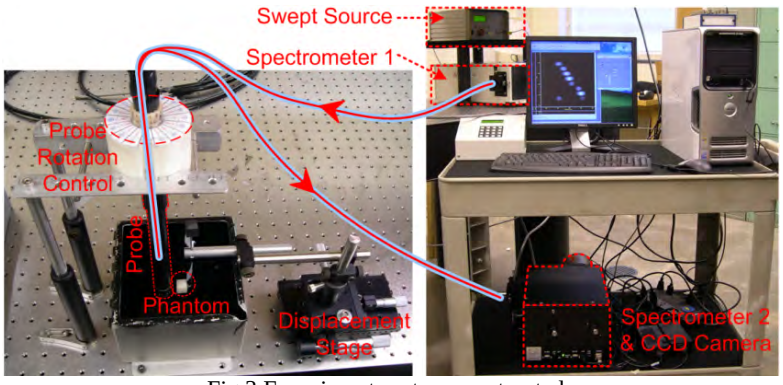

Fig.3 Experiment system constructed

2.3 Examples of signals

With the exposure time and source power described above, the signal intensity detected by the 16-bit CCD camera is in the range of maximum 60000 to minimum 1000. The background count of CCD is approximately 700. One set of images are captured by submerging the probe into 1% intralipid solution. Figure 4(a) shows the images acquired after subtracting dark background. By averaging through the region of interest in the center part of the light spots as seen in Fig.4(b), the extracted data points are used for calibration and reconstruction (Fig.4(c)).

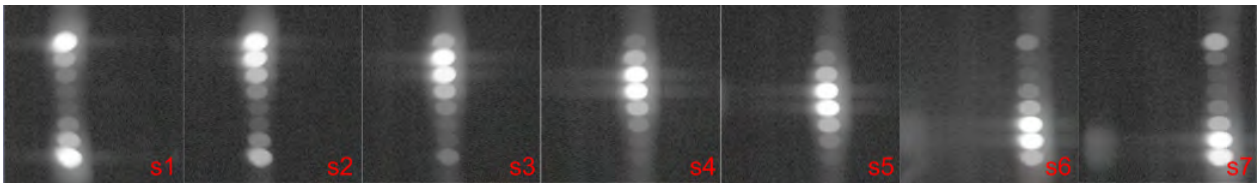

(a) Data spots captured by CCD camera

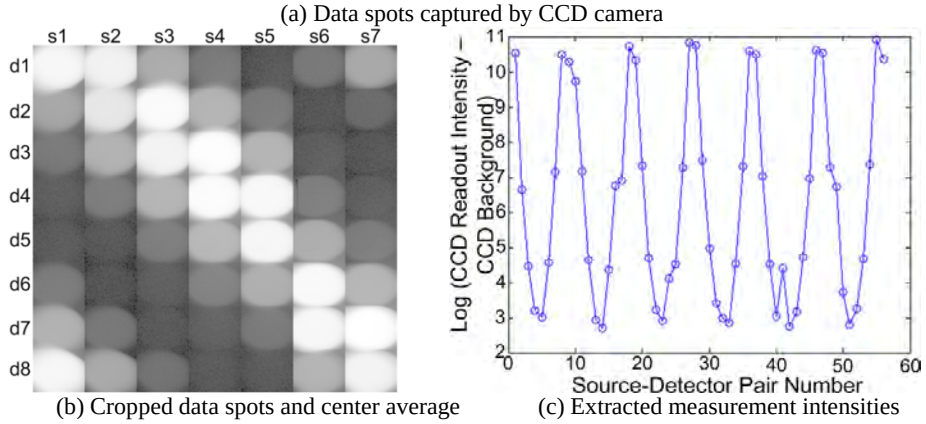

(b) Cropped data spots and center average (c) Extracted measurement intensities

Fig. 4 Raw data processing

2.4 Calibration methods

In this study, the calibration algorithm searches for the offset values between the experimental data, analytical and numerical model in log scale. A bulk 1% intralipid solution with μ_a= 0.0023 mm^{-1} and μ_s'=1mm^{-1} is used in the calibration process. The calibration involves 2 stages: 1) estimation of the optical properties of homogeneous medium with analytical model and; 2) offset between the experimental data and the numerical model.

For the analytical fitting process, many studies use the linear model for semi-infinite homogenous turbid media [14]. However, such model does not accurately represent the light transportation pattern in cylindrical geometry, as is shown in Fig.7(a). Zhang et al [15] have proposed and validated an analytical model for such cylindrical geometry:

$$\Psi = \frac{S}{2\pi^2 D}\int_0^\infty dk\left\{\sum_{m=0}^{\infty}\varepsilon_m I_m\left(k_{eff}R_0\right)K_m\left[k_{eff}\left(R_0+R_a\right)\right]\left\langle 1-\frac{K_m\left(k_{eff}R_0\right)}{I_m\left(k_{eff}R_0\right)}\frac{I_m\left[k_{eff}\left(R_0-R_b\right)\right]}{K_m\left[k_{eff}\left(R_0-R_b\right)\right]}\right\rangle\cos\left[m\left(\varphi-\varphi'\right)\right]\right\} \qquad (2)$$

Where S is the source intensity; D=1/(3(μ_a+μ_s')) is diffusion coefficient; R_0 is the probe radius; R_a=1/ μ_s',is the scattering distance of the imaged medium; ε_m is 2 for m≠0 and 1 for m=0; I_m and K_m are the modified Bessel function of the first and second kind; k_{eff} is the attenuation coefficient; φ and φ' are the angular coordinate of detector and source, respectively. For the evaluation of the model, since the equation consists of infinite series, approximation is applied by cutting off the series at the 60th terms. Such approximation is computationally efficient but introduces discontinuity in the function evaluation, which the commonly used gradient based fitting algorithms does not allow. A heuristic random optimization approach [17] is thus integrated into the analytical calibration process. Since 1) the absolute values are fitted; 2) the duration of the analytical model evaluation increases proportionally to the number of sampling points; and 3) calibration process bases on homogeneous medium, the analytical model is evaluated only at the source-detector separations found in the experimental geometry as shown in Fig. 2. Therefore, only 4 data points are evaluated in each round fitting iteration.

It can be observed that S value is independent of the integral in Equ (2), and in log scale, it is an amplitude bias of the analytical model, which is found to bring in large projection error in the fitting process and might destabilize the searching for other parameters. To suppress such instability, the algorithm first minimizes the log(S) value and starts the overall parametric search, then the result (Fig.5(a) red curve) of which is assigned to the FEM model as the initial guess of the second calibration stage. It can be clearly observed from Fig 7(a) that the algorithm recognized the larger light intensity attenuation in a nonlinear pattern by correcting the μ_a initial guess of 0.005mm^{-1} to 0.0029 mm^{-1}.

The numerical fitting stage integrates finite element method on the ring geometry shown in Fig.2(c), which is disretized to a finite element mesh with 872 nodes and 1620 elements uniformly distributed in the imaging domain. The numerical calibration also starts from searching for the optimum amplitude bias, which is subsequently optimized along with the optical properties of numerical model. And the final model fitting converged to the optical properties of μ_a=0.0023mm^{-1} and μ_s'=0.8982, of which the μ_s' part could be more accurate if analytical model and measurements in frequency domain are available.

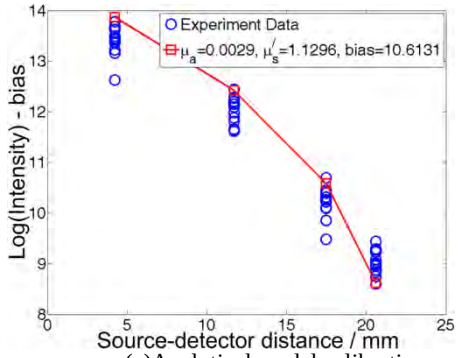

(a)Analytical model calibration

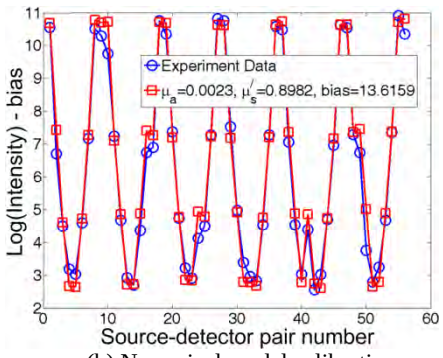

(b) Numerical model calibration

Fig. 5 Data calibration

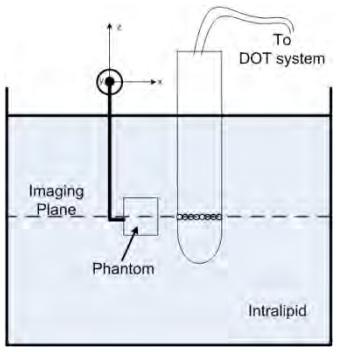

Fig 6 Experiment setup

3. RESULTS ON PHANTOM IMAGING

The performance of this system configuration is evaluated by using liquid and solid phantoms.

3.1 Experiments setup

As is shown in Fig.3 and Fig.6(a), the axial-imaging cylindrical probe was submerged in a tank of 10×10×5 cubic-inch that filled with intralipid. The inner wall of the tank was painted black. The solid phantom targets to be imaged were fabricated from a black plastic material, which was to mimic infinite absorption contrast of the target inclusion over the background intralipid solution, and a phantom with μ_a= 0.0056 mm^{-1} and μ_s'=1.03 mm^{-1}. The sizes of the cubic-shape solid phantom ranged from 5mm to 15 mm. The targets were aligned initially at the imaging plane of the probe and displaced by translation or rotation stages to positions of examination.

3.2 Experiment results

Four sets of experiments were conducted to examine system sensitivity on 1) the size, (Fig. 7(a)); 2) the radial position (Fig. 8(a)); 3) the azimuthal direction (Fig. 9(a)) of the inclusion; and 4) multiple inclusions (Fig. 10(a)).

The first set of results is derived from experiments with target with varied sizes and materials embedded at side-to-probe distance of 5mm. As is expected and demonstrated by the results in Fig.9(b), the reconstructed absorption properties of black plastic materials obviously exceed the solid tissue phantoms. For all five target sizes, the targets made with black plastic were recovered at the same azimuthal location although the recovered volumes decrease with respect to those of the actual targets. For the targets fabricated from solid tissue phantom, the recovered absorption contrast fades as the target volume decreases and background artifacts overwhelms the targets with volumes less than 10×10×10 mm^3.

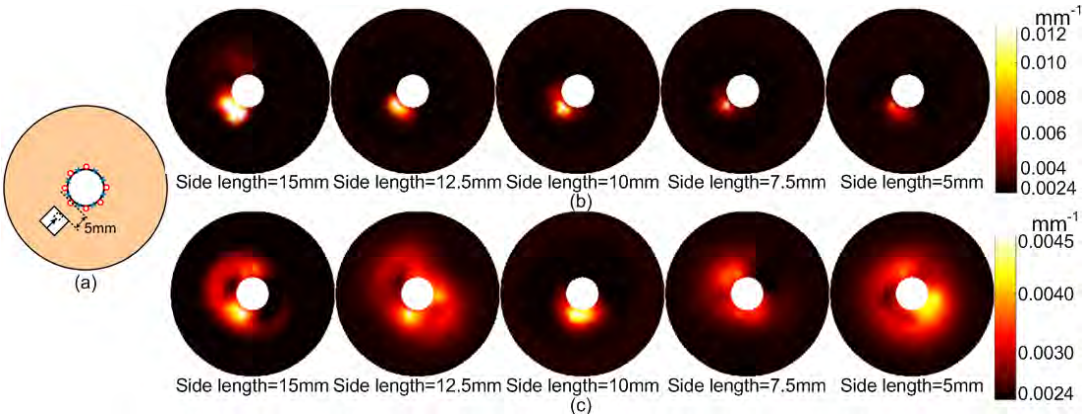

Fig. 7 Experiment on system resolution on inclusion size. (a) Target location and size illustration (b) Reconstruction results on black plastic targets. (c) Reconstruction results on synthetic phantom targets

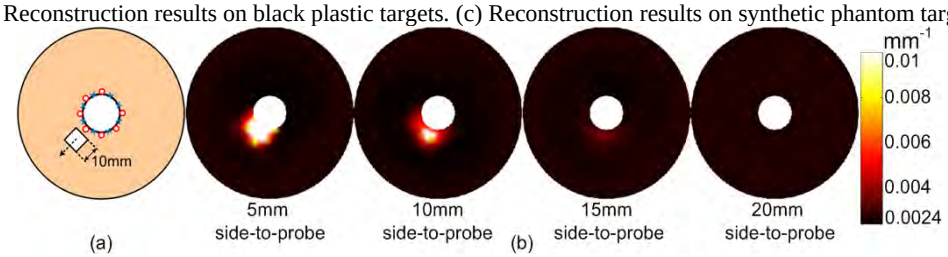

Fig. 8 Experiment on system sensitivity along radial direction
(a) Target location and size illustration (b) Reconstruction results on $10\times10\times10mm^3$ black plastic targets embed at 3mm depth

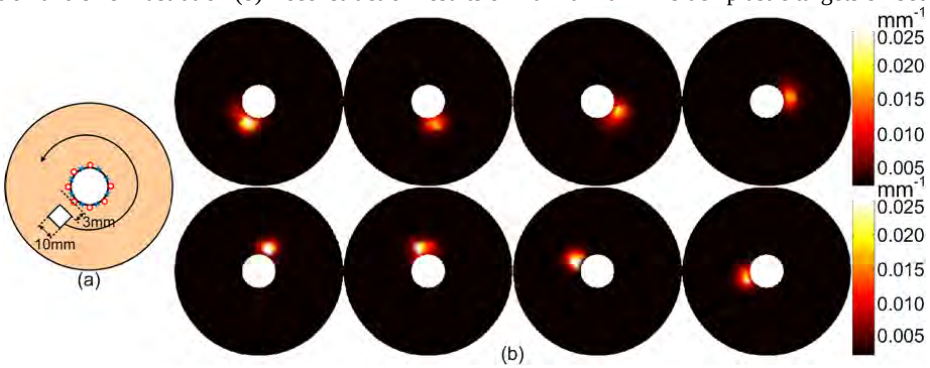

Fig. 9 Experiment on system sensitivity along azimuthal direction
(a) Target location and size illustration (b) Reconstruction results on $10\times10\times10mm^3$ black plastic targets

The second set of experiments examines the system sensitivity along the radial direction. A $10\times10\times10$ mm^3 cube fabricated from black plastic was imaged at side-to-probe distances from 0mm to 15mm (equivalent center depths of 5mm to 20mm). Fig.8(b) shows the recovered absorption distributions. Results indicated that 1) the target could not be recovered beyond 15mm depth; 2) the recovered volume decreased as the depth increased; and 3) similar to experiment shown in Fig.9. Further, all of the target centers were recovered closer to the probe due to the non-uniform sensitivity of the imaging geometry in the radial direction.

However, it is expected that the reconstruction sensitivity should be uniform along the azimuthal direction of the probe in the image plane. Therefore, in the third set of experiments, the $10\times10\times10$ mm^3 black target is embedded 3mm away from the probe and rotated along the azimuthal direction, as is shown in Fig.9(a). Approximately constant target volume and optical properties can be observed in Fig.9(b) as foreseen, and since the targets locate at the most sensitive region of the imaging geometry, all the target depths are desirably recovered.

The fourth set of experiments examine the system capacity of recovering multiple inclusions. Two $7.5\times7.5\times7.5$ mm^3 black cubes were used in this case in consideration that the dimensions of larger targets limit their center separation and smaller targets are more difficult to be resolved. The two targets are both embedded 2mm away from the probe (center

depth = 2+7.5/2= 5.75 mm) at different angular positions with respect to the probe, as is shown in the Fig.10(a). Reconstruction results are shown in Fig.10(b).

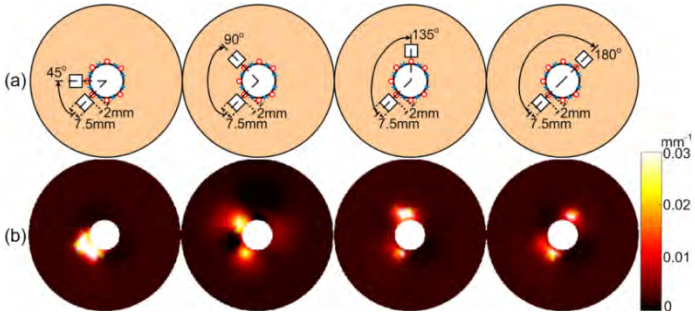

Fig. 10 Experiment on recovery of multiple targets
(a) Target location and size illustration (b) Reconstruction results

It can be observed that for the predetermined depth, angular separation beyond 90 degrees can be recovered accurately by the system. However, at 45 degree separation, the system cannot resolve the gap between the targets and indicates a large light absorbing blob at the correct location. Such result is expected, because the minimum angular separation of two neighboring sources is 45 degree and the signal intensity received by the detector between the two source channels could be substantially reduced by the two targets located in the dominant light propagation path tracing to the detector channel. Hence for the limited source-detector pair in this imaging geometry, reconstruction algorithm recognize the two sources and one detector channel within the 45 degree range as being blocked by one large light absorbing blob.

4. DISCUSSIONS AND FURTURE WORKS

The four sets of experimental evaluations demonstrated the feasibility of DOT using this novel configuration of swept-spectral encoding. It seems that the in most experiments conducted above the rectangular contour of the phantoms was recovered. The ability of such profile-identification may relate to the element geometries of the finite element mesh used in reconstruction algorithm, but similar level of profile-identification was not seen in previous studies wherein identical mesh structures were used [16]. The most likely explanation of such gain in the imaging outcome is that the temporal and spectral encoding of the source light fundamentally reduces the source channel crosstalk between source channels, improving the imaging resolution of a predetermined imaging geometry.

Moreover, with the 4mW source power and 170ms exposure time, targets with center depth up to 20mm (Fig.8) can be detected. Although the previously reported broad-band spectral encoding system possesses higher total power level (20mW), the average power coupled to each source channel could be on the same level as or even lower than the system constructed in this study. The 0.5 frame per second data requisition rate can be readily improved given a stronger wavelength-swept source.

The calibration of the homogenous data with analytical model is proved to be effective and accurate in the circular geometries, although fitting experimental data to the approximately evaluated model could be computationally intensive and impracticable with the gradient based algorithms. The more exhaustive heuristic random optimization approach [17] is implemented in two stages to the calibration process, which is validated by the experimental results. However, the analytical model utilized in this study is limited to steady-state measurement, which is known less accurate in estimating the scattering properties. More accurate calibration may need measurements and models in frequency domain.

Prospectively, this configuration of swept-spectral-encoded sequential source illumination can be extended for rapid fluorescence optical tomography[18], as the source channel for the fluorescence excitation could be differentiated by the temporal encoding of the source channels out of sequential spectral-encoding. Works are planned to validate the use the configuration for fluorescence optical tomography.

5. CONCLUSION

A novel near infrared tomography configuration based on wavelength swept light source is constructed. A data acquisition rate of 0.5 frame per second is demonstrated, which can be improved with more powerful light source. This

source-sequencing configuration based on wavelength-swept source can be extended to rapid fluorescence optical tomography.

ACKNOWLEDGEMENT

This work has been supported in part by the Prostate Cancer Research Program of the U.S. Army Medical Research Acquisition Activity (USAMRAA) through grants #W81XWH-07-1-0247 and #W81XWH-10-1-0836.

REFERENCES

[1] Pogue, B., et al., "Instrumentation and design of a frequency-domaindiffuse optical tomography imager for breast cancer detection," Opt. Express 1(13), 391-403(1997)
[2] Huang, M., et al., "Simultaneous Reconstruction of Absorption and Scattering Maps with Ultrasound Localization: Feasibility Study Using Transmission Geometry," Appl. Opt. 42(19), 4102-4114(2003)
[3] Jiang, Z., et al., "Trans-rectal ultrasound-coupled near-infrared optical tomography of the prostate, Part II: Experimental demonstration," Opt. Express 16(22), 17505-17520(2008)
[4] Andreas, H.H. and et al., "Sagittal laser optical tomography for imaging of rheumatoid finger joints," Physics in Medicine and Biology 49(7),1147(2004)
[5] Yuan, Z., et al., "Tomographic x-ray--guided three-dimensional diffuse optical tomography of osteoarthritis in the finger joints," Journal of Biomedical Optics 13(4), 044006-10(2008)
[6] Boas, D.A. and A.M. Dale, "Simulation study of magnetic resonance imaging-guided cortically constrained diffuse optical tomography of human brain function," Appl. Opt. 44(10), 1957-1968(2005)
[7] Pogue, B.W. and K.D. Paulsen, "High-resolution near-infrared tomographic imaging simulations of the rat cranium by use of a priori magnetic resonance imaging structural information," Opt. Lett. 23(21), 1716-1718(1998)
[8] Hielscher, A.H., "Optical tomographic imaging of small animals," Current Opinion in Biotechnology 16(1), 79-88(2005)
[9] White, B.R. and J.P. Culver, "Phase-encoded retinotopy as an evaluation of diffuse optical neuroimaging," NeuroImage 49(1), 568-577(2010)
[10] Piao, D., et al., "Video-rate near-infrared optical tomography using spectrally encoded parallel light delivery," Opt. Lett. 30(19), 2593-2595(2005)
[11] Piao, D. and B.W. Pogue, "Rapid near-infrared diffuse tomography for hemodynamic imaging using a low-coherence wideband light source," Journal of Biomedical Optics 12(1), 014016-12(2007)
[12] Choma, M., et al., "Sensitivity advantage of swept source and Fourier domain optical coherence tomography," Opt. Express 11(18), 2183-2189(2003)
[13] Strupler, M., et al., "Rapid spectrally encoded fluorescence imaging using a wavelength-swept source," Opt. Lett. 35(11), 1737-1739(2010)
[14] Fantini, S., et al., "Quantitative determination of the absorption spectra of chromophores in strongly scattering media: a light-emitting-diode based technique," Appl. Opt. 33(22), 5204-5213(1994)
[15] Zhang, A., et al., "Photon diffusion in a homogeneous medium bounded externally or internally by an infinitely long circular cylindrical applicator. I. Steady-state theory," J. Opt. Soc. Am. A 27(3), p. 648-662(2010)
[16] Piao, D., et al. "Near-infrared optical tomography: endoscopic imaging approach," Proceeding SPIE 6431, 643103-1(2007)
[17] Li, J. and R. Russell Rhinehart, "Heuristic random optimization," Computers & Chemical Engineering 22(3), 427-444(1998)
[18] Lee, J. and E.M. Sevick-Muraca, "Three-dimensional fluorescence enhanced optical tomography using referenced frequency-domain photon migration measurements at emission and excitation wavelengths," J. Opt. Soc. Am. A 19(4), 759-771(2002)

Transrectal Optical Tomography With Ultrasound Guidance: A Novel Hybrid Imaging Technology Toward Prostate Cancer Detection and Characterization

Daqing (Daching) Piao,[1*] Zhen Jiang,[2] Kenneth E. Bartels,[1] G. Reed Holyoak,[1] Jerry W. Ritchey,[1] Guan Xu,[1] Charles F. Bunting,[1] Gennady Slobodov,[3]

1. Oklahoma State University, Stillwater, Oklahoma, USA; 2. Washington University in St. Louis, St. Louis, Missouri, USA; 3. University of Oklahoma Health Sciences Center, Oklahoma City, Oklahoma, USA.

1. Background

- Needle-based core-biopsy of the prostate relies heavily upon transrectal ultrasound (TRUS). However, TRUS is not a reliable imaging modality for performing focal-biopsy of the prostate cancer.
- ***A novel hybrid imaging technology was explored to address this deficiency in prostate cancer detection***.
- This new technology is based on near-infrared (NIR) optical tomography that is coupled to TRUS.

2. Objectives

- To evaluate if TRUS-coupled optical tomography can non-invasively distinguish malignant from benign lesions in the dog prostate.

3. Methods and Materials

- ***A transrectal NIR array was coupled with an ALOKA bi-plane TRUS transducer to perform concurrent NIR and ultrasound imaging of the prostate*** [1, 2].
- The optical tomography system has evolved from single band (840 nm for NIR absorption) to dual-band (785 nm and 830 nm for [HbT]) and to triple-band (705 nm, 785 nm, and 808 nm for [HbT] and StO2).
- ***A canine model of prostate cancer has also been developed by using canine transmissible venereal tumor (TVT) cells***.
- The technology has been evaluated on one normal dog and three dogs with implanted TVT tumors.

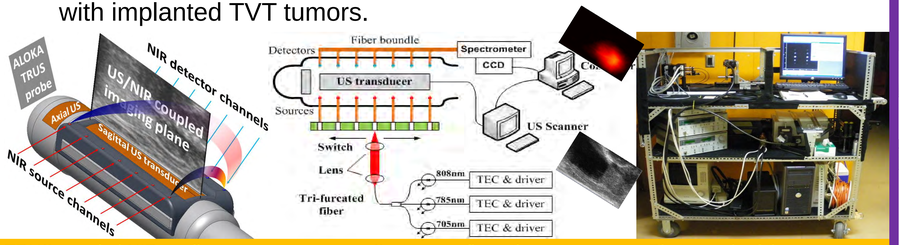

TRUS-coupled NIR applicator. System configuration. Photograph of the system

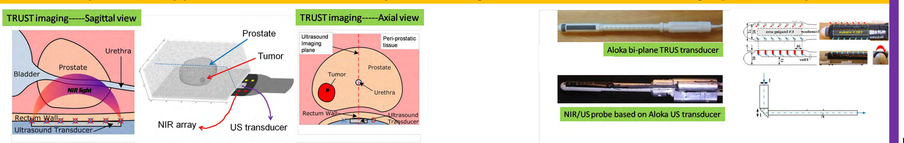

Sagittal imaging geometry. Axial imaging geometry. Development of TRUS/NIR applicator

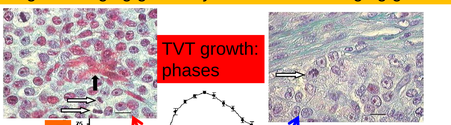

TVT growth: phases

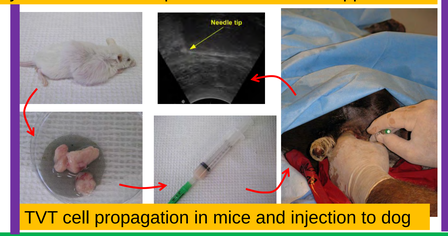

TVT cell propagation in mice and injection to dog

4. Results

Dog #1

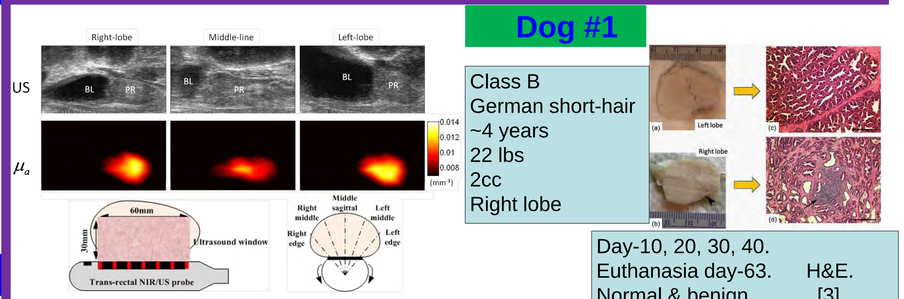

Class B
German short-hair
~4 years
22 lbs
2cc
Right lobe

Day-10, 20, 30, 40.
Euthanasia day-63. H&E.
Normal & benign. [3]

Dog #2

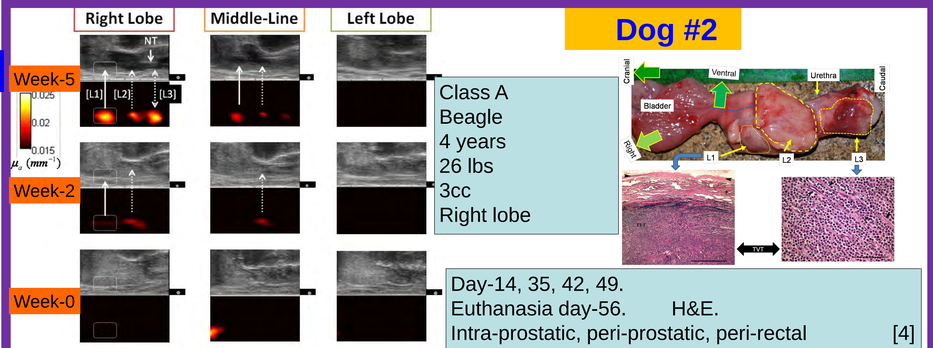

Class A
Beagle
4 years
26 lbs
3cc
Right lobe

Day-14, 35, 42, 49.
Euthanasia day-56. H&E.
Intra-prostatic, peri-prostatic, peri-rectal [4]

Dog #3

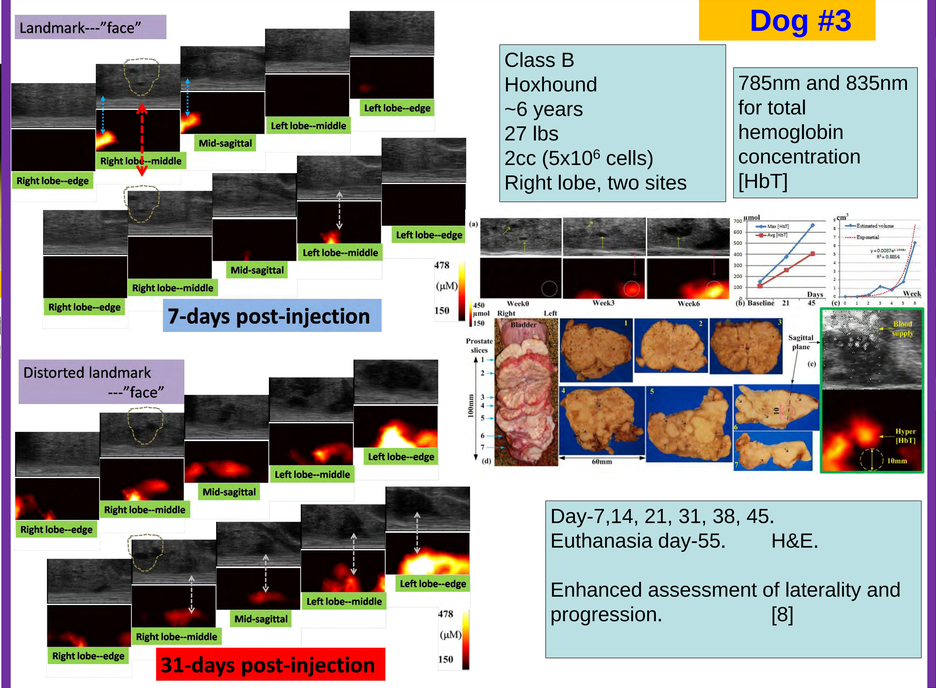

Class B
Hoxhound
~6 years
27 lbs
2cc (5x10⁶ cells)
Right lobe, two sites

785nm and 835nm for total hemoglobin concentration [HbT]

Day-7,14, 21, 31, 38, 45.
Euthanasia day-55. H&E.

Enhanced assessment of laterality and progression. [8]

Dog #4

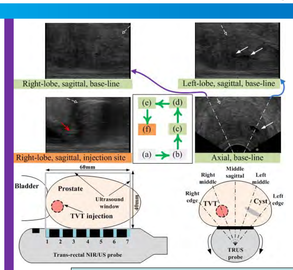

Class B
Hoxhound
~7 years
27 lbs
2cc (5x10⁶ cells)
Right lobe

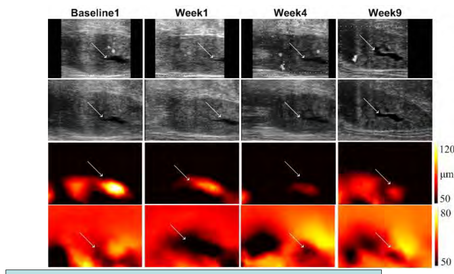

Day-7,14, 21, 28, 35, 42, 49, 56, 63
Euthanasia day-63. H&E, TEM.

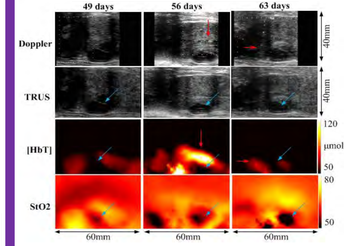

TVT, necrotic

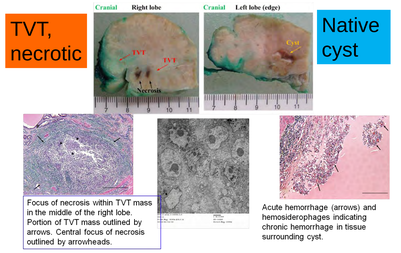

Native cyst

5. Conclusions

TRUS-coupled optical tomography is able to non-invasively image malignant prostatic lesions.

6. Impact

This novel hybrid imaging technology will have notable impact on patient care because the technology has the potential to:

- guide focal-biopsy,
- monitor focal-therapy,
- predict treatment response,
- perform intra-surgical imaging evaluation.

Acknowledgement

This work was supported by the U.S. Army Medical Research and Materiel Command under W81XWH-07-1-0247.

Peer-Reviewed Journal Publications Resulted From This Research

[01]. Xu G et al, ***Optics Express***, 16(22): 17484–17504 (2008)
[02]. Jiang Z et al, ***Optics Express***, 16(22): 17505–17520 (2008)
[03]. Piao D et al, ***J. Innovative Opt. Health Sci.***, 2(3): 215-225 (2009).
[04]. Jiang Z et al, ***J. Biomed. Opt. Letters***, 14(3): 030506 (2009).
[05]. Zhang A et al, ***J. Opt. Soc. Amer., A***, 27(3): 648-662 (2010).
[06]. Xu G et al, ***Applied Optics***, 49(16): 3059-3070 (2010).
[07]. Piao D et al, ***IEEE J. Sel. Top. Quant. Electron.***, 16(4): 715-729 (2010). "Biophotonics 2" Special Issue, invited paper.
[08]. Jiang Z et al, ***Urology,*** 77(1): 237-42 (2011).
[09]. Zhang A et al, ***J. Opt. Soc. Amer., A***, 28(2): 66-75 (2011).
[xx]. Jiang Z et al, ***Urology,*** under preparation

Challenges of and new configurations toward fluorescence diffuse optical tomography of zinc-specific biomarker for prostate cancer detection

Guan Xu and Daqing Piao

School of Electrical and Computer Engineering, Oklahoma State University, Stillwater, OK, 74078-5032

1. Introduction

Zinc is well established as a metabolic bio-marker for prostate cancer, with the concentration of it in prostatic tissue reducing at least an order of magnitude accompanying the cancer [1]. A zinc-tagged fluorescence reagent can therefore be used to detect prostate cancer with high specificity.

However, opposite to the conventional scenario of usually higher uptake of tumor-specific fluorophore within the lesion (Fig.1(a)), the zinc-specific fluorophore is expected to have higher uptake in normal tissue, which produces a "***negative-contrast***" in fluorescence detection (Fig.1(b)).

Two issues arise from such case of "***reverse-uptake***" fluorescence imaging. One is that the strong ambient fluorescence emission challenges detecting of the weak emission from the lesion [2]. Novel approach of differential detection is currently under investigation to tackle this problem.

The other is to allow rapid, steady-state fluorescence excitation and detection for testing the feasibility of such "reverse-uptake" fluorescence emission using our existing ***diffuse optical tomography (DOT***) system. This study proposes implementing a ***wavelength-swept light source*** for rapid steady-state ***fluorescence diffuse optical tomography (FDOT).***

2. Source-encoding configurations in DOT

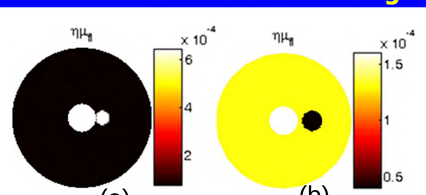

(a) (b)

Fig.1 Fluorescence contrast
(a) Positive contrast (b) Negative contrast

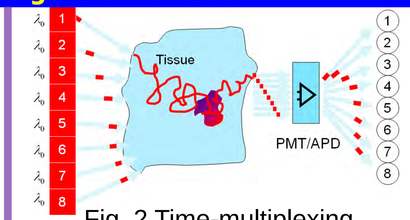

Fig. 2 Time-multiplexing applicable to fluorescence detection

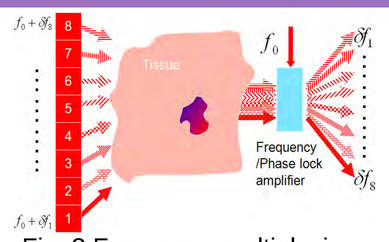

Fig. 3 Frequency-multiplexing applicable to fluorescence detection

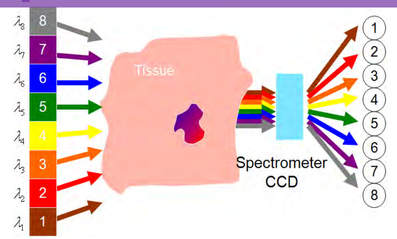

Fig. 4 Spectral-encoding [2, 3] NOT applicable to fluorescence detection.

Spectral-encoding in Fig. 4 allows rapid steady-state DOT, but does not apply to steady-state FDOT due to the need of decoding the source of excitation.

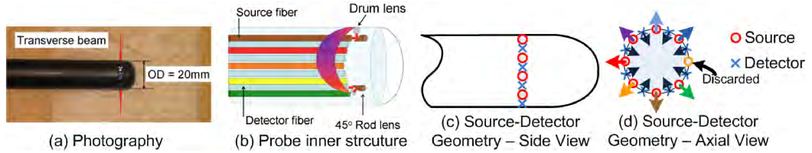

(a) Photography (b) Probe inner strcuture (c) Source-Detector Geometry – Side View (d) Source-Detector Geometry – Axial View

Fig.5 Probe structure and imaging geometry

3. Swept-spectral source-encoding in DOT that is applicable to FDOT

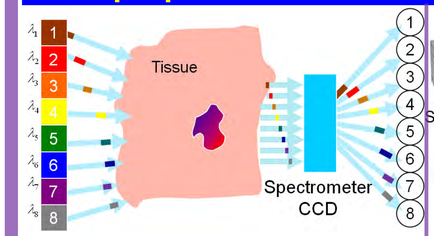

Fig. 6 Swept-spectral-multiplexing applicable to fluorescence detection

Source-sweeping and CCD data acquisition are synchronized. One image is taken for each source channel.

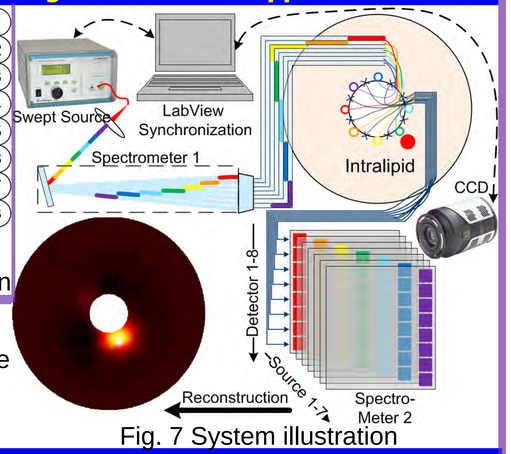

Fig. 7 System illustration

4. Instrumentation

With exposure time of 170ms, the raw data are taken from 1% intralipid (μ_a=0.0023mm^{-1},μ_s'=1mm^{-1}). With data transferring time of 150ms per CCD exposure. The total acquisition time for all 7 sources is ~2s.

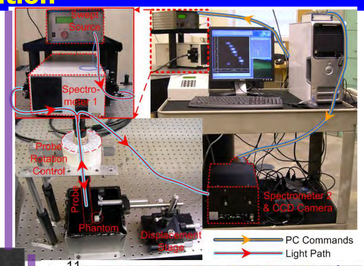

Fig. 8 Experimental system

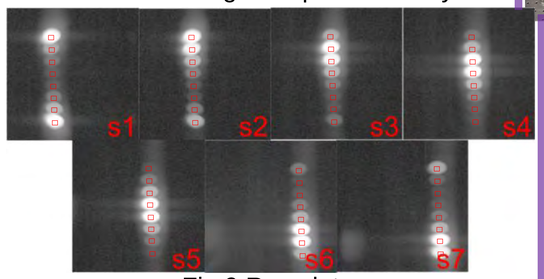

Fig.9 Raw data

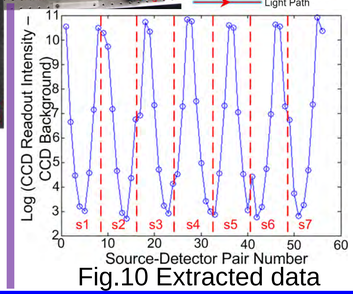

Fig.10 Extracted data

5. Phantom Results

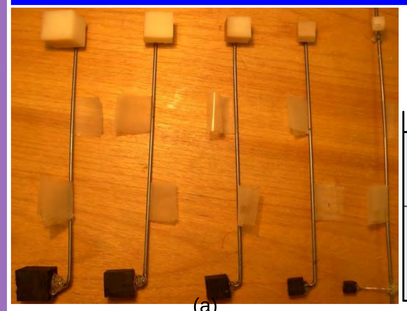

(a)

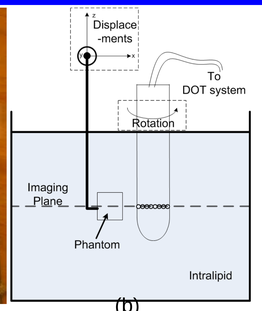

(b)

Fig.11 Experiment setup

Two sets of targets: tissue phantom (μ_a= 0.0056 mm^{-1}, μ_s' = 1.03mm^{-1}) and black plastic (μ_a approx.=Inf).

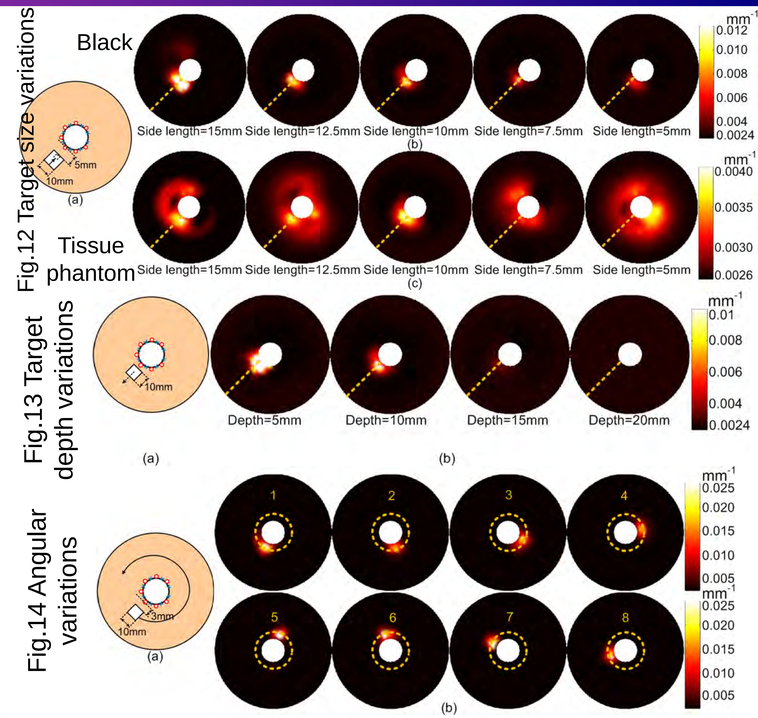

6. Discussion & Conclusion

- Swept-spectral source-encoding is demonstrated for DOT. The encoding mechanism is applicable to FDOT.
- Phantom targets are recovered, with improvements needed in estimations of the target volume and depth.

7. Future Works

- Improving target recovery by optimizing reconstruction algorithm
- Examining DOT of negative targets.
- Extending to FDOT to demonstrate detection of "reverse-uptake" fluorophore concentrations.

Acknowledgement

This work has been supported by the Prostate Cancer Research Program of the U.S. Army Medical Research Acquisition Activity (USAMRAA) through grants #W81XWH-07-1-0247 and #W81XWH-10-1-0836.

References

[1] Zaichick VY et al, "Zinc concentration in human prostatic fluid: normal, chronic prostatitis, adenoma and cancer," Int. Urol. Nephrol. 28, 687-694 (1996).

[2] Piao D, et al., "Video-rate near-infrared optical tomography using spectrally encoded parallel light delivery," Opt. Lett. 30(19), 2593-2595(2005)

[3] Piao D et al, "Endoscopic, rapid near-infrared optical tomography," Opt. Lett. 31(19), 2876-2878(2006).